# Characterisation of Micro-Mechanisms of Cleavage Fracture in SA738Gr.B Steel

By

Weichen Xu

A thesis submitted to the Faculty of Engineering of the University of Birmingham for the degree of Doctor of Philosophy.

School of Metallurgy and Materials.

The University of Birmingham.

Edgbaston,

Birmingham.

B15 2TT.

January 2024.

# Acknowledgements

I want to thank my main supervisor, Prof. P. Bowen, for his encouragement and help with the whole project. Thanks for the opportunity of sponsorship. Also, thank Baosteel Corporation for their financial support with this project and the material provided.

I want to thank my second supervisor Dr Milorad Novovic for his advice on the testing procedures and many valuable discussions.

I want to thank Mr David Price and Dr Tim Doel for their help and advice in testing machines and their kind reminder of safety measures.

Thanks to all members of the Fatigue and Fracture Group. I will miss the time during those years with much of your kindness and help with discussions.

This study is carried out with the help of Zesong Li's work on microscopic fracture stress tests and Charpy specimen SEM fractography images, Huize Fan's help on Charpy specimen optical fractography images, and Yunpeng Gao's help on doing tensile and fracture toughness tests together. Your help is appreciated.

Special thanks to my fiancée Roujia, visiting me from the other side of the globe during the tough time of the pandemic. Your love is giving me the strength to continue my path in science.

# Contents

# Synopsis:

Cleavage fracture is a significant concern for structural materials, as it can lead to sudden and unexpected failures that can have serious consequences, such as the failure of bridges, buildings, or other critical infrastructure. As a fracture mode, cleavage occurs in materials that exhibit brittleness and low toughness under various conditions. The investigation of cleavage fracture micro-mechanisms in conventional steel types has been a subject of research for several decades. Long ago, scientists began locating and predicting the precise cleavage initiation site. In the past, significant emphasis was placed on cleavage nucleation induced by carbides or inclusions and cleavage propagation caused by the fracture of cleavage facets.

This study specifically focusing on the initiation phase. The result of this investigation provides some potential advances for the understanding of the cleavage fracture mechanism by not only identifying cleavage initiation sites with precision but also analysing their role in the fracture process, particularly highlighting the influence of inclusions containing calcium, aluminium, and titanium.

This thesis delves into the cleavage fracture mechanisms in SA738Gr.B steel, a type of high-strength low-alloy (HSLA) steel that is commonly used in the construction of reactor containment vessels. The investigation employed in this study involved two heat treatment processes for SA738Gr.B steel. This included heating the steel to 900°C for two hours, followed by rapid water quenching, and then tempering it at 630°C for three hours (HT1). - Additionally, following HT1, a simulated post-weld heat treatment (PWHT) was conducted, incorporating an additional tempering stage at 620°C for 15 hours, designated as HT2. This HT2 process was introduced and compared with the original HT1 to evaluate the possibility of exempting the need for PWHT. Optical microscopy and scanning electron microscopy (SEM) were employed to conduct an in-depth examination of the steel's microstructure. These techniques facilitated a detailed analysis of the size distribution and chemical composition of inclusions on both polished and the fracture surfaces.

The microstructural characterization of the steel revealed a predominantly granular bainitic structure with carbides precipitated along the grain boundaries. To understand the material's behaviour under stress, Charpy impact tests were conducted across a range of temperatures to determine the ductile to brittle transition temperatures. The transition temperatures, -91 °C for HT1 and -87 °C for HT1, were instrumental in setting the parameters for the subsequent fracture toughness and microscopic cleavage fracture stress tests on pre-cracked and notched specimens.

Tensile tests were then carried out and the material mechanical properties such as yield stress, ultimate tensile strength, and work hardening exponent were measured and calculated at various temperatures. The fracture toughness was measured following ASTM 1820-17 standards and involved using 1T compact tension specimens under the temperature -120 °C, -100 °C and -80 °C. With the obtained test result combined with fracture distance measured from the specimen surface, local cleavage fracture stresses were obtained using McMeeking's FEM analysis results. Additionally, microscopic cleavage fracture stress tests were conducted using a four-point bending method. These tests, performed at temperatures ranging from -196 °C to -160 °C, allowed for a detailed evaluation of the local stress distribution and the cleavage fracture stress, using the Griffith-Owen finite element analysis result.

A significant challenge highlighted in this thesis is the identification of cleavage initiation sites in 55 mm thick compact tension specimens. This required a nuanced understanding of both 'global' and 'local' initiation sites. A comprehensive analysis of 26 sharp-cracked specimens provided detailed insights into the size, location, and chemical composition of the cleavage initiators. One of the critical outcomes of this research is the establishment of a correlation between macroscopic parameters, notably the J-integral, and microscopic local parameters such as fracture distance $X_0$. This correlation is crucial in understanding how microscopic changes in the steel's structure can influence its overall mechanical behaviour and fracture resistance.

The comprehensive results obtained from the two distinct test-piece geometries blunt-notched and sharp-cracked specimens provide robust validation for the

hypothesis that cleavage fracture is governed by a tensile stress-controlled failure criterion and that the cleavage fracture stress is independent of temperature. These principles, critical for interpreting the cleavage behaviour in ferritic steels, have been widely recognized for decades. This study, however, potentially advances the field by offering explicit experimental evidence to substantiate these foundational principles. Furthermore, this research enhances the comprehension of the micro-mechanisms driving cleavage fracture in bainitic steels, especially emphasizing the role of specific inclusions in initiating these fractures.

In conclusion, this thesis contributes significantly to the field of microscopic analysis of the cleavage mechanism in steel, especially in the context of limited data availability and the challenges associated with traditional testing methodologies for characterizing cleavage initiation. The detailed analysis of fracture surfaces, the identification of cleavage initiation sites, and the establishment of relationships between various mechanical parameters not only provide valuable insights for future research but also have practical implications for the design and application of ferritic steels across various industrial sectors.

# Chapter One – Introduction

The investigated material is used in a specially designed nuclear power plant, CAP1000, original designed by Westinghouse AP1000 [1], a notable feature of this type of power plant is its large containment shielding, which significantly enhances safety during operation [2]. The reactor implements passive safety systems to provide core cooling during accidents, which are essential for cooling in small break sizes [3].

In order to fulfil the requirement of the application, one specially designed grade of steel, SA738 Gr.B steel is used. It is a type of high-strength low-alloy (HSLA) steel that is commonly used in the construction of reactor containment vessels. This steel grade is specified by the ASME (American Society of Mechanical Engineers) standards and is designed to withstand extreme temperatures and pressures. In this study, the SA738Gr.B steel is provided by China Baowu Steel Group Corporation Limited.

The SA738Gr.B steel is a low carbon steel with alloying elements such as silicon, manganese, and molybdenum. In ASME standards, SA738B have alloying elements such as manganese, nickel, and small amount of copper, chromium and niobium to enhance its strength and toughness. The microstructure and chemistry are designed for high yield strength, improved toughness and good weldability[4]. SA738Gr.B steel has excellent low temperature tensile properties, Charpy-V notch impact performance, and fracture toughness, making it suitable for use in nuclear containment vessels [5]. It also exhibits good tensile properties and mechanical performance at elevated temperatures, affirming its suitability for nuclear power station purposes [6].

This study involves a simulated post weld heat treatment (PWHT), aimed at - investigating the possibility of exempting the post-weld heat treatment process if the material mechanical behaviour after the simulated post-weld heat treatment is not largely changed. Thus, the comparison results could provide important guidance for the sponsoring steel company

The objective of this research is to precisely describe the cleavage initiation process mechanically, through the mechanical testing, with the testing result parameters $J$, $CTOD$, $K_Q$ and $K_{JC}$ to describe the material condition at the onset of cleavage process, and relate these parameters with the measured microstructural features such as inclusions found at the initiation site, facet diameter for the first cleavage facet. With the help of the existing finite element analysis results from Griffith-Owen and McMeeking, the stress-strain profile ahead of the notch-tip or crack-tip was found and hence the local cleavage fracture stress was estimated. It was found in this material, the cleavage initiation is still controlled by local tensile stress, where the cleavage initiation site is beyond and close to the peak tensile stress location predicted by the finite element analysis.

This thesis contains nine chapters.

Chapter two reviews the possible features that can appear in bainitic steel. Carbides, inclusions and martensite-austenite constituents are considered as they are often present in steel matrix as particles which can act as an essential feature in the cleavage process and influence material toughness significantly. Then, the high-angle grain boundaries, alloying elements, and tempering effect are reviewed.

Chapter Three reviews work conducted by previous researchers on cleavage fracture mechanisms in bainitic steels. Macro fracture mechanics include the development of stress intensity factor K, COD, and J-integral. Their limitations are discussed. Micro-mechanisms of brittle fracture from Stroh's theory, Cottrell's theory and Smith's theory are introduced, then the RKR model and statistical approach, among which the Beremin model and its modifications are illustrated. Lastly, cleavage mechanisms in bainitic steel are discussed where inclusions, martensite-austenite constituents and bainitic facets in the cleavage process are reviewed from existing literature.

Chapter Four describes the material and the experimental methods used in this project. Tensile test, Charpy impact test, microscopic fracture stress test and fracture toughness test procedures are described in detail.

Chapter Five gives the general description of the material characterization results and Charpy tests results and discussions. The chemical composition and size distribution of inclusions are studied.

Chapter Six documents tensile tests results which are used together with the sharp-cracked specimen and blunt-notched specimen toughness test results to investigate the cleavage fracture micro-mechanisms.

In terms of HT1 and HT2 heat treatment conditions, very similar results are obtained for all tests and no differences are observed in microstructures. Hence, in discussion of HT1 and HT2 in blunt-notched specimens and sharp-cracked specimens, they are treated as one population, retaining HT1 and HT2 for identification of specimens only.

Chapter Seven summarizes the main conclusions and suggests ideas for further work.

# Chapter Two – A Review of Prior Research on Low Carbon Bainitic Steel Microstructure

## 2.1 Evolution of Microstructural Features in Bainitic Steel and Its Effect on Cleavage Fracture

### 2.1.1 Bainite

The formation of the plate-like microstructure known as bainite in steels occurs at temperatures ranging from 125 to 550 °C. When austenite is cooled below a temperature at which it can no longer be thermodynamically stable to form ferrite or cementite, this is one of the products that has the potential to form. In the initial description of the microstructure, Davenport and Bain [7] mentioned that it had a look that was comparable to that of tempered martensite. However, when viewed using a light microscope, the microstructure of bainite looks darker than that of un-tempered martensite. This is due to the fact that bainite has a greater number of substructures. In terms of its thermodynamic properties, bainite is not a phase but rather an acicular microstructure that can develop in some steels. Cementite and dislocation-rich ferrite are the two most prevalent components of bainite, which has a fine non-lamellar structure. Because of this, the process is far more difficult than it would otherwise be. The development of bainite can be slowed down by the majority of alloying elements. Other than these, carbon is the most efficient substance in preventing the development of bainite.

Typically, the cementite in bainite is not arranged in parallel arrays or plates. Nonetheless, it exists as a collection of irregularly arranged precipitates within small dislocation-rich ferrite grains.

Temperature effects:

In the event that the temperature is sufficiently elevated, it has been observed that carbon shall expeditiously diffuse away from the newly formed ferrite and subsequently congregate to form carbides within the carbon-enriched residual austenite that is situated between the ferritic plates. This will result in the absence of carbides on the ferritic plates. Carbon will diffuse more slowly at lower temperatures, and it is possible that it will precipitate before it can escape the bainitic ferrite.

Time effects:

During the sufficient time required for bainitic transformation, the carbon atoms in bainitic ferrite are partitioned into the surrounding austenite. Consequently, this type of bainitic ferrite has a minimal carbon content. High carbon content is present in retained austenite. As the transformation time of bainite increases, tensile strength decreases, but elongation and impact toughness increase. This is due to the reduction of martensite and the enhancement of retained austenite's stability. When the austenite is sufficiently stable after being undercooled, the bainite transformation will cease.

Upper Bainite:

In upper bainite, ferrite is distributed as fine plates, with a thickness of around $0.2\ \mu m$ and a length of about $10\ \mu m$. [8] Clusters of these plates are regarded as sheaves.

The hard carbide clusters precipitated in the bainitic ferrite package boundaries (upper bainite) can act as stress raisers and lower crack propagation energy.

Lower Bainite:

Lower bainite is very similar to upper bainite in microstructure and crystallographic sense. The most significant difference comes from the distribution of carbides. In lower bainite, carbides precipitate inside ferrite. Also, carbides in lower bainite are extremely fine, with a thickness of a few nanometres and a length of around $500\ nm$. [8]

Granular Bainite:

In granular bainite, the sheaves are relatively coarse, and the block appearance of blocks of bainite and austenite microstructure gives it a granular morphology. Besides upper and lower bainite, granular bainite is often used in industrial-made steels by continuous cooling. [9] Continuous cooling provides the condition for extensive transformation; for granular bainite formation, the carbon concentration needs to be low enough to limit austenite or carbide existing between sub-unites of bainite.

The martensite-austenite constituents are a distinguishing feature of granular bainite. Carbon is partitioned from bainitic ferrite and stabilizes the remaining austenite. Thus, the final microstructure consists of both retained austenite and a small amount of high-carbon martensite.[9]

### 2.1.2 Martensite

Lath martensite has a low-carbon content and plate martensite has a high-carbon content. Lath martensite exhibits superior toughness and ductility, albeit with lower strength, while plate martensite displays higher strength in comparison to lath martensite, albeit with a tendency towards brittleness.

In the context of a specific alloy composition, it has been observed that an increase in the carbon concentration of the austenitic phase leads to a reduction in both the martensite start temperature $M_s$ and the martensite finish temperature $M_f$ . This phenomenon is associated with an incomplete transformation of austenite to martensite. The quantity of retained austenite present is dependent on the amount of carbon solubilized in the parent austenite phase and the degree of suppression of the $M_s$ and $M_f$ temperatures.

The incorporation of lower bainite into the mixed lower bainite-martensite microstructures has resulted in a notable enhancement of Charpy V-notch impact energy, the reduction in area, and the elongation. The observed phenomenon can be ascribed to the significantly enhanced ductility and impact toughness of the lower bainitic microstructure in contrast to martensitic microstructures. [10]

### 2.1.3 Retained Austenite

Retained austenite is usually found in martensite microstructures where $M_f$ (martensite finish temperature) is lower than room temperature. This is often the case when the martensite transformation is incomplete. There are generally two morphologies of retained austenite: filmy (needle-like) austenite, usually located between martensite laths, and blocky (island-like) austenite which is surrounded by ferrite.

The retained austenite acts as a plasticity enhancer in quenching and partition steels. It appears that the RA grains located at lath boundaries manifest a greater propensity to enhance the toughness of the microstructure. This is attributed to the superior mechanical stability of the film-like RA grains, which exhibit a relatively higher number density owing to their finer size. [11] The retained austenite microstructure, being richer in carbon, has more dislocations than the original austenite.

Historically, retained austenite was undesirable for a number of reasons; first, being soft in nature, it was a concern to be widely avoided in tool steels. Second, retained austenite has the ability to transform into martensite or bainite; the displacive transformation will lead to an increase in volume. This austenite transformation is generally unwanted as the volume change is likely to produce internal stress around it, which may lead to cracks.

However, with the advancement of the steel-making process and the development of new steel grades, researchers found the possibilities of utilising this phase. Firstly, being ductile in nature, it is possible to improve toughness if a small amount (such as 10% in the microstructure) of this austenite phase is well distributed Secondly, with a sufficient quantity in the microstructure, the retained austenite can balance the transformation contraction during heating and the expansion during cooling.

The attainment of full (100%) austenite retention at ambient temperature in plain carbon steels through the implementation of rapid cooling measures is an

unattainable objective. The presence of austenite at ambient temperature is a phenomenon that can be achieved through the incorporation of certain alloying elements, such as nickel or manganese. This is evident in austenitic stainless steels and Hadfield manganese steels.

Although complete retention of austenite is difficult, all austenite former elements can help retain austenite where carbon, manganese and nickel are used in structure steels such as high nickel-based pressure vessel steels. In addition, silicon is widely used in austenite-containing steels due to its excellent ability to restrict carbide precipitation during isothermal holding, which can be used to achieve stabilisation of austenite by carbon partition. Aluminium in austenite-containing steel has a very similar effect to silicon; even better, aluminium showed good abilities in preventing Si/Mn oxide formation and forming an inhibition layer on the steel surface.

Applications based on the nature of austenite:

1. Transformation-induced plasticity (TRIP) steels

TRIP stands for transformation-induced plasticity; when external stress or strain is applied to the microstructure, retained austenite transforms into martensite, associated with a volume expansion and leads to additional plasticity. Being usually as Dual-Phase steels (austenite/martensite), TRIP steel has different varieties depending on the content of the austenite phase, from only minor austenite present (TRIP assisted steel) to fully austenitic. The microstructural features of TRIP steels are characterised by a considerable amount of retained austenite, owing to their high silicon and carbon contents. The microstructural constituents of the material typically comprise a primary matrix of ferrite, within which the retained austenite is commonly embedded with a minimum of 5% amount; other hard phases can also present in the microstructure with varying amounts.

2. Quench & Partitioning (QP) steels:

QP steel is designed for higher tensile strength and elongation based on similar chemical compositions as TRIP steel. The main idea is to hold the steel above the $M_s$ temperature, using carbon partitioning to stabilise the austenite phase.

The fabrication process includes a quenching and a partitioning stage, where in the quenching stage, fully austenitised steels are quenched to a temperature between the $M_s$ and $M_f$ temperatures for a desired martensite volume fraction, then the partition process is carried at a slightly higher temperature than $M_s$ for carbon depletion from martensite into austenite (for austenite to have a lower $M_s$ temperature) to achieve thermally stable austenite after final quenching to room temperature. Finally leading to a microstructure of tempered martensite and retained austenite for desired mechanical properties.

3. Twinning-induced plasticity (TWIP) steels

With TWIP steel's high manganese content (17-24%), bainitic and martensitic phase transformations are postponed during cooling, leaving TWIP steel fully austenitic at room temperature. TWIP Stands for twinning-induced plasticity; twinning as the principal mechanism for deformation refines the microstructure and leads to a high strain hardening rate (n). With the potential of the twinning process, the n value can be as high as 0.4 at an engineering strain of 30% and remains constant until it reaches 50% total elongation. Furthermore, tensile strength can be higher than 1000 MPa.

### 2.1.4 Martensite-Austenite Constituents

The toughness of the steel is sometimes influenced by many 'local brittle zones', such as a mixture of un-tempered martensite and retained austenite, also known as 'martensite-austenite constituents'. [12]

M-A constituents are widely found in welded joints, where the welding heat process facilities the formation of M-A constituents. The presence of the M-A

phase in many situations is regarded as the critical factor that has a detrimental effect on steel toughness. [12][13]

The formation process of M-A constituents in granular bainite has been explained in detail [14]; as a sub-unit grain forms, it rejects its excess carbon into the residual austenite. The carbon content in the retained austenite gradually builds-up until a critical point where the austenite-bainite transformation is thermodynamically unfavourable. Once the high carbon content of austenite is cooled down to a temperature below $M_s$ (martensite transformation start temperature), it will transform into martensite; if there is still untransformed austenite, it will form into martensite-austenite constituents. The amount of martensite formation is controlled by the critical carbon content of the residual austenite when the bainite transformation stops.

It has been reported that the amount of M-A constituents is the dominant factor that affects material toughness [13], [15]–[18], with other researchers suggesting that volume fraction also takes good responsibility for the detrimental effects to the toughness. [19]–[21]

The low toughness of ICCG HAZ is reported to be caused by coarse necklacing of M-A constituents ( $\geq 2$ μm) along prior austenite grain ( $\sim 70$μm) boundaries.[17]. The same author suggested that there is a critical size of M-A constituents, 1.3-2 μm, above which the impact toughness could deteriorate. It was also reported that a size below 1 μm M-A constituents could deflect the crack propagation, which improved toughness.[18]

Following extensive research on M-A constituents, not only does the size of M-A influence toughness, but the shape of M-A also takes good responsibility for lowering the toughness. It was reported [19] that the elongated shape of M-A constituents leads to the lowest toughness among other 'round dot shapes' and massive M-A constituents.

In addition to this, the reduction of toughness in steels is reported not only to be controlled by M-A size, distribution and morphology. It also has relations to the surrounding matrix. [20] The initiation of cracks has been observed to occur predominantly at the interface separating the coarse M-A constituents and the matrix. [21][22]

Recently, Yeong-Do et al. [23] have done extensive work on M-A, and they classified martensite-austenite constituents into three typical types based on their internal arrangement of substructures. (Shown in Figure 2-1) namely, Type 1 is blocky retained austenite surrounded by martensite. Type 2 is lath-like martensite and retained austenite forming for a layered substructure and slender morphology. Type 3 is a random arrangement of martensite and retained austenite.

### 2.1.5 Cementite and Carbide

With a carbon concentration of 6.67 wt%, $Fe_3C$ has high hardness but low ductility and toughness, making it a brittle phase. It appears white under an optical microscope, difficult to be etched by nitric acid etching solutions. As an interstitial compound, it is divided into primary cementite, solidifying directly from the liquid phase; secondary cementite, precipitating from austenite; and tertiary cementite, precipitating from ferrite when carbon is saturated. Secondary cementite is often found within a grain or at grain boundaries; it can appear in flaky, lamellar, net-like, and needle-like structures. After heat treatment, such as tempering and annealing, the cementite might change into a more spheroid or granular shape.

### 2.1.6 Acicular Ferrite

The term 'acicular' denotes a geometrical configuration that is reminiscent of a needle, yet it is widely acknowledged that acicular ferrite exhibits a three-dimensional structure that is characterised by slender plates. [24]

Acicular ferrite is often found in low-alloy steel after cooling from the austenite phase. Because of its good toughness, acicular ferrite is essential in commercial usage. However, research into the microstructure mechanisms suggests that acicular ferrite is only intragranular nucleated bainite. [25]

The steel microstructure that develops into bainite, or acicular ferrite, is strongly dependent on prior austenite grain size and inclusion density. With a larger austenite grain size and higher inclusion density, acicular ferrite is more likely to be nucleated than bainite ferrite, as the bainite sheaves or Widmanstatten ferrite development is stopped by hard impingement between plates nucleated independently at adjacent sites.[24]

With high strength and toughness, acicular ferrite is desirable in low-temperature applications. The acicular ferrite is about 0.1-0.2 um thick and around 1-2 um long because of its interlocking arrangement of plates oriented in diverse directions within the prior austenite grain. (High angle grain boundary misorientation). These two behaviours give a difficult path for crack propagation, as a crack is deflected more times than in other microstructures. In cleavage fracture, the crack deflection in acicular ferrite is superior to bainite and martensite. In bainite and martensite microstructures, adjacent plates are parallel and in similar crystallographic orientations, and the cleavage crack can propagate through the packet undeflected [25]

### 2.1.7 High Angle Grain Boundary (HAGB)

High-angle grain boundary considers the misorientation angles between neighbouring grains. The criterion for HAGB is divided; most researchers take a misorientation angle above 15°, and a few others prefer 45°. In this thesis, it is considered that misorientation has to be above 15° for a HAGB. When the angle is less than 15°, the boundary is considered as a LAGB (low angle grain boundary)

In the context of microstructural analysis, it has been observed that a given prior austenite grain exhibits a discernible partitioning into multiple packets, each of which is characterised by a uniform habit plane. Further examination reveals that these packets are themselves subdivided into distinct blocks, each

of which comprises a collection of laths that share a common crystallographic orientation. When packet, block and lath boundaries are considered, the lath boundaries are LAGBs, while the packet and block boundaries are HAGBs. [26]

Effective grain size is a crucial term in fracture mechanics; it was believed to be packet size in martensitic and bainitic steels. [27] Since the development of EBSD, the effective grain size is considered as both packet and block boundaries. Both packet and block boundaries are considered as HAGBs. The nomenclature "effective grain size" designates the mean size of grains that are encompassed by high-angle grain boundaries (HAGBs) [28]. It is generally considered that increasing the HAGBs and then reducing the effective grain size of steel microstructures can increase their toughness. Cleavage fracture in low carbon steel usually takes place along {100} planes. [29] More recently, Morris et al. suggested that the angle between {100} crystallographic planes is more relevant than overall misorientation angle (OMA) during cleavage fracture for determining the effective grain size. [30]

However, toughness is influenced by many factors, not only from grain boundaries but also the 'soft phase' like retained austenite or 'hard phase' such as carbides. There is still much research focusing on how HAGBs influence toughness. Several experimental results have demonstrated that the presence of high-angle grain boundaries (HAGBs) can effectively impede the occurrence of cleavage fracture, either by halting the propagation of cleavage cracks or by altering their directions. One of the principal directions of the HAGB study is to what extent it influences toughness, finding it as a decisive factor or as additional resistance to the crack.

The grain boundary energy $E$ is directly affected by misorientation angle, Read and Shockley described it in the 1950s: [31]

$$E = E_0\theta\ (A - ln\theta) \qquad \text{Equation (2-1)}$$

Where $E_0$ and $A$ are constants. When the grain boundary misorientation angle $\theta$ is larger than 15°, $E$ tends to be a certain value due to the variation of

electrostatic energy induced by the screening effect. The grain boundaries markedly deflect the brittle cracks with misorientation angles greater than 15°.

This equation from Read and Shockley showed the fundamental mechanism of how high-angle grain boundaries can hinder microcrack propagation and the possibility of helping microcrack deflection.

The cleavage fracture strength $\sigma$ is expressed by a modified Griffith equation: [32]

$$\sigma = (1.4EW)^{1/2} \cdot d^{-1/2} \qquad \text{Equation (2-2)}$$

Where $E$ is elastic modulus, $d$ represents effective grain size, $and\ W$ is the energy required for plastic tearing at effective grain boundaries. From this equation, it is clear that, by refining the effective grain size, fracture stress can be increased. This finding can be related to providing some fundamental importance of the steel matrix in the fracture process.

### 2.1.8 Inclusions

As large oxides, sulphides, and other inclusions are generally unwelcome in steel microstructure, elements such as oxygen, sulphur, phosphorus, and hydrogen are the main focus to be reduced. Traditionally, the oxygen and sulphur content has been used to determine the level of steel cleanliness.

However, this conventional inclusion cleanliness rating method can only give a general indication, sometimes it cannot give reliable scientific proof, and the results from the rating can be misleading in steel fracture properties [33], as some inclusions have little effect on the fracture process. However, due to the conventional rating, these "neutral" inclusions are regarded as harmful. In summary, the conventional rating is based on inclusion composition, shape,

and sizes instead of their effects on the cleavage fracture process and fracture properties.

The effect of inclusions on the fracture properties is based on the combined effect of its shape, size, elastic and thermal properties, and bonding to the matrix. The combined effects lead to different stress concentrations and stress distributions in the matrix around inclusions. A general case is that oxides promote cleavage fracture as they raise tessellated stresses, while sulphides such as MnS are generally considered not to affect cleavage.

From the findings of Kiessling in 1989, calcium aluminates are most detrimental. However, the detrimental effect is decreased in duplex inclusions, such as oxides surrounded by sulphide shells. [34] Brooksbank and Andrews explain the reason in the 1970s. [35]–[38]

The occurrence of a radial stress concentration is frequently observed as a result of the disparities in mechanical properties between an inclusion and the steel matrix. Two aspects mainly cause the radial stress: Tessellated stress raised from cooling as inclusions and the matrix have thermal contraction differences; the second is the elastic modulus difference between inclusions and matrix.

The model proposed by Andrews [36] considers the inclusions as ideal spheres. The radial stress experienced by the surface that separates the inclusion from the steel matrix can be determined by applying Equations (2-3) and (2-4).

$$\sigma_R = \frac{(\alpha_M - \alpha)\Delta T}{\frac{0.5(1+\nu_M)+(1-2\nu_M)d^3}{E_M(1-d^3)}+\frac{(1-2\nu)}{E}} \qquad \text{Equation (2-3)}$$

$$d = R/R_M \qquad \text{Equation (2-4)}$$

Where the radial stress, denoted as $\sigma_R$, occurs in the interface of the inclusion-matrix. The coefficients of linear expansion of the steel matrix and the inclusion are represented by $\alpha_M$ and $\alpha$, respectively.

Specifically, the parameter of interest is the temperature differential, denoted as $\Delta T$, which is defined as the disparity between the holding temperature preceding the vacuum quenching process and the ambient room temperature. Additionally, the Poisson's ratios of both the steel matrix ($v_M$) and the inclusion ($v$) are considered.

The Young's modulus of the steel matrix and inclusion are denoted as $E_M$ and $E$, respectively. The radius of the inclusion and the steel matrix around a single inclusion are represented by $R$ and $R_M$, respectively.

From Equations (2-3) and (2-4), the study conducted by Brooksbank and Andrews has demonstrated that the tessellated stress existing between the inclusion and matrix is contingent solely upon the inclusion type and its volume fraction, and is not subject to variation based on the inclusion size. (Size only influences the stress range) The linear expansion coefficient, elastic modulus, and Poisson's ratio of inclusion are subject to modification by the inclusion type. -The detailed properties of the most commonly seen inclusions was summarised in Table 2.1

Mean linear expansion coefficient- Stress Raising Ability:

In the event that the linear expansion coefficient of the matrix surpasses that of the inclusion, it can be posited that, during the cooling process, the matrix shall undergo a greater degree of shrinkage in comparison to the inclusion. The results indicate that the inclusion's presence leads to a squeezing effect by the matrix, which in turn induces tensile stresses between the inclusion-matrix interface. In instances where the linear expansion coefficient of the matrix is comparatively smaller than that of the inclusion, it can be observed that the inclusion undergoes a greater degree of shrinkage in comparison to the surrounding matrix. The phenomenon of inclusion-matrix interfacial debonding readily occurres, and it is conceivable that the absence of tessellated stress may be observed. It can be easily seen from the table that oxides, calcium aluminates, and nitrides have great potential for raising tessellated stresses. While sulphides, on the contrary, are strong void formers in the microstructure.

Elastic properties:

When the Young's modulus of the matrix is smaller than that of inclusion, a stress difference will generate a radial stress concentration around the inclusion. Such can be seen for inclusions such as, calcium aluminates, $Al_2O_3$ and $TiC$. When the Young's modulus of the matrix is larger than that of inclusion, the inclusion is relatively harmless, such as sulphides.

It is worth noticing that when in the context of ductile fracture, a lower linear expansion coefficient is generally more welcome as it has better bonding with the matrix, making voids is more difficult to nucleate.

### 2.1.9 Element Effects

Aluminium and Titanium are both added for deoxidising purposes; however, these elements will produce corresponding inclusions in the microstructures. The solid particles of $Al_2O_3$ tend to form aggregates of irregular shape, which are commonly referred to as "alumina clusters", this phenomenon is primarily attributed to the process of coalescence and collision. Titanium nitride with sharp edges can act as local stress concentration points. These inclusions in the final product can strongly affect the steel's low-temperature mechanical properties.

Calcium is added into steel mainly to reduce the detrimental effect of $Al_2O_3$ inclusions and improve the castability of molten steel.[39] It is reported that by adding calcium, the $Al_2O_3$ inclusions will go through a transformation process, resulting in the formation of liquid calcium aluminates inclusions. These inclusions are expected to have a spherical morphology and exhibit low melting points. The current review has revealed that these liquid inclusions exhibit a high degree of susceptibility to removal from the melt. The residual inclusions such as $CaO{-}Al_2O_3$ or $CaO - Al_2O_3 - SiO2$ inclusions in steel are less harmful than untreated $Al_2O_3$ inclusion to the low-temperature mechanical properties.[40]

## 2.2 Parameters Affecting the Microstructures of Bainitic Steel

### 2.2.1 Effects of Alloying Elements on Microstructure

**Carbon**:

The influence of carbon on bainitic steels is of paramount importance, as it significantly modulates the temperature range within which the upper bainite and lower bainite transformations take place. In the capacity of an austenite stabilising element, carbon exhibits a greater degree of solubility in austenite as compared to ferrite. Moreover, it exhibits a formidable ability to stabilize austenite, resulting in a widespread deceleration of reaction kinetics.

However, in general, in industry, carbon needs to be restricted below 0.4wt% to ensure reliable mechanical properties.

**Manganese**:

Usually, Manganese content is between 0.4-2.0 wt.%. Larger content of 1.5-2.0 wt% slows down the pearlite reaction significantly and promotes the formation of acicular ferrite or the bainitic transformation. High Mn addition >2.5wt.% is avoided as it results in a brittle banded structure due to Mn segregation.

**Nickel**:

Nickel is usually added to increase hardenability and improve toughness for low-temperature applications. Nickel being an austenite stabiliser, the presence of Ni has been observed to exert a retarding effect on the kinetics of the transformation process of ferrite and pearlite. The introduction of nickel has the potential to induce a rightward shift in the Continuous Cooling Transformation (CCT) curve, thereby conferring a favourable disposition towards the formation of bainitic and martensitic microstructures. Ni exhibits a proclivity towards the promotion of lower bainitic microstructure, while concurrently impeding the formation of upper bainite. With increasing nickel content, the CCT curve can shift to the right, passing ferritic and pearlitic phase regions and even bainitic phase regions to form martensite; thus, the final microstructure is often seen in lower bainite and tempered martensite.

**Silicon**:

As a ferrite stabiliser that refines the ferrite grain size. Silicon is insoluble in cementite, and silicon is very effective in restricting cementite formation.

**Aluminium**:

Similar to silicon, Al is insoluble in cementite, but unlike silicon, it precludes the formation of Si/Mn oxides. Also, it can help the austenite to bainite transformation and is typically introduced in very small quantities as a deoxidizer.

**Calcium**:

As deoxidiser and desulphuriser, Ca decreases the number of inclusions. Also, it modifies inclusion morphology, such as modifying elongated oxides and

sulphides into a globular shape, which can eliminate the steel's anisotropic properties.

e.g., Aluminium oxides, which generally are hard and angular, being very harmful to steel machinability, appears in clusters and are reduced in number or replaced by complex $CaO - Al_2O_3$ or $CaO - Al_2O_3 - SiO_2$ inclusions.

**Molybdenum**:

Molybdenum is recognized for its effectiveness in altering the transformation kinetics and phase distributions in steel. It is highly effective at inhibiting the transformation into pearlite and bainite. In addition, the addition of $Mo$ significantly reduced the dislocation annihilation rate and slowed the coarsening rate of nanometer-sized $(Nb, Mo)C$ carbides during extended tempering at elevated temperatures, thereby enhancing the resistance to subsequent softening after peak hardening.

**Titanium and Niobium**:

Niobium and Titanium are frequently used as microalloying elements to form nanoscale precipitates and prevent austenite grains from becoming coarser. The addition of Niobium and Titanium increased the strength of steel by refining the grains and reinforcing the precipitation. In order to avert the segregation of constituent elements and the concomitant development of macroscopic inclusions, such as nitrides and carbides, it is imperative to exercise stringent control over the steelmaking and continuous casting procedures.

**Titanium**:

Among all kinds of inclusions acting as nucleation sites for acicular ferrite, titanium compounds were more likely to be found. [41]

The presence of titanium nitride (TiN) inclusions within the microstructure of steel has been identified as a probable precursor to the onset of cleavage fracture. This is attributed to the inherent mechanical properties of TiN, which are characterised by high levels of hardness, brittleness, and strong interfacial bonding with the surrounding steel matrix. In the context of heterogeneous materials, it has been observed that the elastic deformation of a hard inclusion embedded within a plastically deforming matrix can lead to stress concentration due to the presence of a strong interfacial bond. This phenomenon may ultimately result in the occurrence of fracture within the inclusion.

**Sulphur and Phosphorus**:

Sulphur and phosphorus are usually considered impurities in steel rather than alloying elements. The formed products are often considered to be inclusions.

### 2.2.2 Tempering Effect

Tempering Effect:

The process of tempering is a widely employed technique in the realm of metallurgy for the purpose of enhancing the ductility and resistance to fracture of steel alloys. This modification in quenched high and medium-carbon steels is a common practise in the application of ultrahigh-strength martensitic steels. Different combinations of tempering temperatures and time can be used depending on the required properties.

Generally speaking, tempering can lower the bainitic steel strength, increasing fracture toughness. However, how much strength is reduced and how much

toughness is raised is a more complicated issue. The tempering process allows for optimising the material strength/toughness ratio. Carbon movements in the tempering process led to different distributions and morphologies of carbides that alter the steel's behaviour. It has been suggested that tempering temperature has a more profound effect than tempering time. [42]

Temperature Effect:

From experimental results, the heat treatment has to be above a temperature of around 500°C for substitutional atoms diffusing in a reasonable period, which is critical for alloy carbide formation. On the other hand, cementite and other transition iron carbides can form at a low temperature of 200°C.

Tempering of Martensite:

The process of tempering martensite is chiefly distinguished by the partitioning of supersaturated carbon to defects or clusters within the martensite lath, thereby leading to the formation of cementite precipitates. The martensite lath featuring low-angle boundaries undergoes a process of combination and recrystallization, leading to the formation of polygonal ferrite grains.

Tempering of Bainite:

The difference in the tempering process between bainite and martensite comes from their different solubility of carbon. As less carbon can exist in bainite than in martensite, the tempering will have much less effect in bainite; also, the mechanical behaviour changes are much less. A significant tempering effect on strength changes is observed as bainite plates coarsen or recrystallize into equiaxed ferrite grains. Conversely, tempering has a minor effect on strength when cementite particles coarsen and dislocation substructures undergo recovery. [8]

Generally, the decomposition during the tempering process is primarily characterised by the formation of cementite, recovery and recrystallization of a highly dislocated ferrite matrix, and the potential precipitation of micro-alloying carbides. For the mechanical aspect: this decomposition and recrystallisation of the bainite ferrite matrix will decrease tensile strength. However, it has been observed that the aforementioned issue may be mitigated through the precipitation of micro-alloying carbides at a tempering temperature exceeding 500 °C.

Tempering of Martensite-Austenite Constituents:

The Martensite-Austenite constituents changed with varying martensite and retained austenite combinations. Therefore, the tempering of M-A constituents is the tempering of both martensite and retained austenite. [43] Decomposition of retained-austenite occurs at temperatures above 400 °C.[44] The retained austenite in M-A constituents is always carbon-rich as a of result of partition. The carbon diffusion out from austenite is the primary process. At elevated tempering temperatures reaching 620 °C, the phenomenon of carbide precipitation and spheroidization within M-A constituents, as well as recovery and recrystallization within the bainitic ferrite matrix, have been observed.[44]

# Chapter Three – A Review of Previous Work on Cleavage Fracture Mechanisms of Bainitic Steels

## 3.1 Macro Fracture Mechanics and Its Limitations

During the time before Fracture Mechanics was developed, the theoretical strength of a crystal was estimated using this equation:

$$\sigma = \left(\frac{E \cdot \gamma}{b}\right)^{1/2} \qquad \text{Equation (3-1)}$$

Where $E$ is Young's modulus, $\gamma$ is the surface energy and $b$ is the atomic spacing.

However, the measured value is much smaller than the theory predicted, making researchers realise that there are different kinds of flaws in crystal structures. Therefore, based on micro-cracks existence and propagation, macro fracture mechanics starts to be developed.

### 3.1.1 Griffith Theory

The first work was done by Griffith [45], who was inspired by the glass making industry and proposed that, in crack propagation, the stored energy is varied based on micro-crack size. The energy transferred between elastic strain energy and surface energy:

For plane-stress conditions:

$$\sigma_f = \left(\frac{2E \cdot \gamma_s}{\pi a}\right)^{1/2} \qquad \text{Equation (3-2)}$$

For plane-strain conditions:

$$\sigma_f = \left(\frac{2E \cdot \gamma_s}{\pi a(1-v^2)}\right)^{1/2} \qquad \text{Equation (3-3)}$$

Where $\gamma_s$ is elastic surface energy, $a$ is half of the micro-crack size, $v$ is the Poisson's ratio.

### 3.1.2 Linear Elastic Stress Intensity Factor K

During the 1940s-1950s, Orowan [46] and Irwin [47] developed Griffith's theory; they believed there is plastic deformation before a crack front in metallic materials. Therefore, crack propagation needs to overcome work done by plastic deformation. If $\gamma_p$ is plastic work in unit area, then in plane-strain:

$$\sigma_f = \left(\frac{2E \cdot \gamma_{eff}}{\pi a(1-v^2)}\right)^{1/2} = \left(\frac{2E \cdot (\gamma_s + \gamma_p)}{\pi a(1-v^2)}\right)^{1/2} \qquad \text{Equation (3-4)}$$

Where $\gamma_{eff}$ is effective surface energy and $\gamma_p$ is the plastic surface energy.

Based on Westergaard's theory [48], Irwin introduced the stress intensity factor $K$, which further developed into the foundation of Linear elastic fracture mechanics ($LEFM$):

$$K = \sigma\sqrt{\pi a} \qquad \text{Equation (3-5)}$$

Where $K$ is the linear elastic stress intensity factor, $\sigma$ is applied stress, $a$ is half of the micro-crack size (strictly for a buried crack under biaxial tensile loading in an infinite test-piece)

This stress intensity factor $K$ is further introduced in the ASTM testing standard; for the specimen testing to be valid in $LEFM$, the specimen size needs to be satisfied:

$$B, a, (W - a) > 2.5(\frac{K_{IC}}{\sigma})^2 \qquad \text{Equation (3-6)}$$

Where $B$ is the specimen thickness, $W, a$ is the specimen width and crack length respectively.

However, in a real testing environment, if the temperature achieved is not low enough, or the material microstructure is ductile then plastic deformation ahead of the crack front cannot be avoided, and linear elastic mechanics must be modified to explain the plastic region. Irwin gives the concept of equivalent crack size; this can work under a relatively small size of the plastic region.

Small scale yielding:

$LEFM$ is considered when the plastic deformation is not present at the crack front.

However, this is very difficult to achieve in real life, small or large; there will always be some level of plastic deformation ahead of crack. To enable $LEFM$ to be working again, Irwin proposed his correction factor:

$$a_{eff} = a + \Delta a_n \qquad \text{Equation (3-7)}$$

Where $a_{eff}$ is effective crack length, $a$ is the physical crack length, and $\Delta a_n$ is the increment in the notational crack length.

The correction factor was introduced by placing the plastic zone within a region following $LEFM$; the nature is by extending the $LEFM$ scope of application to solve more real problems. That can only be used when the plastic deformation is small.

The size of the plastic zone from Irwin's correction gives:

In plane stress condition:

$$r_y = \frac{1}{2\pi}\left(\frac{K_I}{\sigma_{ys}}\right)^2 \qquad \text{Equation (3-8)}$$

In plane strain condition:

$$r_y = \frac{1}{4\sqrt{2}\pi}\left(\frac{K_I}{\sigma_{ys}}\right)^2 \qquad \text{Equation (3-9)}$$

Where $r_y$ is the plastic zone size.

In many structures, the toughness of the material was too great to initiate fracture and $LEFM$ was not applicable anymore; When yielding occurs under a larger scale, usually when $r_y \ / \ a < 1/10$ condition is not met and the plastic zone size $r_y$ is not far less than the crack length $a$, Irwin corrections cannot be

used anymore, this will lead to the introduction of Elastic-Plastic Fracture Mechanics (EPFM).

### 3.1.3 COD Theory

In an actual testing environment, the strain at the crack tip is difficult to measure precisely. Wells found that plastic deformation will lead to crack blunting in an initially sharp crack. He first suggests using that blunted crack opening displacement (COD) to represent the strain indirectly. Furthermore, this can show the material's ability to resist fracture (toughness).

Under this circumstance, Dugdale's strip yield model [49] was introduced with Wells' [50] COD model (crack opening displacement). Then in crack-front under ideal plastic yielding, COD can be written as:

$$\delta_t = \frac{8\sigma_{ys}a}{\pi E} Ln\ sec\frac{\pi\sigma}{2\sigma_{ys}} \qquad \text{Equation (3-10)}$$

Where $\sigma_{ys}$ is the yield stress, $a$ is half the crack length, $E$ is young's modulus, and $\sigma$ is the applied stress.

Different from Irwin, Dugdale considered a strip-shaped plastic zone, which gives the plastic zone size as:

$$r_y \approx \frac{\pi}{8}(\frac{K_I}{\sigma_{ys}})^2 \qquad \text{Equation (3-11)}$$

Furthermore, it can be used when there is a large size of the plastic region, and the linear-elastic fracture mechanics cannot work anymore.

The plastic deformation can either be seen as crack extension (Irwin) or crack blunting (Dugdale). These two models can be equivalent when plastic deformation is small.

The original COD definition of crack opening displacement varies as the crack tip is approached. Crack tip opening displacement (CTOD) is developed to give an experimentally measurable definition by 90° intersection with the crack tip flank. The illustration is shown schematically in Figure 3-1.

To extend the crack and thereby increase the Crack Tip Opening Displacement (CTOD) value, the execution of plastic work is necessary, and the amount of plastic work is representative of the material's fracture toughness. CTOD can then be used to represent the material's fracture toughness. The above led to the idea that fracture occurs when the opening reaches a critical value. CTOD can therefore be related to the stress intensity factor, $K_I$, under LEFM conditions:

$$CTOD = \frac{{K_I}^2}{nC\sigma_{ys}} \qquad \text{Equation (3-12)}$$

where $E =$ Young's Modulus,

$n = 1.0$ for the plane stress and $n = 2.0$ for plane strain,

$\sigma_{ys}$ = yield stress.

CTOD approach is not limited only to $LEFM$ conditions. It is still valid when more significant plastic deformation occurs at the crack tip. However, if total yielding occurs, it will not be applicable.

### 3.1.4 J-Integral

In 1968, Rice [51] proposed an energetic contour path integral $J$, proving that J-integral was path-independent with respect to the contour around a crack. $J$-integral can characterise the intensity of crack-tip stress and strain fields. Then it became the fundamental of elastic-plastic fracture mechanics.

$$W(\epsilon) = \int_0^{\epsilon} \sigma_{ij} d\epsilon_{ij} \qquad \text{Equation (3-13)}$$

The function $W(\epsilon)$ is utilised to denote the energy density of an elastic material. It is shown in Figure 3-2 from a homogeneous material as the considered body, subjected to a deformation field of two dimensions, wherein a crack devoid of any traction was present. It has been observed that the value of the line integral remains invariant for all paths $\Gamma$ that encircle the tip. The present figure involves a traversal of the path in a counterclockwise direction, whereby the traction vector denoted by the symbol $\mathrm{T}$ on the boundary $\Gamma$ is defined in accordance with the outward normal.

$$J = \int_{\Gamma} \left[ W(\epsilon)\, dy - T \cdot \frac{\partial u}{\partial \mathrm{x}} ds \right] \qquad \text{Equation (3-14)}$$

Where, $W = \int \sigma_{ij} d\epsilon_{ij} =$ strain energy density ($\sigma_{ij}$ and $\epsilon_{ij}$ as stress and strain tensors).

$T = \sigma_{ij} n_j =$ components of the traction vector acting on the contour.

$u_i =$ displacement vector, $s$ is the arc length,

$ds =$ increase in length along the contour $\Gamma$.

If the material's response is elastic-plastic, the $J$-integral is equivalent to the reduction in potential energy resulting from an incremental increase in the crack length. It is, therefore, equivalent to the release rate of energy G.

As a crack grows in a material, the J-integral can give a measure of the elastic-plastic work done, and this is shown as a line integral in the Figure 3-2.

Under $LEFM$ conditions, release rate of energy $J$ and $G$ has a direct correlation with the stress intensity factor $K$ under Mode $I$ loading through:

$$J = G = \frac{K^2}{E} \qquad \text{Equation (3-15)}$$

For plane stress conditions and,

$$J = G = \frac{K^2}{E}(1 - v^2) \qquad \text{Equation (3-16)}$$

For plane strain conditions.

As stated in Equation (3-15) and Equation (3-16), in a linear elastic material, under monotonic loading conditions, J-integral can characterise the strain energy release rate for a crack-tip.

With the study and development of $J$-integral, the critical value of fracture energy $J_{IC}$ can be used to characterise material fracture toughness.

To get a valid $J$ value, the specimen needs to satisfy:

$$a, t, L > 25(\frac{J_{IC}}{\sigma}) \qquad \text{Equation (3-17)}$$

Where $a$ is the crack length, $t$ is the thickness of the specimen, $L$ is the width of the specimen minus the crack length.

The seminal work of Hutchinson, Rice and Rosengren [52] demonstrated that the $J$-Integral possesses the ability to delineate the singular stress and strain fields in the vicinity of a crack tip in a power law hardening elastic-plastic material, provided that the plastic zone dimensions are considerably smaller than the crack length.

The material constitutive law employed by Hutchinson was of the form proposed by W. Ramberg and W. Osgood: [53]

$$\frac{\epsilon}{\epsilon_y} = \frac{\sigma}{\sigma_y} + \alpha(\frac{\sigma}{\sigma_y})^n \qquad \text{Equation (3-18)}$$

Where the variable $\sigma$ denotes the stress experienced by a material in a state of uniaxial tension, the symbol $\sigma_y$ denotes the yield stress, the symbol $\epsilon$ denotes the strain and $\epsilon_y = \sigma_y/E$ is the corresponding yield strain, the parameter denoted by $E$ represents the Young's modulus of the material under consideration. $n$ is the work hardening coefficient.

The present model is characterised by parameter α, which is a dimensionless constant that is representative of the material under consideration.

However, there are assumptions and limitations of the HRR model: First, it only considers the case of monotonically increased load (proportional loading), the stress components generally remain in the same ratios when load increases and unloading is not allowed.

The second limitation is that the crack-tip blunting effect is not considered; thus, large strains at the crack tip are not considered.

Shih [54] used the HRR field to express a relationship between the CTOD and the $J$-integral:

$$J = m\sigma_y CTOD \qquad \text{Equation (3-19)}$$

Where $m =$ plastic constraint factor,

$\sigma_y =$ yield stress.

The plastic constraint factor, $m$, is an empirical parameter.

Regarding Linear Elastic Fracture Mechanics (LEFM), it is optimal for the plastic zone to be governed by the surrounding $J$ dominant zone, thereby enabling the characterization of crack tip loading conditions through $J$.

Eventually, in order to operationalize the theoretical framework, it is imperative to ascertain that both the test specimen and component meet the requisite criteria for $J$ dominance, as previously expounded upon.

### 3.1.5 Macro Fracture Mechanics Limitations

Although there are significant developments in macro fracture mechanics, there are still great limitations.

3.1.5.1. Toughness values, such as $K_{IC}$, $J_{IC}$, and COD, do not have unique value, there are large variability of measuring values. Thus, when designing materials for critical projects and applications, a safety margin is still necessary.

3.1.5.2. Macro-fracture mechanics was built on continuum mechanics. The heterogeneous behaviour of materials, the differences in material microstructure, and the randomness of cleavage fracture nucleation were not considered.

## 3.2 Micro-Mechanisms of Brittle Fracture

### 3.2.1 Cleavage Fracture

As the {100} plane of iron is the primary cleavage plane, the general criterion for cleavage in mild steel is the stress criterion which suggests that cleavage took place when local tensile stress reached a specific threshold value.

Low [55], [56] conducted a comprehensive investigation on the influence of ferrite grain size on the compressive yield stress and cleavage fracture stress in

mild steels. The findings of the investigation have unveiled that the fracture stress in unnotched specimens was either equivalent to or exceeded the yield stress. The widely held consensus in this field of research is that the occurrence of cleavage necessitates the presence of localised plastic deformation.

Griffith gives the general cause of cleavage fracture, which is pre-existing microcracks in the material.

### 3.2.2. Stroh's Theory

Zener [57] and Stroh [58] inferred that plastic stain initiated the cleavage fracture instead of pre-existing microcracks. Based on this, a dislocation lead micro-crack nucleation model has been proposed:

He postulates that microcrack nucleation is the critical event; thus, cleavage is nucleation controlled when dislocation pile-up leads to increased stress level:

$$\tau_{eff} = \tau_y\text{-}\tau_i \geq \left[\frac{12\mu\gamma_p}{\pi(1-v^2)d}\right]^{1/2} \qquad \text{Equation (3-20)}$$

Where the symbol $\tau_y$ denotes the shear yield stress, variable $\tau_i$ denotes the lattice friction shear stress, symbol μ denotes the shear modulus, $v$ denotes Poisson's Ratio, the effective surface energy of ferrite is denoted by the symbol $\gamma_p$ and the slip band half-length is represented by $d$.

At the same time, local cleavage fracture stress $\sigma_F$ is:

$$\sigma_F = \sigma_0 + k_F d^{-1/2} \qquad \text{Equation (3-21)}$$

Where $\sigma_F$ is the local cleavage fracture stress, $d$ is the grain diameter, $k_F$ is a constant.

The schematic illustration of Stroh proposed model is shown in Figure 3-3.

### 3.2.3 Cottrell's Theory

On the contrary, Cottrell [59] postulates cleavage is not all nucleation controlled. He suggested a model that two dislocations intersecting each other at {101} slip planes leading to a sessile dislocation formation in which Burgers vector is normal to the cleavage plane:

$$\frac{a}{2}[\bar{1}\bar{1}1](101) + \frac{a}{2}[111](\bar{1}01) \rightarrow a[001](001) \quad \text{Equation (3-22)}$$

As the interaction of dislocations is intrinsically linked to a reduction in energy, then the crack nucleation is easy to achieve, the critical event is controlled by the crack propagation, so the fracture stress is then related to the grain size:

$$\sigma_F \geq \frac{2\mu\gamma_p}{k_y} d^{-1/2} \quad \text{Equation (3-23)}$$

The parameter denoted as $k_y$ corresponds to the constant of shear Hall-Petch yielding. The symbol $\mu$ denotes the shear modulus, the effective surface energy is denoted by the symbol $\gamma_p$, and the grain diameter is represented by the symbol $d$.

Stroh and Cottrell's theory provided the basics of the cleavage fracture model in steels. The argument is still proceeding for whether a specific type of material fracture is nucleation or propagation controlled.

Because Cottrell's model only considered grain size, it ignored the brittle particles which generally existed in steel. The influence of the second phase and carbides is still missing in cleavage models.

The schematic illustration of Cottrell proposed model is shown in Figure 3-4.

### 3.2.4 Smith's Theory

McMahon and Cohen [60] investigated the carbide influence on cleavage fracture by showing grain boundary carbide cracking firstly and propagated into ferrite matrix; because the effective surface energy of ferrite is larger than the second phase, the microcrack cannot propagate further, which gives evidence that fracture is propagation controlled. They showed that the presence of coarse carbides in the microstructure of the material under investigation facilitated the occurrence of cleavage fracture, whereas the presence of fine carbides enabled the material to exhibit ductile behaviour.

Based on the above, Smith [61] proposed that the critical event of cleavage is second phase particle cracks propagating into contiguous grains under applied tensile stress and induced dislocation pile-ups. The schematic illustration of Smith proposed model is shown in Figure 3-5.

As he found that cleavage fracture was always related with cracked carbides. He concluded that carbide cracking is the critical event and the intermediate process between dislocation pile-up and cleavage crack propagation. His findings on cleavage fracture were always related to cracked carbides.

$$\left(\frac{C_0}{d}\right)\sigma_f{}^2 + \tau_e{}^2\left[1 + \frac{4}{\pi}\left(\frac{C_0}{d}\right)^{1/2}\frac{\tau_i}{\tau_e}\right]^2 \geq \frac{4E\gamma_p}{\pi(1-\nu^2)d} \quad \text{Equation (3-24)}$$

The equation elucidates the relationship between the grain size denoted by $d$, the grain boundary carbide thickness represented by $C_0$, and the effective shear stress denoted by $\tau_e$. The variable $\tau_i$ denotes the friction shear stress. the effective surface energy of ferrite, denoted by the symbol $\gamma_p$. Poisson's ratio is represented by the symbol $v$, and Young's modulus is represented by the symbol $E$.

The second term in the left-hand side equation yields a negligible contribution to the overall, if it is neglected, then the Smith model can be re-written as:

$$\sigma_F = \left(\frac{4E\gamma_p}{\pi(1-v^2)d}\right)^{1/2} \qquad \text{Equation (3-25)}$$

From studying spheroidised plain carbon steel, Curry and Knott [62] regard the spheroidal carbide particles as micro-crack nuclei for the cleavage fracture process. As the carbide shape is penny-shaped, it was considered as a Griffith-type micro-crack, and under plane strain conditions, local cleavage fracture stress can be written as:

$$\sigma_F = \left(\frac{\pi E\gamma_p}{2(1-v^2)r}\right)^{1/2} \qquad \text{Equation (3-26)}$$

Where $r$ is the radius of the carbide spheroid, and $L = 2r$ gives the carbide length.

Equation (3-26) can also be seen as a cleavage criterion especially considering the largest carbide particles under sufficient local stress. Furthermore, this equation is extensively used when considering a penny-shaped microcrack in the microstructure.

Temperature dependence:

Knott and Griffiths [63], [64] have studied the temperature dependence of cleavage fracture. Knott [63] proposed that in cases of slip-induced cleavage, evidence indicates that the fracture stress in mild steels demonstrates negligible dependence on both strain rates and temperatures. He applied slip-line field theory to notched bend specimens to evaluate the fracture stress when general yielding takes place. However, the early studies were limited to a narrow temperature range that could be applied.

In 1971, Griffiths and Owen [64] applied elastic-plastic finite element analysis to simulate the maximum principal stress along the notch in the blunt-notch specimen for a pure bending test. With the loading to the maximum yielding load and assuming that fracture will take place at maximum local principal stress, as shown in Figure 3-6, the finite element analysis gives a profile of stress distribution. The maximum principal stress is regarded as microscopic cleavage fracture stress with its location in the plastic zone. Griffiths and Owen [64] have measured the fracture stress values over -196 °C to 50 °C for a roughly constant value of around 1000 $MN/m^2$. Based on the results, it was generally assumed that cleavage fracture stress in medium to high carbon steels is temperature independent.

### 3.2.5 Ritchie, Knott and Rice (RKR model)

Ritchie, Knott and Rice [65] proposed the RKR model, which suggested that there is a characteristic distance ahead of the pre-crack tip for pre-cracked specimens where the cleavage happens only when normal stress is larger than the cleavage fracture stress. They chose two ferritic grain diameters as characteristic distance; However other researchers have demonstrated the

inapplicability of the proposed model for predicting the cleavage fracture in low alloy steels, higher carbon steels and mild steel across a variety of grain sizes.

Bowen [66] proposed the concept of a 'process zone' of 0.95 $\sigma_F$; he used the FEM analysis results to define the process zone, which is an area exhibiting tensile stress larger or equal to 0.95 $\sigma_F$. Only in this zone can tensile stress propagate microcracks. He suggests that the limitation of the RKR model is that it doesn't consider how the process zone size changes with temperature.

The authors Chen et al. [67] have put forth a proposed mechanism for cleavage fracture process. This process has been identified to be slip-induced and is comprised of three consecutive and uninterrupted stages:

1. Criterion for microcrack nucleation, strain must exceed the critical strain $\epsilon_p \geq \epsilon_{pc}$

2. Criterion for microcrack blunting, stress triaxiality must exceed the critical triaxiality.

$\sigma_m/\sigma_c \geq T_c$

3. Criterion for microcrack propagation, local tensile stress must exceed critical cleavage fracture stress

$\sigma_{yy} \geq \sigma_F$

In addition, a 'minimum distance' and 'active zone' concept are also used in Chen's model; they suggested a fracture active zone ahead of the crack/notch tip, which is generated by the triaxial stress state, only weak particles in the active zone can nucleate microcracks and lead to total fracture.

Teleman et al. [68] used slip line theory to investigate the effect of notch radius on cleavage fracture stress. It was found that when the notch radius is above 0.25 mm, the cleavage fracture stress decreases with increasing notch radius.

Many researchers[69]–[71] have measured cleavage fracture stress in blunt-notched and sharp-cracked specimens. After years of research, it was generally accepted that in blunt-notched specimens, the critical event is a grain-sized microcrack propagating into neighbouring grains. The cleavage fracture stress $\sigma_F$ and toughness measured mainly depend on the 5% largest ferrite grain size [66]. While in sharp-cracked specimens, the critical event is microcrack propagation from the brittle second-phase particle into the matrix. The cleavage fracture stress and toughness are determined by the largest brittle second-phase particles such as carbides, nitrides, oxides or M-A constituents.

Application of RKR: using HRR theory:

Curry [72] suggested that the RKR fracture criterion can be written as:

$$\sigma_{yy}(X) > \sigma_F \; for\; all\; X\; satisfying\; 0 < X < X_0 \quad \text{Equation (3-27)}$$

Where $\sigma_{yy}(X)$ is the maximum tensile stress at a point $X$,

$\sigma_F$ is the microscopic fracture stress

$X_0$ is the characteristic distance.

Combining Ramberg-Osgood stress-strain law in plane strain, small-scale yielding conditions can be written as: [51]

$$\frac{\sigma_{yy}(X)}{\sigma_y} = \beta\left(X\left(\frac{\sigma_y}{K_{IC}}\right)^2\right)^{-1/(N+1)} \quad \text{Equation (3-28)}$$

Where $\beta$ is the amplitude of HRR crack-tip stress singularity,

$\sigma_y$ is the yield stress

$N$ is the reciprocal of the strain hardening exponent.

Furthermore, it can then be written as:

$$K_{IC} = \beta^{-(N+1)/2} {X_0}^{1/2} \frac{{\sigma_F}^{(N+1)/2}}{{\sigma_y}^{(N+1)/2}} \qquad \text{Equation (3-29)}$$

Where $N$ is the strain hardening exponent's reciprocal and N equals $1/n$.

$\beta$ is the amplitude of HRR crack-tip stress singularity.

Substitute $N = 1/n$, and we can get:

$$K_{IC} = \beta^{-(n+1)/2n} {X_0}^{1/2} \frac{{\sigma_F}^{(1+n)/2n}}{{\sigma_y}^{(1-n)/2n}} \qquad \text{Equation (3-30)}$$

### 3.2.6 Statistical Approach

Based on the fact that the variability of toughness and local cleavage fracture stress results, as well as the nature of measured fracture initiation sites, were always some distance from notch-tips and crack-tips.

Many researchers[64][69][70] have made attempts to explain this phenomenon. As mentioned above, the RKR model has proposed a "characteristic distance" into the micro-mechanisms. Suggesting the cleavage must overcome a minimum distance before propagating for final failure.

Bowen[73] suggested that the process zone within 0.95 maximum principal stress is most likely to be the initiation site where cleavage begins. And the process zone changes with temperature, which modifies the RKR approach.

### 3.2.7 Beremin Model and Its Modifications

While it has been established that cleavage fracture stress plays a pivotal role in the fracture process, comprehending the variability in cleavage fracture stress remains complex. This variability has necessitated the development of statistical models.

The models proposed by Curry [72] and Beremin [75] in the context of ferritic steels suggest that cleavage microcracks originate due to plastic strain. The Beremin model, in particular, is built upon an assumption: it posits that while cleavage is governed by stress, it is invariably preceded by plastic deformation. Furthermore, the model implies that failure events conform to the weakest-link principle.

The original Beremin model addresses the statistical challenges of test data by introducing the Weibull stress [76] $\sigma_w$ as a probabilistic fracture parameter. This model conceptualizes Weibull stress under an applied load as the driving force for cracking, proposing that crack propagation occurs when the Weibull stress attains a critical threshold.

It is hypothesized that initial microcracks emerge due to the uneven distribution of plastic deformation within the grains. The determination of Weibull stress is thus crucial for understanding this process:

$$\sigma_w = \sqrt[m]{\sum_j (\sigma_1^j)^m \frac{V_j}{V_0}} \qquad \text{Equation (3-31)}$$

Where $V_j$ is the volume of the $j^{th}$ th element experiencing the maximum stress $\sigma_1^j$.

In the context of notched specimens, the probability of failure shall be determined:

$$P_R = 1 - \exp - (\frac{\sigma_w}{\sigma_u})^m \qquad \text{Equation (3-32)}$$

Where $P_R$ is the cumulative probability of failure.

$m$ is the Weibull constant.

$\sigma_w$ is calculated from Equation (3-31), where the size effect is considered.

In the three steel conditions studied by Beremin, $m$ was calculated for a value of $m$ = 22, while $\sigma_u$ was found to be related to grain size. The parameters m and $\sigma_u$ were considered independent of temperature, over the temperature range at least between 77 K and 170 K.

The probability of failure Equation (3-32) can also be written as following Equation (3-33) when in a uniformly loaded volume $V$, assuming there are statistically independent elements $V / V_u$:

$$P_R = 1 - \exp [-\frac{V}{V_u} P(\sigma)] \qquad \text{Equation (3-33)}$$

The distribution may be produced if it is assumed that the material has a population of micro-defects (particles or microcracks of grain size), and that

this population is distributed in accordance with a straightforward power or exponential laws, denoted by p(a). According to the theory of the weakest link, the probability of failure $P(\sigma)$ of a typical volume element, $V_u$, may be expressed as the following formula:

$$P(\sigma) = \int_{a_c(\sigma)}^{\infty} p(a)\, da \qquad \text{Equation (3-34)}$$

Where the critical micro-defect size $a_c$ is simply given by Equation (3-35), i.e.:

$$a_c = \frac{2E\gamma_s}{\alpha\sigma^2} \qquad \text{Equation (3-35)}$$

Given the population distribution function $p(a)$, it is thus feasible to compute the probability of failure $P(\sigma)$.

However, it is often the case when the microcrack distribution is difficult to know; under these circumstances, approximations are used. The distribution $p(a)$ is assumed to follow a power law.

$$p(a) = \gamma \cdot a^k \qquad \text{Equation (3-36)}$$

Where '$k$' represents the power law exponent, which is a constant.

In general, the function $p(a)$ is unknown. However, the empirical determination of the distribution function $p(a)$ is feasible in cases where the

critical stage of cleavage fracture is governed by the advancement of microcracks that originate from particles.

There are several modified models developed from the original Beremin model; among them two models and one concept are worth investigating in this thesis:

3.2.7.1. Threshold Stress:

Some researchers [77], [78] introduced a threshold stress $\sigma_{\mathrm{w\,min}}$

$$P_R = 1 - \exp[-(\frac{\sigma_{\mathrm{w}} - \sigma_{\mathrm{w\,min}}}{\sigma_{\mathrm{u}} - \sigma_{\mathrm{w\,min}}})^m] \qquad \text{Equation (3-37)}$$

The present method concerns the determination of the critical threshold of $\sigma_{\mathrm{w}}$, denoted as $\sigma_{\mathrm{w\,min}}$, beyond which cleavage fracture may occur. In order to achieve a threshold toughness value $K_{I\,min}$ that facilitates cleavage fracture, it is imperative that the process zone size exceed a critical size $X_c$.

In the original Beremin model, threshold Weibull stress is only implicated; the threshold stress concept emphasises the importance of a critical value of Weibull stress and the critical size of a plastic zone $X_c$. It suggested that the cleavage cannot take place if the threshold stress is not met.

$$K_{I\,min} \approx \sigma_{YS} \sqrt{3\pi X_c} \qquad \text{Equation (3-38)}$$

3.2.7.2. Multiple-Barrier Model:

The original Beremin model is oversimplified as cleavage was considered either nucleation or growth controlled during that stage. After many years of modification, the Beremin model's cleavage process was recognised to have two

or three major steps. Microcrack initiation and propagation are two main steps, with the possible deviation of particle-matrix propagation or matrix-matrix propagation as three major consideration steps. Under the base of the weakest-link concept, the cleavage fracture probability of the specimen is a combined conditional two to three events probabilities taking place at the same location successively. [79], [80]

$$P_R = P_{nucleation} + P_{propagation} \qquad \text{Equation (3-39)}$$

Where $P_{\text{nucleation}}$ and $P_{\text{propagation}}$ are the probability of microcrack nucleation and propagation, respectively.

In order to calculate respective probability, critical values of both particle and grain size were considered as $C^*$ and $D^*$ [80], where M-A constituents are considered brittle particles in bainitic steel.

$$C^* = (\frac{\delta \cdot K_I^{c/f}}{\sigma_1})^2 \; and \; D^* = (\frac{\delta \cdot K_I^{f/f}}{\sigma_1})^2 \qquad \text{Equation (3-40)}$$

Where $K_I^{c/f}$ is local toughness of fracture of M-A constituents at the interface with the matrix.

Furthermore, $K_I^{f/f}$ is the local toughness of fracture of neighbouring grains.

In the multiple-barrier model, the weakest link theory provides a solid foundation, and it is imperative to ascertain the distribution of the particle size and the grain (packet) size.

3.2.7.3. Strain Effect:

This concept assumes only newly nucleated microcracks can be effective cleavage initiation points. The theoretical construction of the strain effect posits that the number of nucleated microcracks will grow concomitantly with augmenting plastic strain and diminishing temperature.

This concept adopted some ideas from previous researchers [81] and then introduced a strain correction into the original Beremin model as:

$$P_R = 1 - \exp\left[-\frac{\int_{PZ} \sigma_1^m \exp\left(-m\epsilon_1/\alpha\right)\cdot dV}{\sigma_u^m V_u}\right] \qquad \text{Equation (3-41)}$$

Where the plastic strain, denoted as $\epsilon_1$, occurs in the direction of the highest principal stress within a given element of volume, represented as $dV$.

$\alpha$ is a constant and is postulated to be in close proximity to the value of 2.

3.2.7.4. Master Curve Concept:

One advance of the weakest-link and Beremin model is the Master Curve concept introduced by Wallin [82], [83].

He proposed that the fracture toughness scatter can be expressed by Equation (3-42)

$$P_R = 1 - \exp\left\{-\frac{B}{B_0}\left[\frac{K_{Ic} - K_{I\,min}}{K_0 - K_{I\,min}}\right]^b\right\} \qquad \text{Equation (3-42)}$$

Where $B_0$ is an arbitrary (normalised) thickness.

$K_{Imin}$ represents a critical threshold value, below which the occurrence of fracture is deemed unfeasible. ($K_{Imin} \cong 20\ MPa\ m^{1/2}$)

$K_0$ represents the critical value of toughness that corresponds to a probability of failure of 63.2%, and $K_0 - K_{I\,min}$ is the scale parameter.

$b$ is the Weibull slope and is approximately 4.

The Master Curve framework posits that the configuration of the median $K_{JC}$ toughness, $K_{JC}$(medium) for 1T specimens, is postulated to be explicated by a universal rule:

$$K_{Jc}(med) = 30 + 70 \exp\left[0.019(T - T_0)\right] \quad \text{Equation (3-43)}$$

The parameter denoted by $T_0$ represents the temperature at which the average fracture toughness of a specimen with a thickness of 25 mm attains a magnitude of 100 $MPa\ m^{1/2}$.

The fulfilment of rigorous plane-strain small-scale yielding (SSY) prerequisites is an essential requirement throughout the entirety of the crack front at fracture.

## 3.3 Cleavage Fracture in Bainitic Steels

The debate on cleavage fracture mechanisms in lath-type microstructures such as bainitic and martensitic steels has been going on for a long time. Unlike other types of microstructures, the high matrix strength is impossible to ignore, and the focus of these debates can generally be divided into brittle particle control and matrix control.

Brittle particles such as carbides or inclusions have been found as the cause of the cleavage fracture process, and there are theories of cleavage that were based on the existence of these cracked 'brittle phases' as Griffith microcracks. There

is much evidence that suggests that the critical factor to be considered is these brittle particles. Such as Curry and Knott have proposed that the cracked spheroidal carbides can act as Griffith-type microcracks; being penny-shaped, the propagation of such microcracks causes cleavage. [62]

Among those, it is well known that Bowen and Knott. [84] suggested that the largest observed carbides determined cleavage fracture stress in an A533B PV steel with a martensitic microstructure. Later, Bowen et al. [85] showed evidence that in an A533B bainitic and martensitic steel, the cleavage fracture is controlled by carbide size distribution through precise microscopic observations.

Wallin et al. [86] also postulated that the cleavage fracture in bainitic steels is controlled by carbide and not by bainite packet. Chen et al. [87] studied the effect of M-A constituents in the ferritic matrix. They suggested that M-A constituents, being a 'local brittle phase', raise the stress concentrations and triaxiality locally, which is the critical factor.

With the existing research on brittle particles, the importance of bainite, martensite packets have also been discovered. Kamada et al. [88] investigated the cleavage fracture stress in a bainitic microstructure, which is a complex phenomenon influenced by multiple factors. Specifically, the cleavage fracture stress is determined by the internal resistance of the crystal, a Griffith Stress, and a strain hardening and probability term. The interplay between these factors is critical in understanding the underlying mechanisms governing the fracture behaviour of bainitic microstructures.

It was postulated that the magnitude of Griffith stress was influenced by the size of the bainitic packet. The cleavage mechanism of a low-carbon 2Mn-3Cr bainitic steel has been investigated by Brozzo et al. [89] The investigation has yielded a significant finding that the local cleavage fracture stress exhibits a

direct proportionality with the reciprocal square root of the bainitic packet size. The study employs the Griffith equation to evaluate the local cleavage fracture stress. The measured values of cleavage fracture stress and packet size are utilised to obtain an effective surface energy value of the bainite packet, which is estimated to be approximately 120 $J/m^2$.

# Chapter Four – Material Characterization and Mechanical Experimental Methods

## 4.1 Materials

The material used in this study was a SA738Gr.B steel provided by China Baowu Steel Group Corp. Ltd. It was produced by rolling a continuous casting slab in the form of a 55 mm thick plate. The specimen sampling scheme for Charpy Impact Toughness (CVN), Fracture Stress, Fracture Toughness and Tensile samples is illustrated in Figure 4-1 to Figure 4-4.

The material studied was focused on two heat-treated conditions, HT1 and HT2. Chemical Compositions of material used in this study with a comparison of ASME standard is presented in Table 4-1. A salient distinction between the steel manufactured for this study and that specified by the ASME standard resides in the carbon content; specifically, the carbon concentration in the manufactured steel has been reduced by approximately 50% relative to the ASME standard.

### 4.1.1 Heat Treatment History

The two heat treatment conditions are designated Heat Treatment 1 (HT1) and Heat Treatment 2 (HT2). HT1 condition material was austenised at 900 °C for 2 hours, then water quenched, and then tempered at 630 °C for 3 hours. HT2 condition material underwent the same treatment as HT1, followed by a tempering treatment of 620 °C for 15 hours. A schematic diagram is shown in Figure 4-5.

Both heating and cooling rates were maintained below 56 °C/h above 425 °C.

HT1: 900 °C/2h WQ+630 °C/3h

HT2: 900 °C/2h WQ+630 °C/3h + 620 °C/15h

In the current investigation, Heat Treatment 2 (HT2) was employed as a simulated post-weld heat treatment (PWHT) with the primary objective of investigating the possibility of exempting the post-weld heat treatment process if the material's mechanical behaviour remains largely unchanged after simulation.

## 4.2 Metallographic Examination

In order to apply metallographic examination, a transverse slice of the tested Charpy sample from the specimen ends were taken. They were mounted in bakelite, ground by SiC metallographic abrasive paper, from 400, 800, 1200, to 2500 grit sizes. Polishing was done on the freshly ground surface to a final 0.25 μm alumina paste. The polished surface was cleaned with ethanol before etching in 2% Nital solution.

### 4.2.1 Optical Microscopy

The optical microscope used was a VHX-7000 Digital Keyence Microscope. The optical microscope was used in microstructure analysis to examine the polished and etched steel metallography samples.

### 4.2.2 Secondary Electron Microscopy

A Philips XL30 Environmental SEM with A qualitative Energy Dispersive X-ray Spectroscopy (EDX) and a Hitachi S-4000 Field Emission Gun scanning electron microscope were used in microstructure analysis of polished and etched steel metallography samples and fractography examinations after mechanical tests.

### 4.2.3 Grain Size Measurement

The grain size measurement was carried out by the line intercept method, from polished metallography samples etched in 2% nital of HT1 and HT2. 10 images of each sample were taken from SEM randomly for grain size measurement.

### 4.2.4 Inclusion Size Distribution Measurement

The inclusion distribution was obtained from polished metallographic samples cut from the tested Charpy specimens. Labelled HT1-23 and HT2-23, both were from the longitudinal section (L-S) which is parallel to the steel rolling direction.

The specimen cut from the Charpy sample exhibit a surface area of 10mm × 10mm, after mounting, grinding, and polishing using the same metallographic method stated before. The inclusion size distribution analysis was carried out under the backscattered mode of the Philips XL30-ESEM machine with a built-in INCA EDX system. The machine was set under 20 kV beam voltage, a spot size of 3.0, a working distance of 10 mm and a scale magnitude of 250 times. With the magnification, each image covers area of around 370 μm x 500 μm.

The sampling method is illustrated in Figure 4-6. 50 equally spaced areas were examined, a backscattered image was taken from each. The inclusion can be found due to the brightness difference, (inclusions exhibit dark colour compared with matrix). From the horizontal direction, each inspected image area has 2000 μm spacing; while from the vertical direction, each inspected image area has 900 μm spacing. The precise spacing was controlled by Philips XL30-ESEM built-in software for stage position control. The inclusion was also checked with EDX analysis to confirm the appearance. One cut and polished specimen from each heat treatment condition was used to estimate the steel inclusion distribution for each condition.

After backscattered images were taken (50 from each condition) the result was analysed by ImageJ software. The particle-analysis system in the software identifies inclusions within a steel matrix through the utilisation of a backscattered electron (BSE) detector generated image. The identification process is facilitated by utilising the contrast differences between the inclusions

and the steel matrix, which are discernible through grayscale thresholding. Equivalent circular diameter (ECD) was used to define the effective inclusion size. The threshold was controlled to identify only ECD larger than 0.4 μm inclusions, below this threshold, the result is unreliable as the chances of counting non-inclusion black dots (the noise) in the image increases markedly.

### 4.2.5 Inclusion Elemental Analysis

The present study employed a qualitative approach with Energy Dispersive X-ray Spectroscopy (EDX), whereby point analysis was conducted to perform the EDX analysis. The points were selected on the inclusion itself and the surrounding matrix. By comparing element differences between inclusions and the matrix, inclusion chemistries could be established. Quantitative analysis is not possible from fracture surfaces but qualitative analysis is still powerful.

## 4.3 Charpy Impact Testing

### 4.3.1 Charpy Impact Specimen

The Charpy impact specimen geometry was 10×10×55 $mm^3$ with a 2 mm deep V-notch in the centre, as shown in Figure 4-7.

### 4.3.2 Test Setup

Charpy impact tests were carried out on a calibrated Instron-Wolpert PW30 impact testing machine of a 300 J capacity. The tests were carried out following the standard of BS 131 and ASTM E23-16b. The test temperatures were -196°C, -120°C, -100°C, -90°C, -80°C, -70°C, -60°C and -40 °C. A set of type T thermocouples with an accuracy of ±1°C was placed in the Charpy specimen to monitor the specimen temperature (on the specimen surface, small holes were drilled at various locations around the notch area with a depth of 5mm and a

diameter of 1.6 mm for thermocouple wire to be inserted). The drilling locations are shown in Figure 4-8.

For the test temperature of -196°C, the Charpy specimen was immersed in liquid nitrogen; monitored by a thermocouple positioned at the sample surface. Upon the sample surface temperature reaching the designated test temperature of -196°C, the specimen was allowed to thermally stabilize for an additional 10 minutes to ensure uniform temperature distribution throughout the material's entirety. This duration was predicated on the assumption that a cooling period of 1 minute per millimetre of specimen thickness is required for achieving temperature equilibration. The impact test was executed within a span of four seconds subsequent to the removal of the specimen from the liquid nitrogen bath.

For a test temperature of -120°C, a prepared temperature-time calibration curve was used. To get the temperature-time curve, the specimen was kept in liquid nitrogen (-196°C) and the sample with a thermocouple was submerged in liquid nitrogen for 10 minutes, then put it above the cooled support rolls of the impact machine. a 'T' type thermocouple was connected with the specimen to measure the specimen temperature every 10 seconds. The temperature and temperature data were logged by the readout apparatus, facilitating the construction of the temperature versus time curves. The procedure was repeated several times in order to get an average temperature-time calibration curve. (As shown in Figure 4-9.)

For the actual test at -120°C, the specimen was first kept in liquid nitrogen, taken out, and placed in the impact test machine; an effort was made to do the impact test on the 28$^{th}$ second (derived from the temperature-time calibration curve).

For the temperatures of -100°C, -90°C, -80°C, -70°C, -60°C and -40 °C, mixtures of ethanol and liquid nitrogen were used as the cooling agent. The temperatures of the mixture were controlled to ±1°C. After the specimen achieved the desired temperature, it was soaked for 10 minutes and then proceed with the impact test within 4 seconds.

This study used a total of 105 CVN samples (52 for HT1 condition and 53 for HT2 condition).

### 4.3.3 Test Procedures

Based on the industrial test results previously obtained by Baowu Steel, the Ductile-to-Brittle Transition Temperature (DBTT) is anticipated to reside within the range of -80°C to -100°C. The quantity of test specimens designated for each temperature was judiciously selected in accordance with their proximity to the DBTT. The number of tests were increased when industrial test results suggested temperatures close to the ductile to brittle transition temperature.

Fifty-two test-pieces from HT1 condition and fifty-three test-pieces from HT2 condition were tested. Three tests for each condition were carried out at -196°C and three for each condition at -40°C to establish lower and upper shelf values. Six tests for each condition were carried out at temperatures of -60°C, -70°C and -120°C.

For HT1 condition, nine tests were carried out at -80°C, eight tests were carried out at -90°C and eleven tests were performed at -100°C. For HT2 condition, eight tests were carried out at -80°C, nine tests were carried out at -90°C and twelve tests were performed at -100°C.

### 4.3.4 Procedures for Data Analysis

Determination of the Ductile to Brittle Transition Temperature:

For typical ferritic steels, there are three regions for Charpy Impact Energy: the lower shelf region where the material exhibits fully brittle behaviour and the upper shelf region where the material behaves in a fully ductile manner. Horizontal lines at certain temperatures can represent these two regions. In between is the transition region where the material behaves partly brittle and partly ductile. A sigmoidal curve can represent this region as the transition behaviour occurs over a range of temperatures.

There are different methods for describing the ductile to brittle transition behaviour in steel. One is the nil ductility temperature (NDT) where the fracture surface becomes fully cleavage. Another is the fracture appearance transition temperature (FATT) where the temperature corresponding to half fibrous half cleavage on the fracture surface. The commonly used method also includes defining the temperature corresponding to an average impact energy value of 27 J. The same principal also is applied in the nuclear industry, where a temperature corresponding to 40 J is accepted. This study uses the Tanh fit curve to obtain the transition temperature.

Tanh Fitting of Charpy Impact Energy Data:

Statistical analysis is applied to the Charpy Impact energy results. In summary, general statistical modelling includes model formulation, estimation of model parameters and validation of the model, and it can be written as below for the Charpy Impact result:

$$CVN(T) = \overline{CVN}(T) + \epsilon\,(T) \qquad \text{Equation (4-1)}$$

There are two essential parameters for describing the statistical relationship:

$\overline{CVN}(T)$ shows the tendency of impact energy to vary with temperature in a systematic relation.

$\epsilon\,(T)$ shows the data scattering for the statistical model. (The component of variation)

Among many statistical models, the most widely accepted method, tanh fitting, is used in this study.

$$CVN(T) = A + B \tanh\left(\frac{T-T_0}{C}\right) \qquad \text{Equation (4-2)}$$

The tanh function takes the values from a (-1,1) interval; constants A and B are the scaling parameters. The energy value of A is the energy value that corresponds to the transition temperature.

$T_0$ is the location parameter that 'pins' the curve at a reference temperature. (DBTT)

$C$ is the gradient parameter.

The transition temperature (also in here $T_0$) is obtained from the tanh fitting curve.

The utilization of the hyperbolic tangent (tanh) method offers significant convenience in computational and analytical applications. However, there are limitations: Firstly, the symmetrical shape of this tanh curve limited the flexibility for describing the actual curve shape, as the natural impact energy curve is not necessarily symmetrical. Secondly, a slight change in starting values of the parameters will change the final curve. Thus, after the fitting curve is generated, care is needed to re-evaluate the physical meaning of the curve.

## 4.4 Tensile Testing

Tensile tests were carried out at -196 °C, -170 °C, -160 °C, -140°C, -120°C, -100°C, -80°C, and -60°C using procedures as defined in ASTM E8/E8M-16a.

The tensile tests carried out at –196 °C were tested on a Zwick Roell ZMART PRO screw-driven machine with the load capacity of 200kN. A heat-isolated tank filled with nitrogen (–196 °C) was attached to the machine. The specimens were immersed in a liquid nitrogen bath for at least 10 minutes before starting the tests. The obtained load and displacement data were converted into engineering stress-strain curves. No extensometer was attached for tests at –196 °C due to the limited space inside the nitrogen tank.

Tensile tests at other temperatures were carried out using a Denison Mayes Group (DMG) screw-driven machine with a calibrated load cell of 100 kN capacity. The temperature was controlled by an Instron environmental chamber with an accuracy of ±1°C which was connected to a pressurized liquid nitrogen vessel. The chamber temperature is controlled by the influx of the vaporised liquid nitrogen into the chamber. A built-in air fan was switched on to make sure vaporised nitrogen was distributed evenly. A separate thermocouple was attached to the specimen surface inside the chamber for accurate measurements of the test-piece temperature. The extension of the samples was monitored using an external extensometer with low-temperature capability, and the load was recorded from the calibrated load cell of 100 kN capacity. All tensile tests were carried out in displacement control mode and the crosshead displacement rate was controlled at 0.5 mm per minute. The tests were carried out under the standard procedure from ASTM E8/E8M-16a.

### 4.4.1 Tensile Specimen

The test specimens were prepared as standard tensile specimens of 10 mm diameter and a gauge length of 50 mm. The geometrical illustration is shown in Figure 4-10.

### 4.4.2 Analysis Procedures

The conversion of load-displacement curves into engineering stress-strain curves was performed, and subsequently, individual test results were plotted. Yield stress $\sigma_y$ were obtained from the engineering stress-strain curve at lower yield point stress value. Engineering stress and strain were obtained through expressions of the following:

$$s = P/A_0 \qquad \text{Equation (4-3)}$$

And

$$e = (L - L_0)/L_0 \qquad \text{Equation (4-4)}$$

Where, $s$ is the engineering stress. (Also known as nominal stress)

$P$ is the applied load.

$A_0$ is the original area.

$e$ is the engineering strain. (Also known as nominal strain)

$L$ is the gauge length, and $L_0$ is the original gauge length. True stress and true strain were obtained through expressions of the following:

$$\sigma_t = s(1 + e) \qquad \text{Equation (4-5)}$$

$$\varepsilon_t = \ln(1 + e) \qquad \text{Equation (4-6)}$$

Work hardening exponent ($n$) were obtained through expressions of the following:

$$\sigma_t = \mathrm{K} \cdot {\varepsilon_t}^n \qquad \text{Equation (4-7)}$$

Where $\sigma_t$ is the true stress.

K is the strength coefficient.

$\varepsilon_t$ is the true strain.

$n$ is work hardening exponent.

In order to get the work hardening exponent, the natural log will be applied, the work hardening region of the true stress-strain curve will be replotted as Ln σ verse Ln ε, where the slope of the curve will be calculated as $n$, and the intercept value will be calculated to get $K$.

$$\mathrm{Ln}\ \sigma = \mathrm{Ln}\ \mathrm{K} + n\mathrm{Ln}\ \varepsilon \qquad \text{Equation (4-8)}$$

## 4.5 Fracture Toughness Testing

The present study involved the conduction of fracture toughness testing, wherein the procedures outlined in the BS 7448 and ASTM E1820-15a testing standards were followed. The testing was carried out utilising a digitally controlled Denison-Mayes servo electric testing machine equipped with a 100 kN load cell. The test procedure used in this study was carried out by applying a monotonically increased load to the specimen at a controlled rate, continuously monitor load, notch mouth opening displacement and stable crack propagation. The point at which crack propagation becomes unstable is critical for determining fracture toughness. Record the load-displacement data and note the load at the onset of unstable crack growth. The test temperatures of -120°C, -100°C and -80°C were selected based primarily on the lower shelf to transition temperatures obtained from Charpy impact tests result. The temperature for this investigation was chosen to preserve the cleavage fracture to the steel under study.

### 4.5.1 Sharp-cracked Specimen

The present study employed compact tension specimens with a thickness of 25 mm as the designated specimen type. The specimens underwent machining with internal knife edges to enable the facile application of the clip gauge device, which was utilized to document the notch mouth opening displacement and load line displacement during loading. The configuration of the specimen is visually depicted in Figure 4-11.

### 4.5.2 Plane Strain Stress Intensity Factor $K_{IC}$

In compliance with the guidelines stipulated in BS 7448 and ASTM E1820 standards, the evaluation of plane strain stress intensity factor, denoted as $K_{IC}$, mandates the determination of a specific parameter, $K_Q$. This parameter serves as a requisite measure for ascertaining the material's resistance to crack

propagation under conditions of plane strain. If the test meets the requirements of the plane strain condition, then the provisional value of $K_Q$ will be accepted as $K_{IC}$.

The present investigation employed the Compact Tension Specimen as the primary experimental apparatus, wherein the dimensions of the specimen's width denoted by W and thickness denoted by B were interrelated in such a manner that B is equal to one-half of W.

The pre-cracking process was conducted in accordance with standard procedures. It is required that the length of the fatigue crack must be no less than 0.025 times the width of the specimen. Additionally, the ratio of the crack length to the width of the specimen, denoted as a/W, must fall within the interval of 0.45 to 0.55 as determined by post-fracture measurements.

Under the plane strain regime, it is imperative that the magnitude of the plastic zone at the point of fracture is significantly small in comparison to the dimensions of the specimen. From this requirement, it follows:

$$a, W - a, B \geq 2.5 \left(\frac{K_{IC}}{\sigma_y}\right)^2 \qquad \text{Equation (4-9)}$$

Where,

$B =$ Specimen thickness

$W, a =$ Specimen width and crack length

The provisional plane strain fracture toughness $K_Q$ for Compact Tension geometry is given as:

$$K_Q = (P_q / BW^{\frac{1}{2}}) \cdot f(a/W) \qquad \text{Equation (4-10)}$$

Where,

$$f\left(\frac{a}{W}\right) = \frac{\left(2+\frac{a}{W}\right)\left(0.886+\frac{4.64a}{W}-\frac{13.32a^2}{W^2}+\frac{14.72a^3}{W^3}-\frac{5a^4}{6W^4}\right)}{(1-a/W)^{3/2}} \quad \text{Equation(4-11)}$$

$P_q =$ Maximum load from the load diagram

### 4.5.3 Fatigue Pre-Cracking

The present study involved the fatigue pre-cracking of specimens at ambient temperature utilizing an Amsler Vibrophore machine. Throughout the fatigue cycle, a R ratio of 0.1 between the minimum and maximum loads was applied. At the final stage of fatigue crack propagation, the maximum stress intensity factor was maintained below 25 $MPam^{\frac{1}{2}}$.

When a specimen has been broken, the resultant crack length was precisely determined via examination of the fracture surface. This involved measuring not only the original crack length but also any observable stable crack extension that may have preceded the onset of brittle fracture. Crack length assessment was performed at nine equidistant points at the tip of the fatigue pre-crack. The adopted methodology entails calculating the mean of two measurements taken at the peripheral points and subsequently averaging this resultant value with the measurements ascertained from the seven interior points.

### 4.5.4 Procedures to Determine $K_{IC}$

The present study conducted fracture toughness testing utilizing the procedures as prescribed in the ASTM Standard E1820-17. After fatigue pre-cracking of the

specimens, a monotonically increasing load was applied to the specimen at a controlled rate to conduct the test. And the experimental investigations were conducted utilizing the plot generated from the load versus the notch mouth opening displacements. The notch mouth opening displacements were measured through the utilization of a clip gauge, which was strategically positioned upon the knife edges that accurately embedded in the specimens. The fracture load $P_Q$ is discerned from the plot and subsequently employed in the computation of $K_Q$.

The verification of $K_Q$ as a linear-elastic plane-strain fracture toughness $K_{IC}$ was conducted in accordance with ASTM Standard E399. This involves ensuring that the ratio of the maximum load $P_{Max}$ to $P_Q$ does not exceed 1.10. Additionally, the value of $2.5(K_Q/YS)^2$ (as delineated in Equation (4-9)) must be less than the ligament size $(W - a)$, where $YS$ denotes the 0.2% offset yield strength of the specimen at the testing temperature. The $K_Q$ value is considered a valid representation of $K_{IC}$ only if it meets both of these criteria.

Should $K_Q$ fail to satisfy the specified requirements, the elastic-plastic stress intensity factor $K_{JC}$ will be employed to characterize the condition at the crack tip. In this study, $K_{JC}$ was derived from the $J$-integral as follows:

### 4.5.5 Procedures to Determine J-Integral

When linear elastic fracture mechanics cannot be satisfied, the J-integral can be used to evaluate the crack-tip stress-strain condition.

$$J = J_{el} + J_{pl} \qquad \text{Equation (4-12)}$$

Where:

$J_{el} =$ elastic component of $J$, and

$J_{pl} =$ plastic component of $J$.

Following the ASTM E1820 standard method for the compact specimen:

$$J = \frac{K^2(1-\nu^2)}{E} + J_{pl} \qquad \text{Equation (4-13)}$$

Where $K$ is from Equation (4-10), with $a = a_0$, which is the initial measured crack size, and

$$J_{pl} = \frac{\eta_{pl} A_{pl}}{B_N b_0} \qquad \text{Equation (4-14)}$$

Where:

$A_{pl} =$ area under load-displacement curve corresponding to point studied.

$B_N =$ net specimen thickness ($B_N = B$ if no side grooves are present),

$b_0 =$ uncracked ligament, $(W - a_0)$, and

$\eta_{pl} = 2 + 0.522 b_0/W$

### 4.5.6 CTOD Measurement

Owing to the forthcoming computations associated with the microscopic cleavage fracture parameters that require the integration of the McMeeking FEM model, the measurement of CTOD becomes necessary. Furthermore, CTOD can also be employed as a benchmark for comparison with other steels. The CTOD values obtained in this study are derived from $J - Integral$ as follows:

$$CTOD = J/m\sigma_Y \qquad \text{Equation (4-15)}$$

And

$$\sigma_Y = (\sigma_{YS} + \sigma_{TS})/2 \qquad \text{Equation (4-16)}$$

Where:

$m =$ plastic constraint factor

$\sigma_y =$ effective yield strength.

$\sigma_{YS} =$ yield strength.

$\sigma_{TS} =$ ultimate tensile strength.

The plastic constraint factor, $m$, is an empirical parameter that varies with yield strength and ultimate tensile strength [90]:

$$m = 3.62 - 4.21\left(\frac{\sigma_{YS}}{\sigma_{TS}}\right) + 4.33\left(\frac{\sigma_{YS}}{\sigma_{TS}}\right)^2 - 2\left(\frac{\sigma_{YS}}{\sigma_{TS}}\right)^3 \qquad \text{Equation (4-17)}$$

### 4.5.7 Elastic-Plastic Stress Intensity Factor $K_{JC}$

In the present study, the elastic-plastic stress intensity factor $K_{JC}$ will be employed for investigative purposes. The rationale for utilizing $K_{JC}$ stems from previous industrial tested data provided by Baowu Steel, indicating that the toughness of this particular steel at low temperatures surpasses that of many other common steel types. Consequently, traditional $K_{IC}$ methods may be inadequate for capturing the material behaviour in such conditions. Thus, $K_{JC}$

has also been introduced to facilitate the characterisation of the stress intensity at the crack-tip even beyond the range that $K_Q$ or $K_{IC}$ can adequately describe.

$$K_{JC}=(E' \cdot J_C)^{1/2} \qquad \text{Equation (4-18)}$$

Where $E' = E/(1-v^2)$ for plane strain condition and $E' = E$ for plane stress condition, $E$ is Young's modulus of the material, $J_C$ is the critical J-integral value at the onset of unstable crack tearing.

### 4.5.8. McMeeking Analysis of Local Tensile Stresses

In order to obtain a stress analysis for the sharp-cracked specimens under tensile loading, the stress distribution analysis at a (blunted) crack tip proposed by McMeeking [91] was used in this study. The crack-tip shape and near-tip deformation field are taken into consideration. In McMeeking's finite element analysis, the stress distribution ahead of the blunt crack-tip can then be compared with the actual fracture initiation site (distance, $X_0$) measured on the fracture surface and the crack-tip opening displacement (CTOD), b.

In this study, the material studied is considered to be a power-law hardening material (work hardening exponent N=0.1 and 0.2) and $\frac{\sigma_0}{E} = 1/300$ in the McMeeking model. Figure 4-12 and Figure 4-13., are the plots of this stress and strain distribution around the blunted crack-tip. In these figures: $\sigma_{\theta\theta}$ is the true stress; $\sigma_y$ is the yield (proof) stress; R is defined for the position of material in the undeformed configuration; in this case, when $\theta = 0$, R is the mode I distance ahead of a blunted crack-tip, which at fracture is defined as $X_0$; and, b is the crack tip opening displacement CTOD.

Using the measured initiation sites with measured fracture toughness values, values of R/b for each specimen were obtained. These R/b values were used to obtain the $\sigma_{\theta\theta}/\sigma_y$ values read from McMeeking FEM curve. With a knowledge of the yield stress at each temperature, local failure values $\sigma_{\theta\theta}$ can be calculated.

## 4.6 Microscopic Cleavage Fracture Stress Testing

### 4.6.1 Blunt-notched Specimen

Shown in Figure 4-14, the specimen exhibits 12.7×12.7×80 $mm^3$ dimensions with a notch depth of 4.23 mm in the centre and two 1 mm depth notches at 31.75 mm away from the centre of each side. The radius ρ of the notch is 0.25 mm. The angle of the notch, denoted by φ is 45°.

As shown in Figure 4-15, The experimental procedure involved the application of a four-point bending load to the specimen, thereby facilitating a meticulous investigation on the manner in which the stress is distributed below the notch, as originally predicted by the Finite Element Method. [64]

### 4.6.2 Four Point Bend Test Set-up

The present investigation concerns the evaluation of the nominal stress $\sigma_{nom}$ of the fracture surface of specimens, based on the obtained maximum load P from the test:

$$\sigma_{nom} = \frac{3P(l_1 - l_2)}{2bh^2} \qquad \text{Equation (4-19)}$$

whereby the distance between two outer rollers is denoted as $l_1$, the distance between two inner rollers is denoted as $l_2$, and the width and height of the fracture surface are denoted as $b$ and $h$, respectively.

### 4.6.3 Temperature Control

The fracture stress tests were carried out at temperatures of -196 °C, -170 °C and -160 °C.

The four-point bending tests carried out at –196 °C were tested on a Zwick Roell machine. A heat-isolated container filled with liquid nitrogen was attached to the machine, for the specimen to be entirely immersed in the liquid nitrogen bath.

A DMG testing machine was used for testing at -170 °C and -160 °C, and the temperature was controlled by an Instron environmental chamber connected to a liquid nitrogen vessel. The temperature was controlled by an Instron low-temperature chamber which connected to a liquid nitrogen vessel. The chamber temperature was controlled by the influx of the vaporised liquid nitrogen into the chamber. A built-in air fan was switched on to make sure vaporised nitrogen was distributed evenly. A separate thermocouple was attached to the specimen surface inside of the chamber for accurate measurements of the test-piece temperature.

The experimental apparatus utilized for the present study involved the utilization of two different testing machines for specific testing temperatures, the machines were both operated in stroke control mode and the displacement rate were set at a constant value of 0.5 mm per minute.

### 4.6.4 Griffith-Owen FEM Analysis of Stress Distribution

The present study uses the Griffith-Owen finite element model's result [64], using the stress distribution below the notch root of the blunt-notched

specimens, for fracture loads that range from the general yield load to slightly beyond to conduct an estimation of the local fracture stress $\sigma_F$ at the point of fracture. The results of this analysis are depicted in Figure 4-16, where the lines represent the stress distributions under various loading conditions. With the specific testing load conditions, corresponding curves were plotted by the same method of Figure 4-16 shown.

With the corresponding curve, the highest point in each curve can be measured with a stress intensification $R_{max}$ value, using the equation below, maximum principal stress $\sigma_{yy}^{max}$ can be obtained:

$$\sigma_{yy}^{max} = R_{max} \cdot \sigma_y \qquad \text{Equation (4-20)}$$

Where $\sigma_y$ is the yield stress of the studied steel, and it will be obtained from tensile test results.

The initiation of the cleavage crack is not necessarily confined to the point of maximum intensification. Using the corresponding curve plotted and accurate fracture distance $X_0$ (The distance between the point of initiation of cleavage and the root of the notch was measured and recorded as $X_0$), the microscopic parameter $\sigma_F$ can be determined using the local $R$-value at the precise location $R_{(X_0)}$. By Equation (4-21), the local cleavage fracture stress at initiation site $\sigma_F$ can be obtained where $\sigma_F = \sigma(X_0)$.

$$\sigma_F = \sigma(X_0) = R_{(X_0)} \cdot \sigma_y \qquad \text{Equation (4-21)}$$

Where $\sigma_y$ is the yield stress of the studied steel.

## 4.7 Fractography and EDX Analysis for All Mechanical Test Specimens

After each test was finished, broken specimens were cleaned with acetone and stored safely with desiccants. If there are unbroken specimens such as in fracture toughness tests, following the completion of data recording and the cessation of tests, the specimens were subjected to fatigue cracking. Subsequent to this process, both the original crack length and the final crack extension of the broken specimen halves were measured using a Keyence VHX7000 Digital Microscope.

Detailed fracture surface examinations such as fracture distance measurement and initiation identification were done using a Hitachi S 4000 Field Emission Gun scanning electron microscope operating at an accelerating voltage of 20 kV, a Philips XL30 Field Emission Gun Environmental Scanning Electron microscope, equipped with qualitative Energy Dispersive X-ray Spectroscopy (EDX) system, and a Jeol 6060 Electron microscope, equipped with an Oxford Inca EDX system, were used at an accelerating voltage of 20 kV. The qualitative EDX technique has been used to analyse the observed inclusion at dominant cleavage fracture initiation sites as well as some inclusions found on fracture surfaces of local cleavage initiation sites.

The general and specific characteristics of the initiation site feature on the fracture surface such as initiation reason, chemical composition and fracture facet size were identified. In blunt-notched specimens, the distances from the notch root edge to the initiation site of cleavage micro-crack were measured from the specimen fractured surfaces and marked as fracture distance $X_0$. In sharp-cracked specimens, the distances from the end of ductile crack extension to the initiation site of cleavage micro-crack were measured and marked as

fracture distance $X_o$. In sharp-cracked specimen fracture surfaces, the extensions of stable crack were measured.

# Chapter Five – Material Microstructure and Charpy Impact Tests

## 5.1 Material Microstructure

### 5.1.1 Microstructure

The microstructures of the material in HT1 and HT2 conditions are shown in Figure 5-1 to Figure 5-3. From both optical microscopy and electron microscopy, it appears that both HT1 and HT2 microstructures are of the granular bainitic type. After etching with a nitric acid-alcohol solution, the bainitic ferrite is more susceptible to etching, appearing indented and displaying a grey-black colour under scanning electron microscopy (SEM). Conversely, the austenite is less affected by etching, appearing more protruding and exhibiting a grey-white colour under SEM.

With large volume of granular bainite morphology, the microstructure consists of irregularly shaped grains of ferrite, with the second phase (possibly retained austenite) distributed throughout in a globular manner. It lacks the distinct plate-like or needle-like structure of classic bainite.

There is very limited difference in grain size between HT1 and HT2, however, some difference is seen from the precipitate distribution and the morphology of the precipitates. HT2 have possibly carbide precipitates at the bainitic ferrite grain boundaries, comparing with HT1, the precipitates exhibit more distinct shapes and a greater extent of precipitation, and are well-distributed.

Then the final product appears as granular bainite with a number of carbides precipitating along the ferrite grain boundary and inside the grain in both HT1 and HT2 conditions. Possible martensite-austenite constituents are in the microstructure as well (labelled in Figure 5-3).

### 5.1.2 Grain Size Measurement Result

The overall grain sizes (mainly bainitic ferrite grain size) appear to be very similar for the two heat treatments. The result of the average grain diameter of the analysed HT1 and HT2 metallography specimens was measured as 14 μm and 15 μm respectively.

Grain size was measured based on the bainitic ferrite grain boundaries, utilizing the line-intercept method on SEM images for an approximate estimation of the grain size.

### 5.1.3 Inclusion Size Distribution

The inclusion was distinguished using the Backscattered Electron (BSE) mode of the electron microscope, as depicted in Figure 5-4 (A) and (B). The dark, globular morphology identified in the image corresponds to the inclusion, which has been verified through multiple Energy Dispersive X-ray (EDX) analyses, examples of EDX analysis was in Figure 5-6 (a) and (b).

From polished HT1-23 and HT2-23 samples, 50 equally spaced areas were examined, and a backscattered image was taken from each area. The results from two samples added up to 100 images and typical images are shown in Figure 5-4 (A) and (B) with the illustration of threshold setting examples using by ImageJ software. The inclusions can be found with the help of differences in contrast between matrix and inclusions via grayscale thresholding (inclusions exhibit dark compared with matrix). The threshold was controlled so that only an equivalent circular diameter larger than 0.4 μm can be measured. Inclusion chemical composition was also checked with EDX analysis to confirm the chemical composition.

The inclusion size distribution result from metallography analysis prepared from HT1 and HT2 samples cut from Charpy specimens with the longitudinal direction is shown in Figure 5-5 (a). The HT1 and HT2 combined distribution is shown in Figure 5-5 (b).

### 5.1.4 Inclusion Chemical Analysis

Chemical analysis of inclusions was conducted on the polished surface utilizing Energy-Dispersive X-ray Spectroscopy (EDX) to examine the elemental composition of the inclusions present. In Figure 5-6 (a) and (b), typical polished surface inclusion compositions are shown. Results give calcium, aluminium, titanium and sulphur to be present in the inclusions. The inclusions can be mainly divided into two groups, one is the calcium containing spherically shaped inclusions and the other one is titanium containing cubic shaped inclusions.

## 5.2 Charpy Impact Test Results

### 5.2.1 Charpy Impact Energy

Charpy impact energy values for HT1 and HT2 conditions are summarized in Table 5-1 and Table 5-2.

The impact energy plots with the temperature of HT1 and HT2 conditions are shown in Figure 5-7 and Figure 5-8, respectively. The combined plot is presented in Figure 5-9.

The comparison of the two conditions presented in Figure 5-9 reveals a minimal difference in the Charpy impact energy at temperatures above -80 °C and below -100 °C. The ductile to brittle transition region appears to be narrow, within the temperature range of -80°C and -100°C.

At the temperature of -100°C, most specimens showed low impact energy in both HT1 and HT2 conditions. At the temperature of -70°C, all specimens showed high impact energy, indicating upper shelf behaviour. At the temperature of -80°C, an apparent separation behaviour can be seen in the distribution of impact energy values in both conditions; most specimens showed upper shelf behaviour; however, one out of nine specimens showed lower shelf behaviour. The separation is more pronounced at -90°C for the HT1 condition; there were five out of nine specimens showed upper shelf behaviour, and four showed lower shelf behaviour. At -90°C for HT2 condition, the separation was less severe.

In summary, the impact energy values shown in Table 5-1, Table 5-2, and Figure 5-9 indicate a sharp ductile-to-brittle transition behaviour in both HT1 and HT2 conditions around -80°C to -90°C.

### 5.2.2 Ductile to Brittle Transition

At the temperature above -60 °C, the material behaviour is fully ductile with micro-void coalescence as the fracture micro-mechanism. When temperature was reduced to around -110 °C, the material changes into brittle behaviour, cleavage was seen as the fracture micro-mechanism. In terms of Charpy impact energy, the impact toughness exhibits high values from 250 J to 300 J at the upper shelf region compared with 2 J to 36 J at the lower shelf. For the

specimens tested in the transition temperature region, both micro-void coalescence and cleavage occurred in the same specimen, and the impact toughness exhibits value somewhere between the upper and lower shelf values. Then the ductile to brittle transition region can be roughly determined from the temperature between -110 °C to -60 °C.

### 5.2.3 Tanh Fitting of Charpy Impact Energy Data

The tanh fitting curves corresponding to HT1 and HT2 condition impact test results are presented in Figure 5-10 and Figure 5-11 respectively. The combined tanh fitting curve was plotted in Figure 5-12. The transition temperature value was measured, and a minimal difference was shown in the two condition transition temperatures. (-91°C for HT1 compared with -87°C for HT2)

### 5.2.4 Charpy Impact Test Fractography

5.2.4.1 General Information of Fracture Surface Overview

Fracture surfaces of all tested samples with information on Charpy impact energy (CVN) with cleavage area percentage (CA), lateral expansion (LE) and the ductile thumbnail (DT) were measured and listed in Table 5-1 and Table 5-2. Overviews of tested Charpy impact specimens with information of cleavage area percentage (CA) and lateral expansion (LE) are presented in Figure 5-13 and Figure 5-14.

On the lower shelf, the Charpy specimens exhibits a 'shiny' appearance on the fracture surface. 'River patterns' are usually found on cleavage facets; by tracing back the river lines, cleavage initiation can sometimes be identified.

From Figure 5-15, the measured cleavage area percentage is strongly related to the Charpy impact energy, where higher impact energy corresponds to a lower cleavage area measured from the fracture surface.

A strong relationship is also seen in the Charpy impact energy with lateral expansion from Figure 5-16. With higher impact energy, more lateral expansion is usually seen.

From Figure 5-17, the correlation between ductile thumbnail and Charpy impact energy can be seen, and generally a larger ductile thumbnail extension value corresponds to a higher Charpy impact energy value.

5.2.4.2 Detailed Information on Cleavage Initiation

Fourteen specimens exhibiting cleavage morphology were selected for detailed examination of their fracture surface features. Among these, six specimens initiated from inclusions, five initiated from the matrix, and three initiated from matrix-related features. Detailed fractography images are given in Figure 5-18 to Figure 5-31.

Table 5-3 gives the summary of the fourteen selected Charpy impact specimen fracture initiation feature information. Fracture distance $X_o$ , cleavage initiation reason with size, first facet size and ductile crack growth extension measurements are included in the table.

From the fourteen measured initiation sites, fracture distance $X_o$ is in the range from 229 μm to 693 μm, the initiator diameter is in the range from 1.6 μm to 2.7 μm, first facet diameter is in the range from 24 μm to 54 μm. The ductile crack growth extension is in the range of 23 μm to 3803 μm.

5.2.4.3 Initiation Reason

For the determination of initiation reasons in Charpy specimens, it is typically the case that only one half of the fractured specimen is observed. Without confirmation from the matching half, it is not possible to confirm initiation reasons, such as inclusions cracking or decohering. However, for six out of

fourteen of the selected Charpy specimens that failed under cleavage fracture, the presence of inclusions at initiating sites is clear.

## 5.3 Charpy Impact Test Discussion

### 5.3.1 Upper Shelf Charpy Test Behaviour

From Figure 5-15, it is observed that the Charpy specimen failing at around 250J exhibited a cleavage area percentage of 20%. For the specimen failing at 300J, the cleavage area percentage was reduced to zero. Fractography reveals that the ductile fracture region of Charpy specimens exhibits the micro-void coalescence (MVC) mechanism.

The generally accepted process for micro-void coalescence mechanism consists of three stages, which include nucleation of micro-void by second phase particle debonding or cracking from the matrix, strain-controlled micro-void growth under plastic flow (work hardening has a huge influence in this stage as it indicates the amount of energy needed for extension) and coalescence of micro-voids by necking between adjacent micro-voids or different micro-void linking together.

Charpy specimens exhibiting an impact energy of approximately 300J are predominantly fully ductile. Due to the limitations of the testing machine's capacity, which can only measure up to 300J, the Charpy specimens did not fracture completely during testing. Instead, they were separated after the impact testing while ensuring the preservation of the fracture surfaces. Regarding the upper shelf Charpy impact energy value, data obtained from Baosteel's in-house laboratory indicate a value of around 320J, suggesting that the transition curve should be slightly elevated and the transition temperature should be slightly increased. Utilizing the same hyperbolic tangent fitting

method (tanh fit), the derived temperatures for actual transition temperature are higher: the ductile to brittle Transition Temperature (DBTT) for HT1 is determined to be -70 °C, while for HT2, it is -64 °C.

### 5.3.2 Ductile to Brittle Transition

From Figure 5-10 and Figure 5-11, it is noted that only a few specimens failed within the 50J to 200J range, where the ductile-to-brittle transition is expected to occur. Although numerous tests were conducted at -80°C, -90°C, and -100°C, most specimens failed either on the upper or lower shelf.

From Figure 5-12, the tanh curve generated from both populations shows a sharp transition from the upper shelf to the lower shelf. The transition temperature interval is only around 20°C and falls within the range of -80°C to -100°C.

This phenomenon is expected since ferritic steel typically exhibits a sharp change in fracture mechanism, where the material behaviour transitions from ductile to brittle rapidly if the working temperature falls below the ductile-to-brittle transition temperature. The ductile to brittle transition in ferritic steel is influenced by various factors such as grain size and other microstructural factors [92]–[95], specimen geometries or dimensions [96]–[98], and loading rates [94], [98].

### 5.3.3 Fractography and EDX Analysis

Table 5-3 shows a summary of measured fracture surface features of Charpy specimens. The initiator was identified as a clear feature with measurable sizes, not only inclusions were identified as initiator, non-inclusion related or matrix related features are also considered as initiators, this is the same principle also to the following blunt-notched and sharp-cracked specimen analysis.

In most specimens, fracture distances and first facet sizes can be measured because the cleavage initiation point can be traced back from river patterns. Most initiator sizes can be obtained by measuring the area of the initiator feature and then calculating an equivalent diameter. However, not all initiators can be obtained, especially when the initiation comes from the matrix or in the case when it is not measurable. There are 14 specimens where a clear initiation site was identified, results are shown in Table 5-3, and detailed fractography results can be found in Figure 5-18 to Figure 5-31

### 5.3.4 Charpy Impact Energy Relationship to Cleavage Area, Lateral Expansion and Ductile Thumbnail Extension.

The cleavage area refers to the region of the fracture surface where brittle cleavage initiated. It is typically characterized by a smooth and flat fracture surface, often with a distinctive "chevron" pattern that indicates the direction of crack propagation. The cleavage area is an indicator of the material's susceptibility to brittle fracture. The size and location of the cleavage area can provide important information about the specimen's fracture behaviour and susceptibility to brittle failure. Figure 5-15 shows the good correlations between cleavage area percentage with the Charpy impact energy in both HT1 and HT2 conditions.

The lateral expansion is the amount of plastic deformation that occurs on the side of the specimen opposite to the notch during fracture. It is the distance between the original width of the specimen and the maximum width of the shear lip. The lateral expansion is an indicator of the material's ability to deform plastically and absorb energy during the fracture process at the tested temperature. In Figure 5-16, a good correlation is also seen between the lateral expansion and the Charpy impact energy in both HT1 and HT2 conditions.

Ductile crack growth behaviour in Charpy specimen shows a 'thumbnail' appearance, thus in Charpy specimens, ductile thumbnail extension is often considered a certain term and it is used to describe the ductile crack extension of the Charpy test-piece. It is also the result of the stable crack growth during the test, indicating the material's ability to absorb energy during the ductile fracture. By measuring the extent of how much ductile crack travels (the amount of the extension) before the unstable cleavage fracture takes place from post-fractured specimen surfaces, important information of the material's ability to resist fracture can be obtained. If the material is ductile, the stable crack can travel significantly before final fracture, and the ductile thumbnail extension is large. If the material is brittle, it may fracture before any significant ductile cracking occurs, and the resulting ductile thumbnail extension is small. As can be seen from Figure 5-17, with increasing ductile thumbnail extension, there is a trend of Charpy impact energy increase. Significant scattering occurs in the higher value region, mainly the region with Charpy impact energy from 150J to 250J. In this region, at relatively similar impact energies, there can be relatively substantial differences in ductile thumbnail. The correlation between ductile thumbnail extension and Charpy impact energy is clearer in the lower value region than in the higher value region.

### 5.3.5 Charpy Impact Test Analysis at Lower Shelf Region

5.3.5.1 The Relationship between Charpy Impact Energy and the Ductile Thumbnail Extensions

Figure 5-32 illustrates the relationship between Charpy impact energy and temperature, delineating the sampling range of the test specimens selected for detailed characterization of cleavage fracture. Samples demonstrating cleavage fracture were specifically chosen for an in-depth examination of their fracture surface features.

Figure 5-33 depicts the relationship between ductile thumbnail extensions in Charpy specimens, selected from the lower shelf region, and their Charpy impact energy at temperatures of -196°C, -120°C, -90°C, and -100°C. The trend shown in this figure confirms the good correlation between ductile thumbnail extension with Charpy impact energy especially at the lower shelf to transition region. In this region, the ductile thumbnail also can be seen as an indication of the material's ability to resist crack propagation.

5.3.5.2 The Relationship between Charpy Impact Energy, Initiator Sizes, and First Facet Sizes

Figure 5-34 shows the relationship between Charpy impact energy values and initiator diameters. Initially, it is observed that initiator diameters fall within the range of 1.5 to 3.0 μm.

Figure 5-35 presents the relationship between Charpy impact energy values and the first facet diameters. Here, it can be seen that the first facet diameters fall within the range of 20 to 60 μm.

5.3.5.3 The Relationship between Initiator Sizes and First Facet Sizes

Figure 5-36 illustrates the relationship between the first facet diameter and the initiator diameter. The results suggest that there appears to be a correlation between the size of the initiator and the size of the initial facet. Generally, with a larger initiator, a larger initial facet can be expected.

Nevertheless, the presence of a larger initiator or first facet does not necessarily correlate with increased absorption of impact energy. This observation may imply that the relationship between initiation characteristics and Charpy impact energy is more complex than what is delineated by the current method of investigation.

## 5.4 Conclusions

5.4.1 The Charpy impact toughness ranges from 2J to 299J, corresponding to test temperatures from -196 °C and -40 °C, respectively. The ductile to brittle transition region was between -100 °C to -80 °C, where a sharp increase of impact energy can be seen from 12.5J to 298J. The ductile to brittle transition temperatures for HT1 and HT2 conditions are estimated at -91°C and -87°C, respectively, based on the Tanh model fit.

5.4.2 From the fracture surface measurement of Charpy specimen halves, the increased lateral expansion and decreased cleavage area percentage are strongly related to the Charpy impact energy and test temperature.

5.4.3 From lower shelf temperatures to ductile to brittle transition temperatures, for tested Charpy impact specimens, the cleavage initiation reason is most likely to be the same, which is initiating from the cracking of calcium or titanium-based inclusions.

5.4.4 Regarding the Charpy impact test results, very similar results were seen in HT1 and HT2 heat treatment conditions.

# Chapter Six –Tensile, Fracture Toughness and Microscopic Cleavage Fracture Stress Tests

## 6.1 Tensile Test Results

A total of 30 specimens were tested at temperatures from -196°C to -60°C, 15 samples from each of the two heat-treatment conditions. For each condition, three specimens were tested at -196°C; one was tested at -170°C and one was tested at -160°C. Two specimens were tested at each temperature of-140°C, -120°C, -100°C, -80°C and -60°C.

Among 30 tests, seven tests were interrupted deliberately before the final fracture as they experienced cracking in the centre of the specimen along the loading axis after the attainment of the maximum load plateau. The loading process was ceased when the crack at the specimen surface along the loading axis could be visually confirmed. The engineering stress-strain curves of selected tensile tests were presented in Figure 6-1 and Figure 6-2.

### 6.1.1 Lower Yield Stress and Ultimate Tensile Strength

Apart from the seven intentionally terminated test specimens, the other 23 specimens were tested to fracture.

For tests performed at temperatures at -196°C, only small work hardening (average n=0.1) was found, and as a result, the ultimate tensile stress was only slightly higher than the yield stress. For instance, an average of 952 MPa of UTS compared with 927 MPa yield stress from HT1 condition. Moreover, an average of 947 MPa of UTS compared with 927 MPa yield stress from HT2 condition. For tests conducted at -120°C and higher temperatures, the ultimate tensile strength becomes much larger than the yield stress.

The tensile testing results for both HT1 and HT2 conditions are summarised in Table 6-1 and Table 6-2. The lower yield stress, ultimate tensile strength (UTS) and work hardening exponent values are shown in these tables.

The yield stresses and the ultimate tensile strengths for the two heat treatment conditions showed similar trends even though HT2 consistently exhibits a marginally lower value compared to the results for HT1. Shown in Figure 6-3, the yield stress for the HT1 condition showed a value of an average 563 MPa at -60°C to 927 MPa at -196°C. In the meantime, the yield stress for HT2 condition increases from an average 535 MPa at -60°C to 927 MPa at -196°C. In terms of the ultimate tensile strength, seen from Figure 6-4, it changes from average 654 MPa at -60°C to 952 MPa at -196°C in HT1 condition and from 640 MPa at -60°C to 947 MPa at -196°C in HT2 condition.

### 6.1.2 Work Hardening Exponents

The work hardening can have an important effect on the fracture behaviour of steels and the work hardening exponent is an important parameter affecting the stress state ahead of the stress concentration factor such as a sharp crack. [91]

The work hardening exponent values have therefore been calculated from engineering stress-strain curves and are listed in Tables 6-1 and Table 6-2 for HT1 and HT2 conditions, respectively.

For n values at -140°C, -120°C, -100°C, -80°C and -60°C, load-displacement response was obtained using an extensometer attached to the specimen, the load-displacement curves were then converted into engineering stress-strain and true stress-strain curves. The work hardening exponent n is derived from the slope of the linear relationship in a plot of natural logarithm of true stress versus natural logarithm of true strain at the uniform plastic deformation region (Figure 6-5 and Figure 6-6). The result gives a work hardening exponent at a value of around 0.15 at temperatures from -140°C to -60°C (Figure 6-7).

The work hardening result did increase the complexity in the cleavage mechanism analysis, as the existing McMeeking [91] finite element analysis model is available based on individual work hardening exponents of n=0, n=0.1 or n=0.2. This result of work hardening exponent might suggest an analysis considering n=0.1 and n=0.2 results as upper and lower bound.

### 6.1.3 Tensile Specimen Fractography

Some typical fracture surfaces of tested tensile specimens are shown in Figure 6-8 to Figure 6-10. At -196°C, Figure 6-9, which shows the fracture surfaces of HT1-01, reveals very similar characteristics of quasi-cleavage. In Figure 6-10, which depicts the fracture surface of HT2-03, a large proportion of cleavage fracture is evident from both optical and SEM images. At a temperature of -120°C, the fracture surface is dominated by cleavage, but slight necking of the specimen diameter is visible, suggesting some extent of ductile failure. From -80°C and above, the tensile fracture surface start to show “star” shape, which possibly indicates a large amount of ductile deformation taking place.

## 6.2 Summary of Tensile Test Results

6.2.1. The tensile tests give results of lower yield stress, ultimate tensile stress and work hardening exponent n. The overall results show very subtle differences between the two heat-treatment conditions. Despite the fact that the yield stress and the Ultimate tensile strength of HT2 are consistently exhibits a marginally lower value than those of HT1.

6.2.2 Yield stress results of -196°C, -170°C will be used in the blunt-notched test analysis. And yield stress, ultimate tensile strength, work hardening exponent results of -120°C, -100°C and -80°C will be used in the sharp-cracked test analysis. As the McMeeking FEA results in the following discussion are only

available for work hardening exponents of 0.1 and 0.2 and the estimated work hardening exponent appear to be around 0.15, both n=0.1 and n=0.2 conditions of analysis will need to be analysed.

## 6.3 Fracture Toughness Test Results

### 6.3.1 Load-Displacement Curve Results

The load-displacement curves of the fracture toughness test carried out from sharp-cracked specimens are shown in Figure 6-11. First of all, linear behaviour is seen in the initial stages of loading, where small increments in load produce proportionate increments in displacement. In this phase, elastic behaviour prevails, and the material can return to its original form when unloaded. However, as the material reaches and surpasses its elastic limit, the load-displacement relationship becomes non-linear. This non-linearity reveals that plastic deformation is occurring alongside elastic deformation, and irreversible changes in the material are taking place. The non-linearity in a load-displacement curve during the J-integral fracture toughness test is indication of material behaviour transitioning from elastic to plastic responses.

With the help of the load-displacement curve, $K_Q$ and the J-integral can be accurately calculated, as previous shown in Equation (4-10) and Equation (4-11) the $K_Q$ is measured from the peak load $P_Q$ and the crack size $a$; from Equation (4-12) to Equation (4-14) the J-integral is measured as $J_{el} + J_{pl}$, where $J_{pl}$ is the area under the load-displacement curve beyond the yielding point up to the point of crack initiation.

For the J-integral test, the non-linearity is especially significant because the J-integral is an energetic measure designed to account for such complex material

behaviour. As the material undergoes plastic deformation, a significant portion of the mechanical energy input is irreversibly absorbed by the material. This energy contributes to the total energy release rate, which the J-integral aims to quantify.

From Figure 6-11, it's observable that as the temperature increases from -120°C to -80°C, the peak load tends to increase as well.

### 6.3.2 Fracture Toughness Calculations

The results of the fracture toughness tests conducted on twenty-seven 1T C(T) samples are summarised in Table 6-3 and Table 6-4.

#### 6.3.2.1 $K_{IC}$ Validity.

Following on Equation (4-9), there are four valid $K_{IC}$ tests based on the ASTM E1820 requirements. For the other tests that did not fulfil the $K_{IC}$ requirement, they were analysed using the elastic-plastic stress intensity factor $K_{JC}$.

#### 6.3.2.2. Results of J-integral, CTOD and $K_{JC}$

Based on Equation (4-12) to Equation (4-14), the J-integral was calculated at the point of fracture for each specimen. CTOD was calculated by Equation (4-15) to Equation (4-17) and $K_{JC}$ was calculated by Equation (4-18) based on the result of J-integral results. The $K_{JC}$ value versus temperature as well as $K_Q$ value versus temperature plots were present in Figure 6-12 and Figure 6-13.

Confirming from Table 6-3 and Table 6-4, both **J-integral** and the Crack Tip Opening Displacement (**CTOD**) values vary significantly with temperature, confirming the notion that temperature plays a crucial role in the fracture mechanics of this steel. J-integral values increase with temperature for both HT1 and HT2 specimens. Higher J-integral and CTOD values at -80°C compared to -120°C possibly indicate increased ductility or a transition from a brittle to a ductile fracture mechanism.

The variability in J-integral values also appears to increase with temperature, particularly for specimens tested at -100°C, indicated by a wider spread of the J-integral values from 17 to 218 $kJ/m^2$ compared with J-integral ranges from 15 to 55 $kJ/m^2$ at -120°C.

### 6.3.3 Fractography

6.3.3.1 Quasi-Cleavage Fracture

The fracture toughness test procedure is to ensure Mode I fracture toughness is able to be quantified, with shear stress kept to a minimum. However, with the CT specimen geometry, shear stress may not be entirely negated. The low-constraint condition in a sharp-cracked compact tension specimen has a great chance to enable the quasi-cleavage mode of fracture. Unlike pure cleavage fracture which occurs along specific crystallographic planes [99], [100], quasi-cleavage fracture often shows ridges or terraces and may appear wavy at the microscopic level, the appearance can be seen in almost all fracture surfaces of sharp-cracked specimens, e.g. Figure 6-14 to Figure 6-39.

The extent of morphological changes on the surface of sharp-cracked specimens is closely related to temperature. As the temperature shifts, these specimens exhibit varying degrees of morphological alteration. Specifically, the changes observed at -120 °C are generally less marked compared to those at -100 °C. Evaluating these changes, particularly from the perspective of surface morphology, is subjective, as there is currently no established quantitative standard. However, a notable correlation exists between these morphological variations and the magnitude of the J-integral. This correlation is exemplified in Figure 6-16, Figure 6-32, Figure 6-36 and Figure 6-37, which shows several typical examples with corresponding J-integral values of 55.4 $kJ/m^2$, 64.9 $kJ/m^2$, 36.1 $kJ/m^2$ and 86.2 $kJ/m^2$. In these examples, the J-integral values

are among the highest within their specimen categories, and the features of quasi-cleavage are more prominently displayed.

#### 6.3.3.2 Cleavage Initiation in Sharp-Cracked Specimens

In the present study, a total of twenty-seven compact tension specimens were subjected to fracture toughness testing. Of those, only one specimen, designated as HT2-24 and tested at a temperature of -80°C, lacked an identifiable initiation site. The remaining twenty-six specimens exhibited discernible global initiation sites responsible for initiating cleavage fracture. Comprehensive details pertaining to these twenty-six fracture initiation sites are listed in Table 6-5.

#### 6.3.3.3 Dominant Initiation Site and Local Initiation Site

From the observation of the fracture surfaces, it is often found that there are several cleavage sites from a single specimen Based on the observed variations in cleavage initiation morphologies, it can be inferred that a single dominant initiation site, manifesting a significant cleavage affected area on the fracture surface, governs the global fracture behaviour of the specimen. Other observed initiation sites serve merely as localized cleavage initiation points. River patterns emanate from both dominant and localized initiation sites within the fracture surface. The key distinction between the localized and dominant site lies in their respective zones of influence; for the dominant initiation site, the impact on the fracture surface is more extensive, thereby wielding a greater influence over the overall cleavage process. It is often the case that it can be seen that the river pattern went across the whole specimen.

For all specimen investigated, there is a dominant initiation site which governs the cleavage. However, the local cleavage initiation sites such as the cases found in Figure 6-30 (e), Figure 6-32 (e) and Figure 6-37 (e) are also on the fracture

surface and could be potential competitors if the dominant initiation site fails to initiate the global cleavage fracture.

#### 6.3.3.4 Cleavage Initiation Reason

To ascertain the underlying cause of initiation, Energy Dispersive X-ray (EDX) analysis was employed. When both corresponding fracture surfaces exhibited identical inclusion compositions, this was designated as inclusion cracking, signifying that the inclusion had cracked into two distinct halves.

In instances where only one-half of the fracture surface displays an inclusion composition while the opposing half manifests a void-like feature, the phenomenon is categorically labelled as inclusion decohesion.

#### 6.3.3.5 Information of Cleavage Initiation and Fracture Distance

Table 6-5 provides a comprehensive summary of the fracture initiation characteristics for the 26 sharp-cracked specimens. Incorporated within the table are variables such as the fracture distance $X_o$, cleavage initiation reason with sizes, first facet sizes and stable crack extension measurements. Complementary fractographic imagery for each test specimen is delineated in Figures 6-14 to 6-39, combined with the Energy-Dispersive X-ray (EDX) spectroscopic data corresponding to the initiation sites.

From the 26 measured initiation sites, fracture distance $X_o$ is in the range from 21 μm to 657 μm, the ductile crack growth extension is in the range from 2 μm to 70 μm. The initiator diameter is in the range from 0.6 μm to 3.2 μm, and the first facet diameter is in the range from 20 μm to 46 μm, with the majority of facet diameters come down to 20-40 μm in 23 out of 26 measurements.

#### 6.3.3.6 Information on All Initiators

Figure 6-40 and 6-41 gives the size distribution of all initiators and the size distribution of solely inclusions.

There are 5 initiation sites related to matrix cracking, although the location and fracture distance can be measured the initiator is not able to be measured. 16 specimens initiated from inclusions. For the remaining 5 initiators, related to possibly carbides or martensite-austenite constituents, their sizes can be estimated using equivalent diameter by measuring their area.

6.3.3.7 Detailed Information on Inclusions

Both halves of the broken fracture toughness samples were examined. There are 16 specimens where fracture initiated from a calcium, aluminium and titanium inclusion. Clearly, there were 15 out of 16 specimens where initiation is due to inclusion cracking. Only 1 (HT1-1) out of 16 specimens initiated because of inclusion decohesion.

The majority (11 out of 16) of inclusion sizes fall into the region of 1 to 2 μm. From fractography, the inclusions can be divided into two different types, calcium-based inclusions often present as a spherical shape, and titanium-based inclusions often present as a cubic shape with sharp edges.

Within the set of 16 initiating inclusions, 11 are characterized as spherical in shape and are predominantly associated with calcium. The equivalent diameters of these calcium-based inclusions range from 0.7 to 2.5 μm. Conversely, five inclusions are categorized as cubic in shape and are principally associated with titanium. The dimensions of these titanium-based inclusions are as follows: 1.0, 1.5, 1.6, 1.7, and 1.8 μm, respectively.

### 6.3.4 McMeeking FEM Analysis Results

Using the measured fracture distance values (R in McMeeking analysis) with measured fracture CTOD values (b in McMeeking analysis), values of R/b for

each specimen were obtained and listed in Table 6-7 (n=0.1) and Table 6-10 (n=0.2). These R/b values were used to correspond to the $\sigma_F/\sigma_y$ values read from McMeeking FEM curves. With a knowledge of the yield stress at each temperature, local failure values of $\sigma_F$ were calculated and listed in Table 6-6 (n=0.1) and Table 6-9 (n=0.2).

The present study reveals that most of the sites of initiation, as determined from the fractured sample surfaces, are situated in close proximity to, or surpassing, the location of the maximum tensile stress. Four out of twenty-six samples with initiation sites far ahead of the peak stress location with an R/b value larger than 10, exceeding the limits of the graph provided in Figure 4-12 and Figure 4-13. In order to make the analysed result comparable, the $\sigma_F/\sigma_0$ values corresponding to the R/b values larger than 10 were obtained by extrapolating the existing graph of McMeeking's and estimated values were obtained and summarized in Table 6-7 (n=0.1) and Table 6-10 (n=0.2).

There is a natural increase in uncertainty regarding the local stresses at these remote sites, but extrapolation beyond the limits of Figures 4-12 and Figure 4-13 is anticipated to result in an even shallower stress gradient and so estimates made are likely to be reasonable.

## 6.4 Microscopic Cleavage Fracture Stress Test Results

### 6.4.1 Specimens Valid from the FEM Analysis

The load-displacement curves of these seven tests were presented in Figure 6-42.

Among all the tested specimens, only seven specimens failed within the general yield limit predicted by the FEM model of Griffiths and Owen. They were six tests at the temperature of -196°C and one (HT2-04) at the temperature of -170°C.

### 6.4.2 Fractography

A comprehensive analysis of the fractographic features has been conducted on the blunted-notched specimens of both halves of the fractured surfaces. Detailed fractography images are shown in Figure 6-43 to Figure 6-49. Examination of the blunt-notched specimen fracture surfaces involved identifying the location of the cleavage initiation and measurement of the initiation features (non-metallic inclusions and other possible features) from the notch root $X_o$. EDX spectrums of the initiation inclusions were also presented with the fractography images.

A single failure initiation site led to the overall specimen failure for the specimen studied. The initiation site was traced back after the river lines across large cleavage facets. The empirical findings have evinced that the sites of initiation were consistently situated at some distance beneath the notch root. Moreover, the precise distances from the initiation sites to the notch root, denoted as $X_o$, were able to be measured. The result of $X_o$ is listed in Table 6-12, together with the measurements of inclusion diameter and the cleavage facet diameter.

### 6.4.3 Microscopic Cleavage Fracture Stress Test Results

Table 6-13 gives the fracture stress test results and maximum principal stress $\sigma_{yy}^{max}$ at fracture.

Using the method described in Chapter four, the calculated maximum stress intensification factor $R_{Max}$ was found to be in the range of 1.98 to 2.55, with the maximum principal stress ranging from 1835 MPa to 2076 MPa.

Table 6-14 gives the local cleavage fracture stress $\sigma_F$ at the distance of $X_o$ measured from fracture surfaces using SEM.

An estimated curve corresponding to each specific test result of $L/L_{GY}$ was plotted, (estimated curves were not shown) according to the fracture distance $X_0$ measured from each specimen, the local stress intensification $R_{(X0)}$ can be obtained from the curve. Then local cleavage fracture stress was calculated based on the $R_{(X0)}$ value.

The result of local stress intensification $R_{(X0)}$ is slightly lower than the maximum stress intensification, with the result range from 1.81 to 2.44.

6.4.3.1 Results from Griffith-Owen FEM Analysis

Stress distributions ahead of a blunt notch were evaluated using results generated by Griffiths and Owen FEM analysis. [64] The analysis is not dependent on the work hardening exponent. This analysis is used to interpret the experimental results obtained using blunt-notched specimens. The Griffith-Owen analysis gives a comprehensive analysis of the location of cleavage fracture initiation sites in relation to the stress intensification factor $R$, the fracture distance $X_0$ below the notch tip to the initiation point, at various loads. The analysis was conducted with a notch root radius of 250 μm, as in the original Griffith-Owen work. The results based on the FEM analysis are depicted in Figure 6-50, which demonstrates the relevant cleavage fracture initiation sites plotted against the aforementioned stress intensification factor R.

Six results were located at the left side of the maximum principal stress of the corresponding curve, while one is at the right side of the maximum principal stress of the corresponding curve. For the result on the right-side, it may because of its $L/L_{GY}$ is much lower than other test results and the initiator size is only 1.1 μm. However, it is difficult to say which factor has the largest influence on the relative position against the maximum principal stress.

From the Griffith-Owen analysis result of seven blunt-notched specimen tests, the values of the local stress intensification ratio, $R_{(X_0)}$, were measured. Then the local cleavage fracture stress was calculated and presented in Figure 6-51 with measured fracture distances $X_0$.

The FEM result of the test stress intensification R is in the range from 1.81 to 2.44. Combined with the yield stress reported in Section 6.1, the local cleavage fracture stress is calculated to vary from 1678 MPa to 2039 MPa.

### 6.4.4 Cleavage Initiation Reason

EDX analysis was used in this study to determine the cleavage fracture initiation. Cleavage initiation sites were generally analysed on both fracture surfaces of a broken sample. If the cleavage fracture was initiated by an inclusion and an EDX analysis of the inclusion initiation site resulted in the same (or very similar) chemical composition, the cleavage fracture was deemed to be initiated by the cracking of an inclusion. If an inclusion was found at the initiation site on only one fracture surface, and a void was observed at the matching location on the other fracture surface, the cleavage initiation was deemed to be caused by the inclusion decohesion.

### 6.4.5 Cleavage Initiation Feature

The sizes of the cleavage initiators identified in all seven specimens are summarized in Table 6-12. In addition to the size of the initiating feature, the cleavage facet sizes corresponding to the cleavage initiators were also measured, and the results are shown in the same table.

Cleavage fracture in four out of seven samples was initiated by an inclusion, while in three samples the fracture initiated from a matrix-related (non-inclusion) feature.

The sizes of these inclusions are 1.6 μm, 1.8 μm, 2.6 μm, and 2.6 μm; the sizes of matrix-related initiators (possibly M-A or carbides) are estimated to be 1.1 μm, 1.8 μm, and 2.6 μm. The EDX analysis on inclusions showed they were all calcium containing inclusions.

From the seven measured initiation sites, the fracture distance $X_o$ ranges from 220 μm to 420 μm, the initiator diameter varies from 1.1 μm to 2.6 μm, and the first facet diameter spans from 20 μm to 34 μm.

## 6.5 Fracture Toughness Test Discussion

### 6.5.1 Load-Displacement Curve

The bulk mechanical properties response to the loading of the material has been plotted in Figure 6-11. At a test temperature of -120 °C, the load-displacement response is generally linear for all specimens. At the test temperature of -100 °C and -80 °C, linear behaviour is seen in the initial stages of loading, where small increments in load produce proportionate increments in displacement. In this phase, elastic behaviour prevails. However, as the material reaches and surpasses its elastic limit, the load-displacement relationship becomes non-linear. This non-linearity reveals that plastic deformation is occurring alongside elastic deformation, and irreversible changes in the material are taking place.

### 6.5.2 Stress Intensity Factor $K_Q$, $K_{IC}$ and $K_{JC}$

$K_Q$ is known as the provisional fracture toughness and is essentially an experimental measure of fracture toughness for a specific specimen and loading conditions. However, it must be ascertained whether $K_Q$ can be considered as

a valid approximation of $K_{IC}$. This is evaluated by meeting certain size criteria, stated as Equation (4-9) to ensure that plane strain conditions prevail.

$K_{IC}$ is the plane-strain fracture toughness, considered a material property independent of specimen geometry, when tested under plane strain conditions. $K_{IC}$ is widely regarded as a critical material parameter for design in fracture mechanics. It is typically used for brittle materials or ductile materials that operate at lower temperatures or higher strain rates, where conditions favour plane-strain fracture.

$K_{JC}$ is the fracture toughness in terms of the J-integral, specific to ductile materials. It's based on elastic-plastic fracture mechanics, which gives it the ability to account for both the elastic and plastic deformations near the crack tip. $K_{JC}$ is employed in conditions where extensive plastic deformation is present, and when $K_{IC}$ no longer remains valid.

The results indicate that the fracture toughness values ($K_Q$ and $K_{JC}$) exhibit a dependency on the temperature, being generally higher at -80 °C compared to -120 °C. $K_Q$ and $K_{JC}$ values against temperatures of -120 °C, -100 °C and -80°C are drawn in Figure 6-12 and Figure 6-13; There is a clear trend that with elevated temperature, $K_Q$ values remain roughly the same but the $K_{JC}$ values are increased significantly, which indicates the extents of the plastic deformation increases with higher temperatures.

### 6.5.3 Plastic Zone Sizes

$K_Q$ based calculation assumes Linear Elastic Fracture Mechanics (LEFM) conditions, whereas $K_{JC}$ based calculation is used under Elastic-Plastic Fracture Mechanics (EPFM) conditions. $K_Q$ is generally used for brittle materials or conditions where plastic deformation is limited, while $K_{JC}$ is applicable to ductile materials where plasticity plays a significant role.

By assuming that the plastic zone is a circular region around the crack tip then according to Equation (3-9), the nominal plastic zone and true plastic zone sizes can be estimated by taking $K_Q$ and $K_{JC}$ value into the equation. The results are listed in Table 6-7 and Table 6-10, for McMeeking analysis of n=0.1 and n=0.2 conditions respectively. In all tested and measured specimens, the cleavage initiation sites were always located well within both the nominal and true plastic zone.

In addition to this, using the measurements of these two physical quantities $K_Q$ and $K_{JC}$, one can make comparative assessments between the nominal and actual sizes of the plastic zone in the specimens. It can be explicitly gauged comparing the sizes of the plastic zones for the characterisation of the degree of plastic deformation. Specifically, a specimen that generates a larger plastic zone would be less compliant with Linear Elastic Fracture Mechanics (LEFM) and, correspondingly, would necessitate a description using Elastic-Plastic Fracture Mechanics (EPFM).

It is imperative to articulate that the primary objective of this study is to provide a precise description of the micro-mechanical processes involved in cleavage, and to correlate these with discernible physical quantities. Therefore, parameters including the size of the plastic zone, the J-integral, and quantified measurements of stable crack extension possess substantial physical relevance within this framework. Following this, the study attempts to delineate the relationship between the J-integral and stable crack extension.

### 6.5.4 J-integral Relation with Measured Stable Crack Extensions

The $J$-integral values were plotted against measured stable crack extension at the fracture surface from different specimens. In this section, due to the inherent correlation between the $J$-measured stable crack extension ($J$-$\Delta a$)

curve and the generalized $J$-resistance curve ($J-R$) curve, the analysis is conducted by juxtaposing the characteristics of both the $J$-$\Delta a$ and the general $J$-$R$ curves.

Generally, the $J-R$ curve is a graphical representation that captures the relationship between the $J$-integral, (an energy release rate), and the stable crack extension $\Delta a$. The $J$-$R$ curve captures the material's ability to resist crack propagation during stable crack growth. Usually, different J integral and stable crack extension were measured from a single test from several unloading sequences. The curve is used to characterize the fracture toughness of materials, offering insights into how the material will behave after a stable crack has initiated. In the physical aspect, a higher J-integral suggests a stronger stress field capable of extending the crack further. [101][102]

From Figure 6-52, firstly, a **linear** correlation can be seen, where a larger stable crack extension is correlated with a greater energy release rate at the crack-tip ($J$-integral). In a general $J$-$R$ curve, if the resistance to crack extension remains relatively constant, that will indicate a direct linear correlation between crack growth and the energy release. While a non-linear $J$-$R$ curve suggests that the material's resistance to crack propagation changes with the extension of the crack. Next, the J-integral and stable crack extension in this figure is closely related. Among different temperatures, the tread shown in this figure is largely the same from -80 °C to -120 °C, which confirms that the material's ability to resist crack propagation is not changed in this temperature range.

An essential aspect observed in Figure 6-52 is the significance of the lower and upper bounds of the measured values for stable crack growth extensions. This range is critical as it represents the conditions under which the material is anticipated to undergo cleavage. At the temperature of -120 °C, the stable crack extension ranges from 3 μm to 14 μm, at -100 °C, the stable crack extension ranges from 2 μm to 70 μm.

It is worth noting that the **largest** stable crack growth is less than 70 μm, and the **average** stable crack growth for tested specimens at -120 °C, -100 °C and -80 °C are 6, 17 and 44 μm respectively. These values could be difficult to precisely obtain from conventional stable crack size determination methods.

Furthermore, a benefit from the direct measurements of $J_C$, $K_{JC}$, and the stable crack size '$\Delta a$' at the time of fracture, data obtained from this study is that they are considered more accurate for description of stable crack size compared to conventional methods that employ unloading compliance, wherein compliance is converted into crack size. [90] The traditional and standard approach is less reflective of the real case, particularly when ductile cracks are sufficiently small, making it difficult to accurately calibrate the position of the onset of cleavage or the stable crack size using unloading compliance load-displacement curves alone. This discrepancy also arises from the difference in scale: conventional experimental apparatus typically measures on the millimetre scale, while fractography measures in this study was on the order of micrometres.

For a general $J$-$R$ curve, there is an intersecting point between the $J$-$R$ curve and the $y$-axis [90], which naturally corresponds to a critical J-integral value. However, in Figure 6-52, the $J$-$\Delta a$ curve does not intersect with $y$-axis. The lower bound value for stable crack growth is extracted directly from the curve itself. Specifically, at a temperature of -80 °C, the lower bound for stable crack growth is found to be 34 μm. Similarly, at -100°C, the lower bound is ascertained to be 2 μm and at -120°C, the lower bound is 3 μm. The physical meaning is that from 26 tested results, there is always stable crack growth prior to the cleavage initiation. This could give evidence to show that plastic deformation is a precursor condition for cleavage initiation.

For a general $J$-$R$ curve, the point where the curve begins usually corresponds to the initiation of stable crack growth. $J_{IC}$ is often used as the indication of the point. This $J_{IC}$ value serves as a quantifiable measure of the material's resistance to the initiation of ductile fracture. Which is to say that the value $J_{IC}$ is identified as the $J$-integral value at the onset of stable crack growth, often at the lower bound of the non-linear region of the $J$-$R$ curve. $J_C$ measured in this study, is the onset of unstable crack extensions (cleavage fracture initiation).

In order to provide sufficient safety margins for engineering materials, the quantification of stable crack growth extension can be difficult to measure and monitor under real-world conditions. However, the J-integral could be more readily determined in certain geometries and operational scenarios. The $J_C$ integral represents the energy release rate at the crack tip at the onset of brittle fracture. Consequently, in this chapter, the range of $J_C$ integral values at varying temperatures of this investigated material have been delineated. This delineation effectively defines the ranges within which global cleavage fracture occurs. This could provide a robust methodology for identifying the initiation of cleavage fracture by monitoring the changing of the J-integral of material in operation. Specifically, data obtained from this study gives the result that the J-integral ranges are 71-156 $kJ/m^2$ at -80°C, 17-86 $kJ/m^2$ at -100 °C (except for HT1-01, which registered at 218 $kJ/m^2$), and 15-55 $kJ/m^2$ at -120 °C which does indicate the material is susceptible to cleavage at these J integral ranges of the corresponding temperatures. For large-scale machinery in practical applications, maintaining the J-integral below the lower bound of these identified ranges could serve as a proactive strategy to minimize the occurrence of cleavage initiation.

The general $J$-$R$ curve offers insights into the material's behaviour subsequent to stable crack initiation, while the curve presented in this context elucidates

the relationship between unstable crack initiation and the $J_C$ value. In some respects, both types of graphs offer their own unique value. Moreover, the curve of $J$-$\Delta a$ could be considered even more rarefied due to the increased challenges associated with obtaining this specific data.

### 6.5.5 The Importance of Fracture Distance $X_0$

6.5.5.1 The Relationship Between J-integral and the Fracture Distance $X_0$

The $J_C$ integral, representing the J-integral at the onset of specimen cleavage fracture, carries distinct physical significance. Likewise, the parameters fracture distance $X_0$ and the stable crack size $\Delta a$, which are quantifiable characteristics directly related to the material's current state, correlate with the intrinsic physical properties of the material. Consequently, these measurements are of significant importance for a detailed interpretation of the material's mechanical behaviour.

The $J_C$ relation with measured onset of unstable crack growth distance (fracture distance $X_0$) is plotted in Figure 6-53. First of all, the scatter of the location of cleavage initiation is seen from the figure, at the same J-integral and same temperature, the fracture distance $X_0$ can be largely different. Then, although fracture distance $X_0$ result is largely scattered, $X_0$ is still slightly increased with the $J_C$ value. As it can be seen from the figure, two trends (slopes) can still be seen from the figure at -80 °C and -120 °C, the data from -100 °C is distributed into the two slopes of -80 °C and -120 °C.

The range of $X_0$ at a temperature of -120 °C spans from 21 μm to 657 μm, with an arithmetic mean value of 139 μm. At a temperature of -100 °C, the $X_0$ range is observed to be between 53 μm and 655 μm, with an average of 245 μm. For the two specimens measured at -80 °C, the $X_0$ values were found to be 295 μm and 486 μm, yielding a mean value of 395 μm. The mean value difference

repeatedly confirmed that the $X_0$ distribution conspicuously increases with temperature. This corroborates, from a thermal perspective, that the relationship between $X_0$ and $J_C$, is positively correlated. That is to say, in regions where the crack-tip energy release rate is higher, $X_0$ correspondingly increases.

At the same fracture distance $X_0$, the energy release rate at -120 °C will be higher. Take an example of two data points at around 300 μm in Figure 6-53. The two data points at -80 °C and -120 °C around 300 μm gives a $J_C$ value difference of around 50 $kJ/m^2$. This may suggest that there could be an inherent potential energy within the material that contributes to significant variations in the initiation of cleavage at different temperatures. Specifically, at -120 °C, the material may accumulate enough potential energy to exhibit a more pronounced tendency toward initiation even when the fracture distance ($X_0$) remains the same. This hypothesis can be substantiated by comparing the $X_0$ values at a constant critical energy release rate ($J_C$). By treating $J_C$ as an indicative measure of the material's inclination towards cleavage, it can be inferred that the propensity for cleavage initiation intensifies at lower temperatures, as evidenced by the increasing magnitude of $J_C$ values.

Understanding the $J–X_0$ relationship allows for more accurate safety margins in engineering components, particularly where brittle fracture is a major concern. Also, the $J-X_0$ relationship can be used as a material selection criterion for applications where cleavage fracture is a critical failure mode. Then in the material selection criterion, it is essential to understand the J integral relationship with the lower and higher bounds of $X_0$ due to the implications for safety.

6.5.5.2 The Relationship Between Stable Crack Extensions and the Fracture Distances $X_0$

Furthermore, due to the strong correlation between the J-integral and stable crack growth (Figure 6-52), as evidenced by a given correlation coefficient ($R^2 = 0.95$), it can also be inferred—perhaps even directly plotted as $X_0$ against stable crack extension (Figure 6-54)—that greater stable crack extension leads to a more extensive fracture distance $X_0$. It is worth stating again, the $X_0$ is measured starting from the end point of stable crack extension to the onset of unstable crack extension.

6.5.5.3 The Relationship Between the True Plastic Zone Size and the Fracture Distances $X_0$

The fundamental rationale for the observed phenomena for fracture distance $X_0$ with $J_C$ or stable crack extensions can be also clearly elucidated by considering the directly proportional relationship between the fracture distance $X_0$ and the size of the true plastic zone. Specifically, empirical observations indicate a positive correlation between the two: from Figure 6-55, as the size of the plastic zone expands, $X_0$ correspondingly shifts further away from the terminal location of the stable crack.

In certain analytical theory frameworks, notably the RKR model [65], the $X_0$ fracture distance is anchored to a critical value ascertained by a localised fracture criterion. Within this specific model, $X_0$ serves as a characterizing distance, connecting macroscopic and microscopic scales in fracture mechanics.

According to the Ritchie-Knott-Rice (RKR) model, cleavage is initiated when the stress at a critical distance ahead of the crack tip surpasses the material's

tensile strength. Empirical evidence from initial studies on coarse-grained mild steel suggested that this characteristic distance may approximate two grain diameters to facilitate an unstable cleavage fracture. However, later research has not substantiated a uniform correlation between this critical cleavage distance and the grain size.

Currently, measurements of the J-integral at the onset of cleavage fracture in sharp-cracked specimens are rather scarce, as are measurements of the local fracture distance on the tested specimens. This scarcity stems from the necessity of conducting measurements on multiple specimens. Traditional J-integral testing typically relies on single specimen assessments employing the unloading compliance method. Such methodologies are predominantly effective for the ductile domain of the tested materials and seldom executed at temperatures favourable for the observation of predominantly cleavage behaviour.

### 6.5.6 Tensile Stress Control Fracture Criterion

Figure 6-56 and Figure 6-57 illustrate the stress distributions based on McMeeking's analysis using the measured fracture distances $X_0$ and CTOD values of 26 sharp-cracked specimens.

In order to analyse the local cleavage behaviour, the local cleavage fracture stress was compared with the maximum principal stress ahead of the blunted crack tip. From Figure 6-58 and Figure 6-59, the relative percentage of local cleavage fracture stress compared to maximum principal stress under both n=0.1 and n=0.2 conditions are plotted and it can be seen that the local cleavage fracture stress values are relatively close to the position of maximum principal stress.

According to Table 6-7 and Table 6-10, it can be seen that there are only two specimens, HT2-03 with R/b value of 1.7 and HT2-07 with R/b value of 1.07, where the fracture initiation locations are located before the maximum principal stress location (R/b=2) along the stress distribution curve. The majority (24 out of 26) are located beyond the maximum principal stress location.

Figure 4-12 and Figure 4-13 give the original McMeeking FEM analysis results of stress and strain distributions for n=0.1 and n=0.2, respectively. From these two figures, it can be seen that before the location of the maximum principal stress, the strain distribution shows that strain is much higher than at a distance further beyond the location of maximum principal stress. Most significant in this analysis the peak values of tensile stresses (and strains) are not predicted to change as the CTOD (or stress intensity factor, K) increases, but rather they move forward then extend over a greater absolute distance. Thus, when a fracture site is found and compared with the peak position of local tensile stress, if it is shown to be before the current position (based on the applied CTOD/K at failure) then at this position it would have seen a higher local tensile stress at a lower value of applied CTOD/K and if under tensile stress control then it must fail. This is the reason why the fracture taking place before attaining the maximum principal stress places doubt on a purely tensile stress-controlled failure criterion. However, when the failure location is beyond the maximum principal stress position, failure occurs when this site first experiences a high enough local stress to promote failure. This is consistent with a purely tensile stress-controlled failure criterion with a local stress trying to find a potent enough initiation site through sampling as the low stresses sweep out with increasing applied CTOD/K. Thus, in the current study the vast majority (25 out of 26 in n=0.2 condition and 24 out of 26 in n=0.1 condition) of fracture

sites support a purely tensile stress-controlled failure criterion, as has been suggested for several decades.

### 6.5.7 Local Cleavage Fracture Stress Compared with the Maximum Principal Stress

In Table 6-6 and Table 6-9, the $\sigma_F/\sigma_{Max}$ value is listed, indicating the relation of the local cleavage fracture stress to the maximum principal stress. Additionally, the plastic zone sizes are listed in Table 6-7 and Table 6-10

The calculated $\sigma_{\theta\theta}/\sigma_{Max}$ value is in the range of 78% to 99% for McMeeking analysis of n=0.1 and in the range of 65% to 99% for McMeeking analysis of n=0.2.

Researchers have been discussing the conditions for microcracks to propagate, the microcrack propagation is typically occurring under sufficient stress and within the plastic zone of the loaded specimen ahead of the notch root or pre-crack tip.

Bowen have shown in a A533B steel [66], the area with most possibility of cleavage fracture is within 95% of the maximum principal stress. Bose has shown in a HSLA steel of blunt-notched specimen, there were 19 out of 49 specimens with a local cleavage fracture stress higher than 90% of the maximum principal stress, and another 19 out of 49 specimens had a local cleavage fracture stress lower than 90% of the maximum principal stress but still in the plastic zone. [103] Farron has shown in a material of MnMoNi steel that cleavage initiated reasonably close to the maximum principal stress and within the area covered by 85% of the maximum principal stress.[104]

Among 26 test results in this study, if 95% maximum principal stress is used as the criterion for predicting cleavage fracture, 11 specimens have measured local stress values that are greater than 95% maximum principal stress under the condition of n=0.1 and 6 specimens have measured local stress values that are greater than 95% maximum principal stress under the condition of n=0.2.

If 85% maximum principal stress is used as the criterion for predicting cleavage fracture, 21 out of 26 specimens having $\sigma_{\theta\theta}/\sigma_{Max}$ values greater than 85% for the McMeeking analysis of n=0.1 and 14 out of 26 specimens having $\sigma_{\theta\theta}/\sigma_{Max}$ values greater than 85% for the McMeeking analysis of n=0.2.

### 6.5.8 Local Cleavage Fracture Stress in Different Steel Microstructures

The material investigated in this research is a type of high strength low alloy steel with large amount of granular bainite microstructure. The local cleavage fracture stresses from blunt-notched specimen tests were in the range from 1835 MPa to 2076 MPa at temperatures from -170 °C to -196 °C, and the result from sharp-cracked specimen tests at temperature from -80 °C to -120 °C was in the range from 1870 MPa to 2478 MPa under the condition n=0.1 in McMeeking analysis and 2053 MPa to 3267 MPa under the condition n=0.2 in McMeeking analysis. The results are worth comparing with the reported results from T.Saario [105] where local cleavage fracture stress from a ferritic and bainitic steel CrMoV at 75 K to 200 K was tested which result from 1700 MPa to 2250 MPa for blunt-notched tests and 2250 MPa to 3000 MPa from sharp-cracked tests. Although this study considered carbide distribution as the controlling factor for the cleavage process, the local cleavage fracture stress results are still very similar to the current study.

For pearlitic steel microstructures, Alexander [106] has shown that at -90 °C the local cleavage fracture stress was in the range from 1100 MPa to 1400 MPa,

and Li [107] showed that for a pearlitic eutectoid steel, the local cleavage fracture stress is in the range from 900 MPa to 1200 MPa for four heat-treatment conditions of the same material. Linaza [108] has calculated the local cleavage fracture stress of ferritic-pearlitic steels varies from 1050 MPa to 2160 MPa.

For Martensitic steel microstructures, Linaza [108] has obtained the local cleavage fracture stress from SENB specimens of a pure and tempered martensitic steel from 2250 MPa to 3550 MPa. Virginia [109] recently has estimated the nominal stress was from 1800 MPa to 3000 MPa ahead of SENB specimens at -100 °C for a tempered bainitic and martensitic steel microstructure. Similarly, the microstructural link was found as (Mg, Al, Ca) (O, S) and (Nb, Ti) (C) inclusions.

Although the initiation reason and type of initiator are all different, it still can be seen that local cleavage fracture stress is expected to be higher in bainitic and martensitic steels. This comparison shows that the local cleavage fracture stress is very likely to be strongly linked with the matrix microstructure.

A considerable volume of empirical evidence suggests that the inherent characteristics or the intrinsic strength of the matrix cannot be overlooked. While investigators have endeavoured to identify 'potent' particles, it is increasingly evident that these may span a range of sizes. Importantly, the size distribution is predominantly governed by the characteristics of the existing matrix which is related with the cleavage facet size.

### 6.5.9 Active Cleavage Initiation First Facet Size Distribution

Regardless of whether particles are situated inside the grain or along the grain boundaries, the resulting facets generated upon cleavage transform a finite distance of the surrounding grain on the same cleavage plane into a cleavage facet. Consequently, the dimensions of these facets serve as a critical parameter governing the fracture mechanism within the material. Therefore, provided that the facet size can be accurately determined, it assumes greater significance than the grain size in governing the dynamics of the cleavage process and acts as a primary microstructural parameter.

With respect to the association with local cleavage fracture stress, the correlation coefficients for both initiator and facet diameters remain suboptimal, as depicted in Figure 6-60 and Figure 6-61. However, it is noteworthy that the correlation between the first facet diameter and local cleavage fracture stress exhibits a marginally superior R-squared value of 0.24, as opposed to an R-squared value of 0.1 observed in the initiator diameter with local cleavage fracture stress result (with the McMeeking analysis conducted at n=0.1). This outcome intimates that the local cleavage initiation mechanism is not solely modulated by the initiator dimensions; rather, the size of the first facet serves as a significantly influential parameter. Consequently, it may be inferred that facet dimensions exert a greater impact on local cleavage initiation than do initiator dimensions by just comparing the R-squared values. In this study of 26 sharp-cracked specimens, the first facet diameter ranged from 20 μm to 46 μm, with the majority of facet diameters falling between 20-40 μm in 23 out of the 26 measurements.

For many researchers [110]–[113], the correlation with initiator and the facet will determine the critical event of micro-crack nucleation [113], [114] or micro-crack propagation. [115], [116] This thesis was carried out by assuming the critical event is an initiator sized micro-crack nucleation. From the evidence in this chapter, the critical event is more likely to be related with both the initiator

sized micro-crack and the adjacent facet. Consequently, the initiation of cleavage is most plausibly controlled by a synergistic interplay between a potent initiator and its corresponding facet.

For the discussion of the relationship between particle size and grain size, it was also reported from other researchers [117] that in the cleavage initiation process, a critical particle size might exist for a given steel microstructure. The particle size and grain size were combined into one graph, Figure 6-62. It was suggested that in cleavage of a Ti-containing high strength low alloy steel mainly containing ferrite and pearlite, a one-to-one correspondence between the critical size of initiator and the critical size of the grain exists, thereby supporting the assertion in this thesis that a range of facet sizes is closely related to the range of active initiators. Unlike the approach that considers a singular value, namely the critical size, and identifies grain size as the crucial microstructural parameter, this thesis correlates the active size range of the initiator with the facet size, directly regarding the latter as the primary microstructural parameter in cleavage.

### 6.5.10 Active Global Cleavage Initiator Size Distribution

It can be seen from Figure 6-40, for all cleavage initiators (both inclusions and matrix related), 95% of initiators are sized below 3 μm. If inclusions alone are considered (Figure 6-41), 100% (16 out of 16) of inclusion initiators sizes are below 3 μm.

It is worth comparing inclusion size distribution with the general inclusion distribution of the material. Figure 5-5 (a) and Figure 5-5 (b) show the inclusion distribution from metallography analysis prepared from HT1 and HT2 samples cut from Charpy specimens in the longitudinal direction. In both HT1 and HT2 conditions, the majority of inclusions found on polished surfaces are below 3 μm. The smallest initiator was found to be a matrix related feature with a diameter of 0.6 μm, and smallest inclusion initiating fracture had a diameter of 0.7 μm.

An important point to be noticed here is that in all fractured surfaces of sharp-cracked specimens, the largest initiator size on the fracture surface is 3.2 μm as a matrix related initiator, and the largest inclusion size is 2.5 μm. However, it is clear that in the polished metallographic specimen result, there is a distribution of inclusion sizes larger than 2.5 μm, to be precise, from 2.5 μm to 8 μm.

Generally speaking, because the percentage of large-sized (3 μm and larger) inclusions is low within the material, the likelihood of sampling these inclusions can be very low compared to sampling inclusions smaller than 3 μm.

Nevertheless, if the sampling effect can be neglected, with the condition that the fracture stress does not vary significantly and the probability of sampling inclusions of various sizes is assumed to be equal, then the absence of large-sized inclusions perhaps implies that the very largest-sized inclusions are inactive in this cleavage process.

Some supporting evidence can be found in other researcher's work [108]. The fractographic analysis showed in their material that TiN particles act as the cleavage initiator. However, in the majority of the cleavage cases, the originating cleavage initiated from TiN sized from 2 to 6 μm, far less than the largest TiN size population of 12 μm. This work also shows that there is an 'active inclusion size range' in the cleavage initiation process.

According to the weakest link theory [118], and the Weibull volume effect introduced from Equation (3-31), the larger the particles, the smaller the stress that is required to break it. However, in the research from Linaza [108], it is reported that the coarsest particles do not invariably act as the most deleterious entities in the material. The reason is very likely to be these particles may fracture at stress levels insufficient to instigate cleavage propagation across the particle-matrix interfaces.

### 6.5.11 Local Cleavage Initiation Sites at Fracture Surfaces

Figure 6-30 (e), 6-32 (e), and 6-37 (e) illustrate typical examples of localised cleavage initiation sites. Across these examples, it becomes evident that within a comparable fracture distance, an inclusion can function as a localised site for cleavage initiation. However, only those initiations that are capable of facilitating micro-crack propagation across the entire specimen will predominate in the overall cleavage mechanism and contribute to the whole sample failure. Such localized initiations sites serve as potential contenders in the global cleavage fracture initiation process, with the primary distinguishing factor between a dominant and a non-dominant initiation residing in the favourability of their respective conditions.

If the inclusion sizes are outside of the active size range, the chance of global cleavage initiation will be largely decreased. However, it still can initiate local cleavage fracture. These can be found at the fracture surface below the ductile crack end, the wavy appearance of fracture surface are local cleavage initiation sites, they are believed to initiate at the almost the same time, leading to the fracture surface of an irregular topography or the undulating surface.

### 6.5.12 Global Cleavage Initiator and Inclusion Elemental Analysis

#### 6.5.12.1 Global Cleavage Initiator and its First Facet Size Relationship

Firstly, from the first facets size alone, comparing the facet size where non-inclusion initiated and inclusion initiated, there was no clear evidence showing the facets differed in size or nature.

Secondly, based on the relationship between all initiator sizes and first facet sizes in Figure 6-63, the detailed relationship must be complex, with the fact that a range of initiator diameters can be observed at the same first facet diameter. Also, within the same initiator size, there exists a range of first facet sizes. However, a very weak correlation between the initiator and facet size is still conceivable in general.

#### 6.5.12.2 Inclusion Type and the J-integral Relationship

In some recent works [109], researchers did find evidence that in a largely bainitic microstructure, the (Mg, Al, Ca) (O, S) oxides triggered fracture were related to the highest CTOD values, among all oxides, carbides, nitrides, and niobium-rich inclusions. The niobium-rich inclusions that triggered fracture were related with the lowest CTOD. Consequently, the research substantiated that niobium-rich inclusions exhibit a more detrimental effect.
In this thesis, findings consistent with those reported in recent studies were not observed. The initiating inclusions identified were exclusively oxide inclusions, specifically calcium-based spherical oxide inclusions or titanium-based cubic inclusions. Furthermore, calcium and titanium were frequently found to co-exist, with no significant distinction in their respective J-integral values.

However, this research did observe in the only specimen (HT1-01) where inclusion decohesion was identified as the cause of initiation, that the J-integral value (and consequently, the CTOD value) was the highest among all specimens examined. The highest J-integral value, indicating the largest plastic deformation, suggests that cleavage fracture could potentially be delayed if

initiation is supplanted by inclusion decohesion instead of inclusion cracking. Many researchers believe that the relationship between inclusion decohesion and cracking is competitive. [119]–[121] So it may be feasible to consider enhancing low-temperature toughness by making inclusion decohesion more favourable at lower temperatures [122], if the quantity and size of inclusions remain relatively unchanged.

#### 6.5.12.3 Inclusion Decohesion and Inclusion Cracking Initiation

Within all 16 inclusion related initiation events, the result of 15 cracked inclusion compared with only one decohered inclusion firstly indicates that for cleavage to initiate widely for the whole specimen to fracture, the probability of finding a cracked inclusion is significantly higher than finding a decohered inclusion as the global initiation site for the whole specimen.

Second and more importantly, it may imply that inclusions are more likely to crack than to decohere in cleavage fracture at -120 °C, -100 °C, and -80 °C, which suggests that the interface strength between these inclusions and the matrix is greater than the stresses required to break the inclusion. Therefore, when the stress concentration progressively builds up at both the inclusion-matrix interface and inclusion itself, inclusion cracking is more likely to occur due to its lower energy and stress required.

For the specimen where initiation was from inclusion decohesion (HT1-01), the inclusion's chemical composition was primarily calcium and aluminium. The inclusion diameter, measuring 1.1 μm, was not different from that of the cracked inclusions. The first facet diameter of 24 μm was also similar to those in the rest of the specimens. The local cleavage fracture stress was calculated to be 2212 MPa (McMeeking analysis of n=0.1). The chemical composition of the cleavage-

initiating inclusion, as well as the inclusion size and first facet size, were the same as those of other initiating inclusions.

This particular case is distinguished by examining Tables 6-3 to 6-5, which reveal that the stable crack extension is the largest across all specimens, measuring 70 μm. This value exceeds the average stable crack extension of 44 μm, observed in specimens tested at -80°C, by 60%.

Further examination of this specimen result indicates that the $J$-integral registers the maximum value at 218 $kJ \cdot m^{1/2}$ and the corresponding $K_{JC}$ is also the highest among all specimens at 212 $MPa \cdot m^{1/2}$. The large amount of plastic deformation in the specimen, very likely facilitates decohesion as a mode of initiation, effectively serving as the dominant cleavage initiation site of crack formation.

#### 6.5.12.4 Inclusion Element Composition

The EDX analysis was carried out by point analysis. The points were determined on the inclusion itself and the inclusion surrounding matrix, by comparing the element difference between inclusion and the matrix, the inclusion element was confirmed.

For the role of titanium in steel deoxidation process, it was reported [123], that the presence of crystalline patches containing titanium were detected towards the edges of inclusions. As titanium monoxide formation requires strongly reducing conditions, it is reasonable to assume that the titanium-rich crystalline patches observed at the edges of inclusions are possibly $TiC$, $NbC$ or $(Ti, Nb)(C, N)$.[124], [125] This was also be confirmed as EDX analysis results from Figure 6-14 (d).

A sufficient amount of aluminium was added to molten steel as a deoxidizing element, but this will produce solid particles of $Al_2O_3$ and these particles form aggregates of irregular shape termed “alumina clusters” by collision and coalescence. [126] These clusters in the final steel product can have a strong detrimental effect to the mechanical properties.

Calcium added into steel is mainly to reduce the detrimental effect of $Al_2O_3$ inclusions and improve the castability of molten steel. It is reported [127][128] that by adding calcium, the $Al_2O_3$ inclusions will be transformed into liquid calcium aluminate inclusions with low melting points and spherical morphology. These liquid inclusions are easily removable from the melt and the residual inclusions in the steel are less harmful than un-treated $Al_2O_3$ inclusion to the mechanical properties.

The modification of $Al_2O_3$ inclusion into calcium aluminates by adding calcium is reported to exhibit the following reaction sequence: $Al_2O_3 \rightarrow CaO \cdot 6Al_2O_3 \rightarrow CaO \cdot 2Al_2O_3 \rightarrow CaO \cdot Al_2O_3 \rightarrow CaO \cdot (Al_2O_3)_x(liquid)$ [128]

Inclusions of the $CaO - MgO - Al_2O_3$ system are very likely to be found in both HT1 and HT2 steel samples. This was reported owing to the reaction between $[Ca]$ and $MgO - Al_2O_3$ inclusions as listed by Equation 6-1 and Equation 6-2. [129] [130]

$$[Al] + \frac{3}{2}(CaO) = \frac{3}{2}[Ca] + \frac{1}{2}(Al_2O_3) \quad \text{Equation (6-1)}$$

$$x[Ca] + (MgO \cdot Al_2O_3) = [xCaO \cdot (1-x)MgO \cdot Al_2O_3] + x[Mg] \quad \text{Equation (6-2)}$$

6.5.12.5 Inclusions That Do Not Initiate Cleavage

In Figure 6-37 (f) and Figure 6-37 (g) of HT2-21 site2, an inclusion is shown on the fracture surface, but there is no river pattern spreading from it, indicating that the inclusion is not responsible for either global or the local cleavage initiation. The EDX analysis of the two inclusions in HT2-21 site2 with equivalent diameters of 1.8 μm and 2.0 μm reveals the presence of calcium, aluminium, sulphur, and a small quantity of titanium.

This demonstrates that not all inclusions will be active in initiating cleavage, despite the fact that inclusions are detrimental to the cleavage process. There are a number of other inclusions that behave similarly throughout the observation.

Inclusions may not initiate cleavage fracture for many possible reasons. Among them all, one could be that the inclusion is not on the cleavage plane of the entire specimen which results in a stress concentration that could differ from that of inclusions located on the specimen's cleavage plane. (example seen from Figure 6-37 (f)) Which is to say, the stress concentration could be a lot less for the inclusions that are not on the cleavage plane.

### 6.5.13 Local Cleavage Fracture Stress $\sigma_F$ and Effective Surface Energy $\gamma_p$

$\sigma_F$ is the calculated stress for an initiation site, where a penny-shaped crack was assumed and using a modified Griffith-type equation:

$$\sigma_F = \left[\frac{\pi E \gamma_p}{(1-\nu^2)d}\right]^{1/2} \qquad \text{Equation (6-3)}$$

Where $d$ is the critical crack length.

(If inclusion is considered, then d is inclusion diameter instead of radius)

$\gamma_p$ is effective surface energy.

$E$ is Young's modulus taken as 210 GPa, and $v$ is Poisson's ratio taken as 0.28.

Based on the initiators' measured size, with the help of the modified Griffith equation stated in Equation (6-3) for a penny-shaped microcrack, the effective surface energy is calculated. It is assumed that the critical event of cleavage in these specimens was the fracture of these initiators, and the cracked or decohered initiator acted as a penny-shaped crack in the material. The diameter of the initiator can be regarded as critical crack length. The calculated $\gamma_p$ estimated from the general form Griffith equation can be found in Table 6-8 and Table 6-11 for n=0.1 and n=0.2 conditions respectively. The effective surface energy for initiator sizes between 0.6-3.2 μm ranges within 5 $J/m^2$ to 22 $J/m^2$ for the n=0.1 condition and 7 $J/m^2$ to 34 $J/m^2$ in the n=0.2 condition. With a linear fit in the initiator diameter-local cleavage fracture stress plot (Figure 6-60), the slope gives the surface energy of 9.2 $J/m^2$ in the n=0.1 condition and the surface energy of 13.6 $J/m^2$ in the n=0.2 condition. This result can be seen as support for previous values of 7-14 $J/m^2$ deduced in the literature. [85]

The calcium based spherical shape inclusion surface energy result is in the range from 7.4 $J/m^2$ to 33.5 $J/m^2$, the titanium based cubic shape inclusion surface energy is in the range from 9.7 $J/m^2$ to 24.2 $J/m^2$ and non-inclusion initiator surface energy result is in the range from 7.2 $J/m^2$ to 30.0 $J/m^2$

From the result of surface energy distribution, it appears that there may not be a strong difference in the calculated surface energy between these different types of initiators.

### 6.5.14 Local Cleavage Fracture Stress Relationship to Microstructural Features

The relationship between local cleavage fracture stress and the reciprocal square root of initiator diameter and the first facet diameter are shown in Figure 6-60 to Figure 6-61. Generally, the scattered nature of the data can be seen; however, there is also a tendency of increasing local cleavage fracture stress with decreasing initiator sizes and facet sizes. The general trend can be represented by the slope. Thanks to the modified Griffith equation for a penny-shaped microcrack (Equation 6-3), when the particle-matrix crack is considered critical, the slope gives a surface energy of 9.2 $J/m^2$ under condition of n=0.1 and surface energy of 13.6 $J/m^2$ under n=0.2 condition.

Moreover, if the facet size is assumed to be the initiating micro-cracks and cracking of the facet considered as the critical event, the slope gives 203 $J/m^2$ under n=0.1 condition and 300 $J/m^2$ under n=0.2 condition. The calculated surface energy result may be worth comparing with the data in the literature of around 120 $J/m^2$ [89].

## 6.6 Microscopic Cleavage Fracture Stress Test Discussion

### 6.6.1 Local Cleavage Fracture Stress $\sigma_F$ Compared with the Maximum Principal Stress $\sigma_{yy}^{max}$

Plotted in Figure 6-64 is the relationship between local cleavage fracture stress $\sigma_F$ and the maximum principal stress $\sigma_{yy}^{max}$.

It can be seen from both Figure 6-64 and Table 6-14 that six specimens exhibited measured local cleavage fracture stresses very close to the corresponding maximum principal stresses.

Considering the ratio of $\sigma_F/\sigma_{yy}^{max}$, six data points yield a result higher than 93%, which is very close to the 'process zone' threshold of 95% of the maximum principal stress.[66] Only one specimen HT2-07, had a slightly larger difference between local cleavage fracture stress and maximum principal stress ($\sigma_F = 0.91\sigma_{yy}^{max}$).

### 6.6.2 Initiator Size and the first Facet Size Relationship with the Local Cleavage Fracture Stress

In order to evaluate the size effect of initiation features during the cleavage process, the local cleavage fracture stress $\sigma_F$ is compared with the reciprocal square root of fractographic initiator size as well as facet size.

From Figure 6-65 and Figure 6-66, it is observed that although the correlation of facet size with $\sigma_F$ is slightly stronger than that of initiator size with $\sigma_F$, the overall correlation of both initiator and first facet size with local cleavage fracture stress is relatively weak.

From Figure 6-67, there is a weak correlation between the size of all-type initiators and the first facet size in seven blunt-notched specimens.

### 6.6.3 Local Cleavage Fracture Stress $\sigma_F$ and the Effective Surface Energy $\gamma_p$

The calculated surface energy from each test is summarised in Table 6-15. The surface energy results for four inclusion related specimens were 8.0 $J/m^2$, 10.4 $J/m^2$, 12.3 $J/m^2$, and 13.6 $J/m^2$, and the surface energy results for the three specimens with matrix related initiation were 4.3 $J/m^2$, 9.6 $J/m^2$ and 13.3 $J/m^2$.

### 6.6.4 Fractography

The blunt-notched specimens produced a high-constraint condition at the crack tip, increasing the likelihood of plane-strain conditions, where pure cleavage is more likely to occur. The high constraint minimizes the crack-tip plastic zone, reducing the amount of energy absorbed during crack propagation, thus favouring cleavage fracture over quasi-cleavage fracture.

## 6.7 Comparison of Cleavage Fracture Between the Sharp-cracked and Blunt-notched Specimens

### 6.7.1 Stress-Condition Difference Between the Sharp-cracked and Blunt-notched Specimens

Based on the Griffith-Owen analysis and the McMeeking analysis, when loading increases in blunt-notched specimens, the $L/L_{GY}$ will increase, which will lead to a larger maximum principal stress. Hence it is possible to increase the local cleavage fracture stress. This means the local stress-state ahead of the notch-root will change and a larger stress is likely to occur ahead of the notch-root. However, in sharp-cracked specimens, according to the McMeeking analysis, the stress distribution ahead of the pre-crack tip stays the same. The load

increase will only increase the sampling distance for cleavage fracture ahead of the pre-crack tip.

### 6.7.2 Fracture Surface Appearance

As discussed before, in blunt-notched specimens, the local cleavage fracture stress at fracture is close to the maximum principal stress and the crack propagates perpendicular to the direction of the applied stress. It results in a generally flat, featureless appearance, with the cleavage facets meeting at a 90° angle. This can be compared with sharp-cracked specimens, when the cleavage path is not perpendicular to the direction of the applied stress, and the resulting fracture surface may have a more jagged or rough appearance. Additionally, the crack may branch and interact with other cracks in the material, leading to a more complex fracture surface. Some typical examples are illustrated in Figure 6-16, Figure 6-32, Figure 6-36 and Figure 6-37, where their respective J-integral values are 55.4 $kJ/m^2$, 64.9 $kJ/m^2$, 36.1 $kJ/m^2$ and 86.2 $kJ/m^2$. These values were higher than the average of their corresponding sample populations.

In conclusion, fractographic analyses of cleavage surfaces for specimen tested at -100 °C and -80 °C frequently reveal discrete zones of quasi-cleavage fracture, as documented in [131] The underlying reason for this observation is that a propagating cleavage crack may encounter intricate hindrances, such as highly disoriented grains, which are impervious to fracturing. Consequently, the cleavage crack is compelled to navigate around these impediments, resulting in the formation of isolated intact ligaments. These residual ligaments undergo tearing, necessitating a relatively high energy expenditure, when the crack openings widen sufficiently. This microscale process enhances fracture toughness and becomes increasingly prevalent at elevated temperatures.

### 6.7.3 Effect of Temperature

Figure 6-68 gives the local cleavage fracture stress results for different test temperatures in sharp-cracked specimens (for n=0.1 and n=0.2) as well as for blunt-notched specimens.

Based on the blunt-notched specimen test results obtained at –196 and -170°C, although the local cleavage fracture stress does not appear to have a strong dependency on temperature, the single valid failure stress obtained at the higher temperature makes this suggestion very tentative.

However, as seen in Figure 6-68 average values from blunt-notched specimens and lower bound values from sharp-cracked specimens, the local cleavage fracture stress does indeed seem to be temperature independent. This is strong support for the widely held interpretation of the origin of the brittle to ductile transition with a decreasing yield stress with increasing temperature, combined with a temperature independent cleavage fracture stress.

Work hardening exponent is assumed to have no effect on the stress distribution in the Griffiths and Owen analysis for blunt-notched specimens, resulting in an average local cleavage fracture stress of approximately 1985 MPa at -196 °C and -170 °C. For the actual work hardening exponent estimated at around n=0.15, analysis of the sharp-cracked specimen tests based on McMeeking FEA resulted in the lower bound local cleavage fracture stress values of 2060, 1961 and 2144 MPa, for -120 °C, -100 °C, and -80 °C test temperatures, respectively.

The local cleavage fracture stress results from blunt-notched specimens at 196 °C and -170 °C are comparable with the lower bound local cleavage fracture stress results from sharp-cracked specimens at -120 °C, -100 °C, and -80 °C. This shows that the local cleavage fracture stress does not appear to be affected by temperature changes ranging from –100 °C to -196 °C.

### 6.7.4 Fracture Distance Analysis

In the present study, the majority of measured fracture distances in sharp-cracked specimens are within 200 μm, but in blunt-notched specimens, cleavage fracture distances are all measured to be larger than 200 μm.

Figure 6-69 gives the fracture distance comparison for sharp-cracked specimens and blunt-notched specimens. The measured fracture distances show the sampling distance ranging from 220 to 440 μm in blunt-notched specimens and 21 to 657 μm in sharp-cracked specimens.

A red dashed line at 200 μm shows the difference between these different specimens. On the left side of the red dashed line (fracture distance < 200 μm), sharp-cracked specimen fracture distance values are concentrated in the high stress region. The concentration level is clearly higher than results on the right side of red dashed line (fracture distance > 200 μm). Compared with the blunt-notched specimens, high stress facilitates sharp-cracked specimens cleavage initiating at the locations much closer to the pre-crack tip than the blunt-notch tip.

One important point to note here is that on the right side of red dashed line, which is when the fracture distance exceeds 200μm, the local cleavage fracture stress results seen in sharp-cracked specimens can be very similar to blunt-notched specimen values. This may suggest that the local stress condition in sharp-cracked specimens where the fracture distance exceeds 200μm and blunt-notched specimens ahead of notch root are similar.

Figure 6-70 depicts the relationship between all types of initiators and the local cleavage fracture stresses, and Figure 6-71 shows the relationship between all facet sizes and the local cleavage fracture stresses. Since n=0.1 and n=0.2 give equivalent results, only the n=0.1 condition is shown for clarity. Initiators and facets located beyond 200μm exhibit the lowest local cleavage fracture stress. This phenomenon is attributed to the McMeeking analysis result, which reveals

that stress distribution varies with the distance from the tip of a ductile crack. Essentially, as the fracture distance increases, the local cleavage fracture stress decreases progressively until the material ultimately fractures.

### 6.7.5 Surface Energy of the Cracked Inclusion

The local cleavage fracture stress and the calculated surface energy of each cracked inclusion is summarized in Table 6-16 and Table 6-17. Based on the assumption that the critical event in the cleavage fracture process is the cracking of the inclusions, the calculated surface energy will be more accurate than calculated previously from all initiators. - In the study, four blunt-notched specimens exhibited cracked inclusions, with surface energy results calculated at 8.0 $J/m^2$, 10.4 $J/m^2$, 12.3 $J/m^2$, and 13.6 $J/m^2$, respectively. Conversely, fifteen sharp-cracked specimens were observed to contain cracked inclusions and the calculated surface energy result from sharp-cracked specimen with cracked inclusion initiation is in the range of 5.0-21.0 $J/m^2$ in the n=0.1 condition and 7.4-33.5 $J/m^2$ in the n=0.2 condition.

The reciprocal square root of cracked inclusion diameter and corresponding local cleavage fracture stress is plotted in Figure 6-72 and Figure 6-73. The slopes of these figures show a surface energy value of 10.6 $J/m^2$ from blunt-notched specimens, 9.6 $J/m^2$ from sharp-cracked specimens using n=0.1 and 14.0 $J/m^2$ from sharp-cracked specimens using n=0.2.

## 6.8 Conclusions

6.8.1. In sharp-cracked specimens, the inclusions found at cleavage initiation sites using EDX analysis showed the presence of calcium, aluminium and

titanium, with a size distribution of equivalent diameter from 0.7 to 2.5 μm and related first facet size distribution in the range from 20 to 46 μm in equivalent diameter. There appears to be no significant differences in the cleavage micro-mechanism for calcium related spherical shape inclusions and titanium related cubic shape inclusions.

6.8.2. The surface energy of all initiators in sharp-cracked specimens is 9.2 $J/m^2$ in the n=0.1 condition and 13.6 $J/m^2$ in the n=0.2 condition. If only cracked inclusions are considered, the surface energy in sharp-cracked specimens is estimated at 9.6 $J/m^2$ in the n=0.1 condition and 14.0 $J/m^2$ in the n=0.2 condition.

6.8.3. In sharp-cracked specimens, 21 out of 26 specimens have $\sigma_F/\sigma_{Max}$ values greater than 85% for the McMeeking analysis of n=0.1 and 14 out of 26 specimens have $\sigma_{\theta\theta}/\sigma_{Max}$ values greater than 85% for the McMeeking analysis of n=0.2.

6.8.4. In blunt-notched specimens, both non-metallic inclusions and non-inclusion features were identified as cleavage initiation sites. The size of seven initiators was within 1.1 μm to 2.6 μm. And four inclusions sizes are within 1.6 μm to 2.6 μm.

6.8.5. In blunt-notched specimens, by assuming the initiator as penny-shaped micro-cracks, using a modified Griffith-type equation, the calculated surface energy gives a distribution from 4.3 $J/m^2$ to 13.6 $J/m^2$.

6.8.6. In blunt-notched specimens, the FEM calculated local cleavage fracture stress $\sigma_F$ was very close to the maximum principal stress. The local cleavage fracture stress of one test was 91% of the maximum principal stress, and the other six tests were above 93% of the maximum principal stress.

6.8.7. Overall results presented from both test-piece geometries provide very strong support both for a purely tensile stress-controlled failure criterion of

cleavage fracture, and for the temperature independence of the cleavage fracture stress. Although such important tenets for the interpretation of the brittle to ductile transition in ferritic steels have been accepted for several decades, this study has provided very clear experimental validation of these tenets.

# Chapter Seven – Main Conclusions and Future Work

## 7.1 Main Conclusions

1. In the wide range of sharp-cracked specimens, blunt-notched specimens and Charpy specimens (failed in the lower shelf region), inclusions have been observed to initiate cleavage fracture. Chemical analysis has shown the inclusions at cleavage initiation sites to contain either calcium, sometimes combined with aluminium which appear to be spherical in shape or to have titanium and to be cubic in shape.
2. For the majority of samples that failed by cleavage fracture, fracture initiation was caused by a cracked inclusion. Compared with decohered inclusions, cracked matrix and matrix related features, cracked inclusions appear to be the most detrimental feature to trigger cleavage fracture in the whole specimen for the studied steel material.
3. The tensile stress control criterion is generally valid for prediction of cleavage fracture in both blunt-notched and sharp-cracked specimens. The cleavage fracture for the entire specimen to occur is most likely to be around the location where the maximum principal stress is anticipated.
4. There was a weak tendency for the local cleavage fracture stress to rise in sharp-cracked specimens with the decrease of the cracked non-metallic inclusion size. But it was challenging to discern whether there is such a tendency in the blunt-notched specimens.
5. The average local cleavage fracture stress value measured in blunt-notched specimens is 1985 MPa. If the lower bound value of measured local cleavage fracture stress from sharp-cracked specimens is considered, the result of 2055 MPa is closely similar with the average value from blunt-notched specimens results. The local cleavage fracture stress in this steel appears to

be temperature independent.

6. In the wide range of Charpy impact specimens, sharp-cracked specimens and blunt-notched specimens, although the detailed relationship is complex, for all types of initiators, the initiator size seems to have a weak correlation with the first facet size.
7. Overall results demonstrated by the two distinct test-piece geometries offer compelling corroboration for a purely tensile stress-controlled failure criterion of cleavage fracture, and for the temperature independence of the cleavage fracture stress. Such important tenets for the interpretation of the brittle to ductile transition in ferritic steels have been widely accepted for numerous decades. However, this study has contributed significantly to the field by providing explicit experimental validation of these fundamental tenets.

## 7.2 Future work

1. The current fracture toughness tests were conducted at -120 °C, -100 °C, and -80 °C using 1T CT pre-cracked specimens, while the microscopic fracture stress tests were conducted at -196 °C, -170 °C, and -160 °C using notched specimens. There is no direct comparison between the two types of specimens at the same temperature, so future research of fracture toughness tests can be conducted at temperatures such as -196 °C, -170 °C, and -160 °C so that a direct comparison can be made.
2. Griffiths and Owen and McMeeking FEM analyses from the 1970s are used in the current research. Although the fundamental principle of fracture mechanics has not changed in the past 50 years, this study would benefit from a specific Finite Element Analysis based on the material under investigation and the appropriate work hardening behaviour.

3. The most significant aspect of this study's fractography analysis is the presence of non-metallic inclusions at the cleavage initiation locations. However, non-inclusion features were also observed at some initiation sites; based on their appearance, these features are likely to be carbides or martensite-austenite constituents. The investigation can be enhanced by a qualitative examination of these characteristics.

References:


[1] H. B. Liu, H. Q. Zhang, and J. F. Li, “Toughness of SA738Gr.B steel used for nuclear containment vessel,” *International Journal of Pressure Vessels and Piping*, vol. 168, no. April, pp. 200–209, 2018, doi: 10.1016/j.ijpvp.2018.10.017.

[2] L. Tuñón-Sanjur, R. S. Orr, S. Tinic, and D. P. Ruiz, “Finite element modeling of the AP1000 nuclear island for seismic analyses at generic soil and rock sites,” *Nuclear Engineering and Design*, vol. 237, no. 12–13, pp. 1474–1485, Jul. 2007, doi: 10.1016/j.nucengdes.2006.10.006.

[3] J. Montero-Mayorga, C. Queral, and J. Gonzalez-Cadelo, “AP1000® SBLOCA simulations with TRACE code,” *Ann Nucl Energy*, vol. 75, pp. 87–100, 2015, doi: 10.1016/j.anucene.2014.07.045.

[4] L. Z. Ding, Y. Lei, J. Zhang, and Q. S. Meng, “An investigation into the weldability of SA-738Gr.B steel,” in *Materials Research Innovations*, Maney Publishing, May 2015, pp. S51197–S51201. doi: 10.1179/1432891714Z.0000000001277.

[5] Y. L. Zhang and H. Hui, “Investigation of Mechanical Properties and Ductile-Brittle Transition Behaviors of SA738Gr.B Steel Used as Reactor Containment,” in *Structural Integrity Assessment*, in Key Engineering Materials, vol. 795. Trans Tech Publications Ltd, Dec. 2019, pp. 66–73. doi: 10.4028/www.scientific.net/KEM.795.66.

[6] S. Wei-hua, “Microstructure and Mechanical Properties of Q and T Heavy Plate for Nuclear Power Station Purpose,” *Journal of Iron and Steel Research*, 2011, [Online]. Available: https://api.semanticscholar.org/CorpusID:138430302

[7] E. S. Davenport, “Transformation of austenite at constant subcritical temperatures,” *Metallurgical Transactions*, vol. 1, no. 12, pp. 3479–3501, 1970, doi: 10.1007/BF03037891.

[8] H. Bhadeshia and R. Honeycombe, *Bainite*, 4th ed. Elsevier Ltd, 2017. doi: 10.1016/b978-0-08-100270-4.00006-8.

[9] H. K. D. H. BHADESHIA, “Other Morphologies of Bainite,” in *BAINITE IN STEELS Transformations, Microstructure and Properties SECOND EDITION*, 2001, pp. 277–284.

[10] K. Abbaszadeh, H. Saghafian, and S. Kheirandish, “Effect of Bainite Morphology on Mechanical Properties of the Mixed Bainite-martensite Microstructure in D6AC Steel,” *J Mater Sci Technol*, vol. 28, no. 4, pp. 336–342, 2012, doi: 10.1016/S1005-0302(12)60065-6.

[11] H. Luo, X. Wang, Z. Liu, and Z. Yang, “Influence of refined hierarchical martensitic microstructures on yield strength and impact toughness of ultra-high strength stainless steel,” *J Mater Sci Technol*, vol. 51, pp. 130–136, 2020, doi: 10.1016/j.jmst.2020.04.001.

[12] H. K. D. H. Bhadeshia, “Proceedings of the International Seminar on Welding of High Strength Pipeline Steels,” *Proceedings of the International Seminar On Welding of High Strength Pipeline Steels CBMM and TMS, 2013*, pp. 99–106, 2013.

[13] L. Lan, C. Qiu, D. Zhao, X. Gao, and L. Du, “Analysis of microstructural variation and mechanical behaviors in submerged arc welded joint of high strength low carbon bainitic steel,” *Materials Science and Engineering A*, vol. 558. pp. 592–601, 2012. doi: 10.1016/j.msea.2012.08.057.

[14] Shyi-Chin Wangand Jer-Ren Yang, “Effects of chemical composition, rolling and cooling conditions on the amount of martensite/austenite (M/A) constituent formation in low carbon bainitic steels.” 1992.

[15] Y. Li and T. N. Baker, “Effect of morphology of martensite-austenite phase on fracture of weld heat affected zone in vanadium and niobium microalloyed steels,” *Materials Science and Technology*, vol. 26, no. 9, pp. 1029–1040, 2010, doi: 10.1179/026708309X12512744154360.

[16] B. zhou Li, C. sheng Li, X. Jin, and J. Zhang, “Effect of M–A constituents formed in thermo-mechanical controlled process on toughness of 20CrNi2MoV steel,” *Journal of Iron and Steel Research International*, vol. 26, no. 12, pp. 1340–1349, 2019, doi: 10.1007/s42243-019-00244-8.

[17] X. Li, C. Shang, X. Ma, and S. V. Subramanian, “Study on the toughness of X100 pipeline steel heat affected zone,” *Energy Materials 2014, Conference Proceedings*, no. December 2019, pp. 597–604, 2014, doi: 10.1002/9781119027973.ch72.

[18] H. F. Lan, L. X. Du, and R. D. K. Misra, “Effect of microstructural constituents on strength-toughness combination in a low carbon bainitic steel,” *Materials Science and Engineering A*, vol. 611, pp. 194–200, 2014, doi: 10.1016/j.msea.2014.05.084.

[19] X. Luo, X. Chen, T. Wang, S. Pan, and Z. Wang, “Effect of morphologies of martensite–austenite constituents on impact toughness in intercritically reheated coarse-grained heat-affected zone of HSLA steel,” *Materials Science and Engineering A*, vol. 710. pp. 192–199, 2018. doi: 10.1016/j.msea.2017.10.079.

[20] C. L. Davis and J. E. King, “Cleavage initiation in the intercritically reheated coarse-grained heat-affected zone: Part I. Fractographic evidence,” *Metallurgical and Materials Transactions A*, vol. 25, no. 3, pp. 563–573, 1994, doi: 10.1007/BF02651598.

[21] F. G. Caballero *et al.*, “Influence of bainite morphology on impact toughness of continuously cooled cementite free bainitic steels,” *Materials Science and Technology*, vol. 28, no. 1, pp. 95–102, 2012, doi: 10.1179/1743284710Y.0000000047.

[22] J. Chen, S. Tang, Z. Y. Liu, and G. D. Wang, “Microstructural characteristics with various cooling paths and the mechanism of embrittlement and toughening in low-carbon high performance bridge steel,” *Materials Science and Engineering A*, vol. 559, pp. 241–249, 2013, doi: 10.1016/j.msea.2012.08.091.

[23] D. C. Ramachandran *et al.*, “Classification of martensite-austenite constituents according to its internal morphology in high-strength low alloy steel,” *Mater Lett*, vol. 278, p. 128422, 2020, doi: 10.1016/j.matlet.2020.128422.

[24] J. R. Yang and H. K. D. H. Bhadeshia, “Thermodynamics of the Acicular Ferrite Transformation in Alloy-Steel Weld Deposits.” pp. 187–191, 1986.

[25] S.S. Babu and H.K.D.H.Bhadeshia, “Mechanism of the Transition from Bainite to Acicular Ferrite,” *Materials Transactions,JIM*, vol. 32, no. 8, pp. 679–688, 1991.

[26] S. Morito, X. Huang, T. Furuhara, T. Maki, and N. Hansen, “The morphology and crystallography of lath martensite in alloy steels,” *Acta Mater*, vol. 54, no. 19, pp. 5323–5331, 2006, doi: https://doi.org/10.1016/j.actamat.2006.07.009.

[27] N. J. Kim, A. H. Nakagawa, and A. H. Nakagawa, “Effective grain size of dual-phase steel,” *Materials Science and Engineering*, vol. 83, no. 1, pp. 145–149, 1986, doi: 10.1016/0025-5416(86)90181-3.

[28] J. Kang, C. N. Li, G. Yuan, and G. D. Wang, “Improvement of strength and toughness for hot rolled low-carbon bainitic steel via grain refinement and

crystallographic texture," *Mater Lett*, vol. 175, pp. 157–160, 2016, doi: 10.1016/j.matlet.2016.04.007.

[29] M. Díaz-Fuentes, A. Iza-Mendia, and I. Gutiérrez, "Analysis of different acicular ferrite microstructures in low-carbon steels by electron backscattered diffraction. Study of their toughness behavior," *Metall Mater Trans A Phys Metall Mater Sci*, vol. 34 A, no. 11, pp. 2505–2516, 2003, doi: 10.1007/s11661-003-0010-7.

[30] J. W. Morris, C. S. Lee, and Z. Guo, "The nature and consequences of coherent transformations in steel," *ISIJ International*, vol. 43, no. 3, pp. 410–419, 2003, doi: 10.2355/isijinternational.43.410.

[31] R. W. T. and S. W., "Dislocation Models of Crystal Grain Boundaries," *Physical Review*, vol. 78, no. 3, p. 275, 1950.

[32] J. Naylor and R. Blondeau, "The respective roles of the packet size and the lath width on toughness," *Metallurgical Transactions A*, vol. 7, no. 5, pp. 891–894, 1976, doi: 10.1007/BF02644090.

[33] J. Y. Monnot, J., Heritier, B. & Cogne, "Relationship of melting practice, inclusion type, and size with fatigue resistance of bearing steels," *Effect of Steel Manufacturing Processes on the Quality of Bearing Steels, Phoenix, Arizona, USA, 4-6 Nov. 1986, ASTM*. pp. 149–165.

[34] R. Kiessling, *Non-metallic inclusions in steel, Part V*. The Institute of Metals, 1989.

[35] D. B. and K. W.Andrews, "Thermal expansion of some inclusions found in steels and relation to tessellated stresses.," *Journal of the Iron and Steel Institute*, vol. 206, no. 6, pp. 595-599., 1968.

[36] D. B. and K. W.Andrews, "Tessellated stresses associated with some inclusions in steel.," *Journal of the Iron and Steel Institute*, vol. 207, no. 4, pp. 474–483, 1969.

[37] D. Brooksbank, "Thermal expansion of calcium aluminate inclusions and relation to tessellated stresses," *Journal of the Iron and Steel Institute*, vol. 208, no. 5, pp. 495–499, 1970.

[38] D. B. and K. W.Andrews, "Stress fields around inclusions and their relation to mechanical properties," *Journal of the Iron and Steel Institute*, vol. 210, no. 4, pp. 246–255, Apr. 1972.

[39] Y. Jun, C. Bo-Tao, T. Wei, Z. Fan-Zheng, Y. Gang, and S. Feng, “Experimental study to improve the castability of aluminum killed cold heading steel,” *Steel Res Int*, vol. 84, no. 8, pp. 703–712, Aug. 2013, doi: 10.1002/srin.201200246.

[40] J. Yang, X. H. Wang, M. Jiang, and W. J. Wang, “Effect of calcium treatment on non-metallic inclusions in ultra-low oxygen steel refined by high basicity high Al2O3 slag,” *Journal of Iron and Steel Research International*, vol. 18, no. 7, pp. 8–14, 2011, doi: 10.1016/S1006-706X(11)60083-6.

[41] H. Bhadeshia and R. Honeycombe, *Acicular Ferrite*, 4th ed. Elsevier Ltd, 2017. doi: 10.1016/b978-0-08-100270-4.00007-x.

[42] W. S. Lee and T. T. Su, “Mechanical properties and microstructural features of AISI 4340 high-strength alloy steel under quenched and tempered conditions,” *J Mater Process Technol*, vol. 87, no. 1–3, pp. 198–206, 1999, doi: 10.1016/S0924-0136(98)00351-3.

[43] G. Yan, L. Han, C. Li, X. Luo, and J. Gu, “Characteristic of retained austenite decomposition during tempering and its effect on impact toughness in SA508 Gr.3 steel,” *Journal of Nuclear Materials*, vol. 483, pp. 167–175, 2017, doi: 10.1016/j.jnucmat.2016.11.011.

[44] H. Bhadeshia and R. Honeycombe, *Tempering of Martensite*, 4th ed. Elsevier Ltd, 2017. doi: 10.1016/b978-0-08-100270-4.00009-3.

[45] A. A. Griffith, “The Phenomena of Rupture and Flow of Solids.,” *Philosophical Transcations of the Royal Society*, no. A221. pp. 162–198, 1920.

[46] E. Orowan, “Fracture and Strength of Solids,” *Reports in Progress in Physics*, vol. XII, p. 185, 1948.

[47] G. R. Irwin, “Fracture Dynamics.,” *Fracture of Metals*, no. American Society for Metals, Cleveland, pp. 147–166, 1948.

[48] H. M. Westergaard, “Bearing Pressures and Cracks: Bearing Pressures Through a Slightly Waved Surface or Through a Nearly Flat Part of a Cylinder, and Related Problems of Cracks,” *J Appl Mech*, vol. 6, no. 2, pp. A49–A53, Mar. 1939, doi: 10.1115/1.4008919.

[49] D. S. Dugdale, “Yielding of steel sheets containing slits,” *J Mech Phys Solids*, vol. 8, no. 2, pp. 100–104, 1960, doi: https://doi.org/10.1016/0022-5096(60)90013-2.

[50] A. A. Wells, “Application of fracture mechanics at and beyond general yielding[J],” *British Welding Journal*, vol. 10, pp. 563–570, 1963.

[51] J. R. Rice and G. F. Rosengren, “Plane strain deformation near a crack tip in a power-law hardening material,” *J Mech Phys Solids*, vol. 16, no. 1, pp. 1–12, 1968, doi: 10.1016/0022-5096(68)90013-6.

[52] J. W. Hutchinson, “Plastic stress and strain fields at a crack tip,” *J Mech Phys Solids*, vol. 16, no. 5, pp. 337–342, 1968, doi: 10.1016/0022-5096(68)90021-5.

[53] W. Ramberg and W. R. Osgood, “Description of stress-strain curves by three parameters,” *National Advisory Committee For Aeronautics*. p. Technical Note No. 902.NACA, 1943.

[54] C. F. Shih and R. J. Asaro, “Elastic-plastic and asymptotic fields of interface cracks,” *Int J Fract*, vol. 42, no. 2, pp. 101–116, 1990, doi: 10.1007/BF00018380.

[55] J. R. Low, *Relation of Properties to Microstructure*. Cleveland, OH: ASM, 1954.

[56] J. R. Low, *Deformation and Flow of Solids*. Berlin: Springer Verlag, 1956.

[57] C. Zener, “Fracturing of Metals,Cleveland,” *ASM*. pp. 3–31, 1948.

[58] A. N. Stroh, “The Formation of Cracks as a Result of Plastic Flow,” *Proc R Soc Lond A Math Phys Sci*, vol. 223, no. 1154, pp. 404–414, Jun. 1954.

[59] A. H. S. Cottrell, “THEORY OF BRITTLE FRACTURE IN STEEL AND SIMILAR METALS,” 1958.

[60] C. J. Mcmahon and M. Cohen, “Initiation of cleavage in polycrystalline iron,” *Acta Metallurgica*, vol. 13, pp. 591–604, 1965.

[61] E. Smith, “Cleavage fracture in mild steel,” *International Journal of Fracture Mechanics*, vol. 4, no. 2, pp. 131–145, 1968, doi: 10.1007/BF00188940.

[62] D. A. Curry and J. F. Knott, “Effects of microstructure on cleavage fracture stress in steel,” no. November, pp. 511–514, 1978.

[63] Knott J. F., *J. Iron and Steel Inst.*. , vol. 204. 1966.

[64] J. R. Griffiths and D. R. J. Owen, “An elastic-plastic stress analysis for a notched bar in plane strain bending,” *J Mech Phys Solids*, vol. 19, no. 6, pp. 419–431, 1971, doi: 10.1016/0022-5096(71)90009-3.

[65] R. O. Ritchie, J. F. Knott, and J. R. Rice, “On the relationship between critical tensile stress and fracture toughness in mild steel,” *Journal of the Mechanics*

*and Physics of Solids*, vol. 21, no. 6. pp. 395–410, 1973. doi: 10.1016/0022-5096(73)90008-2.

[66] P. Bowen, S. G. Druce, and J. F. Knott, "Micromechanical modelling of fracture toughness," *Acta Metallurgica*, vol. 35, no. 7, pp. 1735–1746, 1987, doi: 10.1016/0001-6160(87)90119-2.

[67] J. H. Chen and G. Z. Wang, "Study of mechanism of cleavage fracture at low temperature," *Metallurgical Transactions A*, vol. 23, no. 2, pp. 509–517, 1992, doi: 10.1007/BF02801168.

[68] T. R. Tetelman, D.A and Wilshow, *J.Mech Fracture*. 1969.

[69] G. T. Hahn, "Influence of Microstructure on Brittle Fracture Toughness.," *Metallurgical transactions. A, Physical metallurgy and materials science*, vol. 15 A, no. 6, pp. 947–959, 1984, doi: 10.1007/bf02644685.

[70] G. R. Odette, G. E. Lucas, R. Maiti, and J. W. Sheckherd, "The mumechanical mechanisms of cleavage fracture in martensitic stainless steels," *Journal of Nuclear Materials*, vol. 122, no. 1, pp. 442–447, 1984, doi: https://doi.org/10.1016/0022-3115(84)90637-8.

[71] M. Holzmann, L. Jurášek, and I. Dlouhý, "Fracture behaviour and cleavage initiation in hypoeutectoid pearlitic steel," *Int J Fract*, vol. 148, no. 1, pp. 13–28, 2007, doi: 10.1007/s10704-007-9173-3.

[72] D. A. Curry, "Cleavage micromechanisms of crack extension in steels," *Metal Science*, vol. 14, no. 8–9, pp. 319–326, 1980, doi: 10.1179/msc.1980.14.8-9.319.

[73] P. B. Martin Strangwood, "Micromechanisms of Brittle Fracture in 2.25Cr-1Mo Weld Metal,"

[74] D. A. Curry and J. F. Knott, "Effect of microstructure on cleavage fracture toughness of quenched and tempered steels," *Metal Science*, vol. 13, no. 6, pp. 341–345, 1979, doi: 10.1179/msc.1979.13.6.341.

[75] F. M. Beremin, A. Pineau, F. Mudry, J. C. Devaux, Y. D'Escatha, and P. Ledermann, "A local criterion for cleavage fracture of a nuclear pressure vessel steel," *Metallurgical Transactions A*, vol. 14, no. 11, pp. 2277–2287, 1983, doi: 10.1007/BF02663302.

[76] W. Weibull, "A Statistical Distribution Function of Wide Applicability," *J Appl Mech*, vol. 18, no. 3, pp. 293–297, Apr. 1951, doi: 10.1115/1.4010337.

[77] X. Gao, C. Ruggieri, and R. H. Dodds, “Calibration of Weibull stress parameters using fracture toughness data,” *Int J Fract*, vol. 92, no. 2, pp. 175–200, 1998, doi: 10.1023/A:1007521530191.

[78] X. Gao and R. H. Dodds, “Constraint effects on the ductile-to-brittle transition temperature of ferritic steels: a Weibull stress model,” *Int J Fract*, vol. 102, no. 1, pp. 43–69, 2000, doi: 10.1023/A:1007526006632.

[79] A. Martín-Meizoso, I. Ocaña-Arizcorreta, J. Gil-Sevillano, and M. Fuentes-Pérez, “Modelling cleavage fracture of bainitic steels,” *Acta Metallurgica Et Materialia*, vol. 42, no. 6, pp. 2057–2068, 1994, doi: 10.1016/0956-7151(94)90031-0.

[80] A. Lambert-Perlade, A. F. Gourgues, J. Besson, T. Sturel, and A. Pineau, “Mechanisms and modeling of cleavage fracture in simulated heat-affected zone microstructures of a high-strength low alloy steel,” *Metall Mater Trans A Phys Metall Mater Sci*, vol. 35, no. 13, pp. 1039–1053, 2004, doi: 10.1007/s11661-004-1007-6.

[81] L. E. Kaechele, “A statistical investigation of microcrack formation,” *Acta Met.*, vol. 17, pp. 463–475, 1969.

[82] K. Wallin, “Statistical modelling of fracture in the ductile to brittle transition region,” in *Defect assessment in components*, 1991, pp. 415–445.

[83] K. Wallin, “Fracture Toughness Transition Curve Shape for Ferritic Structural Steels BT - Fracture of Engineering Materials and Structures,” S. H. Teoh and K. H. Lee, Eds., Dordrecht: Springer Netherlands, 1991, pp. 83–88. doi: 10.1007/978-94-011-3650-1_10.

[84] P. Bowen and J. F. Knott, “Cleavage fracture of A 533 B pressure vessel steel in martensitic condition,” *Metal Science*, vol. 18, no. 5, pp. 225–235, 1984, doi: 10.1179/030634584790420131.

[85] P. Bowen, S. G. Druce, and J. F. Knott, “Effects of microstructure on cleavage fracture in pressure vessel steel,” *Acta Metallurgica*, vol. 34, no. 6, pp. 1121–1131, 1986, doi: 10.1016/0001-6160(86)90222-1.

[86] K. Wallin, T. Saario, and K. Törrönen, “Statistical model for carbide induced brittle fracture in steel,” *Metal Science*, vol. 18, no. 1, pp. 13–16, Jan. 1984, doi: 10.1179/030634584790420384.

[87] J. H. Chen, Y. Kikuta, T. Araki, M. Yoneda, and Y. Matsuda, “Micro-fracture behaviour induced by M-A constituent (Island Martensite) in simulated welding heat affected zone of HT80 high strength low alloyed steel,” *Acta*

*Metallurgica*, vol. 32, no. 10, pp. 1779–1788, 1984, doi: https://doi.org/10.1016/0001-6160(84)90234-7.

[88] A. Kamada, N. Koshizuka, and T. Funakoshi, "Effect of Austenite Grain Size and C Content on the Substructure and Toughness of Tempered Martensite and Bainite.," *Trans Iron Steel Inst Jpn*, vol. 16, no. 8, pp. 407–416, 1976, doi: 10.2355/isijinternational1966.16.407.

[89] P. Brozzo, G. Buzzichelli, A. Mascanzoni, and M. Mirabile, "Microstructure and cleavage resistance of low-carbon bainitic steels," *Metal Science*, vol. 11, no. 4, pp. 123–130, Apr. 1977, doi: 10.1179/msc.1977.11.4.123.

[90] ASTM Standard E1820, "Standard Test Method for Measurement of Fracture Toughness," *ASTM Book of Standards*, no. January, pp. 1–54, 2013, doi: 10.1520/E1820-13.Copyright.

[91] R. M. McMeeking, "Finite deformation analysis of crack-tip opening in elastic-plastic materials and implications for fracture," *J Mech Phys Solids*, vol. 25, no. 5, pp. 357–381, 1977, doi: 10.1016/0022-5096(77)90003-5.

[92] N. Igata and R. R. Hasiguti, "A phenomenological theory of the irradiation embrittlement of iron and steel," *Journal of Nuclear Materials*, vol. 30, no. 1, pp. 234–241, 1969, doi: https://doi.org/10.1016/0022-3115(69)90184-6.

[93] C. C. Koch, D. G. Morris, K. Lu, and A. Inoue, "Ductility of Nanostructured Materials," *MRS Bull*, vol. 24, no. 2, pp. 54–58, 1999, doi: 10.1557/S0883769400051551.

[94] G. Z. Wang, Y. L. Wang, F. Z. Xuan, S. T. Tu, and Z. D. Wang, "Cleavage fracture behavior of a C-Mn vessel steel at various loading rates in notched specimens," *International Journal of Pressure Vessels and Piping*, vol. 85, no. 10, pp. 720–727, 2008, doi: 10.1016/j.ijpvp.2008.03.002.

[95] C. Wang, M. Wang, J. Shi, W. Hui, and H. Dong, "Effect of microstructural refinement on the toughness of low carbon martensitic steel," *Scr Mater*, vol. 58, no. 6, pp. 492–495, 2008, doi: https://doi.org/10.1016/j.scriptamat.2007.10.053.

[96] A. Moitra, S. A. Krishnan, G. Sasikala, A. K. Bhaduri, and T. Jayakumar, "Effect of specimen size in determining ductile to brittle transition temperature," *Materials Science and Technology*, vol. 31, no. 14, pp. 1781–1787, Nov. 2015, doi: 10.1179/1743284715Y.0000000006.

[97] V. Tvergaard and A. Needleman, “Analysis of the Charpy V-notch test for welds,” *Eng Fract Mech*, vol. 65, no. 6, pp. 627–643, 2000, doi: https://doi.org/10.1016/S0013-7944(99)00146-0.

[98] A. Ya. Krasovskii, “Ductile-to-brittle transition temperature as a measure of the crack resistance of steels,” *Strength of Materials*, vol. 17, no. 10, pp. 1439–1446, 1985, doi: 10.1007/BF01534035.

[99] R. Honda, “Cleavage Fracture in Single Crystals of Silicon Iron,” *J Physical Soc Japan*, vol. 16, no. 7, pp. 1309–1321, Jul. 1961, doi: 10.1143/JPSJ.16.1309.

[100] M. J. Kaufman and A. J. Forty, “A detailed fractographic analysis of cleavage steps in silicon,” *J Mater Sci*, vol. 21, no. 9, pp. 3167–3172, 1986, doi: 10.1007/BF00553353.

[101] D. W. Beardsmore, “JEDI: A Code for the Calculation of J for Cracks Inserted in Initial Strain Fields and the Role of J and Q in the Prediction of Crack Extension and Fracture,” 2008. [Online]. Available: https://api.semanticscholar.org/CorpusID:137364424

[102] R. H. Rigby and M. H. Aliabadi, “Mixed-mode J-integral method for analysis of 3D fracture problems using BEM,” *Eng Anal Bound Elem*, vol. 11, no. 3, pp. 239–256, 1993, doi: https://doi.org/10.1016/0955-7997(93)90026-H.

[103] W. W. Bose Filho, A. L. M. Carvalho, and P. Bowen, “Micromechanisms of cleavage fracture initiation from inclusions in ferritic welds. Part I. Quantification of local fracture behaviour observed in notched testpieces,” *Materials Science and Engineering A*, vol. 460–461, pp. 436–452, 2007, doi: 10.1016/j.msea.2007.01.115.

[104] V. J. Farron, “Effects of Microstructure and Strain Ageing on Toughness of Nuclear PWR Reactor Weld Metals. Volume I,” 2009.

[105] T. Saario, K. Wallin, and K. Törrönen, “On the Microstructural Basis of Cleavage Fracture Initiation in Ferritic and Bainitic Steels,” *J Eng Mater Technol*, vol. 106, no. 2, pp. 173–177, Apr. 1984, doi: 10.1115/1.3225695.

[106] D. J. Alexander and I. M. Bernstein, “Cleavage fracture in pearlitic eutectoid steel,” *Metallurgical Transactions A*, vol. 20, no. 11, pp. 2321–2335, 1989, doi: 10.1007/BF02666667.

[107] D. M. Li and F. Ye, “Microstructural effect on cleavage fracture behavior of pearlitic eutectoid steel,” *Mater Chem Phys*, vol. 26, no. 3, pp. 367–373, 1990, doi: https://doi.org/10.1016/0254-0584(90)90024-5.

[108] M. A. Linaza, J. M. Rodriguez-Ibabe, and J. J. Urcola, “Determination of the energetic parameters controlling cleavage fracture initiation in steels,” *Fatigue Fract Eng Mater Struct*, vol. 20, no. 5, pp. 619–632, 1997, doi: 10.1111/j.1460-2695.1997.tb00296.x.

[109] V. Bertolo, Q. Jiang, U. Tiringer, C. L. Walters, J. Sietsma, and V. Popovich, “Cleavage fracture micromechanisms in thick-section quenched and tempered S690 high-strength steels,” *J Mater Sci*, vol. 57, no. 42, pp. 20033–20055, Nov. 2022, doi: 10.1007/s10853-022-07841-1.

[110] S. R. Yu, Z. G. Yan, R. Cao, and J. H. Chen, “On the change of fracture mechanism with test temperature,” *Eng Fract Mech*, vol. 73, no. 3, pp. 331–347, 2006, doi: 10.1016/j.engfracmech.2005.08.005.

[111] B. Z. Margolin, V. A. Shvetsova, and G. P. Karzov, “Brittle fracture of nuclear pressure vessel steels-I. Local criterion for cleavage fracture,” 1997.

[112] A. Echeverría and J. M. Rodriguez-Ibabe, “BRITTLE FRACTURE MICROMECHANISMS IN BAINITIC AND MARTENSITIC MICROSTRUCTURES IN A C-Mn-B STEEL,” 1999.

[113] J. H. Chen, G. Z. Wang, and Q. Wang, “Change of critical events of cleavage fracture with variation of microscopic features of low-alloy steels,” *Metallurgical and Materials Transactions A*, vol. 33, no. 11, pp. 3393–3402, 2002, doi: 10.1007/s11661-002-0327-7.

[114] G. Z. Wang, X. C. Ren, and J. H. Chen, “Change of critical events of cleavage fracture with variation of loading rate in notched specimens of steel,” *Int J Fract*, vol. 119, no. 3, pp. 61–66, 2003, doi: 10.1023/A:1023929310530.

[115] J. H. Chen, C. Yan, and J. Sun, “Further study on the mechanism of cleavage fracture at low temperatures,” *Acta Metallurgica Et Materialia*, vol. 42, no. 1, pp. 251–261, 1994, doi: 10.1016/0956-7151(94)90067-1.

[116] J. H. Chen, G. Z. Wang, C. Yan, H. Ma, and L. Zhu, “Advances in the mechanism of cleavage fracture of low alloy steel at low temperature. Part I: Critical event,” *Int J Fract*, vol. 83, no. 2, pp. 105–120, 1997, doi: 10.1023/A:1007306932437.

[117] A. Ghosh, A. Ray, D. Chakrabarti, and C. L. Davis, “Cleavage initiation in steel: Competition between large grains and large particles,” *Materials Science and Engineering A*, vol. 561, pp. 126–135, 2013, doi: 10.1016/j.msea.2012.11.019.

[118] S. B. Batdorf and J. G. Crose, “A Statistical Theory for the Fracture of Brittle Structures Subjected to Nonuniform Polyaxial Stresses,” *J Appl Mech*, vol. 41, no. 2, pp. 459–464, Jun. 1974, doi: 10.1115/1.3423310.

[119] J. F. Knott, “Microstructural Aspects of the Resistance to Crack Extension of Engineering Alloys,” in *Application of Fracture Mechanics to Materials and Structures*, G. C. Sih, E. Sommer, and W. Dahl, Eds., Dordrecht: Springer Netherlands, 1984, pp. 3–26.

[120] L. Babout, Y. Brechet, E. Maire, and R. Fougères, “On the competition between particle fracture and particle decohesion in metal matrix composites,” *Acta Mater*, vol. 52, no. 15, pp. 4517–4525, 2004, doi: https://doi.org/10.1016/j.actamat.2004.06.009.

[121] A. Bergsmo and F. P. E. Dunne, “Competing mechanisms of particle fracture, decohesion and slip-driven fatigue crack nucleation in a PM nickel superalloy,” *Int J Fatigue*, vol. 135, Jun. 2020, doi: 10.1016/j.ijfatigue.2020.105573.

[122] S. tong Zhou *et al.*, “An investigation into the role of non-metallic inclusions in cleavage fracture of medium carbon pearlitic steels for high-speed railway wheel,” *Eng Fail Anal*, vol. 131, no. July 2021, 2022, doi: 10.1016/j.engfailanal.2021.105860.

[123] A. O. Kluken and Grong, “Mechanisms of inclusion formation in Al-Ti-Si-Mn deoxidized steel weld metals,” *Metallurgical Transactions A*, vol. 20, no. 8, pp. 1335–1349, 1989, doi: 10.1007/BF02665492.

[124] T. Thorvaldsson and G. L. Dunlop, “Effect of stabilizing additions on precipitation reactions in austenitic stainless steel,” *Metal Science*, vol. 16, no. 4, pp. 184–190, Apr. 1982, doi: 10.1179/msc.1982.16.4.184.

[125] Y. Xu, D. Tang, and Y. Song, “Equilibrium Modeling of (Nb, Ti, V)(C, N) Precipitation in Austenite of Microalloyed Steels,” *Steel Res Int*, vol. 84, no. 6, pp. 560–564, Jun. 2013, doi: https://doi.org/10.1002/srin.201200248.

[126] K. Wasai, K. Mukai, and A. Miyanaga, “Observation of inclusion in aluminum deoxidized iron,” *ISIJ International*, vol. 42, no. 5, pp. 459–466, 2002, doi: 10.2355/isijinternational.42.459.

[127] L. Holappa, M. Hämäläinen, M. Liukkonen, and M. Lind, “Thermodynamic examination of inclusion modification and precipitation from calcium treatment to solidified steel,” *Ironmaking and Steelmaking*, vol. 30, no. 2, pp. 111–115, 2003, doi: 10.1179/030192303225001748.

[128] G. Ye, P. Jönsson, and T. Lund, “Thermodynamics and Kinetics of the Modification of $Al_2O_3$ Inclusions,” *ISIJ International*, vol. 36, no. Suppl, pp. S105–S108, 1996, doi: 10.2355/isijinternational.36.Suppl_S105.

[129] H. Yu, X. Wang, J. Zhang, H. Li, and W. Wang, “Cleanliness of Alloying Structural Steel,” *Journal of Iron and Steel Research International*, vol. 18, no. 12, pp. 6–11, 2011, doi: 10.1016/S1006-706X(12)60002-8.

[130] X. Wang, M. Jiang, B. Chen, and H. Li, “Study on formation of non-metallic inclusions with lower melting temperatures in extra low oxygen special steels,” *Sci China Technol Sci*, vol. 55, no. 7, pp. 1863–1872, 2012, doi: 10.1007/s11431-012-4874-x.

[131] B. Djordjevic, S. Mastilovic, A. Sedmak, A. Dimic, and M. Kljajin, “Ductile-to-brittle transition of ferritic steels: A historical sketch and some recent trends,” *Eng Fract Mech*, p. 109716, Nov. 2023, doi: 10.1016/j.engfracmech.2023.109716.

Table 2-1. Summary of Mechanical properties of selected inclusions and the steel matrix. [35]–[38]

| ***Inclusion Type*** | | ***Mean Linear Expansion Coefficient*** $\boldsymbol{\alpha}$ $\boldsymbol{(10^{-6}\cdot{}^{\circ}C)}$ | ***Elastic Modulus*** $\boldsymbol{E}$ $\boldsymbol{(GPa)}$ | ***Poisson's Ratio*** $\boldsymbol{v}$ |
|---|---|---|---|---|
| *Calcium aluminates* | $CaS \cdot 2Al_2O_3$ | 5.0 | | |
| | $CaS \cdot 6Al_2O_3$ | 8.8 | | |
| | $CaO \cdot Al_2O_3$ | 6.5 | | |
| | $12CaO \cdot 7Al_2O_3$ | 7.6 | | |
| *Alumina* | $Al_2O_3$ | 8.0 | 390 | 0.25 |
| *Nitrides* | $TiN$ | 9.4 | 320 | 0.19 |
| *Simple oxides* | $FeO$ | 14.2 | | |
| | $CaO$ | 13.5 | 183 | 0.21 |
| | $MgO$ | 13.5 | 306 | 0.18 |
| | $MnO$ | 14.1 | | |
| *Spinels* | $MnO \cdot Al_2O_3$ | 8.0 | | |
| | $MgO \cdot Al_2O_3$ | 8.4 | 271 | 0.26 |
| | $FeO \cdot Al_2O_3$ | 8.6 | | |
| *Sulphides* | $CaS$ | 14.7 | | |
| | $MnS$ | 18.1 | 103 | 0.30 |
| *Matrix* | | 12.5 | 206 | 0.29 |

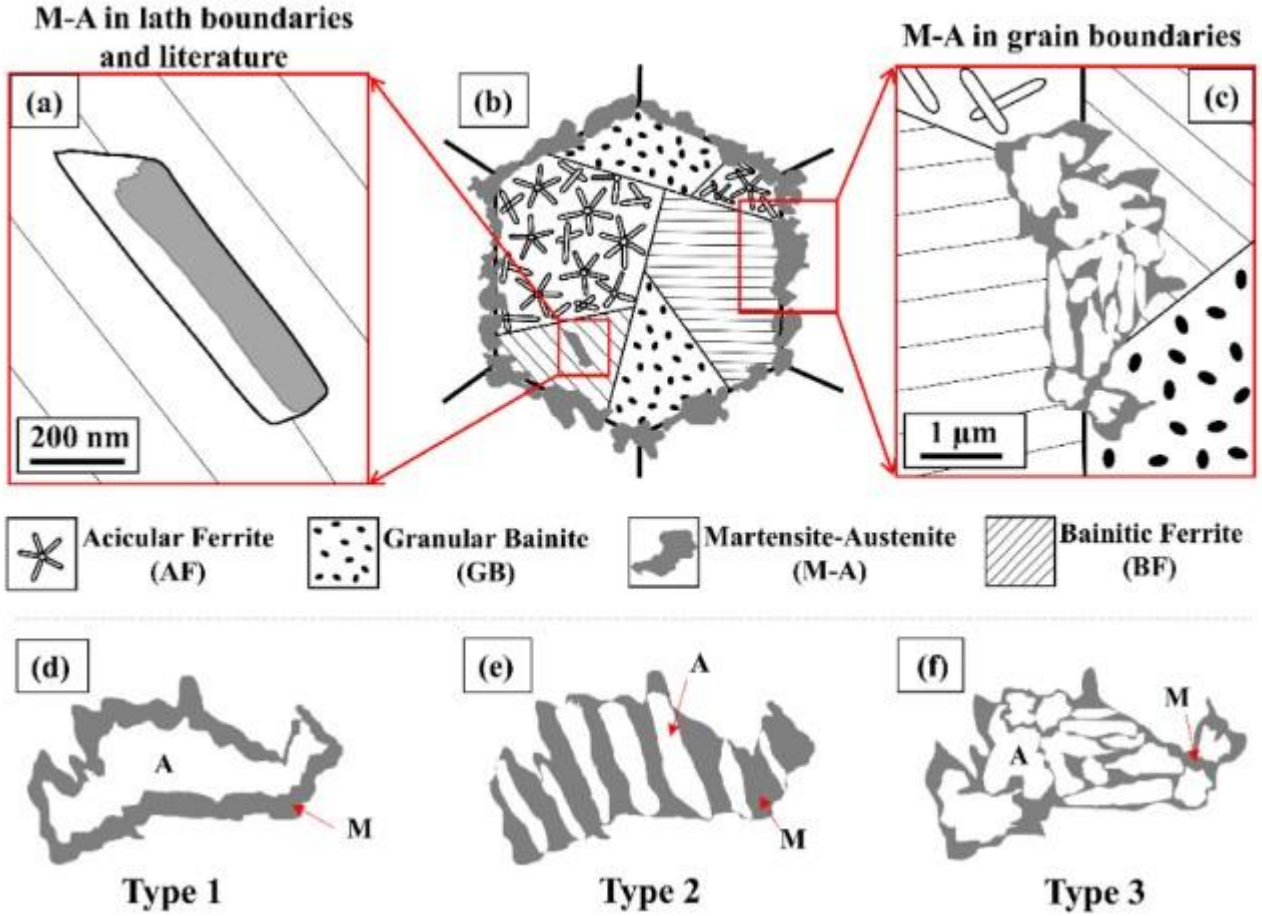


Figure 2-1. The schematic representation of M-A constituent types. [23]

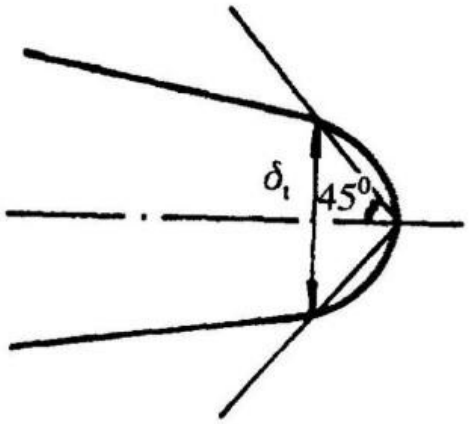


Figure 3-1. Schematic diagram of CTOD definition.

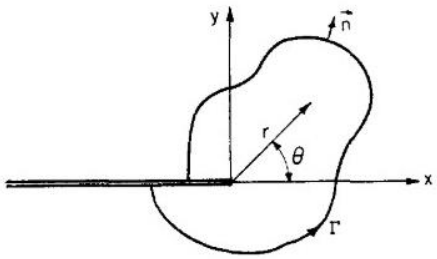


Figure 3-2. Schematic diagram of coordinates for crack tip deformation field and contour $\Gamma$ for evaluating path-independent line integral.

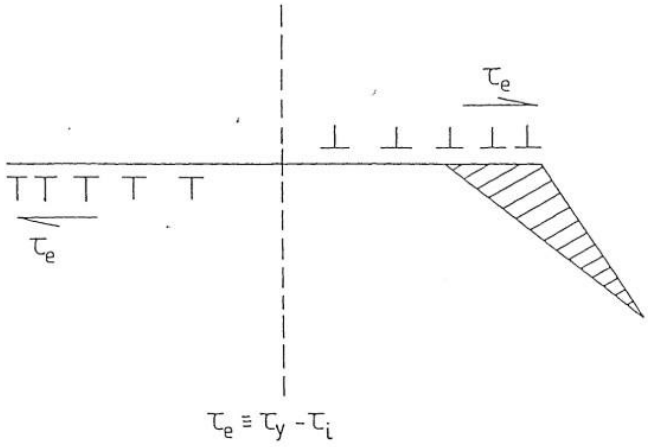


Figure 3-3. Schematic diagram of Stroh model as cleavage nucleation ahead of a dislocation pile-up.

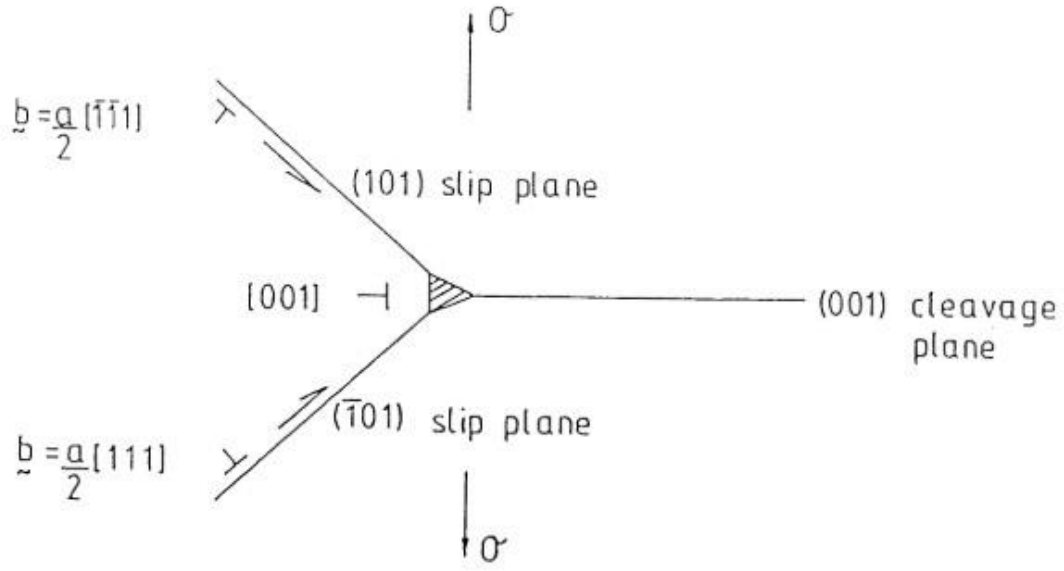


Figure 3-4. Cleavage fracture nucleation in a bcc metal suggested by Cottrell.

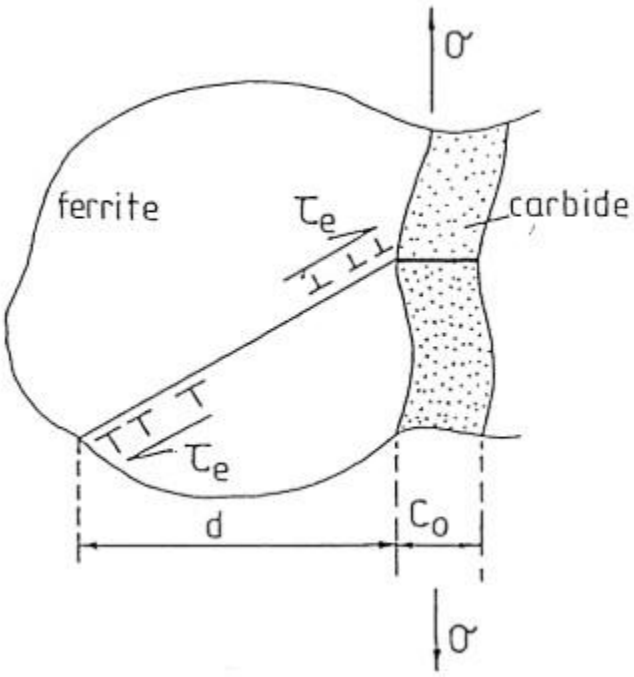


Figure 3-5. Cleavage fracture process in mild steel suggested by Smith.

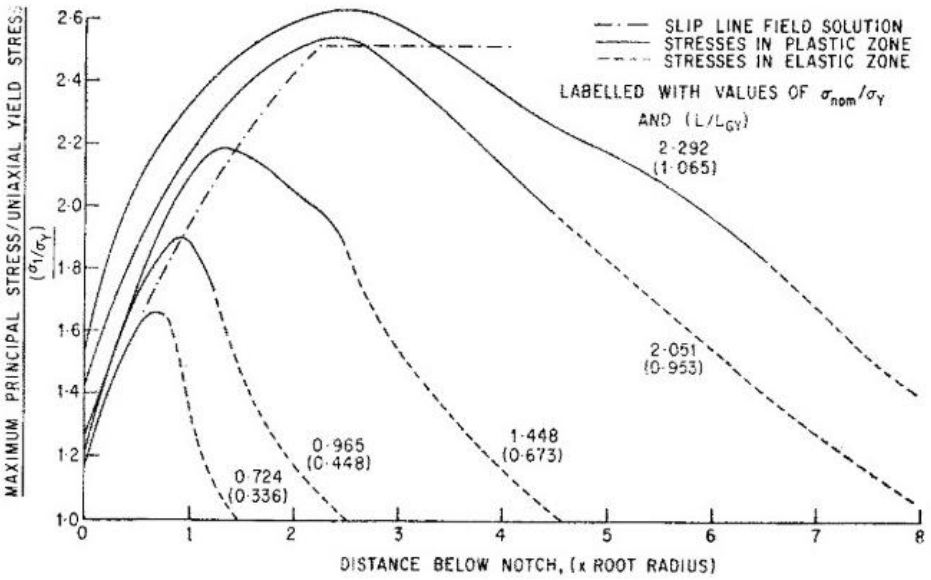


Figure 3-6. Stress distribution below the notch root generated by finite element analysis. [64]

Table 4-1. Chemical Compositions of material used in this study with comparison of ASME standard.

| $\boldsymbol{Element}$ [$\boldsymbol{wt}$%] | $\boldsymbol{C}$ | $\boldsymbol{Si}$ | $\boldsymbol{Mn}$ | $\boldsymbol{P}$ | $\boldsymbol{S}$ | $\boldsymbol{Cu + Ni + Cr}$ | $\boldsymbol{Mo}$ | $\boldsymbol{V + Nb}$ | $\boldsymbol{CE}$ |
|---|---|---|---|---|---|---|---|---|---|
| ***Baowu Steel*** | 0.088 | 0.18 | 1.47 | 0.003 | 0.0002 | 0.37 | 0.19 | 0.063 | 0.40 |
| ***ASME BPVD Requirements*** | $\leq 0.20$ | $0.15 - 0.55$ | $0.90 - 1.50$ | $\leq 0.003$ | $\leq 0.003$ | $\leq 1.25$ | $\leq 0.30$ | $\leq 0.08$ | $\leq 0.48$ |

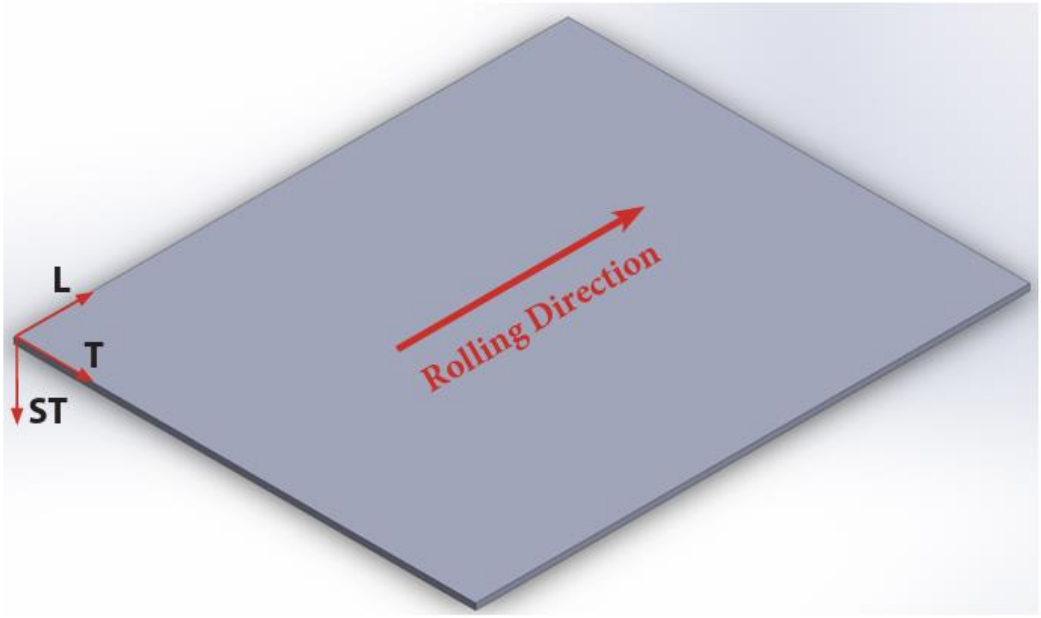


L Longitudinal Direction
T Transverse Direction
ST Short Transverse Direction

Figure 4-1. SA.738 Gr. B steel plate rolling direction.

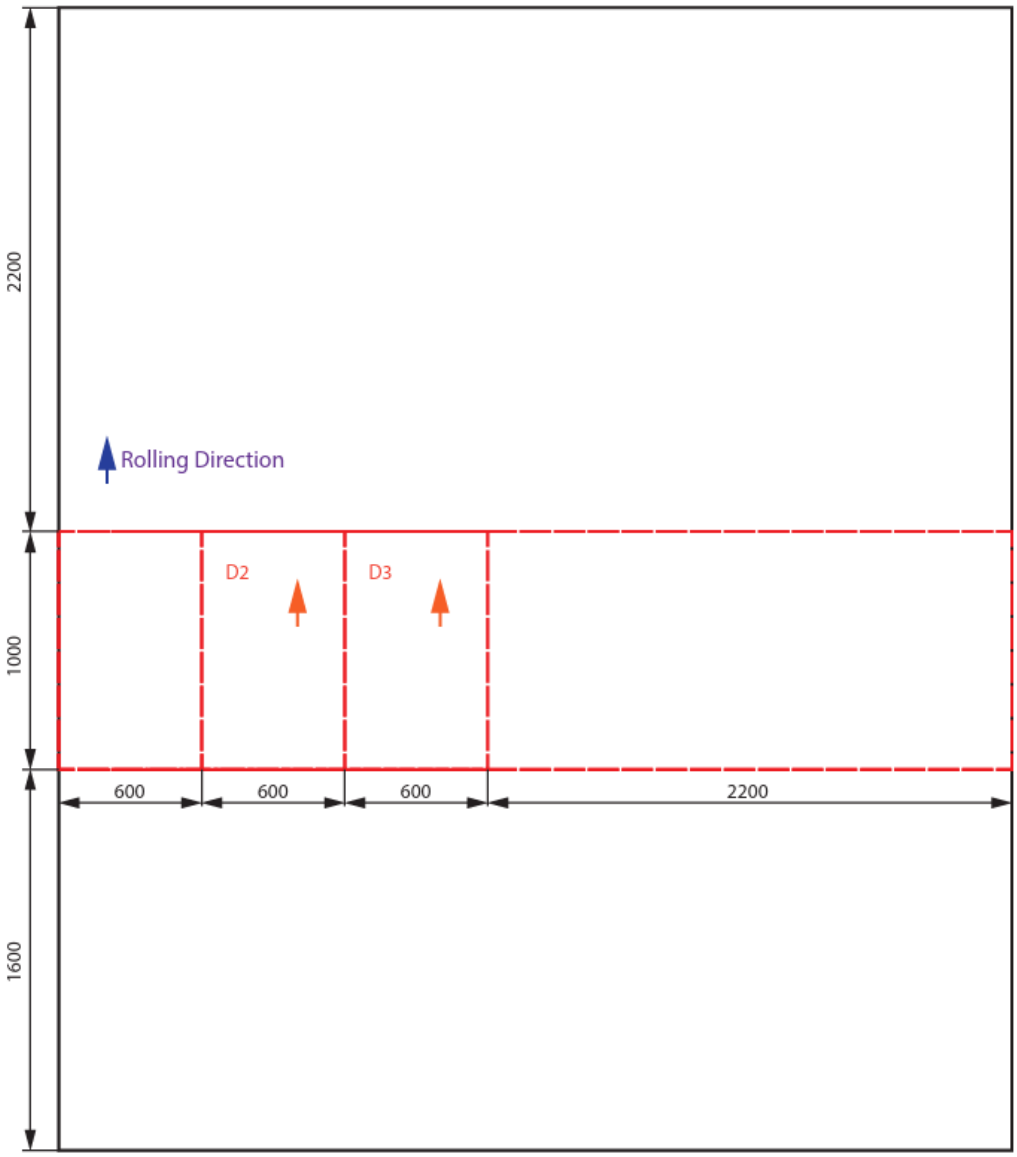


Figure 4-2. SA.738 Gr. B steel plate and sampling orientation.

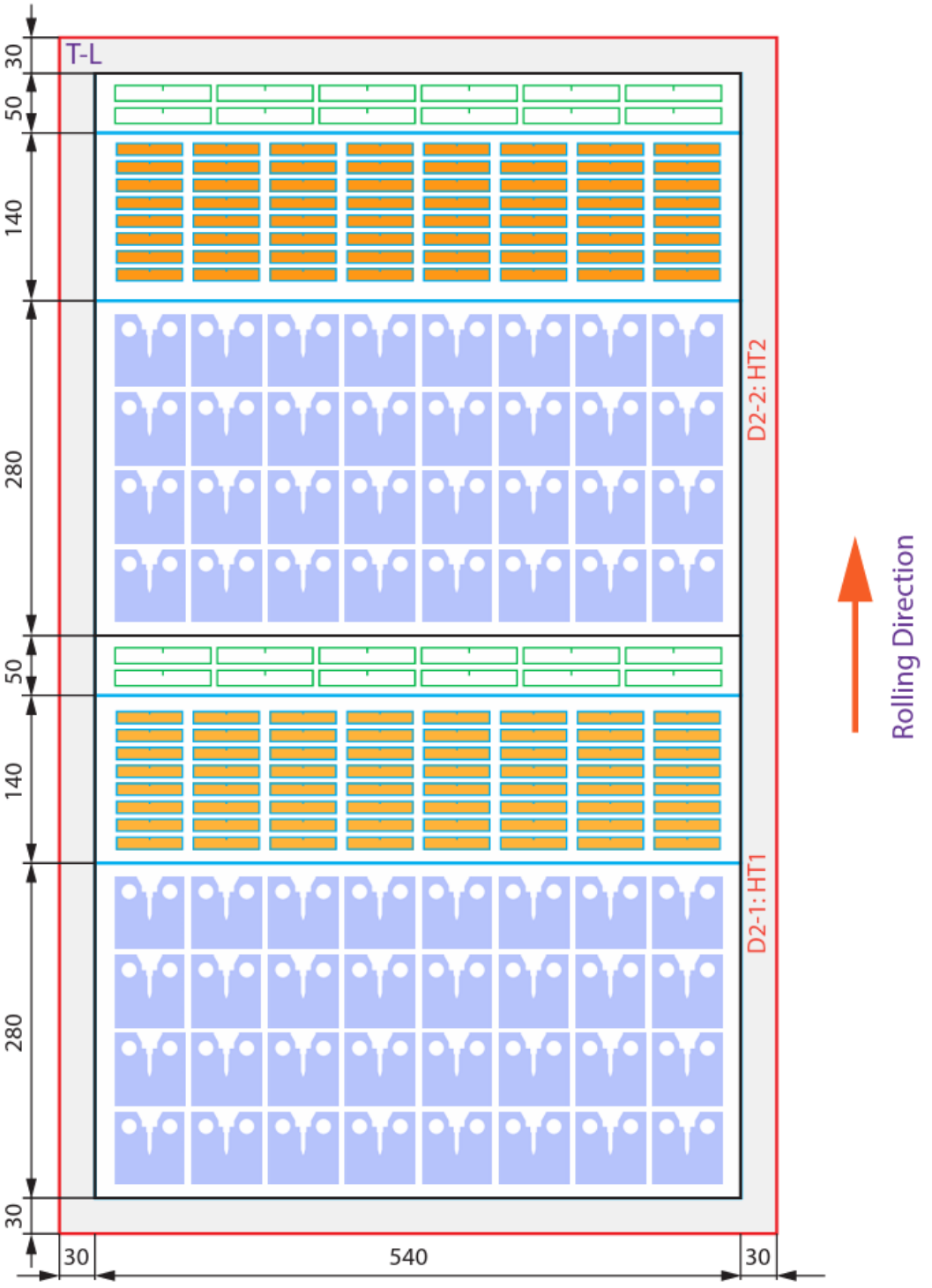


Figure 4-3. SA.738 Gr. B steel plate and Charpy test, fracture stress, and fracture toughness sampling orientation.

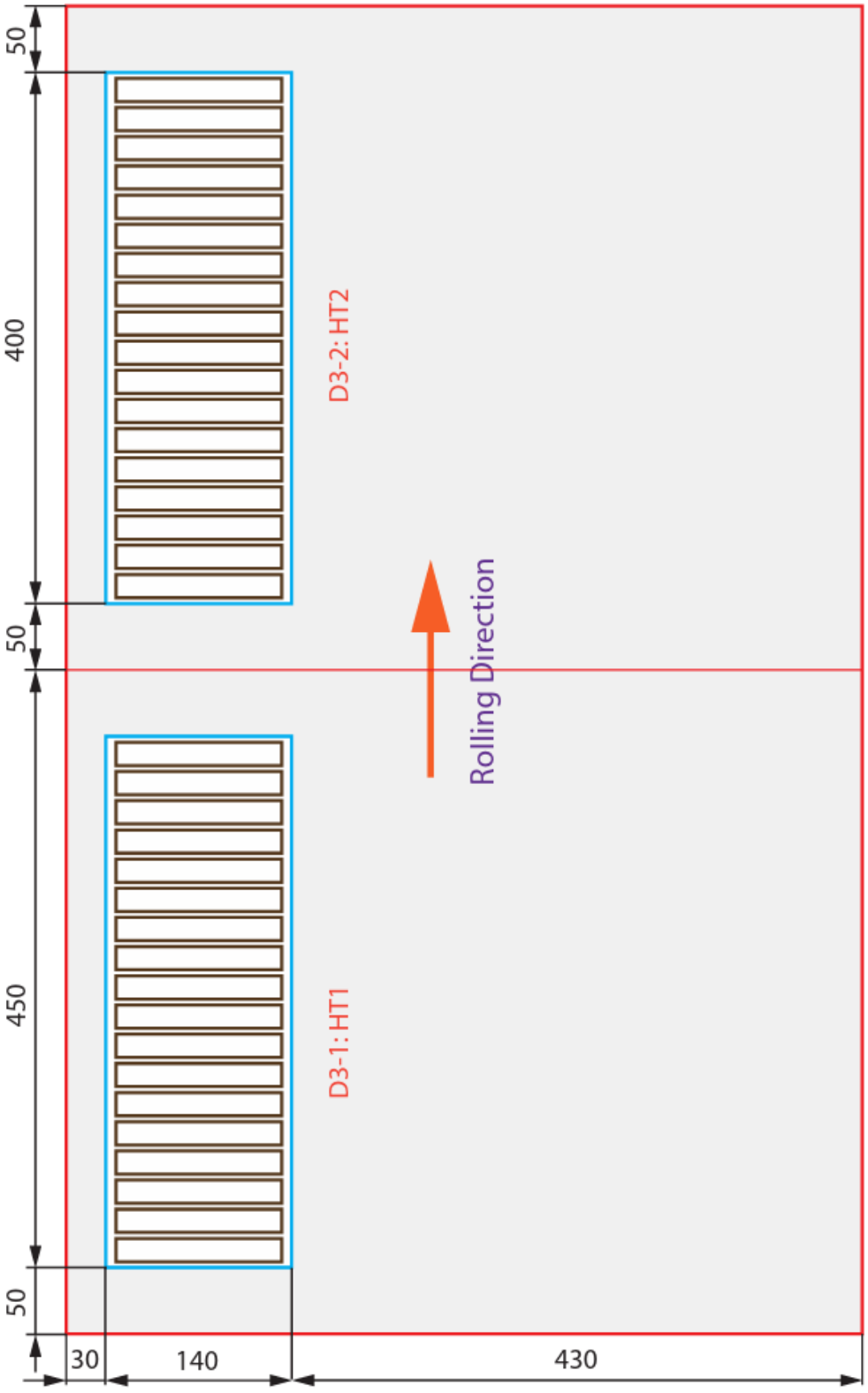


Figure 4-4. Tensile specimen sampling orientation.

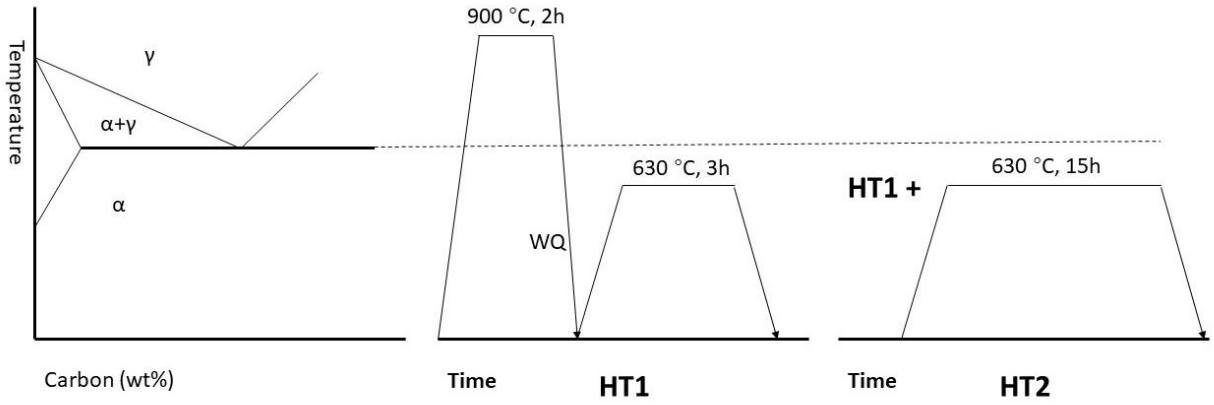


Figure 4-5. HT1 and HT2 heat treatment history.

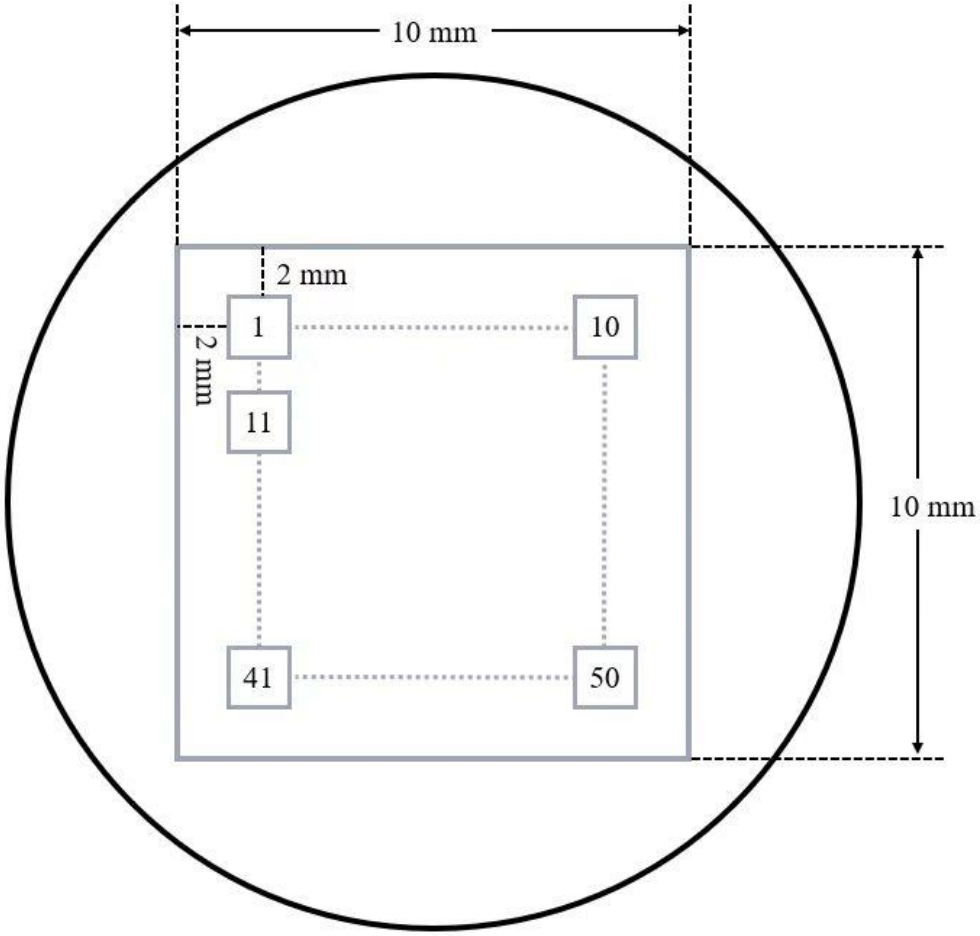


Figure 4-6. Geometrical illustration of the inclusion distribution sampling method.

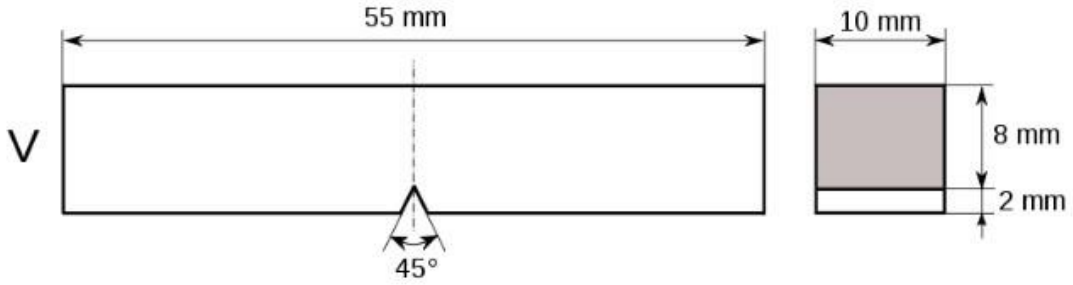


Figure 4-7. Charpy Specimen geometry.

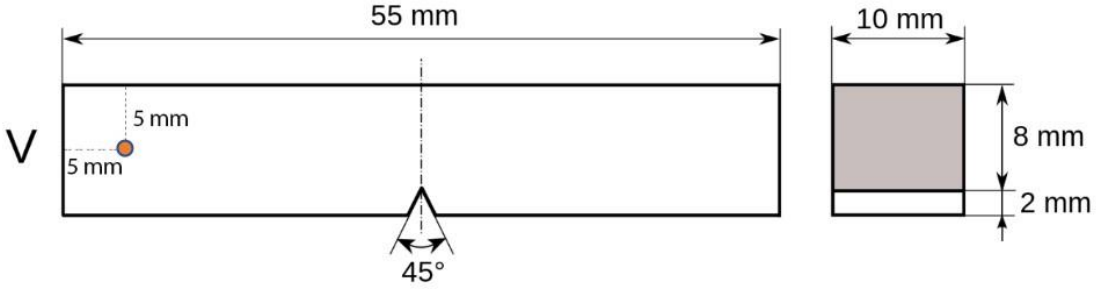


Figure 4-8. Charpy specimen geometry with drilling position for the thermocouple to be inserted.

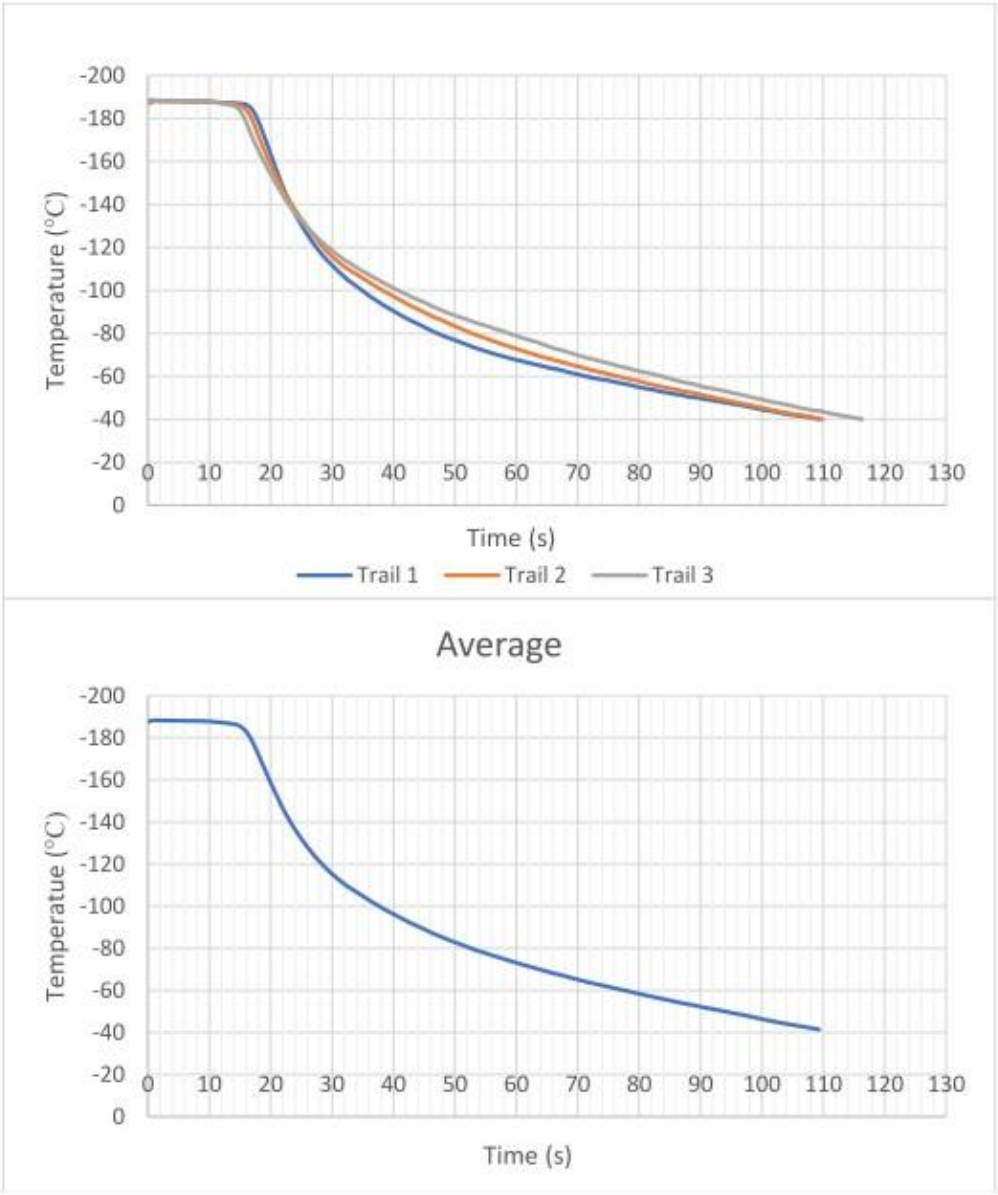


Figure 4-9. Temperature-Time calibration curve used for Charpy impact test at -120°C.

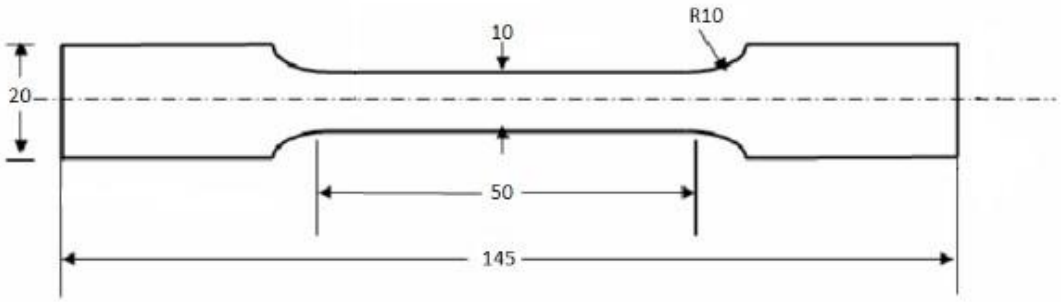


Figure 4-10. Geometrical illustration of the tensile test specimen.

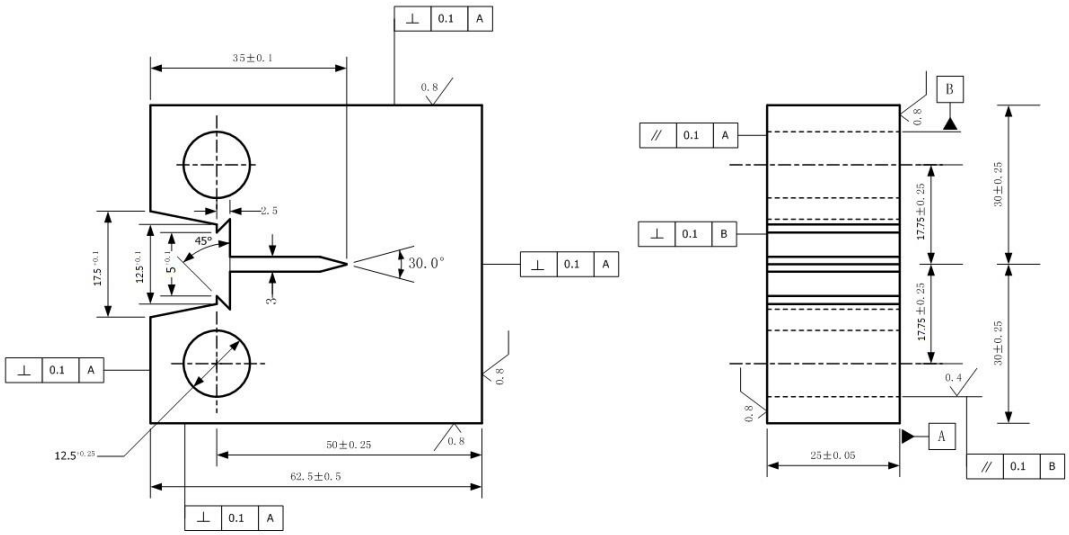


Figure 4-11. The dimensions of Compact Tension specimens.

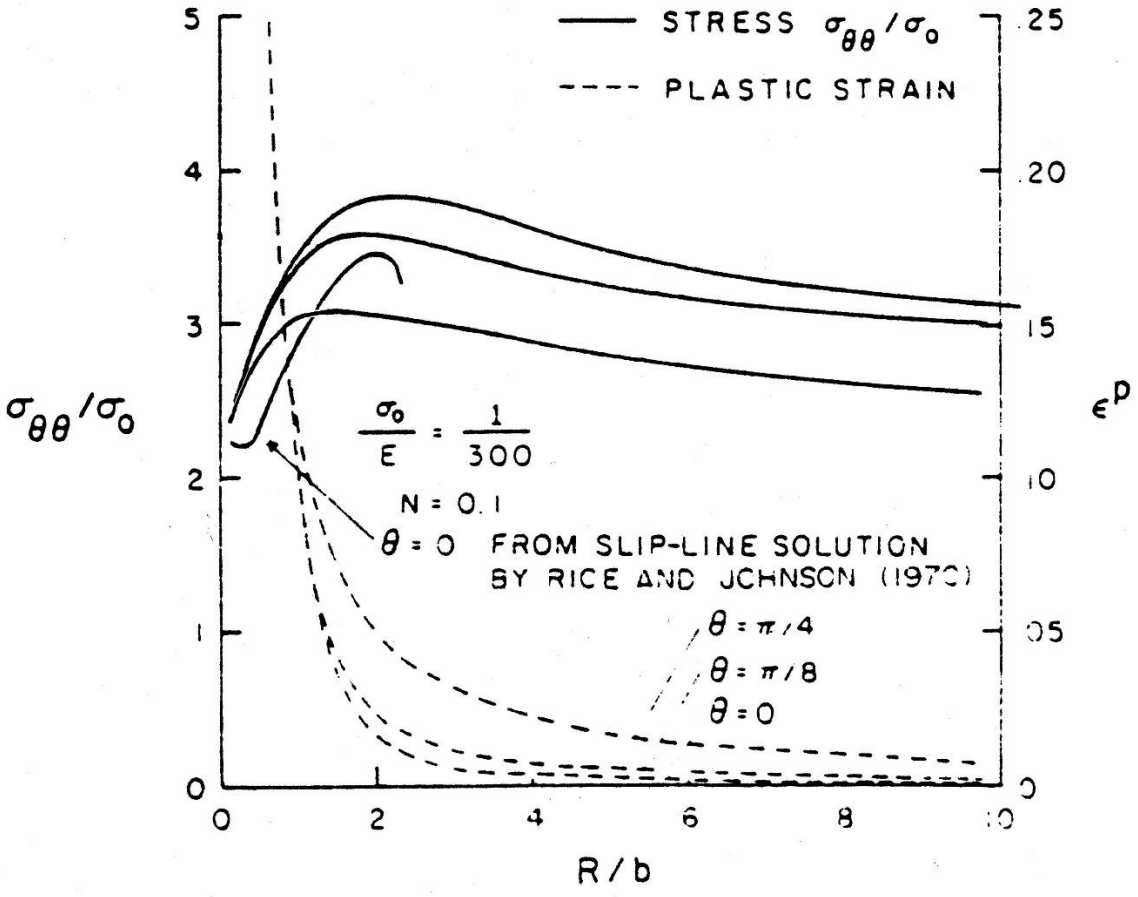


Figure 4-12. Stress and plastic strain distribution ahead of pre-crack tip for $\frac{\sigma_0}{E} = 1/300$ and N=0.1. (N is the work hardening exponent in McMeeking analysis) [91]

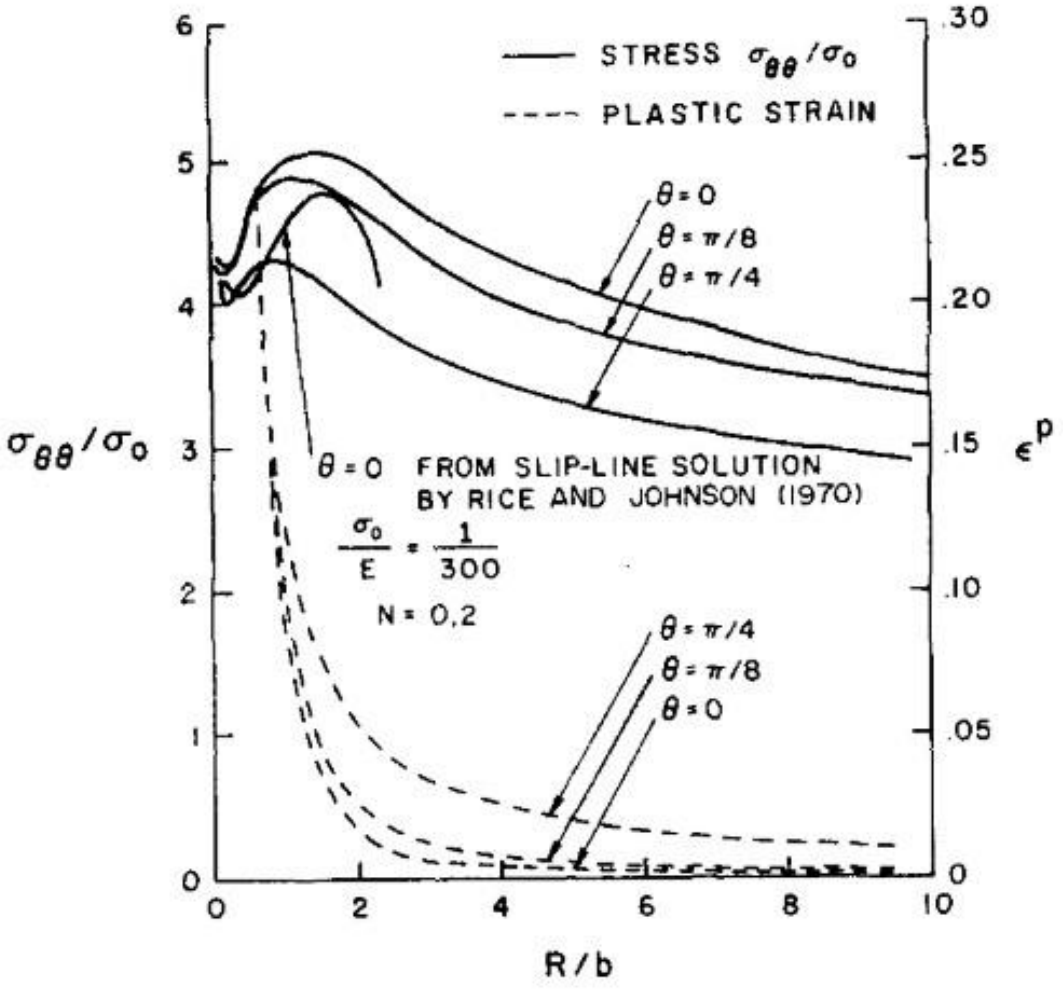


Figure 4-13. Stress and plastic strain distribution ahead of pre-crack tip for $\frac{\sigma_0}{E} = 1/300$ and N=0.2. (N is the work hardening exponent in McMeeking analysis) [91]

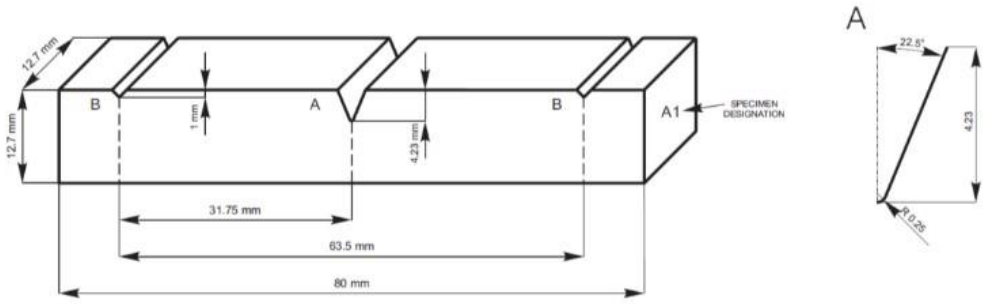


Figure 4-14. Blunt-notched specimen geometry.

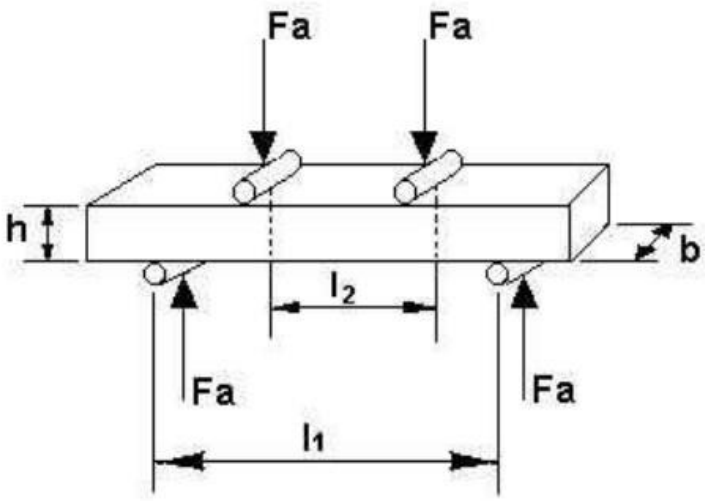


Figure 4-15. Illustration of the four-point bending test setup.


Figure 4-16. Variation of the maximum principal stress below the notch root at various loads.[64]

Table 5-1. HT1 Charpy Test Results Summary

| *Specimen No.* | *Temperature oC* | *CVN J* | *DT mm* | *LE mm* | *CA %* | *Specimen No.* | *Temperature oC* | *CVN J* | *DT mm* | *LE mm* | *CA %* |
|---|---|---|---|---|---|---|---|---|---|---|---|
| HT1-1 | -196 | 2.5 | 0.000 | 0.14 | 100.0 | HT1-40 | -90 | 299.0 | 5.252 | 2.15 | 0.0 |
| HT1-2 | | 3.0 | 0.000 | 0.12 | 100.0 | HT1-41 | | 298.5 | 3.437 | 1.98 | 0.0 |
| HT1-3 | | 2.0 | 0.000 | 0.14 | 100.0 | HT1-13 | -80 | 299.0 | 2.460 | 2.30 | 0.0 |
| HT1-7 | -120 | 5.0 | 0.063 | 0.12 | 99.1 | HT1-14 | | 236.0 | 4.571 | 2.53 | 26.2 |
| HT1-8 | | 5.0 | 0.000 | 0.12 | 99.3 | HT1-15 | | 298.5 | 1.651 | 2.20 | 0.0 |
| HT1-9 | | 5.0 | 0.059 | 0.14 | 98.4 | HT1-19 | | 297.0 | 1.640 | 2.50 | 0.0 |
| HT1-52 | | 7.5 | 0.011 | 0.23 | 98.7 | HT1-20 | | 297.0 | 2.665 | 2.26 | 0.0 |
| HT1-53 | | 7.5 | 0.001 | 0.15 | 99.2 | HT1-21 | | 246.0 | 2.286 | 2.32 | 21.0 |
| HT1-54 | | 5.0 | 0.038 | 0.17 | 98.0 | HT1-25 | | 299.0 | 2.628 | 2.28 | 0.0 |
| HT1-10 | -100 | 26.0 | 0.088 | 0.37 | 92.9 | HT1-26 | | 273.0 | 2.311 | 2.04 | 15.4 |
| HT1-11 | | 15.0 | 0.116 | 0.25 | 94.8 | HT1-27 | | 13.0 | 0.200 | 0.26 | 90.4 |
| HT1-12 | | 10.5 | 0.275 | 0.35 | 97.0 | HT1-34 | -70 | 298.5 | 3.529 | 1.79 | 0.0 |
| HT1-16 | | 8.5 | 0.188 | 0.16 | 95.1 | HT1-35 | | 298.5 | 3.644 | 2.28 | 0.0 |
| HT1-17 | | 15.0 | 0.188 | 0.27 | 95.9 | HT1-36 | | 283.5 | 3.006 | 2.19 | 14.8 |
| HT1-18 | | 8.0 | 0.090 | 0.17 | 96.5 | HT1-43 | | 298.5 | 1.403 | 2.25 | 0.0 |
| HT1-38 | | 19.5 | 0.265 | 0.31 | 91.9 | HT1-44 | | 258.0 | 3.617 | 1.92 | 20.1 |
| HT1-39 | | 11.5 | 0.157 | 0.22 | 94.8 | HT1-45 | | 272.5 | 2.606 | 2.04 | 19.6 |
| HT1-46 | | 6.0 | 0.010 | 0.14 | 100.0 | HT1-22 | -60 | 297.5 | 3.236 | 2.28 | 0.0 |
| HT1-47 | | 3.0 | 0.000 | 0.08 | 98.1 | HT1-23 | | 297.0 | 2.238 | 2.36 | 0.0 |
| HT1-48 | | 7.5 | 0.000 | 0.20 | 98.7 | HT1-24 | | 297.0 | 3.189 | 2.53 | 0.0 |
| HT1-4 | -90 | 298.0 | 2.711 | 2.54 | 0.0 | HT1-31 | | 299.0 | 1.979 | 2.35 | 0.0 |
| HT1-5 | | 56.5 | 0.427 | 0.72 | 83.5 | HT1-32 | | 299.0 | 4.243 | 2.44 | 0.0 |
| HT1-6 | | 25.0 | 0.157 | 0.27 | 91.5 | HT1-33 | | 298.5 | 3.659 | 2.21 | 0.0 |
| HT1-28 | | 12.0 | 0.088 | 0.23 | 91.9 | HT1-49 | -40 | 298.5 | 4.074 | 2.25 | 0.0 |
| HT1-29 | | 12.0 | 0.144 | 0.25 | 91.8 | HT1-50 | | 298.5 | 3.038 | 2.39 | 0.0 |
| HT1-30 | | 267.0 | 1.975 | 2.23 | 18.2 | HT1-51 | | 298.0 | 1.723 | 2.36 | 0.0 |

*$DT$ is the ductile thumbnail, $LE$ is lateral expansion and $CA$ is cleavage area percentage

Table 5-2. HT2 Charpy Test Results Summary

| *Specimen No.* | *Temperature oC* | *CVN J* | *DT mm* | *LE mm* | *CA %* | *Specimen No.* | *Temperature oC* | *CVN J* | *DT mm* | *LE mm* | *CA %* |
|---|---|---|---|---|---|---|---|---|---|---|---|
| HT2-1 | -196 | 2.0 | 0.023 | 0.00 | 100.0 | HT2-40 | -90 | 247.5 | 2.380 | 2.42 | 23.4 |
| HT2-2 | | 2.5 | 0.064 | 0.15 | 100.0 | HT2-41 | | 18.0 | 0.184 | 0.14 | 94.8 |
| HT2-3 | | 2.0 | 0.000 | 0.08 | 100.0 | HT2-42 | | 90.0 | 1.074 | 1.14 | 79.0 |
| HT2-7 | -120 | 5.0 | 0.000 | 0.18 | 99.4 | HT2-13 | -80 | 23.0 | 0.269 | 0.35 | 94.1 |
| HT2-8 | | 5.5 | 0.000 | 0.10 | 100.0 | HT2-14 | | 258.5 | 2.050 | 2.08 | 22.0 |
| HT2-9 | | 6.0 | 0.000 | 0.10 | 99.9 | HT2-15 | | 250.0 | 2.843 | 2.21 | 20.6 |
| HT2-52 | | 8.5 | 0.000 | 0.13 | 97.5 | HT2-19 | | 241.0 | 2.078 | 2.26 | 25.1 |
| HT2-53 | | 5.0 | 0.021 | 0.13 | 99.5 | HT2-20 | | 203.0 | 1.908 | 2.40 | 35.0 |
| HT2-54 | | 5.0 | 0.000 | 0.15 | 99.9 | HT2-21 | | 212.0 | 2.588 | 2.45 | 30.3 |
| HT2-10 | -100 | 12.5 | 0.106 | 0.17 | 94.6 | HT2-25 | | 261.0 | 3.406 | 2.13 | 18.4 |
| HT2-11 | | 7.5 | 0.076 | 0.27 | 95.6 | HT2-27 | | 298.5 | 3.164 | 2.35 | 0.0 |
| HT2-12 | | 19.0 | 0.154 | 0.22 | 93.3 | HT2-34 | -70 | 298.5 | 3.241 | 2.24 | 0.0 |
| HT2-16 | | 36.0 | 0.224 | 0.47 | 96.9 | HT2-35 | | 240.0 | 2.360 | 2.40 | 28.2 |
| HT2-17 | | 12.0 | 0.079 | 0.18 | 96.9 | HT2-36 | | 233.0 | 2.183 | 2.21 | 27.9 |
| HT2-18 | | 23.0 | 0.197 | 0.15 | 95.4 | HT2-43 | | 229.5 | 2.140 | 2.53 | 27.0 |
| HT2-37 | | 14.0 | 0.174 | 0.18 | 96.6 | HT2-44 | | 298.5 | 3.160 | 2.12 | 0.0 |
| HT2-38 | | 9.5 | 0.052 | 0.15 | 97.3 | HT2-45 | | 298.5 | 3.974 | 2.47 | 0.0 |
| HT2-39 | | 20.0 | 0.322 | 0.32 | 95.2 | HT2-22 | -60 | 297.0 | 3.052 | 2.33 | 0.0 |
| HT2-46 | | 8.0 | 0.021 | 0.25 | 99.4 | HT2-23 | | 297.0 | 3.157 | 2.36 | 0.0 |
| HT2-47 | | 10.0 | 0.143 | 0.17 | 96.2 | HT2-24 | | 297.0 | 3.787 | 2.44 | 0.0 |
| HT2-48 | | 6.0 | 0.038 | 0.27 | 99.8 | HT2-31 | | 299.0 | 2.665 | 2.33 | 0.0 |
| HT2-4 | -90 | 192.0 | 3.803 | 2.04 | 44.5 | HT2-32 | | 299.0 | 2.514 | 2.43 | 0.0 |
| HT2-5 | | 159.0 | 3.040 | 1.74 | 62.5 | HT2-33 | | 237.0 | 3.340 | 2.10 | 6.5 |
| HT2-6 | | 8.5 | 0.095 | 0.32 | 94.8 | HT2-49 | -40 | 299.0 | 5.539 | 2.46 | 0.0 |
| HT2-28 | | 12.0 | 0.136 | 0.30 | 93.5 | HT2-50 | | 299.0 | 3.213 | 2.36 | 0.0 |
| HT2-29 | | 9.5 | 0.000 | 0.10 | 91.0 | HT2-51 | | 299.0 | 3.457 | 2.30 | 0.0 |
| HT2-30 | | 32.0 | 0.273 | 0.29 | 92.3 | | | | | | |

*$DT$ is the ductile thumbnail, $LE$ is lateral expansion and $CA$ is cleavage area percentage

Table 5-3. Detailed information of fracture initiation sites with initiation reason, initiation size, element composition and facet size from the 14 brittle fracture Charpy impact specimens.

| $Temperature$ | $Testpiece$ | $Initiation$ | $CVN$ | $X_0$ | $Ductile\ crack\ growth$ | $Initiation\ diameter$ | $Facet\ diameter$ |
|---|---|---|---|---|---|---|---|
| $°C$ | $No.$ | $reason$ | $(J)$ | $(\mu m)$ | $(\mu m)$ | $(\mu m)$ | $(\mu m)$ |
| -196 | CH HT2-01 | Inclusion related | 2.0 | 229 | 23 | 1.9 | 38 |
| -120 | CH HT1-07 | Matrix cracking | 5.0 | 229 | 63 | N/A | 38 |
| -100 | CH HT1-10 | Matrix cracking | 26.0 | 365 | 88 | N/A | 46 |
| -100 | CH HT1-18 | Inclusion related | 8.0 | 390 | 90 | 1.7 | 24 |
| -100 | CH HT2-11 | Inclusion related | 7.5 | 428 | 76 | 2.3 | 51 |
| -100 | CH HT2-12 | Matrix cracking | 19.0 | 636 | 154 | N/A | 44 |

| | | | | | | | |
|---|---|---|---|---|---|---|---|
| -100 | CH HT2-16 | Matrix related Possible M-A-C | 36.0 | 545 | 224 | 1.6 | 30 |
| -100 | CH HT2-18 | Matrix related Possible M-A-C | 23.0 | 530 | 197 | 2.7 | 54 |
| -90 | CH HT1-05 | Inclusion related | 56.5 | 693 | 427 | 1.6 | 42 |
| -90 | CH HT1-06 | Inclusion related | 25.0 | 596 | 157 | 2.2 | 52 |
| -90 | CH HT2-04 | Matrix cracking | 192.0 | 312 | 3803 | N/A | 40 |
| -90 | CH HT2-30 | Matrix cracking | 32.0 | 413 | 273 | N/A | 33 |
| -90 | CH HT2-41 | Matrix related Possible M-A-C | 18.0 | 619 | 184 | 1.9 | 32 |
| -90 | CH HT2-42 | Inclusion related | 90.0 | 300 | 1074 | 1.8 | 34 |

*$X_0$ indicate the distance from end of ductile thumbnail to the cleavage initiation. M-A-C indicate potential martensite-austenite constituents.

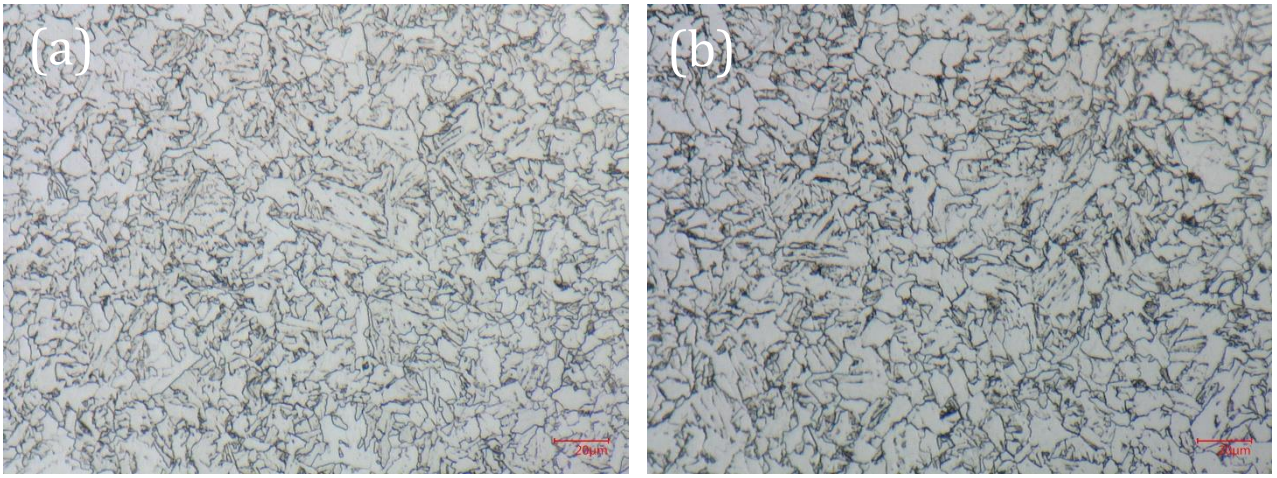


Figure 5-1. Optical microscopy result of (a) HT1 condition and (b) HT2 condition.

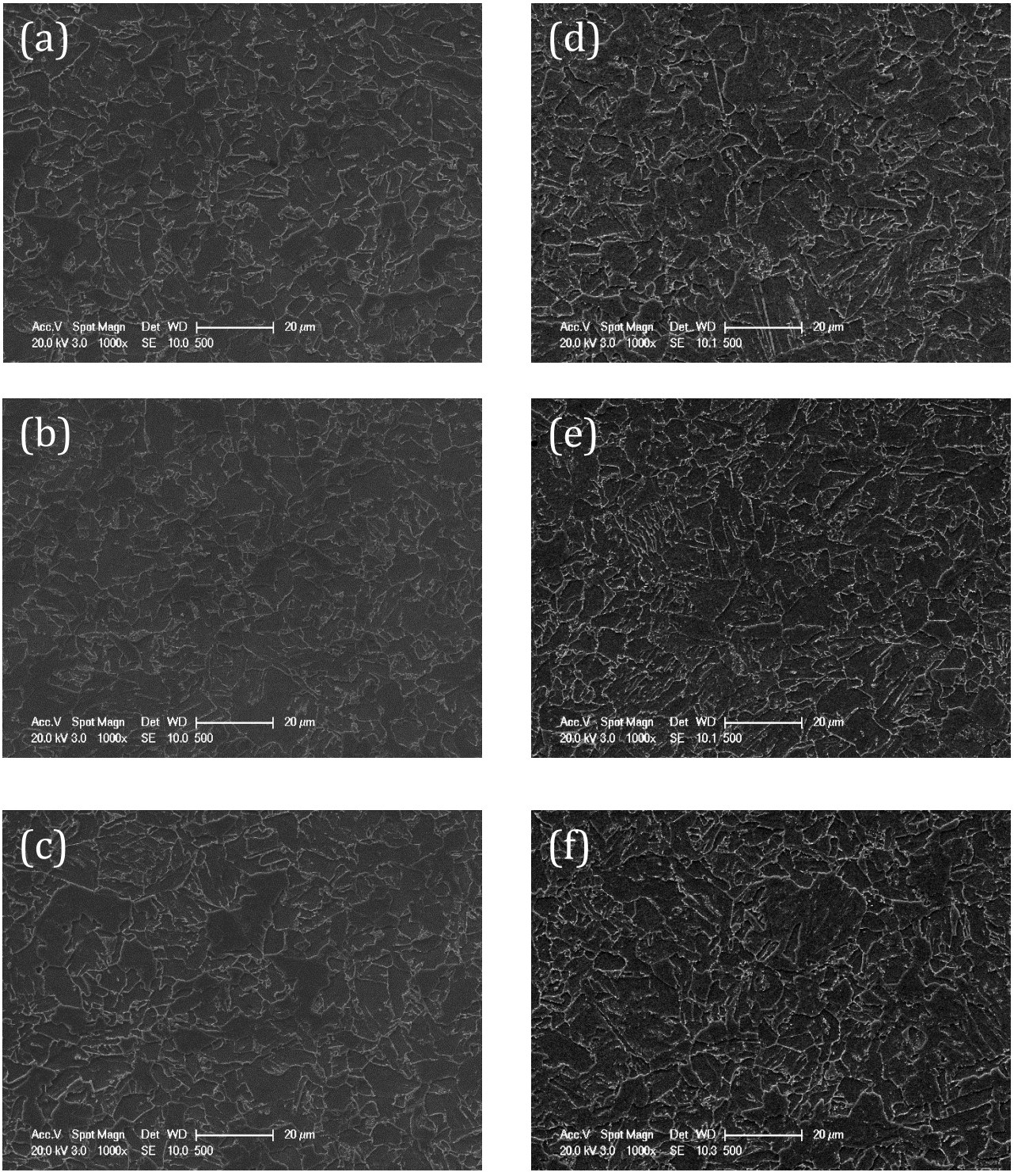


Figure 5-2. Secondary electron microscopy result of random sampled area with magnification of 1000x of HT1 condition (a), (b), (c) and HT2 condition (d), (e), (f).

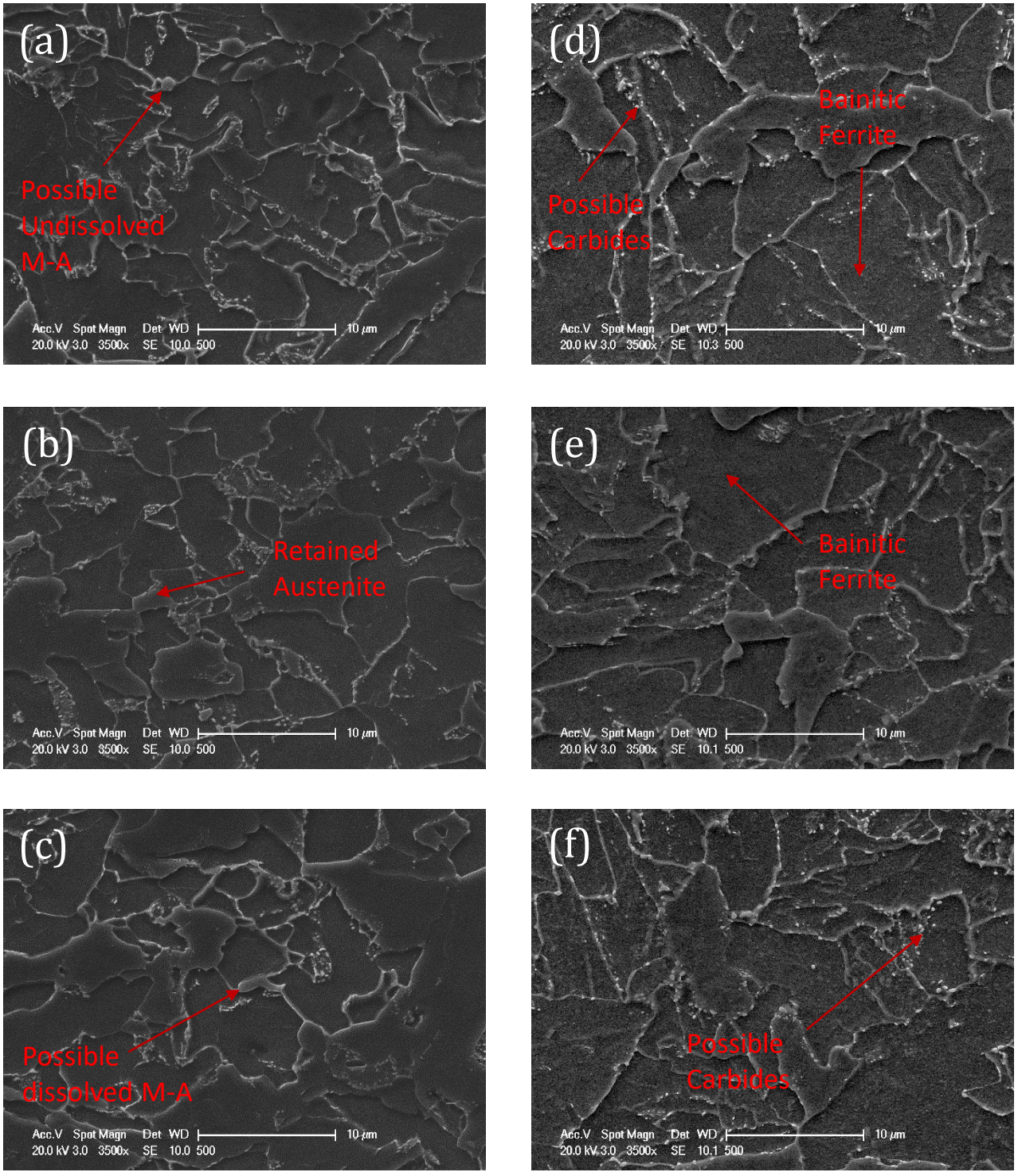


Figure 5-3. Secondary electron microscopy result of random sampled area with magnification of 3500x of HT1 condition (a), (b), (c) and HT2 condition (d), (e), (f).

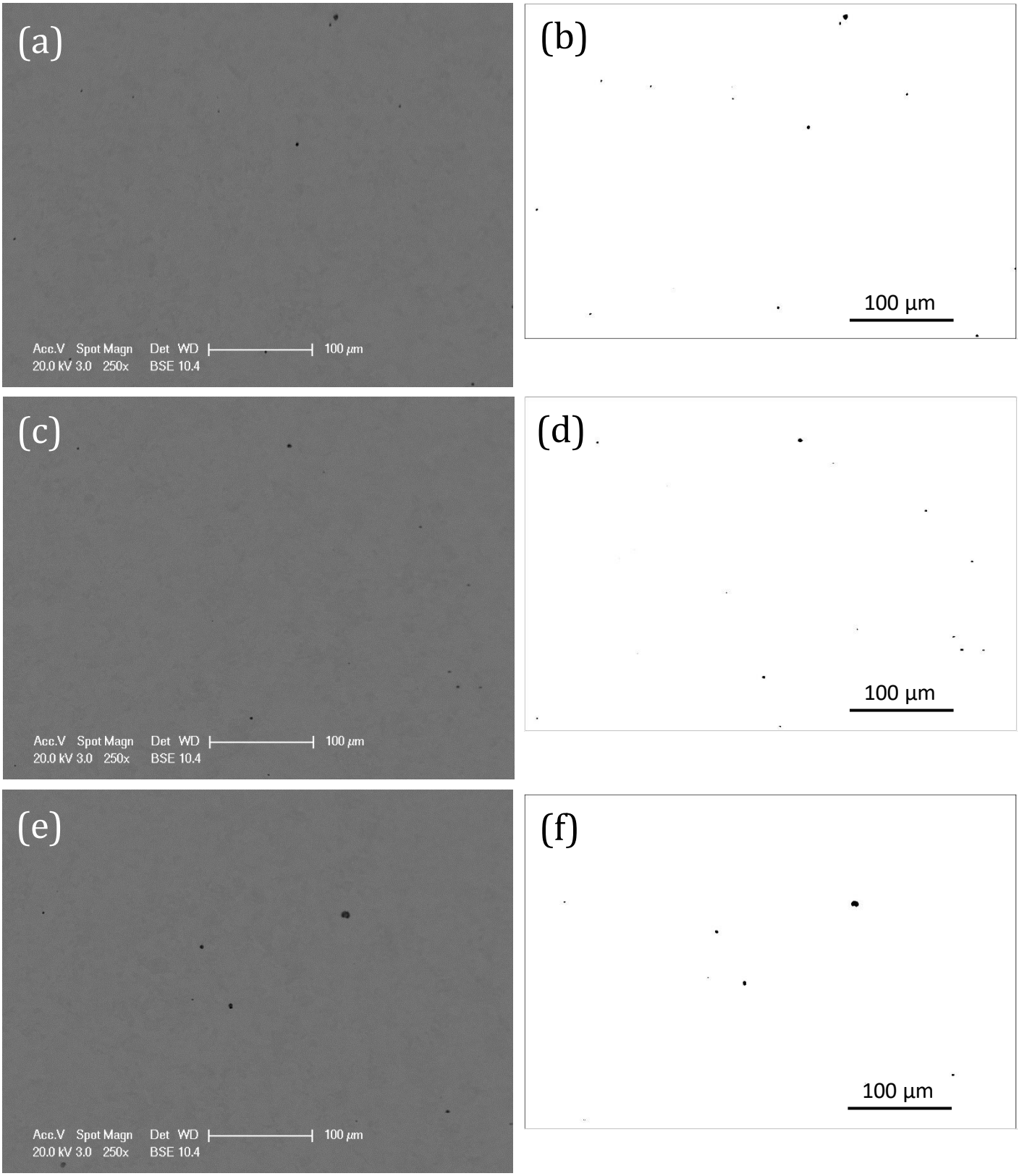


Figure 5-4 (A). Backscattered mode images of random sampled area of polished surfaces from HT1 condition and the ImageJ processed images.

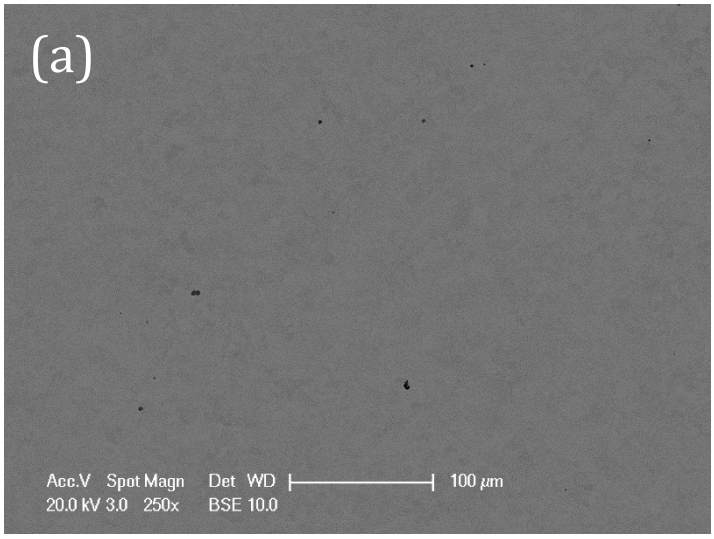


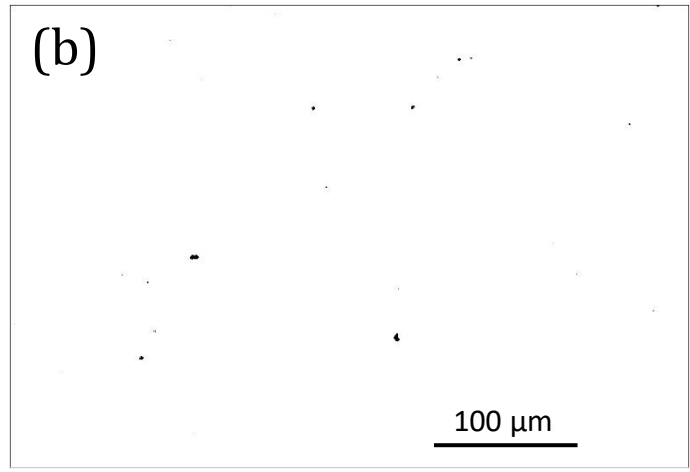


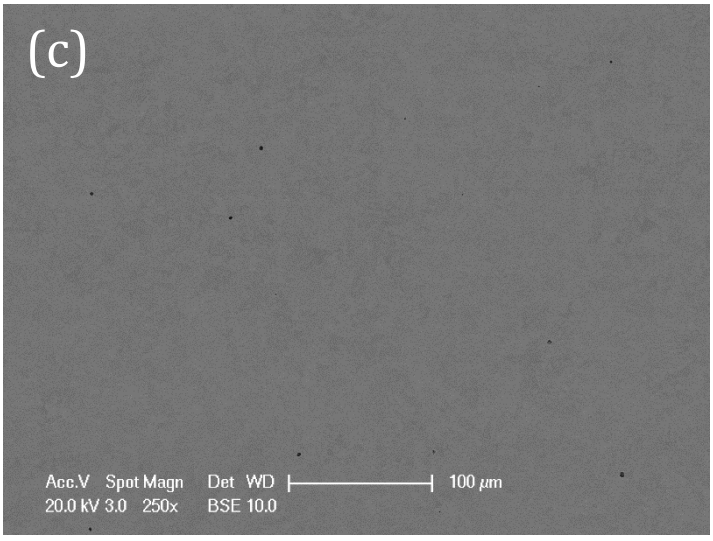


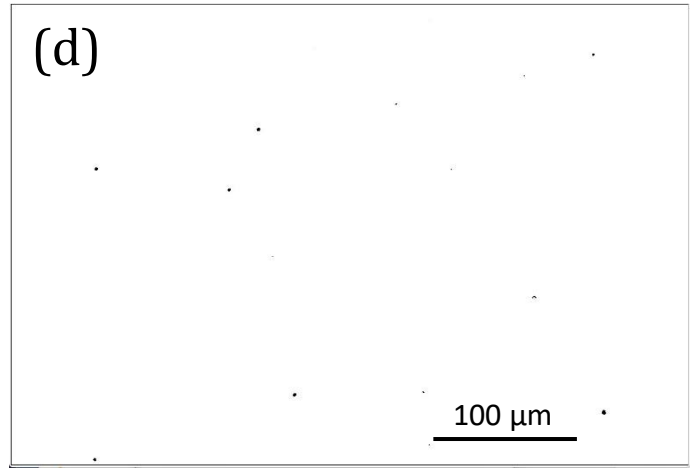


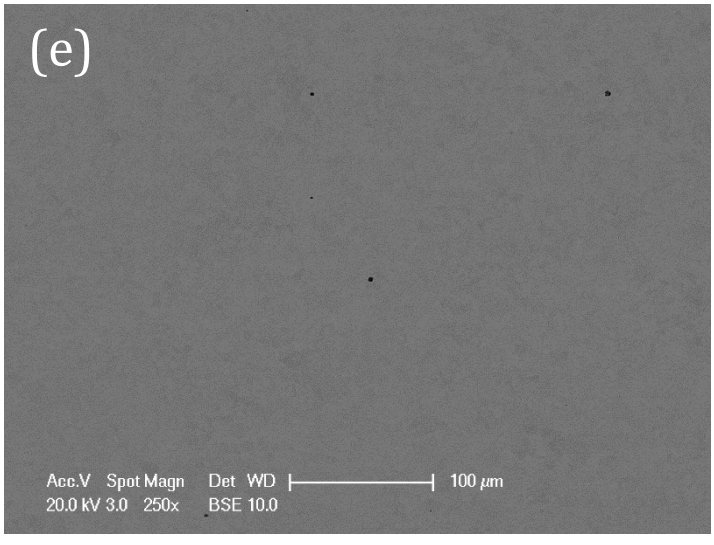


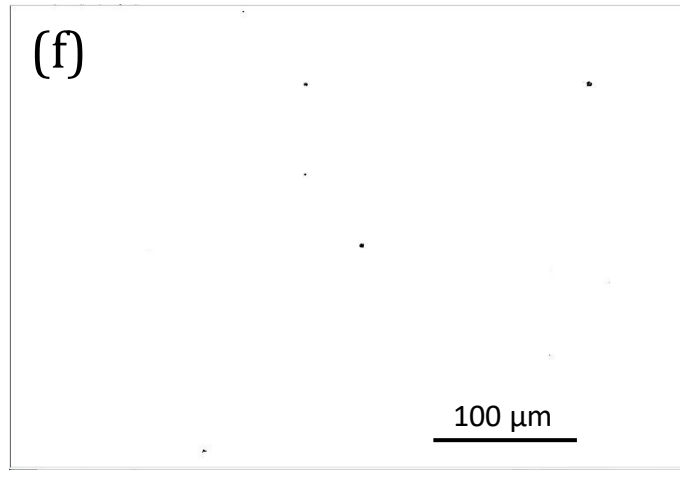


Figure 5-4 (B). Backscattered mode images of random sampled area of polished surfaces from HT2 condition and the ImageJ processed images.

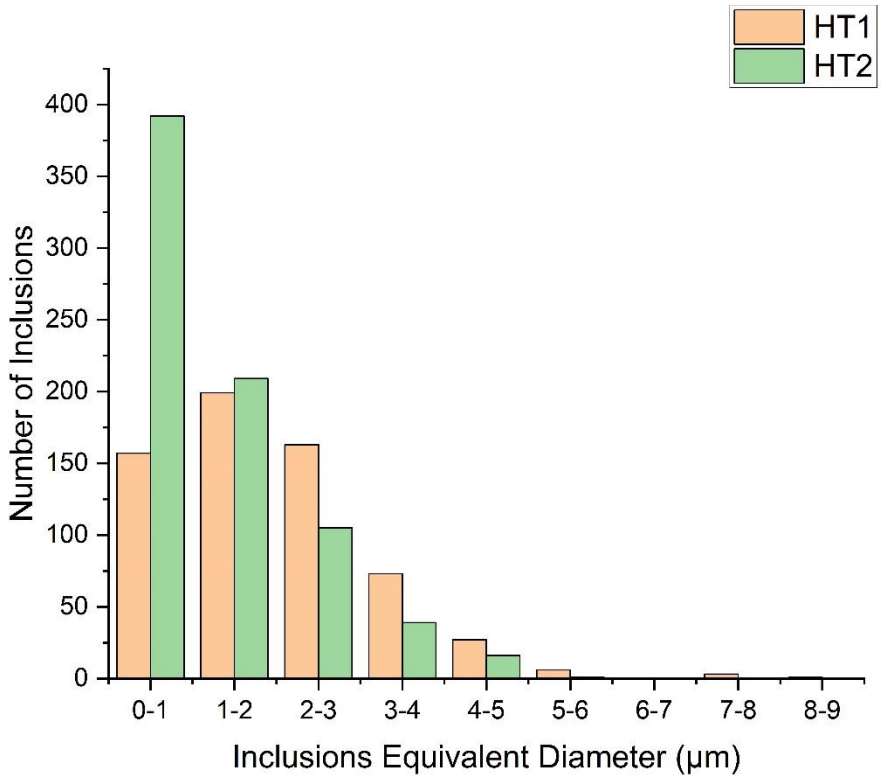


Figure 5-5 (a). Size distribution of inclusions in HT1 and HT2 conditions of polished metallography samples.

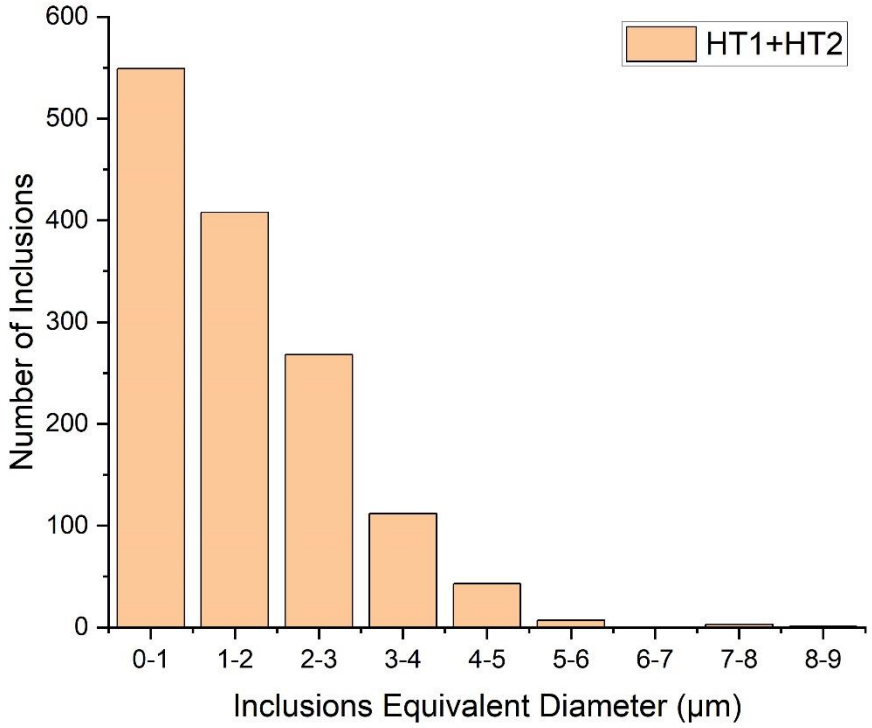


Figure 5-5 (b). Combined size distribution of inclusions in both HT1 and HT2 conditions from polished metallography samples.

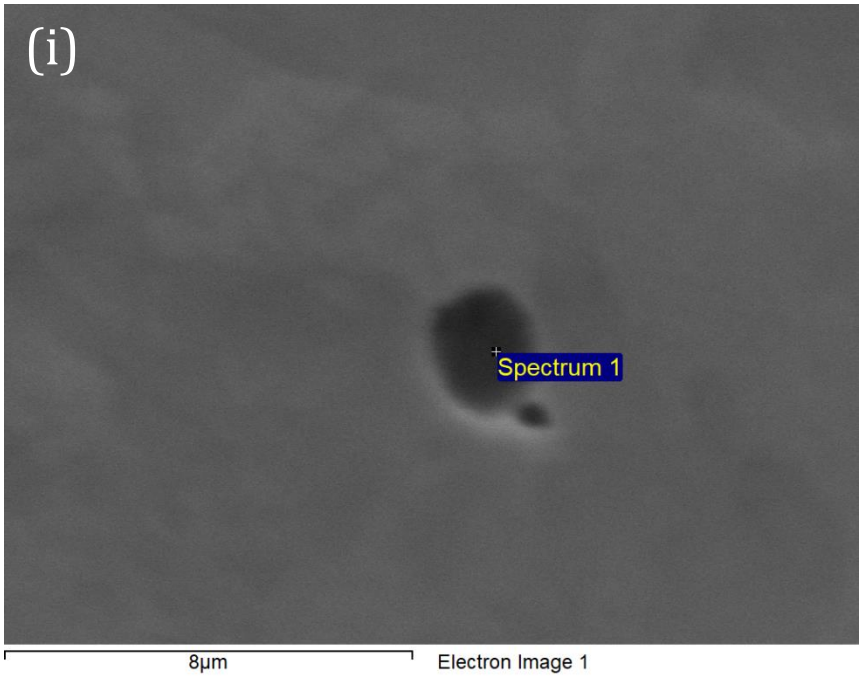


| Element | C | O | Mg | Al | Ca | Ti | Mn | Fe |
|---|---|---|---|---|---|---|---|---|
| Wt% | 6.3 | 16.2 | 6.0 | 5.4 | 3.1 | 1.4 | 0.9 | 60.7 |

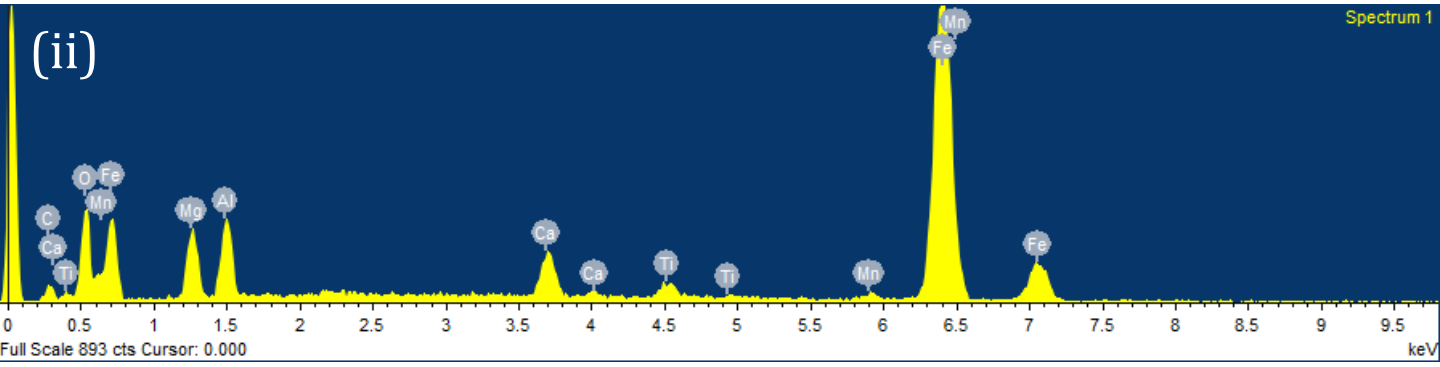


Figure 5-6 (a). Inclusion chemical analysis result from polished metallography samples. (i) shows the SEM image of the inclusion with spectrum location, (ii) is the EDX spectrum result

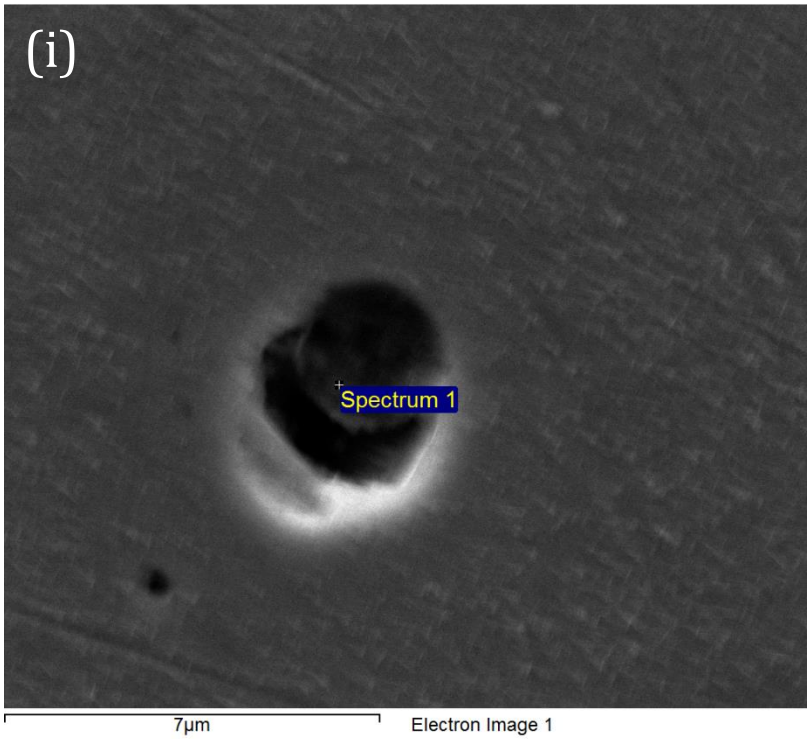


| Element | C | O | Al | S | Ca | Mn | Fe |
|---|---|---|---|---|---|---|---|
| Wt% | 2.5 | 5.2 | 3.6 | 9.8 | 13.1 | 1.1 | 64.7 |

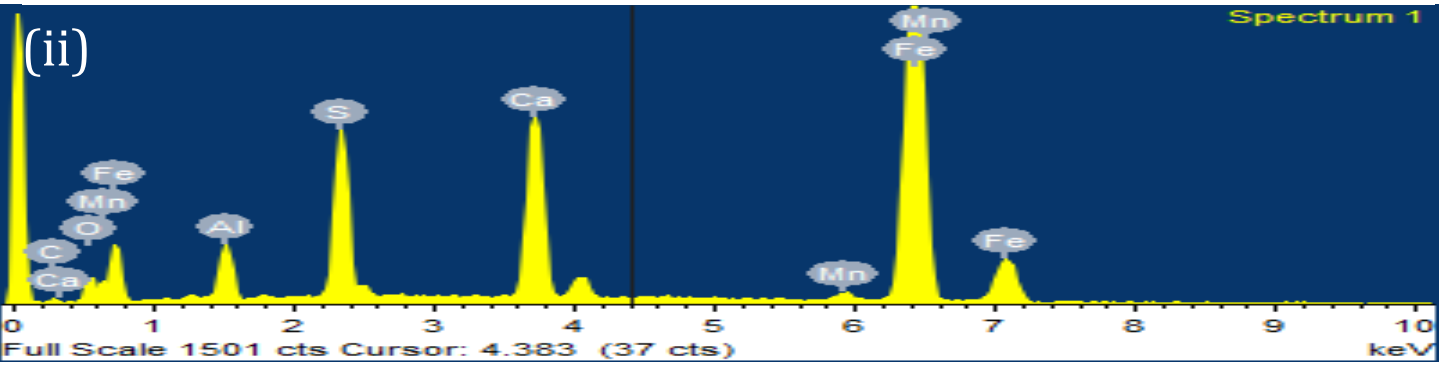


Figure 5-6 (b). Inclusion chemical analysis result from polished metallography samples. (i) shows the SEM image of the inclusion with spectrum location, (ii) is the EDX spectrum result

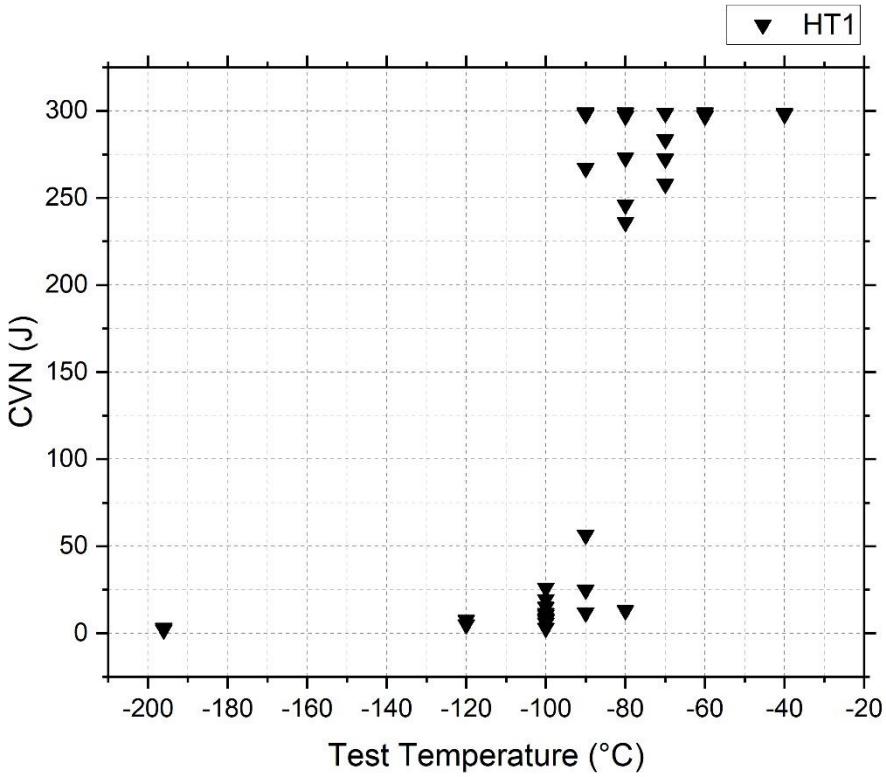


Figure 5-7. Charpy impact energy values plot for HT1 condition.

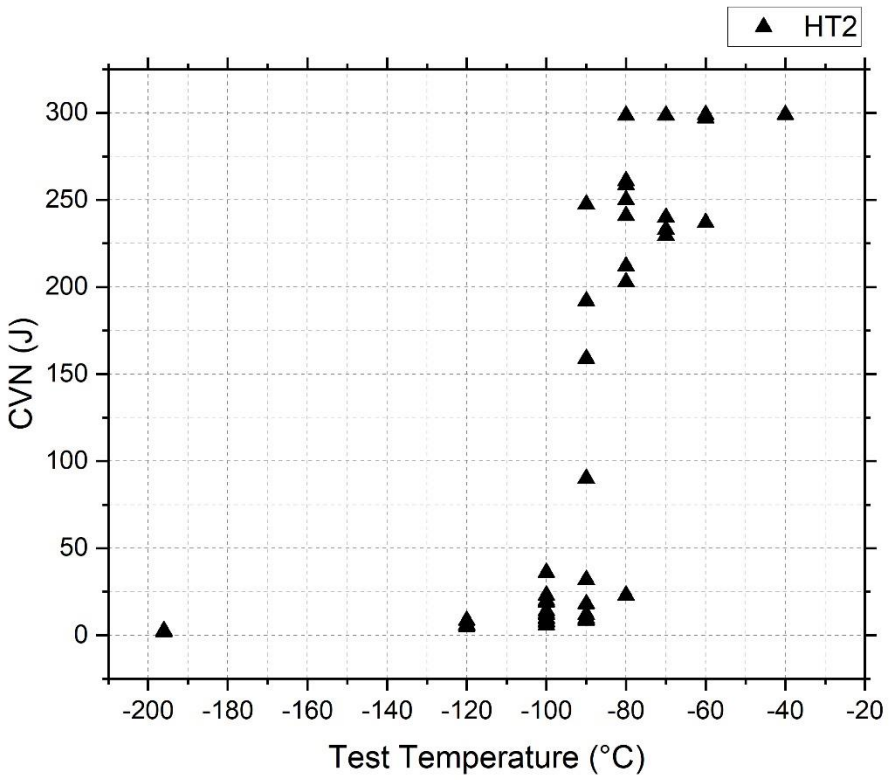


Figure 5-8. Charpy impact energy values plot for HT2 condition.

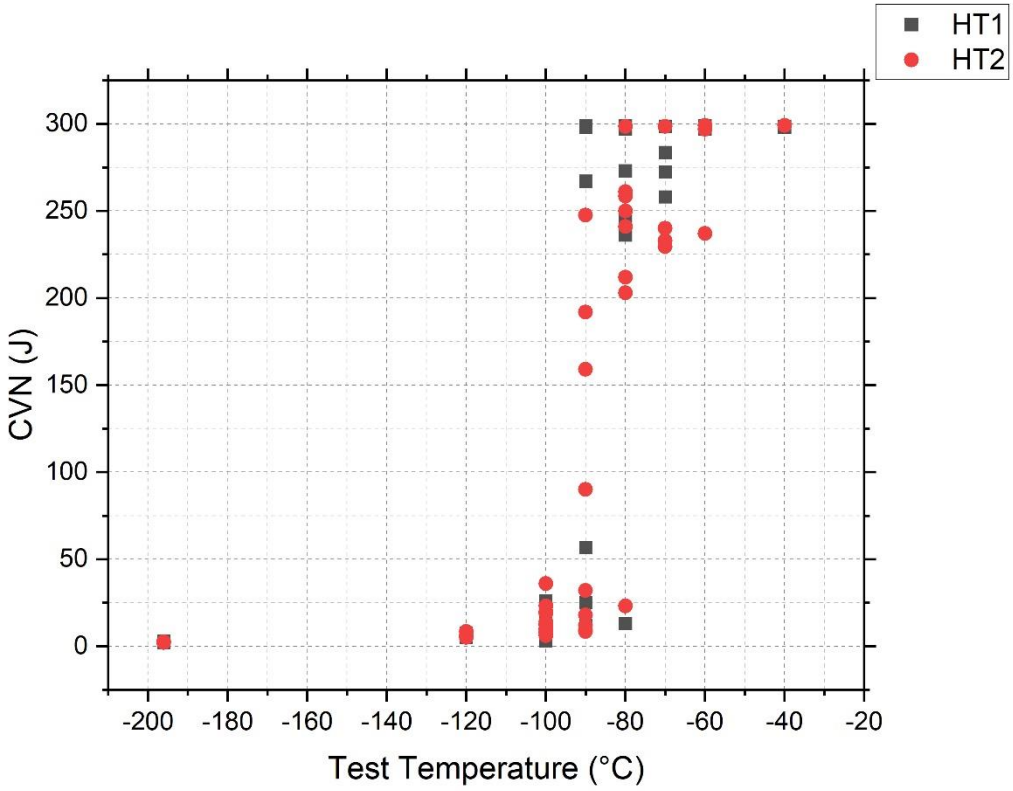


Figure 5-9. Combined Charpy impact energy values plot for both HT1 and HT2 conditions.

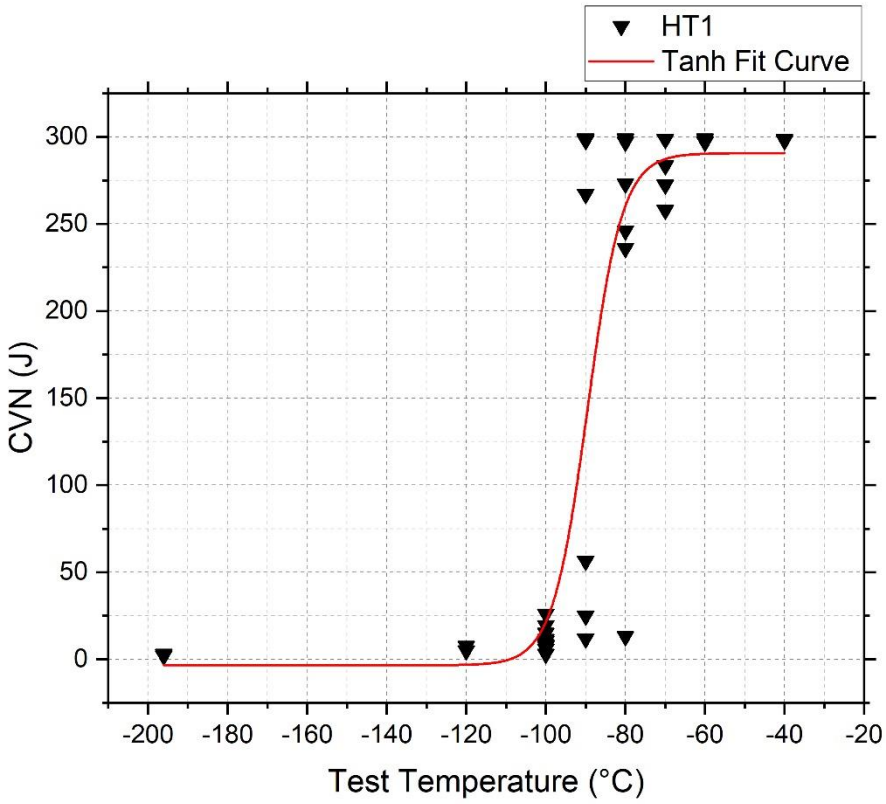


Figure 5-10. Tanh fit curve to Charpy impact energy values of HT1 condition.

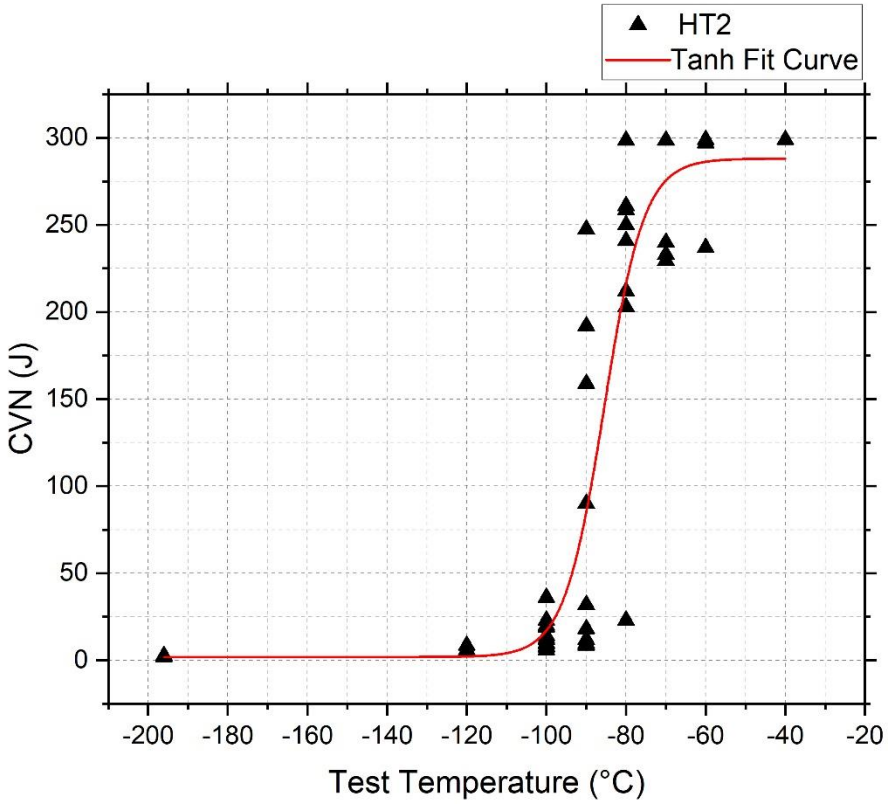


Figure 5-11. Tanh fit curve to Charpy impact energy values of HT2 condition.

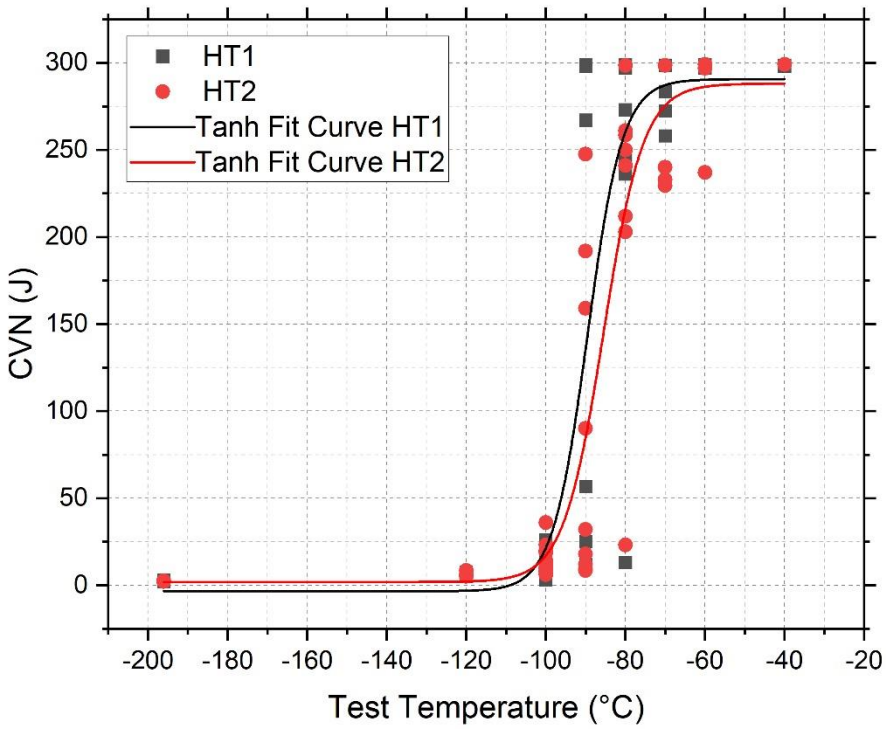


Figure 5-12. Tanh fit curve to Charpy impact energy values of HT1 and HT2 conditions.

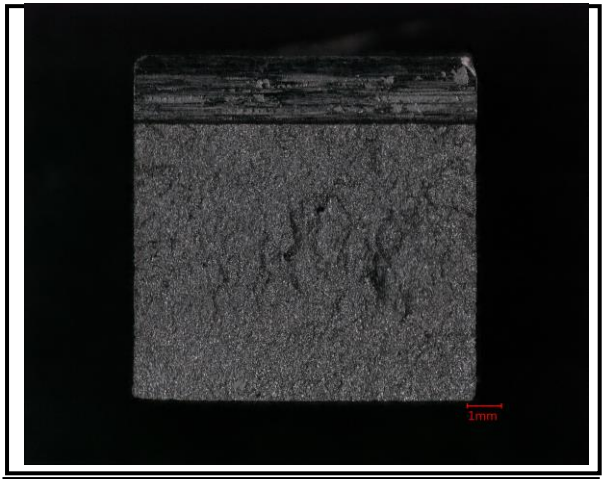

| No. | °C | CVN | CA | LE |
|---|---|---|---|---|
| HT1-1 | -196 | 2.5J | 100% | 0.14mm |

| No. | °C | CVN | CA | LE |
|---|---|---|---|---|
| HT1-2 | -196 | 3.0J | 100% | 0.12mm |

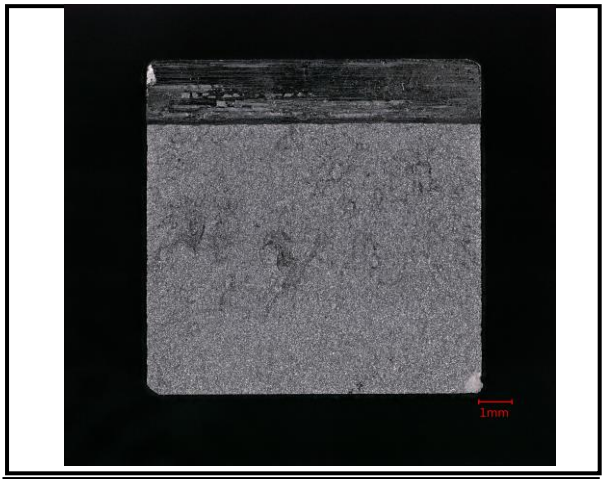

| No. | °C | CVN | CA | LE |
|---|---|---|---|---|
| HT1-3 | -196 | 2.0J | 100% | 0.14mm |

| No. | °C | CVN | CA | LE |
|---|---|---|---|---|
| HT1-7 | -120 | 5.0J | 99.1% | 0.12mm |

| No. | °C | CVN | CA | LE |
|---|---|---|---|---|
| HT1-8 | -120 | 5.0J | 99.3% | 0.12mm |

| No. | °C | CVN | CA | LE |
|---|---|---|---|---|
| HT1-9 | -120 | 5.0J | 98.4% | 0.14mm |

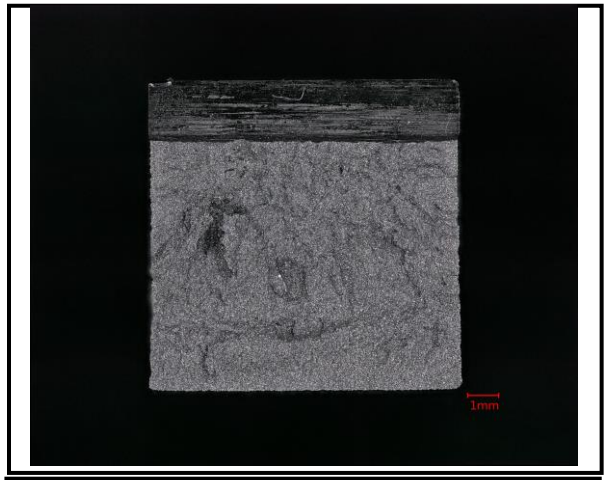

| No. | °C | CVN | CA | LE |
|---|---|---|---|---|
| HT1-52 | -120 | 7.5J | 98.7% | 0.23mm |

| No. | °C | CVN | CA | LE |
|---|---|---|---|---|
| HT1-53 | -120 | 7.5J | 99.2% | 0.15mm |

| No. | °C | CVN | CA | LE |
|---|---|---|---|---|
| HT1-54 | -120 | 5.0J | 98.0% | 0.17mm |

| No. | °C | CVN | CA | LE |
|---|---|---|---|---|
| HT1-10 | -100 | 26.0J | 92.9% | 0.37mm |

| No. | °C | CVN | CA | LE |
|---|---|---|---|---|
| HT1-11 | -100 | 15.0J | 94.8% | 0.25mm |

| No. | °C | CVN | CA | LE |
|---|---|---|---|---|
| HT1-12 | -100 | 10.5J | 97.0% | 0.35mm |

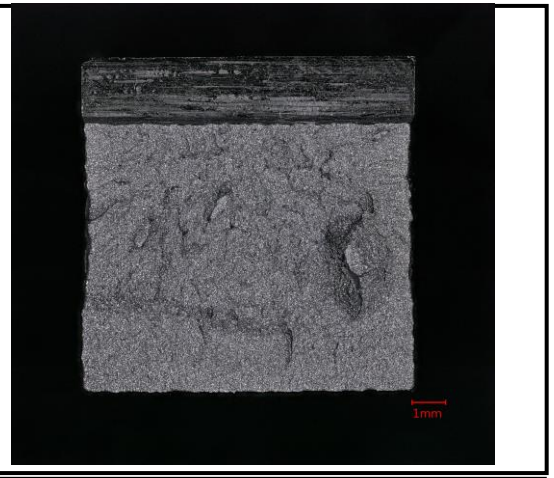

| No. | °C | CVN | CA | LE |
|---|---|---|---|---|
| HT1-16 | -100 | 8.5J | 95.1% | 0.16mm |

| No. | °C | CVN | CA | LE |
|---|---|---|---|---|
| HT1-17 | -100 | 15.0J | 94.8% | 0.25mm |

| No. | °C | CVN | CA | LE |
|---|---|---|---|---|
| HT1-18 | -100 | 8.0J | 96.5% | 0.17mm |

| No. | °C | CVN | CA | LE |
|---|---|---|---|---|
| HT1-38 | -100 | 19.5J | 91.9% | 0.31mm |

| No. | °C | CVN | CA | LE |
|---|---|---|---|---|
| HT1-39 | -100 | 11.5J | 94.8% | 0.22mm |

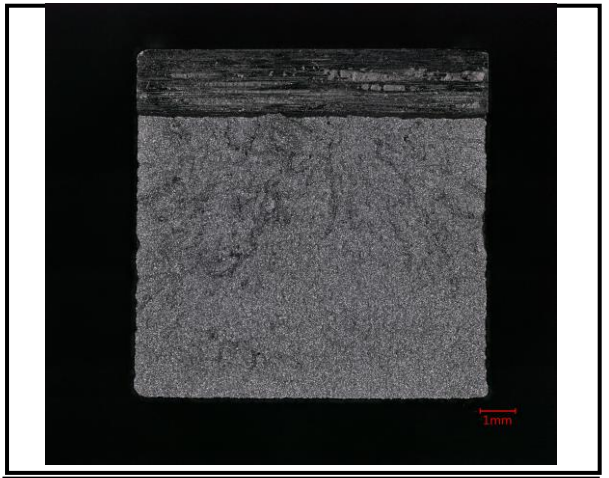

| No. | °C | CVN | CA | LE |
|---|---|---|---|---|
| HT1-46 | -100 | 6.0J | 100% | 0.14mm |

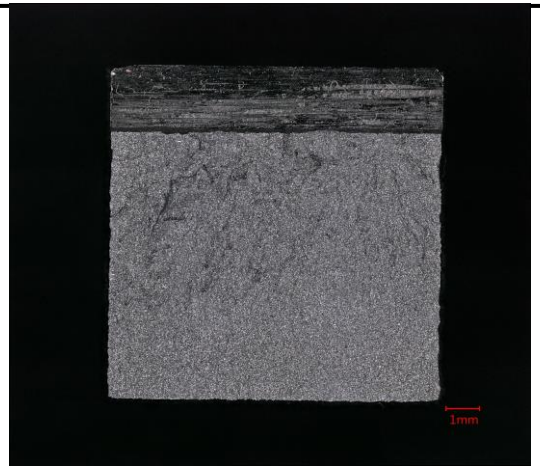

| No. | °C | CVN | CA | LE |
|---|---|---|---|---|
| HT1-47 | -100 | 3.0J | 98.1% | 0.08mm |

| No. | °C | CVN | CA | LE |
|---|---|---|---|---|
| HT1-48 | -100 | 7.5J | 98.7% | 0.20mm |

| No. | °C | CVN | CA | LE |
|---|---|---|---|---|
| HT1-4 | -90 | 298.0J | 0.0% | 2.54mm |

| No. | °C | CVN | CA | LE |
|---|---|---|---|---|
| HT1-5 | -90 | 56.5J | 83.5% | 0.72mm |

| No. | °C | CVN | CA | LE |
|---|---|---|---|---|
| HT1-6 | -90 | 25.0J | 91.5% | 0.27mm |

| No. | °C | CVN | CA | LE |
|---|---|---|---|---|
| HT1-28 | -90 | 12.0J | 91.9% | 0.23mm |

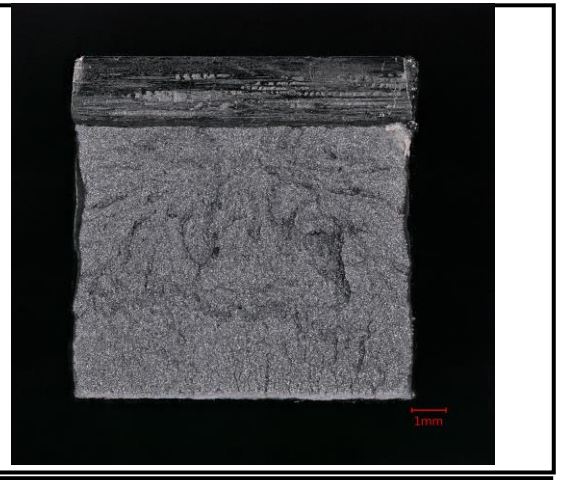

| No. | °C | CVN | CA | LE |
|---|---|---|---|---|
| HT1-29 | -90 | 12.0J | 91.8% | 0.25mm |

| No. | °C | CVN | CA | LE |
|---|---|---|---|---|
| HT1-30 | -90 | 267.0J | 18.2% | 2.23mm |

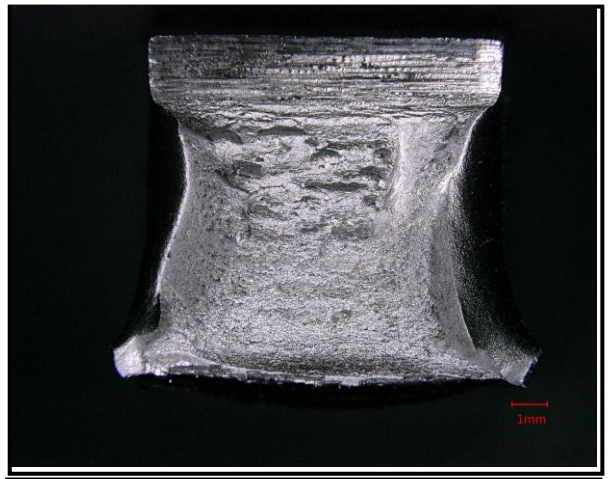

| No. | °C | CVN | CA | LE |
|---|---|---|---|---|
| HT1-40 | -90 | 299.0J | 0.0% | 2.15mm |

| No. | °C | CVN | CA | LE |
|---|---|---|---|---|
| HT1-41 | -90 | 298.5J | 0.0% | 1.98mm |

| No. | °C | CVN | CA | LE |
|---|---|---|---|---|
| HT1-13 | -80 | 299.0J | 0.0% | 2.30mm |

| No. | °C | CVN | CA | LE |
|---|---|---|---|---|
| HT1-14 | -80 | 236.0J | 26.2% | 2.53mm |

| No. | °C | CVN | CA | LE |
|---|---|---|---|---|
| HT1-15 | -80 | 298.5J | 0.0% | 2.20mm |

| No. | °C | CVN | CA | LE |
|---|---|---|---|---|
| HT1-19 | -80 | 297.0J | 0.0% | 2.50mm |

| No. | °C | CVN | CA | LE |
|---|---|---|---|---|
| HT1-20 | -80 | 297.0J | 0.0% | 2.26mm |

| No. | °C | CVN | CA | LE |
|---|---|---|---|---|
| HT1-21 | -80 | 246.0J | 21.0% | 2.32mm |

| No. | °C | CVN | CA | LE |
|---|---|---|---|---|
| HT1-25 | -80 | 299.0J | 0.0% | 2.28mm |

| No. | °C | CVN | CA | LE |
|---|---|---|---|---|
| HT1-26 | -80 | 273.0J | 15.4% | 2.04mm |

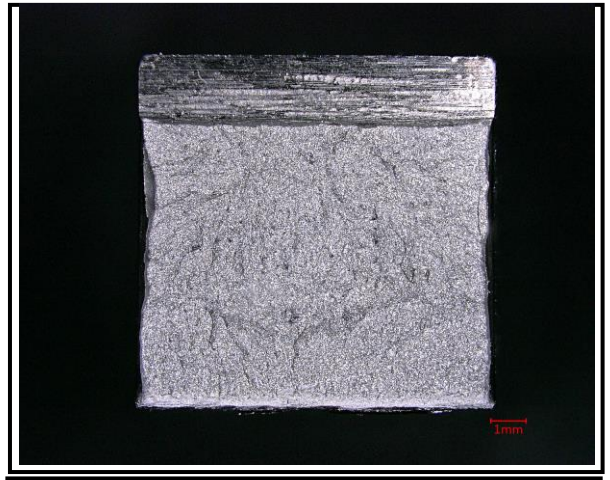

| No. | °C | CVN | CA | LE |
|---|---|---|---|---|
| HT1-27 | -80 | 13.0J | 90.4% | 0.26mm |

| No. | °C | CVN | CA | LE |
|---|---|---|---|---|
| HT1-34 | -70 | 298.5J | 0.0% | 1.79mm |

| No. | °C | CVN | CA | LE |
|---|---|---|---|---|
| HT1-35 | -70 | 298.5J | 0.0% | 2.28mm |

| No. | °C | CVN | CA | LE |
|---|---|---|---|---|
| HT1-36 | -70 | 283.5J | 14.8% | 2.19mm |

| No. | °C | CVN | CA | LE |
|---|---|---|---|---|
| HT1-43 | -70 | 298.5J | 0.0% | 2.25mm |

| No. | °C | CVN | CA | LE |
|---|---|---|---|---|
| HT1-44 | -70 | 258.0J | 20.1% | 1.92mm |

| No. | °C | CVN | CA | LE |
|---|---|---|---|---|
| HT1-45 | -70 | 272.5J | 19.6% | 2.04mm |

| No. | °C | CVN | CA | LE |
|---|---|---|---|---|
| HT1-22 | -60 | 297.5J | 0.0% | 2.28mm |

| No. | °C | CVN | CA | LE |
|---|---|---|---|---|
| HT1-23 | -60 | 297.0J | 0.0% | 2.36mm |

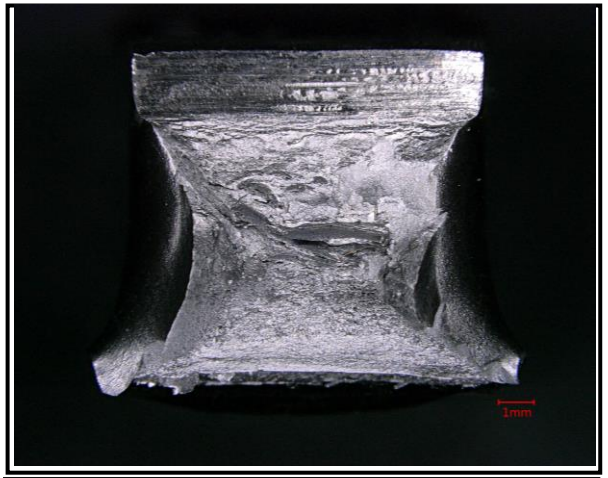

| No. | °C | CVN | CA | LE |
|---|---|---|---|---|
| HT1-24 | -60 | 297.0J | 0.0% | 2.53mm |

| No. | °C | CVN | CA | LE |
|---|---|---|---|---|
| HT1-31 | -60 | 299.0J | 0.0% | 2.35mm |

| No. | °C | CVN | CA | LE |
|---|---|---|---|---|
| HT1-32 | -60 | 299.0J | 0.0% | 2.44mm |

| No. | °C | CVN | CA | LE |
|---|---|---|---|---|
| HT1-33 | -60 | 298.5J | 0.0% | 2.21mm |

| No. | °C | CVN | CA | LE |
|---|---|---|---|---|
| HT1-49 | -40 | 298.5J | 0.0% | 2.25mm |

| No. | °C | CVN | CA | LE |
|---|---|---|---|---|
| HT1-50 | -40 | 298.5J | 0.0% | 2.39mm |

| No. | °C | CVN | CA | LE |
|---|---|---|---|---|
| HT1-51 | -40 | 298.0J | 0.0% | 2.36mm |

Figure 5-13. Charpy Impact Test specimen fracture surfaces for HT1 condition

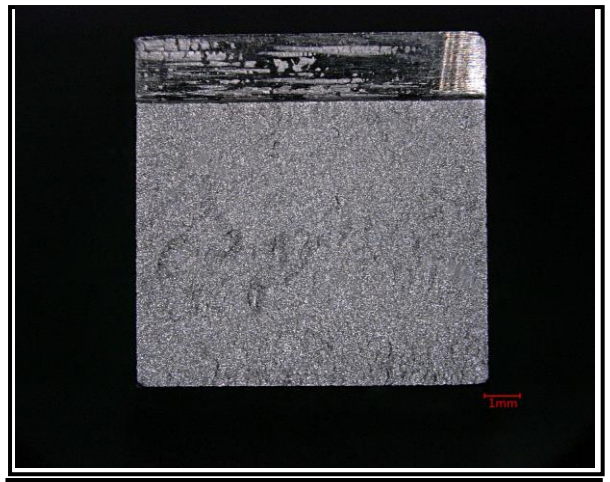

| No. | °C | CVN | CA | LE |
|---|---|---|---|---|
| HT2-1 | -196 | 2.0J | 100% | 0.00mm |

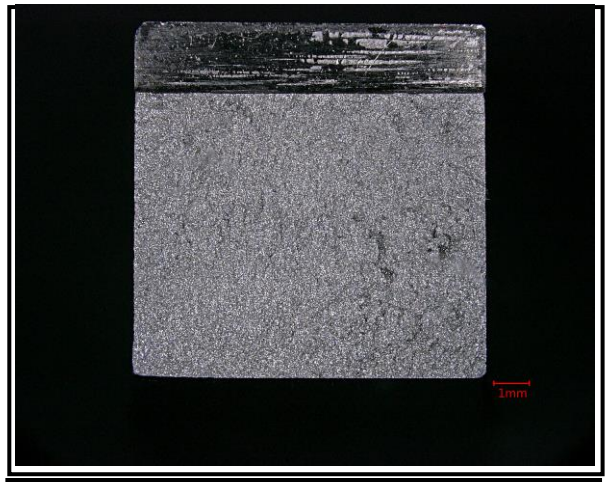

| No. | °C | CVN | CA | LE |
|---|---|---|---|---|
| HT2-2 | -196 | 2.5J | 100% | 0.15mm |

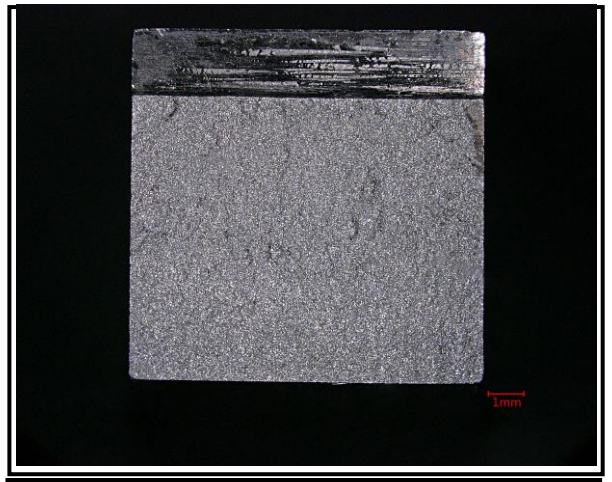

| No. | °C | CVN | CA | LE |
|---|---|---|---|---|
| HT2-3 | -196 | 2.0J | 100% | 0.08mm |

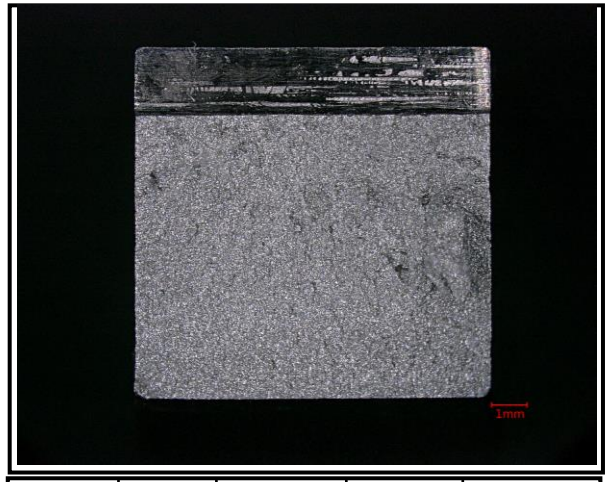

| No. | °C | CVN | CA | LE |
|---|---|---|---|---|
| HT2-7 | -120 | 5.0J | 99.4% | 0.18mm |

| No. | °C | CVN | CA | LE |
|---|---|---|---|---|
| HT2-8 | -120 | 5.5J | 100.0% | 0.10mm |

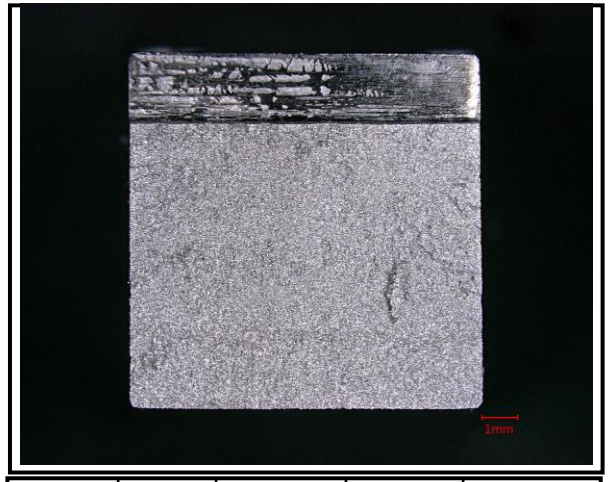

| No. | °C | CVN | CA | LE |
|---|---|---|---|---|
| HT2-9 | -120 | 6.0J | 99.9% | 0.10mm |

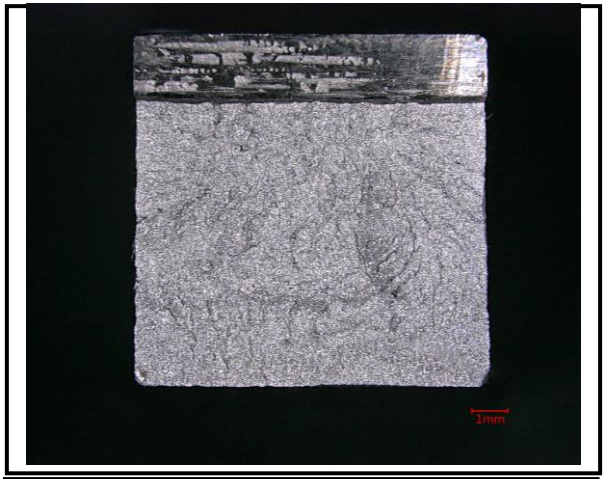

| No. | °C | CVN | CA | LE |
|---|---|---|---|---|
| HT2-52 | -120 | 8.5J | 97.5% | 0.13mm |

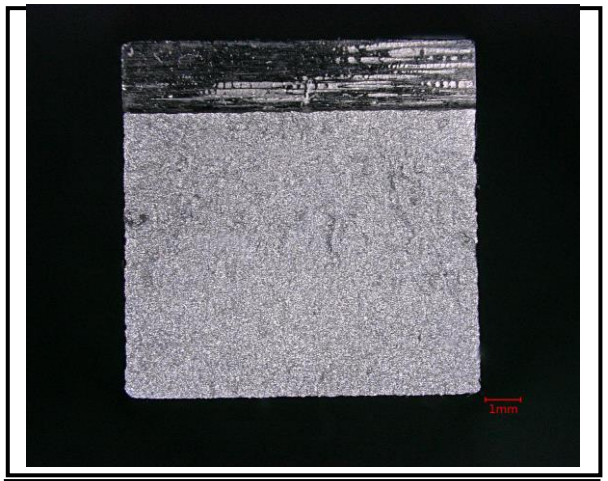

| No. | °C | CVN | CA | LE |
|---|---|---|---|---|
| HT2-53 | -120 | 5.0J | 99.5% | 0.13mm |

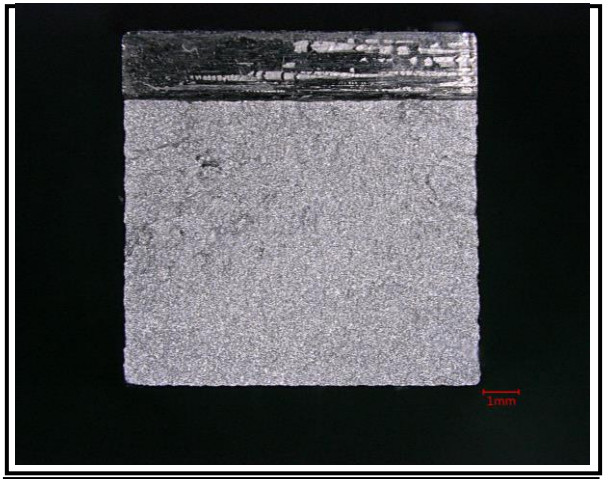

| No. | °C | CVN | CA | LE |
|---|---|---|---|---|
| HT2-54 | -120 | 5.0J | 99.9% | 0.15mm |

| No. | °C | CVN | CA | LE |
|---|---|---|---|---|
| HT2-10 | -100 | 12.5J | 94.6% | 0.17mm |

| No. | °C | CVN | CA | LE |
|---|---|---|---|---|
| HT2-11 | -100 | 7.5J | 95.6% | 0.27mm |

| No. | °C | CVN | CA | LE |
|---|---|---|---|---|
| HT2-12 | -100 | 19.0J | 93.3% | 0.22mm |

| No. | °C | CVN | CA | LE |
|---|---|---|---|---|
| HT2-16 | -100 | 36.0J | 96.9% | 0.47mm |

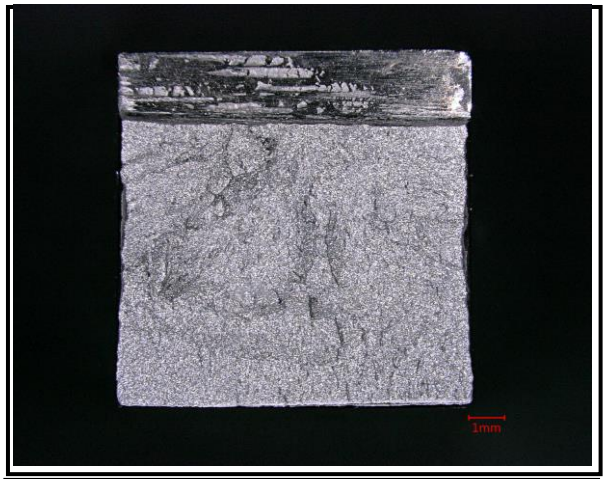

| No. | °C | CVN | CA | LE |
|---|---|---|---|---|
| HT2-17 | -100 | 12.0J | 96.9% | 0.18mm |

| No. | °C | CVN | CA | LE |
|---|---|---|---|---|
| HT2-18 | -100 | 23.0J | 95.4% | 0.15mm |

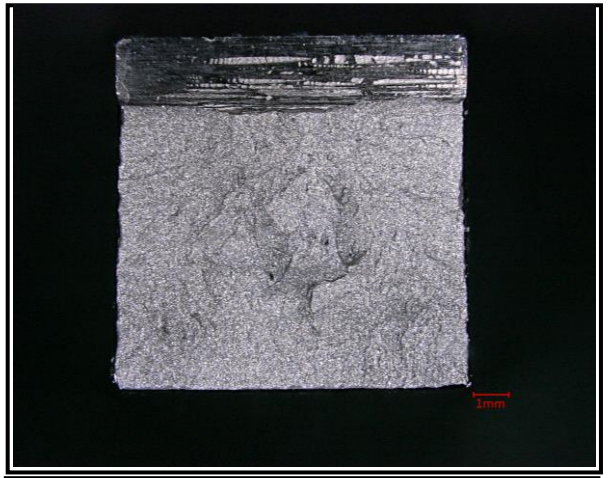

| No. | °C | CVN | CA | LE |
|---|---|---|---|---|
| HT2-37 | -100 | 14.0J | 96.6% | 0.18mm |

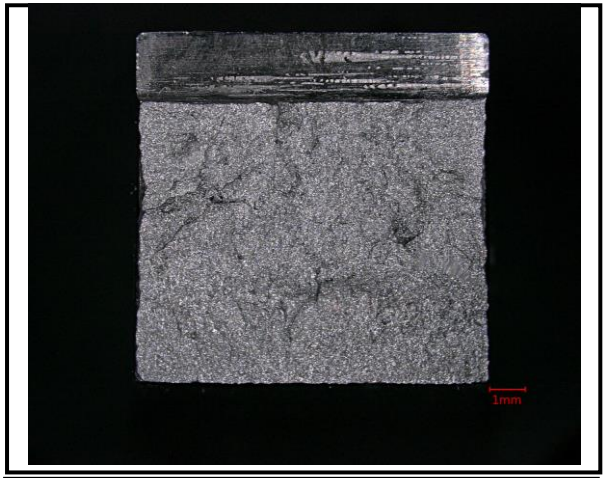

| No. | °C | CVN | CA | LE |
|---|---|---|---|---|
| HT2-38 | -100 | 9.5J | 97.3% | 0.15mm |

| No. | °C | CVN | CA | LE |
|---|---|---|---|---|
| HT2-39 | -100 | 20.0J | 95.2% | 0.32mm |

| No. | °C | CVN | CA | LE |
|---|---|---|---|---|
| HT2-46 | -100 | 8.0J | 99.4% | 0.25mm |

| No. | °C | CVN | CA | LE |
|---|---|---|---|---|
| HT2-47 | -100 | 10.0J | 96.2% | 0.17mm |

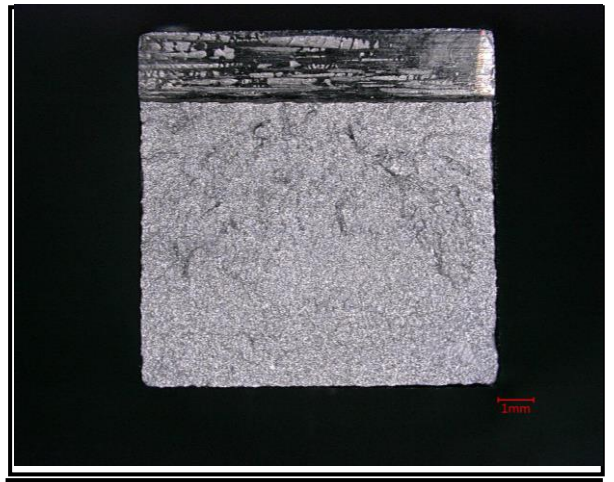

| No. | °C | CVN | CA | LE |
|---|---|---|---|---|
| HT2-48 | -100 | 6.0J | 99.8% | 0.27mm |

| No. | °C | CVN | CA | LE |
|---|---|---|---|---|
| HT2-4 | -90 | 192.0J | 44.5% | 2.04mm |

| No. | °C | CVN | CA | LE |
|---|---|---|---|---|
| HT2-5 | -90 | 159.0J | 62.5% | 1.74mm |

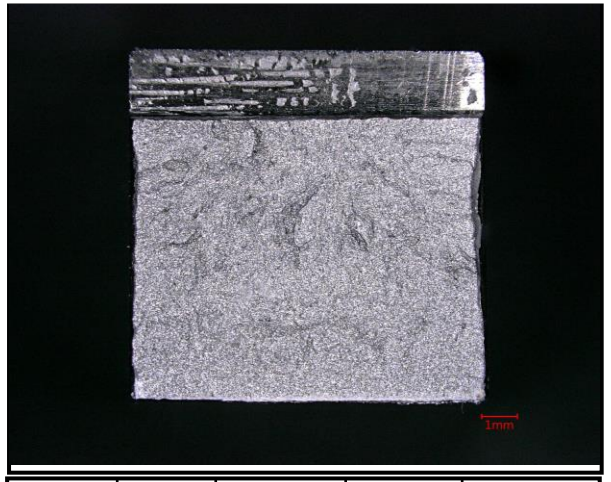

| No. | °C | CVN | CA | LE |
|---|---|---|---|---|
| HT2-6 | -90 | 8.5J | 94.8% | 0.32mm |

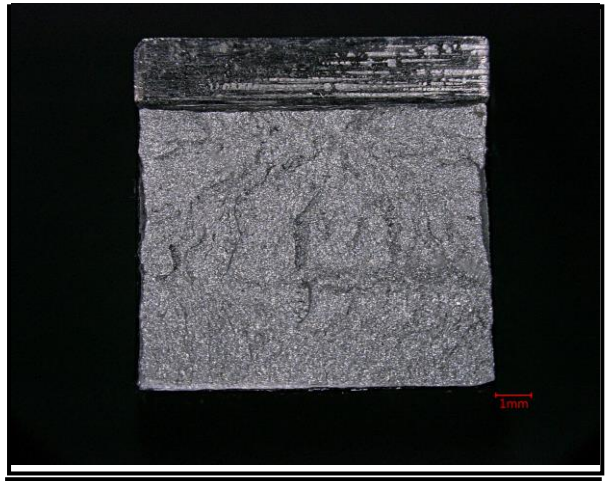

| No. | °C | CVN | CA | LE |
|---|---|---|---|---|
| HT2-28 | -90 | 12.0J | 93.5% | 0.30mm |

| No. | °C | CVN | CA | LE |
|---|---|---|---|---|
| HT2-29 | -90 | 9.5J | 91.0% | 0.10mm |

| No. | °C | CVN | CA | LE |
|---|---|---|---|---|
| HT2-30 | -90 | 32.0J | 92.3% | 0.29mm |

| No. | °C | CVN | CA | LE |
|---|---|---|---|---|
| HT2-40 | -90 | 247.5J | 23.4% | 2.42mm |

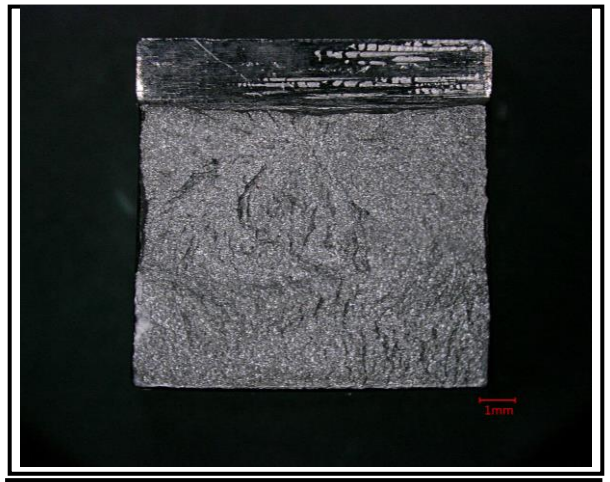

| No. | °C | CVN | CA | LE |
|---|---|---|---|---|
| HT2-41 | -90 | 18.0J | 94.8% | 0.14mm |

| No. | °C | CVN | CA | LE |
|---|---|---|---|---|
| HT2-42 | -90 | 90J | 79.0% | 1.14mm |

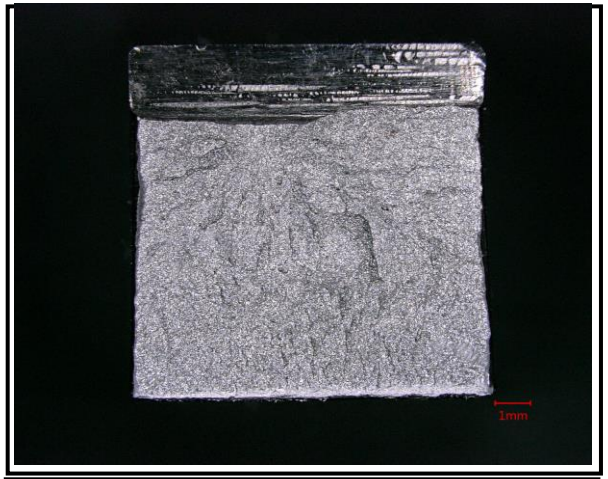

| No. | °C | CVN | CA | LE |
|---|---|---|---|---|
| HT2-13 | -80 | 23.0J | 94.1% | 0.35mm |

| No. | °C | CVN | CA | LE |
|---|---|---|---|---|
| HT2-14 | -80 | 258.5J | 22.0% | 2.08mm |

| No. | °C | CVN | CA | LE |
|---|---|---|---|---|
| HT2-15 | -80 | 250.0J | 20.6% | 2.21mm |

| No. | °C | CVN | CA | LE |
|---|---|---|---|---|
| HT2-19 | -80 | 241.0J | 25.1% | 2.26mm |

| No. | °C | CVN | CA | LE |
|---|---|---|---|---|
| HT2-20 | -80 | 203.0J | 35.0% | 2.40mm |

| No. | °C | CVN | CA | LE |
|---|---|---|---|---|
| HT2-21 | -80 | 212.0J | 30.3% | 2.45mm |

| No. | °C | CVN | CA | LE |
|---|---|---|---|---|
| HT2-25 | -80 | 261.0J | 18.4% | 2.13mm |

| No. | °C | CVN | CA | LE |
|---|---|---|---|---|
| HT2-27 | -80 | 298.5J | 0.0% | 2.35mm |

| No. | °C | CVN | CA | LE |
|---|---|---|---|---|
| HT2-34 | -70 | 298.5J | 0.0% | 2.24mm |

| No. | °C | CVN | CA | LE |
|---|---|---|---|---|
| HT2-35 | -70 | 240.0J | 28.2% | 2.40mm |

| No. | °C | CVN | CA | LE |
|---|---|---|---|---|
| HT2-36 | -70 | 233.0J | 27.9% | 2.21mm |

| No. | °C | CVN | CA | LE |
|---|---|---|---|---|
| HT2-43 | -70 | 229.5J | 27.0% | 2.53mm |

| No. | °C | CVN | CA | LE |
|---|---|---|---|---|
| HT2-44 | -70 | 298.5J | 0.0% | 2.12mm |

| No. | °C | CVN | CA | LE |
|---|---|---|---|---|
| HT2-45 | -70 | 298.5J | 0.0% | 2.47mm |

| No. | °C | CVN | CA | LE |
|---|---|---|---|---|
| HT2-22 | -60 | 297.0J | 0.0% | 2.33mm |

| No. | °C | CVN | CA | LE |
|---|---|---|---|---|
| HT2-23 | -60 | 297.0J | 0.0% | 2.36mm |

| No. | °C | CVN | CA | LE |
|---|---|---|---|---|
| HT2-24 | -60 | 297.0J | 0.0% | 2.44mm |

| No. | °C | CVN | CA | LE |
|---|---|---|---|---|
| HT2-31 | -60 | 299.0J | 0.0% | 2.33mm |

| No. | °C | CVN | CA | LE |
|---|---|---|---|---|
| HT2-32 | -60 | 299.0J | 0.0% | 2.43mm |

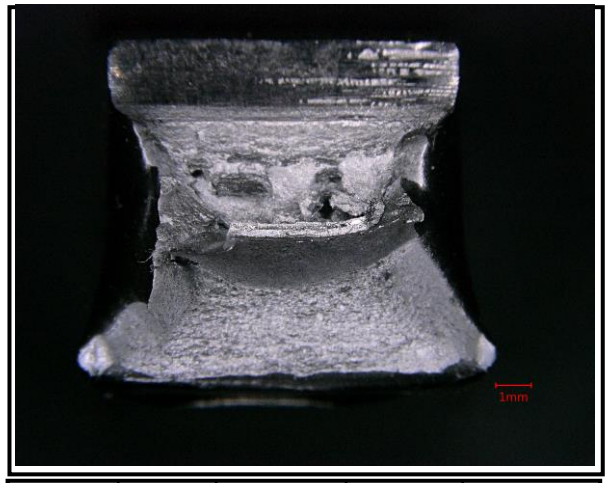

| No. | °C | CVN | CA | LE |
|---|---|---|---|---|
| HT2-33 | -60 | 237.0J | 6.5% | 2.10mm |

| No. | °C | CVN | CA | LE |
|---|---|---|---|---|
| HT2-49 | -40 | 299.0J | 0.0% | 2.46mm |

| No. | °C | CVN | CA | LE |
|---|---|---|---|---|
| HT2-50 | -40 | 299.0J | 0.0% | 2.36mm |

| No. | °C | CVN | CA | LE |
|---|---|---|---|---|
| HT2 -51 | -40 | 299.0J | 0.0% | 2.30mm |

Figure 5-14. Charpy Impact Test specimen fracture surfaces for HT2 condition

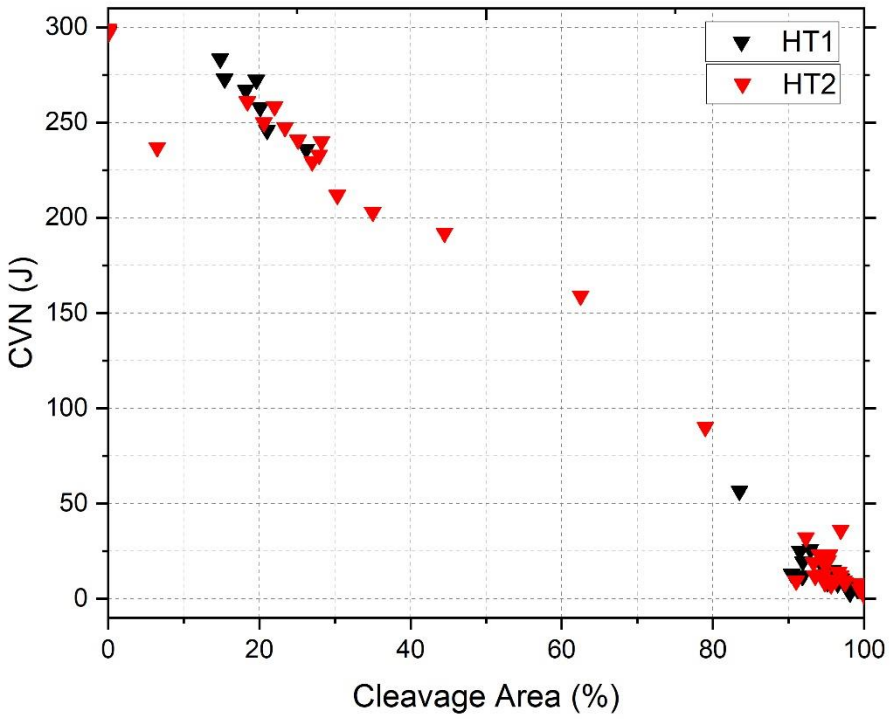


Figure 5-15. Charpy impact energy variation with cleavage area percentage for HT1 and HT2 condition.

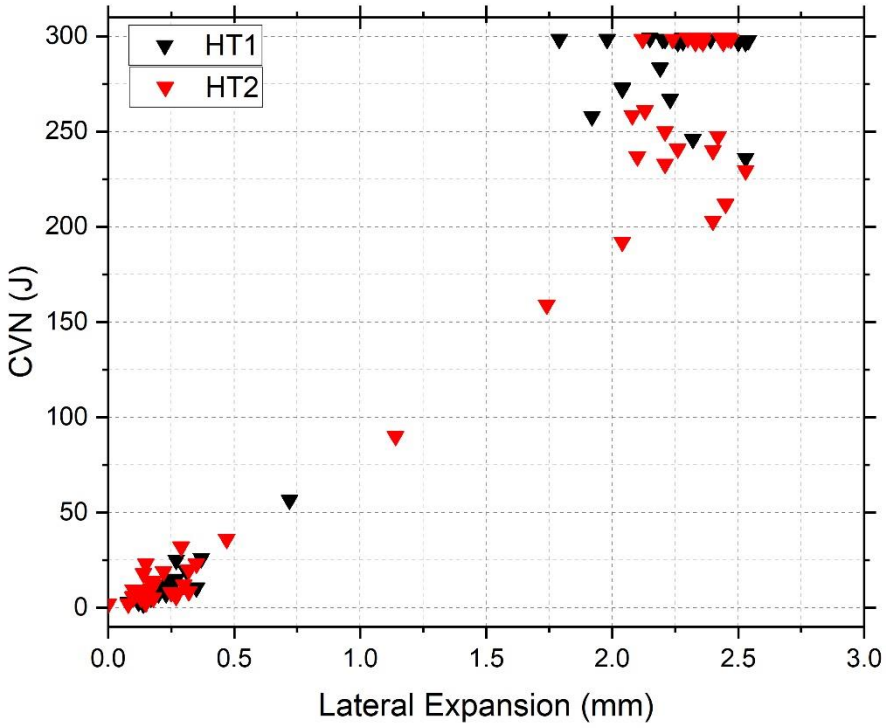


Figure 5-16. Charpy impact energy variation with lateral expansion for HT1 and HT2 condition.

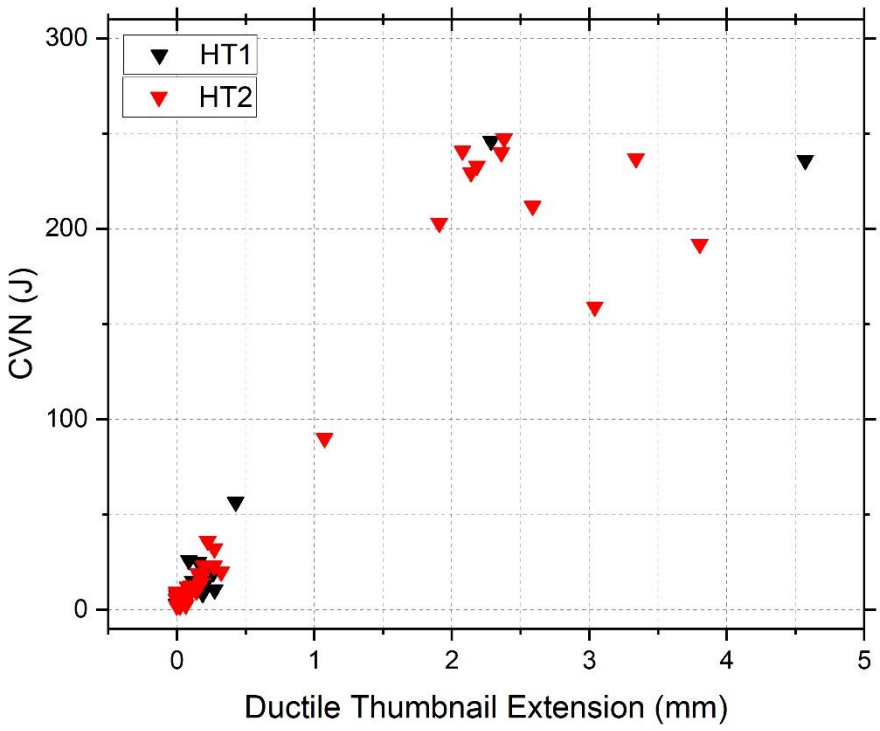


Figure 5-17. Charpy impact energy variation with ductile thumbnail extension for HT1 and HT2 condition.

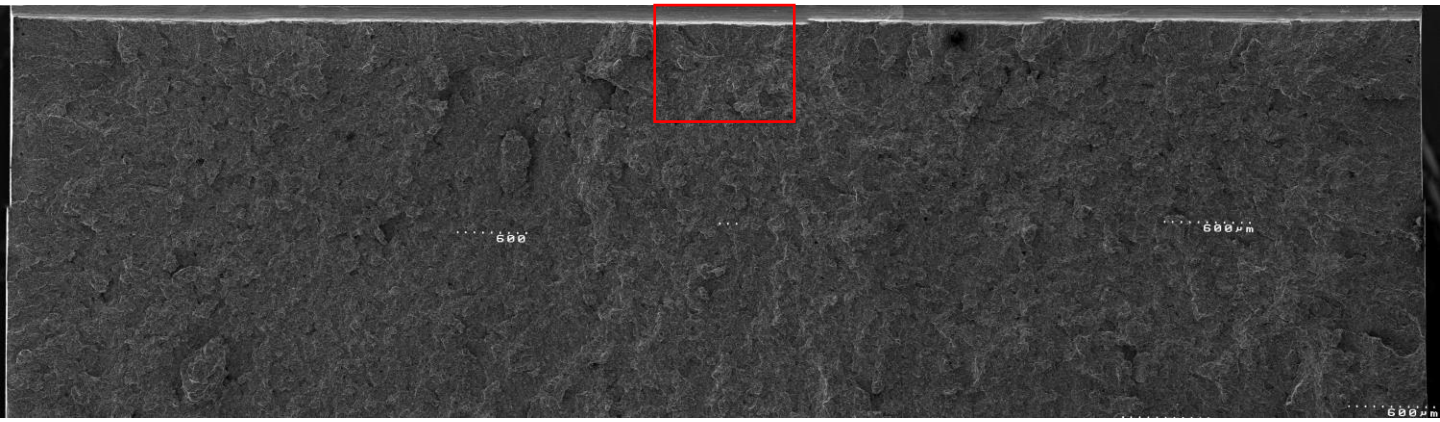

Figure 5-18 (a). Overview of the fracture surface on one side of the Charpy specimen CH HT2-01, tested at -196°C, with a red frame indicating the most probable initiation area. Test results: Charpy impact energy (CVN) of 2 J, fracture initiation distance (X0) of 229 µm, specimen cleavage area of 100%, lateral expansion of 0 mm.

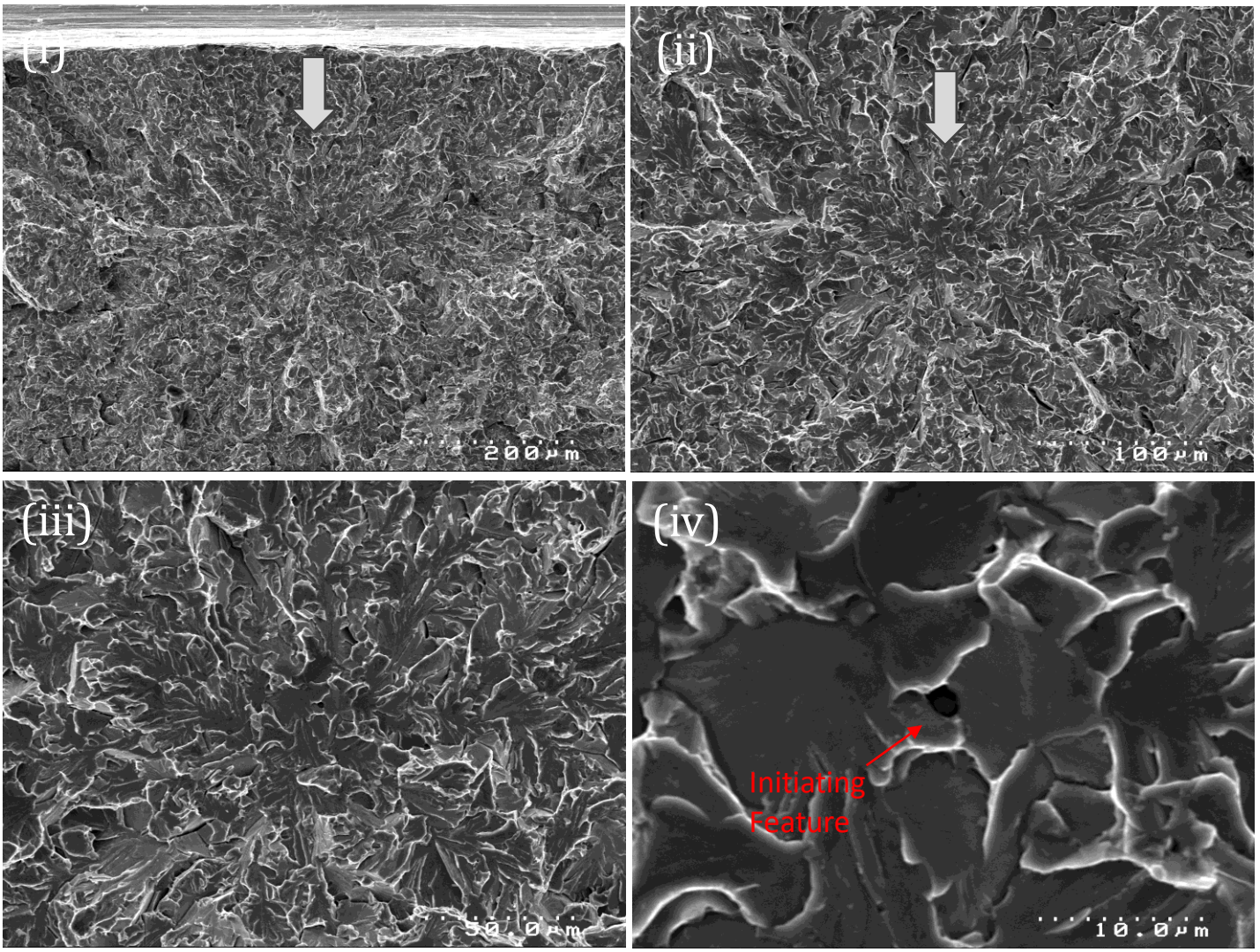


Figure 5-18 (b). Fracture initiation point of one side Charpy specimen CH HT2-01 tested at -196 °C; (i), (ii), (iii) and (iv) are sequential magnification of the same red framed area. Fractographic analysis reveals inclusion related feature as the initiation, with the initiating feature's equivalent diameter at 1.9 µm and the initial facet's equivalent diameter at 38 µm.

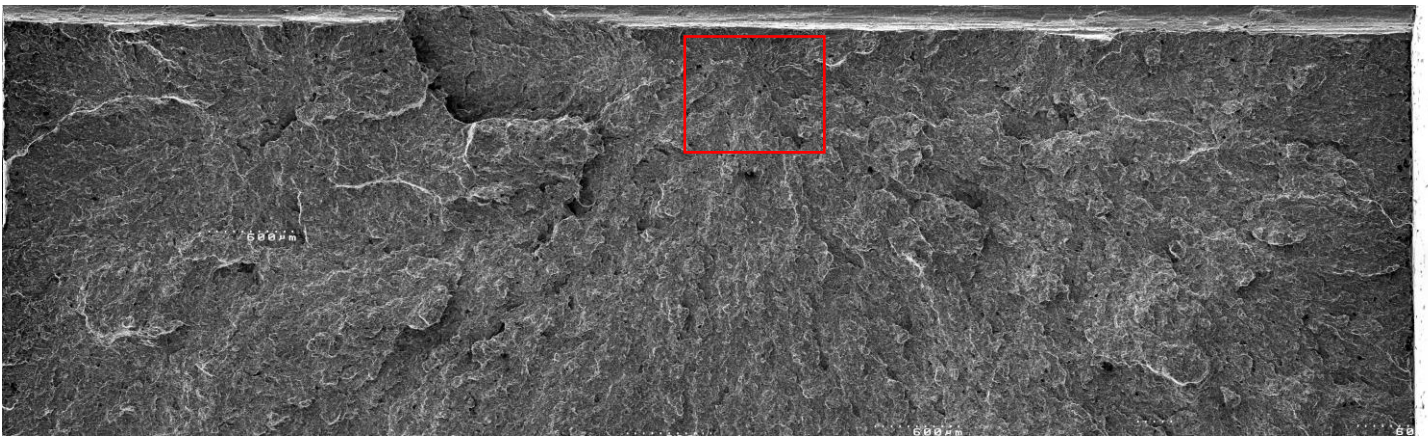

Figure 5-19 (a). Overview of the fracture surface on one side of the Charpy specimen CH HT1-07, tested at -120°C, with a red frame indicating the most probable initiation area. Test results: Charpy impact energy (CVN) of 5 J, fracture initiation distance (Xo) of 229 µm, specimen cleavage area of 99.1 %, lateral expansion of 0.12 mm.

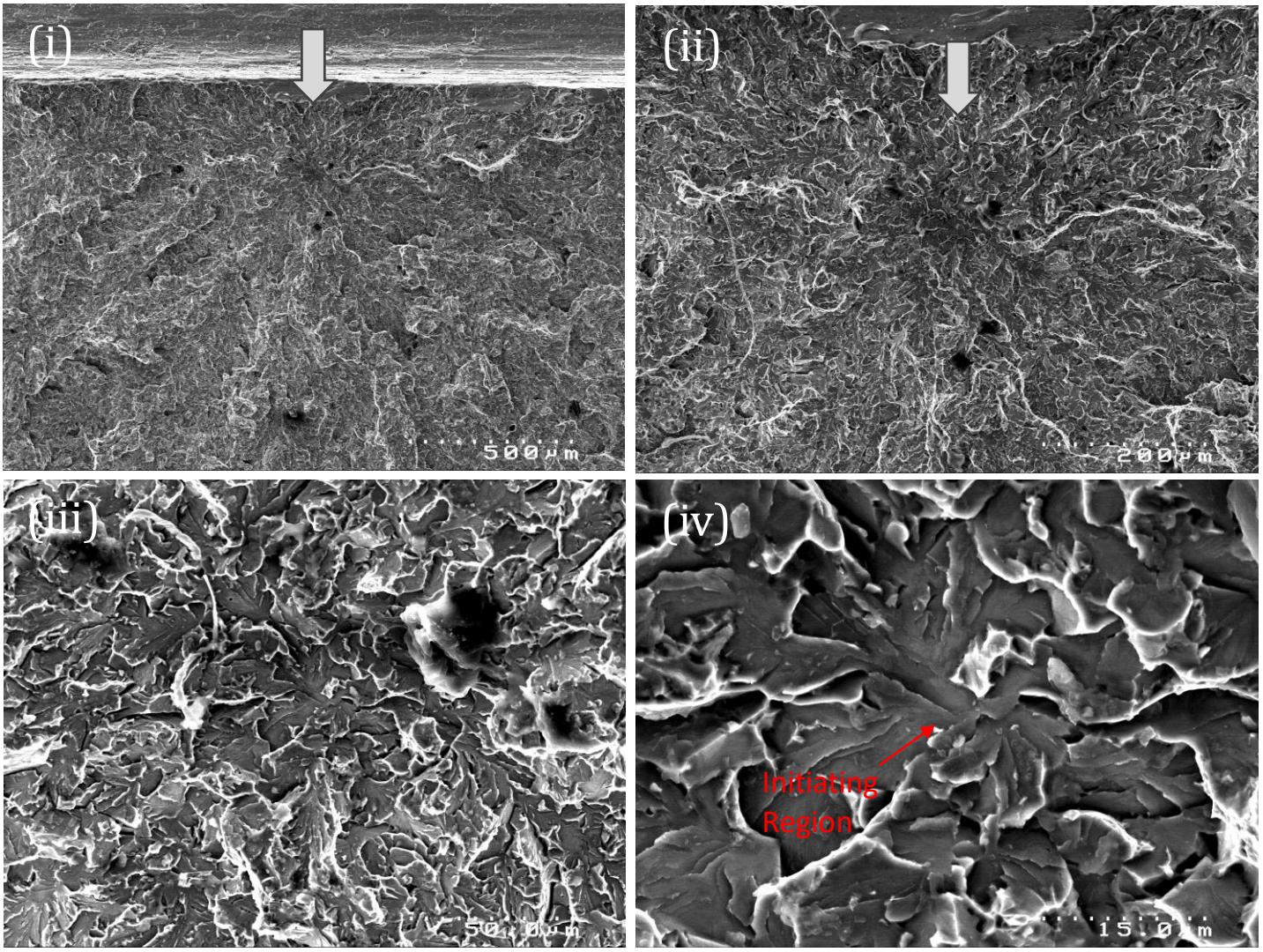


Figure 5-19 (b). Fracture initiation point of one side Charpy specimen CH HT1-07 tested at -120 °C; (i), (ii), (iii) and (iv) are sequential magnification of the same red framed area. Fractographic analysis reveals matrix cracking initiation mechanism, with the initial facet's equivalent diameter at 38 µm.

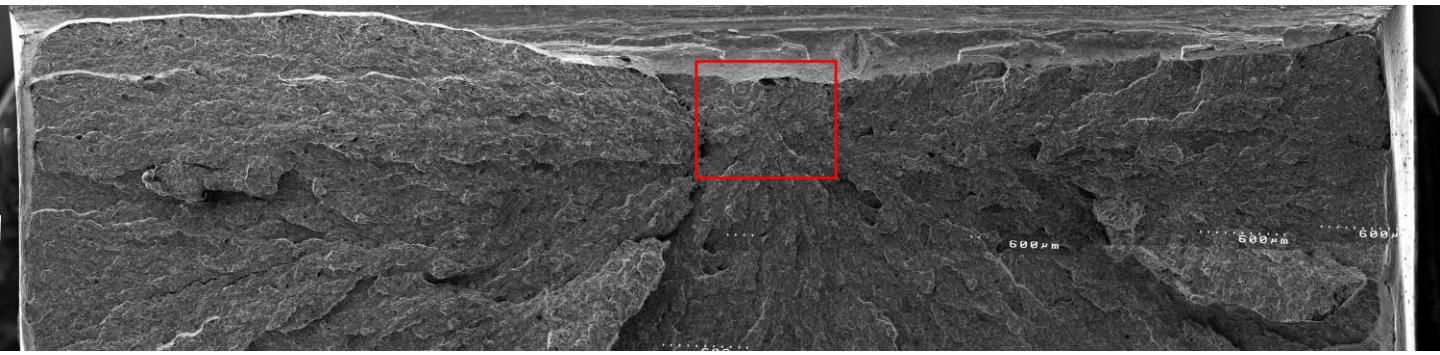

Figure 5-20 (a). Overview of the fracture surface on one side of the Charpy specimen CH HT1-10, tested at -100°C, with a red frame indicating the most probable initiation area. Test results: Charpy impact energy (CVN) of 26 J, fracture initiation distance (Xo) of 365 µm, specimen cleavage area of 92.9 %, lateral expansion of 0.37 mm.

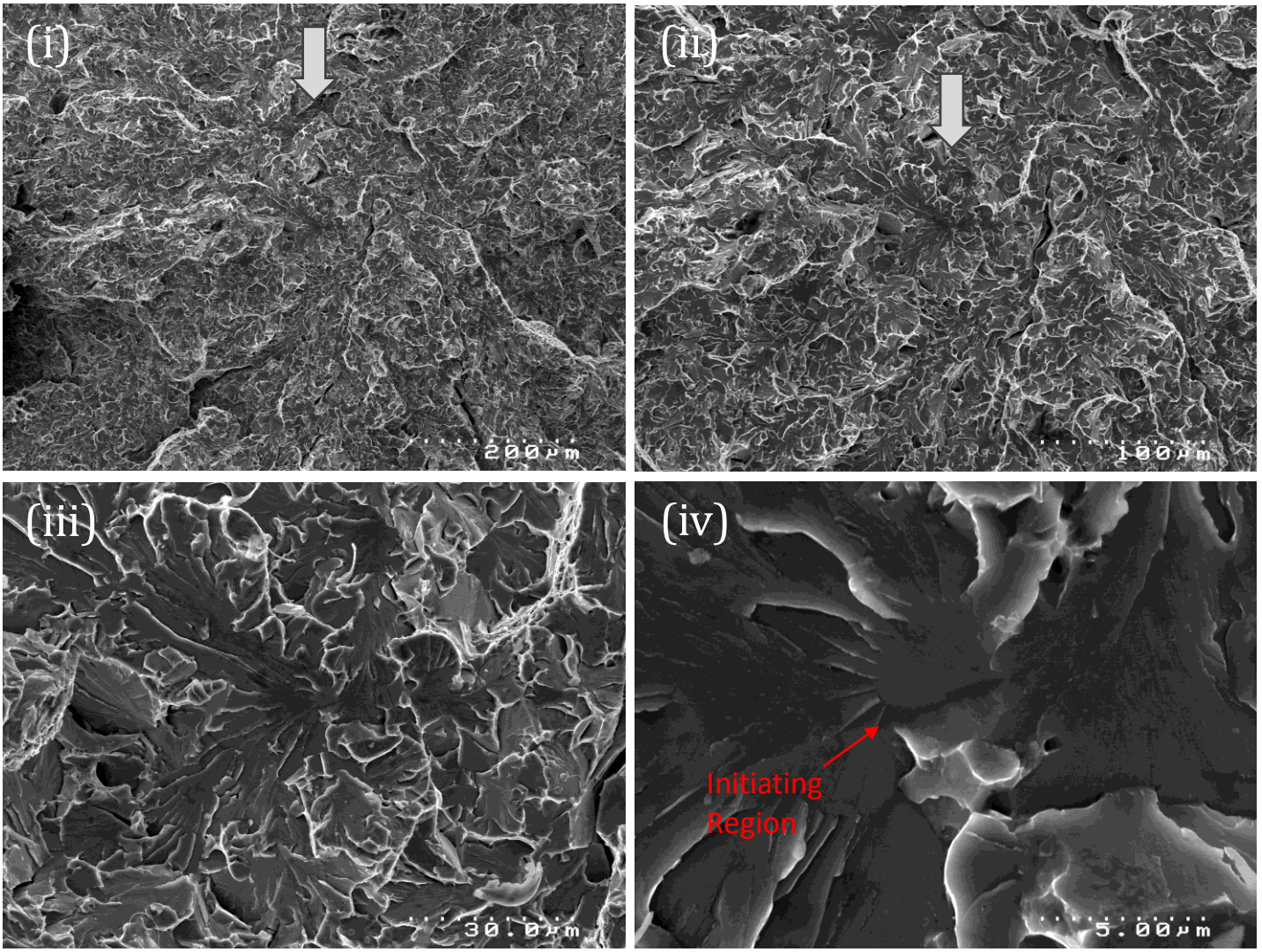


Figure 5-20 (b). Fracture initiation point of one side Charpy specimen CH HT1-10 tested at -100 °C; (i), (ii), (iii) and (iv) are sequential magnification of the same red framed area. Fractographic analysis reveals matrix cracking initiation mechanism, with the initial facet's equivalent diameter at 46 µm.

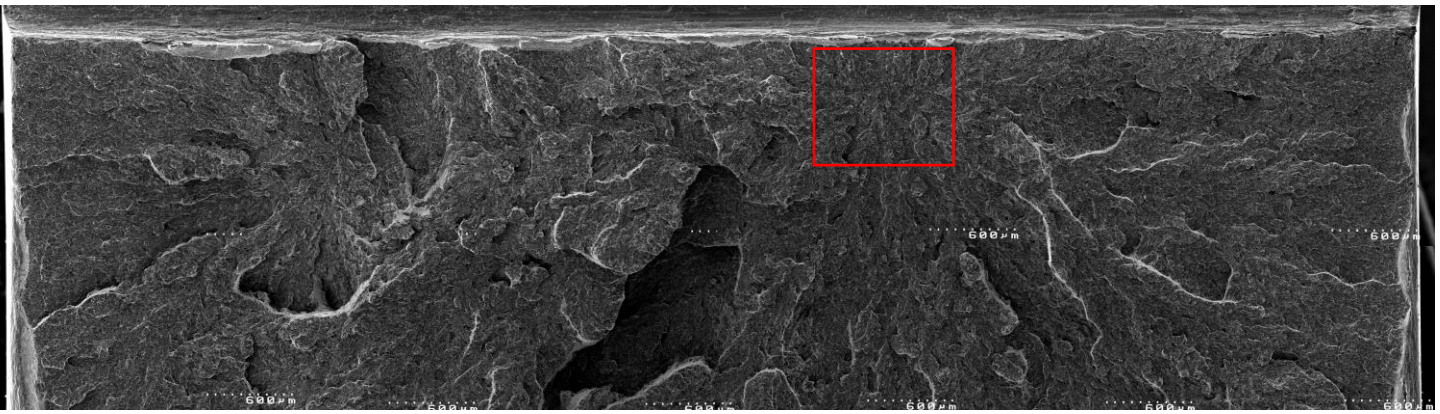

Figure 5-21 (a). Overview of the fracture surface on one side of the Charpy specimen CH HT1-18, tested at -100°C, with a red frame indicating the most probable initiation area. Test results: Charpy impact energy (CVN) of 8 J, fracture initiation distance (Xo) of 390 µm, specimen cleavage area of 96.5 %, lateral expansion of 0.17 mm.

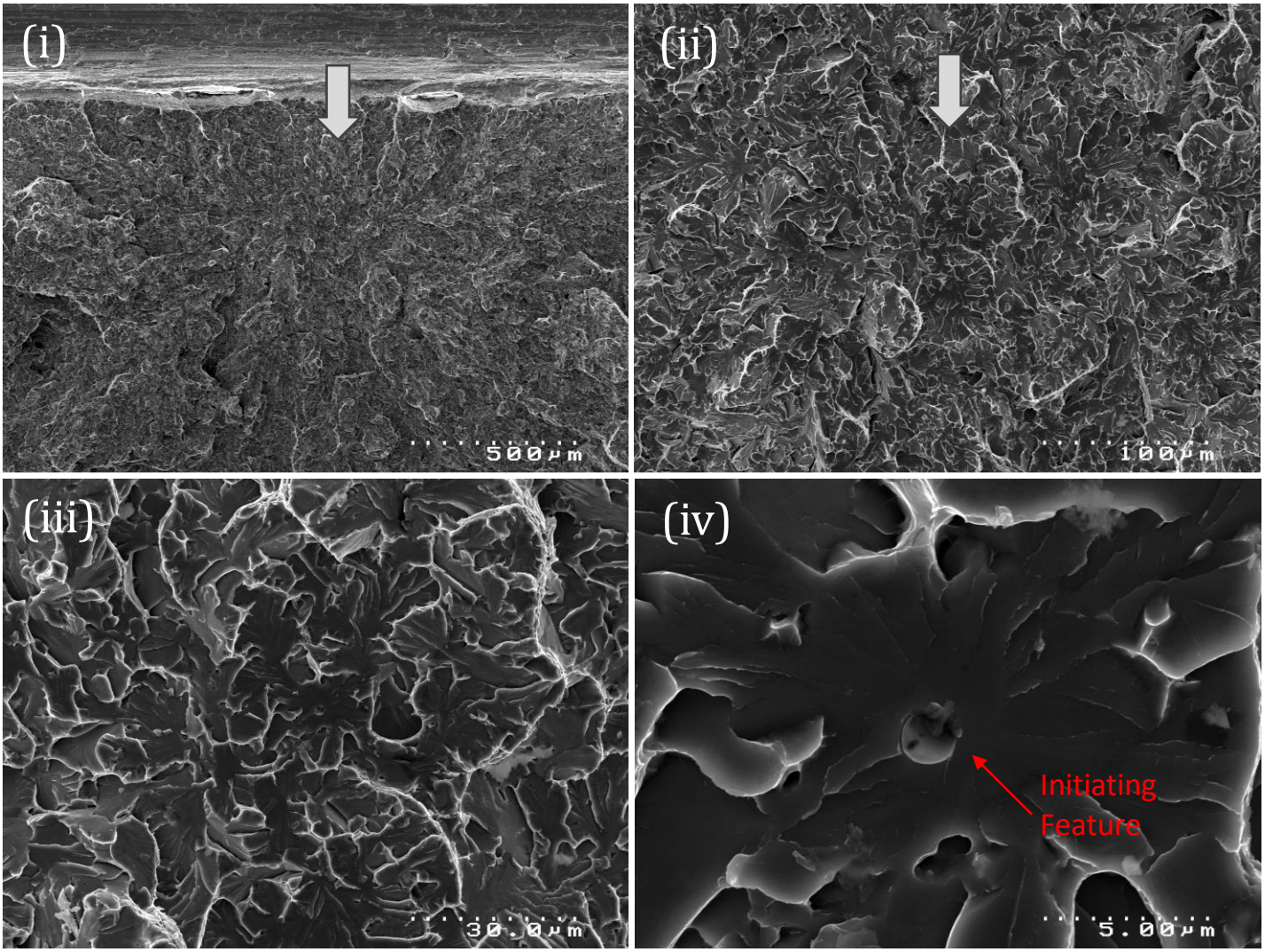


Figure 5-21 (b). Fracture initiation point of one side Charpy specimen CH HT1-18 tested at -100 °C; (i), (ii), (iii) and (iv) are sequential magnification of the same red framed area. Fractographic analysis reveals inclusion related feature as the initiation, with the initiating feature's equivalent diameter at 1.7 µm and the initial facet's equivalent diameter at 24 µm.

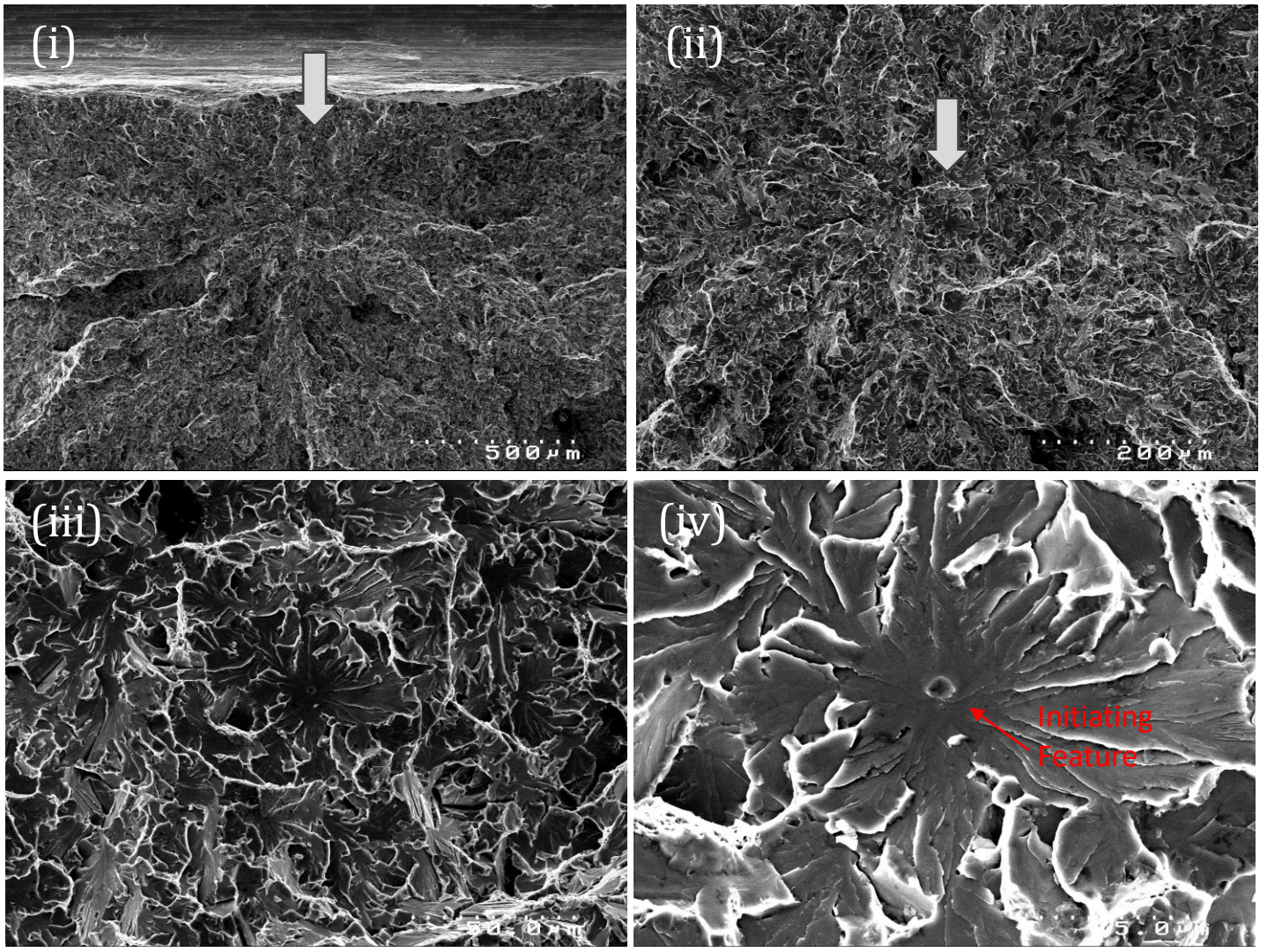


Figure 5-22 (a). Fracture initiation point of one side Charpy specimen CH HT2-11 tested at -100 °C; (i), (ii), (iii) and (iv) are sequential magnification of the most probable initiation area. Fractographic analysis reveals inclusion related feature as the initiation, with the initiating feature's equivalent diameter at 2.3 µm and the initial facet's equivalent diameter at 51 µm.

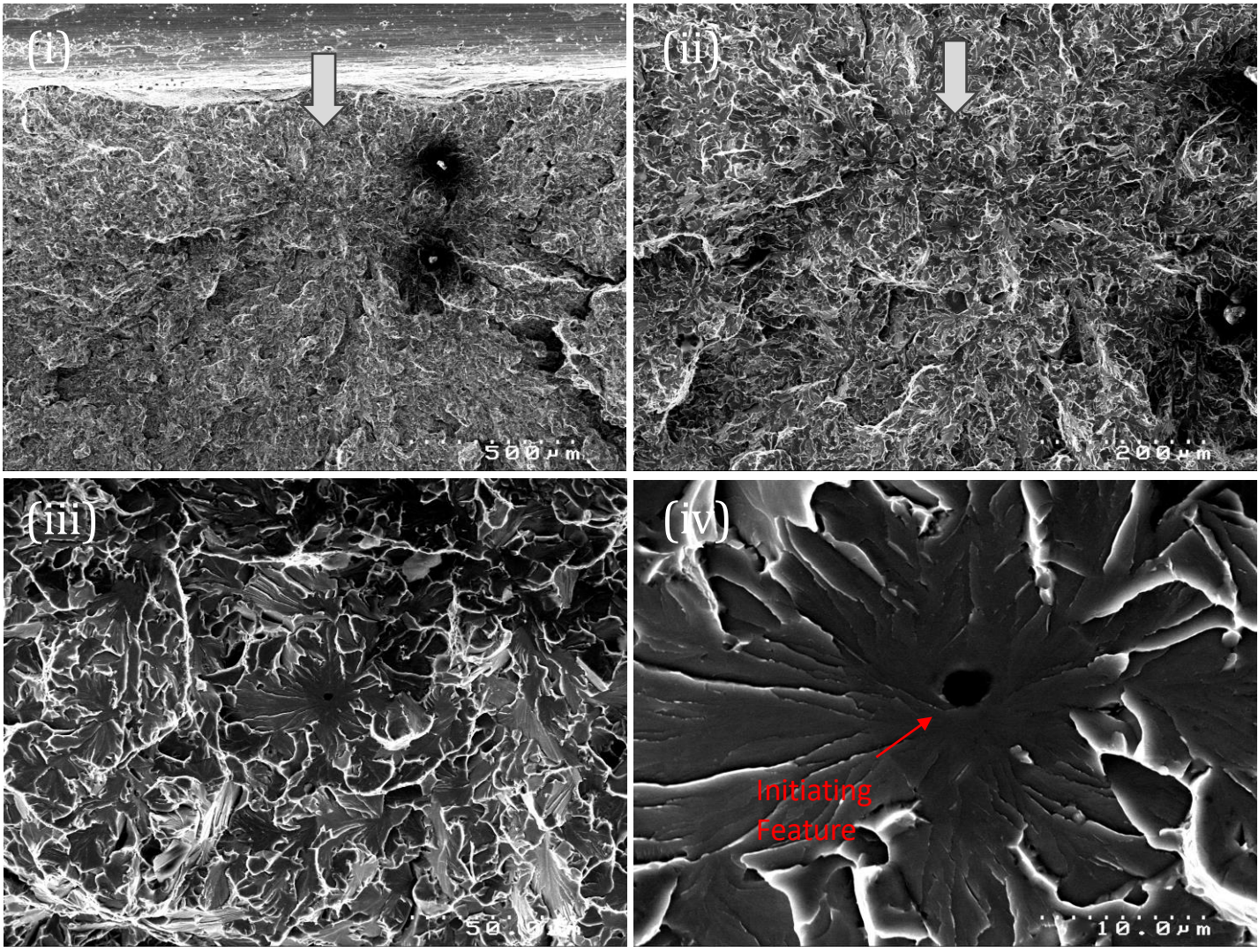


Figure 5-22 (b). Fracture initiation point of the matching side of Charpy specimen CH HT2-11 tested at -100 °C; (i), (ii), (iii) and (iv) are sequential magnification of the most probable initiation area. Fractographic analysis reveals inclusion related feature as the initiation, with the initiating feature's equivalent diameter at 2.3 µm and the initial facet's equivalent diameter at 51 µm.

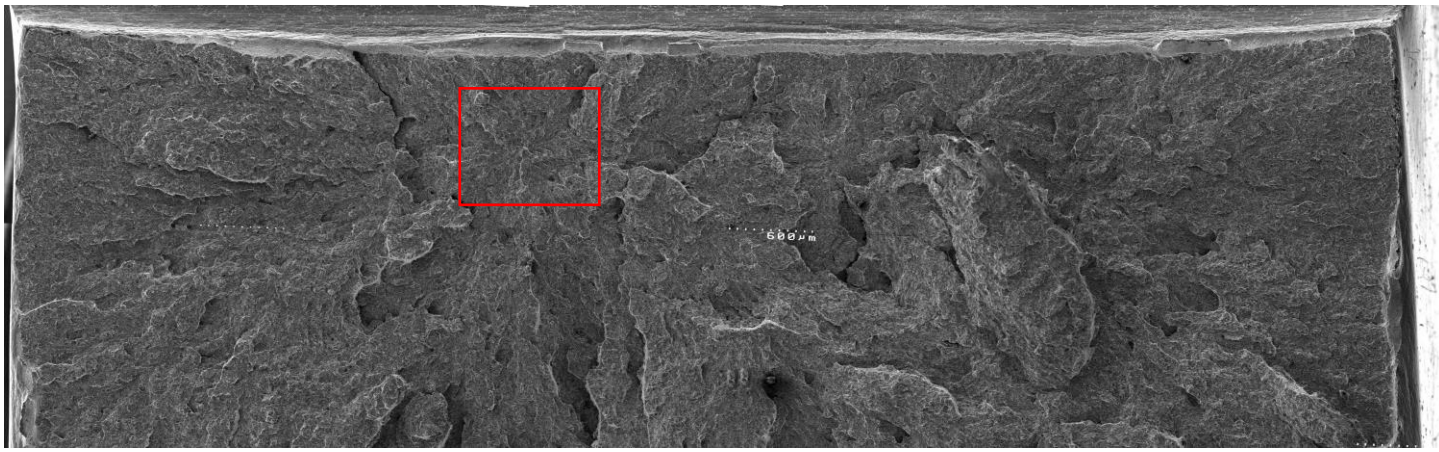

Figure 5-23 (a). Overview of the fracture surface on one side of the Charpy specimen CH HT2-12, tested at -100°C, with a red frame indicating the most probable initiation area. Test results: Charpy impact energy (CVN) of 19 J, fracture initiation distance (Xo) of 636 µm, specimen cleavage area of 93.3 %, lateral expansion of 0.22 mm.

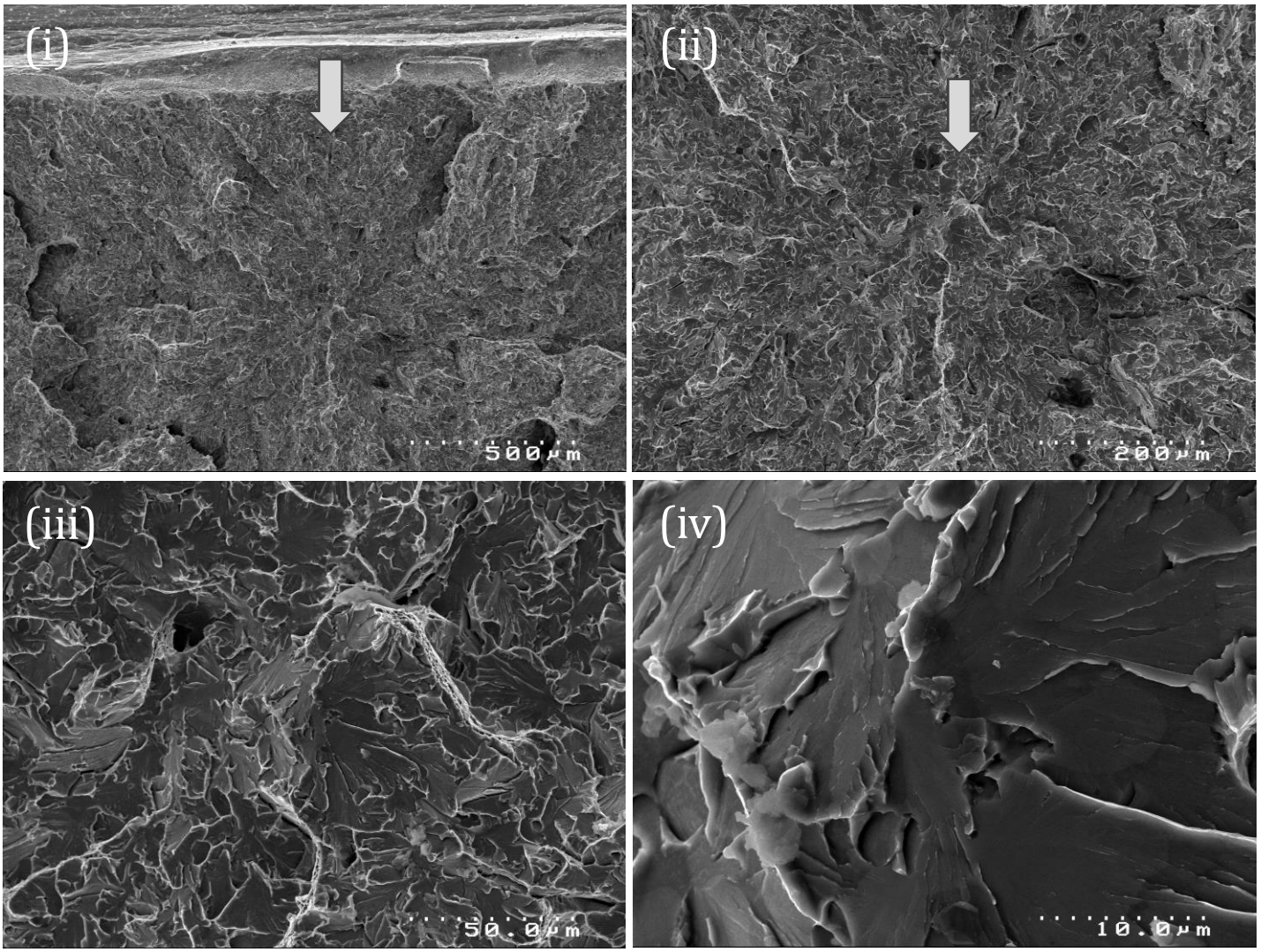


Figure 5-23 (b). Fracture initiation point of one side Charpy specimen CH HT2-12 tested at -100 °C; (i), (ii), (iii) and (iv) are sequential magnification of the same red framed area. Fractographic analysis reveals matrix cracking initiation mechanism, with the initial facet's equivalent diameter at 44 µm.

Figure 5-24 (a). Overview of the fracture surface on one side of the Charpy specimen CH HT2-16, tested at -100°C, with a red frame indicating the most probable initiation area. Test results: Charpy impact energy (CVN) of 36 J, fracture initiation distance (Xo) of 545 µm, specimen cleavage area of 96.9 %, lateral expansion of 0.47 mm.

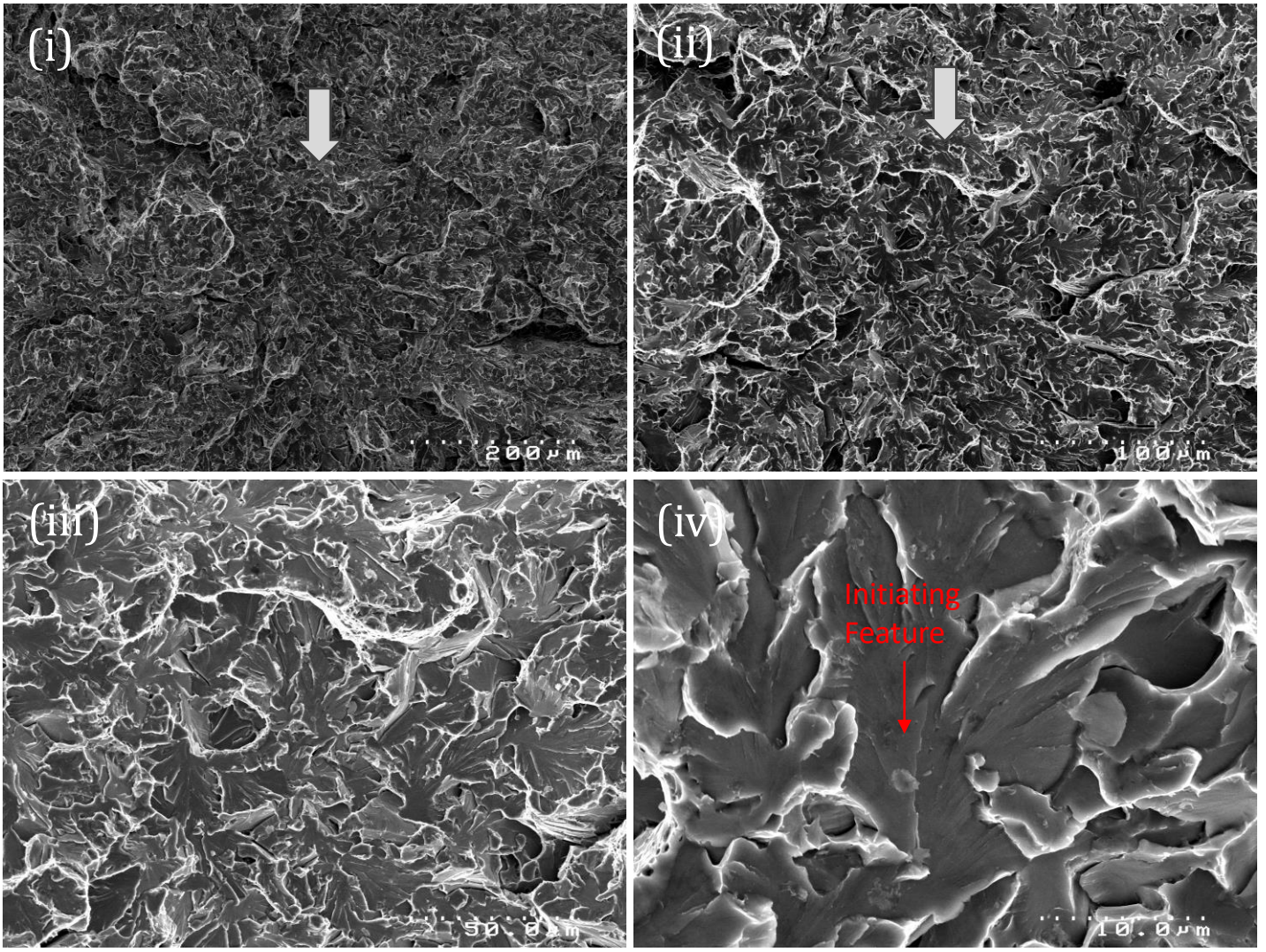


Figure 5-24 (b). Fracture initiation point of one side Charpy specimen CH HT2-16 tested at -100 °C; (i), (ii), (iii) and (iv) are sequential magnification of the same red framed area. Fractographic analysis reveals matrix related initiation mechanism, with the initiating feature's equivalent diameter at 1.6 µm and the initial facet's equivalent diameter at 30 µm.

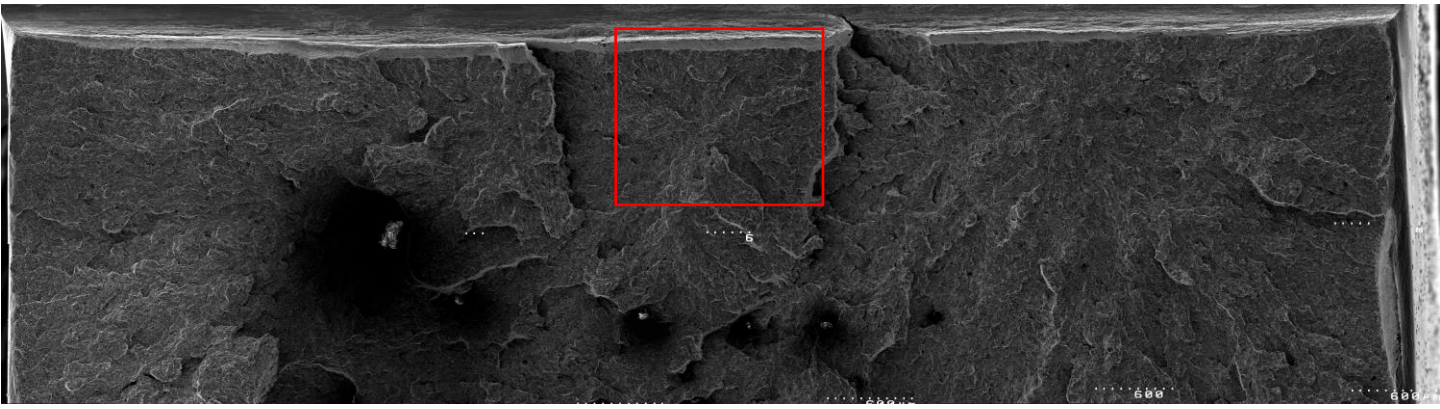

Figure 5-25 (a). Overview of the fracture surface on one side of the Charpy specimen CH HT2-18, tested at -100°C, with a red frame indicating the most probable initiation area. Test results: Charpy impact energy (CVN) of 23 J, fracture initiation distance (Xo) of 530 µm, specimen cleavage area of 95.4 %, lateral expansion of 0.15 mm.

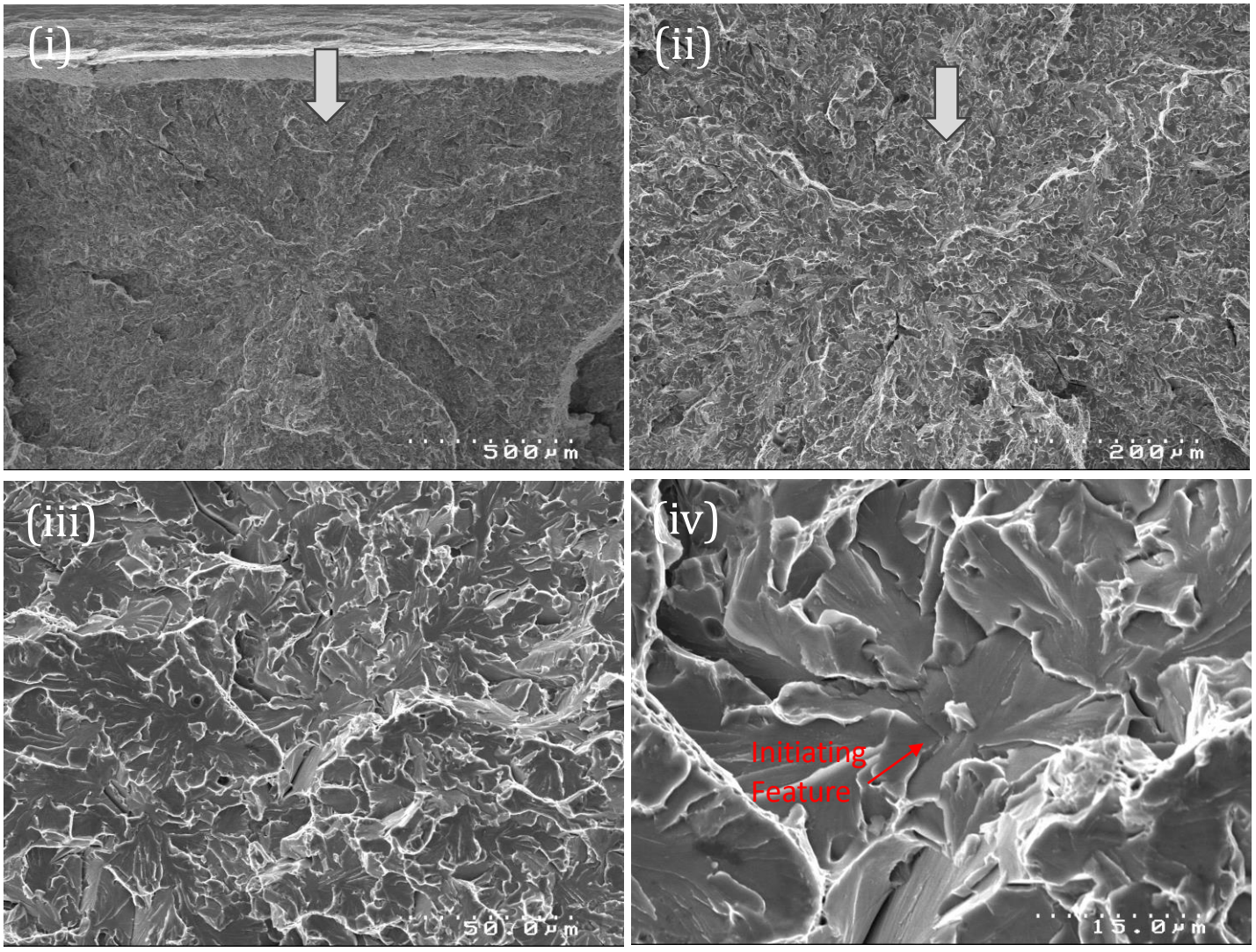


Figure 5-25 (b). Fracture initiation point of one side Charpy specimen CH HT2-18 tested at -100 °C; (i), (ii), (iii) and (iv) are sequential magnification of the same red framed area. Fractographic analysis reveals matrix related initiation mechanism, with the initiating feature's equivalent diameter at 2.7 µm and the initial facet's equivalent diameter at 54 µm.

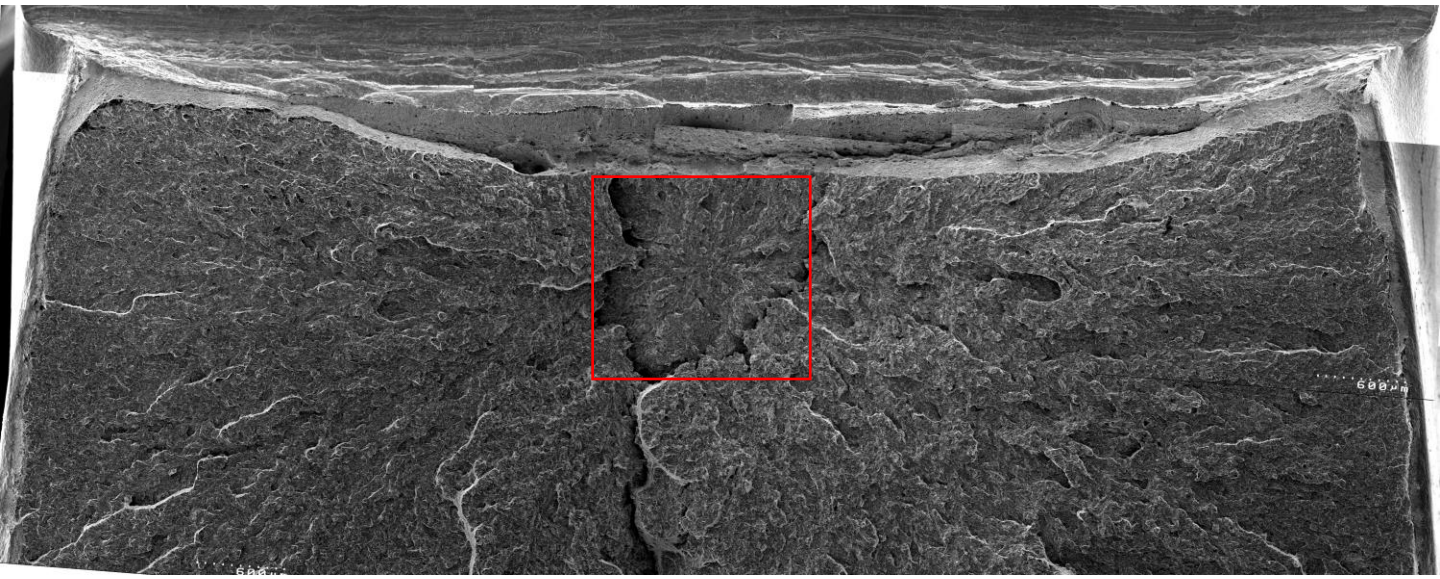

Figure 5-26 (a). Overview of the fracture surface on one side of the Charpy specimen CH HT1-05, tested at -90°C, with a red frame indicating the most probable initiation area. Test results: Charpy impact energy (CVN) of 56.5 J, fracture initiation distance (Xo) of 693 µm, specimen cleavage area of 83.5 %, lateral expansion of 0.72 mm.

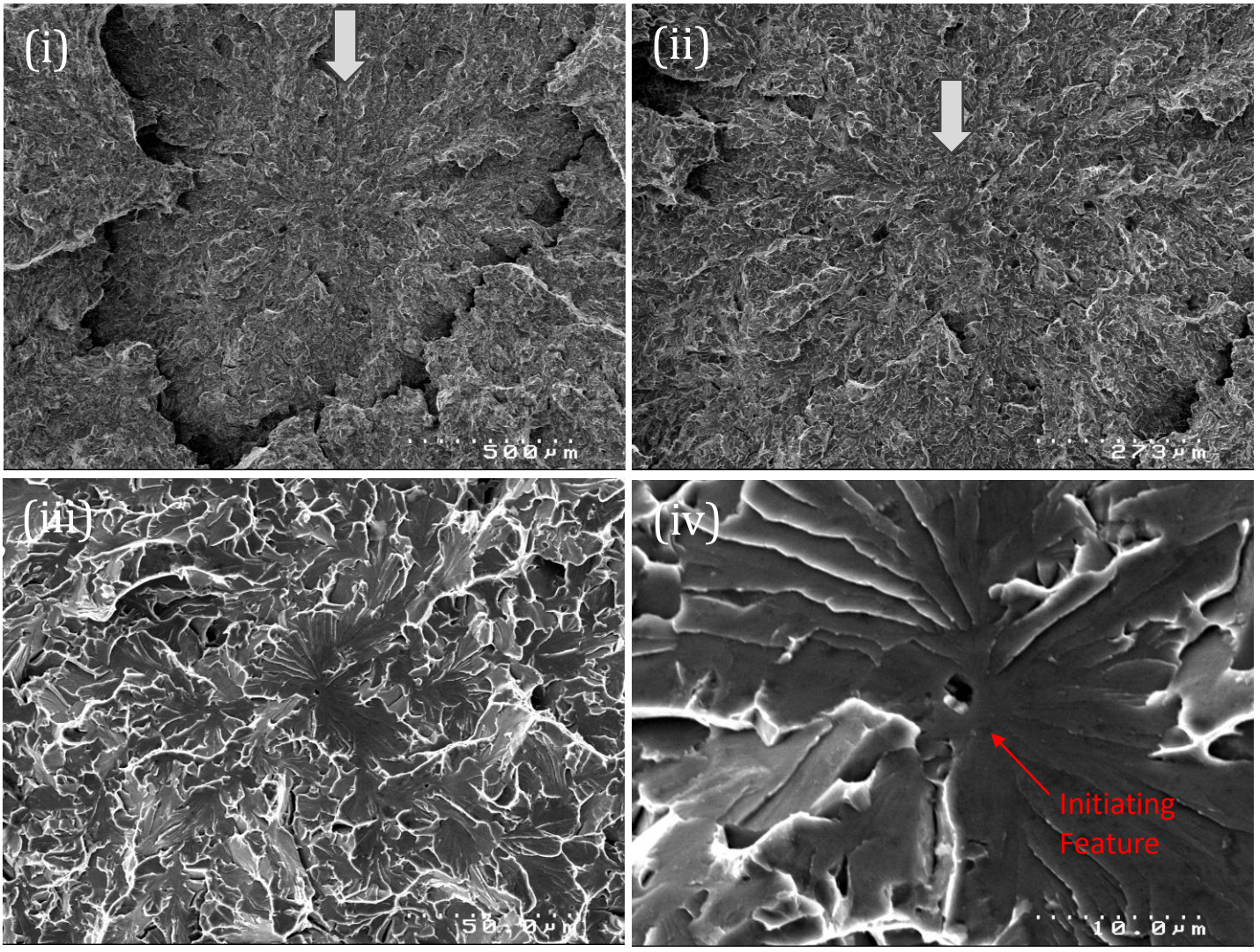


Figure 5-26 (b). Fracture initiation point of one side Charpy specimen CH HT1-05 tested at -90 °C; (i), (ii), (iii) and (iv) are sequential magnification of the same red framed area. Fractographic analysis reveals inclusion related feature as the initiation, with the initiating feature's equivalent diameter at 1.6 µm and the initial facet's equivalent diameter at 42 µm.

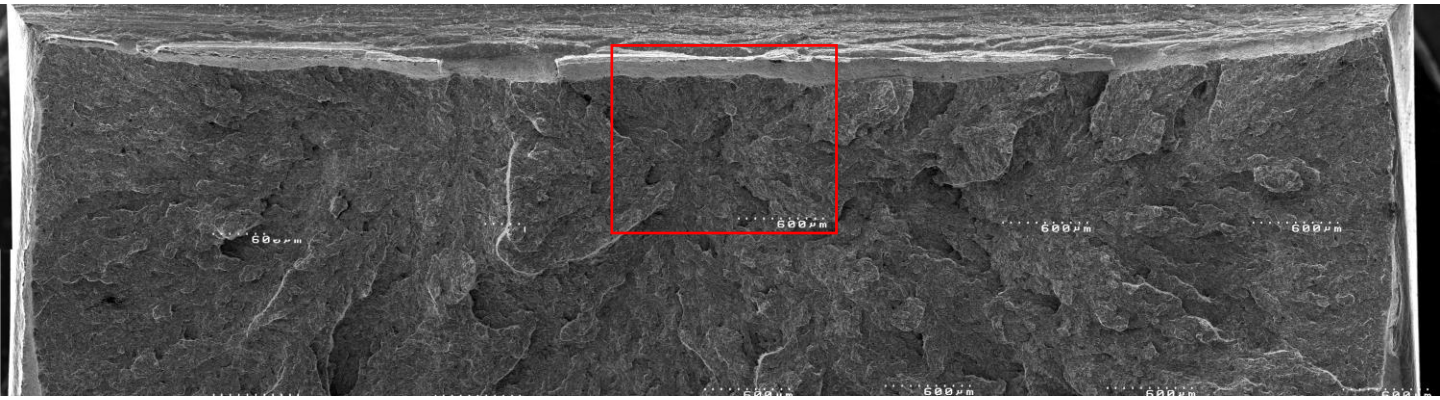

Figure 5-27 (a). Overview of the fracture surface on one side of the Charpy specimen CH HT1-06, tested at -90°C, with a red frame indicating the most probable initiation area. Test results: Charpy impact energy (CVN) of 25 J, fracture initiation distance (Xo) of 596 µm, specimen cleavage area of 91.5 %, lateral expansion of 0.27 mm.

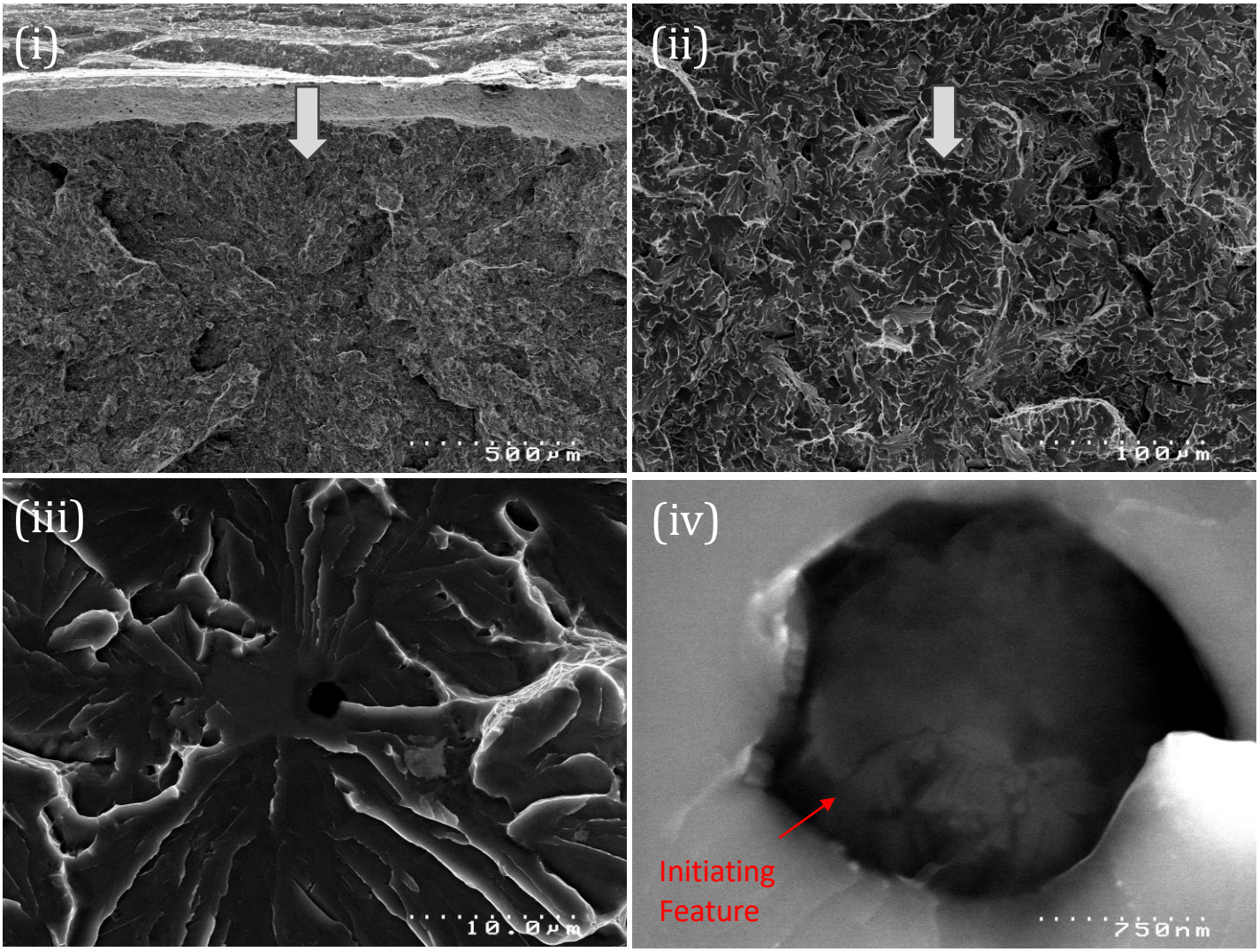


Figure 5-27 (b). Fracture initiation point of one side Charpy specimen CH HT1-06 tested at -90 °C; (i), (ii), (iii) and (iv) are sequential magnification of the same red framed area. Fractographic analysis reveals inclusion related feature as the initiation, with the initiating feature's equivalent diameter at 2.2 µm and the initial facet's equivalent diameter at 52 µm.

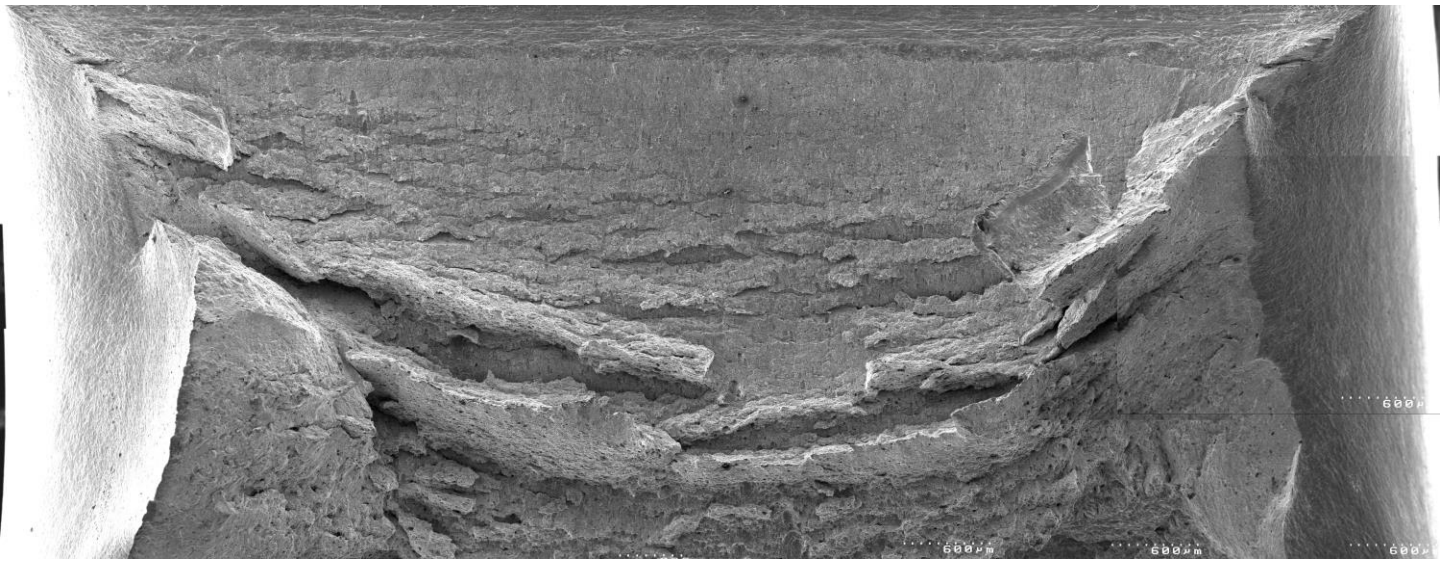

Figure 5-28 (a). Overview of the fracture surface showcasing the ductile region of Charpy specimen CH HT2-04, tested at -90°C. Below the ductile region is the cleavage region, where the initiation of cleavage fracture is observed. Test results: Charpy impact energy (CVN) of 192 J, fracture initiation distance (Xo) of 312 μm, specimen cleavage area of 44.5 %, lateral expansion of 2.04 mm.

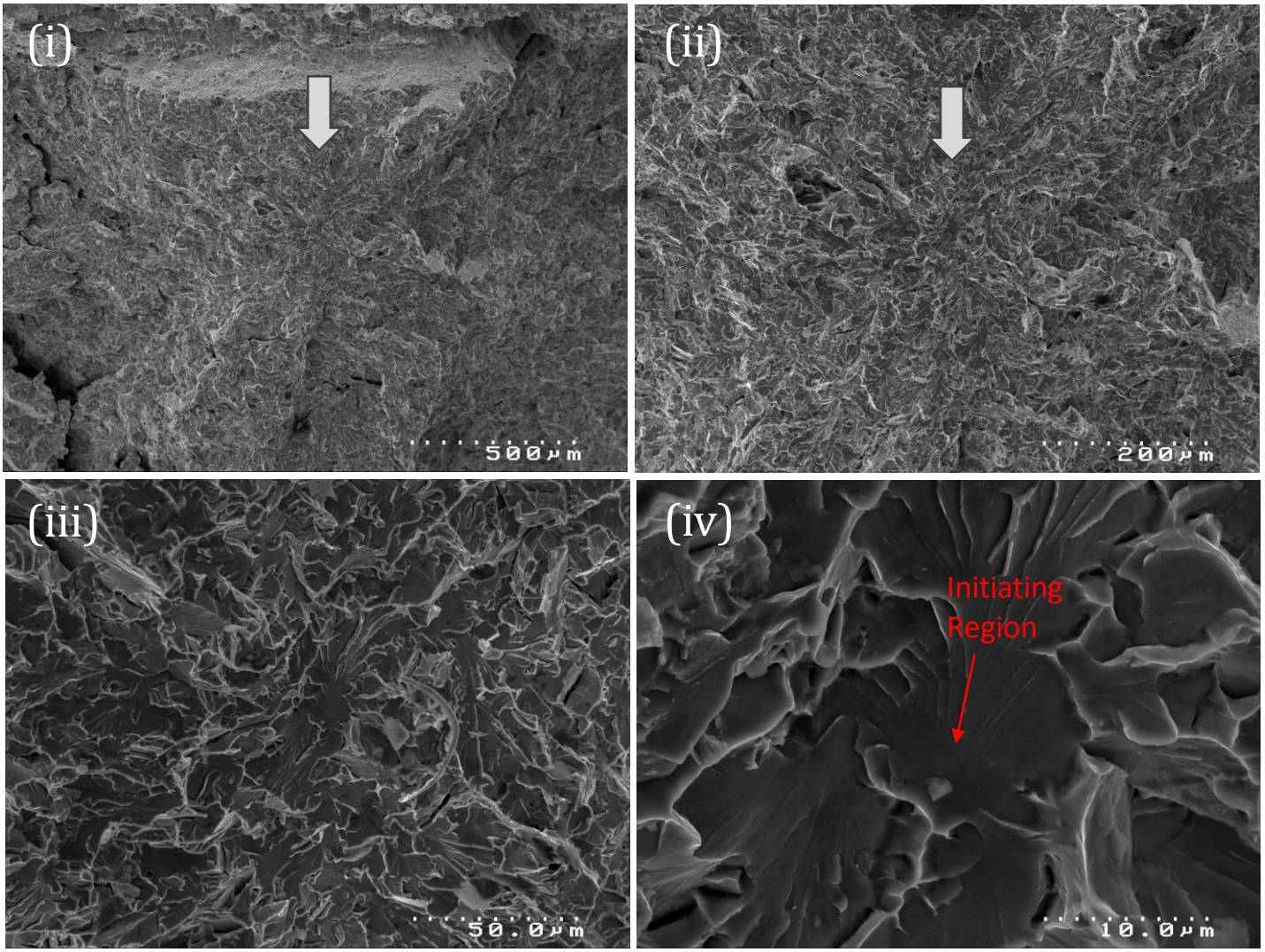


Figure 5-28 (b). Fracture initiation point of one side Charpy specimen CH HT2-04 tested at -90 °C; (i), (ii), (iii) and (iv) are sequential magnification of the most probable initiation area. Fractographic analysis reveals matrix cracking initiation mechanism, with the initial facet's equivalent diameter at 40 µm.

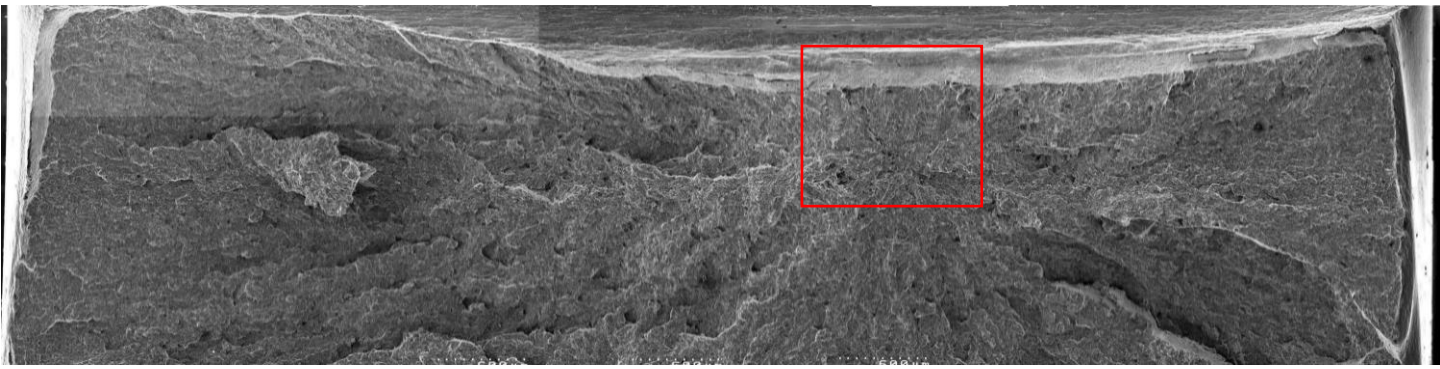

Figure 5-29 (a). Overview of the fracture surface on one side of the Charpy specimen CH HT2-30, tested at -90°C, with a red frame indicating the most probable initiation area. Test results: Charpy impact energy (CVN) of 32 J, fracture initiation distance (Xo) of 413 µm, specimen cleavage area of 92.3 %, lateral expansion of 0.29 mm.

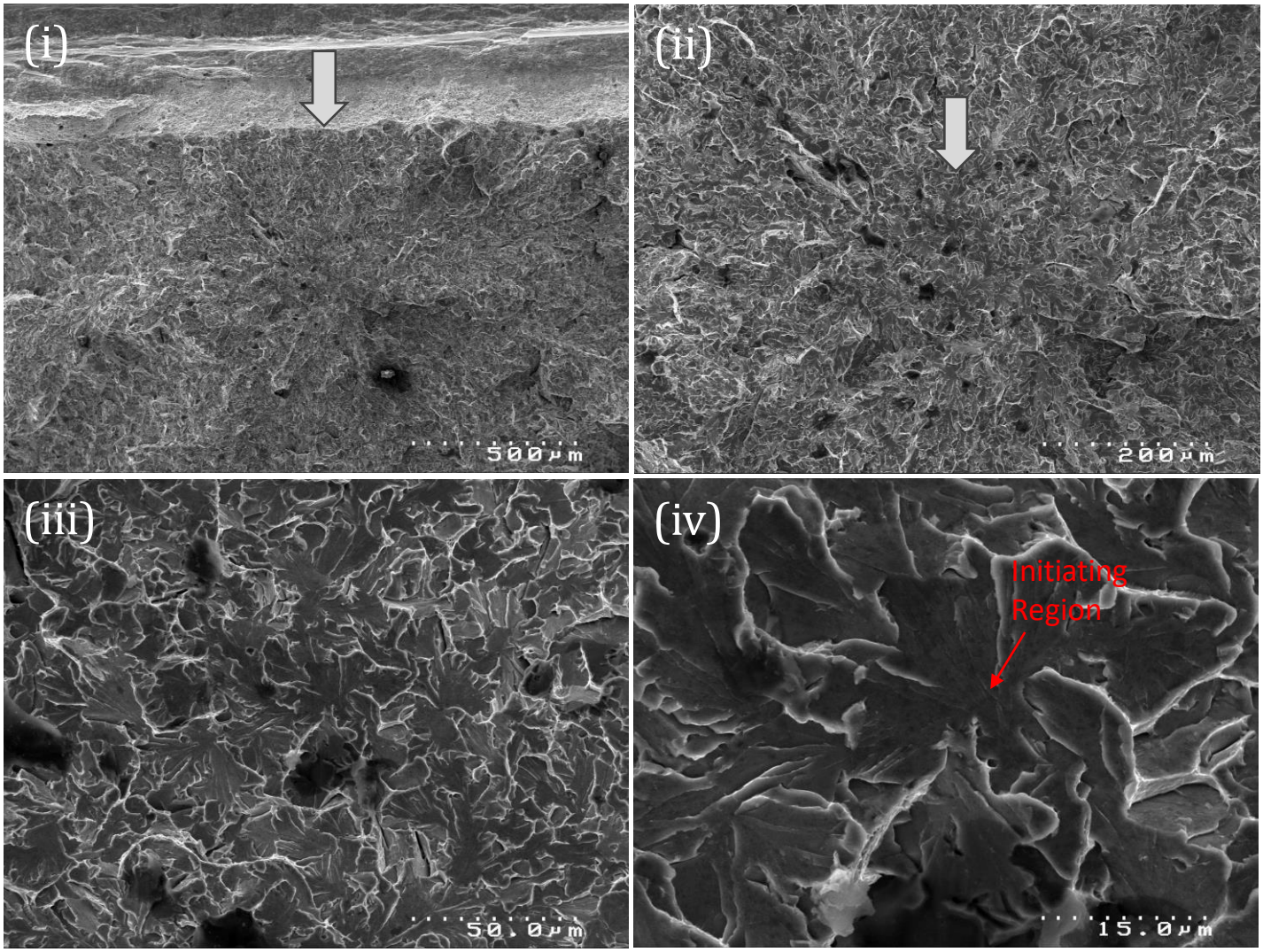


Figure 5-29 (b). Fracture initiation point of one side Charpy specimen CH HT2-30 tested at -90 °C; (i), (ii), (iii) and (iv) are sequential magnification of the same red framed area. Fractographic analysis reveals matrix cracking initiation mechanism, with the initial facet's equivalent diameter at 33 µm.

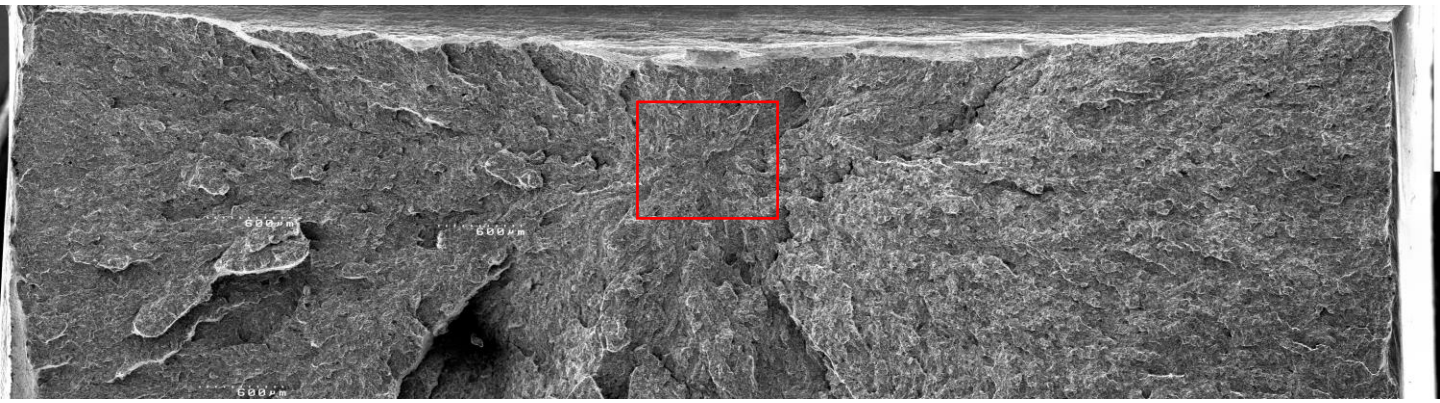

Figure 5-30 (a). Overview of the fracture surface on one side of the Charpy specimen CH HT2-41, tested at -90°C, with a red frame indicating the most probable initiation area. Test results: Charpy impact energy (CVN) of 18 J, fracture initiation distance (Xo) of 619 µm, specimen cleavage area of 94.8 %, lateral expansion of 0.14 mm.

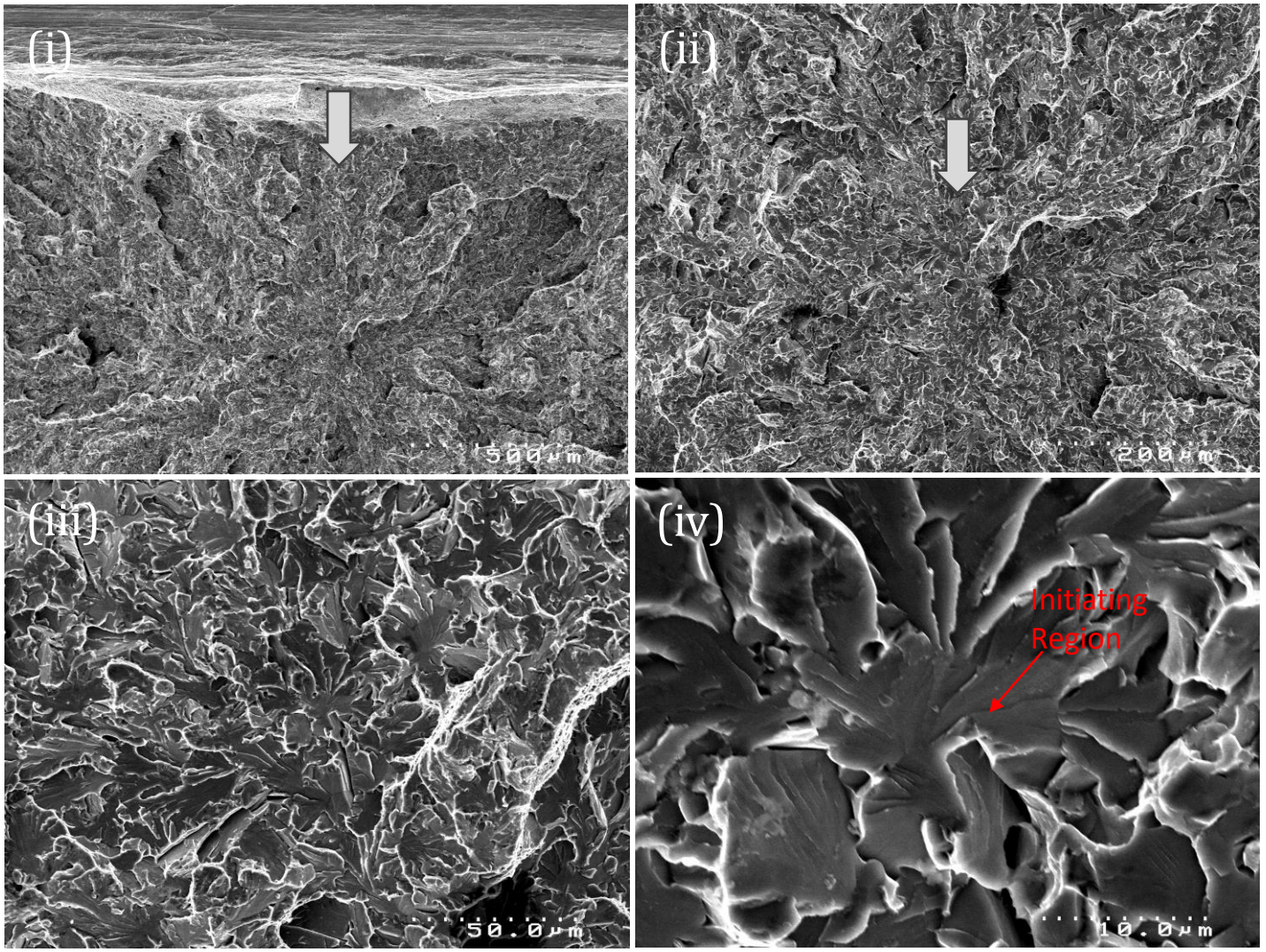


Figure 5-30 (b). Fracture initiation point of one side Charpy specimen CH HT2-41 tested at -90 °C; (i), (ii), (iii) and (iv) are sequential magnification of the same red framed area. Fractographic analysis reveals matrix related initiation mechanism, with the initiating feature's equivalent diameter at 1.9 µm and the initial facet's equivalent diameter at 32 µm.

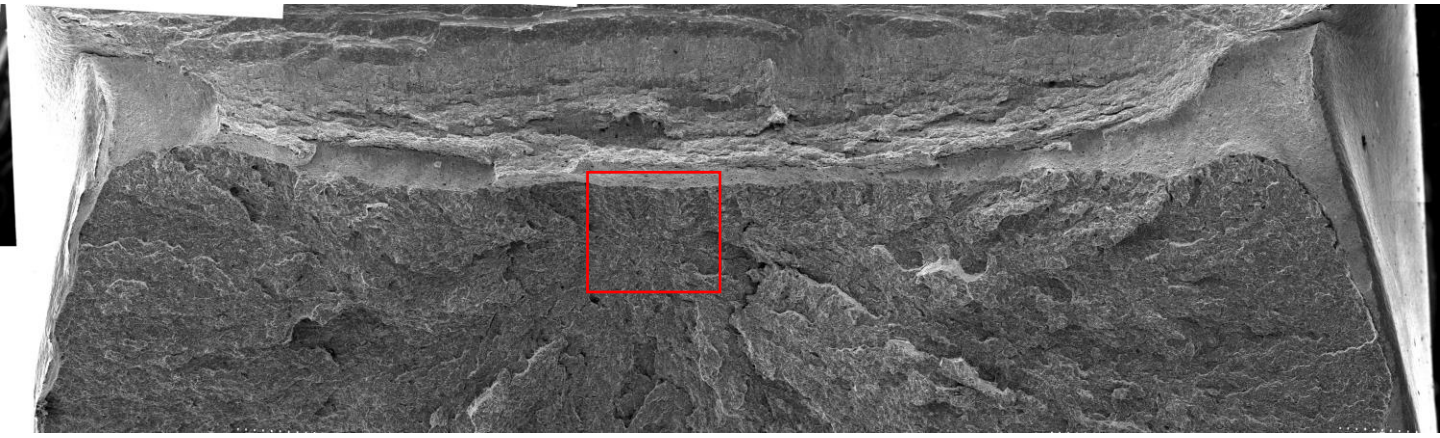

Figure 5-31 (a). Overview of the fracture surface on one side of the Charpy specimen CH HT2-42, tested at -90°C, with a red frame indicating the most probable initiation area. Test results: Charpy impact energy (CVN) of 90 J, fracture initiation distance (Xo) of 300 µm, specimen cleavage area of 79 %, lateral expansion of 1.14 mm.

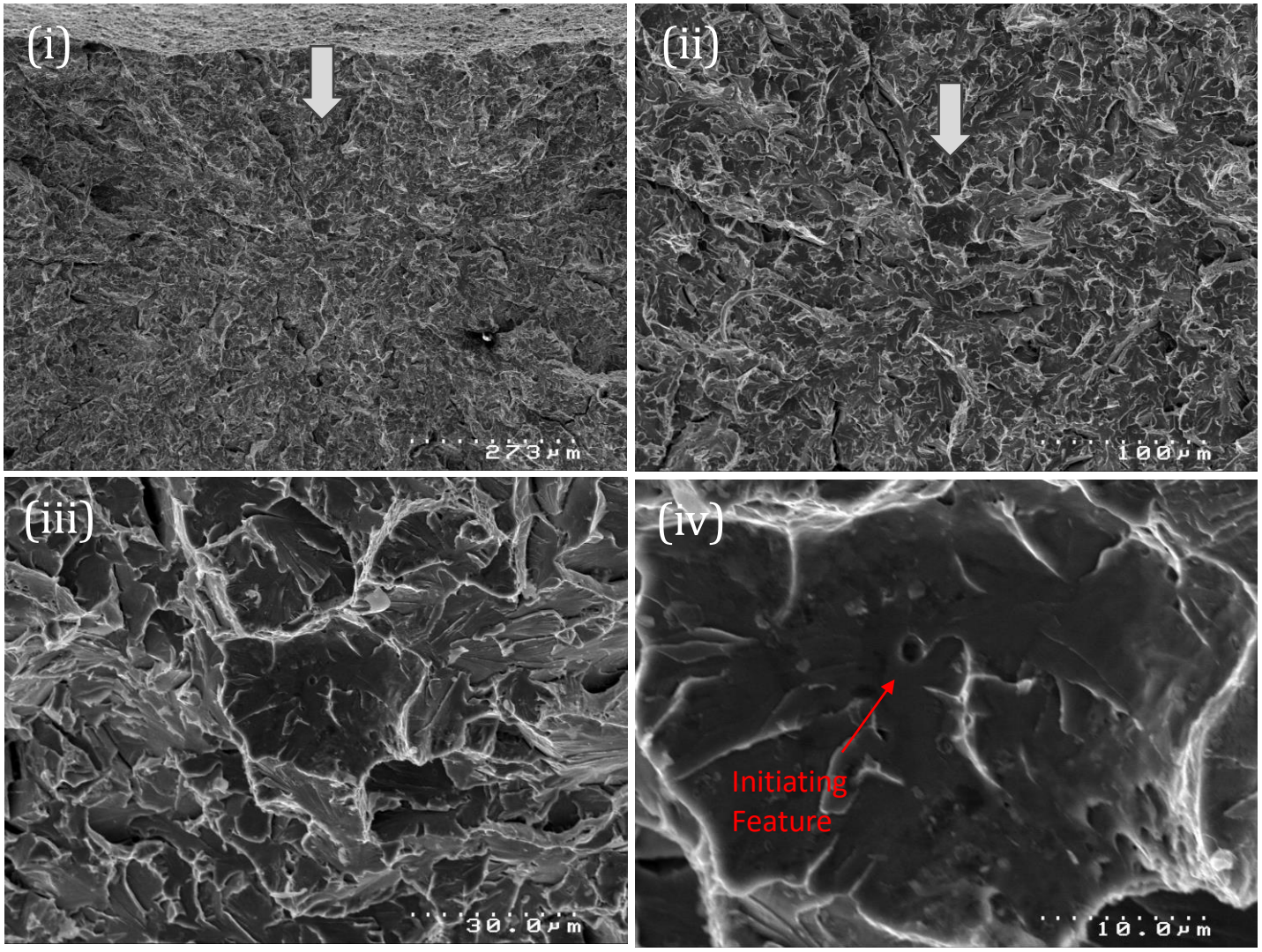


Figure 5-31 (b). Fracture initiation point of one side Charpy specimen CH HT2-42 tested at -90 °C; (i), (ii), (iii) and (iv) are sequential magnification of the same red framed area. Fractographic analysis reveals inclusion related feature as the initiation, with the initiating feature's equivalent diameter at 1.8 µm and the initial facet's equivalent diameter at 34 µm.

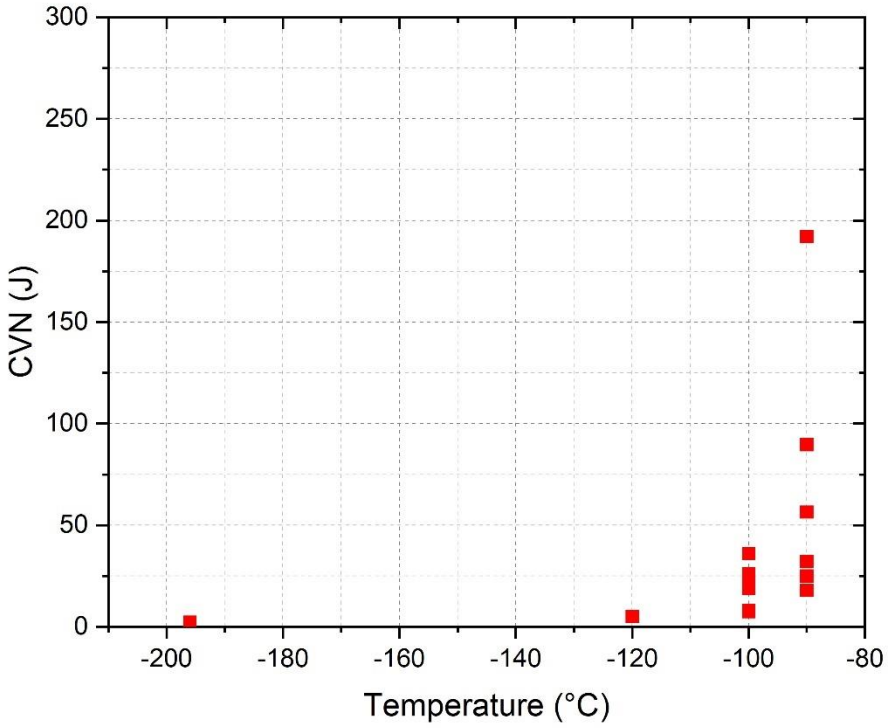


Figure 5-32. Charpy impact energy relation with test temperatures for the fractography measured 14 Charpy specimens at temperature -196°C, -120°C, -100°C and -90°C.

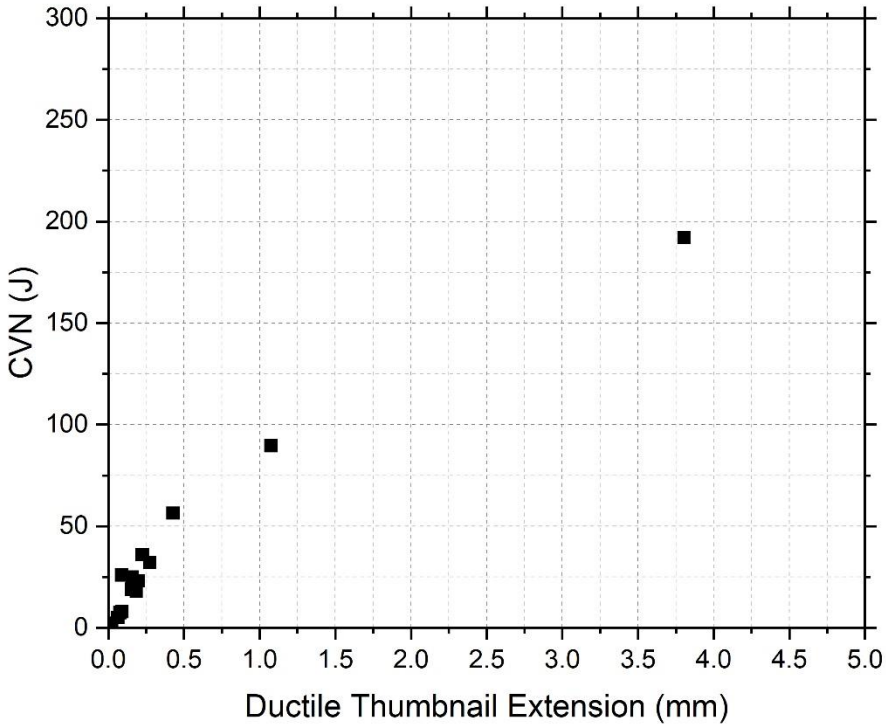


Figure 5-33. Charpy impact energy relation with ductile thumbnail extension for the fractography measured Charpy specimens of test temperature at -196° C, -120°C, -100°C and -90°C.

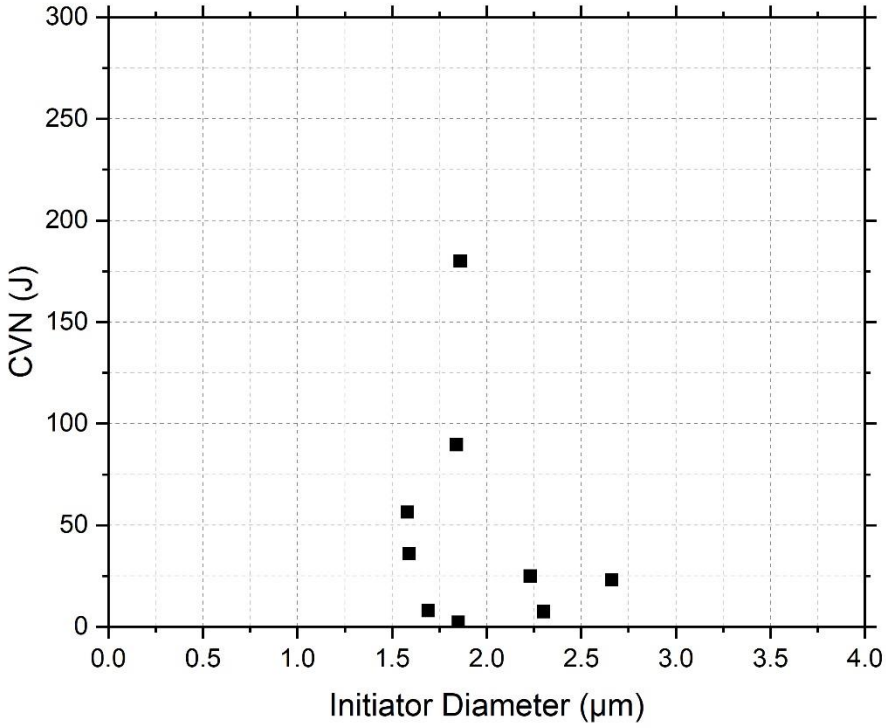


Figure 5-34. Correlation between Charpy impact energy value and the initiator diameter.

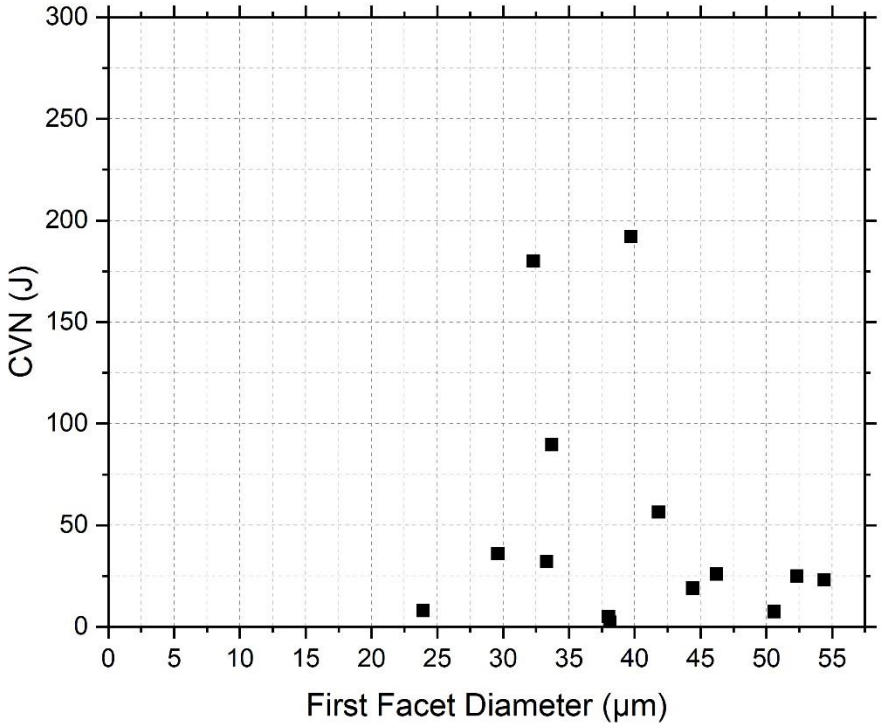


Figure 5-35. Correlation between Charpy impact energy value and the first facet diameter.

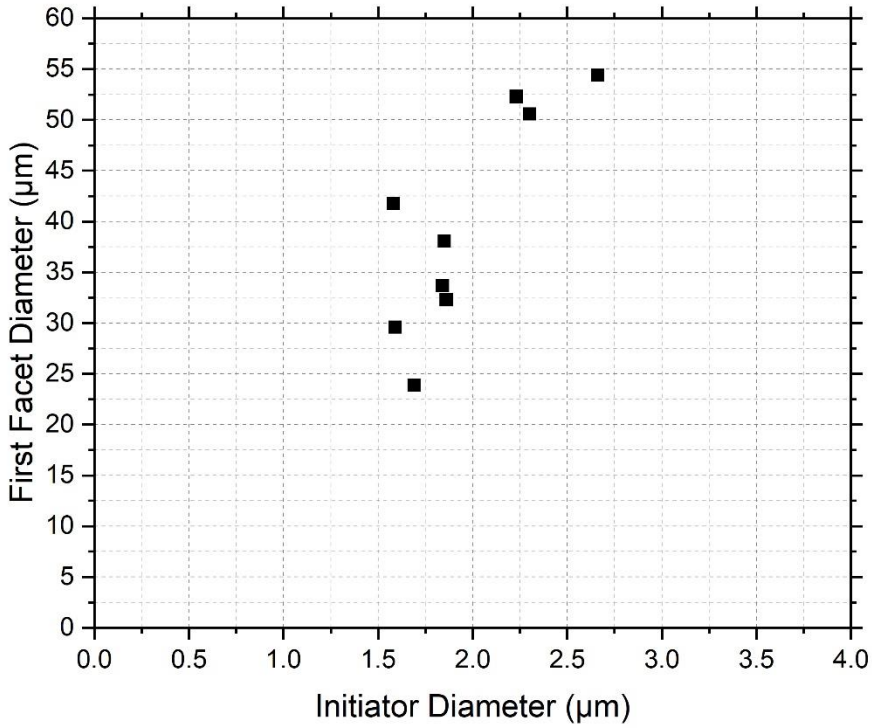


Figure 5-36. Correlation between initiator diameter and first facet diameter in 9 Charpy specimens that initiator was identified and measured.

Table 6-1. HT1 Tensile Tests Results Summary

| ***Test Temperature*** | ***Specimen*** | ***Lower Yield Stress*** | ***UTS*** | ***n*** |
|---|---|---|---|---|
| ***°C*** | ***No.*** | ***MPa*** | ***MPa*** | *(Extensometer)* |
| -196 | **HT1-01** | 921 | 952 | N/A |
| -196 | **HT1-02** | 933 | 954 | N/A |
| -196 | **HT1-03** | 931 | 949 | N/A |
| -170 | **HT1-04** | 804 | 857 | N/A |
| -160 | **HT1-07** | 771 | 828 | N/A |
| -140 | **HT1-06** | 719 | 772 | 0.13 |
| -140 | **HT1-08*** | 711 | N/A | N/A |
| -120 | **HT1-09** | 676 | 733 | 0.12 |
| -120 | **HT1-10** | 636 | 736 | 0.16 |
| -100 | **HT1-11** | 634 | 703 | 0.14 |
| -100 | **HT1-12*** | 612 | N/A | N/A |
| -80 | **HT1-13** | 577 | 678 | 0.14 |
| -80 | **HT1-14** | 581 | 673 | 0.15 |
| -60 | **HT1-15** | 566 | 653 | 0.14 |
| -60 | **HT1-16** | 560 | 655 | 0.16 |

* Indicate the test was ceased at the first longitudinal surface crack occurred to observe cracking.

Table 6-2. HT2 Tensile Tests Results Summary

| ***Test Temperature*** | ***Specimen*** | ***Lower Yield Stress*** | ***UTS*** | ***n*** |
|---|---|---|---|---|
| ***°C*** | ***No.*** | ***MPa*** | ***MPa*** | *(Extensometer)* |
| -196 | **HT2-01** | 934 | 951 | N/A |
| -196 | **HT2-02** | 926 | 941 | N/A |
| -196 | **HT2-03** | 922 | 950 | N/A |
| -170 | **HT2-04** | 785 | 830 | N/A |
| -160 | **HT2-07** | 750 | 814 | N/A |
| -140 | **HT2-06** | 706 | 767 | 0.15 |
| -140 | **HT2-08** | 696 | 769 | 0.15 |
| -120 | **HT2-09** | 646 | 723 | 0.15 |
| -120 | **HT2-10** | 628 | 722 | 0.15 |
| -100 | **HT2-11** | 610 | 693 | 0.14 |
| -100 | **HT2-12** | 588 | 692 | 0.15 |
| -80 | **HT2-13** | 568 | 664 | 0.14 |
| -80 | **HT2-14** | 568 | 663 | 0.15 |
| -60 | **HT2-15** | 528 | 641 | 0.14 |
| -60 | **HT2-16** | 541 | 639 | 0.14 |

Table 6-3. Fracture Toughness Tests Results at -120 °C

| $Temperature$ | $Testpiece$ | $B$ | $W$ | $a_0$ ($compliance$) | $a_0$ | $W$-$a_0$ | $Pmax$ | $PQ$ | $Pmax$ /$PQ$ | $KQ$ | $J$ | $KJc$ | $CTOD$ |
|---|---|---|---|---|---|---|---|---|---|---|---|---|---|
| $°C$ | $No.$ | $[mm]$ | $[mm]$ | $[mm]$ | $[mm]$ | $[mm]$ | $[kN]$ | $[kN]$ | | $(MPa\,m^{1/2})$ | $kJm^{1/2}$ | $(MPa\,m^{1/2})$ | $[mm]$ |
| -120 | **HT1-16** | 24.93 | 49.77 | 25.31 | 25.52 | 24.25 | 37.00 | 37.00 | 1.00 | 66.0 | 21.2 | 66.0 | 0.015 |
| | **HT1-20** | 25.03 | 49.87 | 25.26 | 25.55 | 24.32 | 31.16 | 31.16 | 1.00 | 54.9 | 15.1 | 55.7 | 0.011 |
| | **HT1-21** | 24.94 | 49.66 | 25.48 | 25.91 | 23.75 | 65.93 | 52.12 | 1.26 | 94.4 | 55.4 | 106.9 | 0.040 |
| | **HT1-22** | 24.97 | 49.63 | 25.50 | 25.87 | 23.76 | 47.82 | 47.82 | 1.00 | 86.7 | 39.1 | 89.7 | 0.028 |
| | **HT1-23** | 24.98 | 49.70 | 25.29 | 25.73 | 23.97 | 31.09 | 31.09 | 1.00 | 55.4 | 15.0 | 55.6 | 0.011 |
| | **HT1-24** | 24.98 | 49.70 | 25.46 | 25.68 | 24.02 | 44.42 | 44.42 | 1.00 | 80.0 | 32.4 | 81.7 | 0.023 |
| | **HT2-05** | 24.90 | 49.73 | 25.68 | 25.07 | 24.66 | 37.99 | 37.99 | 1.00 | 69.6 | 23.9 | 70.1 | 0.018 |
| | **HT2-06** | 24.90 | 49.73 | 25.03 | 25.42 | 24.31 | 45.22 | 45.22 | 1.00 | 79.5 | 32.4 | 81.7 | 0.024 |
| | **HT2-07** | 24.90 | 49.88 | 25.12 | 25.46 | 24.42 | 44.63 | 44.63 | 1.00 | 78.4 | 31.6 | 80.7 | 0.023 |
| | **HT2-08** | 24.92 | 49.80 | 25.11 | 25.55 | 24.25 | 49.43 | 49.43 | 1.00 | 87.0 | 40.6 | 91.4 | 0.030 |
| | **HT2-19** | 24.92 | 49.71 | 25.23 | 25.58 | 24.13 | 43.35 | 43.35 | 1.00 | 77.2 | 30.2 | 78.8 | 0.022 |
| | **HT2-22** | 25.01 | 50.00 | 24.93 | 25.60 | 24.40 | 43.08 | 38.52 | 1.12 | 66.3 | 24.1 | 70.4 | 0.018 |

Table 6-4. Fracture Toughness Tests Results at -100 °C and -80 °C

| $Temperature$ | $Testpiece$ | $B$ | $W$ | $a_0$ $(compliance)$ | $a_0$ | $W$-$a_0$ | $Pmax$ | $PQ$ | $Pmax$ /$PQ$ | $KQ$ | $J$ | $KJc$ | $CTOD$ |
|---|---|---|---|---|---|---|---|---|---|---|---|---|---|
| $°C$ | $No.$ | $[mm]$ | $[mm]$ | $[mm]$ | $[mm]$ | $[mm]$ | $[kN]$ | $[kN]$ | | $(MPa\,m^{1/2})$ | $kJm^{1/2}$ | $(MPa\,m^{1/2})$ | $[mm]$ |
| -100 | **HT1-01** | 24.95 | 49.59 | 25.68 | 25.99 | 23.60 | 77.36 | 47.38 | 1.63 | 87.1 | 217.6 | 211.7 | 0.164 |
| | **HT1-07** | 24.97 | 49.75 | 25.41 | 25.74 | 24.01 | 67.30 | 43.44 | 1.55 | 77.9 | 57.7 | 109.1 | 0.044 |
| | **HT1-18** | 25.02 | 49.95 | 25.36 | 25.66 | 24.29 | 63.07 | 36.56 | 1.73 | 64.7 | 38.6 | 89.2 | 0.029 |
| | **HT1-25** | 24.97 | 49.69 | 25.25 | 25.43 | 24.26 | 52.09 | 48.55 | 1.07 | 86.4 | 41.8 | 92.8 | 0.032 |
| | **HT1-26** | 24.96 | 49.75 | 25.26 | 25.58 | 24.17 | 67.67 | 45.63 | 1.48 | 81.1 | 59.4 | 110.6 | 0.045 |
| | **HT1-27** | 24.94 | 49.81 | 25.46 | 25.40 | 24.41 | 54.00 | 44.25 | 1.22 | 79.5 | 37.9 | 88.3 | 0.029 |
| | **HT2-01** | 24.95 | 49.77 | 25.26 | 25.50 | 24.27 | 68.78 | 46.84 | 1.47 | 83.2 | 64.9 | 115.7 | 0.050 |
| | **HT2-02** | 24.99 | 49.94 | 25.04 | 25.30 | 24.64 | 33.74 | 33.74 | 1.00 | 58.6 | 17.2 | 59.6 | 0.013 |
| | **HT2-03** | 24.96 | 49.87 | 25.14 | 25.30 | 24.57 | 54.94 | 47.18 | 1.16 | 82.8 | 40.3 | 91.1 | 0.031 |
| | **HT2-04** | 24.90 | 49.84 | 24.88 | 25.18 | 24.66 | 55.62 | 48.93 | 1.14 | 84.8 | 42.2 | 93.2 | 0.033 |
| | **HT2-09** | 24.94 | 50.00 | 25.94 | 26.10 | 23.90 | 46.25 | 44.60 | 1.04 | 82.0 | 36.1 | 86.3 | 0.028 |
| | **HT2-21** | 24.95 | 49.97 | 25.07 | 25.76 | 24.21 | 74.55 | 36.25 | 2.06 | 63.1 | 86.2 | 133.3 | 0.067 |
| -80 | **HT1-17** | 25.02 | 49.81 | 25.25 | 25.86 | 23.95 | 70.06 | 40.13 | 1.75 | 70.9 | 70.6 | 120.6 | 0.056 |
| | **HT2-24** | 24.96 | 49.74 | 24.65 | 25.03 | 24.71 | 74.63 | 58.33 | 1.28 | 99.9 | 105.8 | 147.6 | 0.086 |
| | **HT2-25** | 24.96 | 50.08 | 25.69 | 25.71 | 24.39 | 72.36 | 45.96 | 1.57 | 82.7 | 155.9 | 179.2 | 0.120 |

Table 6-5. Detailed information of fracture initiation sites from 26 sharp-cracked specimens with initiation reason, chemical composition, fracture distance, initiation diameter, and facet diameter.

| ***Temperature*** | ***Testpiece*** | ***Iniaition reason*** | ***Chemical composition*** | $K_{JC}$ | $X_0$ | ***Stable crack*** | ***Initiator diameter*** | ***Facet diameter*** |
|---|---|---|---|---|---|---|---|---|
| $°C$ | ***No.*** | | | $(MPa\,m^{1/2})$ | $(\mu m)$ | | $(\mu m)$ | $(\mu m)$ |
| -120 | CT HT1-16 | Inclusion cracking | Ti, Nb, Al, Mg | 66 | 30 | 3 | **1.5*** | 21 |
| -120 | CT HT1-20 | Matrix related | Matrix composition | 56 | 52 | 4 | N/A | 30 |
| -120 | CT HT1-21 | Matrix cracking | Matrix composition | 107 | 657 | 14 | N/A | 32 |
| -120 | CT HT1-22 | Inclusion cracking | Ca, Al | 90 | 163 | 8 | 1.5 | 46 |
| -120 | CT HT1-23 | Inclusion cracking | Ti, Nb, Ca | 56 | 21 | 3 | **1*** | 34 |
| -120 | CT HT1-24 | Matrix cracking | Matrix composition | 82 | 61 | 5 | N/A | 36 |
| -120 | CT HT2-05 | Inclusion cracking | Ca, Al | 70 | 256 | 10 | 2.2 | 35 |
| -120 | CT HT2-06 | Matrix related (Possible M-A-C) | Matrix composition | 82 | 79 | 6 | 0.6 | 21 |
| -120 | CT HT2-07 | Inclusion cracking | Ti, Nb | 81 | 25 | 4 | **1.7*** | 34 |
| -120 | CT HT2-08 | Inclusion cracking | Ca, Al, Ti | 91 | 87 | 8 | 2.5 | 28 |
| -120 | CT HT2-19 | Matrix related (Possible M-A-C) | 4wt% Carbon higher than surrounding matrix | 79 | 87 | 4 | 1.7 | 27 |
| -120 | CT HT2-22 | Inclusion cracking | Ca, Al, Ti | 70 | 147 | 6 | 1.6 | 39 |

| *Temperature* | *Testpiece* | *Iniaition reason* | *Element composition* | $K_{JC}$ | $X_0$ | *Stable crack* | *Initiation diameter* | *Facet diameter* |
|---|---|---|---|---|---|---|---|---|
| $°C$ | *No.* | | | $(MPa\ m^{1/2}$ | $(\mu m)$ | | $(\mu m)$ | $(\mu m)$ |
| -100 | CT HT1-01 | Inclusion decohesion | Ca, Al | 212 | 655 | 70 | 1.1 | 24 |
| -100 | CT HT1-07 | Inclusion cracking | Ti, Nb | 109 | 135 | 21 | **1.8*** | 26 |
| -100 | CT HT1-18 | Inclusion cracking | Ca, Ti | 89 | 432 | 8 | 1.7 | 38 |
| -100 | CT HT1-25 | Inclusion cracking | Ca, Al, Ti | 93 | 104 | 7 | 1.4 | 22 |
| -100 | CT HT1-26 | Inclusion cracking | Ca, Al, Ti | 111 | 160 | 19 | 0.7 | 28 |
| -100 | CT HT1-27 | Matrix related (Possible M-A-C) | 11wt% Carbon higher than surrounding matrix | 88 | 94 | 9 | 1.5 | 32 |
| -100 | CT HT2-01 | Inclusion cracking | Ti, Nb | 116 | 649 | 16 | **1.6*** | 34 |
| -100 | CT HT2-02 | Matrix related | Matrix composition | 60 | 63 | 2 | N/A | 43 |
| -100 | CT HT2-03 | Matrix related (Possible M-A-C) | 5wt% Carbon higher than surrounding matrix | 91 | 53 | 9 | 1.1 | 26 |
| -100 | CT HT2-04 | Matrix Cracking | Matrix composition | 93 | 78 | 9 | N/A | 20 |
| -100 | CT HT2-09 | Matrix related (Possible M-A-C) | Matrix composition | 86 | 115 | 8 | 3.2 | 31 |
| -100 | CT HT2-21 | Inclusion cracking | Ca, Ti | 133 | 402 | 32 | 1.4 | 35 |
| -80 | CT HT1-17 | Inclusion cracking | Ca, Al, Ti | 121 | 295 | 34 | 2.1 | 29 |
| -80 | CT HT2-25 | Inclusion cracking | Ca, Al, Ti | 179 | 486 | 54 | 1.4 | 39 |

***** Indicates the inclusion is cubic shape, $X_0$ is the fracture distance measured from end of ductile crack growth extensions to the cleavage initiation.

Table 6-6. CTOD, $X_0$ values and the resulting local cleavage fracture stresses calculated using McMeeking FEM analysis. (n=0.1)

| *Temperature* ($^\circ C$) | *Specimen Number* | *CTOD* ($\mu m$) | $X_0$ ($\mu m$) | *Yield stress* ($MPa$) | $\sigma_{Max}$ ($MPa$) | $\sigma_F$ ($MPa$) | $\sigma_F/\sigma_{Max}$ |
|---|---|---|---|---|---|---|---|
| -120 | CT HT1-16 | 15.2 | 30 | 647 | 2497 | 2484 | 0.99 |
| | CT HT1-20 | 10.9 | 52 | | 2497 | 2271 | 0.91 |
| | CT HT1-21 | 39.9 | 657 | | 2497 | 1954 | 0.78 |
| | CT HT1-22 | 28.2 | 163 | | 2497 | 2200 | 0.88 |
| | CT HT1-23 | 10.8 | 21 | | 2497 | 2484 | 0.99 |
| | CT HT1-24 | 23.4 | 61 | | 2497 | 2478 | 0.99 |
| | CT HT2-05 | 17.6 | 256 | 647 | 2497 | 1986 | 0.80 |
| | CT HT2-06 | 23.9 | 79 | | 2497 | 2420 | 0.97 |
| | CT HT2-07 | 23.3 | 25 | | 2497 | 2290 | 0.92 |
| | CT HT2-08 | 29.9 | 87 | | 2497 | 2459 | 0.98 |
| | CT HT2-19 | 22.2 | 87 | | 2497 | 2349 | 0.94 |
| | CT HT2-22 | 17.7 | 147 | | 2497 | 2090 | 0.84 |
| -100 | CT HT1-01 | 164.3 | 655 | 611 | 2358 | 2212 | 0.94 |
| | CT HT1-07 | 43.6 | 135 | | 2358 | 2303 | 0.98 |
| | CT HT1-18 | 29.1 | 432 | | 2358 | 1870 | 0.79 |
| | CT HT1-25 | 31.6 | 104 | | 2358 | 2285 | 0.97 |
| | CT HT1-26 | 44.8 | 160 | | 2358 | 2261 | 0.96 |
| | CT HT1-27 | 28.6 | 94 | | 2358 | 2285 | 0.97 |
| | CT HT2-01 | 50.2 | 649 | 611 | 2358 | 1900 | 0.81 |
| | CT HT2-02 | 13.3 | 63 | | 2358 | 2145 | 0.91 |
| | CT HT2-03 | 31.1 | 53 | | 2358 | 2322 | 0.98 |
| | CT HT2-04 | 32.6 | 78 | | 2358 | 2340 | 0.99 |
| | CT HT2-09 | 27.9 | 115 | | 2358 | 2206 | 0.94 |
| | CT HT2-21 | 66.6 | 402 | | 2358 | 2071 | 0.88 |
| -80 | CT HT1-17 | 56.2 | 295 | 574 | 2216 | 1992 | 0.90 |
| | CT HT2-25 | 120.4 | 486 | | 2216 | 2078 | 0.94 |

Table 6-7. CTOD, $X_0$ values and the resulting local cleavage fracture stresses calculated using McMeeking FEM analysis. (n=0.1)

| *Temperature* ($^\circ C$) | *Specimen Number* | *R/b* | $\sigma_F/\sigma_y$ *at fracture* | $X_0$ ($\mu m$) | $X_{Max}$ ($\mu m$) | *Plastic zone size* $r_{nominal}$ ($\mu m$) | *Plastic zone size* $r_{true}$ ($\mu m$) |
|---|---|---|---|---|---|---|---|
| -120 | CT HT1-16 | 2.0 | 3.8 | 30 | 30 | 586 | 586 |
| | CT HT1-20 | 4.8 | 3.5 | 52 | 22 | 406 | 418 |
| | CT HT1-21 | 16.5 | 3.0 | 657 | 80 | 1197 | 1536 |
| | CT HT1-22 | 5.8 | 3.4 | 163 | 56 | 1010 | 1083 |
| | CT HT1-23 | 1.9 | 3.8 | 21 | 22 | 413 | 415 |
| | CT HT1-24 | 2.6 | 3.8 | 61 | 47 | 861 | 898 |
| | CT HT2-05 | 14.5 | 3.1 | 256 | 35 | 651 | 661 |
| | CT HT2-06 | 3.3 | 3.7 | 79 | 48 | 849 | 898 |
| | CT HT2-07 | 1.1 | 3.5 | 25 | 47 | 826 | 875 |
| | CT HT2-08 | 2.9 | 3.8 | 87 | 60 | 1018 | 1124 |
| | CT HT2-19 | 3.9 | 3.6 | 87 | 44 | 801 | 836 |
| | CT HT2-22 | 8.3 | 3.2 | 147 | 35 | 591 | 667 |
| -100 | CT HT1-01 | 4.0 | 3.6 | 655 | 329 | 1145 | 6759 |
| | CT HT1-07 | 3.1 | 3.8 | 135 | 87 | 915 | 1793 |
| | CT HT1-18 | 14.8 | 3.1 | 432 | 58 | 631 | 1199 |
| | CT HT1-25 | 3.3 | 3.7 | 104 | 63 | 1126 | 1300 |
| | CT HT1-26 | 3.6 | 3.7 | 160 | 90 | 992 | 1845 |
| | CT HT1-27 | 3.3 | 3.7 | 94 | 57 | 954 | 1176 |
| | CT HT2-01 | 12.9 | 3.1 | 649 | 100 | 1043 | 2017 |
| | CT HT2-02 | 4.7 | 3.5 | 63 | 27 | 518 | 535 |
| | CT HT2-03 | 1.7 | 3.8 | 53 | 62 | 1033 | 1252 |
| | CT HT2-04 | 2.4 | 3.8 | 78 | 65 | 1085 | 1310 |
| | CT HT2-09 | 4.1 | 3.6 | 115 | 56 | 1013 | 1123 |
| | CT HT2-21 | 6.0 | 3.4 | 402 | 133 | 600 | 2678 |
| -80 | CT HT1-17 | 5.2 | 3.5 | 295 | 112 | 859 | 2484 |
| | CT HT2-25 | 4.0 | 3.6 | 486 | 241 | 1170 | 5487 |

Table 6-8. Effective surface energy calculated using the modified Griffith equation for a penny-shaped microcrack. (n=0.1)

| $\boldsymbol{Temperature}$ $(^\circ \boldsymbol{C})$ | $\boldsymbol{Specimen\ Number}$ | $\boldsymbol{Initiation\ diameter}$ $(\boldsymbol{\mu m})$ | $\boldsymbol{Local\ Cleavage\ Fracture\ Stress}$ $\boldsymbol{\sigma_F}$ $(\boldsymbol{MPa})$ | $\boldsymbol{\gamma}$ $(\boldsymbol{J/m^2})$ |
|---|---|---|---|---|
| -120 | CT HT1-16 | 1.5 | 2484 | 12.9 |
| | CT HT1-20 | N/A | 2271 | N/A |
| | CT HT1-21 | N/A | 1954 | N/A |
| | CT HT1-22 | 1.5 | 2200 | 10.1 |
| | CT HT1-23 | 1 | 2484 | 8.6 |
| | CT HT1-24 | N/A | 2478 | N/A |
| | CT HT2-05 | 2.2 | 1986 | 12.1 |
| | CT HT2-06 | 0.6 | 2420 | 4.9 |
| | CT HT2-07 | 1.7 | 2290 | 12.4 |
| | CT HT2-08 | 2.5 | 2459 | 21.0 |
| | CT HT2-19 | 1.7 | 2349 | 13.0 |
| | CT HT2-22 | 1.6 | 2090 | 9.7 |
| -100 | CT HT1-01 | 1.1 | 2212 | 7.5 |
| | CT HT1-07 | 1.8 | 2303 | 13.3 |
| | CT HT1-18 | 1.7 | 1870 | 8.3 |
| | CT HT1-25 | 1.4 | 2285 | 10.2 |
| | CT HT1-26 | 0.7 | 2261 | 5.0 |
| | CT HT1-27 | 1.5 | 2285 | 10.9 |
| | CT HT2-01 | 1.6 | 1900 | 8.0 |
| | CT HT2-02 | N/A | 2145 | N/A |
| | CT HT2-03 | 1.1 | 2322 | 8.2 |
| | CT HT2-04 | N/A | 2340 | N/A |
| | CT HT2-09 | 3.2 | 2206 | 21.6 |
| | CT HT2-21 | 1.4 | 2071 | 8.3 |
| -80 | CT HT1-17 | 2.1 | 1992 | 11.6 |
| | CT HT2-25 | 1.4 | 2078 | 8.4 |

Table 6-9. CTOD, $X_0$ values and the resulting local cleavage fracture stresses calculated using McMeeking FEM analysis (n=0.2).

| *Temperature* ($^\circ C$) | *Specimen Number* | *CTOD* ($\mu m$) | $X_0$ ($\mu m$) | *Yield stress* ($MPa$) | $\sigma_{Max}$ ($MPa$) | $\sigma_F$ ($MPa$) | $\sigma_F/\sigma_{Max}$ |
|---|---|---|---|---|---|---|---|
| -120 | CT HT1-16 | 15.2 | 30 | 647 | 3300 | 3235 | 0.98 |
| | CT HT1-20 | 10.9 | 52 | | 3351 | 2717 | 0.81 |
| | CT HT1-21 | 39.9 | 657 | | 3351 | 2167 | 0.65 |
| | CT HT1-22 | 28.2 | 163 | | 3351 | 2556 | 0.76 |
| | CT HT1-23 | 10.8 | 21 | | 3351 | 3267 | 0.98 |
| | CT HT1-24 | 23.4 | 61 | | 3351 | 3041 | 0.91 |
| | CT HT2-05 | 17.6 | 256 | 647 | 3300 | 2180 | 0.66 |
| | CT HT2-06 | 23.9 | 79 | | 3249 | 2944 | 0.91 |
| | CT HT2-07 | 23.3 | 25 | | 3249 | 3203 | 0.99 |
| | CT HT2-08 | 29.9 | 87 | | 3249 | 3106 | 0.96 |
| | CT HT2-19 | 22.2 | 87 | | 3249 | 2847 | 0.88 |
| | CT HT2-22 | 17.7 | 147 | | 3249 | 2329 | 0.72 |
| -100 | CT HT1-01 | 164.3 | 655 | 611 | 3116 | 2627 | 0.84 |
| | CT HT1-07 | 43.6 | 135 | | 3182 | 2841 | 0.89 |
| | CT HT1-18 | 29.1 | 432 | | 3182 | 2053 | 0.65 |
| | CT HT1-25 | 31.6 | 104 | | 3182 | 2841 | 0.89 |
| | CT HT1-26 | 44.8 | 160 | | 3182 | 2750 | 0.86 |
| | CT HT1-27 | 28.6 | 94 | | 3182 | 2841 | 0.89 |
| | CT HT2-01 | 50.2 | 649 | 611 | 3116 | 2090 | 0.67 |
| | CT HT2-02 | 13.3 | 63 | | 3075 | 2566 | 0.83 |
| | CT HT2-03 | 31.1 | 53 | | 3075 | 3055 | 0.99 |
| | CT HT2-04 | 32.6 | 78 | | 3075 | 2994 | 0.97 |
| | CT HT2-09 | 27.9 | 115 | | 3075 | 2597 | 0.84 |
| | CT HT2-21 | 66.6 | 402 | | 3075 | 2383 | 0.77 |
| -80 | CT HT1-17 | 56.2 | 295 | 574 | 2927 | 2296 | 0.78 |
| | CT HT2-25 | 120.4 | 486 | | 2897 | 2468 | 0.85 |

Table 6-10. CTOD, $X_0$ values and the resulting local cleavage fracture stresses calculated using McMeeking FEM analysis. (n=0.2)

| *Temperature* (°C) | *Specimen Number* | *R/b* | $\sigma_F/\sigma_y$ *at fracture* | $X_0$ ($\mu m$) | $X_{Max}$ ($\mu m$) | *Plastic zone size* $r_{nominal}$ ($\mu m$) | *Plastic zone size* $r_{true}$ ($\mu m$) |
|---|---|---|---|---|---|---|---|
| -120 | CT HT1-16 | 2.0 | 3.8 | 30 | 30 | 586 | 586 |
| | CT HT1-20 | 4.8 | 3.5 | 52 | 22 | 406 | 418 |
| | CT HT1-21 | 16.5 | 3.0 | 657 | 80 | 1197 | 1536 |
| | CT HT1-22 | 5.8 | 3.4 | 163 | 56 | 1010 | 1083 |
| | CT HT1-23 | 1.9 | 3.8 | 21 | 22 | 413 | 415 |
| | CT HT1-24 | 2.6 | 3.8 | 61 | 47 | 861 | 898 |
| | CT HT2-05 | 14.5 | 3.1 | 256 | 35 | 651 | 661 |
| | CT HT2-06 | 3.3 | 3.7 | 79 | 48 | 849 | 898 |
| | CT HT2-07 | 1.1 | 3.5 | 25 | 47 | 826 | 875 |
| | CT HT2-08 | 2.9 | 3.8 | 87 | 60 | 1018 | 1124 |
| | CT HT2-19 | 3.9 | 3.6 | 87 | 44 | 801 | 836 |
| | CT HT2-22 | 8.3 | 3.2 | 147 | 35 | 591 | 667 |
| -100 | CT HT1-01 | 4.0 | 3.6 | 655 | 329 | 1145 | 6759 |
| | CT HT1-07 | 3.1 | 3.8 | 135 | 87 | 915 | 1793 |
| | CT HT1-18 | 14.8 | 3.1 | 432 | 58 | 631 | 1199 |
| | CT HT1-25 | 3.3 | 3.7 | 104 | 63 | 1126 | 1300 |
| | CT HT1-26 | 3.6 | 3.7 | 160 | 90 | 992 | 1845 |
| | CT HT1-27 | 3.3 | 3.7 | 94 | 57 | 954 | 1176 |
| | CT HT2-01 | 12.9 | 3.1 | 649 | 100 | 1043 | 2017 |
| | CT HT2-02 | 4.7 | 3.5 | 63 | 27 | 518 | 535 |
| | CT HT2-03 | 1.7 | 3.8 | 53 | 62 | 1033 | 1252 |
| | CT HT2-04 | 2.4 | 3.8 | 78 | 65 | 1085 | 1310 |
| | CT HT2-09 | 4.1 | 3.6 | 115 | 56 | 1013 | 1123 |
| | CT HT2-21 | 6.0 | 3.4 | 402 | 133 | 600 | 2678 |
| -80 | CT HT1-17 | 5.2 | 3.5 | 295 | 112 | 859 | 2484 |
| | CT HT2-25 | 4.0 | 3.6 | 486 | 241 | 1170 | 5487 |

Table 6-11. Effective surface energy calculated using the modified Griffith equation for a penny-shaped microcrack. (n=0.2)

| $Temperature$ ($^\circ C$) | $Specimen\ Number$ | $Initiation\ diameter$ ($\mu m$) | $Local\ Cleavage\ Fracture\ Stress$ $\sigma_F$ ($MPa$) | $\gamma$ ($J/m^2$) |
|---|---|---|---|---|
| -120 | CT HT1-16 | 1.5 | 3235 | 21.8 |
| | CT HT1-20 | N/A | 2717 | N/A |
| | CT HT1-21 | N/A | 2167 | N/A |
| | CT HT1-22 | 1.5 | 2556 | 13.6 |
| | CT HT1-23 | 1 | 3267 | 14.8 |
| | CT HT1-24 | N/A | 3041 | N/A |
| | CT HT2-05 | 2.2 | 2180 | 14.5 |
| | CT HT2-06 | 0.6 | 2944 | 7.2 |
| | CT HT2-07 | 1.7 | 3203 | 24.2 |
| | CT HT2-08 | 2.5 | 3106 | 33.5 |
| | CT HT2-19 | 1.7 | 2847 | 19.2 |
| | CT HT2-22 | 1.6 | 2329 | 12.1 |
| -100 | CT HT1-01 | 1.1 | 2627 | 10.6 |
| | CT HT1-07 | 1.8 | 2841 | 20.2 |
| | CT HT1-18 | 1.7 | 2053 | 10.0 |
| | CT HT1-25 | 1.4 | 2841 | 15.7 |
| | CT HT1-26 | 0.7 | 2750 | 7.4 |
| | CT HT1-27 | 1.5 | 2841 | 16.8 |
| | CT HT2-01 | 1.6 | 2090 | 9.7 |
| | CT HT2-02 | N/A | 2566 | N/A |
| | CT HT2-03 | 1.1 | 3055 | 14.3 |
| | CT HT2-04 | N/A | 2994 | N/A |
| | CT HT2-09 | 3.2 | 2597 | 30.0 |
| | CT HT2-21 | 1.4 | 2383 | 11.0 |
| -80 | CT HT1-17 | 2.1 | 2296 | 15.4 |
| | CT HT2-25 | 1.4 | 2468 | 11.9 |

Table 6-12. Detailed observations summary of fracture initiation sites from 7 blunt-notched specimens with initiation reason, chemical composition, fracture distance, initiation diameter, and facet diameter.

| ***Test Temperature*** ($°C$) | ***Specimen Number*** | ***Initiation Reason*** | ***Chemical Composition*** | ***Local Cleavage Fracture Stress*** $\sigma_F$ ($MPa$) | ***Xo*** ($\mu m$) | ***Initiator Diameter*** ($\mu m$) | ***Facet Diameter*** ($\mu m$) |
|---|---|---|---|---|---|---|---|
| -196 | HT1-07 | Matrix related Possible M-A-C | Matrix Composition | 1956 | 305 | 1.8 | 34 |
| | HT1-08 | Inclusion cracking | Ca, Al | 2039 | 320 | 1.8 | 20 |
| | HT1-09 | Inclusion cracking | Ca, Ti | 1900 | 239 | 1.6 | 23 |
| | HT2-07 | Matrix related Possible M-A-C | Matrix Composition | 1678 | 335 | 1.1 | 25 |
| | HT2-08 | Inclusion cracking | Ca, Al | 1937 | 268 | 2.6 | 27 |
| | HT2-09 | Inclusion cracking | Ca, Al | 1845 | 220 | 2.6 | 32 |
| -170 | HT2-04 | Matrix related Possible M-A-C | Matrix Composition | 1915 | 420 | 2.6 | 30 |

*M-A-C indicates potential martensite-austenite constituents, Xo is the fracture distance measured from edge of notch root to the cleavage initiation.

Table 6-13. Summary of microscopic cleavage fracture stress test results and the maximum principal stress $\boldsymbol{\sigma_{yy}^{max}}$

| ***Test Temperature*** $(°C)$ | ***Specimen Number*** | ***Lower Yield Stress*** $\sigma_{YS}^{L}$ $(MPa)$ | ***Maximum Load P*** $(kN)$ | ***Nominal Stress*** $\sigma_{nom}$ $(MPa)$ | $\sigma_{nom}/\sigma_{YS}^{L}$ $(max\ 2.292)$ | $L/L_{GY}$ $(max\ 1.065)$ | ***Stress Intensification*** $R_{Max} = \sigma_{yy}^{max}/\sigma_{YS}^{L}$ $(max\ 2.62)$ | ***Maximum Principal Stress*** $\sigma_{yy}^{max}$ $(MPa)$ |
|---|---|---|---|---|---|---|---|---|
| -196 | HT1-07 | 928 | 29.0 | 1213 | 1.307 | 0.608 | 2.14 | 1984 |
| | HT1-08 | | 33.2 | 1388 | 1.496 | 0.696 | 2.24 | 2076 |
| | HT1-09 | | 29.2 | 1221 | 1.316 | 0.612 | 2.15 | 1993 |
| | HT2-07 | 927 | 23.3 | 974 | 1.051 | 0.489 | 1.98 | 1835 |
| | HT2-08 | | 29.7 | 1242 | 1.339 | 0.623 | 2.18 | 2021 |
| | HT2-09 | | 28.7 | 1200 | 1.294 | 0.602 | 2.14 | 1984 |
| -170 | HT2-04 | 785 | 38.4 | 1606 | 2.050 | 0.951 | 2.55 | 2002 |

Table 6-14. Local cleavage fracture stress $\boldsymbol{\sigma_F}$ derived from Griffith-Owen FEM analysis and comparison with maximum principal stress $\boldsymbol{\sigma_{yy}^{max}}$

| ***Test Temperature*** $(°C)$ | ***Specimen Number*** | ***Fracture Distance*** $Xo(\mu m)$ | ***Local Stress Intensification*** $R_{(X0)}$ | ***Local Cleavage Fracture Stress*** $\sigma_F\ (MPa)$ | ***Maximum Principal Stress*** $\sigma_{yy}^{max}\ (MPa)$ | $\sigma_F\ /\sigma_{yy}^{max}$ |
|---|---|---|---|---|---|---|
| -196 | HT1-07 | 305 | 2.11 | 1956 | 1984 | 99% |
| | HT1-08 | 320 | 2.20 | 2039 | 2076 | 98% |
| | HT1-09 | 239 | 2.05 | 1900 | 1993 | 95% |
| | HT2-07 | 335 | 1.81 | 1678 | 1835 | 91% |
| | HT2-08 | 268 | 2.09 | 1937 | 2021 | 96% |
| | HT2-09 | 220 | 1.99 | 1845 | 1984 | 93% |
| -170 | HT2-04 | 420 | 2.44 | 1915 | 2002 | 96% |

Table 6-15. Effective surface energy calculated using the modified Griffith equation for a penny-shaped microcrack.

| $\boldsymbol{Temperature}$ $(\boldsymbol{oC})$ | $\boldsymbol{Specimen\ Number}$ | $\boldsymbol{Initiation\ Diameter}$ $(\boldsymbol{\mu m})$ | $\boldsymbol{Local\ Cleavage\ Fracture\ Stress}$ $\boldsymbol{\sigma_F}$ $(\boldsymbol{MPa})$ | $\boldsymbol{\gamma}$ $(\boldsymbol{J/m^2})$ |
|---|---|---|---|---|
| -196 | FS HT1-07 | 1.8 | 1956 | 9.6 |
| | FS HT1-08 | 1.8 | 2039 | 10.4 |
| | FS HT1-09 | 1.6 | 1900 | 8.0 |
| | FS HT2-07 | 1.1 | 1678 | 4.3 |
| | FS HT2-08 | 2.6 | 1937 | 13.6 |
| | FS HT2-09 | 2.6 | 1845 | 12.3 |
| -170 | FS HT2-04 | 2.6 | 1915 | 13.3 |

Table 6-16. Effective surface energy calculated for **only** cracked inclusions as cleavage origin using the modified Griffith equation for a penny-shaped microcrack. (n=0.1 for McMeeking analysis)

| ***Temperature*** $(o_C)$ | ***Specimen Number*** | ***Initiation diameter*** $(\mu m)$ | ***Local Cleavage Fracture Stress*** $\sigma_F$ $(MPa)$ | $\gamma$ $(J/m^2)$ |
|---|---|---|---|---|
| -196 | FS HT1-09 | 1.6 | 1900 | 8.0 |
| | FS HT1-08 | 1.8 | 2039 | 10.4 |
| | FS HT2-08 | 2.6 | 1937 | 13.6 |
| | FS HT2-09 | 2.6 | 1845 | 12.3 |
| -120 | CT HT1-16 | 1.5 | 2523 | 12.9 |
| | CT HT1-22 | 1.5 | 2234 | 10.1 |
| | CT HT1-23 | 1 | 2523 | 8.6 |
| | CT HT2-05 | 2.2 | 1956 | 12.1 |
| | CT HT2-07 | 1.7 | 2255 | 12.4 |
| | CT HT2-08 | 2.5 | 2421 | 21.0 |
| | CT HT2-22 | 1.6 | 2058 | 9.7 |
| | CT HT1-07 | 1.8 | 2390 | 13.3 |
| | CT HT1-18 | 1.7 | 1940 | 8.3 |
| | CT HT1-25 | 1.4 | 2371 | 10.2 |
| | CT HT1-26 | 0.7 | 2346 | 5.0 |
| | CT HT2-01 | 1.6 | 1888 | 8.0 |
| | CT HT2-21 | 1.4 | 2058 | 8.3 |
| -80 | CT HT1-17 | 2.1 | 2020 | 11.6 |
| | CT HT2-25 | 1.4 | 2060 | 8.4 |

Table 6-17. Effective surface energy calculated for **only** cracked inclusion as cleavage origin using the modified Griffith equation for a penny-shaped microcrack. (n=0.2 for McMeeking analysis)

| ***Temperature*** $(o_C)$ | ***Specimen Number*** | ***Initiation diameter*** $(\mu m)$ | ***Local Cleavage Fracture Stress*** $\sigma_F$ $(MPa)$ | $\gamma$ $(J/m^2)$ |
|---|---|---|---|---|
| -196 | FS HT1-09 | 1.6 | 1900 | 8.0 |
| | FS HT1-08 | 1.8 | 2039 | 10.4 |
| | FS HT2-08 | 2.6 | 1937 | 13.6 |
| | FS HT2-09 | 2.6 | 1845 | 12.3 |
| -120 | CT HT1-16 | 1.5 | 3285 | 21.8 |
| | CT HT1-22 | 1.5 | 2595 | 13.6 |
| | CT HT1-23 | 1 | 3318 | 14.8 |
| | CT HT2-05 | 2.2 | 2147 | 14.5 |
| | CT HT2-07 | 1.7 | 3153 | 24.2 |
| | CT HT2-08 | 2.5 | 3058 | 33.5 |
| | CT HT2-22 | 1.6 | 2293 | 12.1 |
| | CT HT1-07 | 1.8 | 2902 | 20.2 |
| | CT HT1-18 | 1.7 | 2097 | 10.0 |
| | CT HT1-25 | 1.4 | 2902 | 15.7 |
| | CT HT1-26 | 0.7 | 2808 | 7.4 |
| | CT HT2-01 | 1.6 | 2062 | 9.7 |
| | CT HT2-21 | 1.4 | 2352 | 11.0 |
| -80 | CT HT1-17 | 2.1 | 2316 | 15.4 |
| | CT HT2-25 | 1.4 | 2442 | 11.9 |

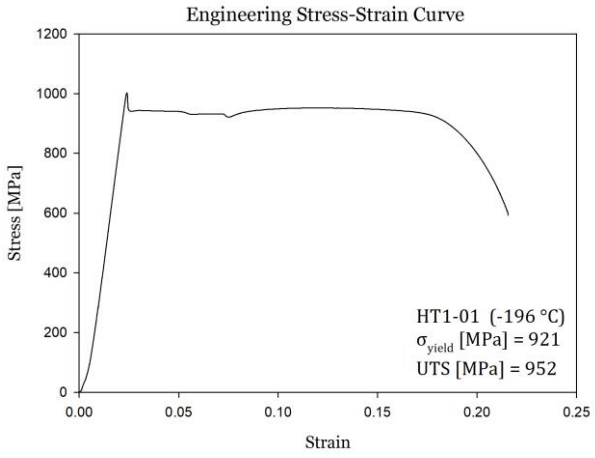
Engineering Stress-Strain Curve
Stress [MPa]
Strain
HT1-01 (-196 °C)
σyield [MPa] = 921
UTS [MPa] = 952

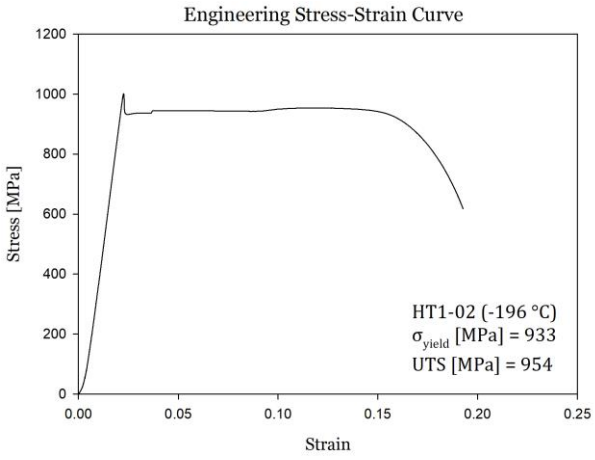
Engineering Stress-Strain Curve
Stress [MPa]
Strain
HT1-02 (-196 °C)
σyield [MPa] = 933
UTS [MPa] = 954

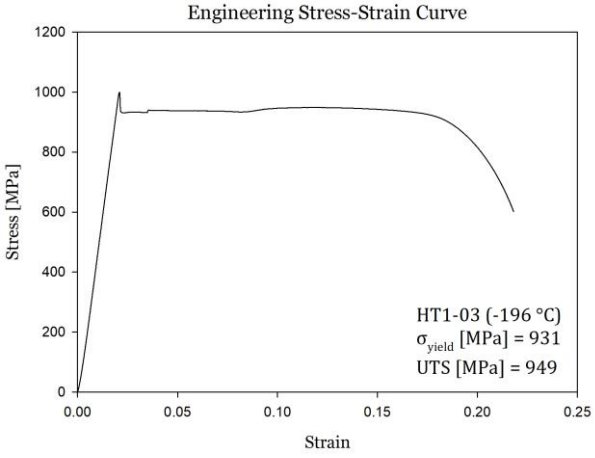
Engineering Stress-Strain Curve
Stress [MPa]
Strain
HT1-03 (-196 °C)
σyield [MPa] = 931
UTS [MPa] = 949

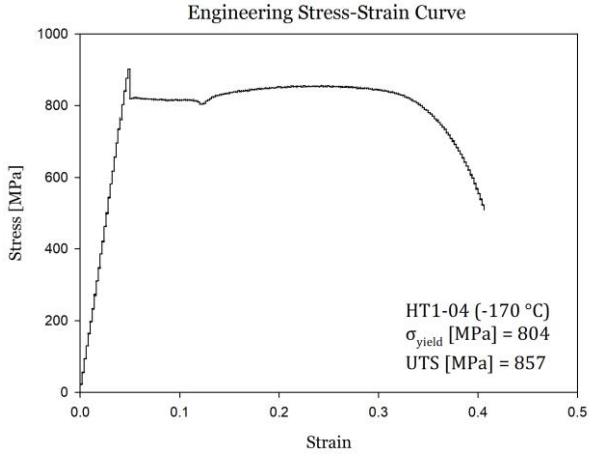
Engineering Stress-Strain Curve
Stress [MPa]
Strain
HT1-04 (-170 °C)
σyield [MPa] = 804
UTS [MPa] = 857

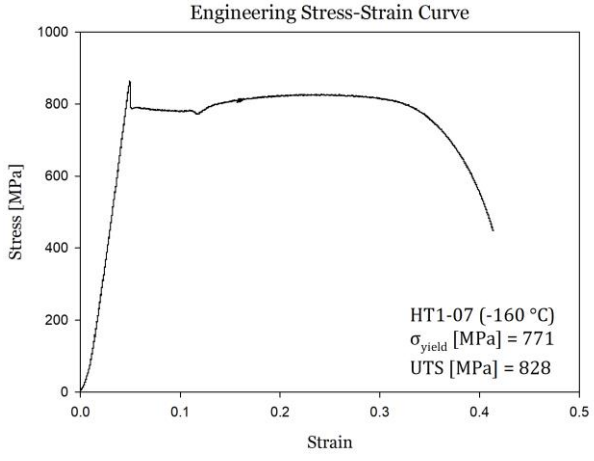
Engineering Stress-Strain Curve
Stress [MPa]
Strain
HT1-07 (-160 °C)
σyield [MPa] = 771
UTS [MPa] = 828

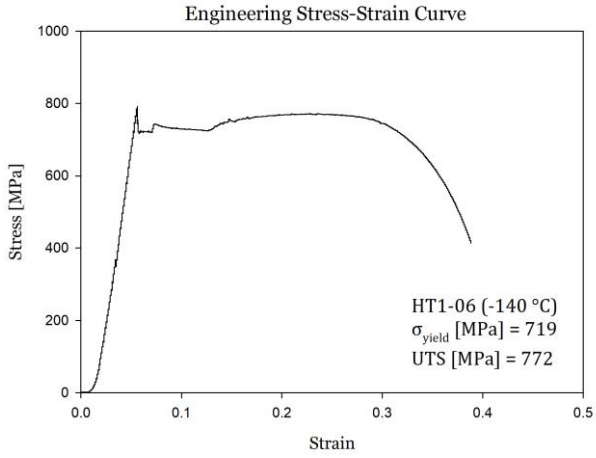
Engineering Stress-Strain Curve
Stress [MPa]
Strain
HT1-06 (-140 °C)
σyield [MPa] = 719
UTS [MPa] = 772

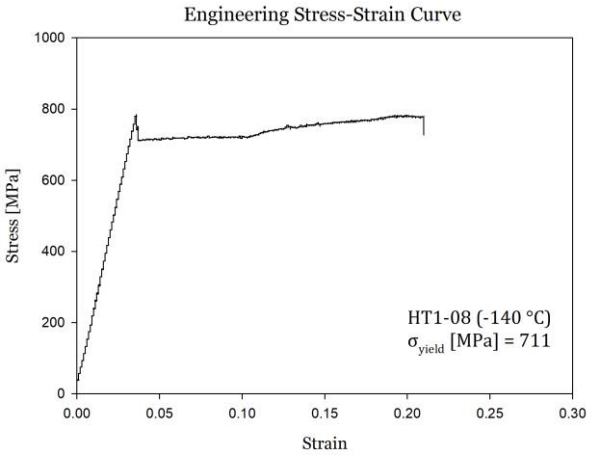
Engineering Stress-Strain Curve
Stress [MPa]
Strain
HT1-08 (-140 °C)
σyield [MPa] = 711

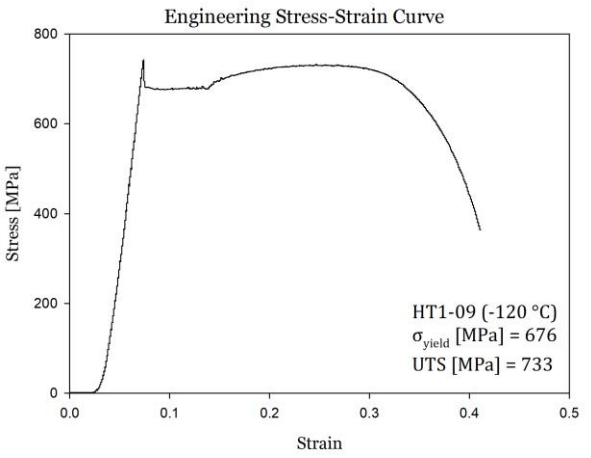
Engineering Stress-Strain Curve
Stress [MPa]
Strain
HT1-09 (-120 °C)
σyield [MPa] = 676
UTS [MPa] = 733

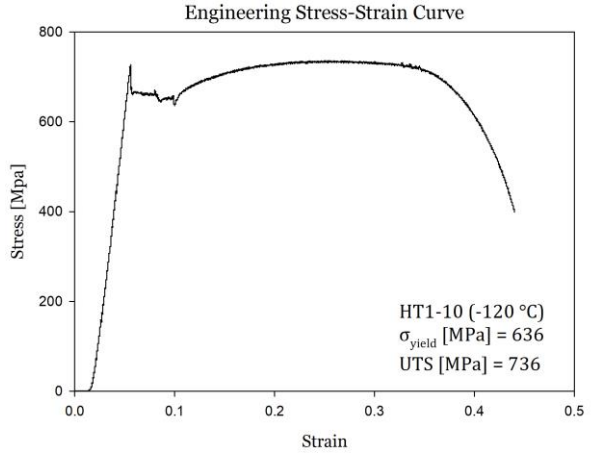
Engineering Stress-Strain Curve
Stress [Mpa]
Strain
HT1-10 (-120 °C)
σyield [MPa] = 636
UTS [MPa] = 736

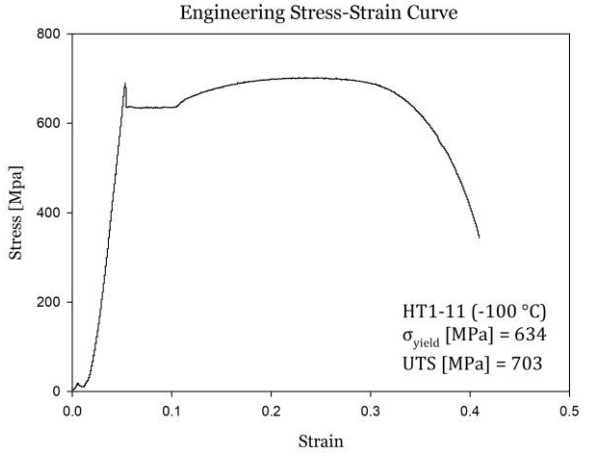
Engineering Stress-Strain Curve
Stress [Mpa]
Strain
HT1-11 (-100 °C)
σyield [MPa] = 634
UTS [MPa] = 703

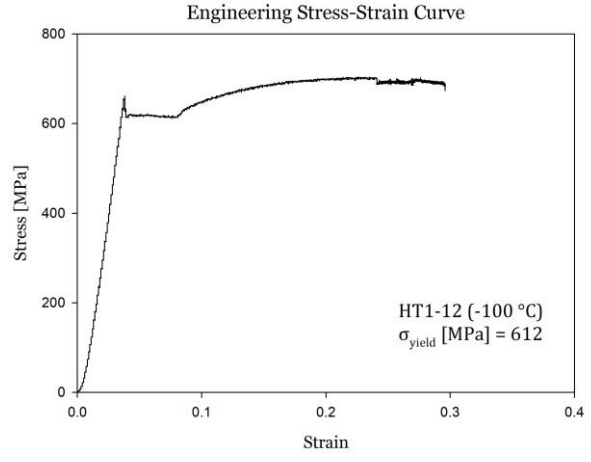
Engineering Stress-Strain Curve
Stress [MPa]
Strain
HT1-12 (-100 °C)
σyield [MPa] = 612

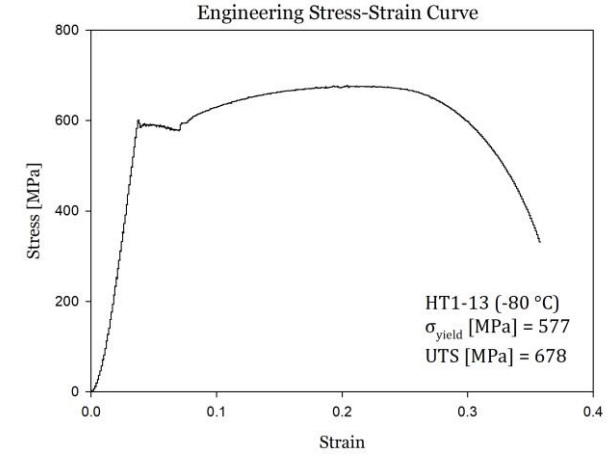
Engineering Stress-Strain Curve
Stress [MPa]
Strain
HT1-13 (-80 °C)
σyield [MPa] = 577
UTS [MPa] = 678

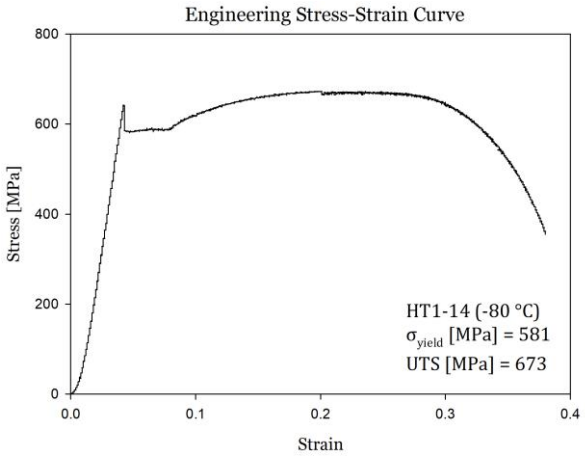


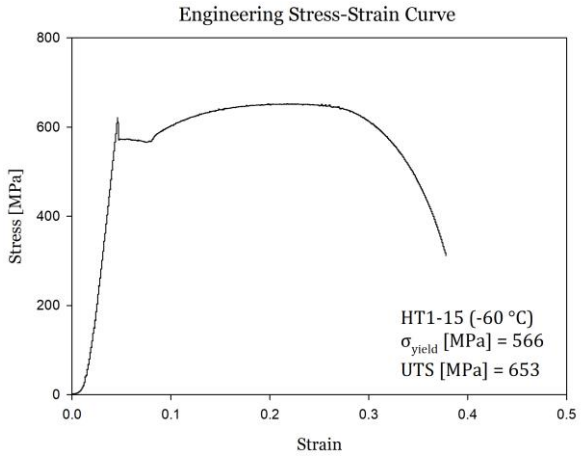


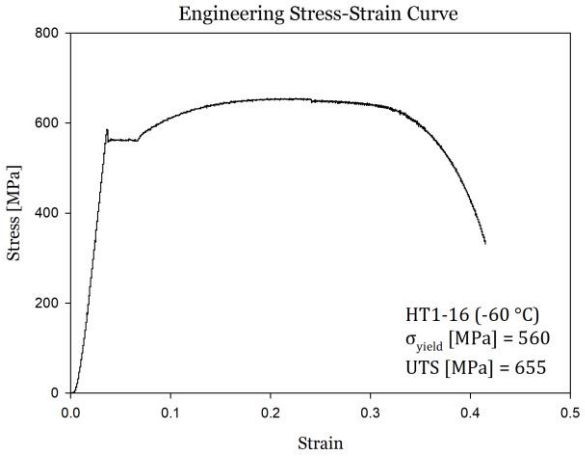


Figure 6-1. Engineering stress-strain curves for HT1 condition of tensile specimens tested at various temperatures

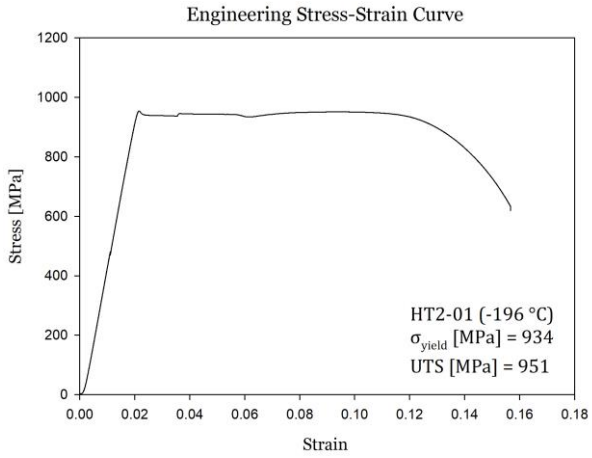
Engineering Stress-Strain Curve
Stress [MPa]
Strain
HT2-01 (-196 °C)
σyield [MPa] = 934
UTS [MPa] = 951

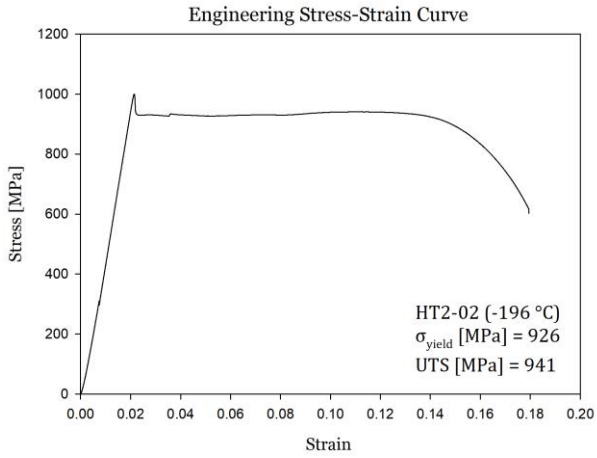
Engineering Stress-Strain Curve
Stress [MPa]
Strain
HT2-02 (-196 °C)
σyield [MPa] = 926
UTS [MPa] = 941

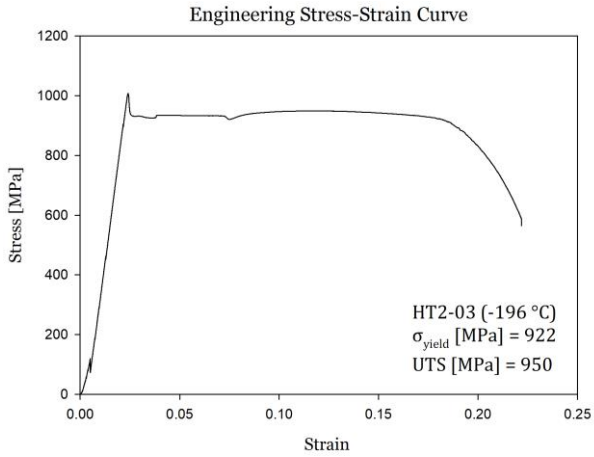
Engineering Stress-Strain Curve
Stress [MPa]
Strain
HT2-03 (-196 °C)
σyield [MPa] = 922
UTS [MPa] = 950

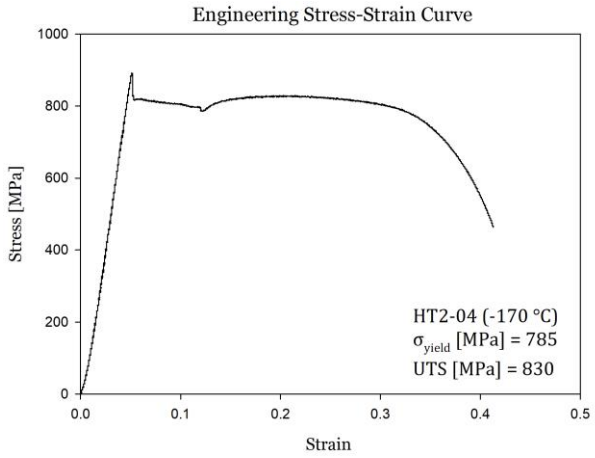
Engineering Stress-Strain Curve
Stress [MPa]
Strain
HT2-04 (-170 °C)
σyield [MPa] = 785
UTS [MPa] = 830

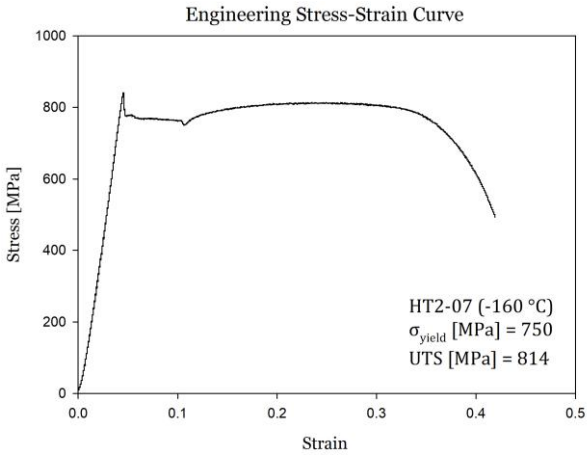
Engineering Stress-Strain Curve
Stress [MPa]
Strain
HT2-07 (-160 °C)
σyield [MPa] = 750
UTS [MPa] = 814

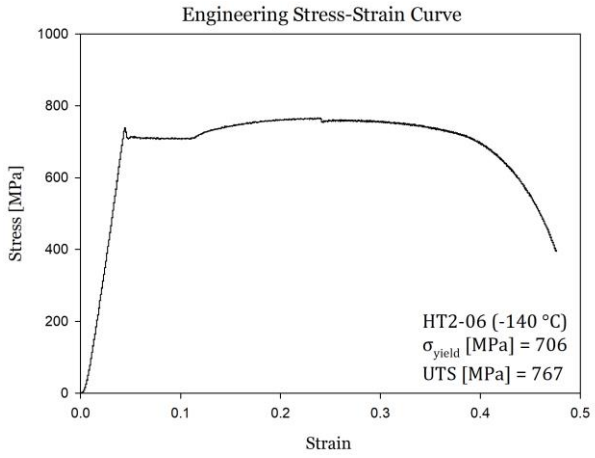
Engineering Stress-Strain Curve
Stress [MPa]
Strain
HT2-06 (-140 °C)
σyield [MPa] = 706
UTS [MPa] = 767

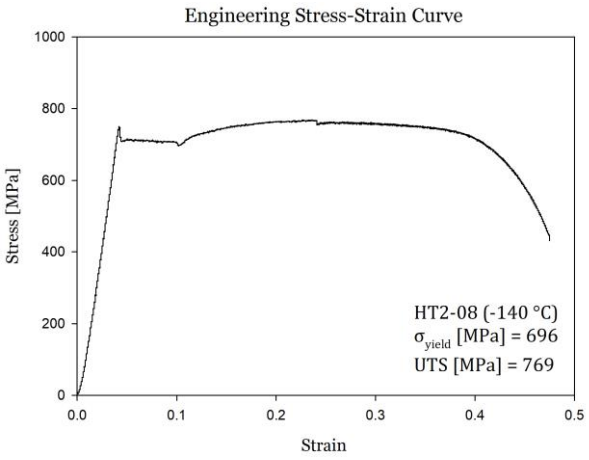
Engineering Stress-Strain Curve
Stress [MPa]
Strain
HT2-08 (-140 °C)
σyield [MPa] = 696
UTS [MPa] = 769

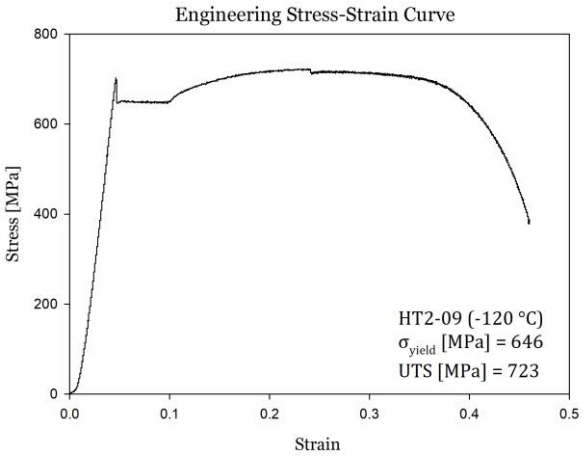
Engineering Stress-Strain Curve
Stress [MPa]
Strain
HT2-09 (-120 °C)
σyield [MPa] = 646
UTS [MPa] = 723

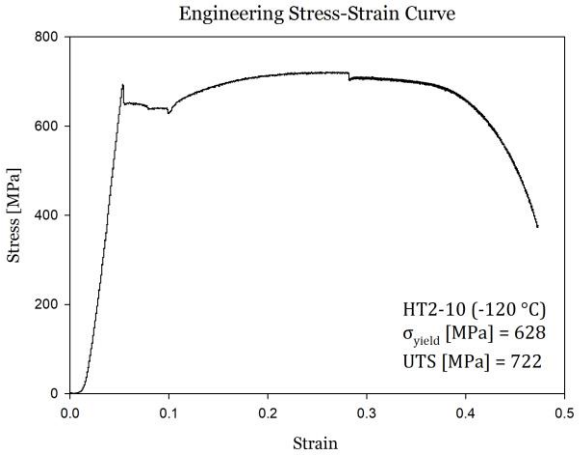
Engineering Stress-Strain Curve
Stress [MPa]
Strain
HT2-10 (-120 °C)
σyield [MPa] = 628
UTS [MPa] = 722

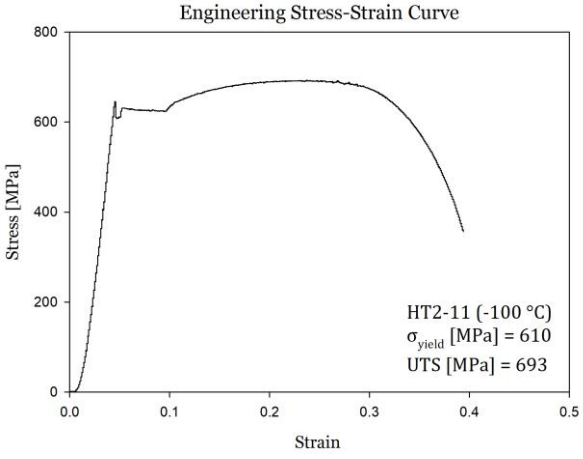
Engineering Stress-Strain Curve
Stress [MPa]
Strain
HT2-11 (-100 °C)
σyield [MPa] = 610
UTS [MPa] = 693

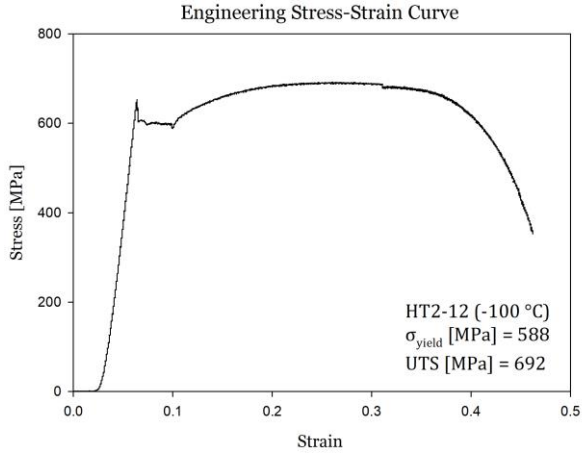
Engineering Stress-Strain Curve
Stress [MPa]
Strain
HT2-12 (-100 °C)
σyield [MPa] = 588
UTS [MPa] = 692

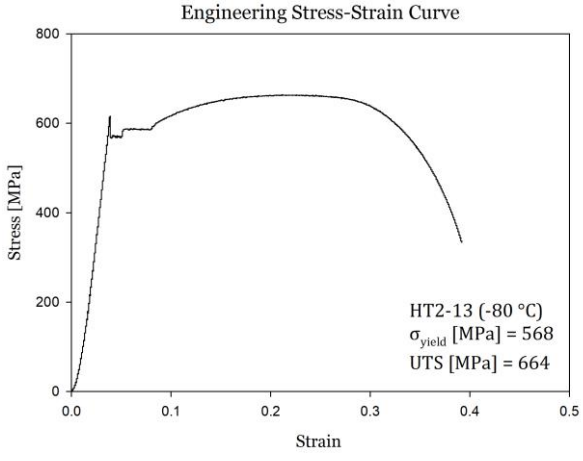
Engineering Stress-Strain Curve
Stress [MPa]
Strain
HT2-13 (-80 °C)
σyield [MPa] = 568
UTS [MPa] = 664

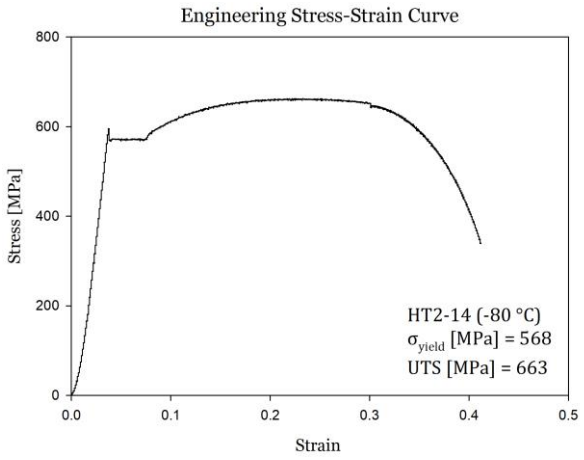


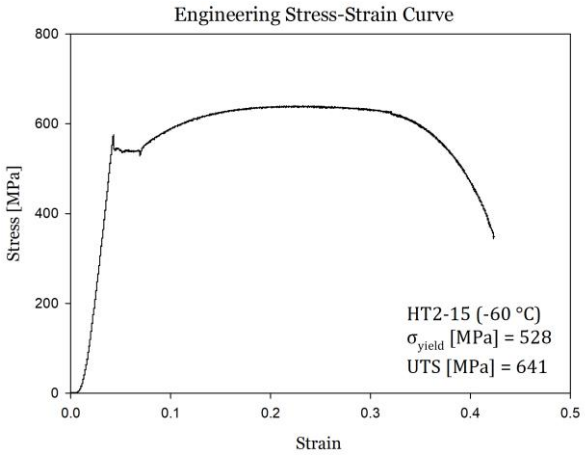


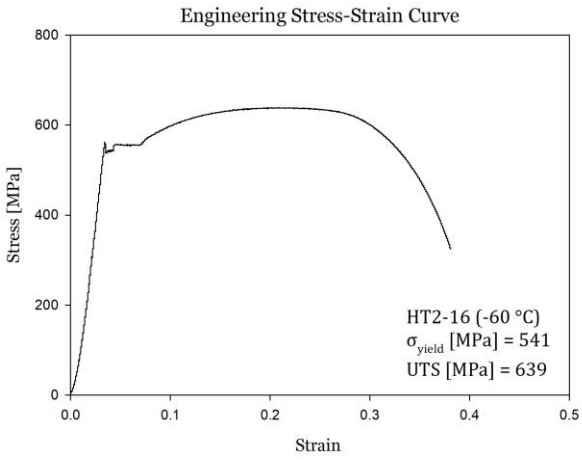


Figure 6-2. Engineering stress-strain curves for HT2 condition of tensile specimens tested at various temperatures

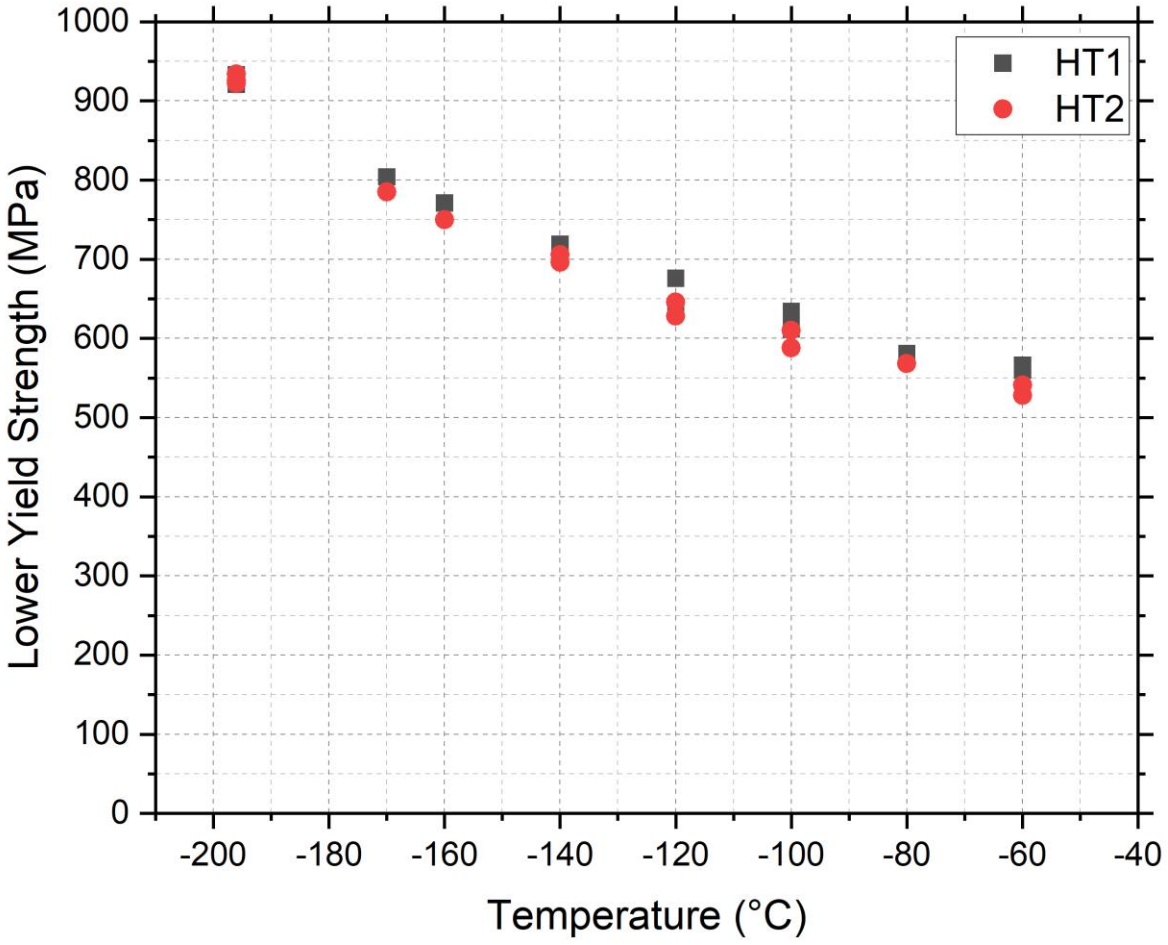


Figure 6-3. Tensile specimens lower yield strength under different temperatures

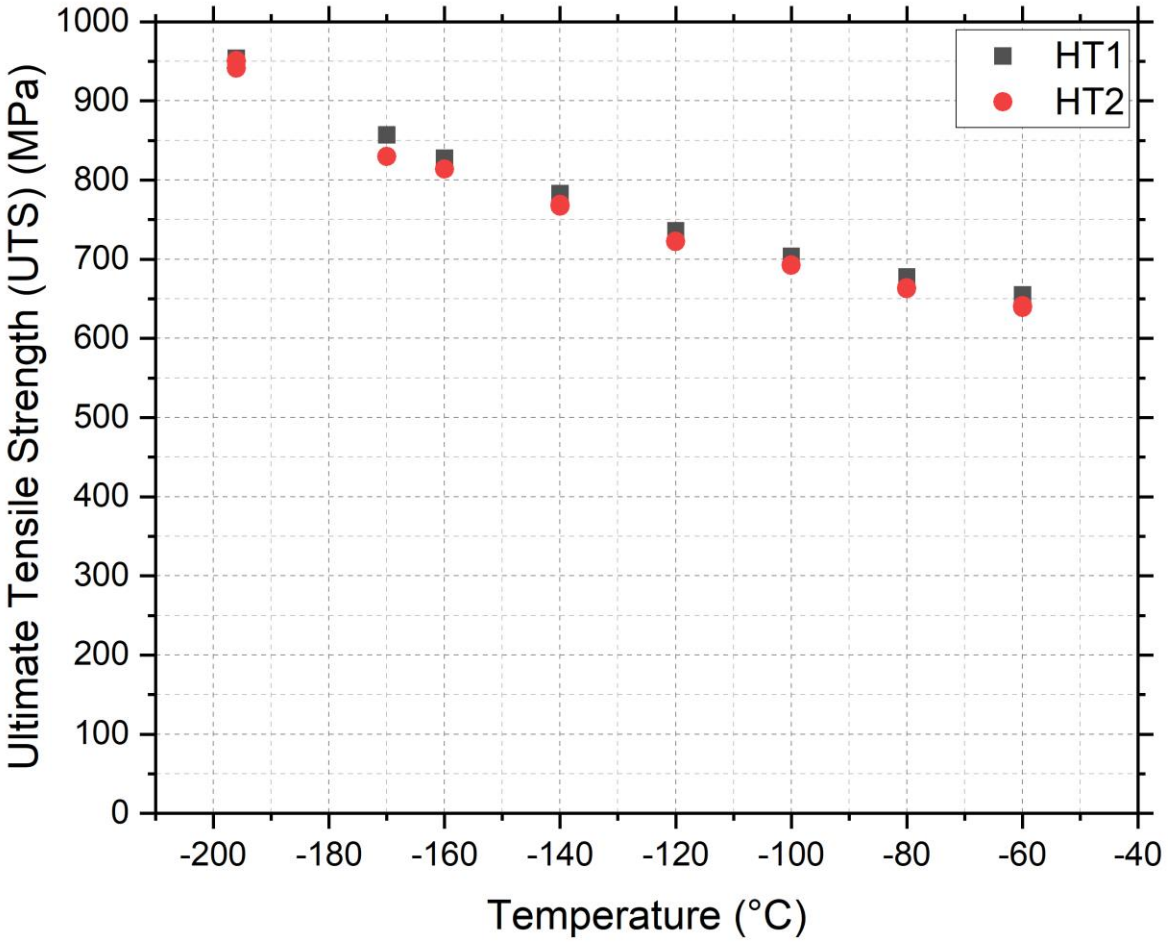


Figure 6-4. Tensile specimens UTS under different temperatures

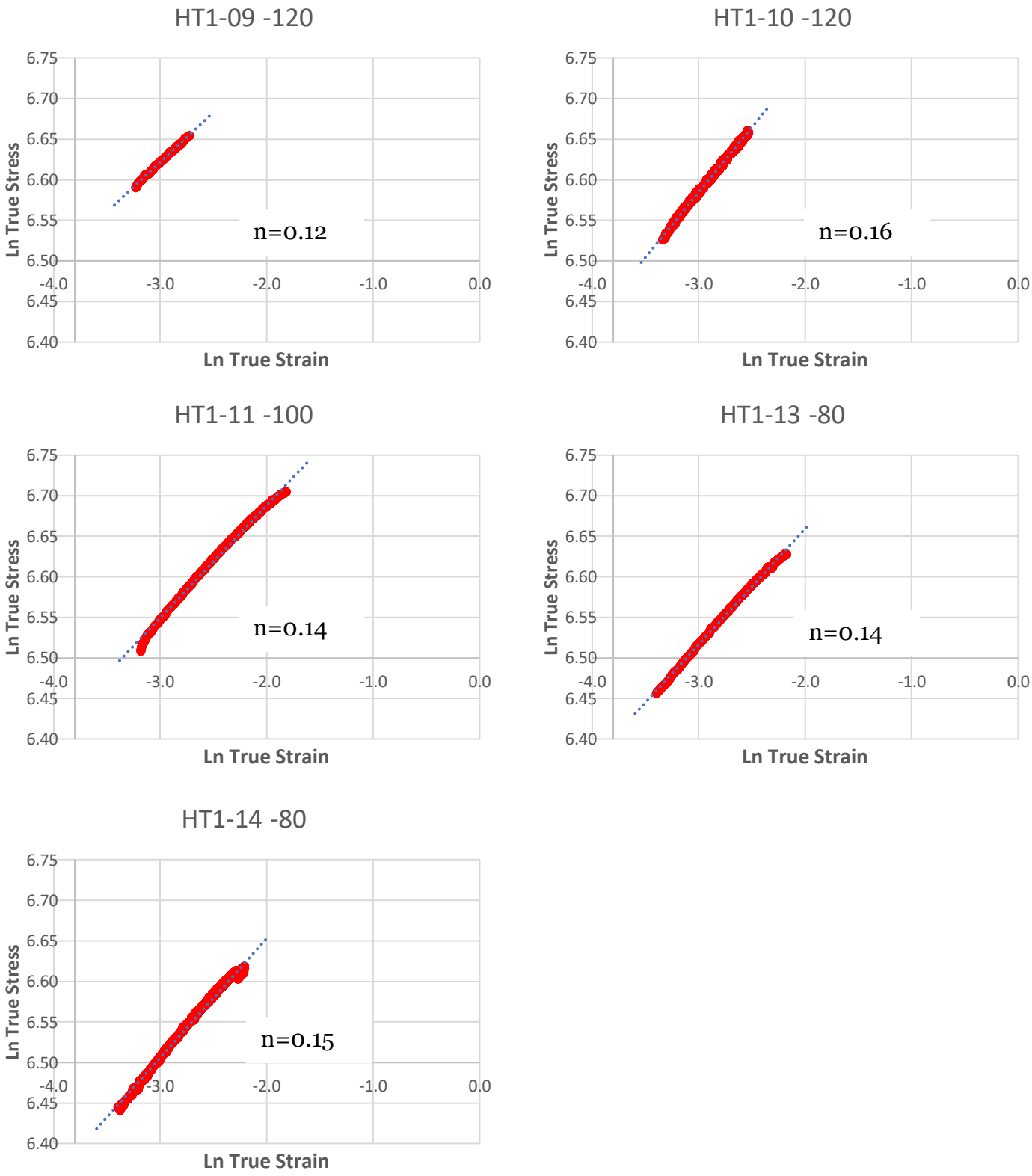


Figure 6-5. Natural logarithm of the true stress-strain curves for HT1 condition of tensile specimens tested at various temperatures

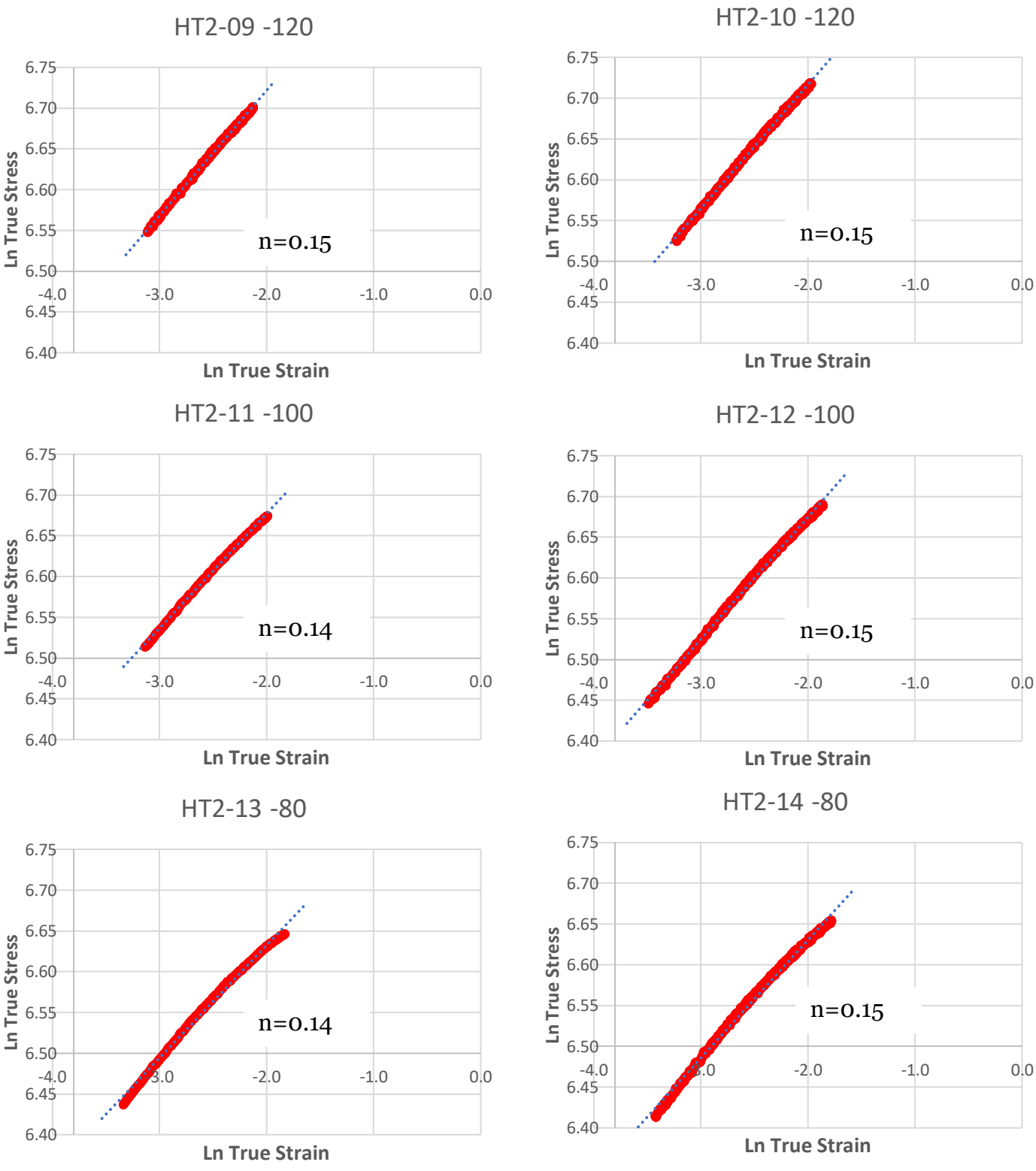


Figure 6-6. Natural logarithm of the true stress-strain curves for HT2 condition of tensile specimens tested at various temperatures

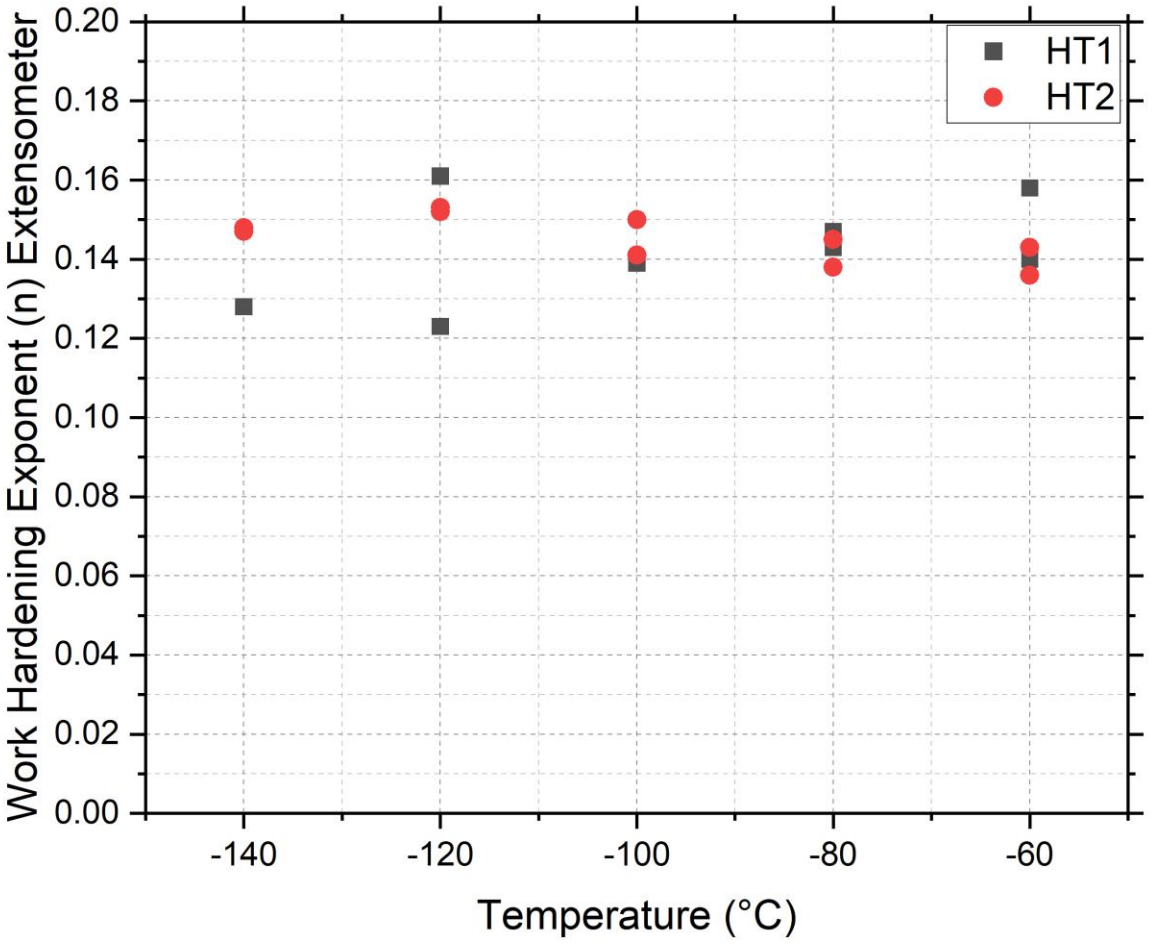


Figure 6-7. Tensile specimens work hardening exponent (extensometer) under different temperatures

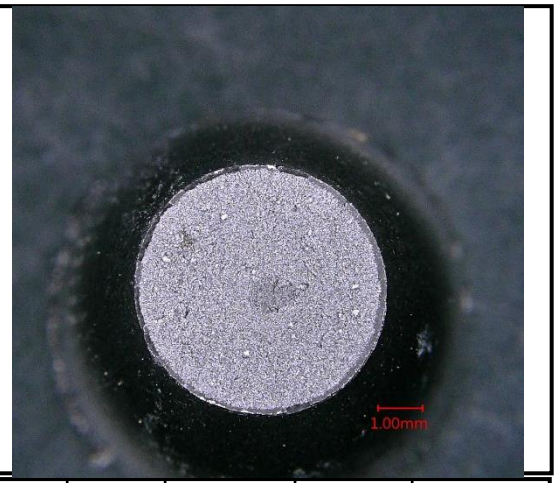


| No. | °C | LYS | UTS | n |
|---|---|---|---|---|
| HT1-1 | -196 | 921MPa | 952MPa | N/A |

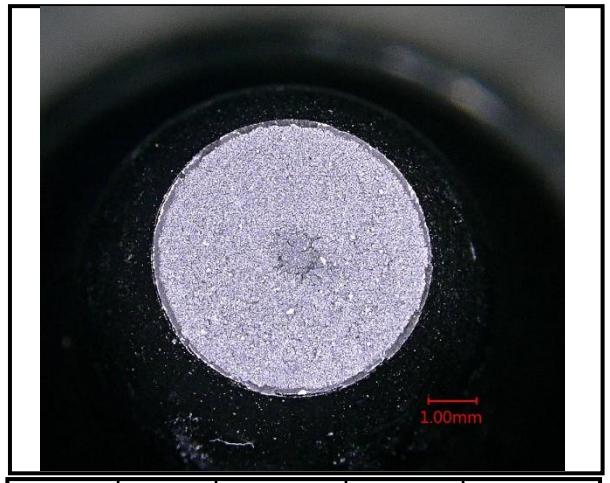


| No. | °C | LYS | UTS | n |
|---|---|---|---|---|
| HT1-2 | -196 | 933MPa | 954MPa | N/A |


| No. | °C | LYS | UTS | n |
|---|---|---|---|---|
| HT1-3 | -196 | 931MPa | 949MPa | N/A |

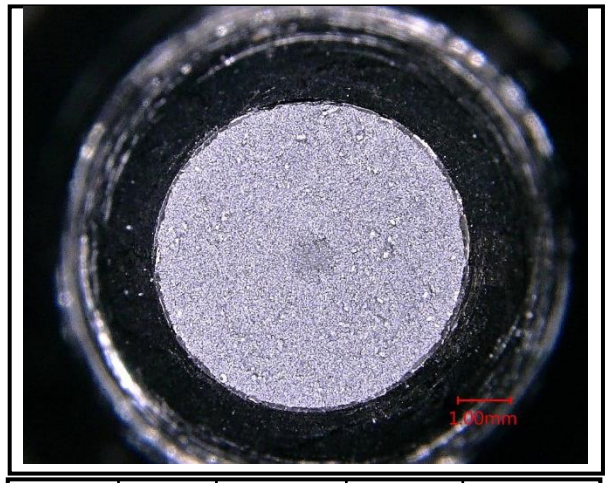


| No. | °C | LYS | UTS | n |
|---|---|---|---|---|
| HT2-1 | -196 | 934MPa | 951MPa | N/A |


| No. | °C | LYS | UTS | n |
|---|---|---|---|---|
| HT2-2 | -196 | 926MPa | 941MPa | N/A |

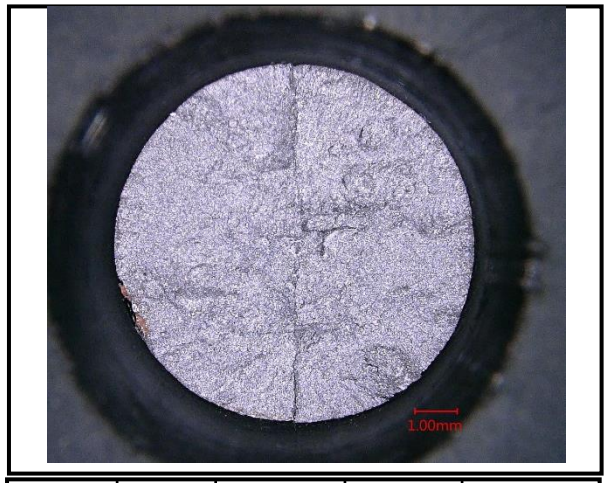


| No. | °C | LYS | UTS | n |
|---|---|---|---|---|
| HT2-3 | -196 | 922MPa | 950MPa | N/A |

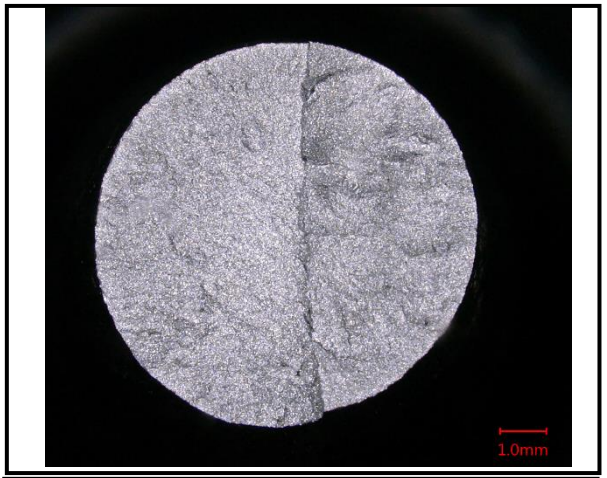


| No. | °C | LYS | UTS | n |
|---|---|---|---|---|
| HT1-10 | -120 | 636MPa | 736MPa | 0.16 |

| No. | °C | LYS | UTS | n |
|---|---|---|---|---|
| HT1-13 | -80 | 577MPa | 678MPa | 0.14 |

| No. | °C | LYS | UTS | n |
|---|---|---|---|---|
| HT1-14 | -80 | 581MPa | 673MPa | 0.15 |

| No. | °C | LYS | UTS | n |
|---|---|---|---|---|
| HT1-15 | -60 | 566MPa | 653MPa | 0.14 |

Figure 6-8. Tensile Test specimen fracture surfaces

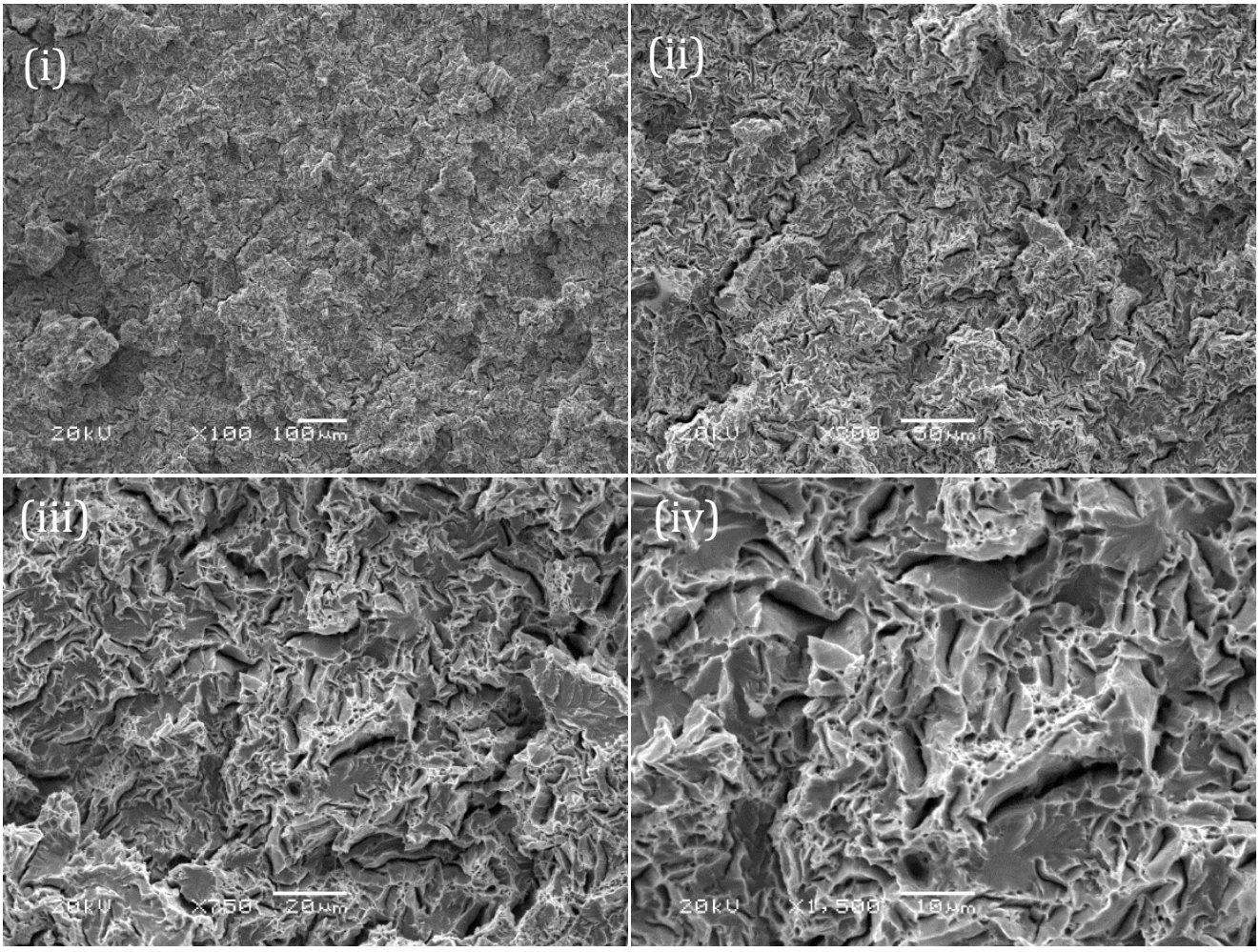


Figure 6-9. Fracture surface morphology of Tensile specimen HT1-01 tested at -196°C; (i), (ii), (iii) and (v) are sequence magnification of the same typical area.

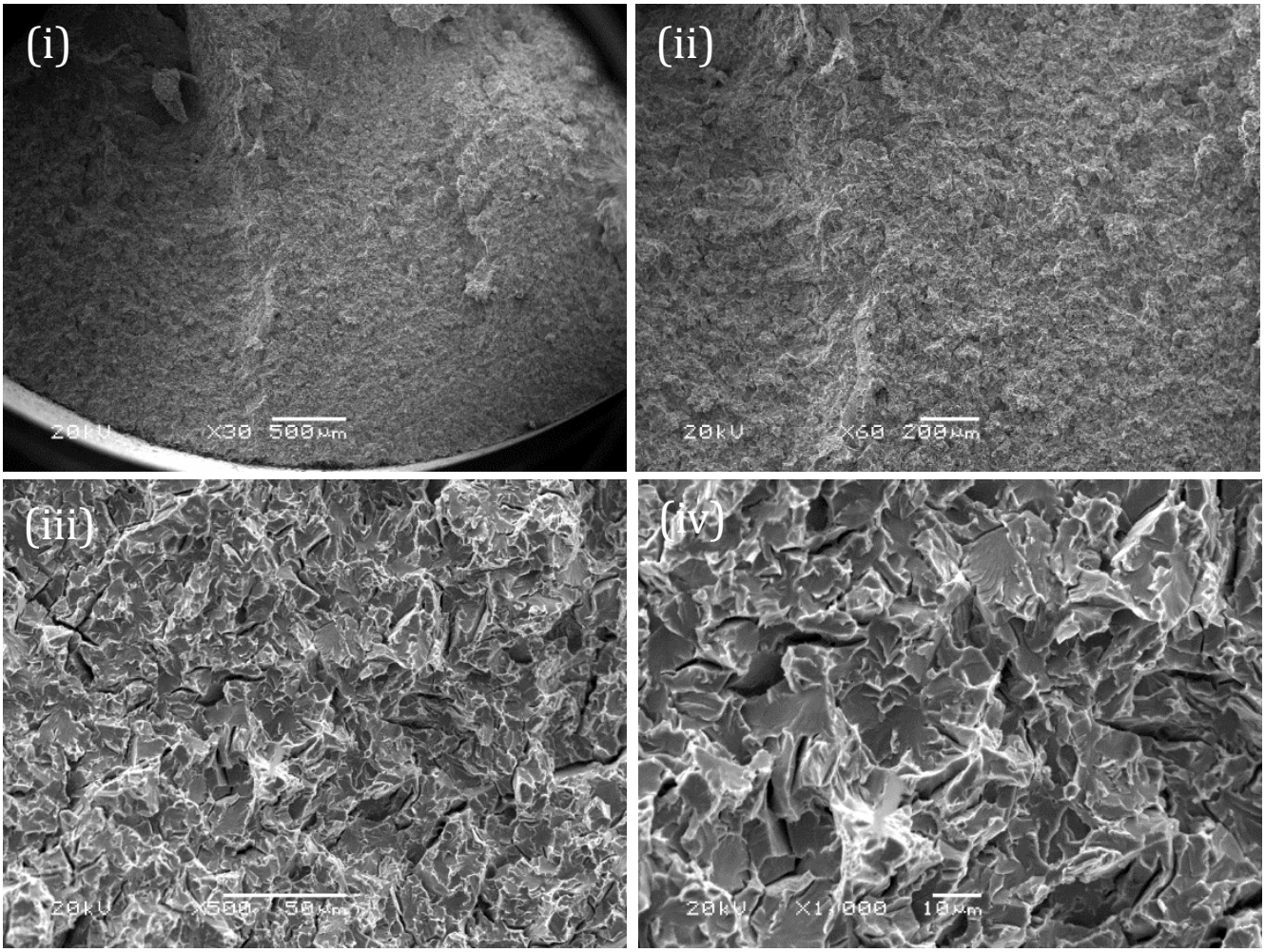


Figure 6-10. Fracture surface morphology of Tensile specimen HT2-03 tested at -196°C; (i), (ii), (iii) and (v) are sequence magnification of the same typical area.

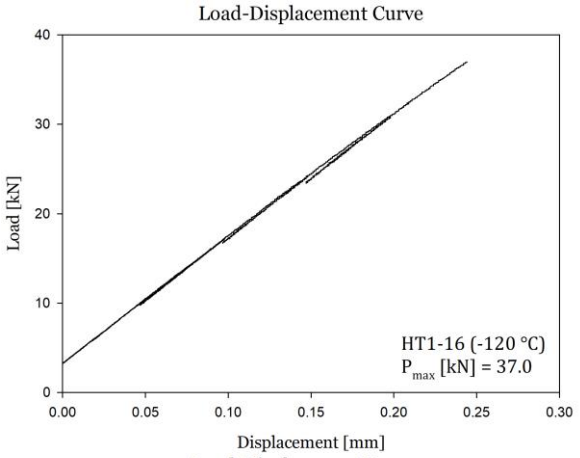
Load-Displacement Curve
Load [kN]
Displacement [mm]
HT1-16 (-120 °C)
P_max [kN] = 37.0

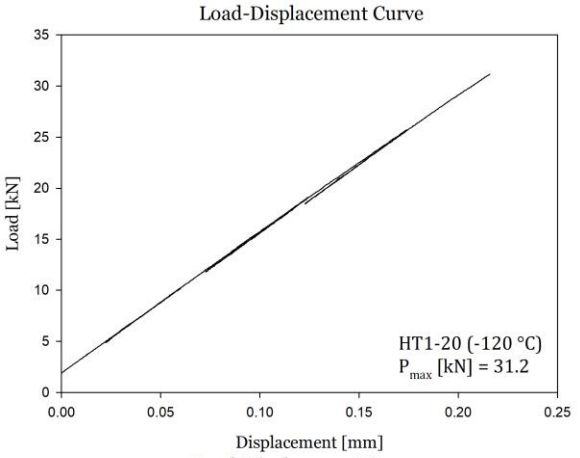
Load-Displacement Curve
Load [kN]
Displacement [mm]
HT1-20 (-120 °C)
P_max [kN] = 31.2

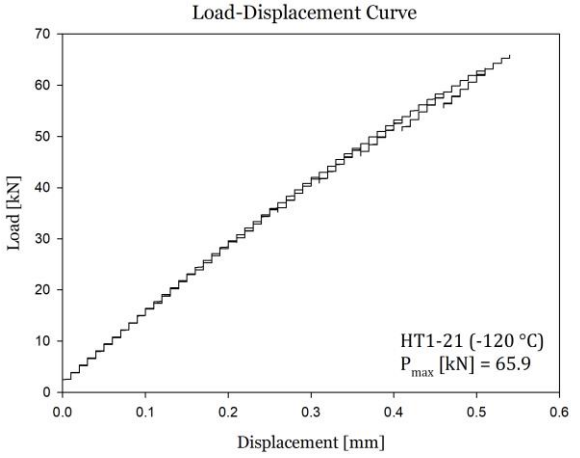
Load-Displacement Curve
Load [kN]
Displacement [mm]
HT1-21 (-120 °C)
P_max [kN] = 65.9

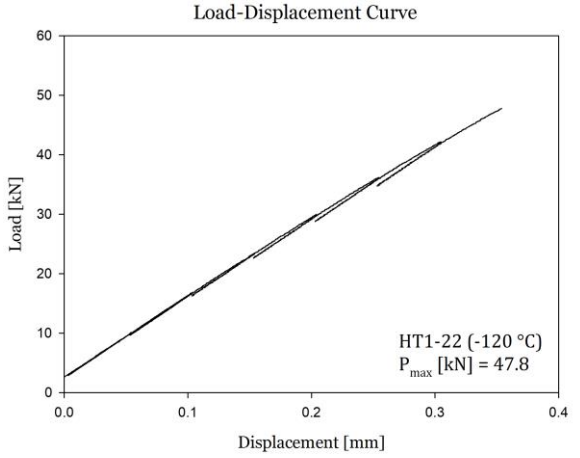
Load-Displacement Curve
Load [kN]
Displacement [mm]
HT1-22 (-120 °C)
P_max [kN] = 47.8

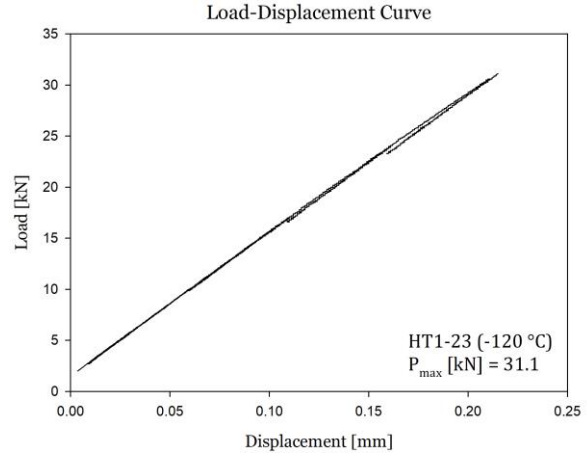
Load-Displacement Curve
Load [kN]
Displacement [mm]
HT1-23 (-120 °C)
P_max [kN] = 31.1

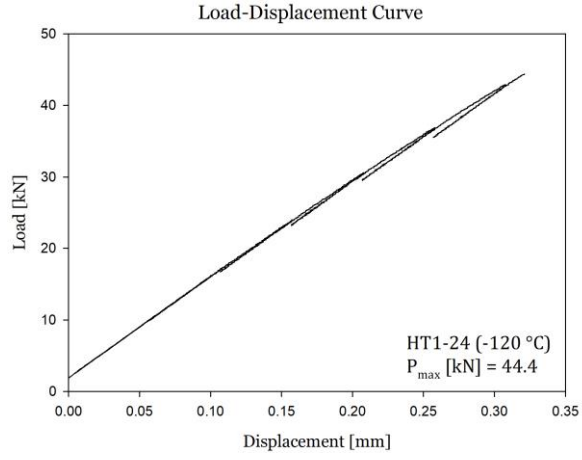
Load-Displacement Curve
Load [kN]
Displacement [mm]
HT1-24 (-120 °C)
P_max [kN] = 44.4

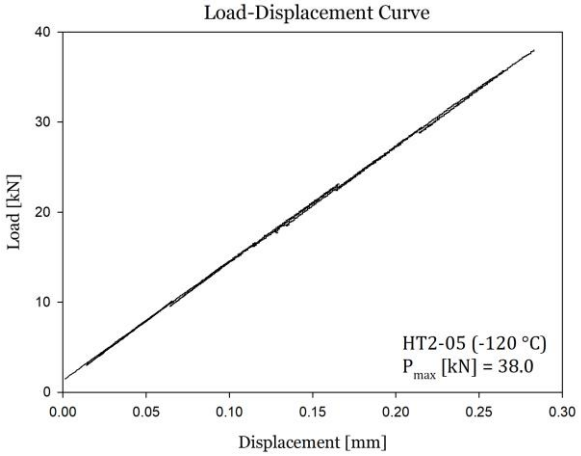
Load-Displacement Curve
Load [kN]
Displacement [mm]
HT2-05 (-120 °C)
P_max [kN] = 38.0

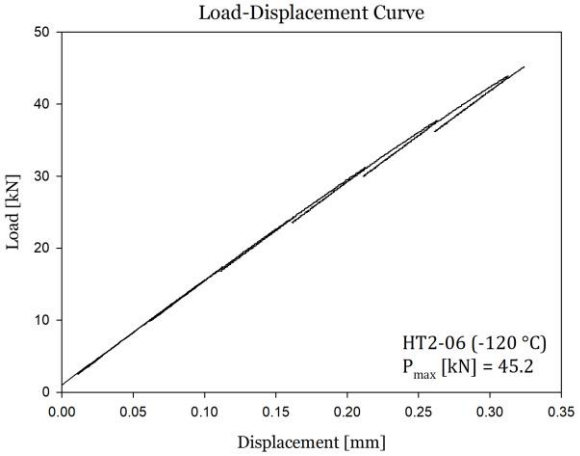
Load-Displacement Curve
Load [kN]
Displacement [mm]
HT2-06 (-120 °C)
P_max [kN] = 45.2

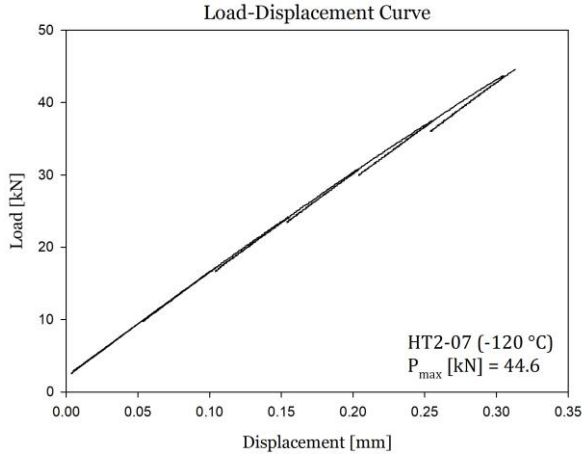
Load-Displacement Curve
Load [kN]
Displacement [mm]
HT2-07 (-120 °C)
P_max [kN] = 44.6

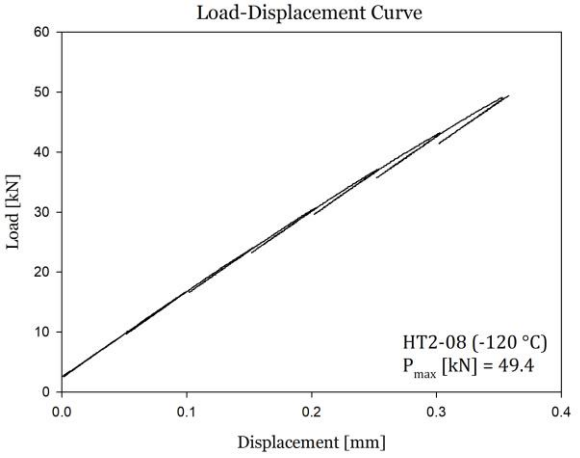
Load-Displacement Curve
Load [kN]
Displacement [mm]
HT2-08 (-120 °C)
P_max [kN] = 49.4

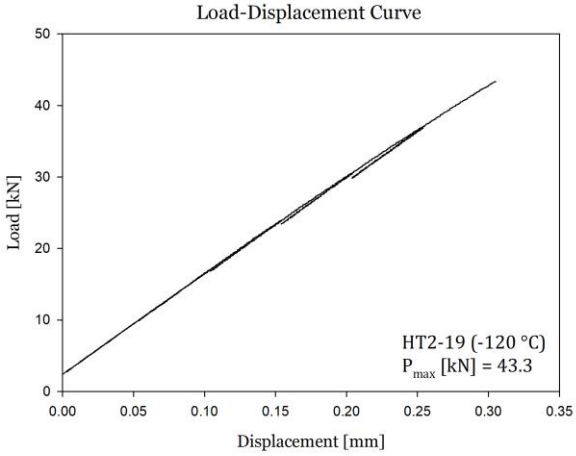
Load-Displacement Curve
Load [kN]
Displacement [mm]
HT2-19 (-120 °C)
P_max [kN] = 43.3

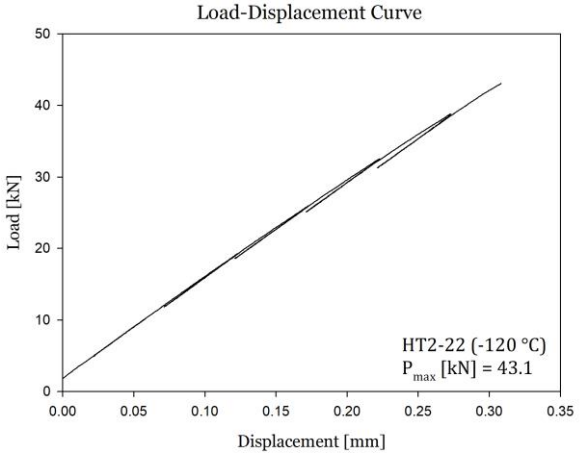
Load-Displacement Curve
Load [kN]
Displacement [mm]
HT2-22 (-120 °C)
P_max [kN] = 43.1

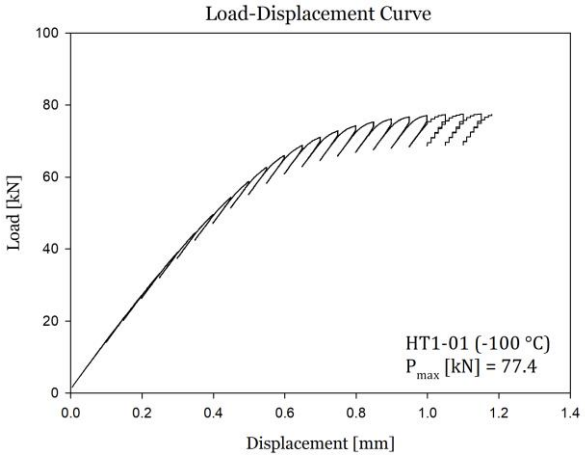
Load-Displacement Curve
Load [kN]
Displacement [mm]
HT1-01 (-100 °C)
P_max [kN] = 77.4

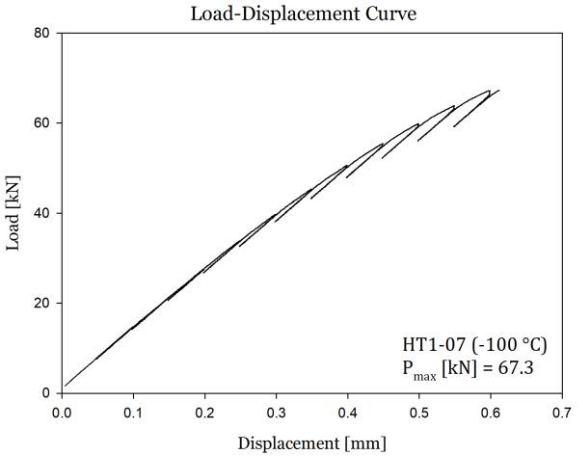
Load-Displacement Curve
Load [kN]
Displacement [mm]
HT1-07 (-100 °C)
P_max [kN] = 67.3

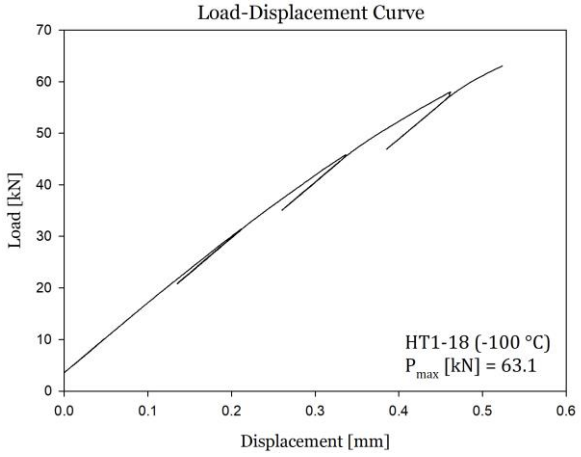
Load-Displacement Curve
Load [kN]
Displacement [mm]
HT1-18 (-100 °C)
P_max [kN] = 63.1

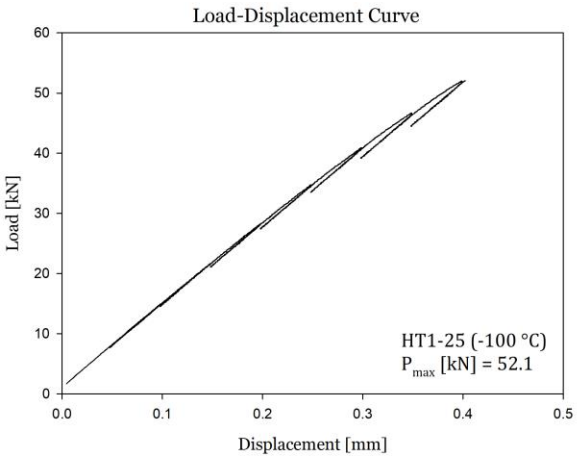
Load-Displacement Curve
Load [kN]
Displacement [mm]
HT1-25 (-100 °C)
P_max [kN] = 52.1

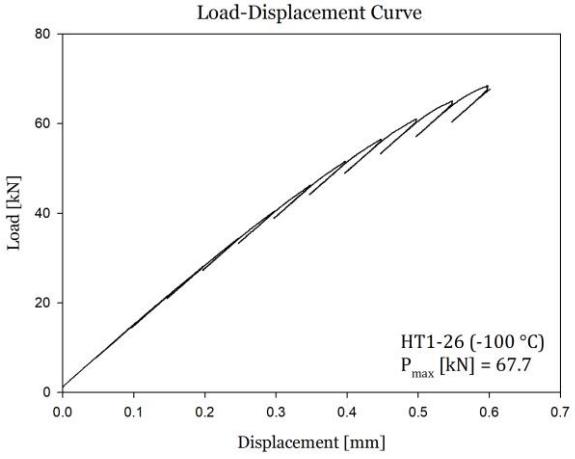
Load-Displacement Curve
Load [kN]
Displacement [mm]
HT1-26 (-100 °C)
P_max [kN] = 67.7

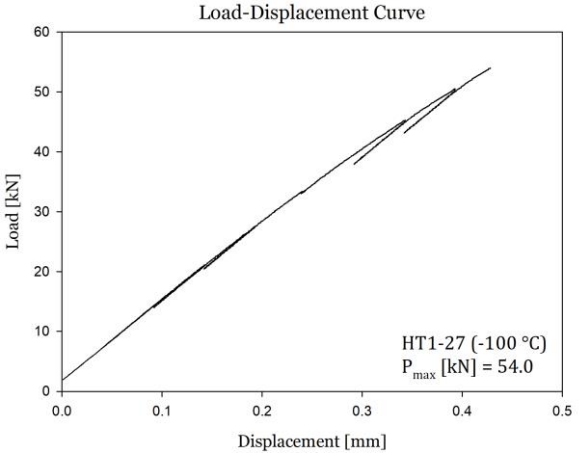
Load-Displacement Curve
Load [kN]
Displacement [mm]
HT1-27 (-100 °C)
P_max [kN] = 54.0

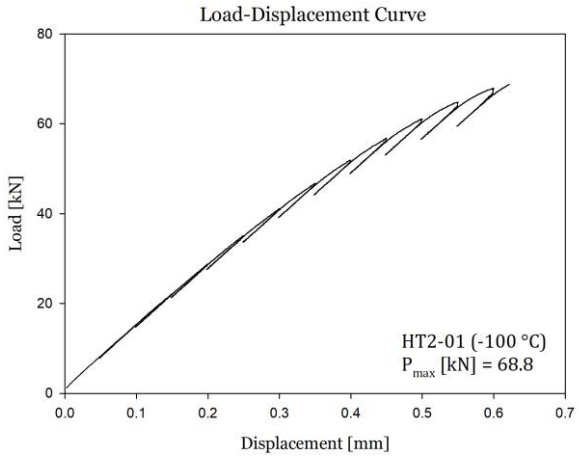
Load-Displacement Curve
Load [kN]
Displacement [mm]
HT2-01 (-100 °C)
P_max [kN] = 68.8

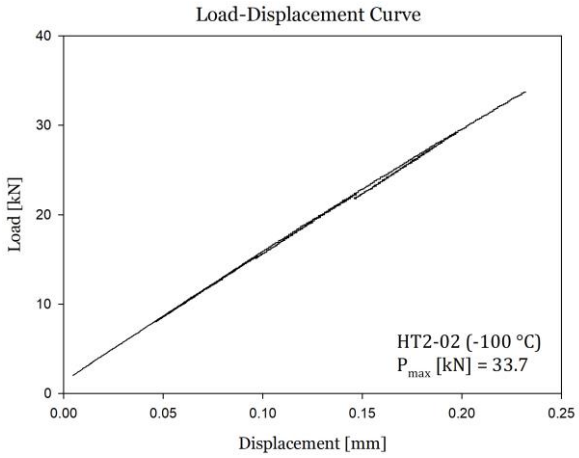
Load-Displacement Curve
Load [kN]
Displacement [mm]
HT2-02 (-100 °C)
P_max [kN] = 33.7

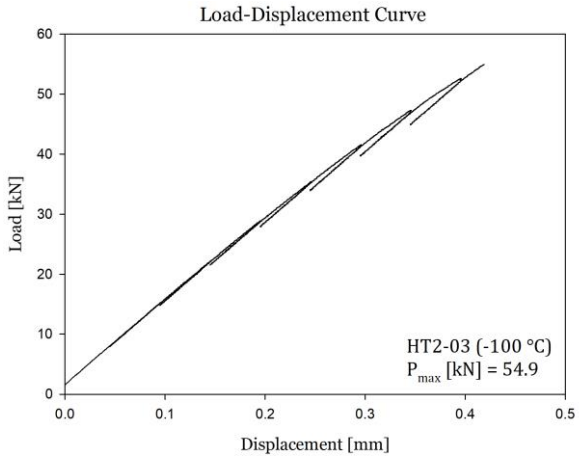
Load-Displacement Curve
Load [kN]
Displacement [mm]
HT2-03 (-100 °C)
P_max [kN] = 54.9

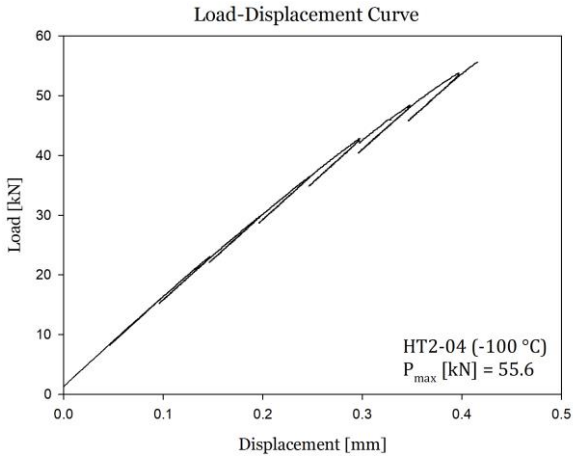
Load-Displacement Curve
Load [kN]
Displacement [mm]
HT2-04 (-100 °C)
P_max [kN] = 55.6

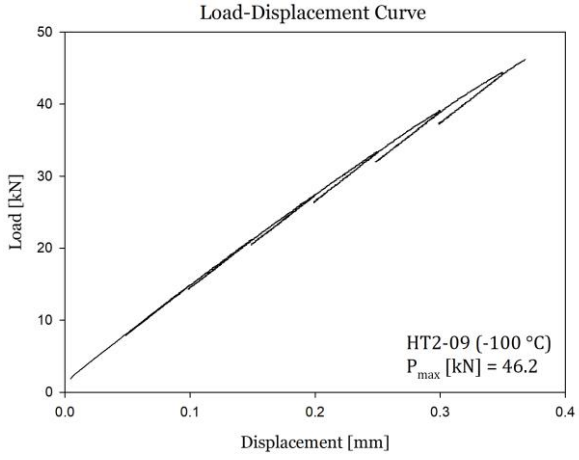
Load-Displacement Curve
Load [kN]
Displacement [mm]
HT2-09 (-100 °C)
P_max [kN] = 46.2

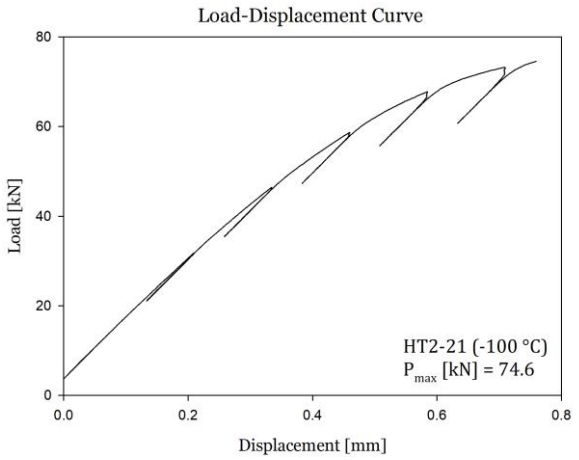
Load-Displacement Curve
Load [kN]
Displacement [mm]
HT2-21 (-100 °C)
P_max [kN] = 74.6

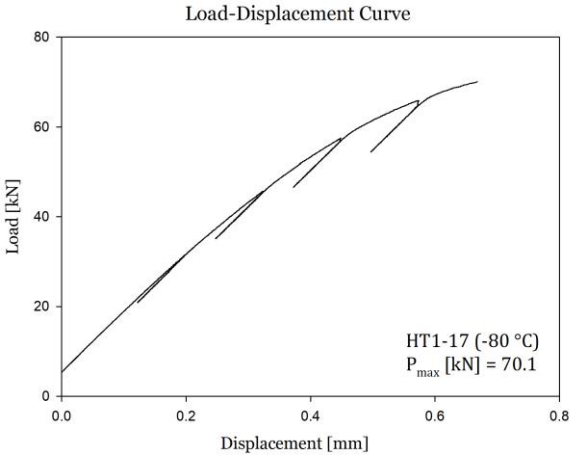


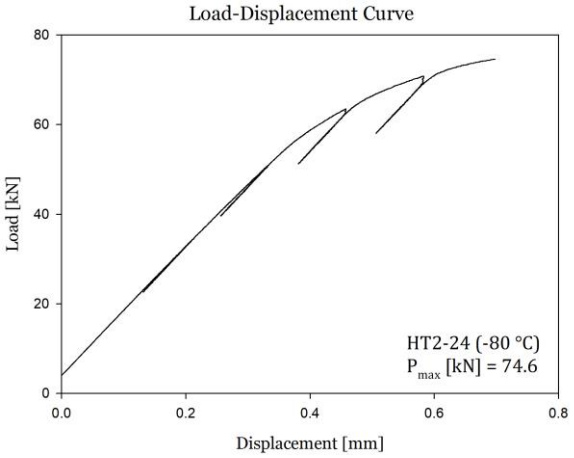


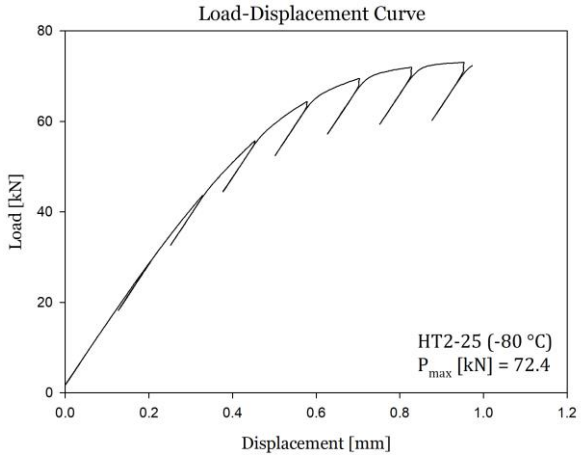


Figure 6-11. Load-displacement curves for all 27 tested sharp-crack specimens at -80 °C, -100 °C and -120 °C

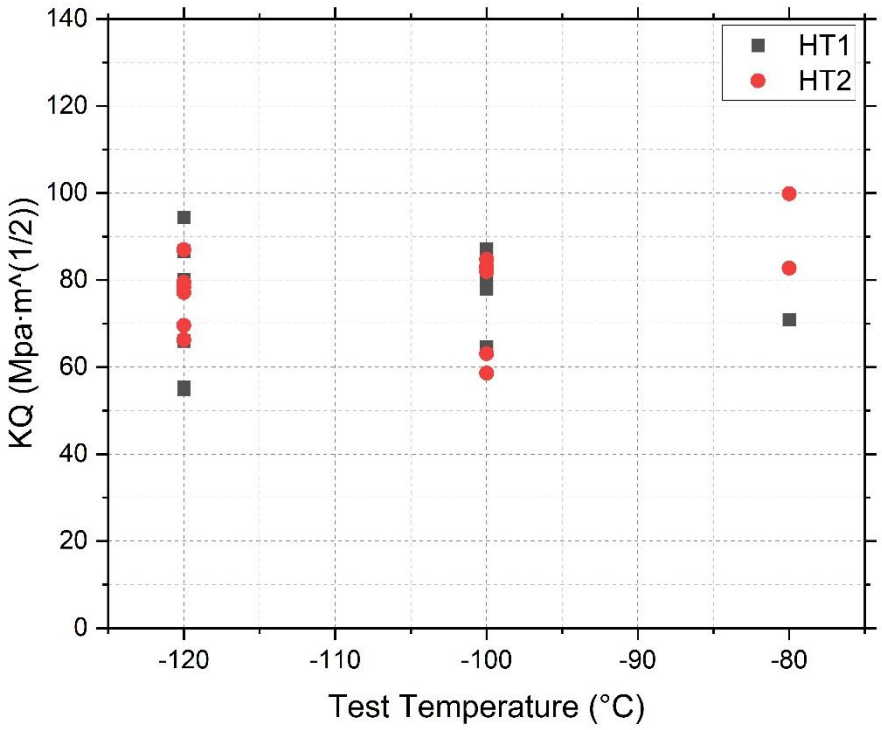


Figure 6-12. $K_Q$ data plot for HT1 and HT2 specimens tested at -120°C, -100°C and -80°C.

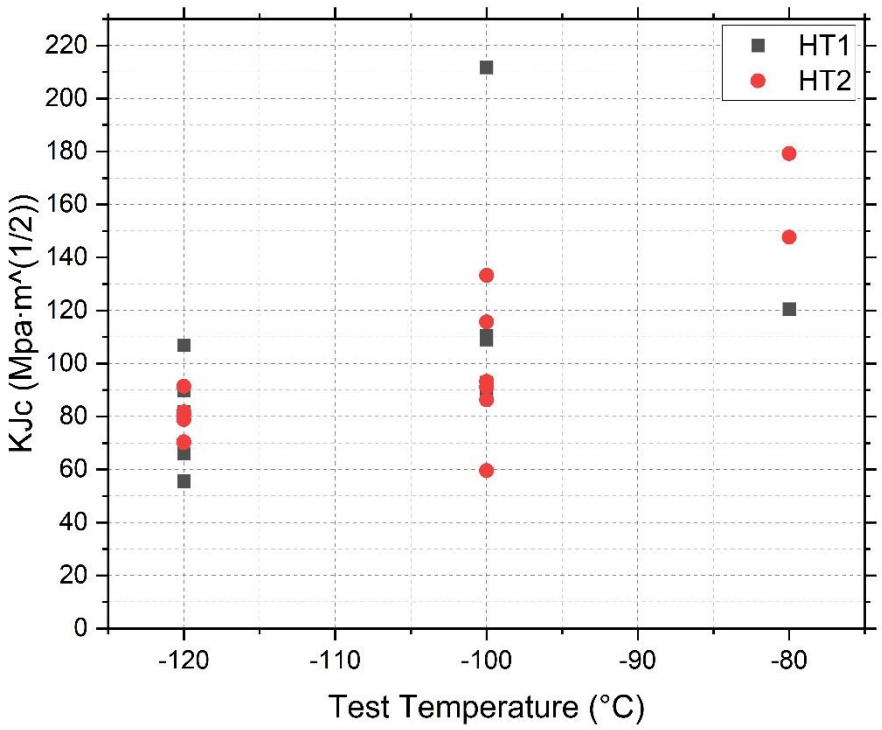


Figure 6-13. $K_{Jc}$ data plot for HT1 and HT2 specimens tested at -120°C, -100°C and -80°C.

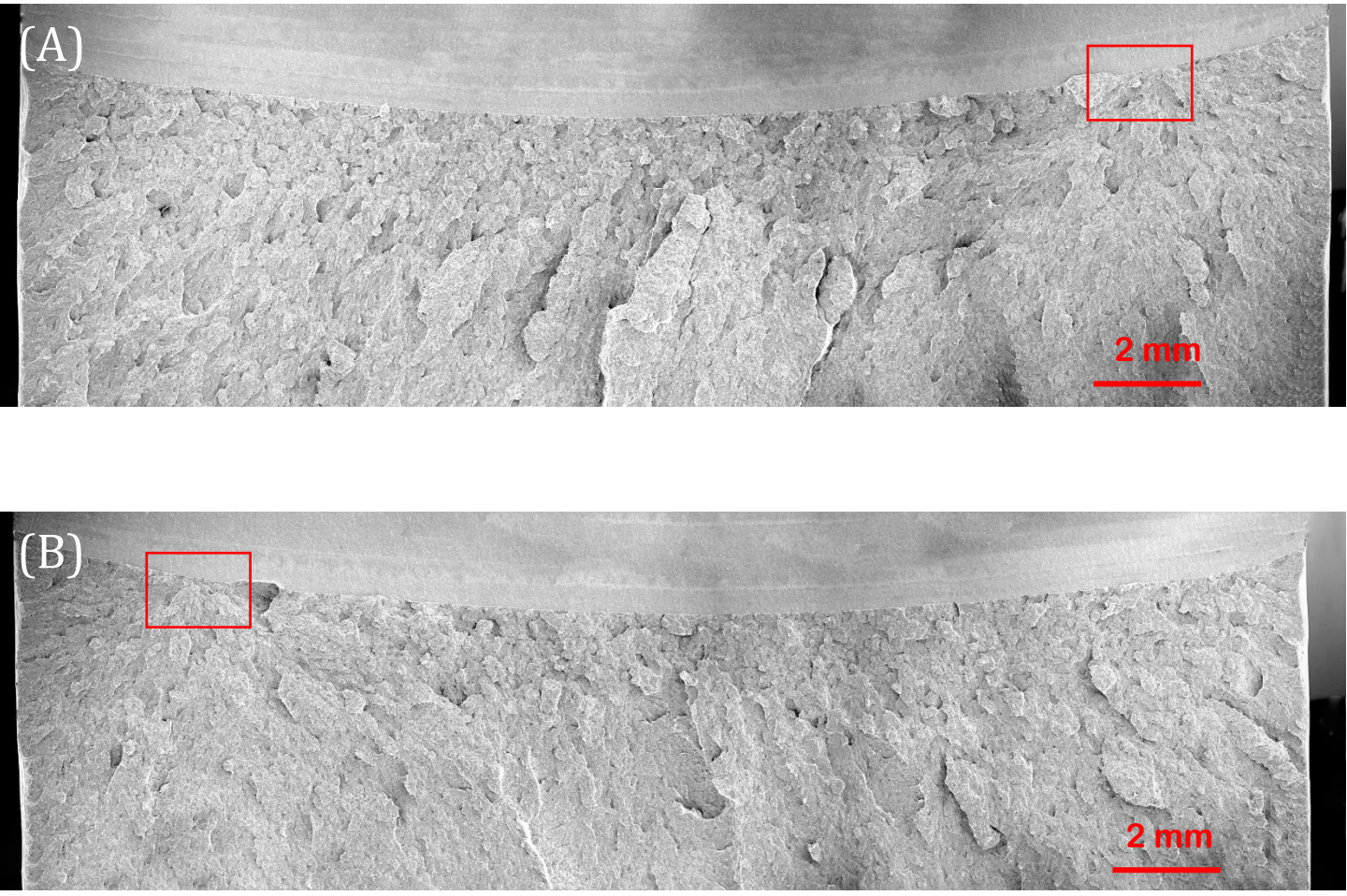


Figure 6-14 (a). Overview of fracture surfaces on a sharp-cracked specimen, designated CT HT1-16, tested at -120 °C. Red frames on matching halves (A) and (B) denote the most probable fracture initiation areas. Test results: Critical J-integral (Jc) value of 21.2 $kJ/m^2$, crack tip opening displacement (CTOD) of 0.015 mm, local cleavage fracture stress of 2484 MPa (n=0.1), fracture initiation distance (Xo) of 30 µm, and an average stable crack extension of 3 µm.

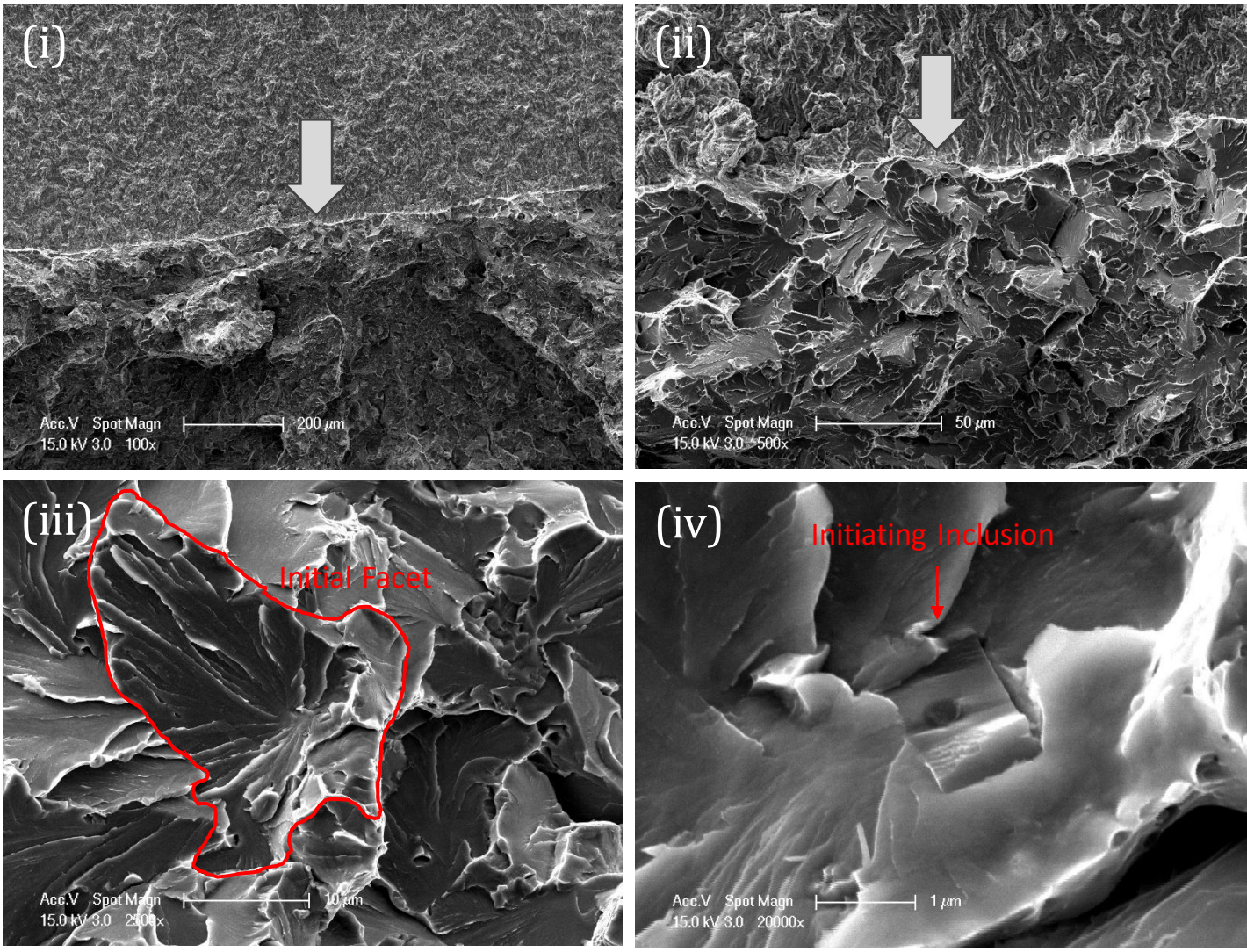


Figure 6-14 (b). Fracture Initiation at side (A) of the sharp-cracked specimen CT HT1-16, test temperature of -120 °C. A sequential magnification of the red-framed area at (i) 100x, (ii) 500x, (iii) 2500x, and (iv) 20000x are shown. Fractographic analysis reveals inclusion cracking as the initiation mechanism, with the inclusion's equivalent diameter at 1.5 µm and the initial facet's equivalent diameter at 21 µm.

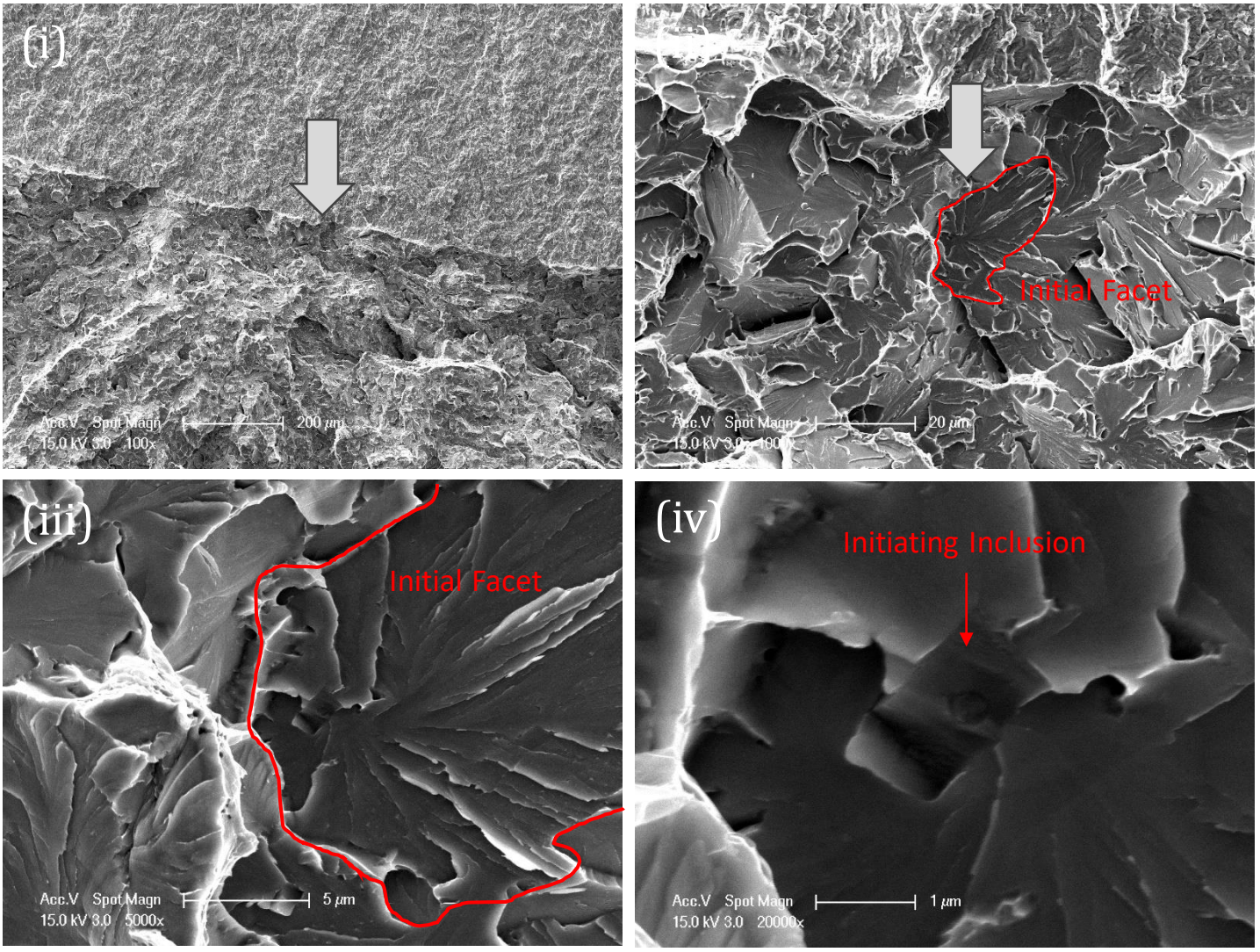


Figure 6-14 (c). Fracture Initiation at matching side (B) of the sharp-cracked specimen CT HT1-16, test temperature of -120 °C. A sequential magnification of the red-framed area at (i) 100x, (ii) 1000x, (iii) 5000x, and (iv) 20000x are shown. Fractographic analysis reveals inclusion cracking as the initiation mechanism, with the inclusion's equivalent diameter at 1.5 µm and the initial facet's equivalent diameter at 21 µm.

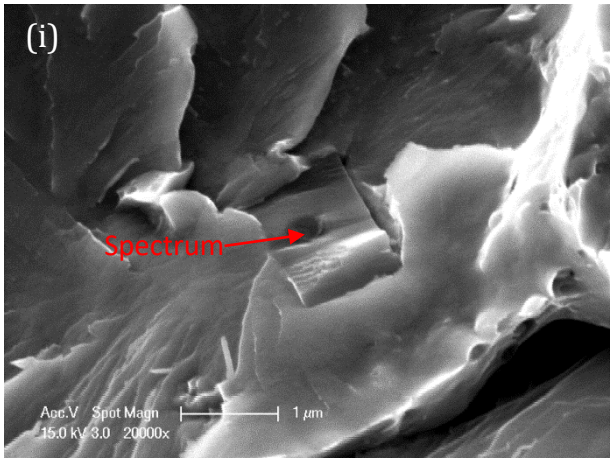


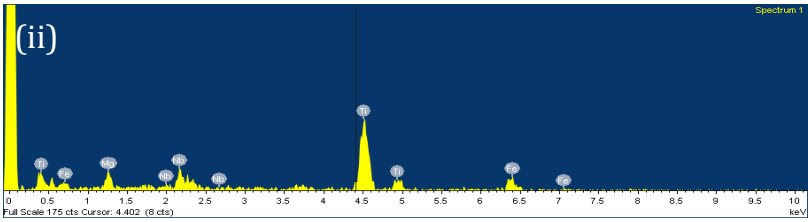


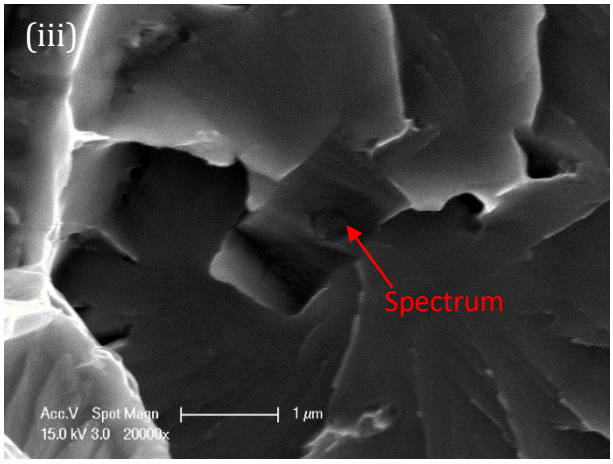


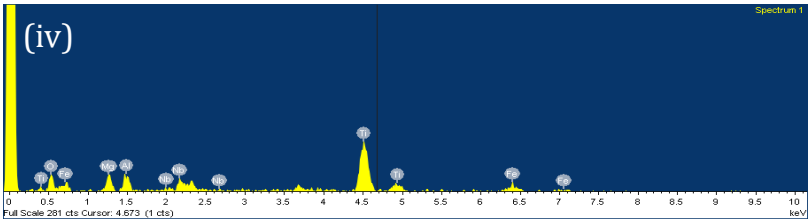


Figure 6-14 (d). Cleavage initiation point (i) and (iii) from matching halves of fracture surfaces of sharp-cracked specimen CT HT1-16 tested at -120 °C with their corresponding EDX spectrums (ii) and (iv) respectively.

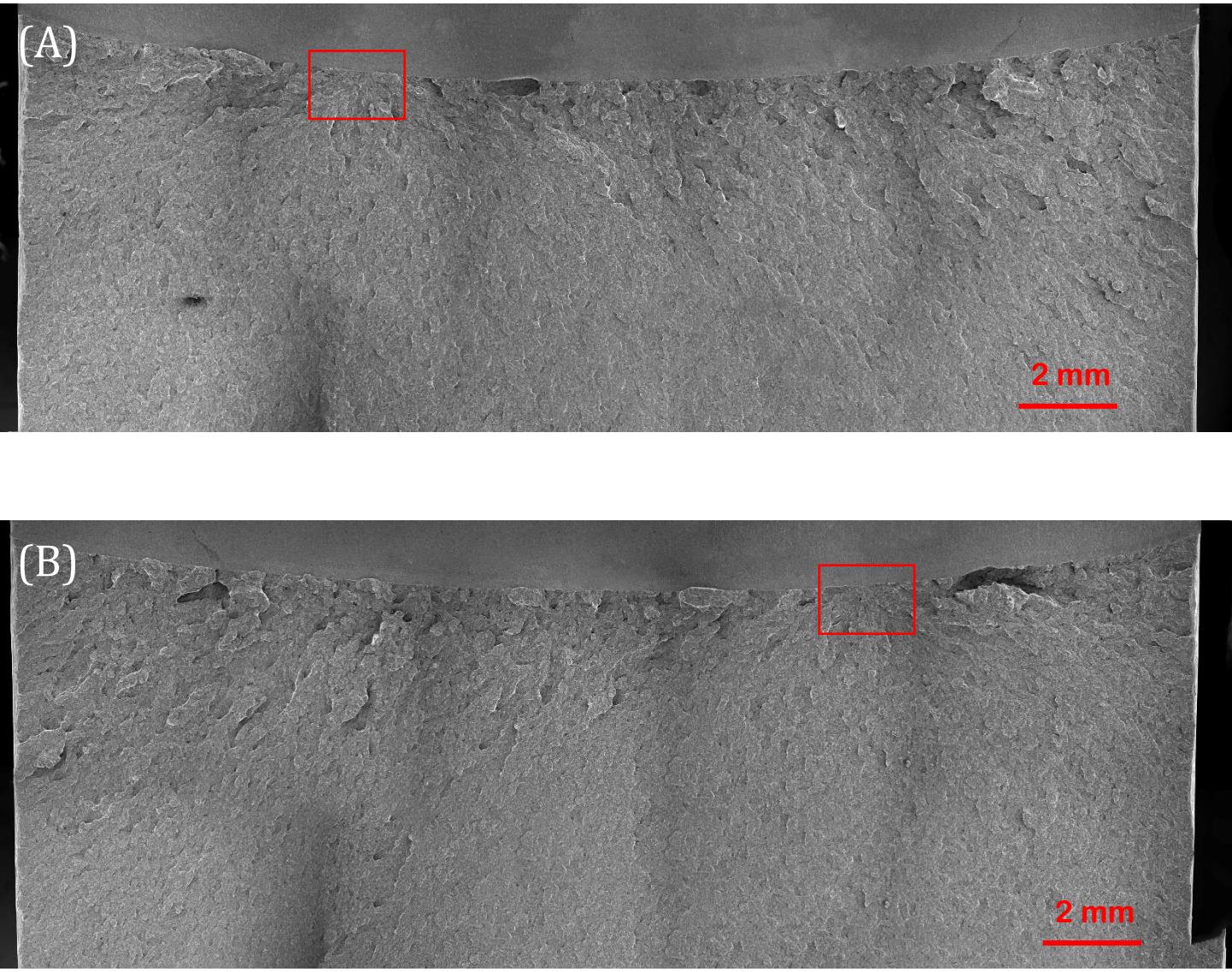


Figure 6-15 (a). Overview of fracture surfaces on a sharp-cracked specimen, designated CT HT1-20, tested at -120 °C. Red frames on matching halves (A) and (B) denote the most probable fracture initiation areas. Test results: Critical J-integral (Jc) value of 15.1 $kJ/m^2$, crack tip opening displacement (CTOD) of 0.011 mm, local cleavage fracture stress of 2271 MPa (n=0.1), fracture initiation distance (Xo) of 52 µm, and an average stable crack extension of 4 µm.

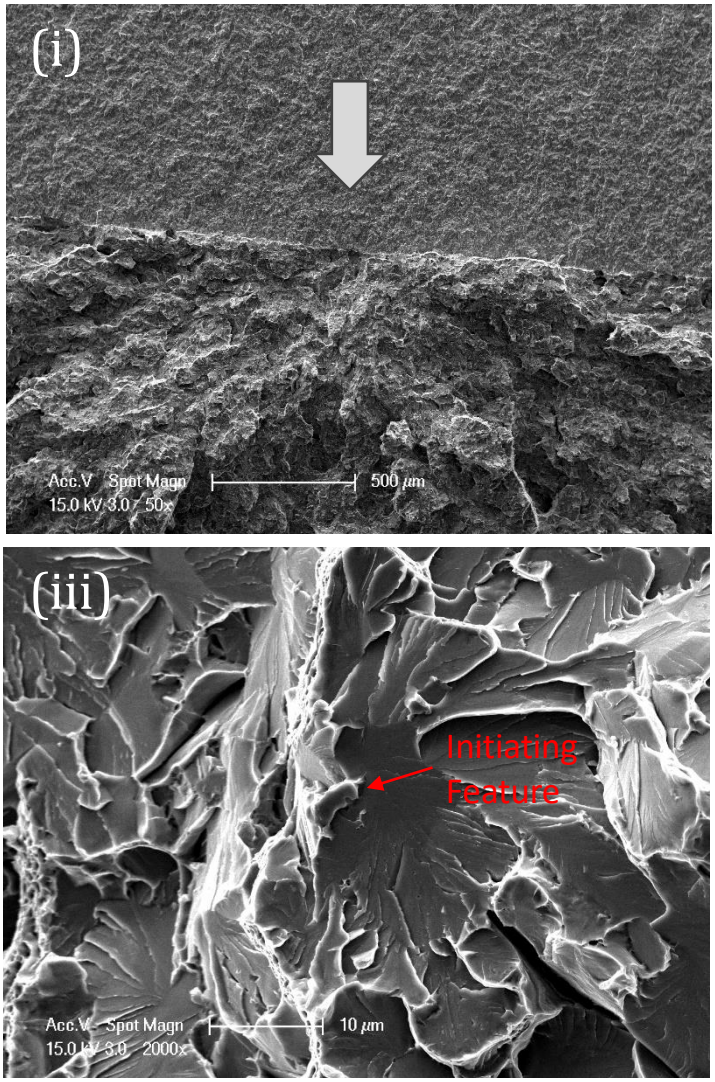


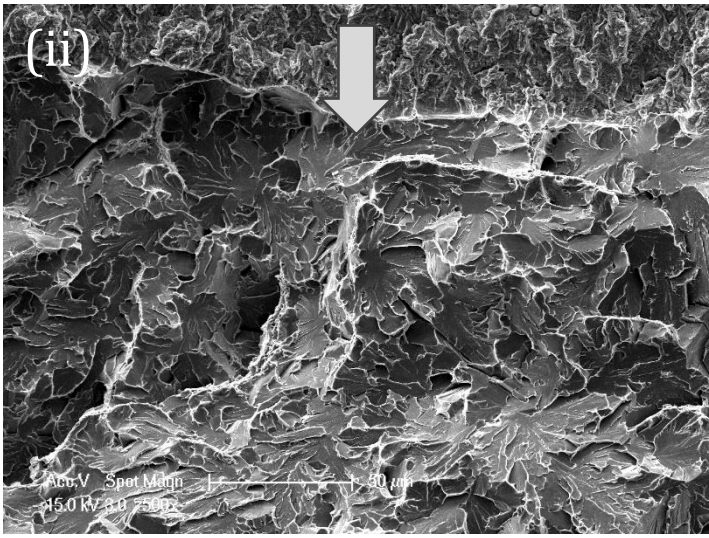





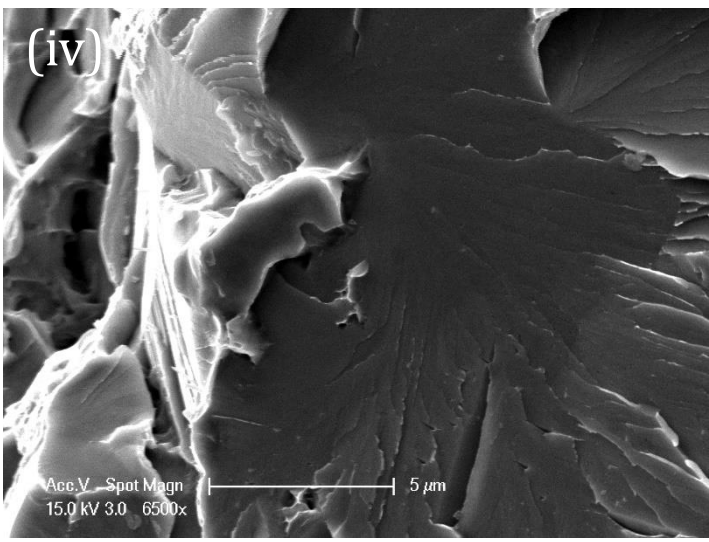


Figure 6-15 (b). Fracture Initiation at side (A) of the sharp-cracked specimen CT HT1-20, test temperature of -120 °C. A sequential magnification of the red-framed area at (i) 50x, (ii) 500x, (iii) 2000x, and (iv) 6500x are shown. Fractographic analysis reveals matrix related initiation mechanism, with the initial facet's equivalent diameter at 30 µm.

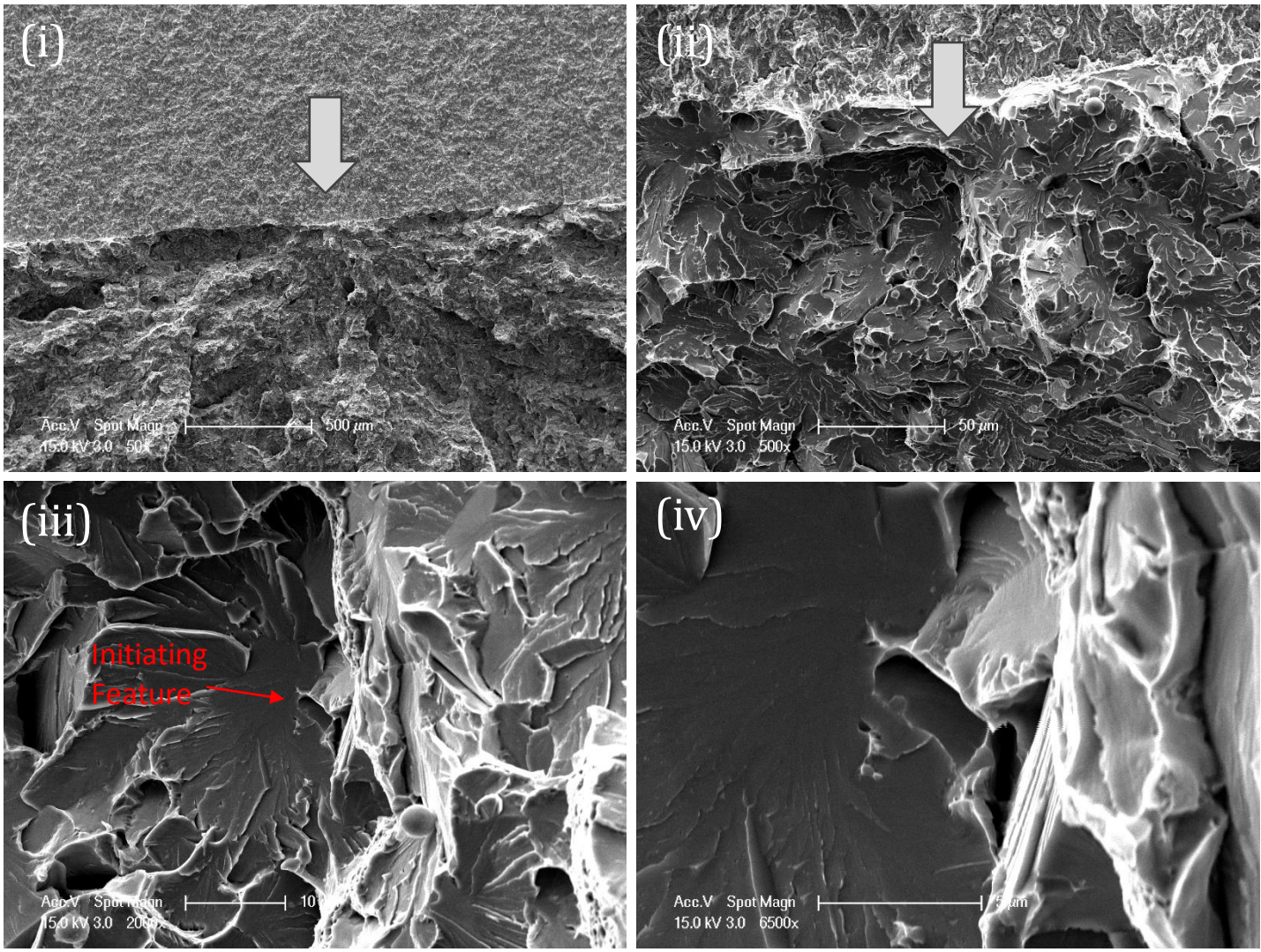


Figure 6-15 (c). Fracture Initiation at matching side (B) of the sharp-cracked specimen CT HT1-20, test temperature of -120 °C. A sequential magnification of the red-framed area at (i) 50x, (ii) 500x, (iii) 2000x, and (iv) 6500x are shown. Fractographic analysis reveals matrix related initiation mechanism, with the initial facet's equivalent diameter at 30 µm.

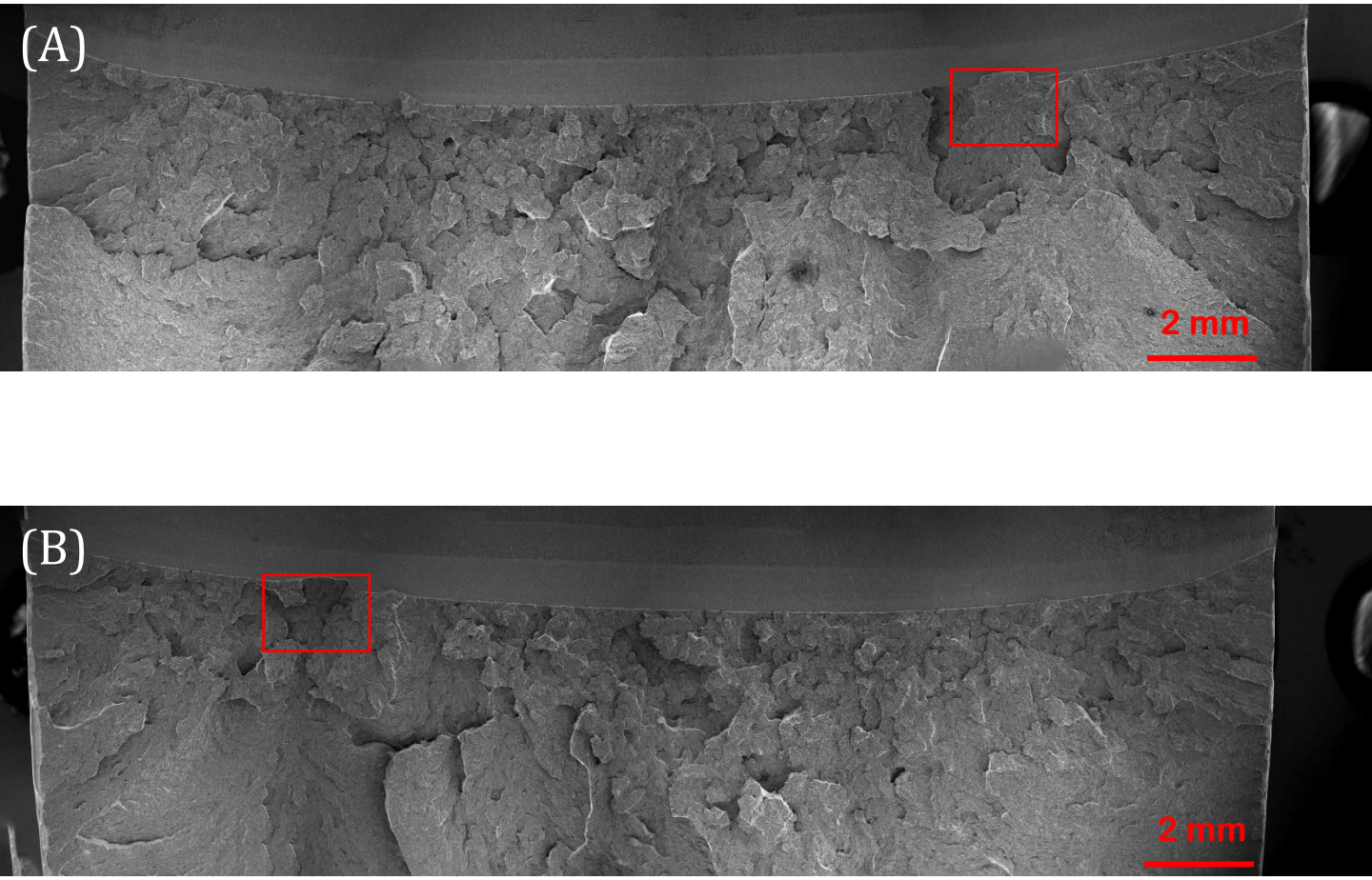





Figure 6-16 (a). Overview of fracture surfaces on a sharp-cracked specimen, designated CT HT1-21, tested at -120 °C. Red frames on matching halves (A) and (B) denote the most probable fracture initiation areas. Test results: Critical J-integral (Jc) value of 55.4 $kJ/m^2$, crack tip opening displacement (CTOD) of 0.040 mm, local cleavage fracture stress of 1954 MPa (n=0.1) , fracture initiation distance (Xo) of 657 µm, and an average stable crack extension of 14 µm.

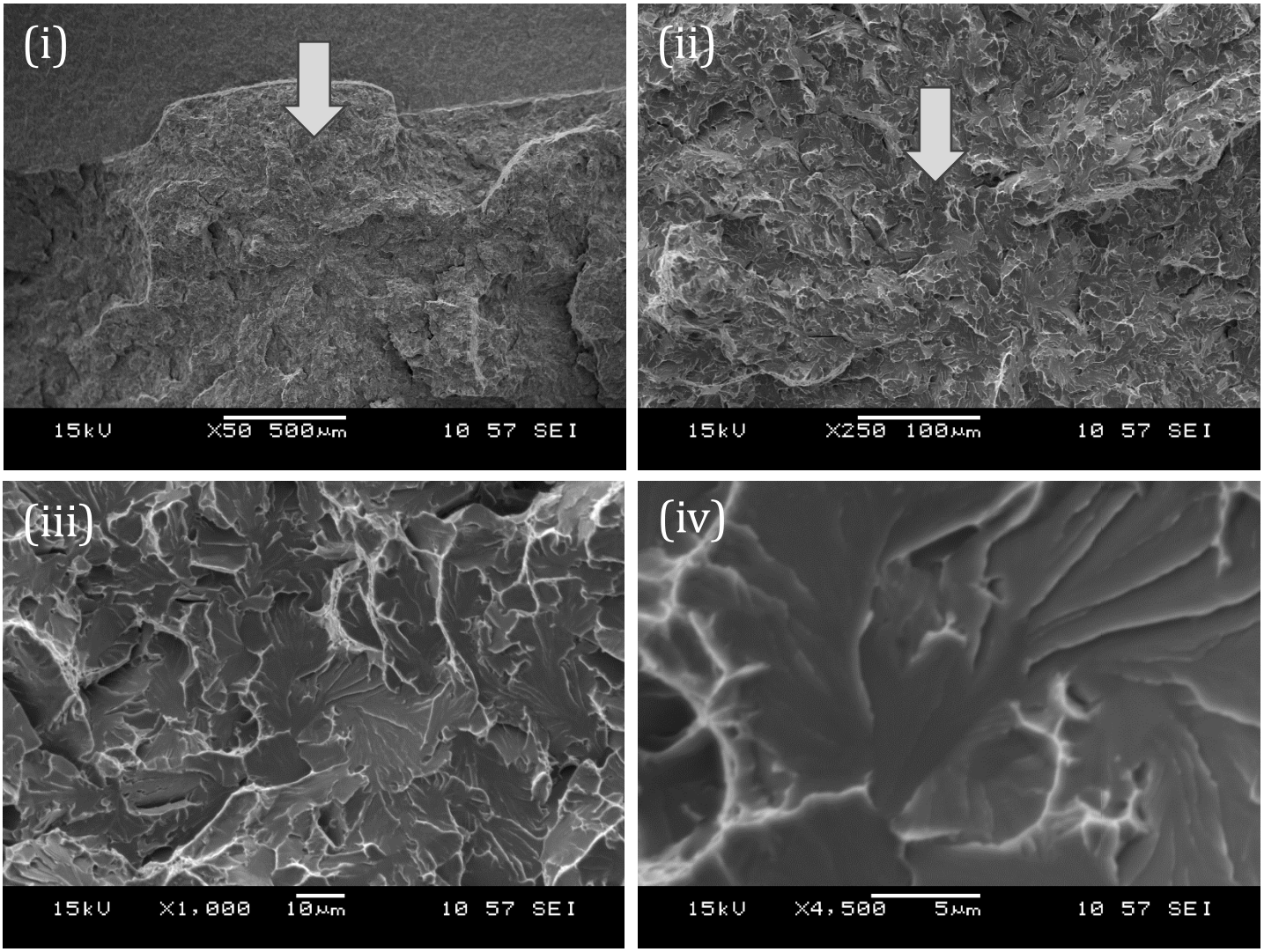


Figure 6-16 (b). Fracture Initiation at side (A) of the sharp-cracked specimen CT HT1-21, test temperature of -120 °C. A sequential magnification of the red-framed area at (i) 50x, (ii) 250x, (iii) 1000x, and (iv) 4500x are shown. Fractographic analysis reveals matrix cracking as the initiation mechanism, with the initial facet's equivalent diameter at 32 µm.

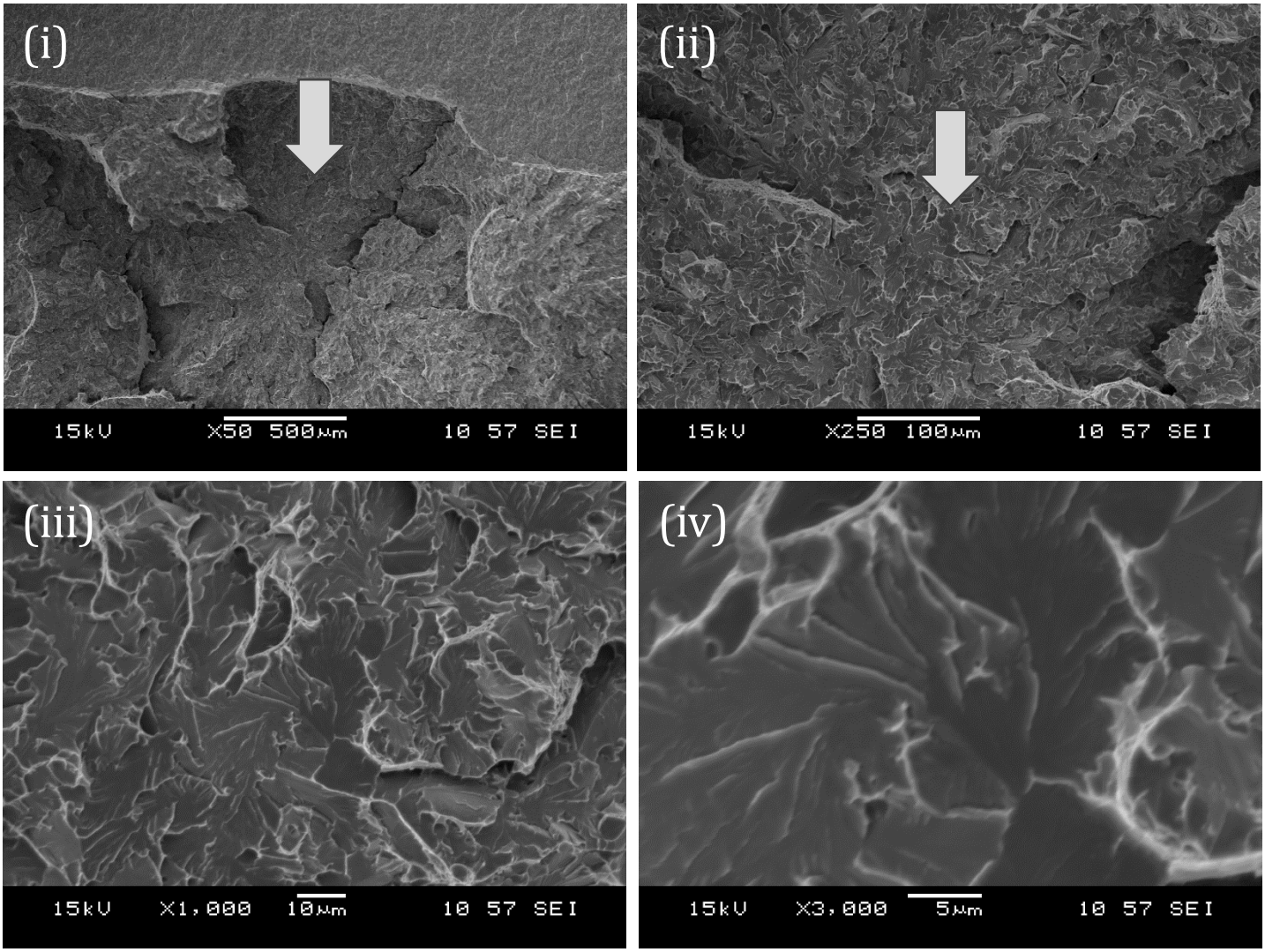


Figure 6-16 (c). Fracture Initiation at matching side (B) of the sharp-cracked specimen CT HT1-21, test temperature of -120 °C. A sequential magnification of the red-framed area at (i) 50x, (ii) 250x, (iii) 1000x, and (iv) 3000x are shown. Fractographic analysis reveals matrix cracking as the initiation mechanism, with the initial facet's equivalent diameter at 32 µm.

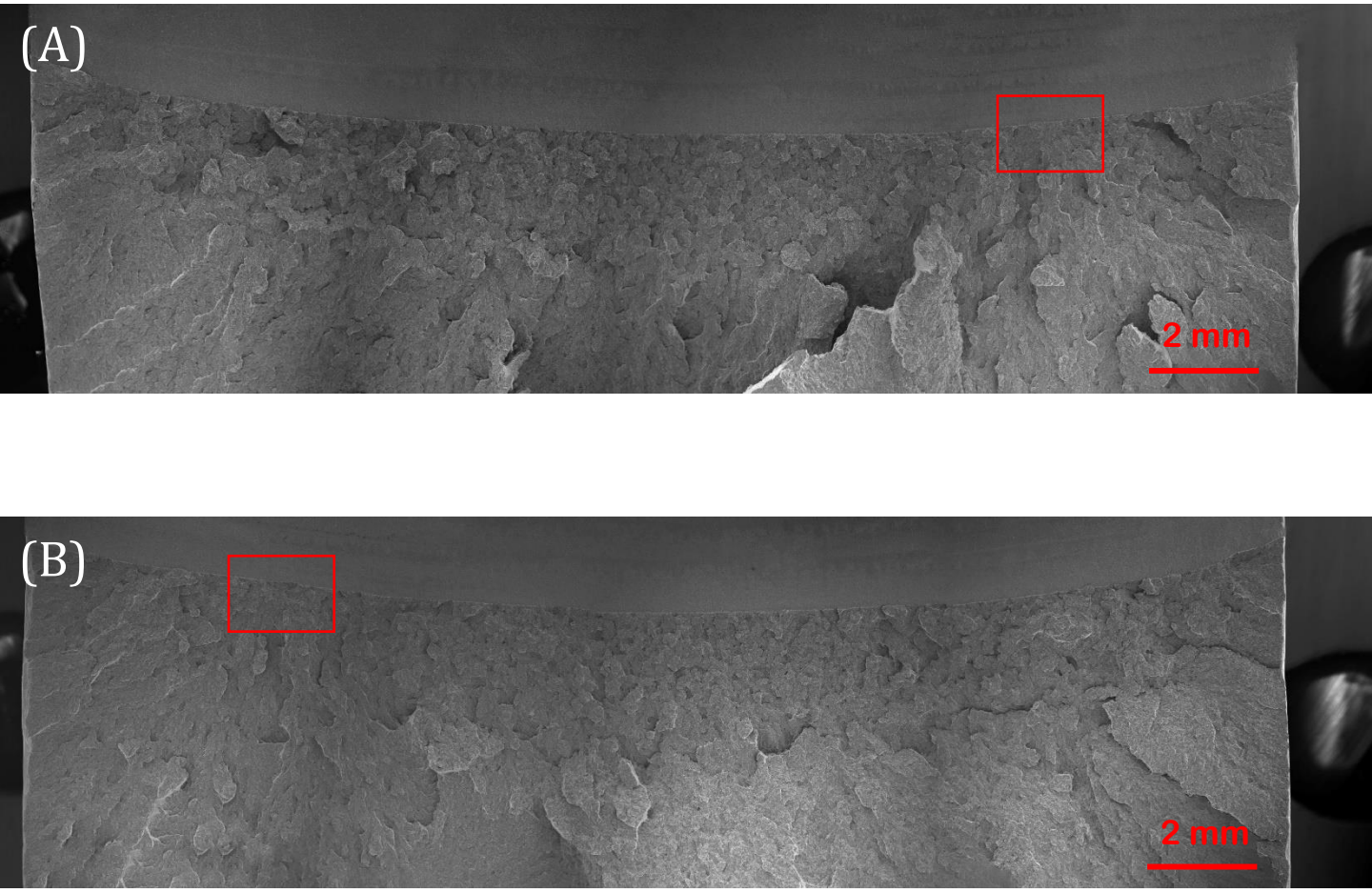


Figure 6-17 (a). Overview of fracture surfaces on a sharp-cracked specimen, designated CT HT1-22, tested at -120 °C. Red frames on matching halves (A) and (B) denote the most probable fracture initiation areas. Test results: Critical J-integral (Jc) value of 39.1 $kJ/m^2$, crack tip opening displacement (CTOD) of 0.028 mm, local cleavage fracture stress of 2200 MPa (n=0.1), fracture initiation distance (Xo) of 163 µm, and an average stable crack extension of 8 µm.

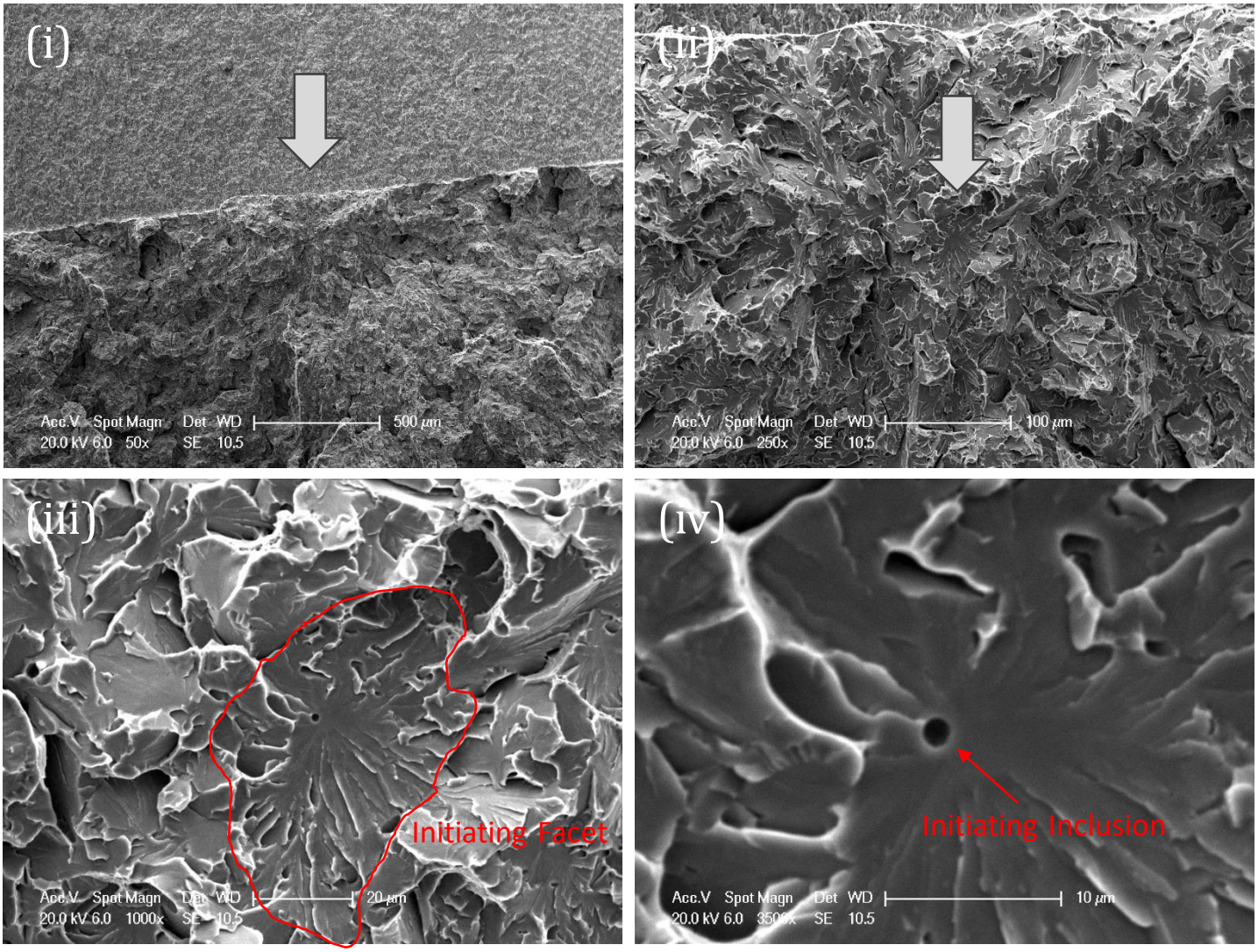


Figure 6-17 (b). Fracture Initiation at side (A) of the sharp-cracked specimen CT HT1-22, test temperature of -120 °C. A sequential magnification of the red-framed area at (i) 50x, (ii) 250x, (iii) 1000x, and (iv) 3500x are shown. Fractographic analysis reveals inclusion cracking as the initiation mechanism, with the inclusion's equivalent diameter at 1.5 µm and the initial facet's equivalent diameter at 46 µm.

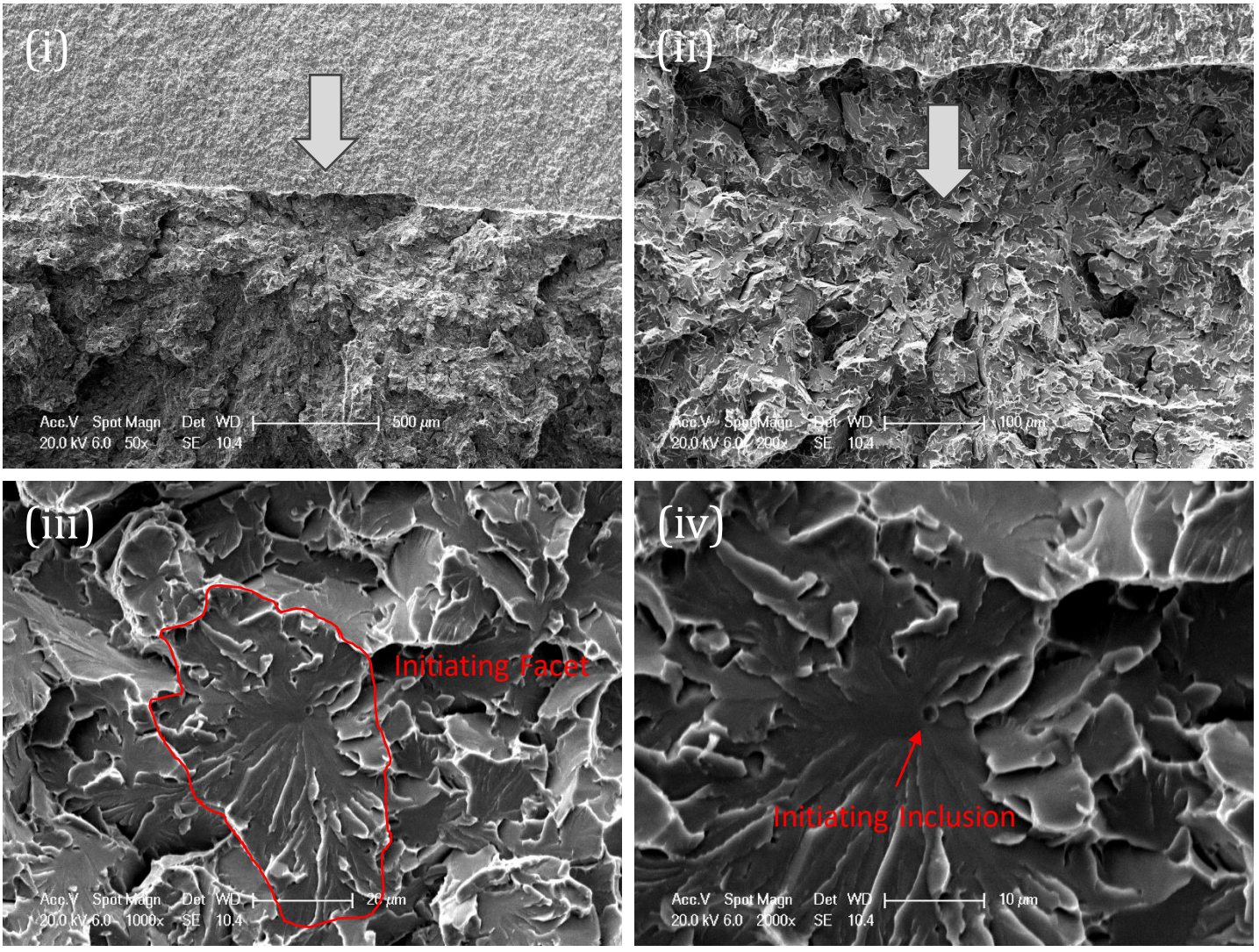


Figure 6-17 (c). Fracture Initiation at matching side (B) of the sharp-cracked specimen CT HT1-22, test temperature of -120 °C. A sequential magnification of the red-framed area at (i) 50x, (ii) 200x, (iii) 1000x, and (iv) 2000x are shown. Fractographic analysis reveals inclusion cracking as the initiation mechanism, with the inclusion's equivalent diameter at 1.5 µm and the initial facet's equivalent diameter at 46 µm.

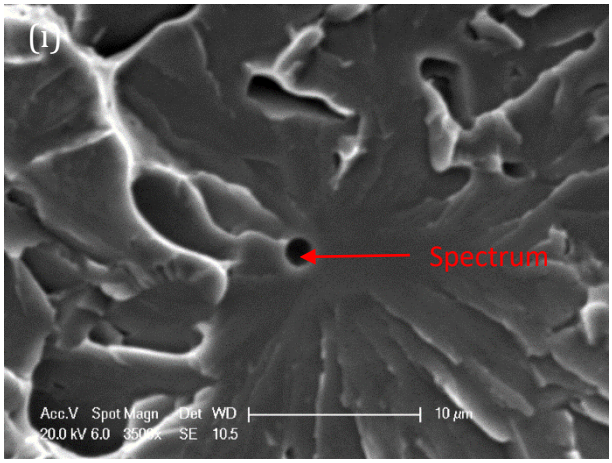


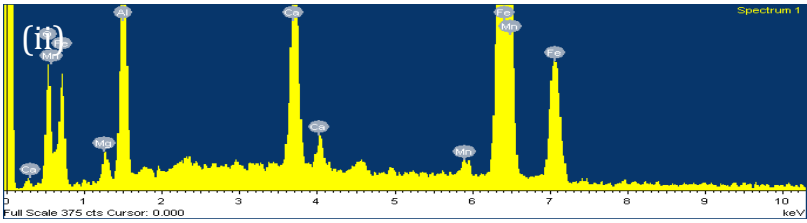


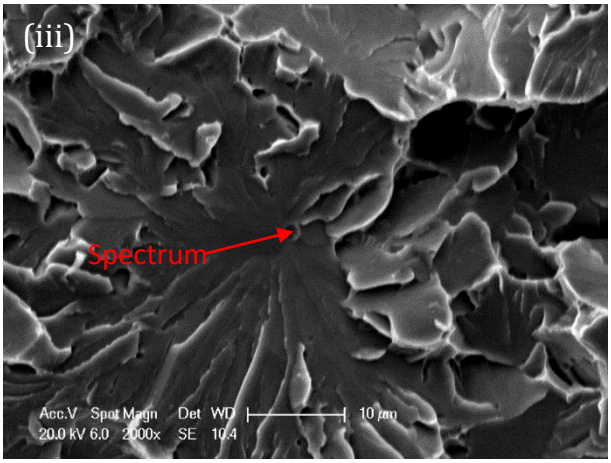


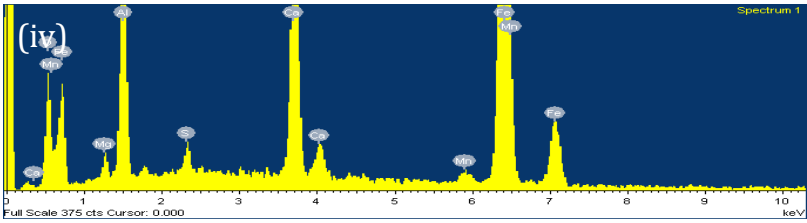


Figure 6-17 (d). Cleavage initiation point (i) and (iii) from matching halves of fracture surfaces of sharp-cracked specimen CT HT1-22 tested at -120 °C with their corresponding EDX spectrums (ii) and (iv) respectively.

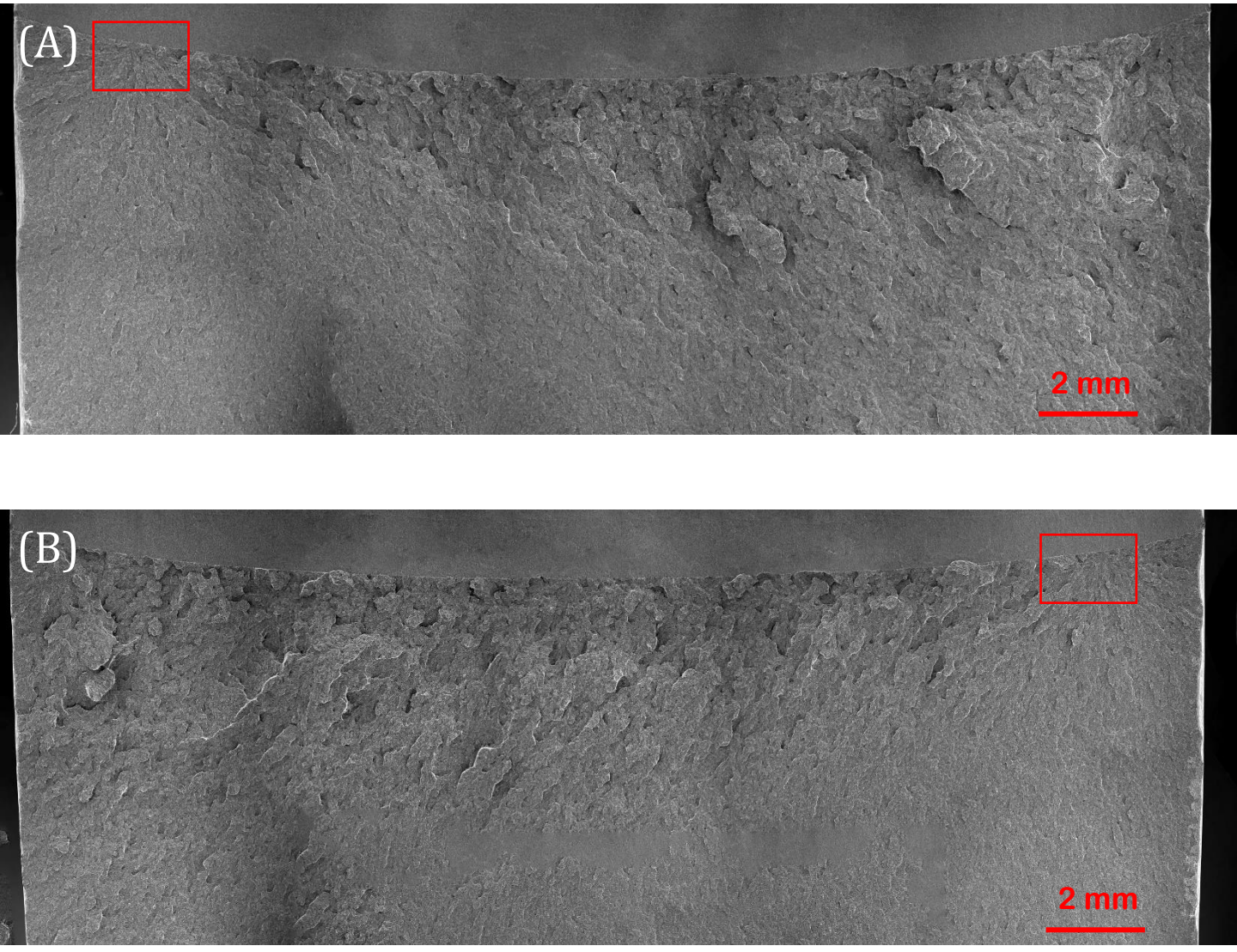


Figure 6-18 (a). Overview of fracture surfaces on a sharp-cracked specimen, designated CT HT1-23, tested at -120 °C. Red frames on matching halves (A) and (B) denote the most probable fracture initiation areas. Test results: Critical J-integral (Jc) value of 15.0 $kJ/m^2$, crack tip opening displacement (CTOD) of 0.011 mm, local cleavage fracture stress of 2484 MPa (n=0.1), fracture initiation distance (Xo) of 21 µm, and an average stable crack extension of 3 µm.

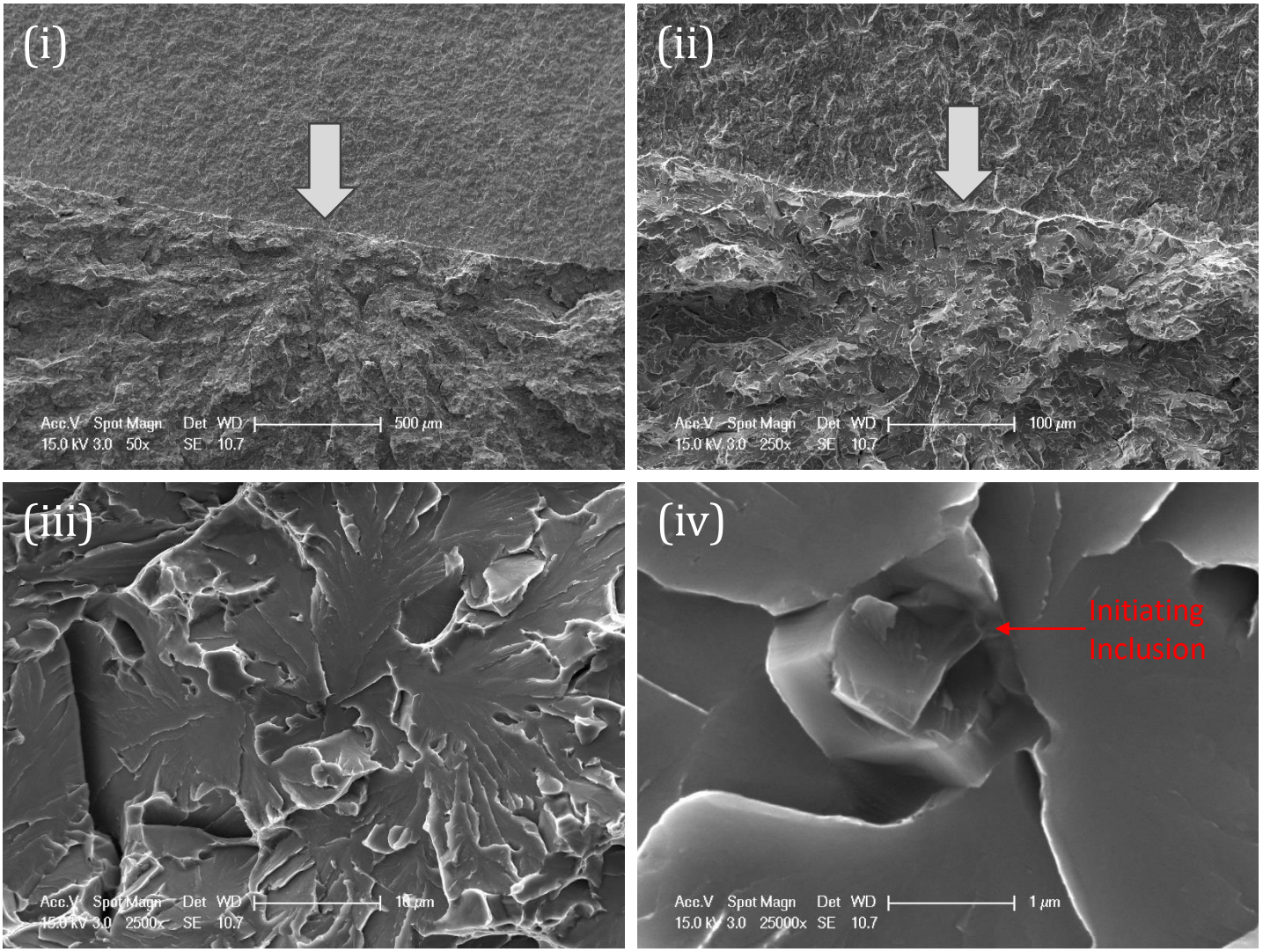


Figure 6-18 (b). Fracture Initiation at side (A) of the sharp-cracked specimen CT HT1-23, test temperature of -120 °C. A sequential magnification of the red-framed area at (i) 50x, (ii) 250x, (iii) 2500x, and (iv) 25000x are shown. Fractographic analysis reveals inclusion cracking as the initiation mechanism, with the inclusion's equivalent diameter at 1.0 µm and the initial facet's equivalent diameter at 34 µm.

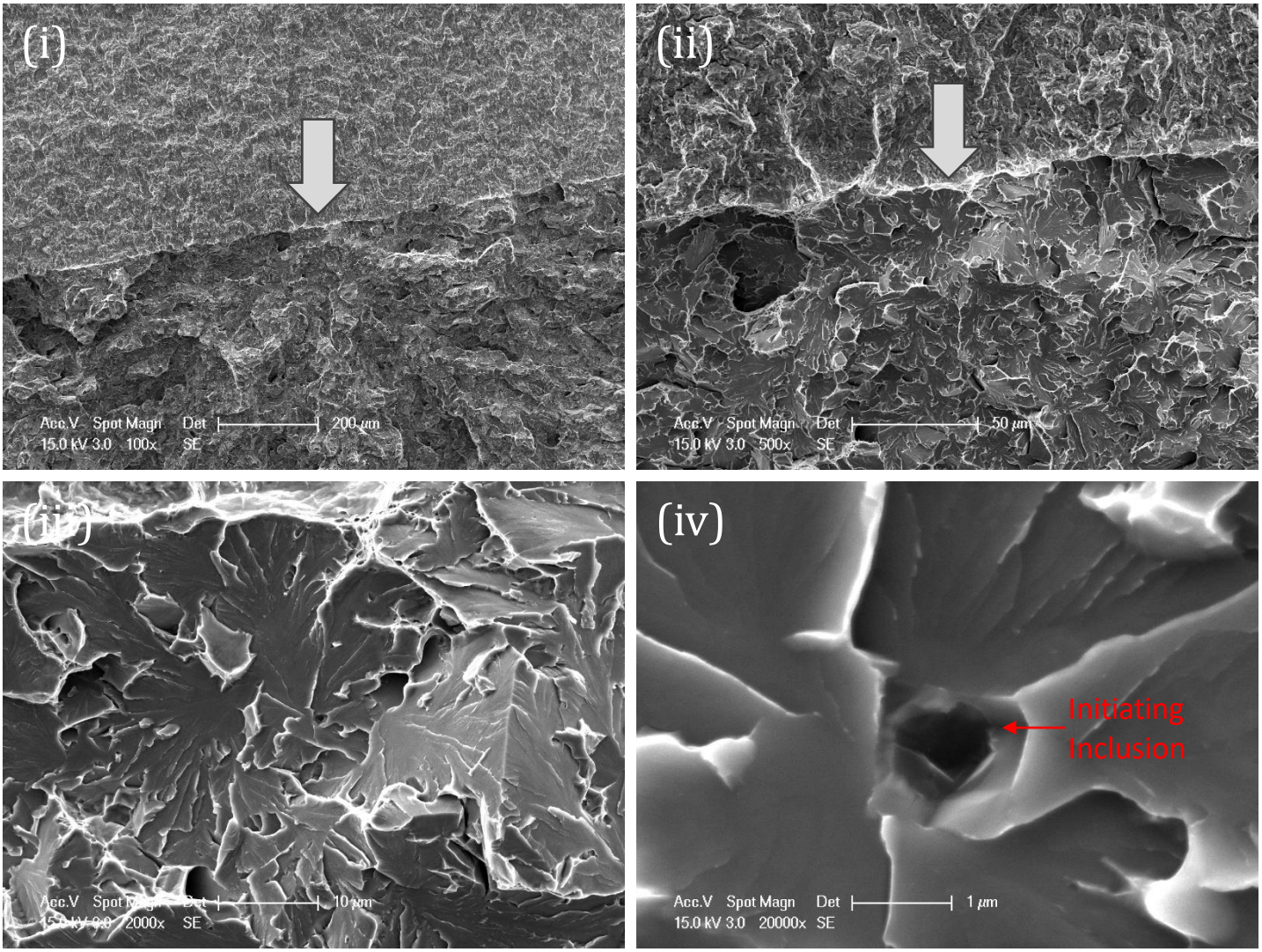


Figure 6-18 (c). Fracture Initiation at matching side (B) of the sharp-cracked specimen CT HT1-23, test temperature of -120 °C. A sequential magnification of the red-framed area at (i) 100x, (ii) 500x, (iii) 2000x, and (iv) 20000x are shown. Fractographic analysis reveals inclusion cracking as the initiation mechanism, with the inclusion's equivalent diameter at 1.0 µm and the initial facet's equivalent diameter at 34 µm.

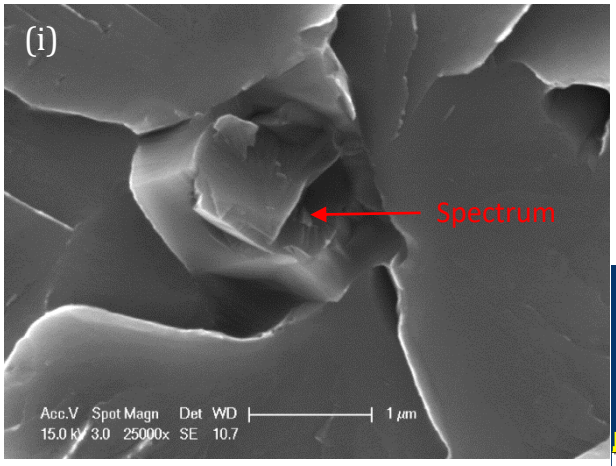


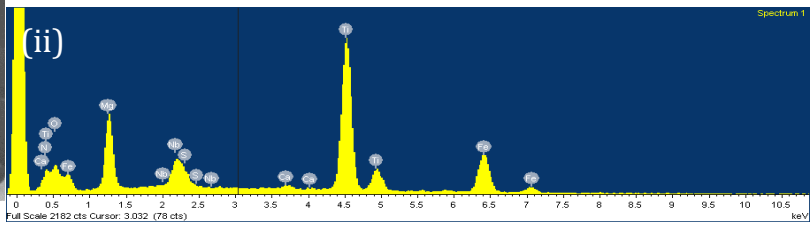


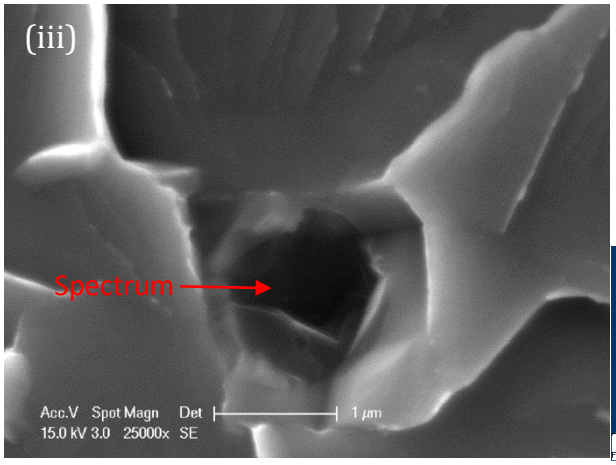


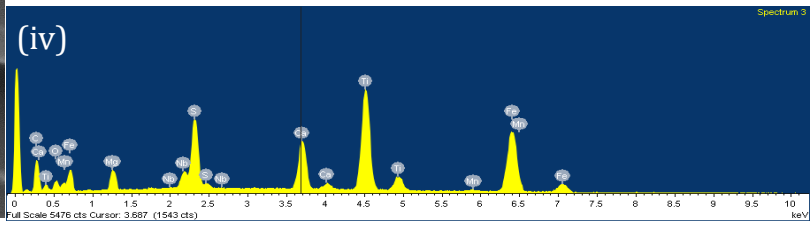


Figure 6-18 (d). Cleavage initiation point (i) and (iii) from matching halves of fracture surfaces of sharp-cracked specimen CT HT1-23 tested at -120 °C with their corresponding EDX spectrums (ii) and (iv) respectively.

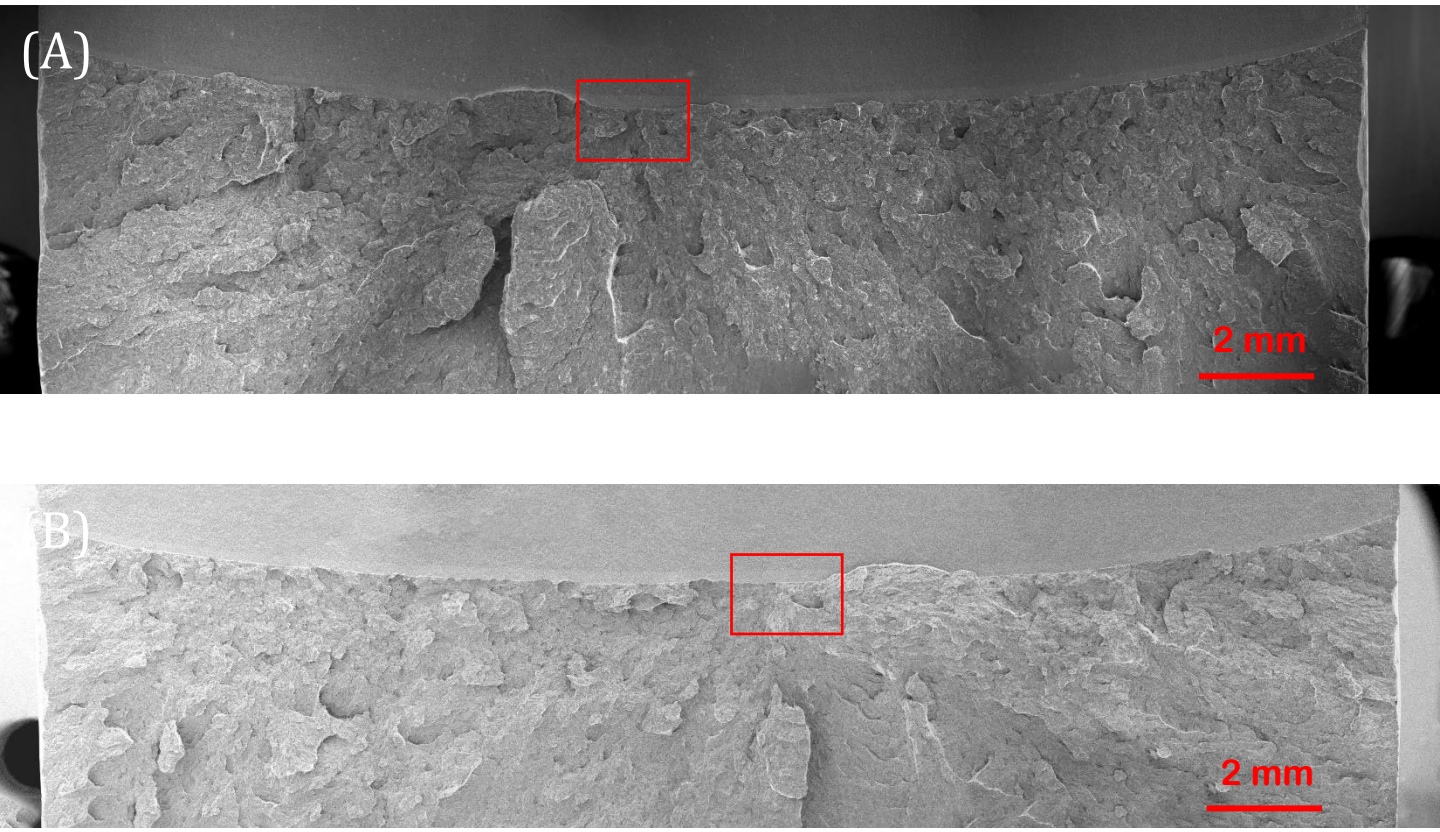


Figure 6-19 (a). Overview of fracture surfaces on a sharp-cracked specimen, designated CT HT1-24, tested at -120 °C. Red frames on matching halves (A) and (B) denote the most probable fracture initiation areas. Test results: Critical J-integral (Jc) value of 32.4 $kJ/m^2$, crack tip opening displacement (CTOD) of 0.023 mm, local cleavage fracture stress of 2478 MPa (n=0.1), fracture initiation distance (Xo) of 61 µm, and an average stable crack extension of 5 µm.

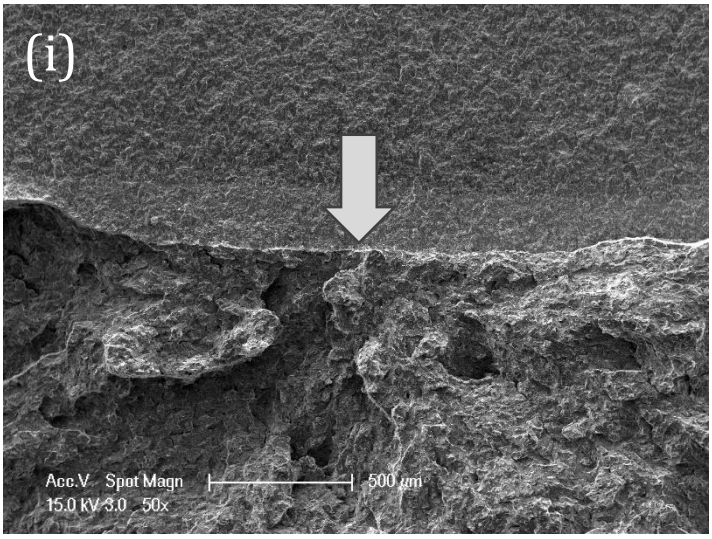


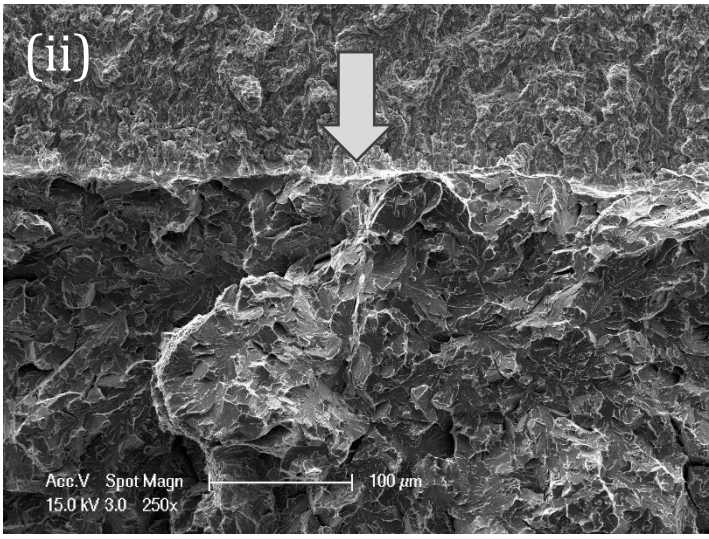


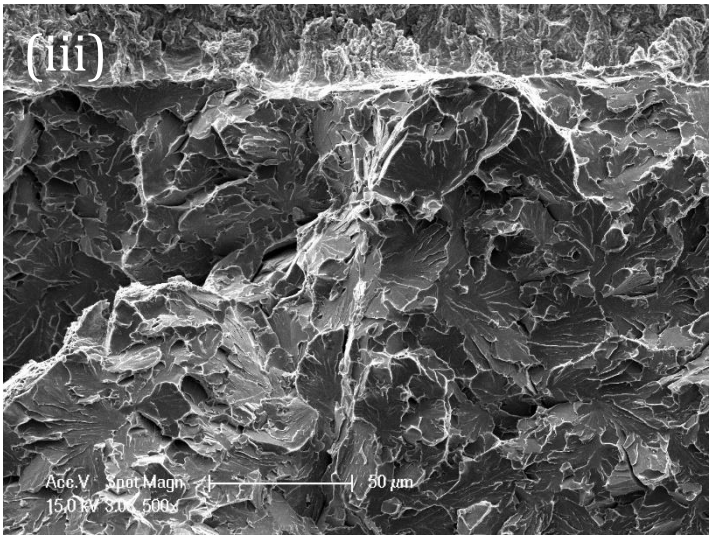


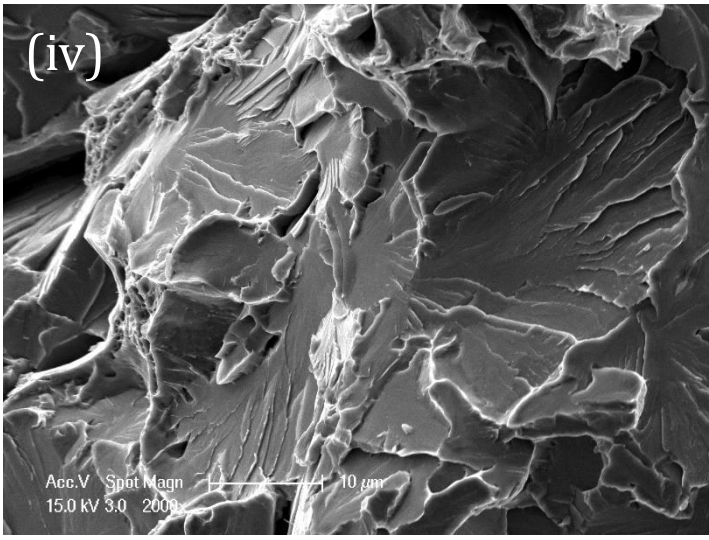


Figure 6-19 (b). Fracture Initiation at side (A) of the sharp-cracked specimen CT HT1-24, test temperature of -120 °C. A sequential magnification of the red-framed area at (i) 50x, (ii) 250x, (iii) 500x, and (iv) 2000x are shown. Fractographic analysis reveals matrix cracking as the initiation mechanism, with the initial facet's equivalent diameter at 36 µm.

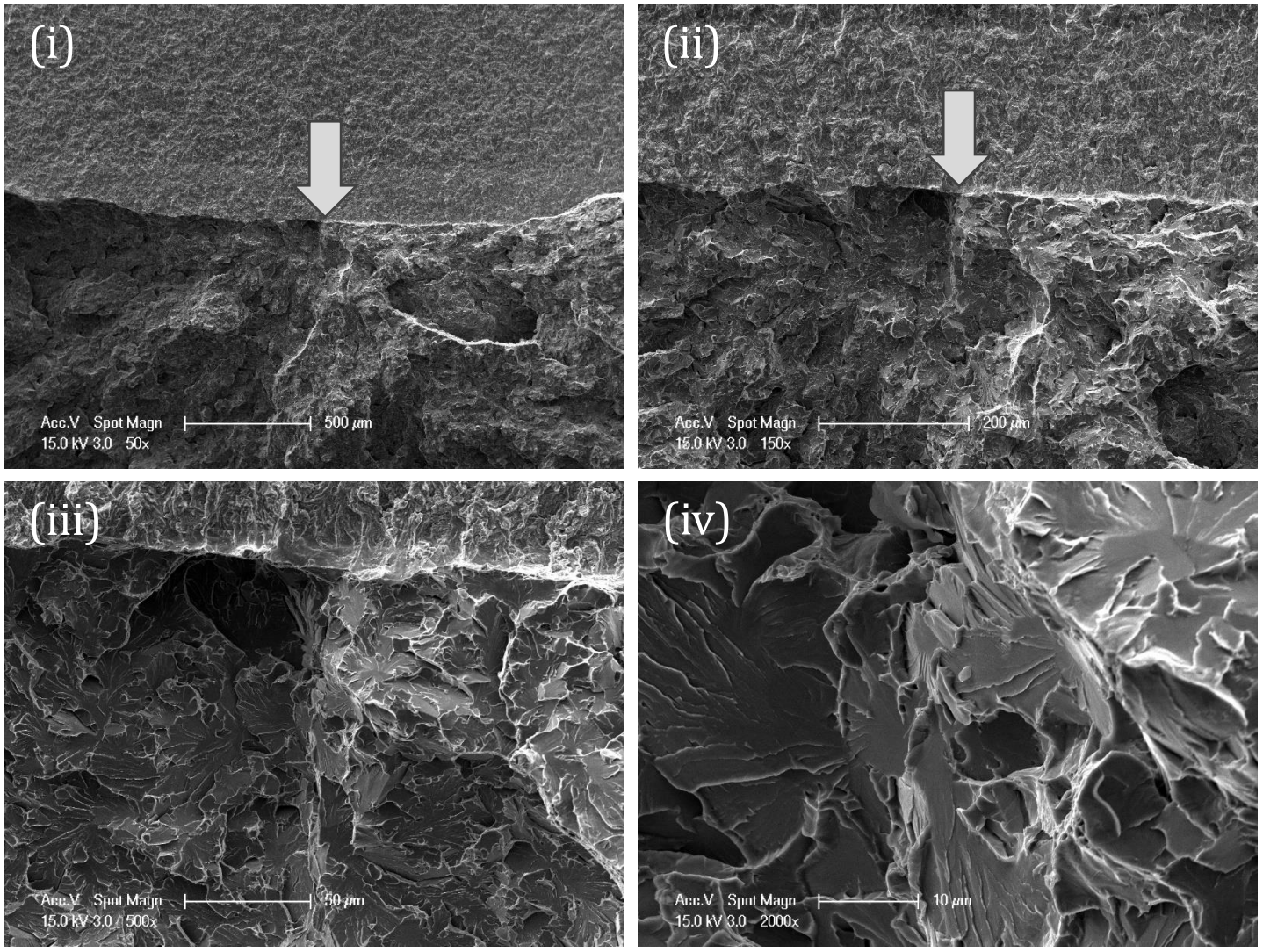


Figure 6-19 (c). Fracture Initiation at matching side (B) of the sharp-cracked specimen CT HT1-24, test temperature of -120 °C. A sequential magnification of the red-framed area at (i) 50x, (ii) 150x, (iii) 500x, and (iv) 2000x are shown. Fractographic analysis reveals matrix cracking as the initiation mechanism, with the initial facet's equivalent diameter at 36 µm.

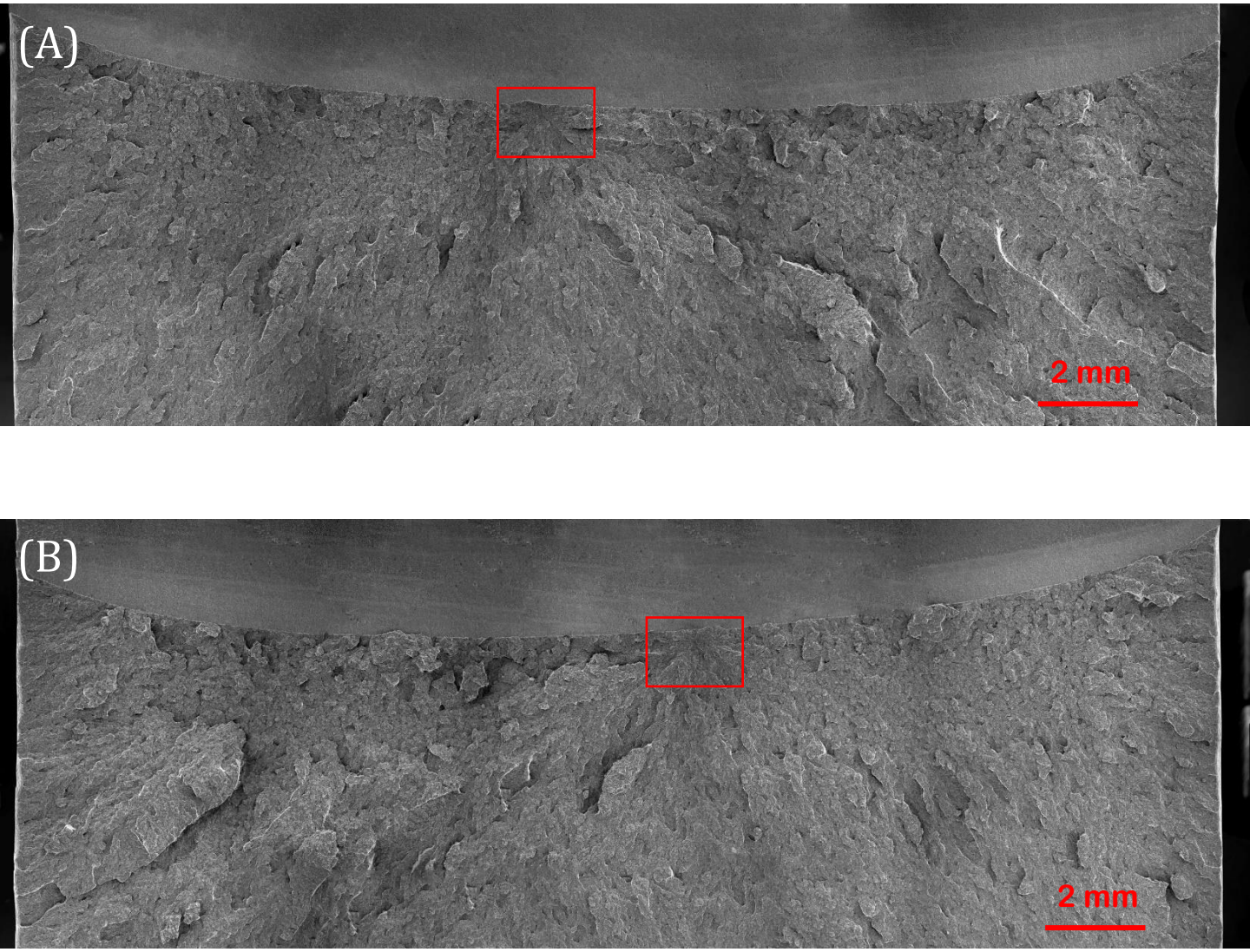


Figure 6-20 (a). Overview of fracture surfaces on a sharp-cracked specimen, designated CT HT2-05, tested at -120 °C. Red frames on matching halves (A) and (B) denote the most probable fracture initiation areas. Test results: Critical J-integral (Jc) value of 23.9 $kJ/m^2$, crack tip opening displacement (CTOD) of 0.018 mm, local cleavage fracture stress of 1986 MPa (n=0.1), fracture initiation distance (Xo) of 256 µm, and an average stable crack extension of 10 µm.

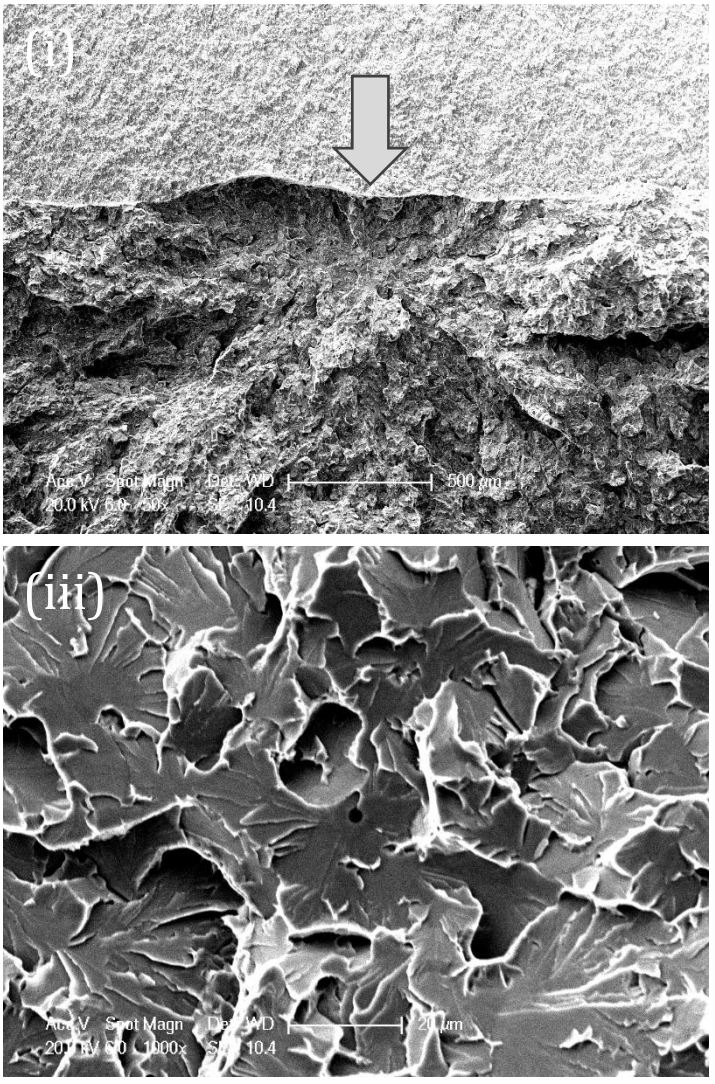


Figure 6-20 (b). Fracture Initiation at side (A) of the sharp-cracked specimen CT HT2-05, test temperature of -120 °C. A sequential magnification of the red-framed area at (i) 50x, (ii) 200x, (iii) 1000x, and (iv) 2500x are shown. Fractographic analysis reveals inclusion cracking as the initiation mechanism, with the inclusion's equivalent diameter at 2.2 μm and the initial facet's equivalent diameter at 35 μm.

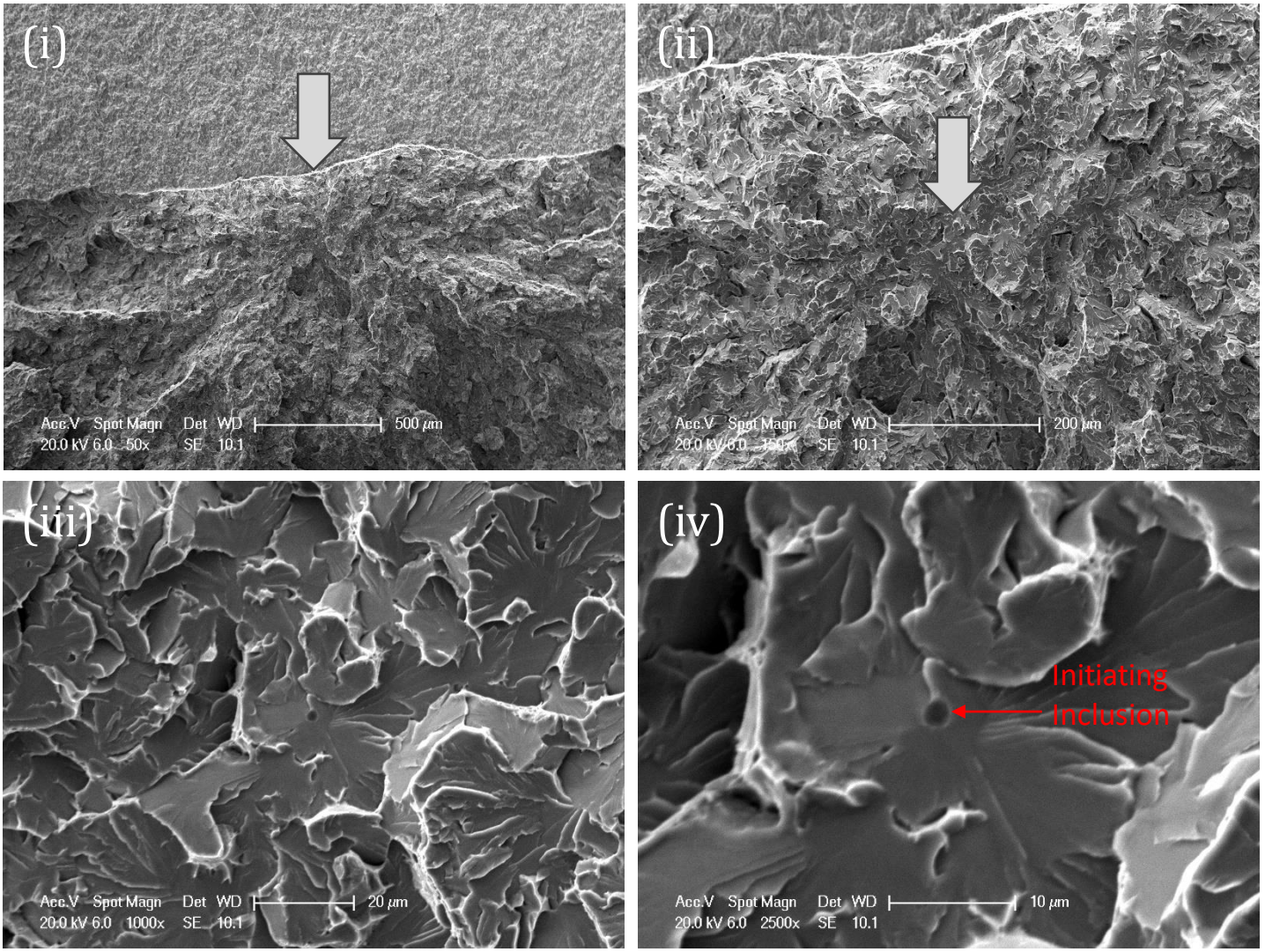


Figure 6-20 (c). Fracture Initiation at matching side (B) of the sharp-cracked specimen CT HT2-05, test temperature of -120 °C. A sequential magnification of the red-framed area at (i) 50x, (ii) 150x, (iii) 1000x, and (iv) 2500x are shown. Fractographic analysis reveals inclusion cracking as the initiation mechanism, with the inclusion's equivalent diameter at 2.2 µm and the initial facet's equivalent diameter at 35 µm.

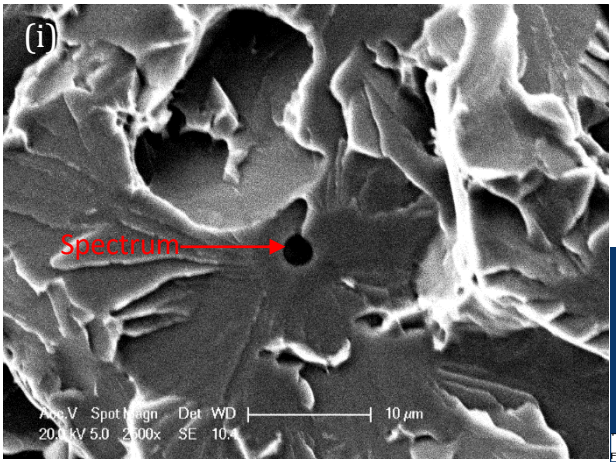


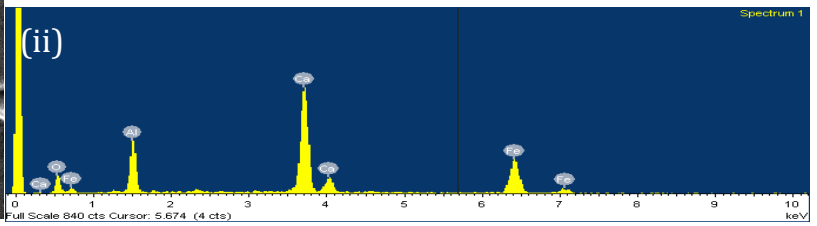


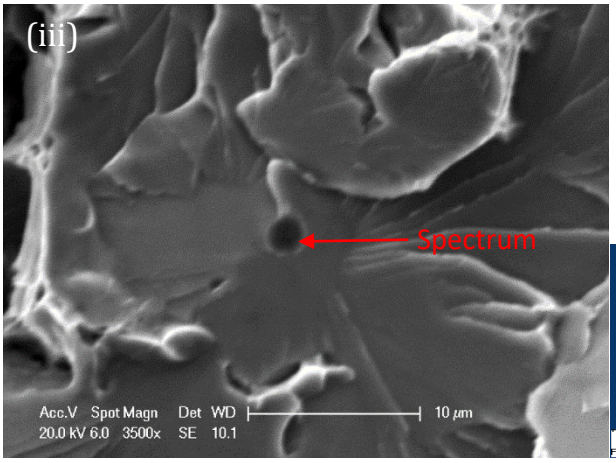


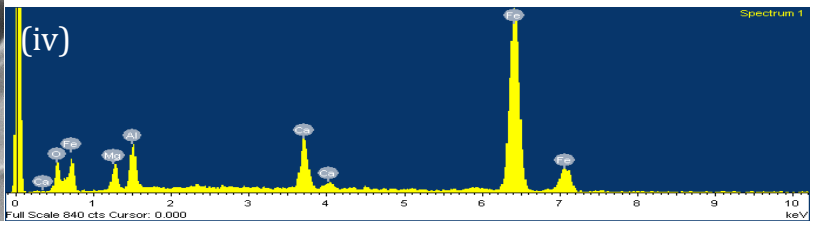


Figure 6-20 (d). Cleavage initiation point (i) and (iii) from matching halves of fracture surfaces of sharp-cracked specimen CT HT2-05 tested at -120 °C with their corresponding EDX spectrums (ii) and (iv) respectively.

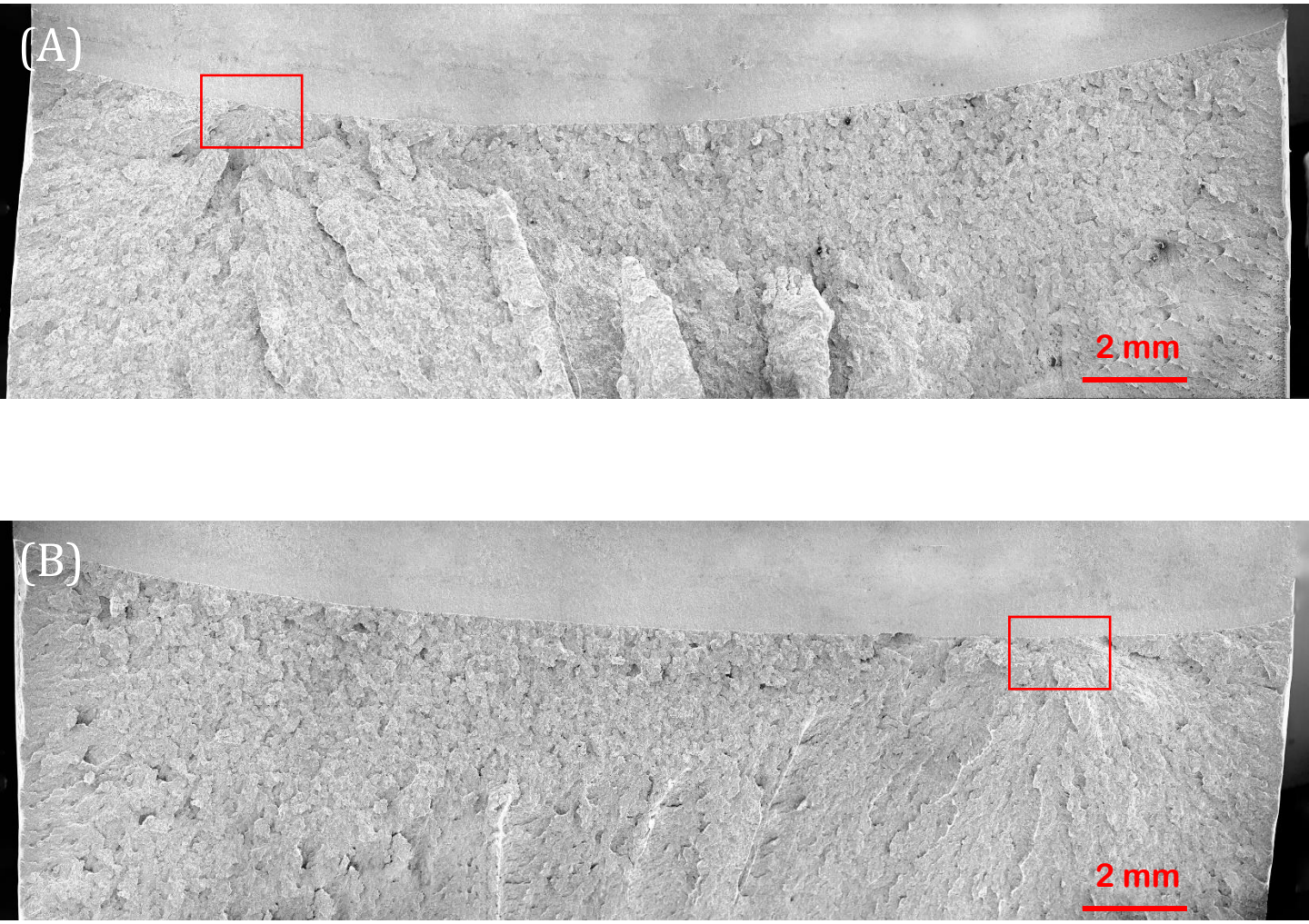


Figure 6-21 (a). Overview of fracture surfaces on a sharp-cracked specimen, designated CT HT2-06, tested at -120 °C. Red frames on matching halves (A) and (B) denote the most probable fracture initiation areas. Test results: Critical J-integral (Jc) value of 32.4 $kJ/m^2$, crack tip opening displacement (CTOD) of 0.024 mm, local cleavage fracture stress of 2420 MPa (n=0.1), fracture initiation distance (Xo) of 79 µm, and an average stable crack extension of 6 µm.

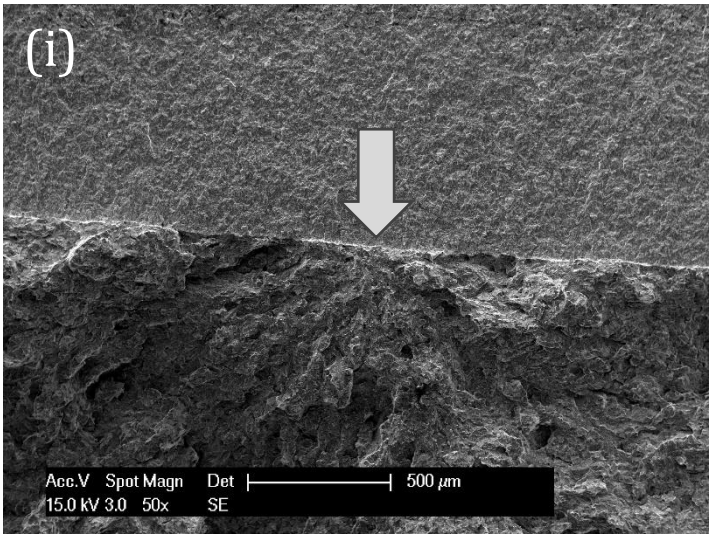


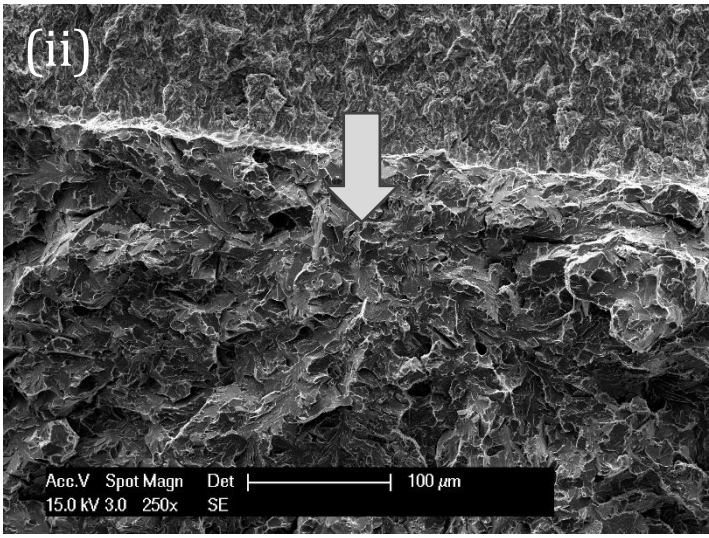


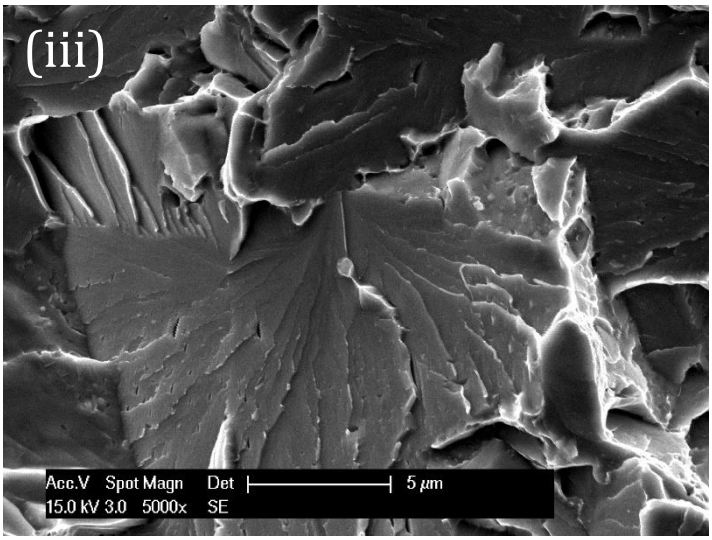


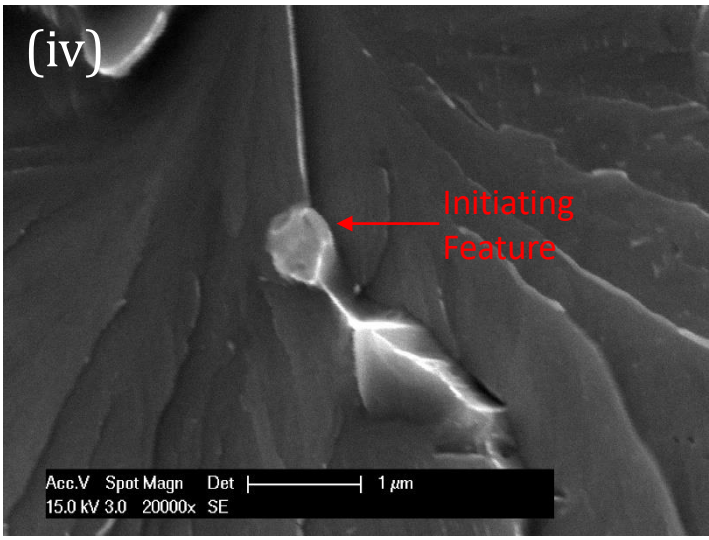


Figure 6-21 (b). Fracture Initiation at side (A) of the sharp-cracked specimen CT HT2-06, test temperature of -120 °C. A sequential magnification of the red-framed area at (i) 50x, (ii) 250x, (iii) 5000x, and (iv) 20000x are shown. Fractographic analysis reveals matrix related initiation mechanism, with the initiating feature's equivalent diameter at 0.6 µm and the initial facet's equivalent diameter at 21 µm.

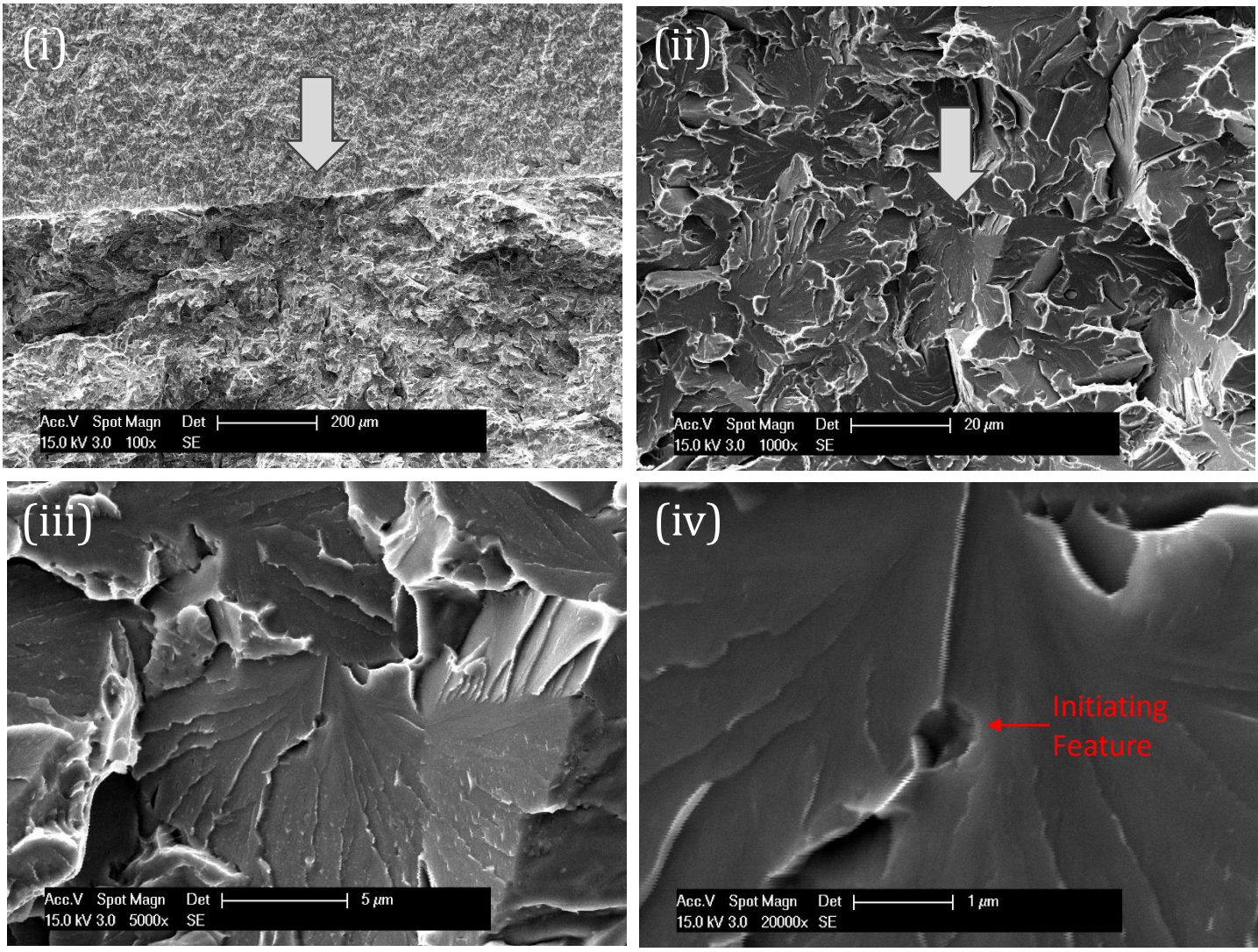


Figure 6-21 (c). Fracture Initiation at matching side (B) of the sharp-cracked specimen CT HT2-06, test temperature of -120 °C. A sequential magnification of the red-framed area at (i) 100x, (ii) 1000x, (iii) 5000x, and (iv) 20000x are shown. Fractographic analysis reveals matrix related initiation mechanism, with the initiating feature's equivalent diameter at 0.6 µm and the initial facet's equivalent diameter at 21 µm.

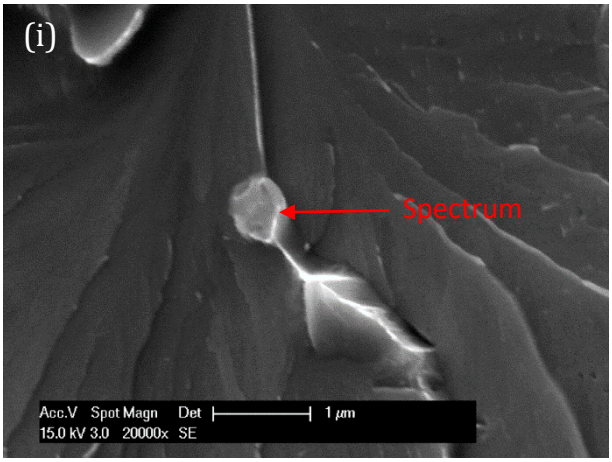


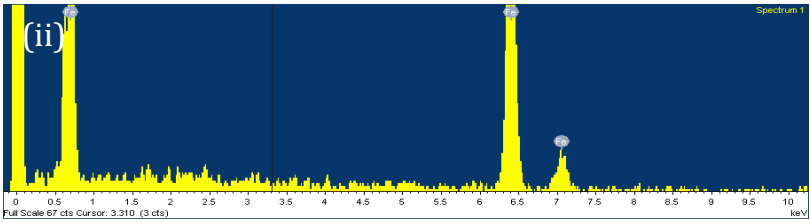


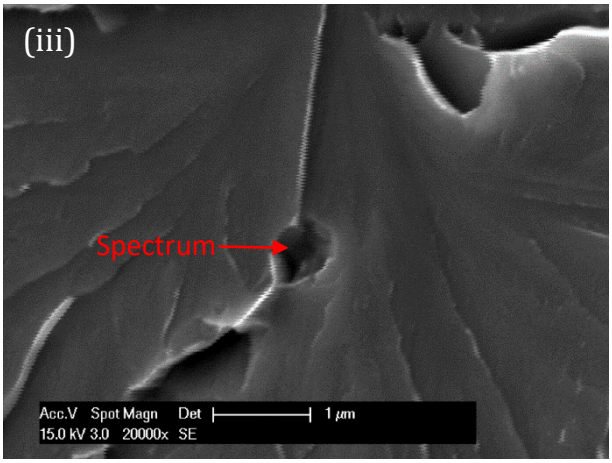


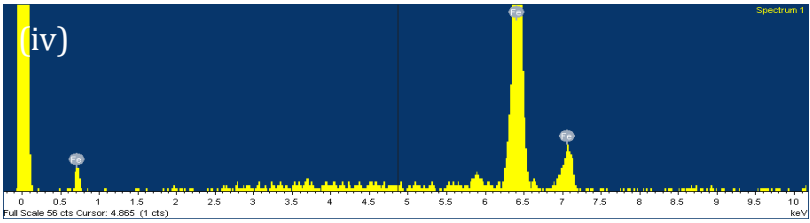


Figure 6-21 (d). Cleavage initiation point (i) and (iii) from matching halves of fracture surfaces of sharp-cracked specimen CT HT2-06 tested at -120 °C with their corresponding EDX spectrums (ii) and (iv) respectively.

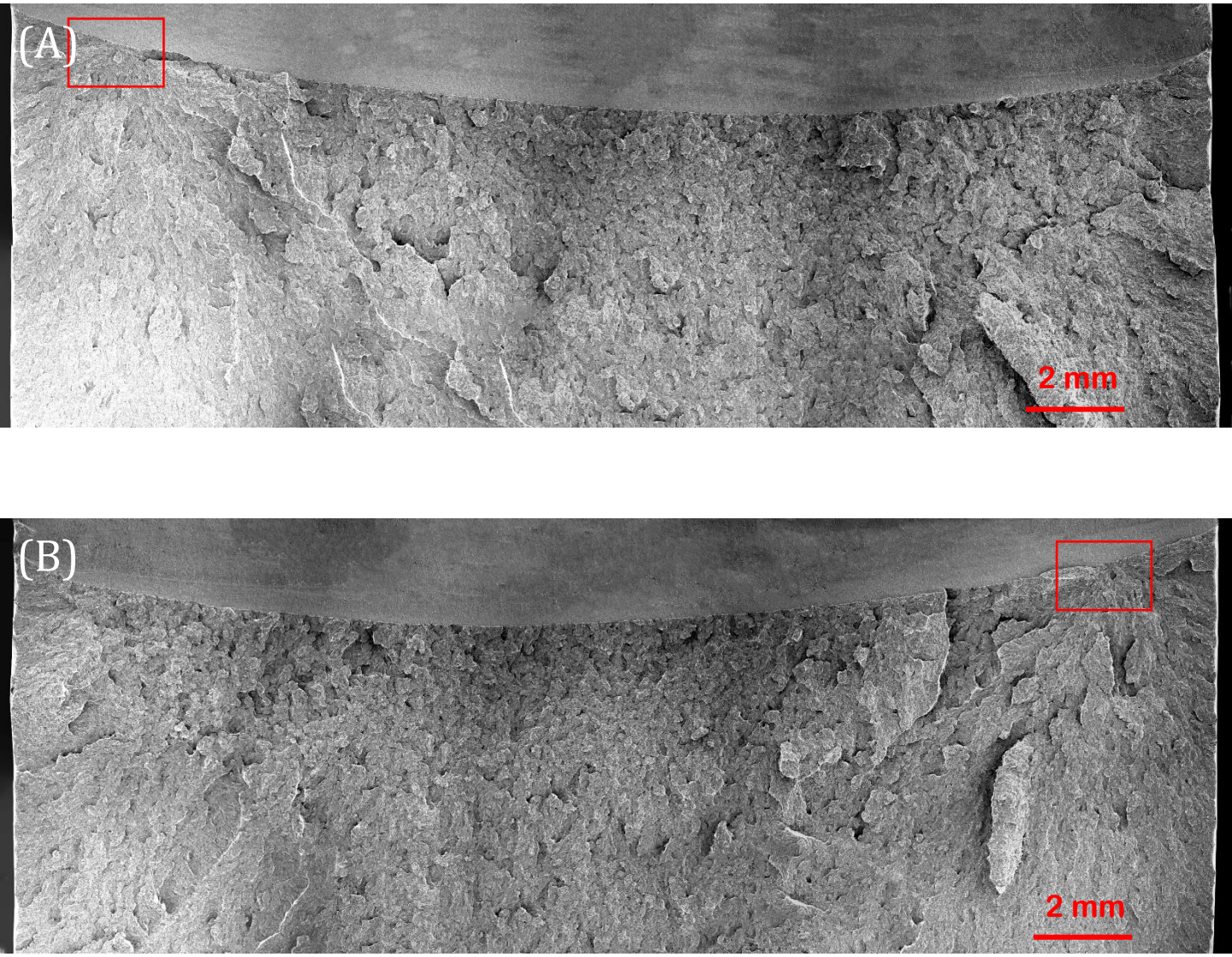


Figure 6-22 (a). Overview of fracture surfaces on a sharp-cracked specimen, designated CT HT2-07, tested at -120 °C. Red frames on matching halves (A) and (B) denote the most probable fracture initiation areas. Test results: Critical J-integral (Jc) value of 31.6 $kJ/m^2$, crack tip opening displacement (CTOD) of 0.023 mm, local cleavage fracture stress of 2290 MPa (n=0.1), fracture initiation distance (Xo) of 25 µm, and an average stable crack extension of 4 µm.

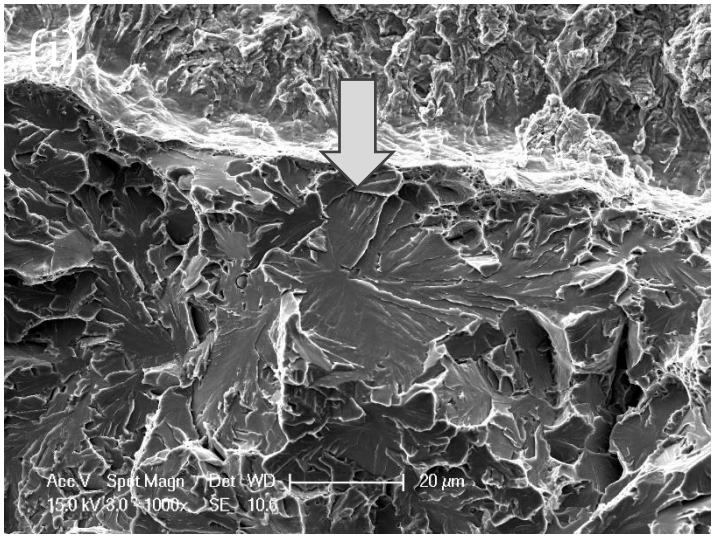


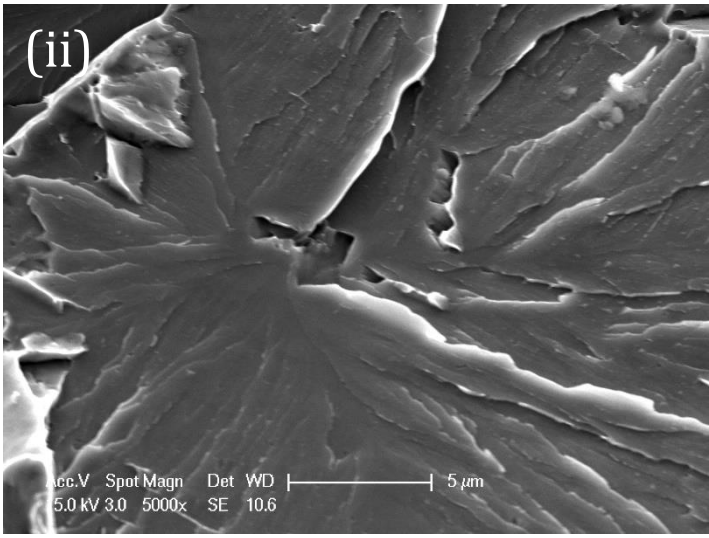


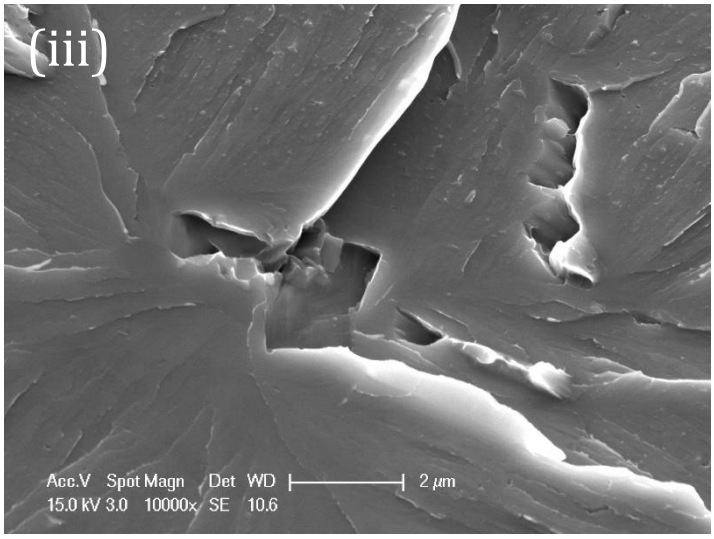


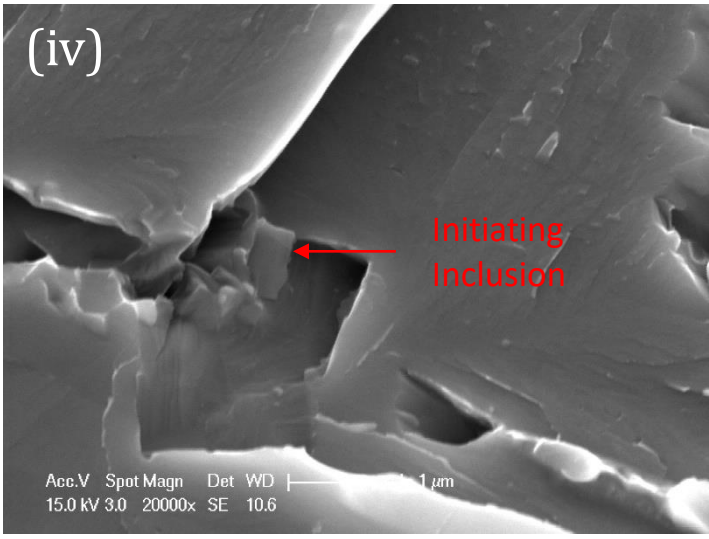


Figure 6-22 (b). Fracture Initiation at side (A) of the sharp-cracked specimen CT HT2-07, test temperature of -120 °C. A sequential magnification of the red-framed area at (i) 1000x, (ii) 5000x, (iii) 10000x, and (iv) 20000x are shown. Fractographic analysis reveals inclusion cracking as the initiation mechanism, with the inclusion's equivalent diameter at 1.7 µm and the initial facet's equivalent diameter at 34 µm.

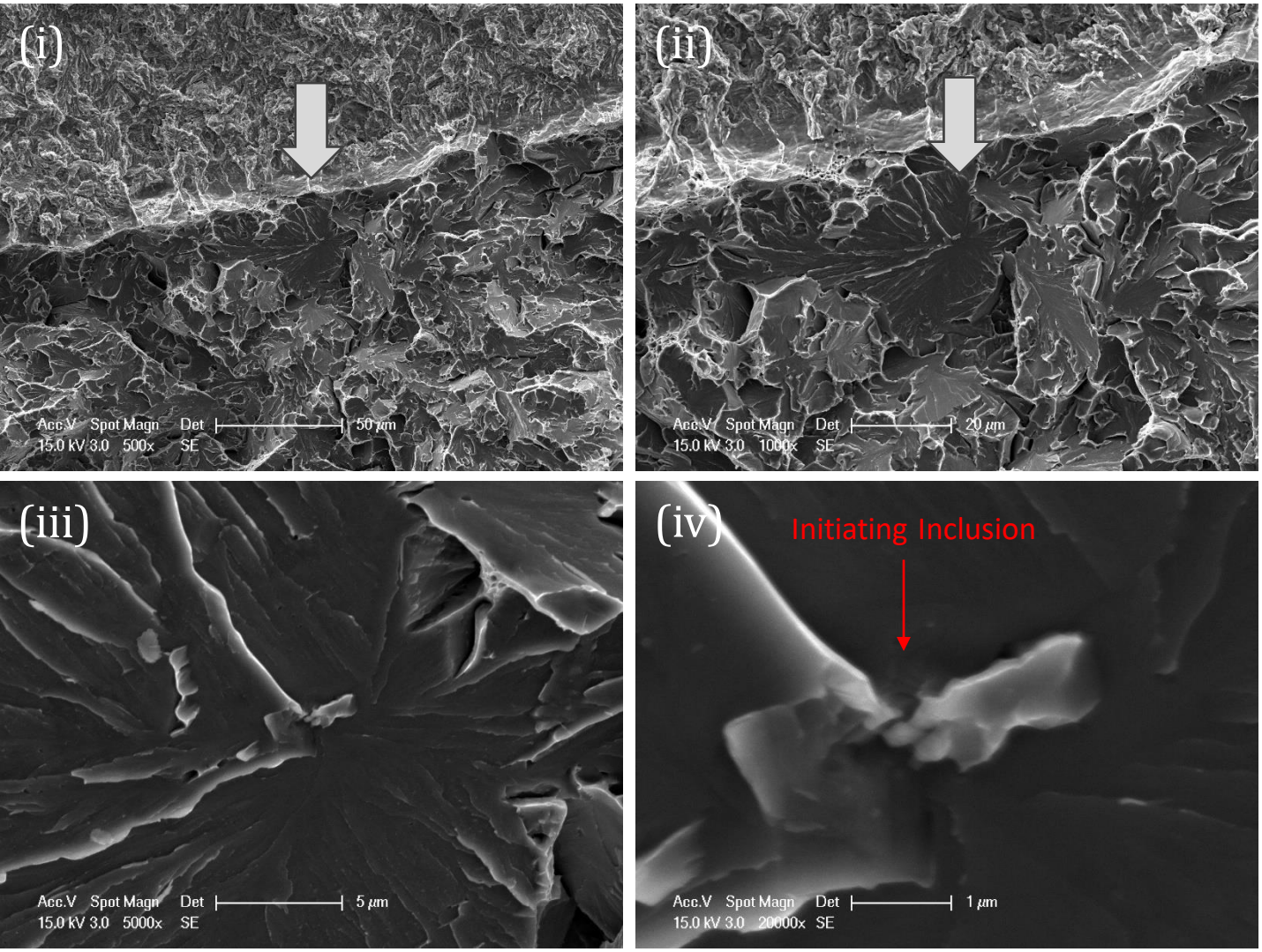


Figure 6-22 (c). Fracture Initiation at matching side (B) of the sharp-cracked specimen CT HT2-07, test temperature of -120 °C. A sequential magnification of the red-framed area at (i) 500x, (ii) 1000x, (iii) 5000x, and (iv) 20000x are shown. Fractographic analysis reveals inclusion cracking as the initiation mechanism, with the inclusion's equivalent diameter at 1.7 µm and the initial facet's equivalent diameter at 34 µm.

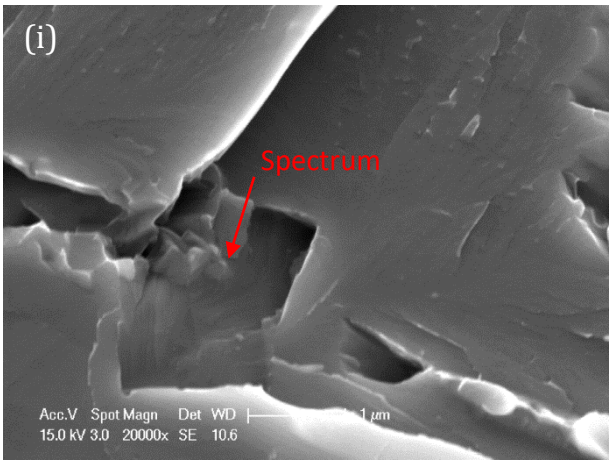


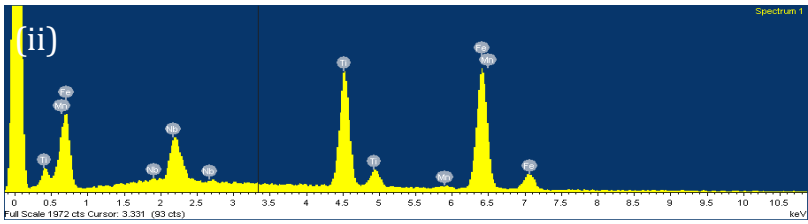


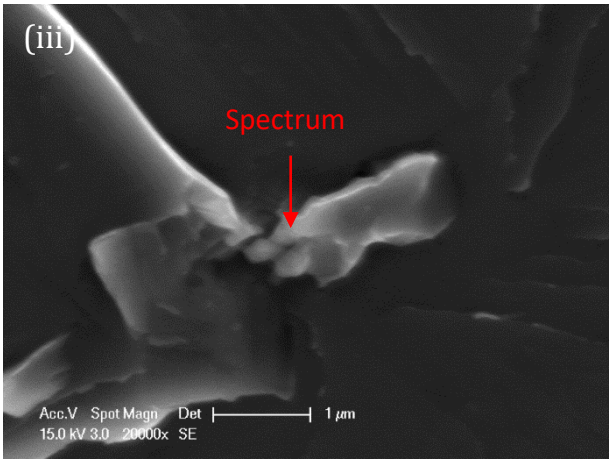


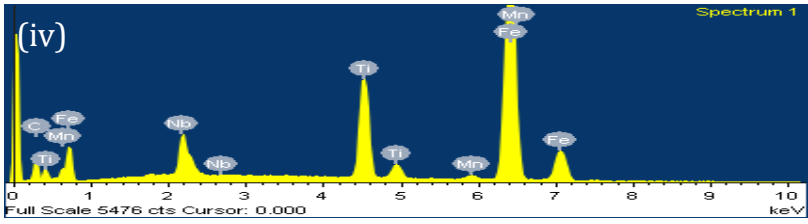


Figure 6-22 (d). Cleavage initiation point (i) and (iii) from matching halves of fracture surfaces of sharp-cracked specimen CT HT2-07 tested at -120 °C with their corresponding EDX spectrums (ii) and (iv) respectively.

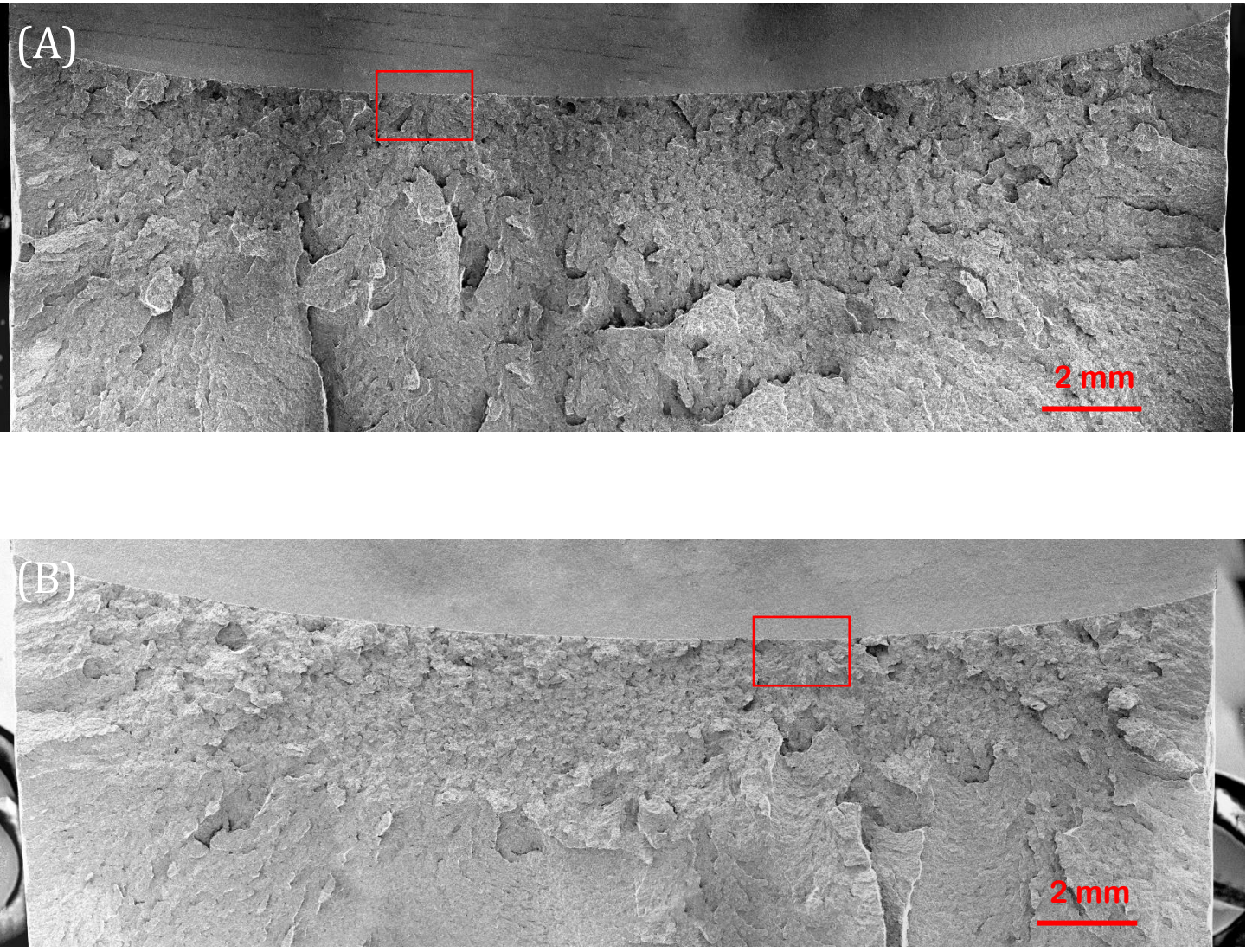


Figure 6-23 (a). Overview of fracture surfaces on a sharp-cracked specimen, designated CT HT2-08, tested at -120 °C. Red frames on matching halves (A) and (B) denote the most probable fracture initiation areas. Test results: Critical J-integral (Jc) value of 40.6 $kJ/m^2$, crack tip opening displacement (CTOD) of 0.030 mm, local cleavage fracture stress of 2459 MPa (n=0.1), fracture initiation distance (Xo) of 87 µm, and an average stable crack extension of 8 µm.

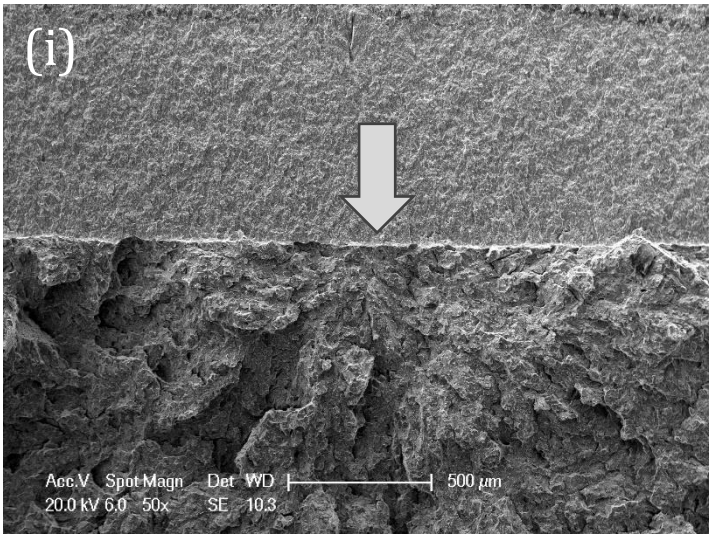


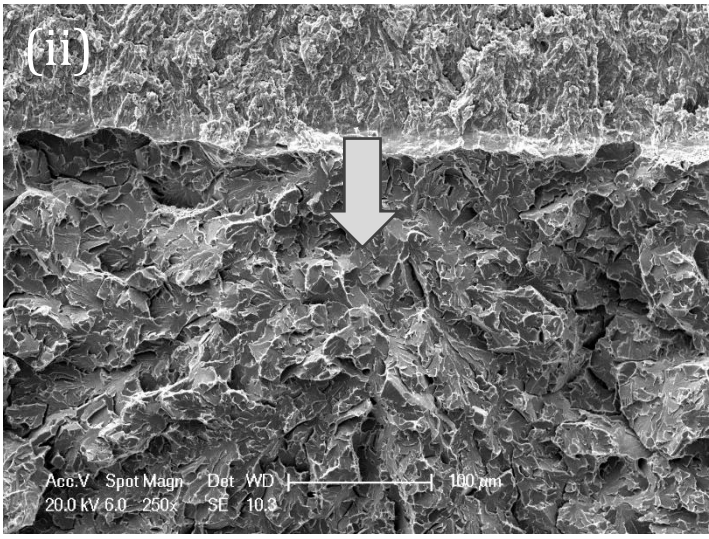


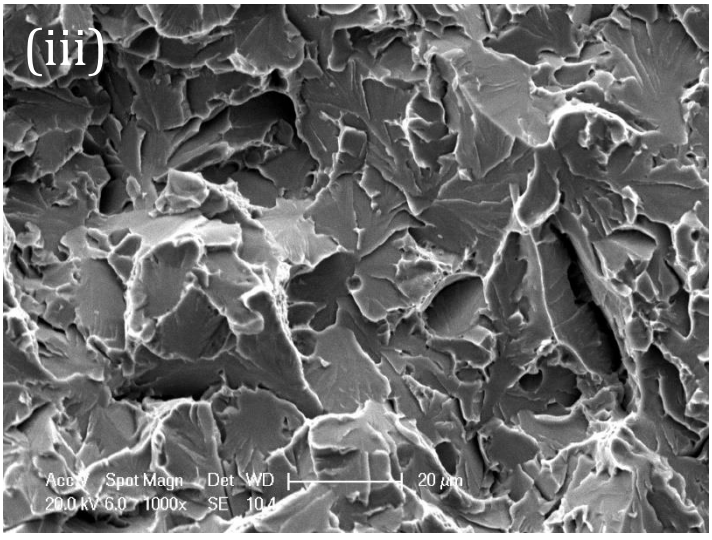


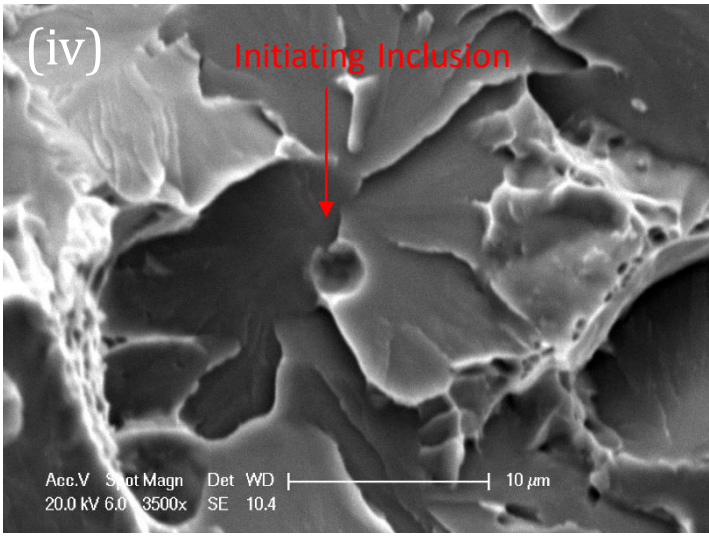


Figure 6-23 (b). Fracture Initiation at side (A) of the sharp-cracked specimen CT HT2-08, test temperature of -120 °C. A sequential magnification of the red-framed area at (i) 50x, (ii) 250x, (iii) 1000x, and (iv) 3500x are shown. Fractographic analysis reveals inclusion cracking as the initiation mechanism, with the inclusion's equivalent diameter at 2.5 µm and the initial facet's equivalent diameter at 28 µm.

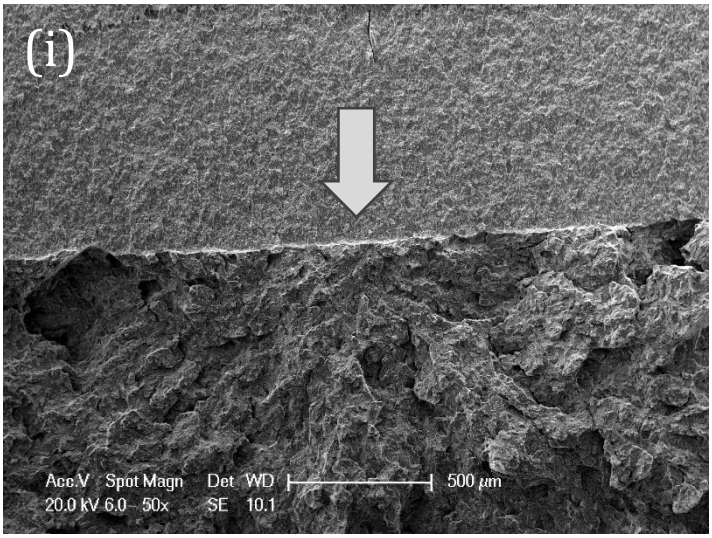


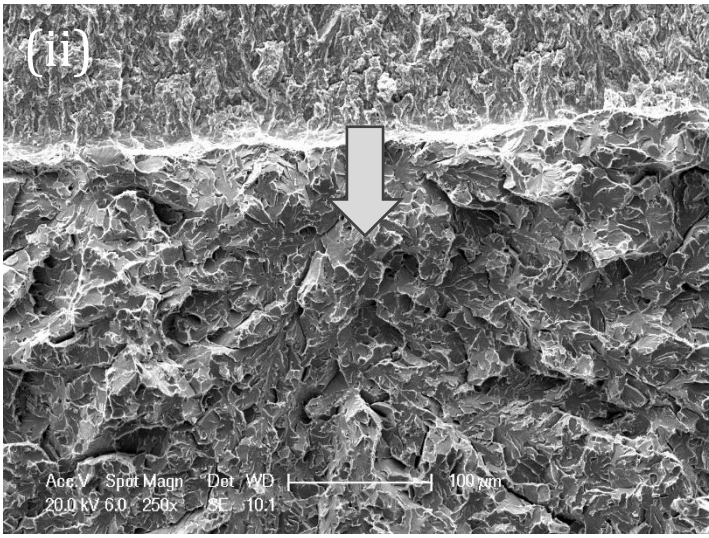


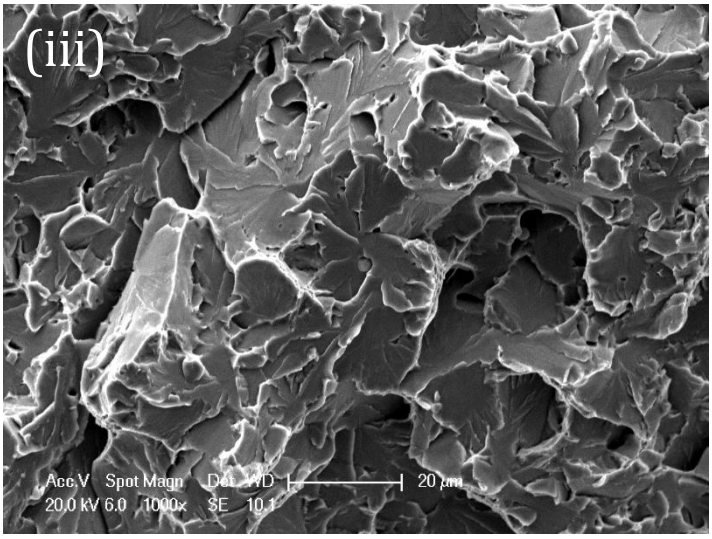


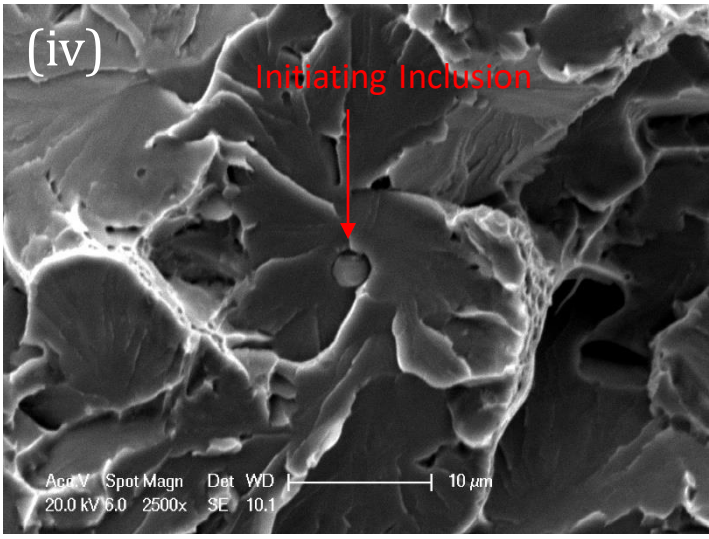


Figure 6-23 (c). Fracture Initiation at matching side (B) of the sharp-cracked specimen CT HT2-08, test temperature of -120 °C. A sequential magnification of the red-framed area at (i) 50x, (ii) 250x, (iii) 1000x, and (iv) 2500x are shown. Fractographic analysis reveals inclusion cracking as the initiation mechanism, with the inclusion's equivalent diameter at 2.5 µm and the initial facet's equivalent diameter at 28 µm.

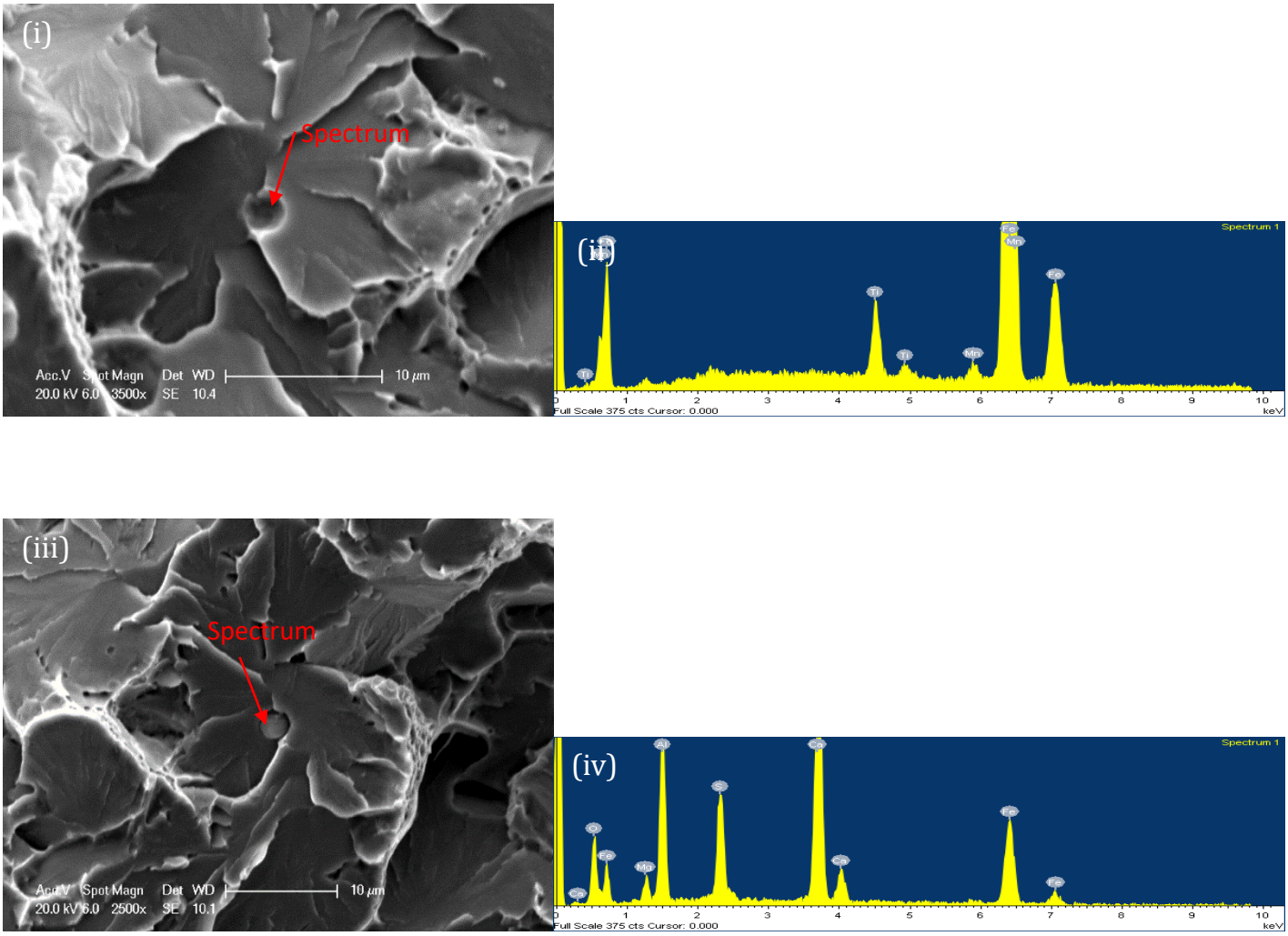


Figure 6-23 (d). Cleavage initiation point (i) and (iii) from matching halves of fracture surfaces of sharp-cracked specimen CT HT2-08 tested at -120 °C with their corresponding EDX spectrums (ii) and (iv) respectively.

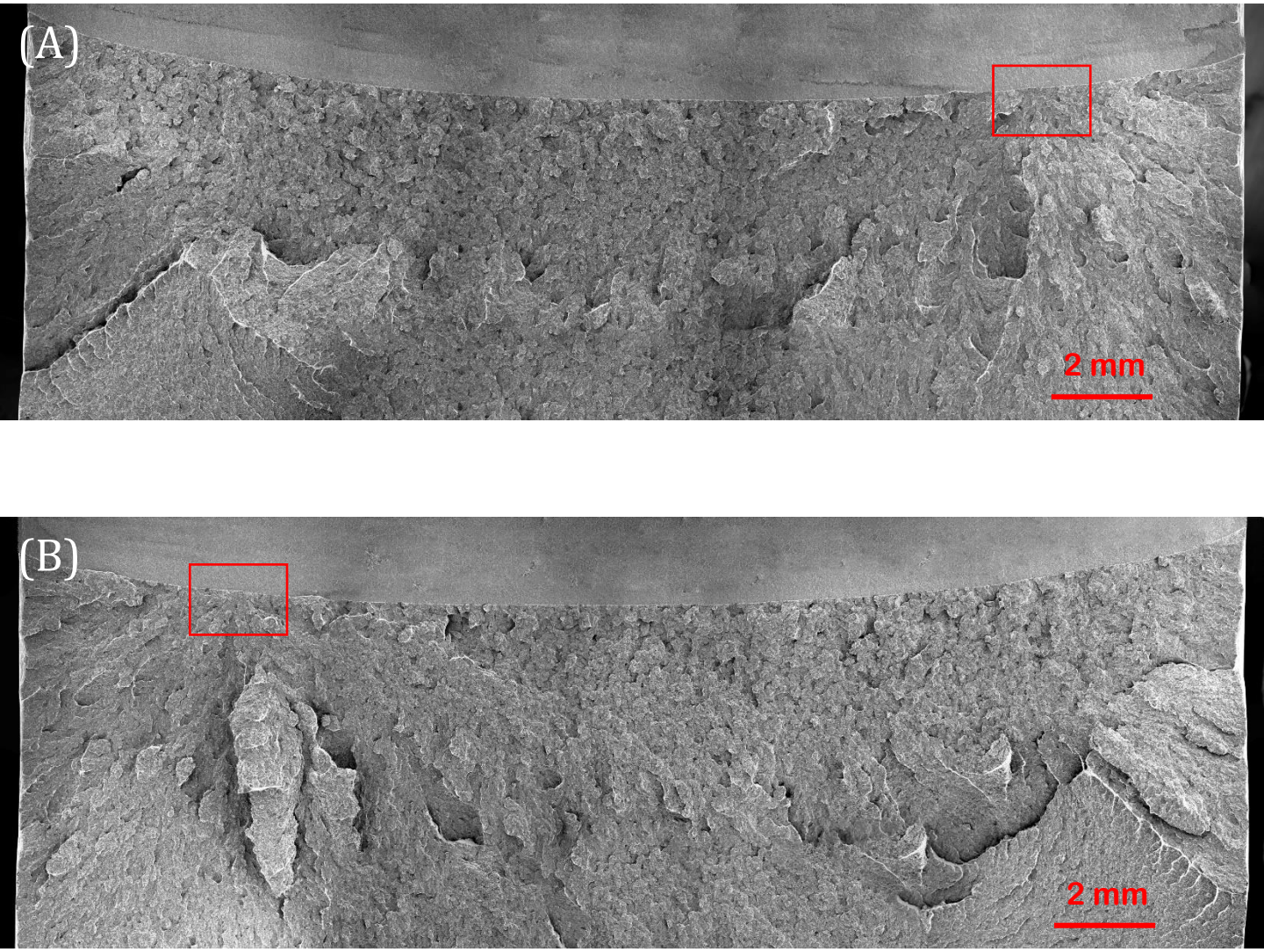


Figure 6-24 (a). Overview of fracture surfaces on a sharp-cracked specimen, designated CT HT2-19, tested at -120 °C. Red frames on matching halves (A) and (B) denote the most probable fracture initiation areas. Test results: Critical J-integral (Jc) value of 30.2 $kJ/m^2$, crack tip opening displacement (CTOD) of 0.022 mm, local cleavage fracture stress of 2349 MPa (n=0.1), fracture initiation distance (X0) of 87 µm, and an average stable crack extension of 4 µm.

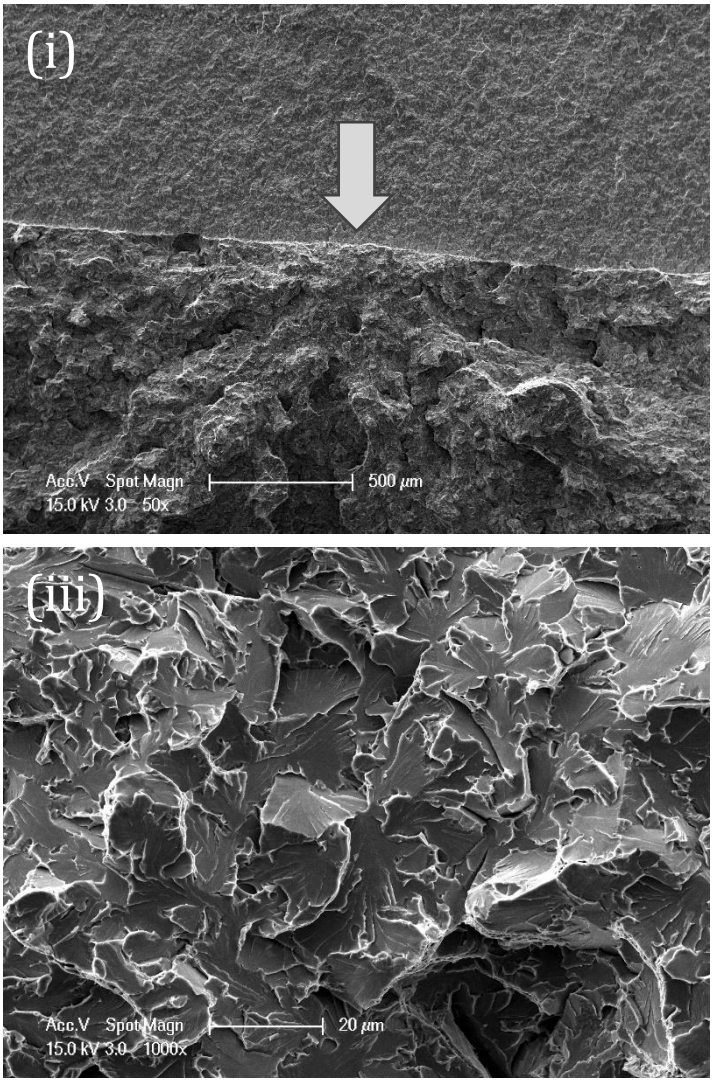


Figure 6-24 (b). Fracture Initiation at side (A) of the sharp-cracked specimen CT HT2-19, test temperature of -120 °C. A sequential magnification of the red-framed area at (i) 50x, (ii) 500x, (iii) 1000x, and (iv) 5000x are shown. Fractographic analysis reveals matrix related initiation mechanism, with the initiating feature's equivalent diameter at 1.7 µm and the initial facet's equivalent diameter at 27 µm.

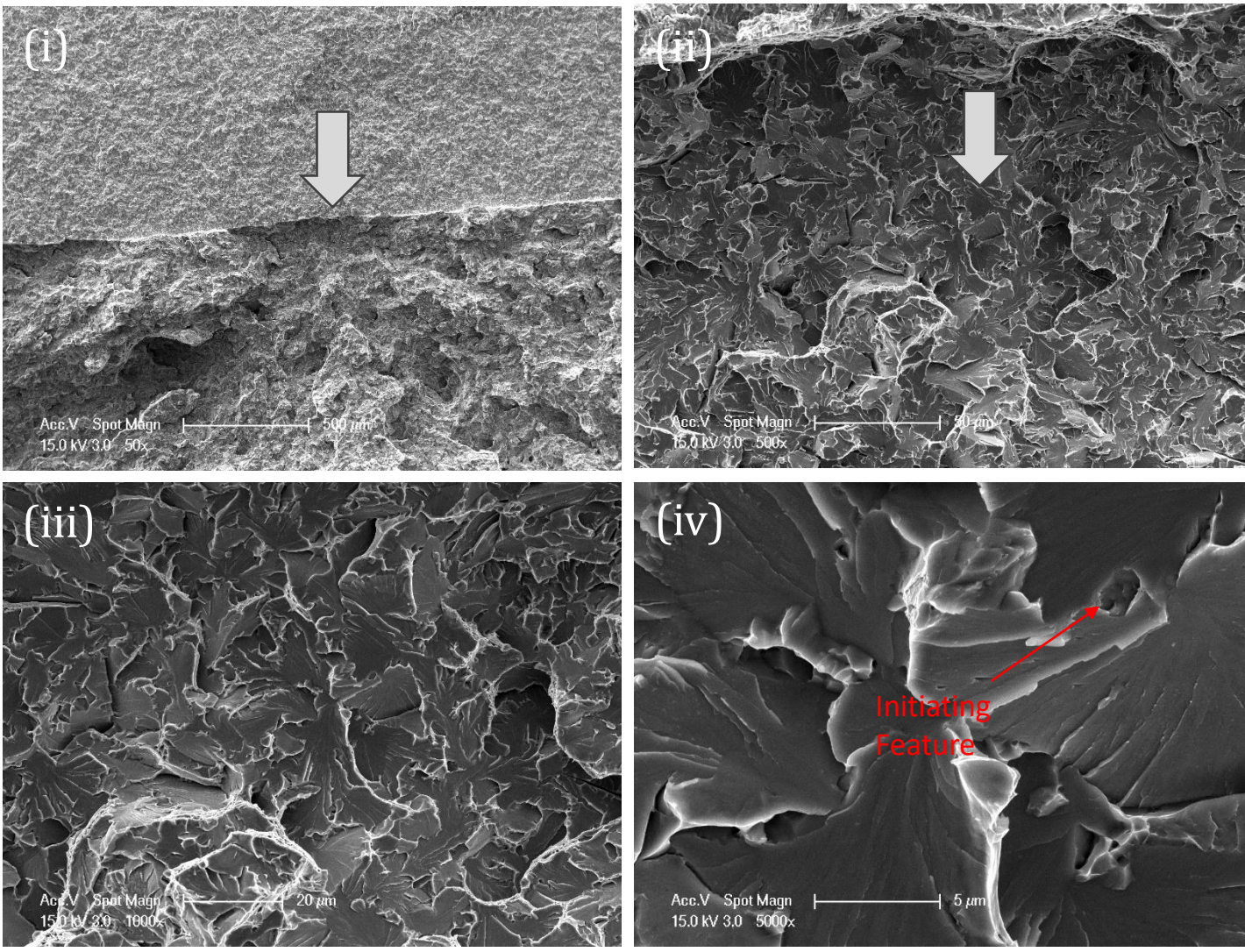


Figure 6-24 (c). Fracture Initiation at matching side (B) of the sharp-cracked specimen CT HT2-19, test temperature of -120 °C. A sequential magnification of the red-framed area at (i) 50x, (ii) 500x, (iii) 1000x, and (iv) 5000x are shown. Fractographic analysis reveals matrix related initiation mechanism, with the initiating feature's equivalent diameter at 1.7 µm and the initial facet's equivalent diameter at 27 µm.

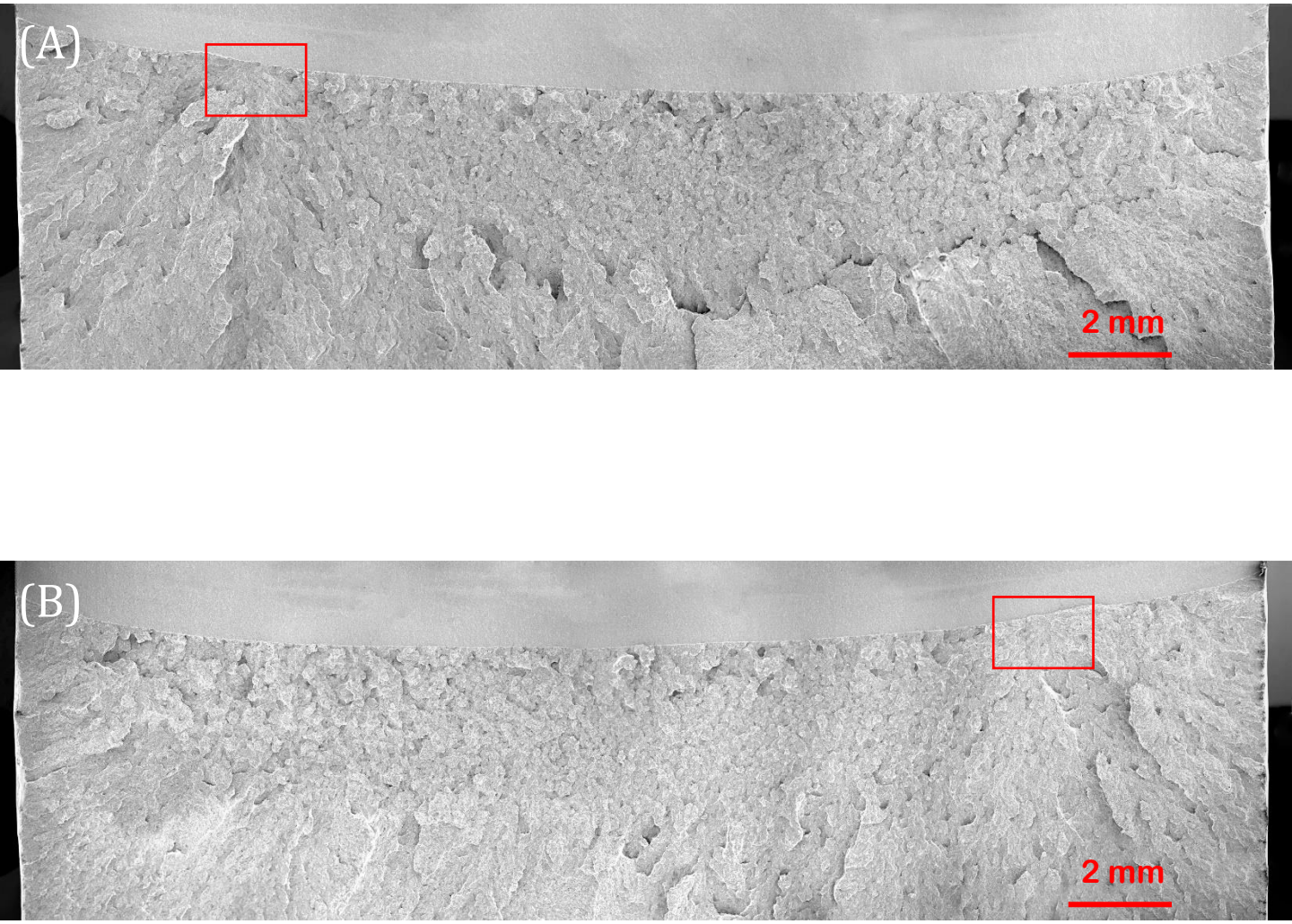


Figure 6-25 (a). Overview of fracture surfaces on a sharp-cracked specimen, designated CT HT2-22, tested at -120 °C. Red frames on matching halves (A) and (B) denote the most probable fracture initiation areas. Test results: Critical J-integral (Jc) value of 24.1 $kJ/m^2$, crack tip opening displacement (CTOD) of 0.018 mm, local cleavage fracture stress of 2090 MPa (n=0.1), fracture initiation distance (Xo) of 147 µm, and an average stable crack extension of 6 µm.

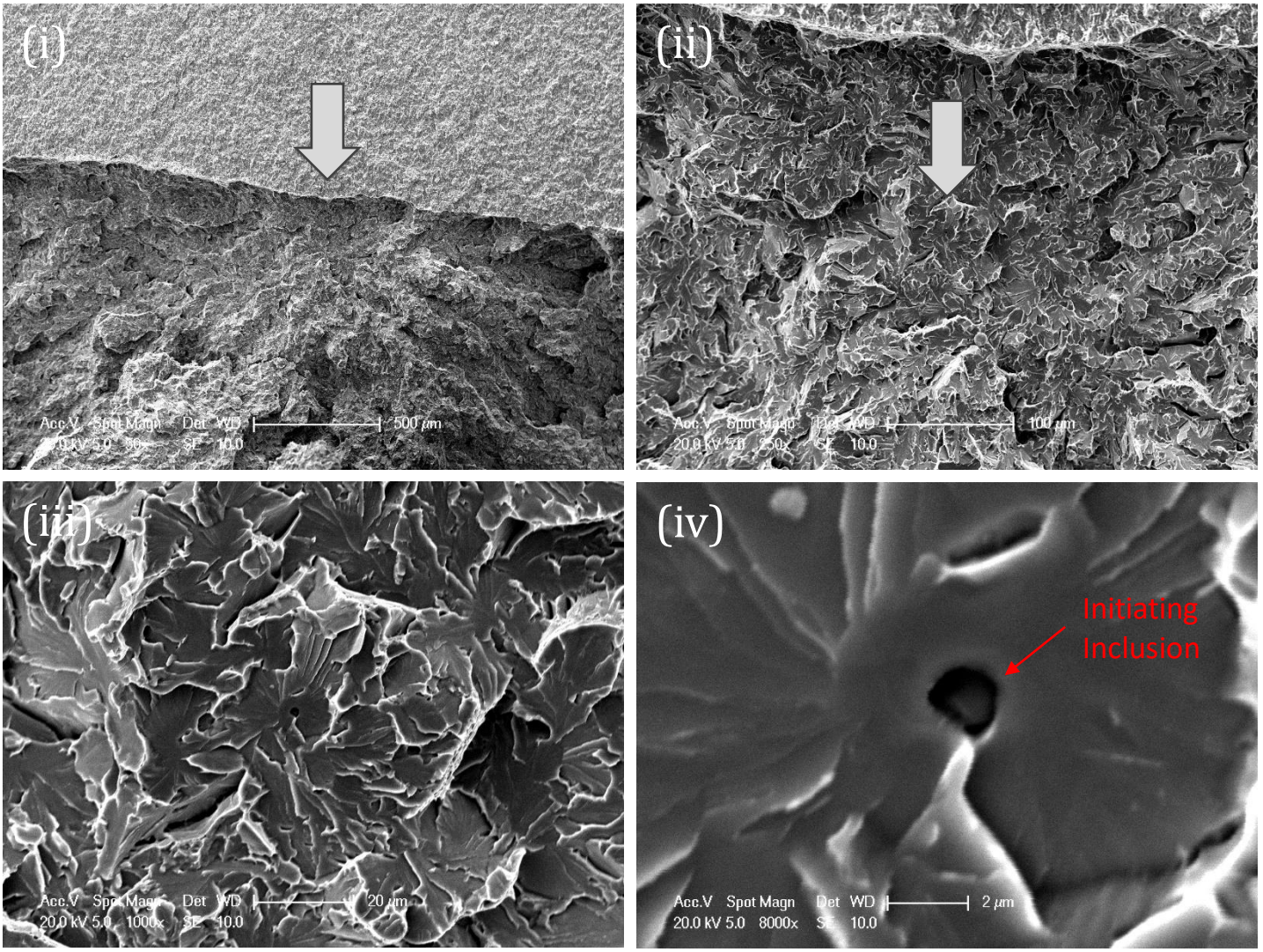


Figure 6-25 (b). Fracture Initiation at side (A) of the sharp-cracked specimen CT HT2-22, test temperature of -120 °C. A sequential magnification of the red-framed area at (i) 50x, (ii) 250x, (iii) 1000x, and (iv) 8000x are shown. Fractographic analysis reveals inclusion cracking as the initiation mechanism, with the inclusion's equivalent diameter at 1.6 µm and the initial facet's equivalent diameter at 39 µm.

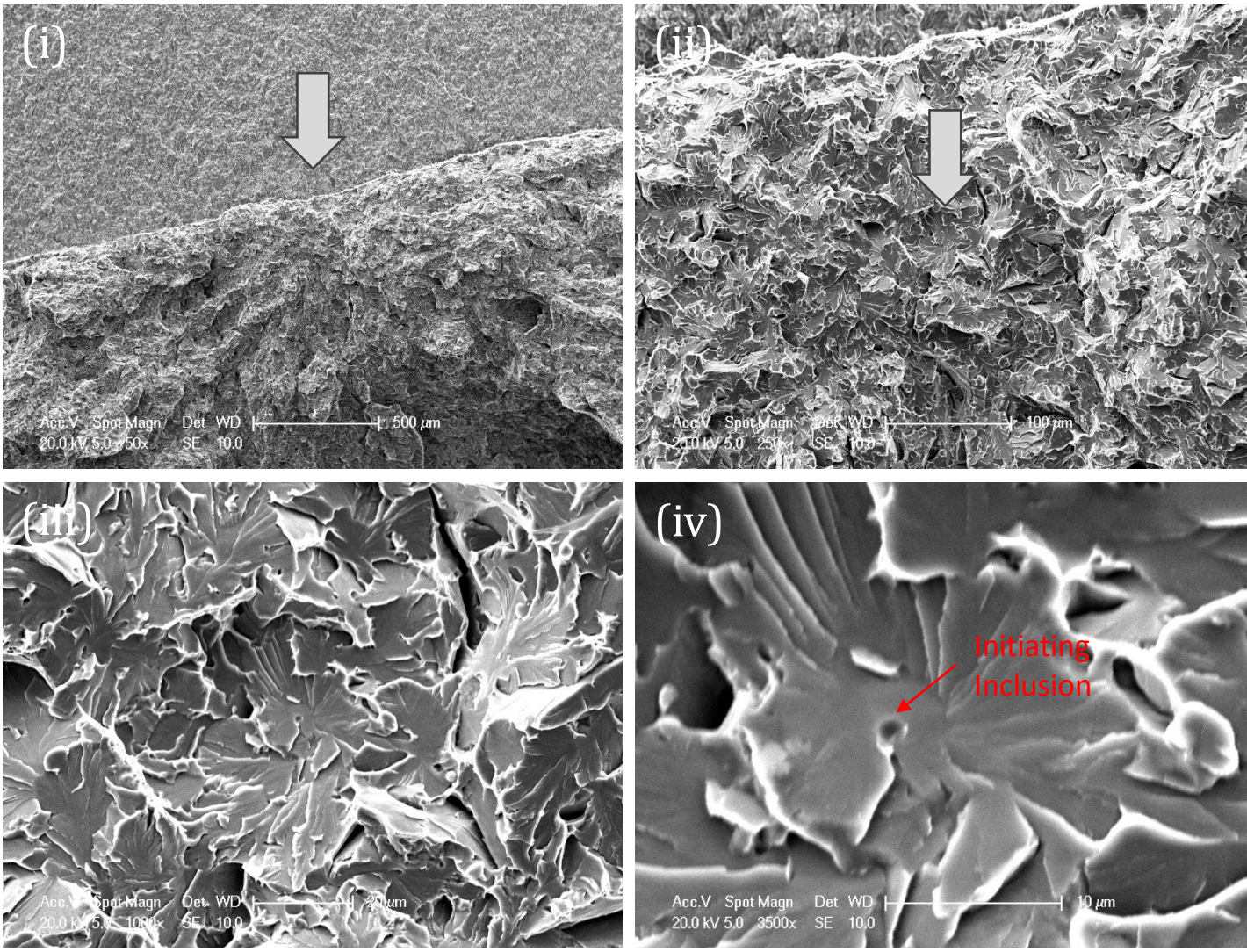


Figure 6-25 (c). Fracture Initiation at matching side (B) of the sharp-cracked specimen CT HT2-22, test temperature of -120 °C. A sequential magnification of the red-framed area at (i) 50x, (ii) 250x, (iii) 1000x, and (iv) 3500x are shown. Fractographic analysis reveals inclusion cracking as the initiation mechanism, with the inclusion's equivalent diameter at 1.6 µm and the initial facet's equivalent diameter at 39 µm.

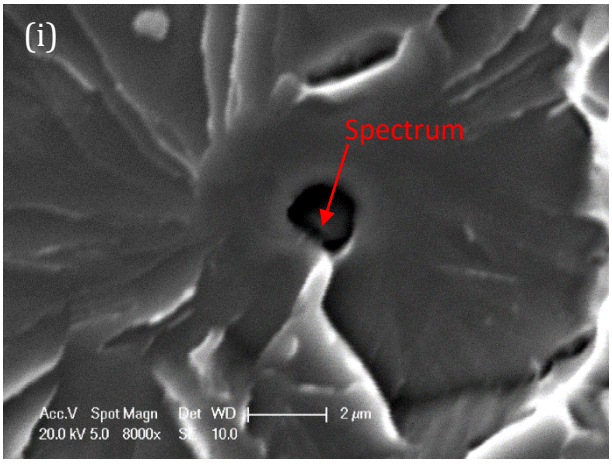


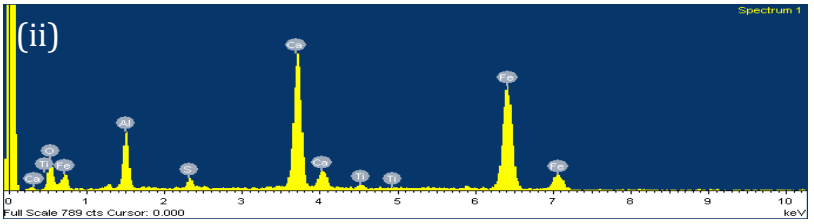


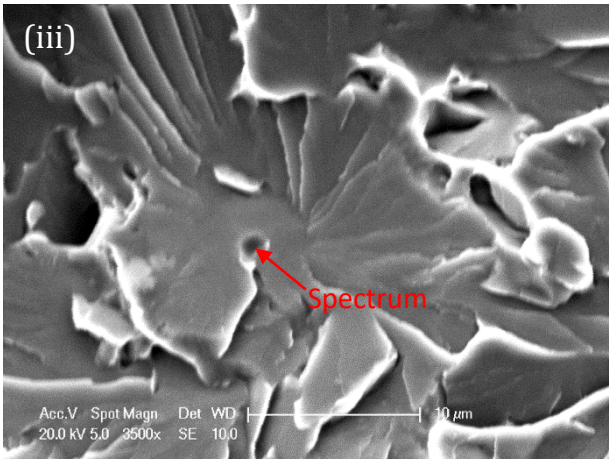


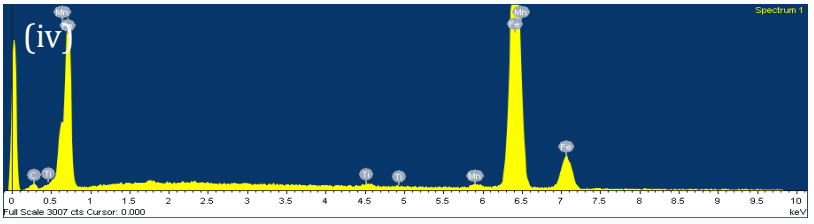


Figure 6-25 (d). Cleavage initiation point (i) and (iii) from matching halves of fracture surfaces of sharp-cracked specimen CT HT2-22 tested at -120 °C with their corresponding EDX spectrums (ii) and (iv) respectively.

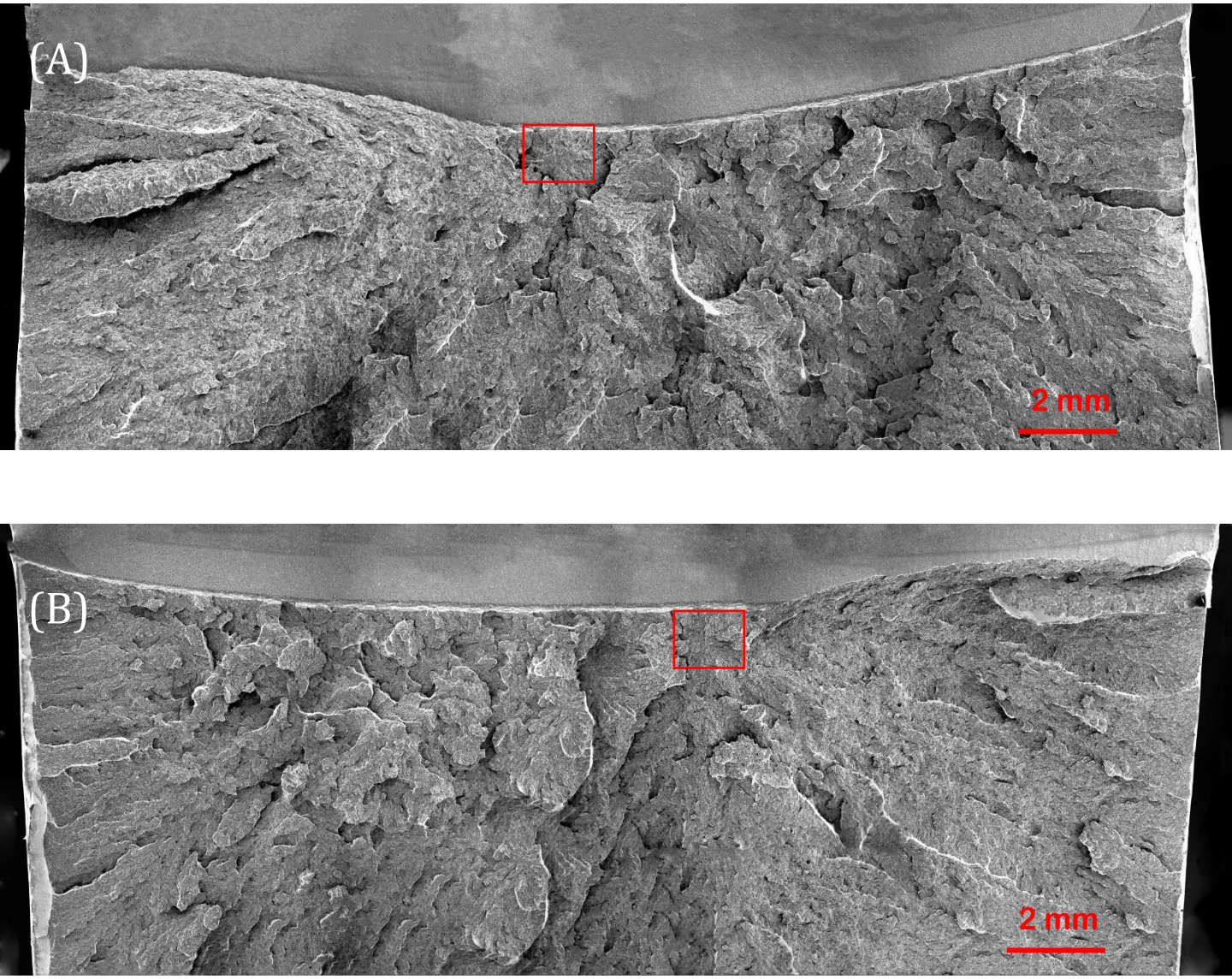


Figure 6-26 (a). Overview of fracture surfaces on a sharp-cracked specimen, designated CT HT1-01, tested at -100 °C. Red frames on matching halves (A) and (B) denote the most probable fracture initiation areas. Test results: Critical J-integral (Jc) value of 217.6 $kJ/m^2$, crack tip opening displacement (CTOD) of 0.164 mm, local cleavage fracture stress of 2212 MPa (n=0.1), fracture initiation distance (Xo) of 655 µm, and an average stable crack extension of 70 µm.

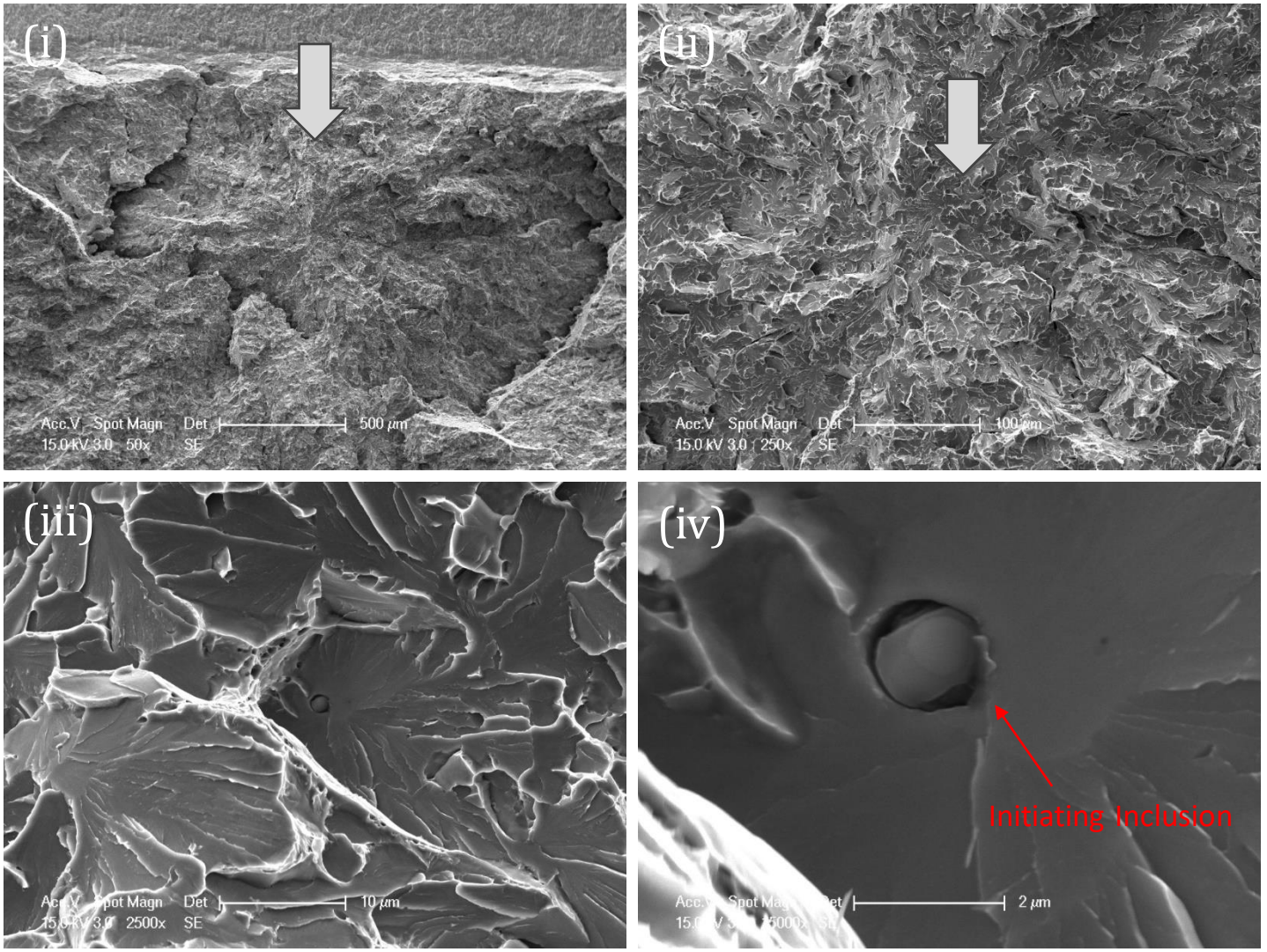


Figure 6-26 (b). Fracture Initiation at side (A) of the sharp-cracked specimen CT HT1-01, test temperature of -100 °C. A sequential magnification of the red-framed area at (i) 50x, (ii) 250x, (iii) 2500x, and (iv) 15000x are shown. Fractographic analysis reveals inclusion decohesion as the initiation mechanism, with the inclusion's equivalent diameter at 1.1 µm and the initial facet's equivalent diameter at 24 µm.

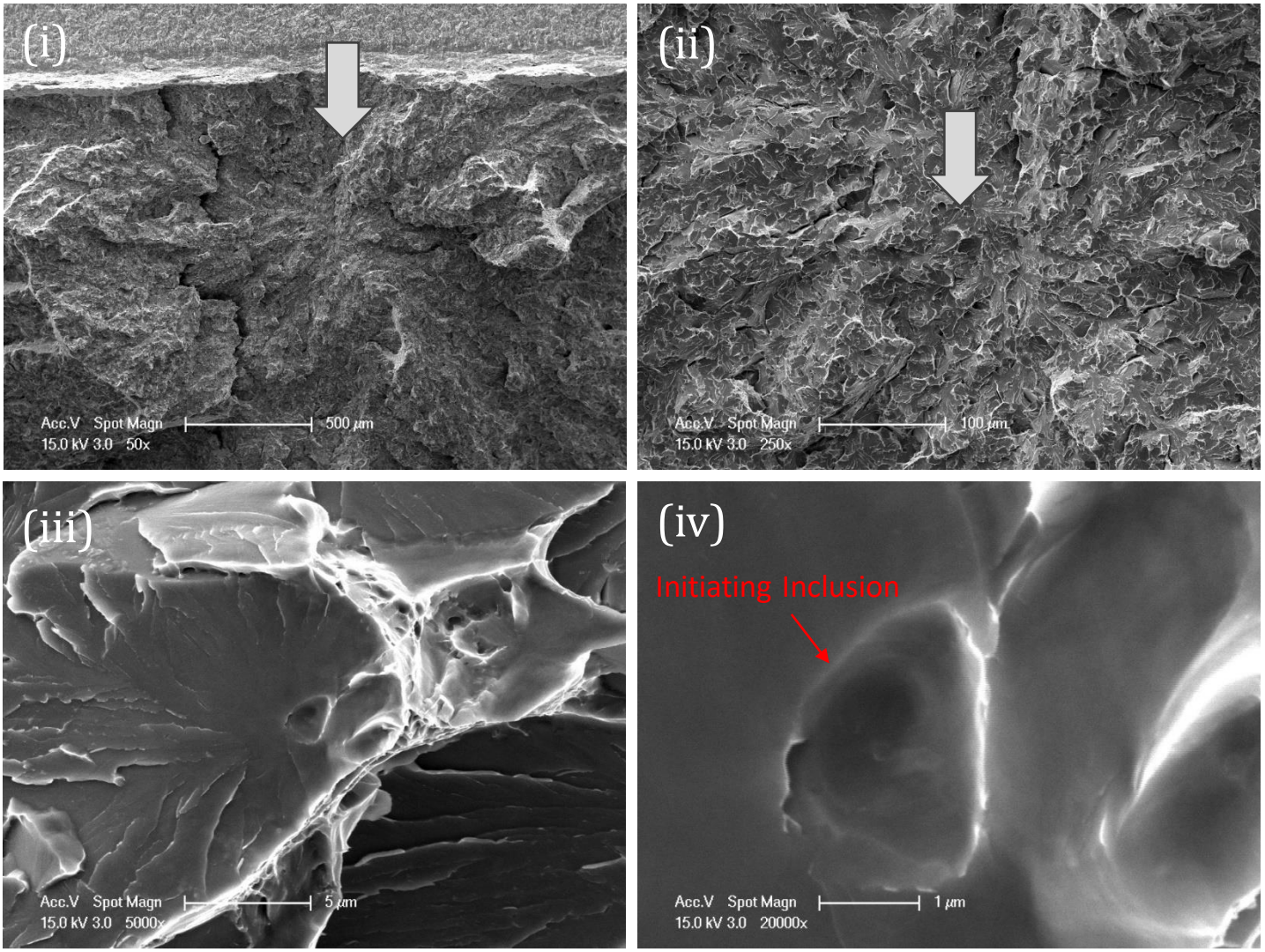


Figure 6-26 (c). Fracture Initiation at matching side (B) of the sharp-cracked specimen CT HT1-01, test temperature of -100 °C. A sequential magnification of the red-framed area at (i) 50x, (ii) 250x, (iii) 5000x, and (iv) 20000x are shown. Fractographic analysis reveals inclusion decohesion as the initiation mechanism, with the inclusion's equivalent diameter at 1.1 µm and the initial facet's equivalent diameter at 24 µm.

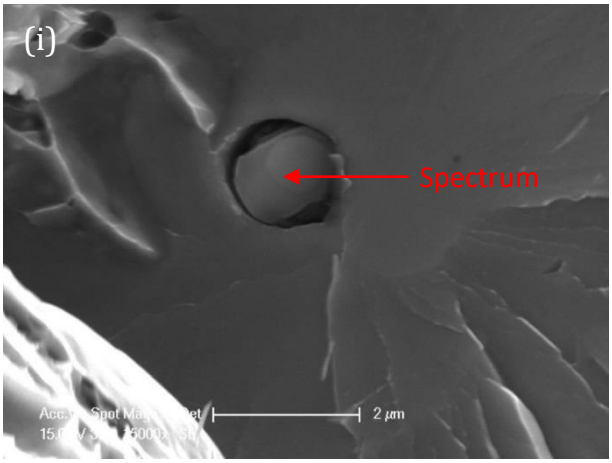


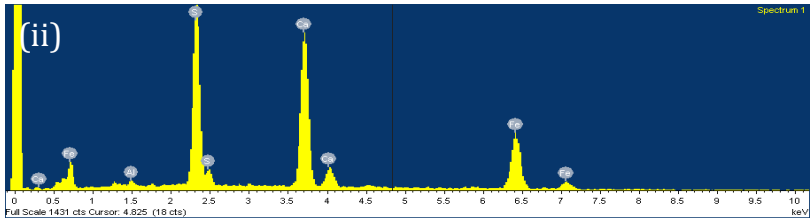


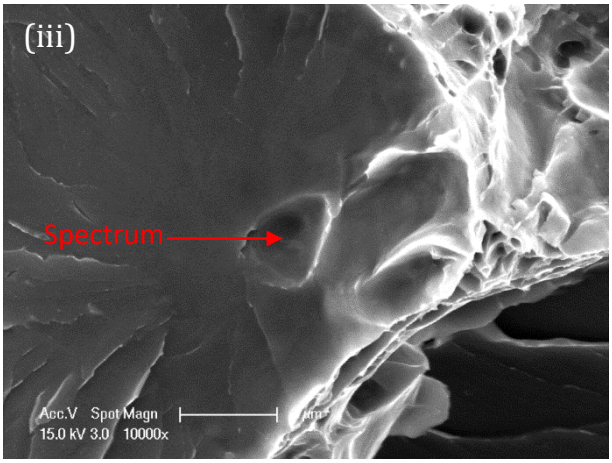


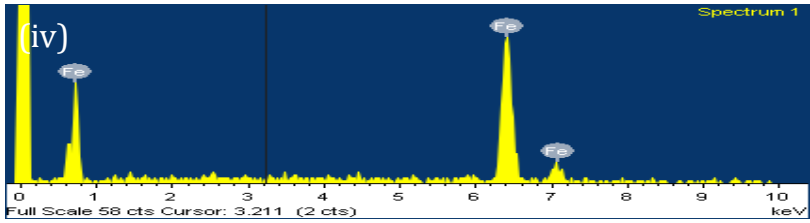


Figure 6-26 (d). Cleavage initiation point (i) and (iii) from matching halves of fracture surfaces of sharp-cracked specimen CT HT1-01 tested at -100 °C with their corresponding EDX spectrums (ii) and (iv) respectively.

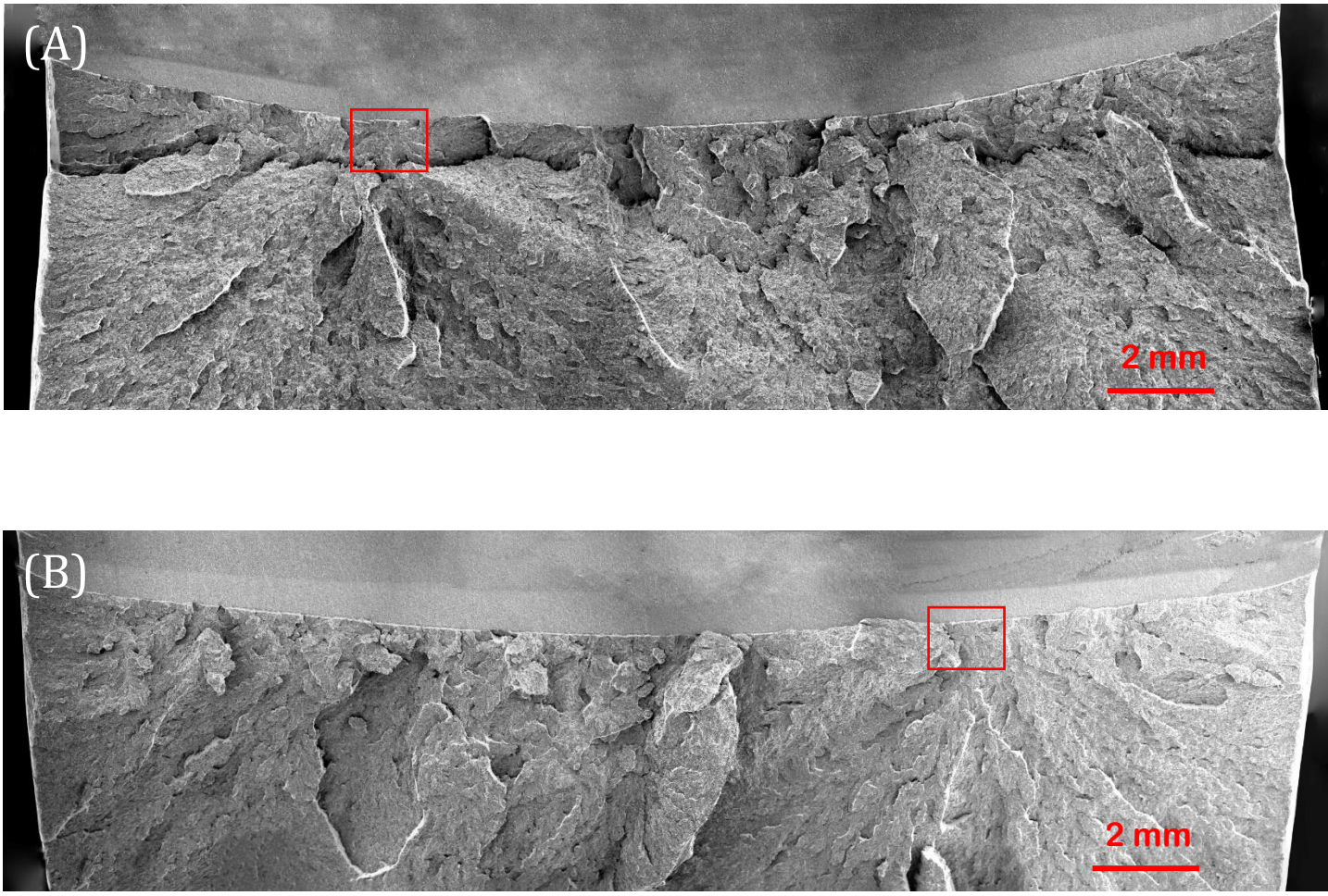


Figure 6-27 (a). Overview of fracture surfaces on a sharp-cracked specimen, designated CT HT1-07, tested at -100 °C. Red frames on matching halves (A) and (B) denote the most probable fracture initiation areas. Test results: Critical J-integral (Jc) value of 57.7 $kJ/m^2$, crack tip opening displacement (CTOD) of 0.044 mm, local cleavage fracture stress of 2303 MPa (n=0.1), fracture initiation distance (Xo) of 135 µm, and an average stable crack extension of 21 µm.

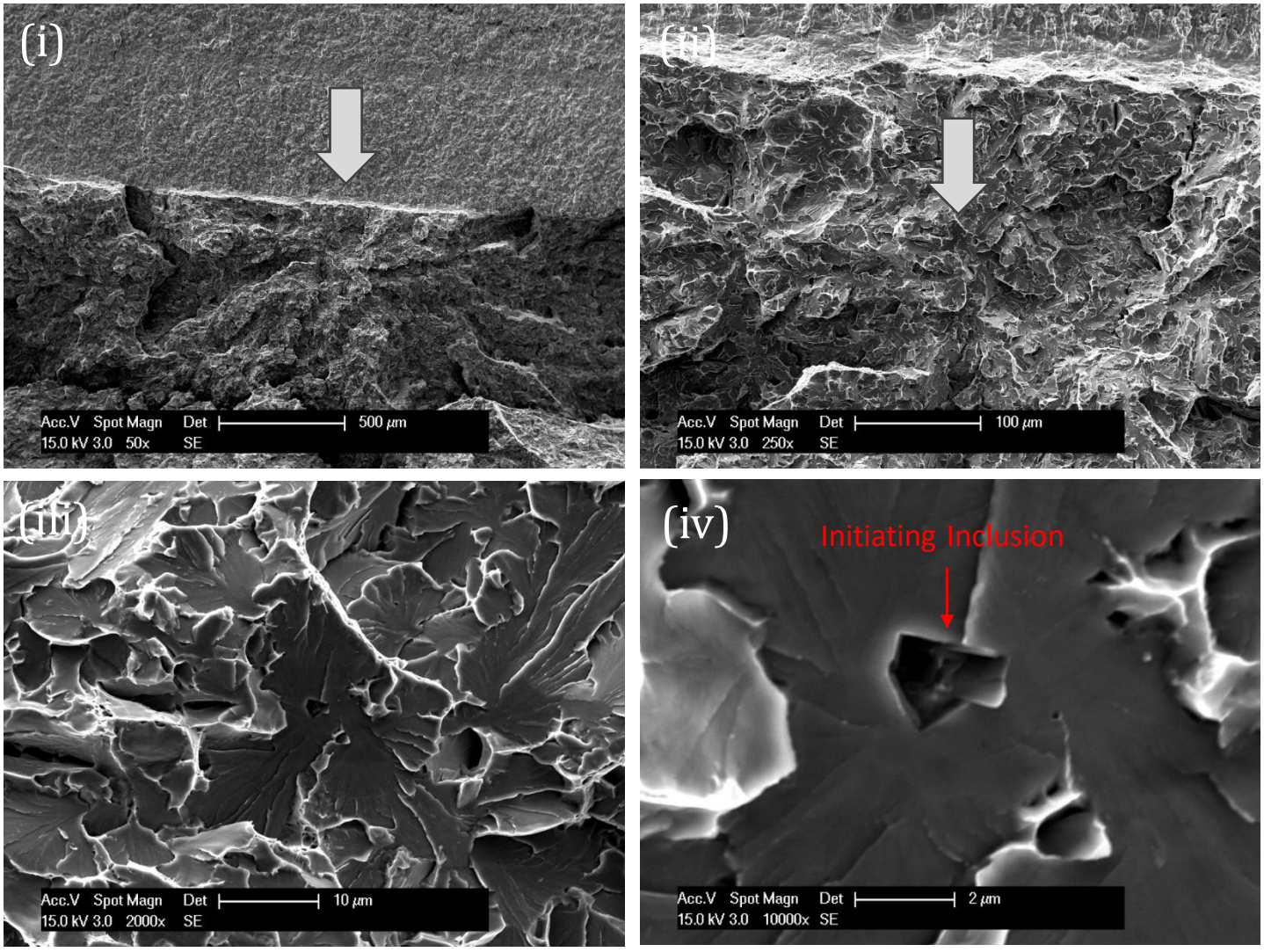


Figure 6-27 (b). Fracture Initiation at side (A) of the sharp-cracked specimen CT HT1-07, test temperature of -100 °C. A sequential magnification of the red-framed area at (i) 50x, (ii) 250x, (iii) 2000x, and (iv) 10000x are shown. Fractographic analysis reveals inclusion cracking as the initiation mechanism, with the inclusion's equivalent diameter at 1.8 µm and the initial facet's equivalent diameter at 26 µm.

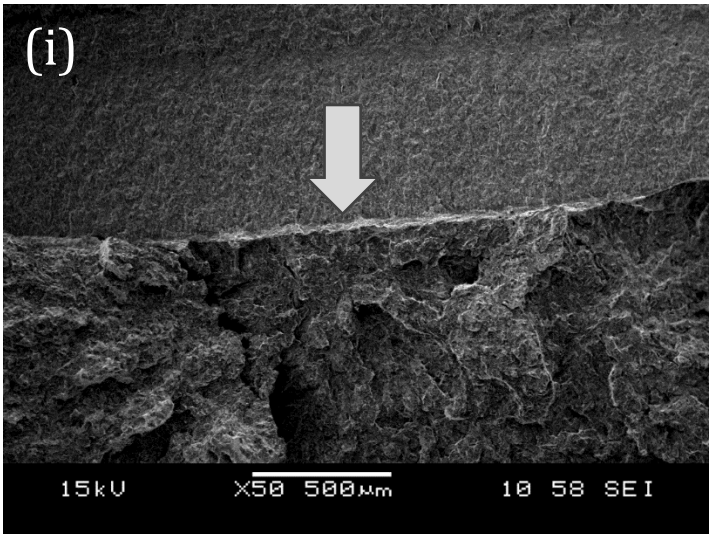


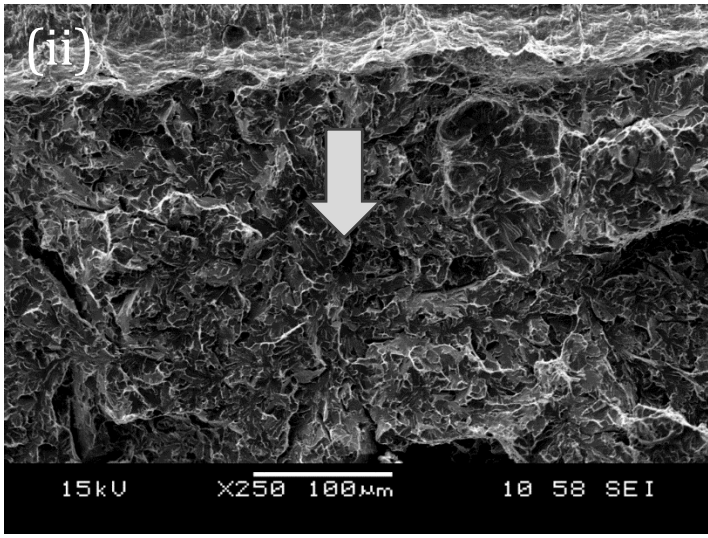


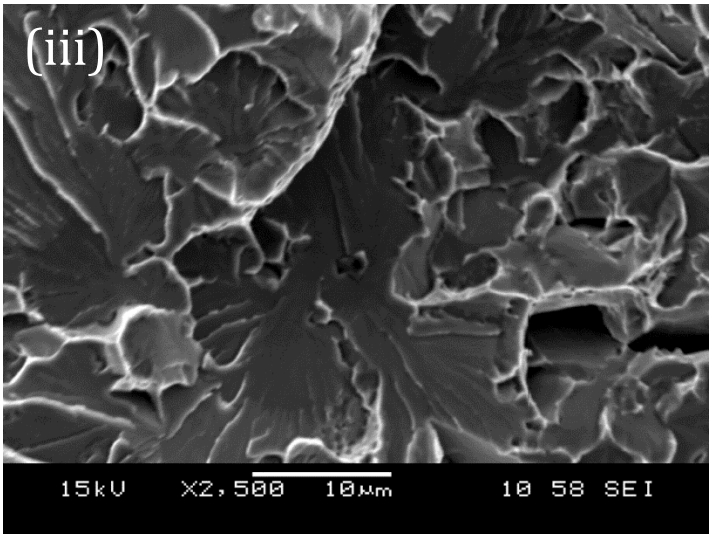


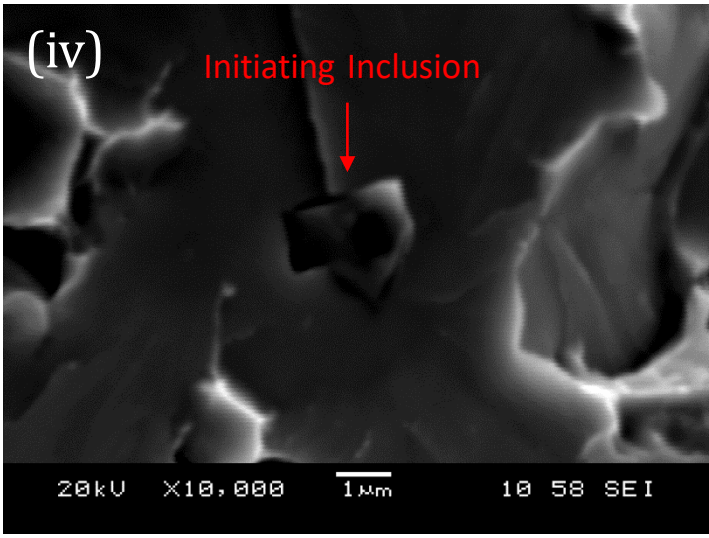


Figure 6-27 (c). Fracture Initiation at matching side (B) of the sharp-cracked specimen CT HT1-07, test temperature of -100 °C. A sequential magnification of the red-framed area at (i) 50x, (ii) 250x, (iii) 2500x, and (iv) 10000x are shown. Fractographic analysis reveals inclusion cracking as the initiation mechanism, with the inclusion's equivalent diameter at 1.8 µm and the initial facet's equivalent diameter at 26 µm.

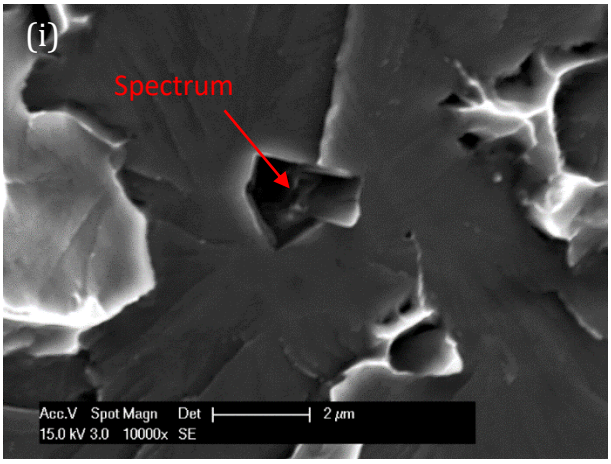


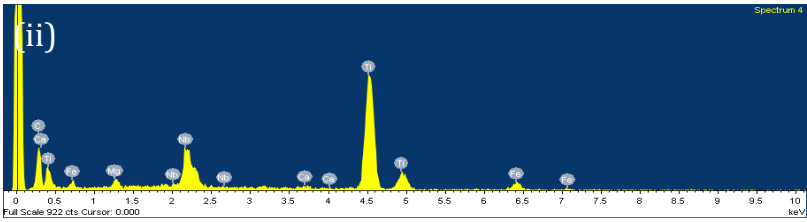


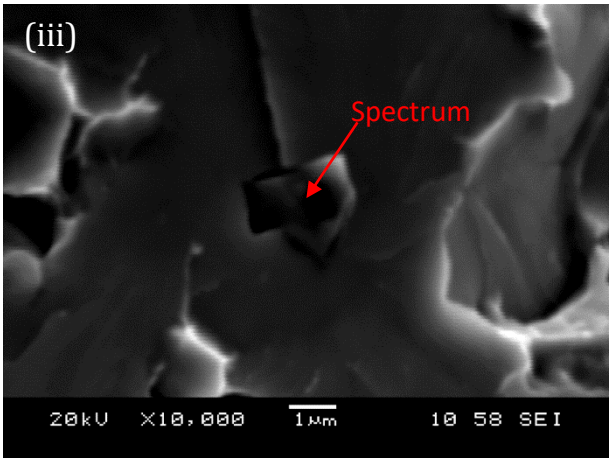


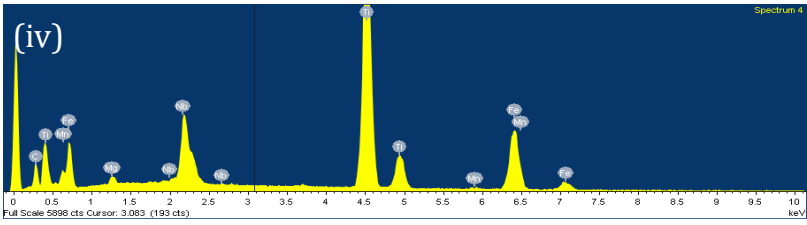


Figure 6-27 (d). Cleavage initiation point (i) and (iii) from matching halves of fracture surfaces of sharp-cracked specimen CT HT1-07 tested at -100 °C with their corresponding EDX spectrums (ii) and (iv) respectively.

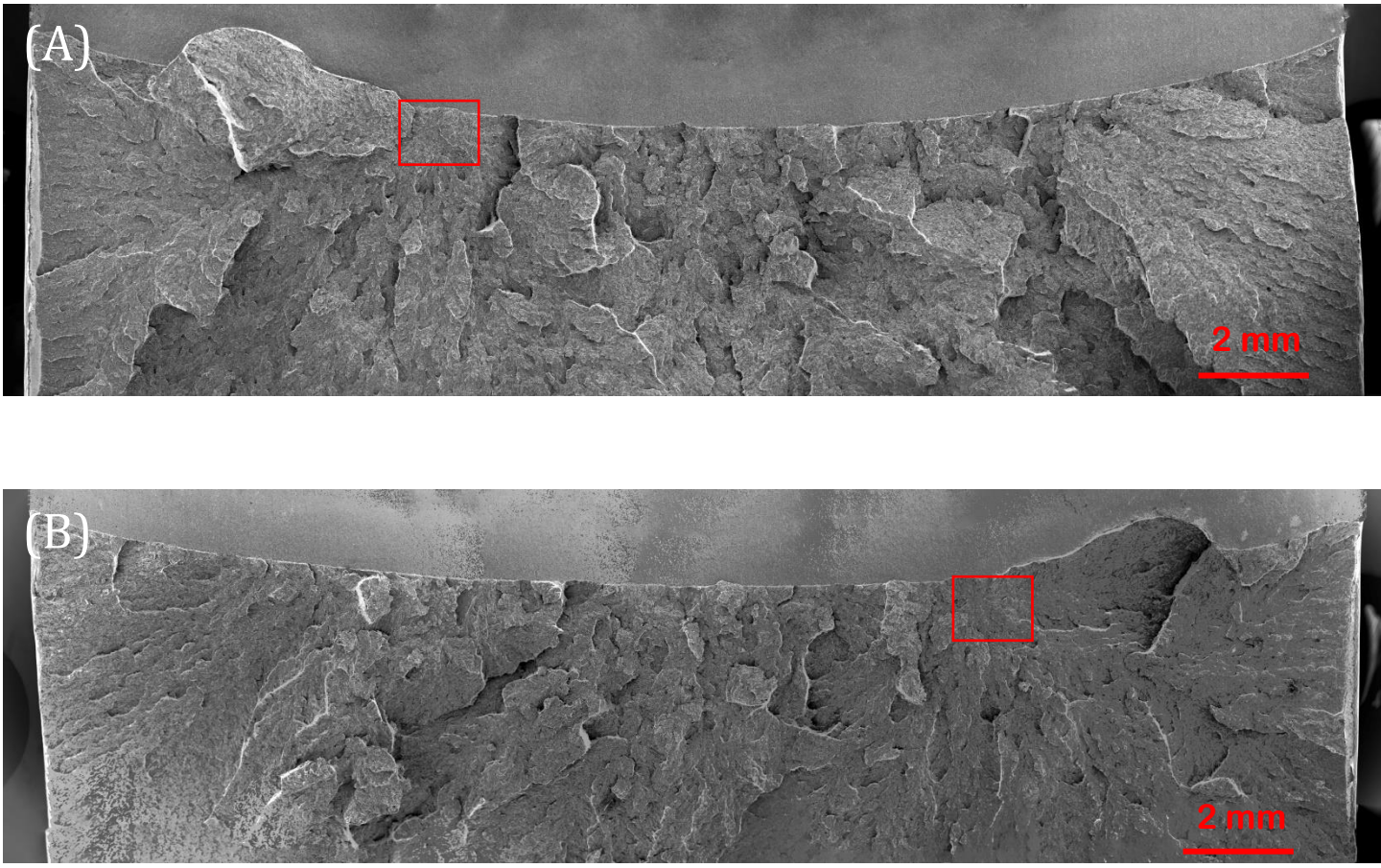


Figure 6-28 (a). Overview of fracture surfaces on a sharp-cracked specimen, designated CT HT1-18, tested at -100 °C. Red frames on matching halves (A) and (B) denote the most probable fracture initiation areas. Test results: Critical J-integral (Jc) value of 38.6 $kJ/m^2$, crack tip opening displacement (CTOD) of 0.029 mm, local cleavage fracture stress of 1870 MPa (n=0.1), fracture initiation distance (X0) of 432 µm, and an average stable crack extension of 8 µm.

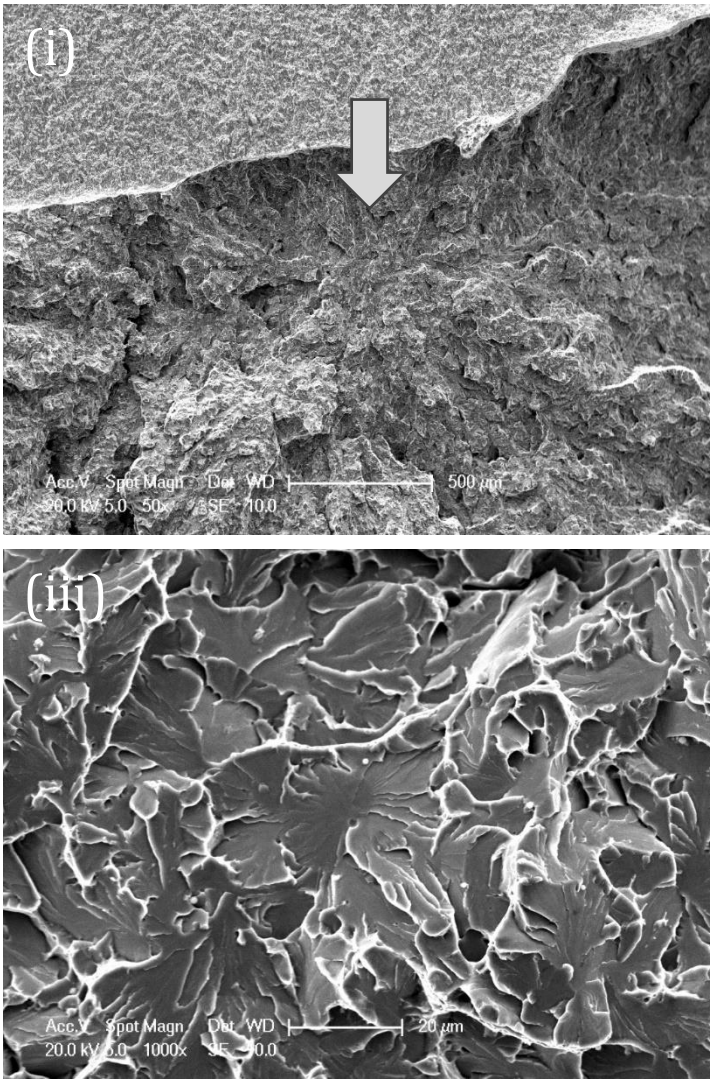


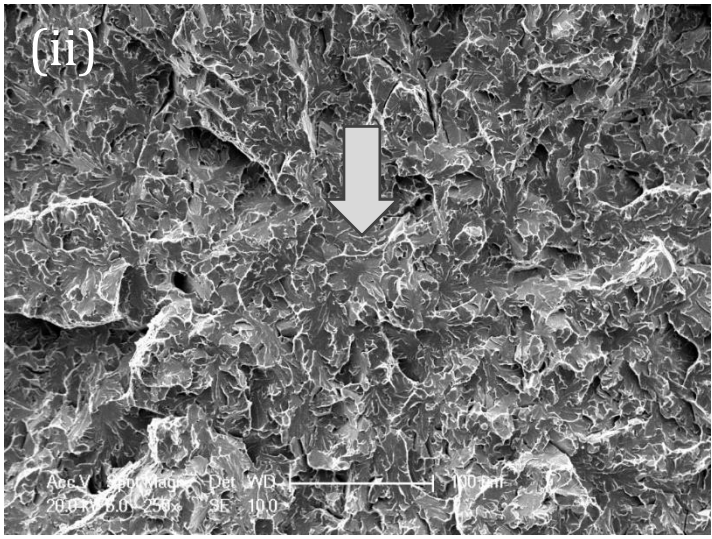





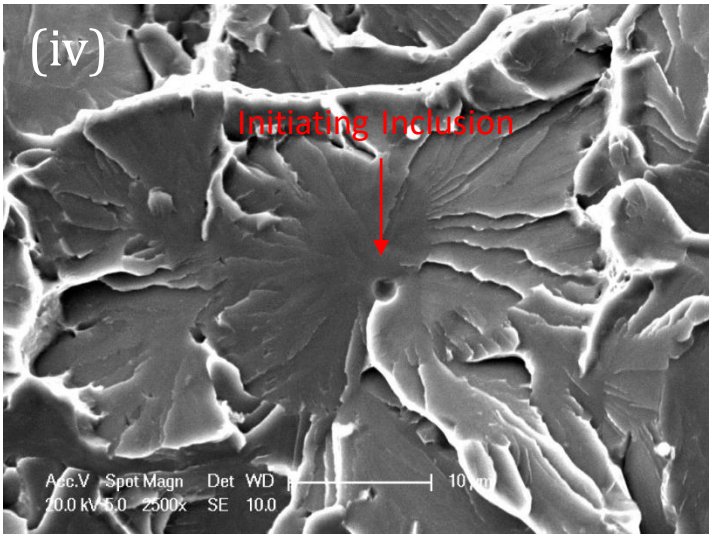


Figure 6-28 (b). Fracture Initiation at side (A) of the sharp-cracked specimen CT HT1-18, test temperature of -100 °C. A sequential magnification of the red-framed area at (i) 50x, (ii) 250x, (iii) 1000x, and (iv) 2500x are shown. Fractographic analysis reveals inclusion cracking as the initiation mechanism, with the inclusion's equivalent diameter at 1.7 µm and the initial facet's equivalent diameter at 38 µm.

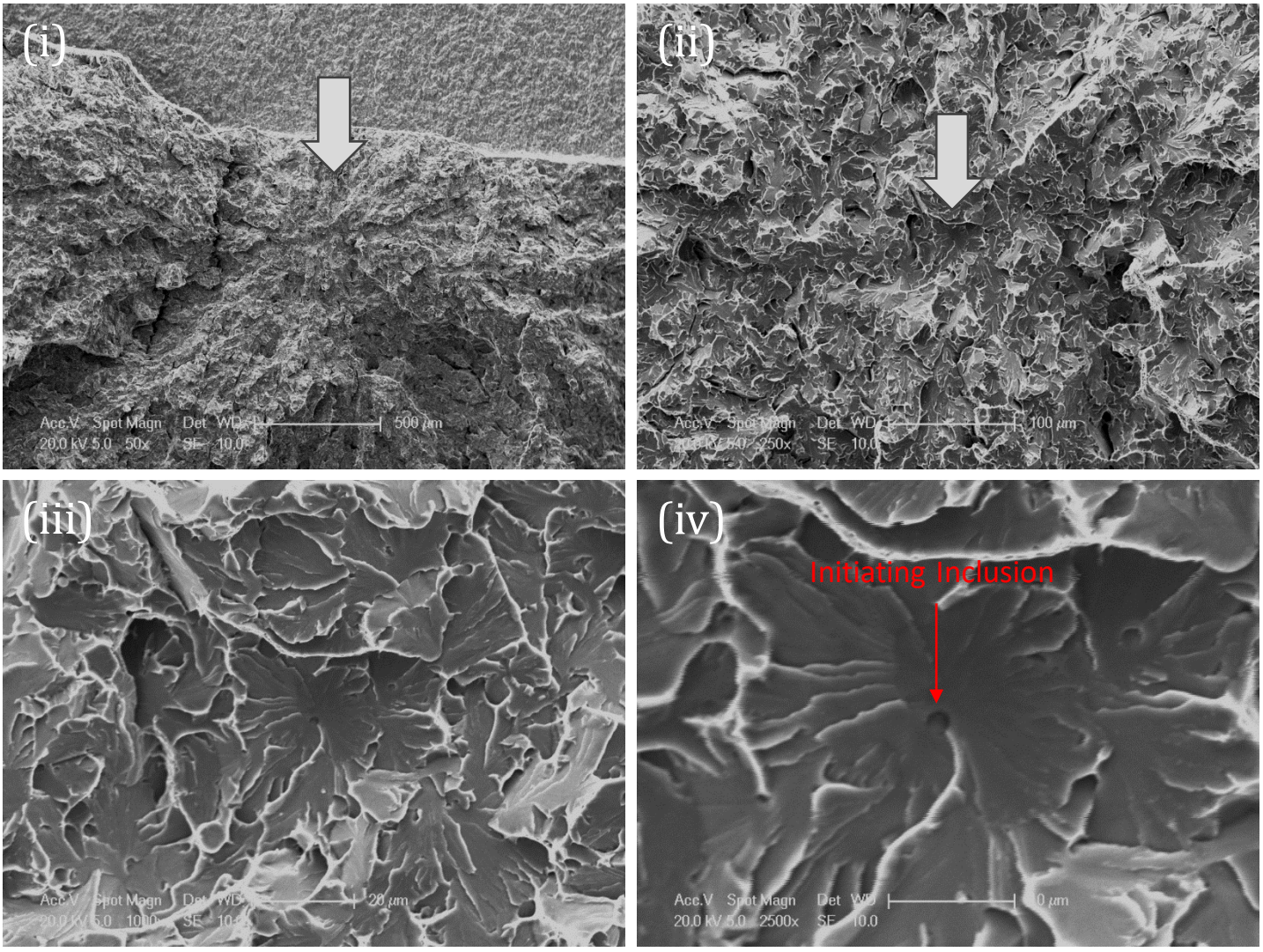


Figure 6-28 (c). Fracture Initiation at matching side (B) of the sharp-cracked specimen CT HT1-18, test temperature of -100 °C. A sequential magnification of the red-framed area at (i) 50x, (ii) 250x, (iii) 1000x, and (iv) 2500x are shown. Fractographic analysis reveals inclusion cracking as the initiation mechanism, with the inclusion's equivalent diameter at 1.7 µm and the initial facet's equivalent diameter at 38 µm.

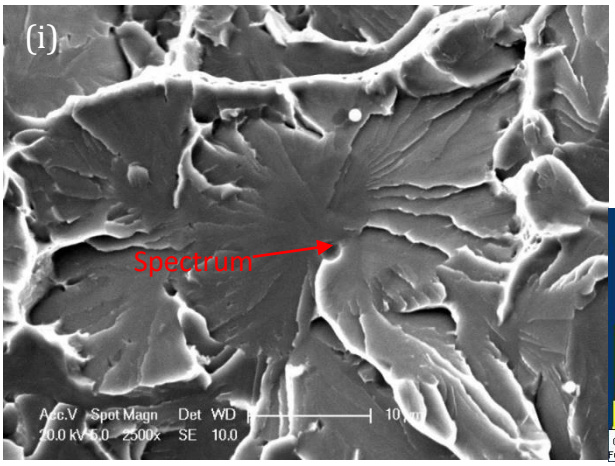


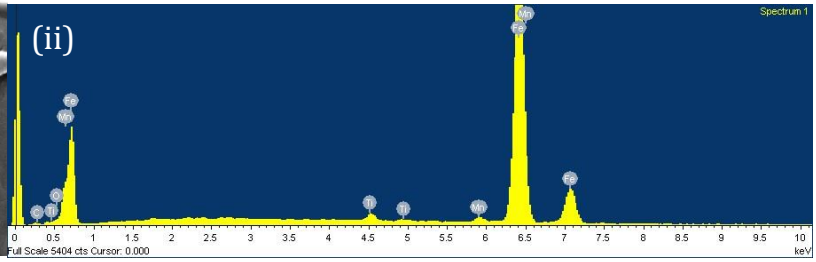


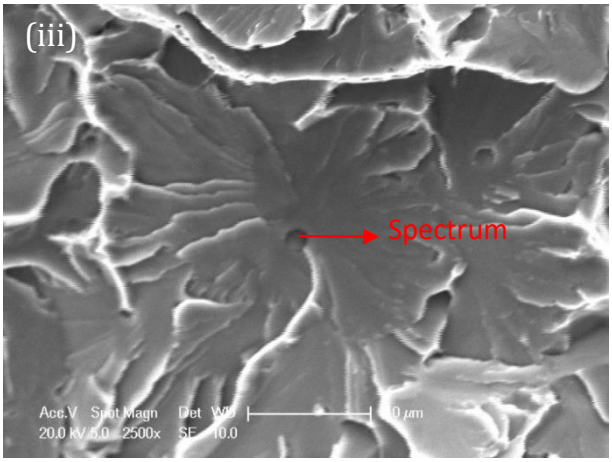


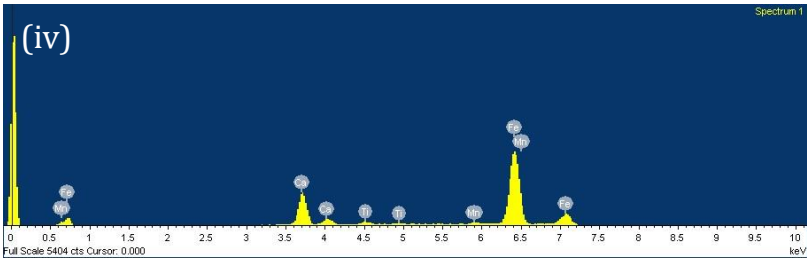


Figure 6-28 (d). Cleavage initiation point (i) and (iii) from matching halves of fracture surfaces of sharp-cracked specimen CT HT1-18 tested at -100 °C with their corresponding EDX spectrums (ii) and (iv) respectively.

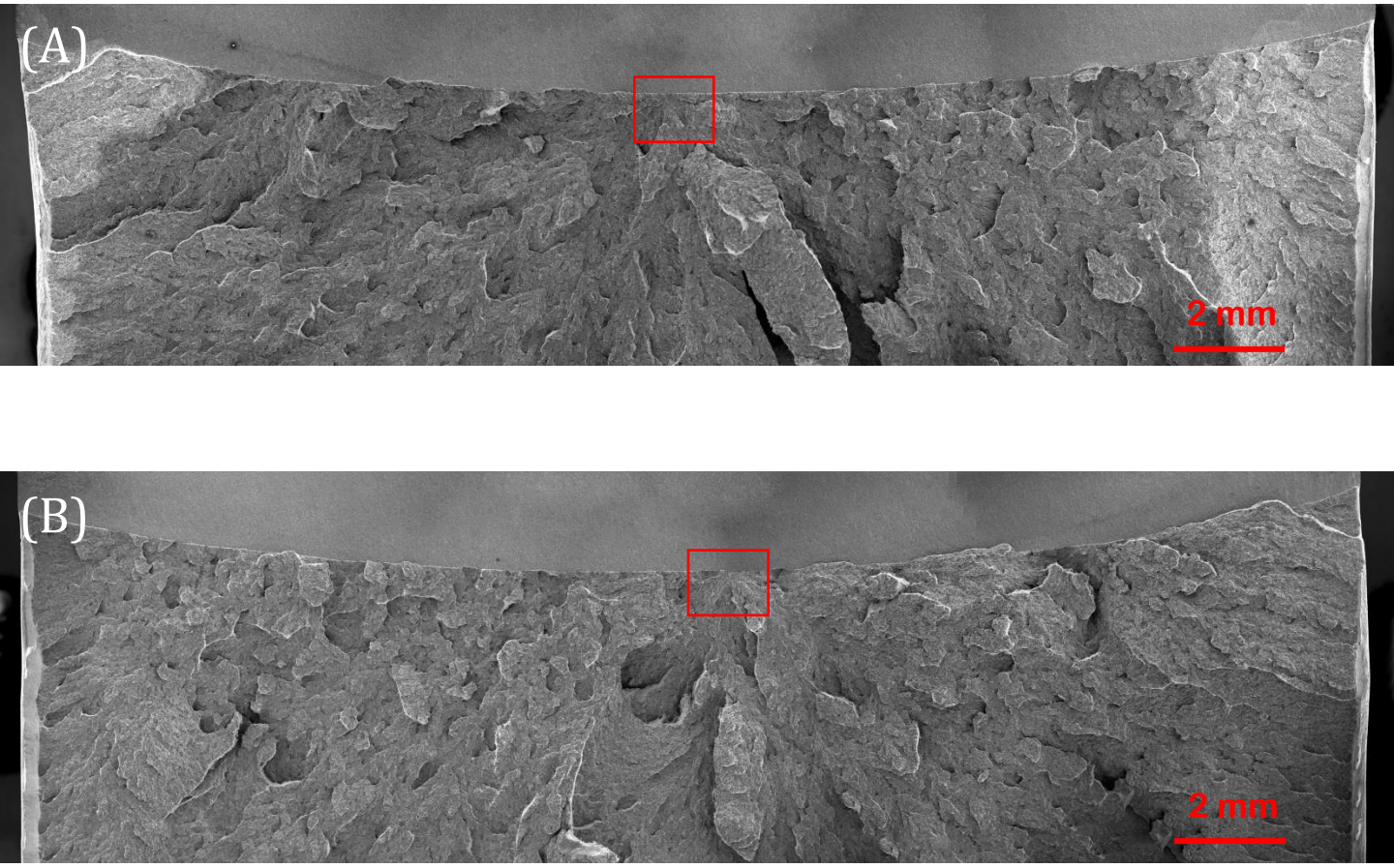





Figure 6-29 (a). Overview of fracture surfaces on a sharp-cracked specimen, designated CT HT1-25, tested at -100 °C. Red frames on matching halves (A) and (B) denote the most probable fracture initiation areas. Test results: Critical J-integral (Jc) value of 41.8 $kJ/m^2$, crack tip opening displacement (CTOD) of 0.032 mm, local cleavage fracture stress of 2285 MPa (n=0.1), fracture initiation distance (Xo) of 104 µm, and an average stable crack extension of 7 µm.

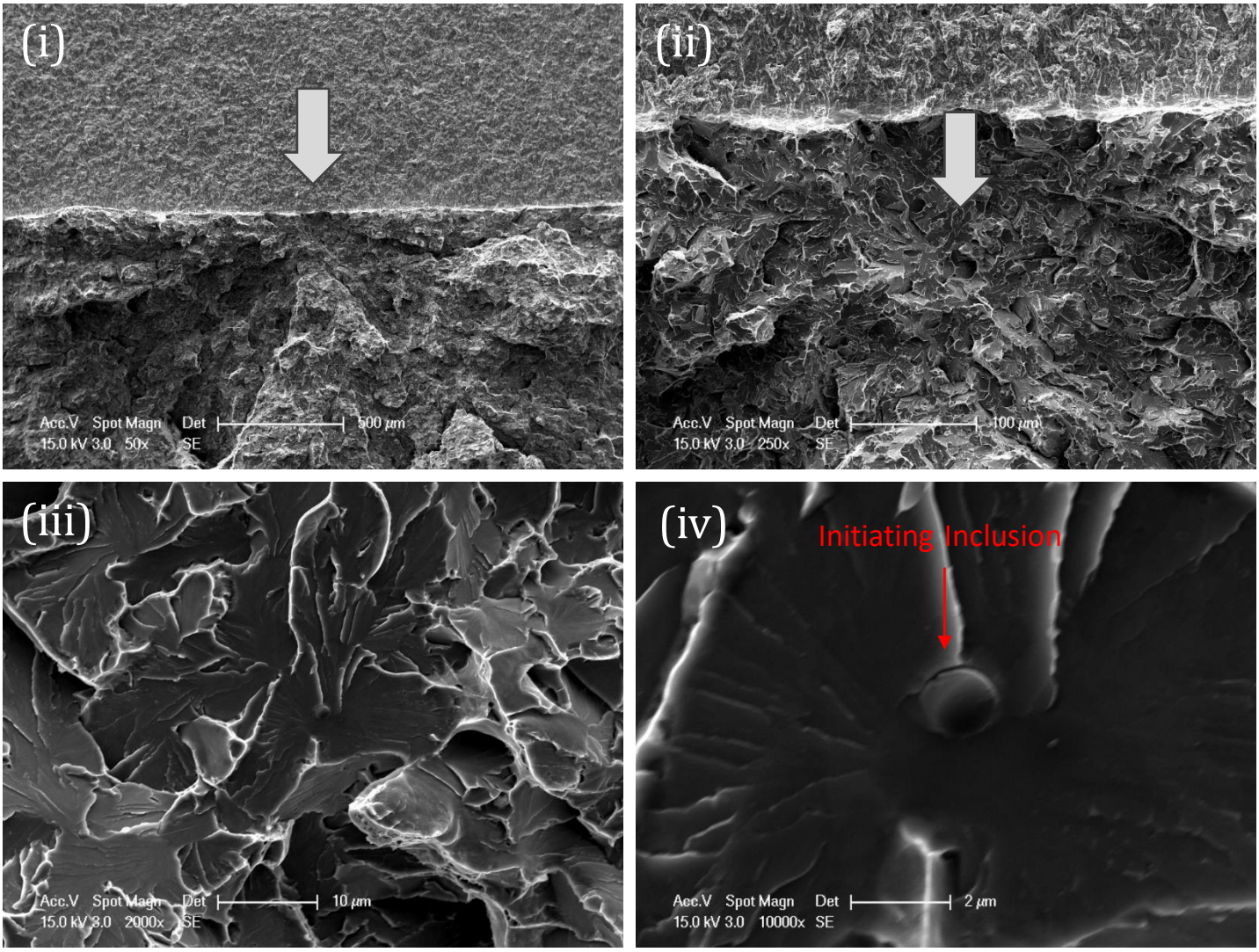


Figure 6-29 (b). Fracture Initiation at side (A) of the sharp-cracked specimen CT HT1-25, test temperature of -100 °C. A sequential magnification of the red-framed area at (i) 50x, (ii) 250x, (iii) 2000x, and (iv) 10000x are shown. Fractographic analysis reveals inclusion cracking as the initiation mechanism, with the inclusion's equivalent diameter at 1.4 µm and the initial facet's equivalent diameter at 22 µm.

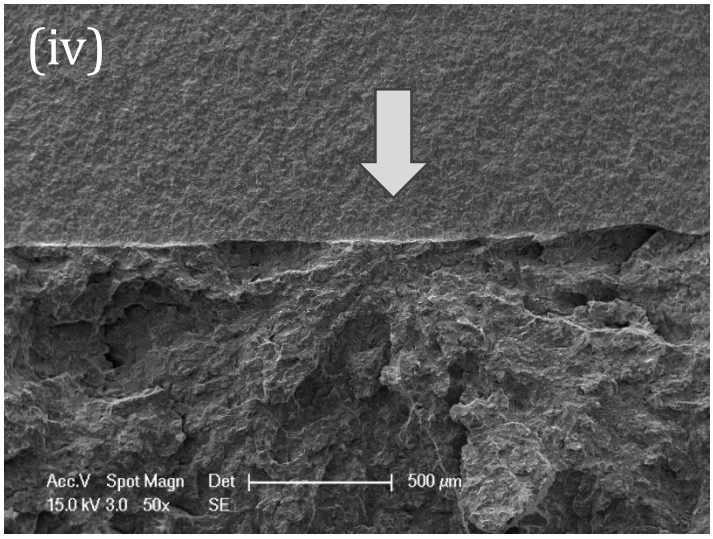


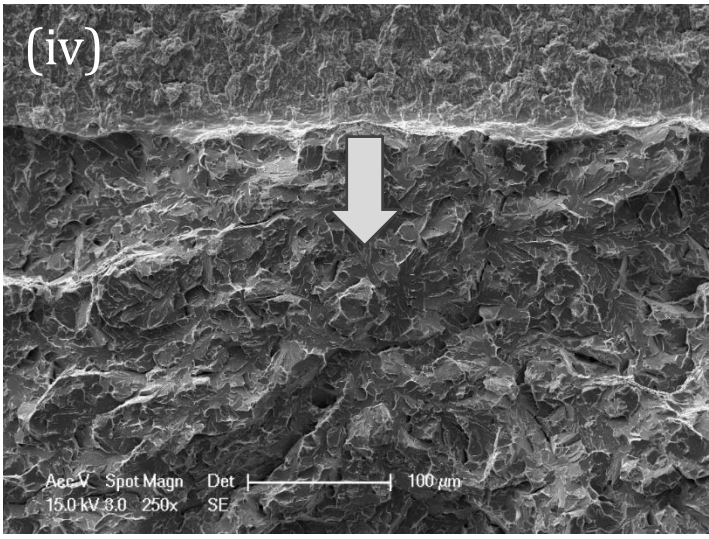


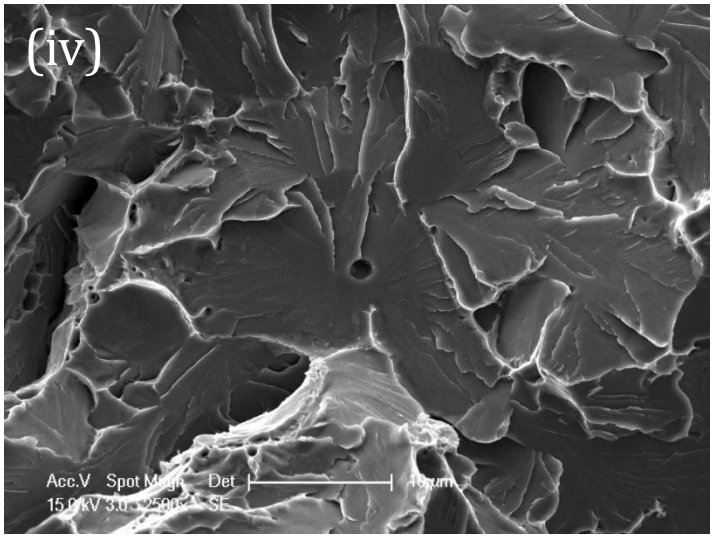


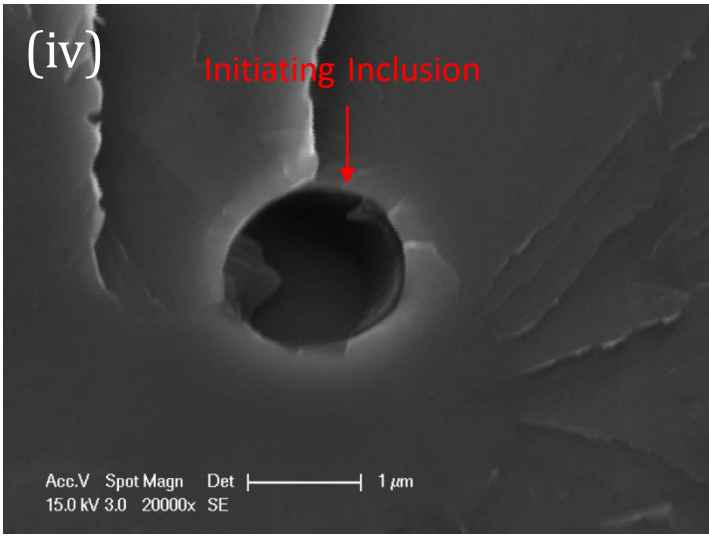


Figure 6-29 (c). Fracture Initiation at matching side (B) of the sharp-cracked specimen CT HT1-25, test temperature of -100 °C. A sequential magnification of the red-framed area at (i) 50x, (ii) 250x, (iii) 2500x, and (iv) 20000x are shown. Fractographic analysis reveals inclusion cracking as the initiation mechanism, with the inclusion's equivalent diameter at 1.4 µm and the initial facet's equivalent diameter at 22 µm.

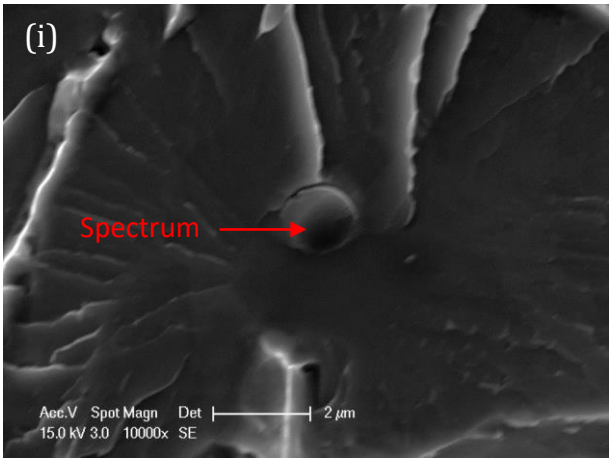


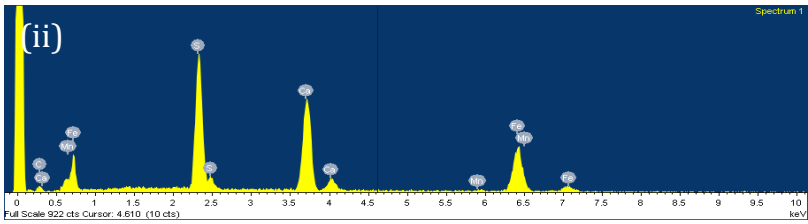


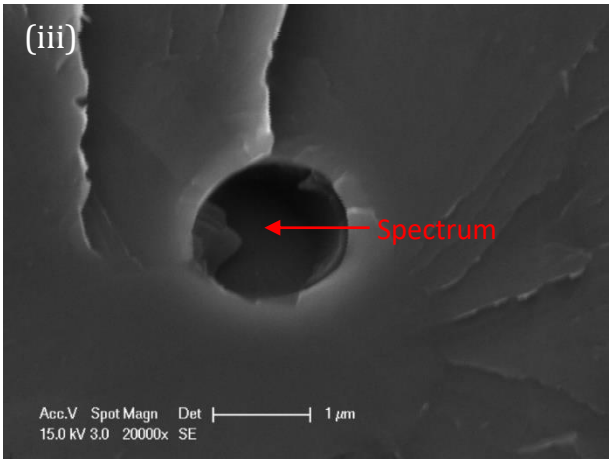


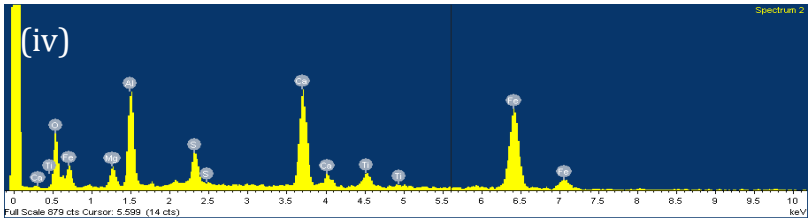


Figure 6-29 (d). Cleavage initiation point (i) and (iii) from matching halves of fracture surfaces of sharp-cracked specimen CT HT1-25 tested at -100 °C with their corresponding EDX spectrums (ii) and (iv) respectively.

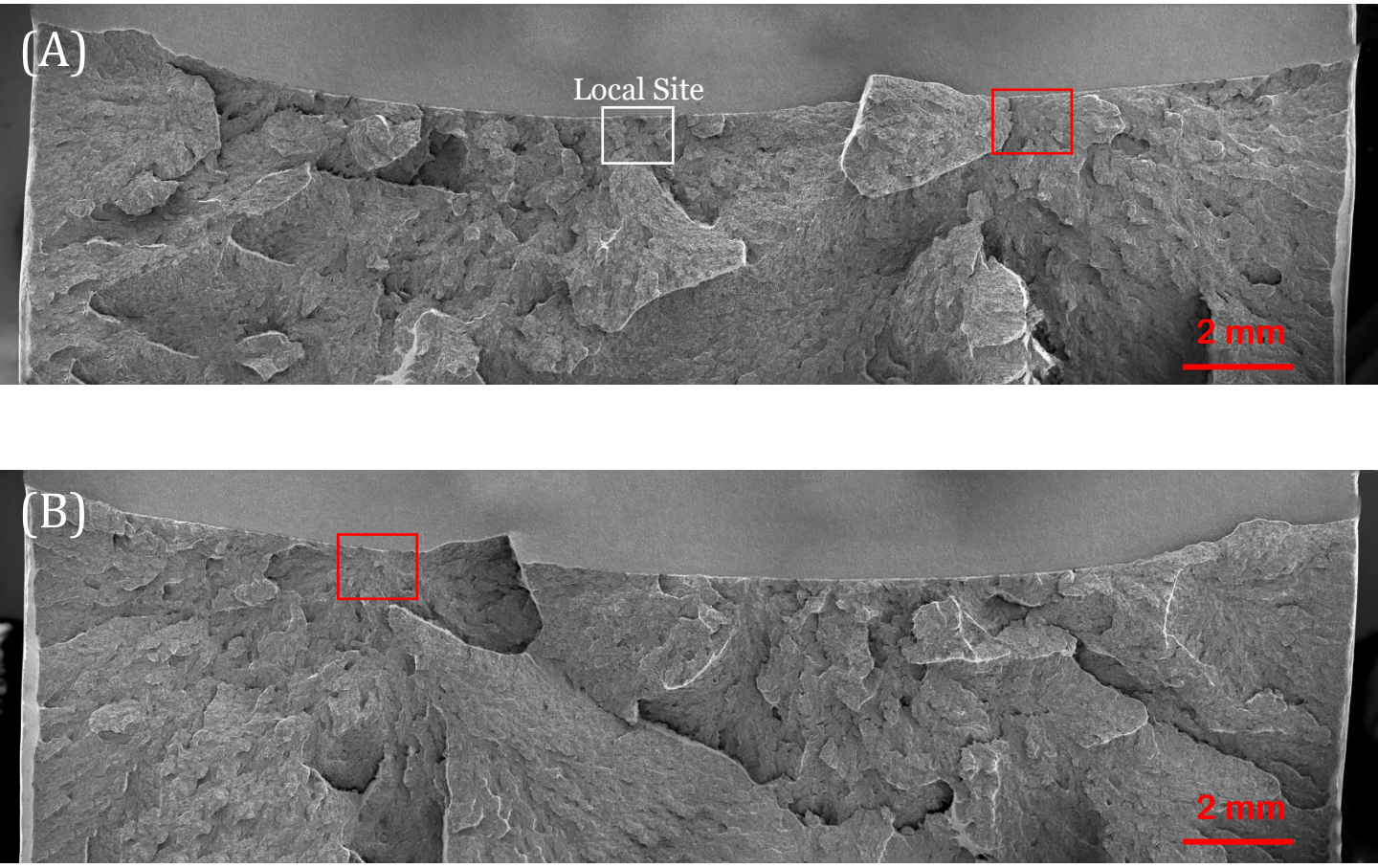


Figure 6-30 (a). Overview of fracture surfaces on a sharp-cracked specimen, designated CT HT1-26, tested at -100 °C. Red frames on matching halves (A) and (B) denote the most probable fracture initiation areas. White frame indicating local cleavage area. Test results: Critical J-integral (Jc) value of 59.4 $kJ/m^2$, crack tip opening displacement (CTOD) of 0.045 mm, local cleavage fracture stress of 2261 MPa (n=0.1), fracture initiation distance (Xo) of 160 µm, and an average stable crack extension of 19 µm.

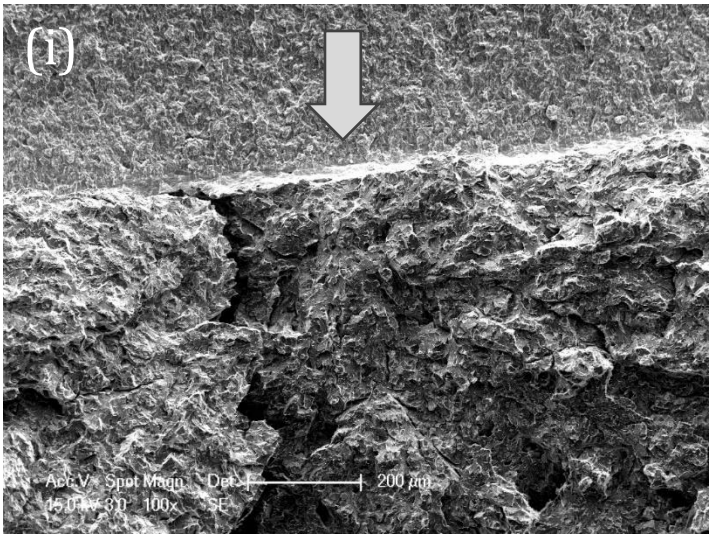


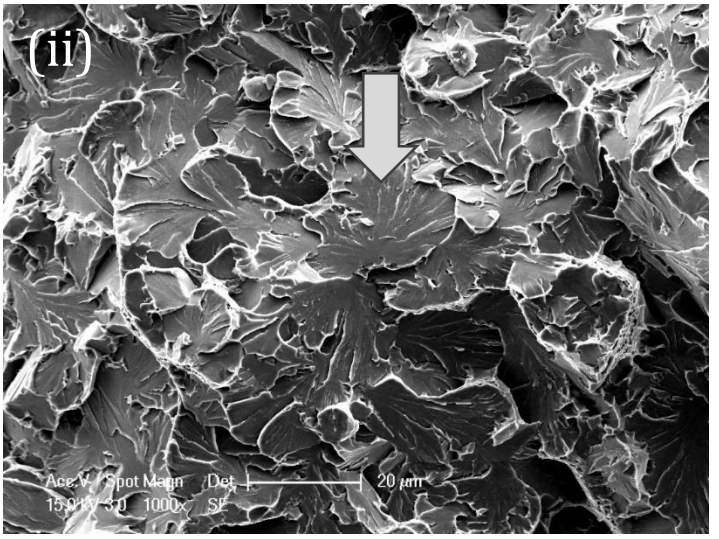


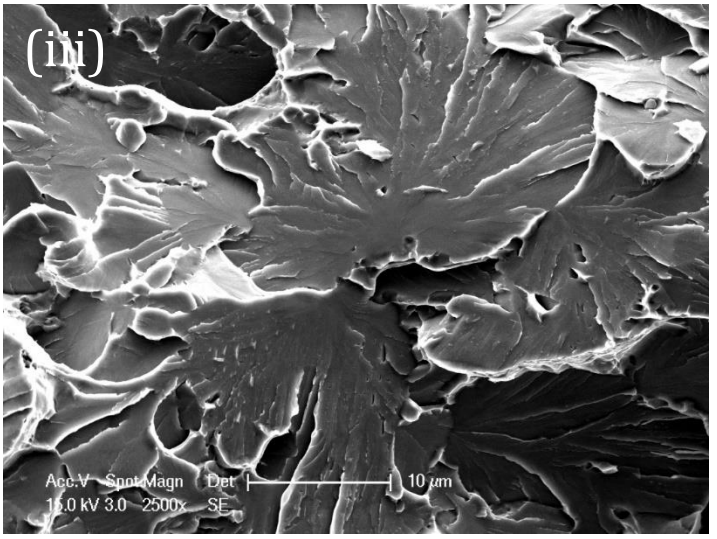


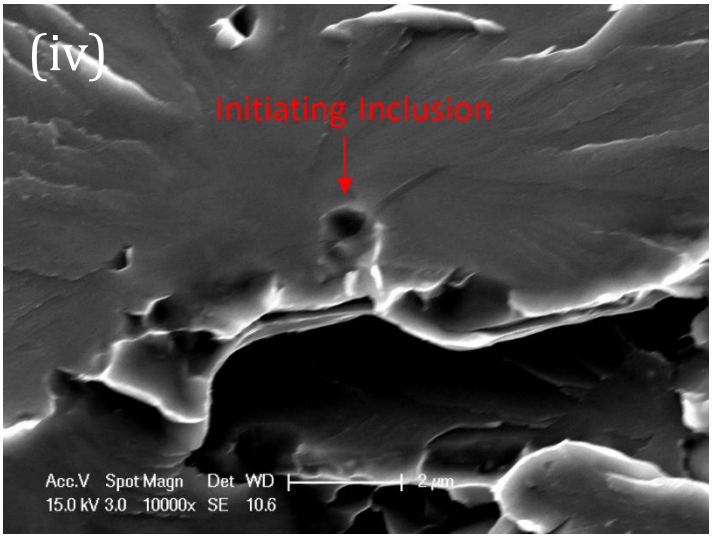


Figure 6-30 (b). Fracture Initiation at side (A) of the sharp-cracked specimen CT HT1-26, test temperature of -100 °C. A sequential magnification of the red-framed area at (i) 100x, (ii) 1000x, (iii) 2500x, and (iv) 10000x are shown. Fractographic analysis reveals inclusion cracking as the initiation mechanism, with the inclusion's equivalent diameter at 0.7 µm and the initial facet's equivalent diameter at 28 µm.

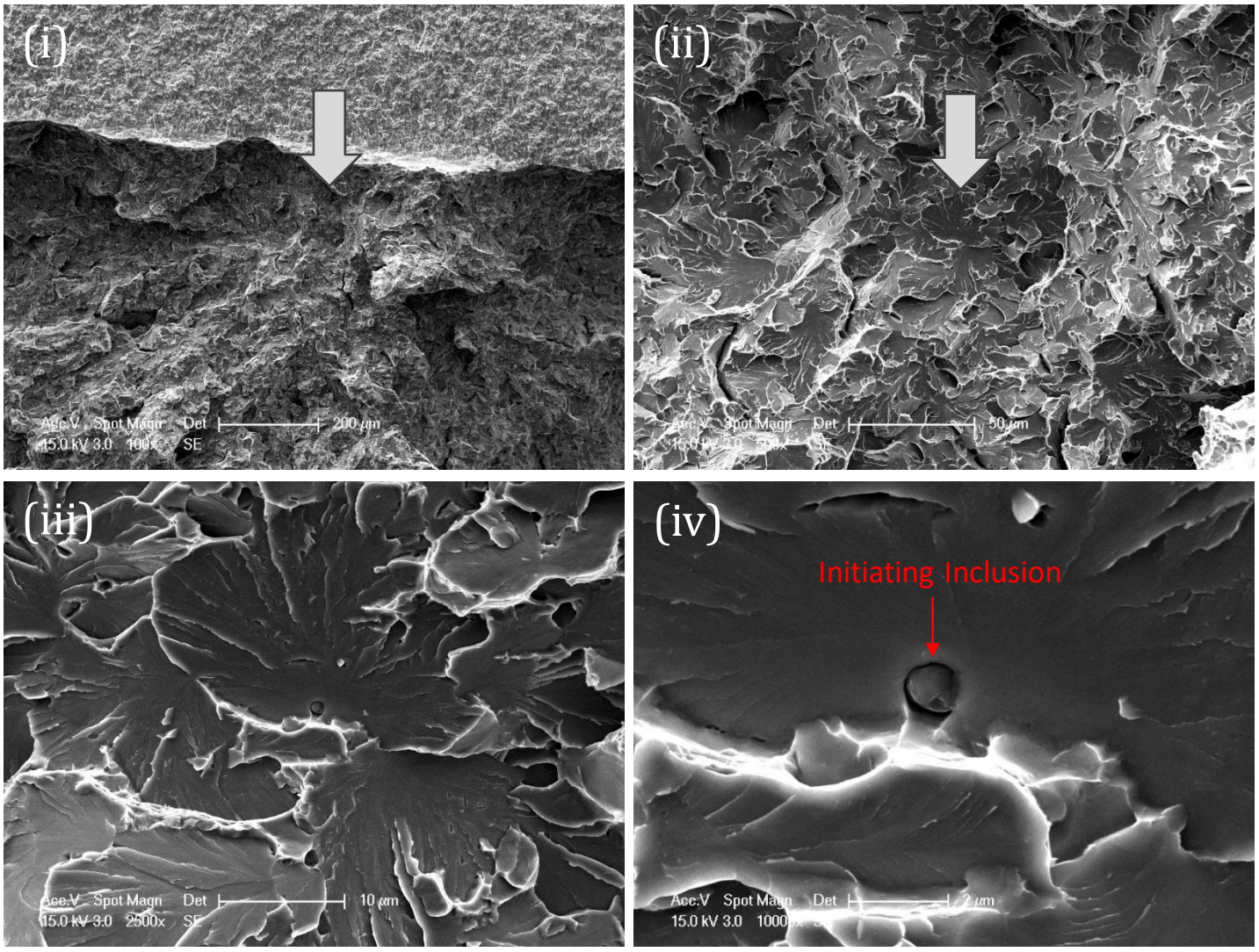


Figure 6-30 (c). Fracture Initiation at matching side (B) of the sharp-cracked specimen CT HT1-26, test temperature of -100 °C. A sequential magnification of the red-framed area at (i) 100x, (ii) 500x, (iii) 2500x, and (iv) 10000x are shown. Fractographic analysis reveals inclusion cracking as the initiation mechanism, with the inclusion's equivalent diameter at 0.7 µm and the initial facet's equivalent diameter at 28 µm.

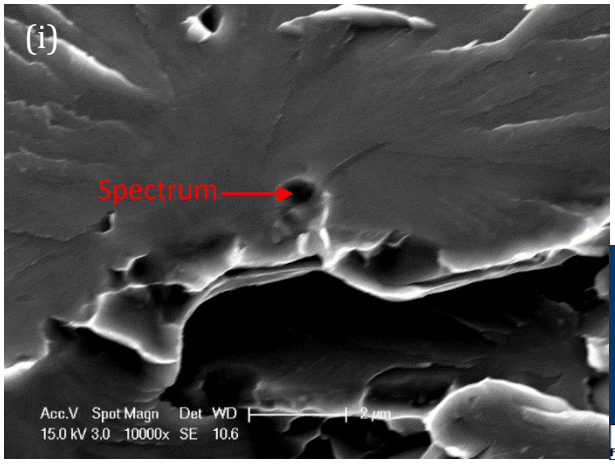


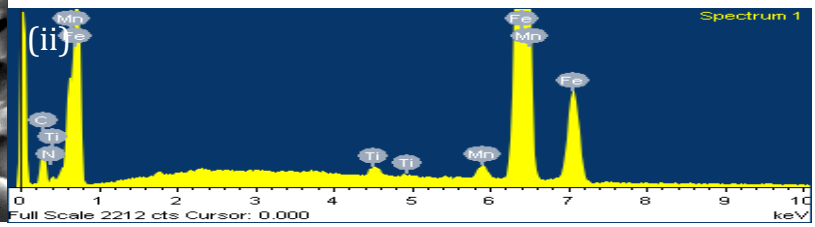


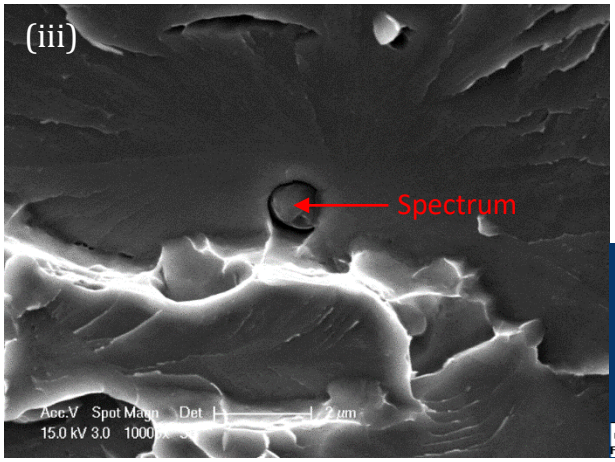


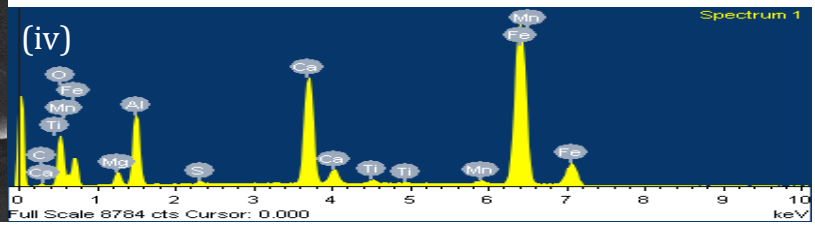


Figure 6-30 (d). Cleavage initiation point (i) and (iii) from matching halves of fracture surfaces of sharp-cracked specimen CT HT1-26 tested at -100 °C with their corresponding EDX spectrums (ii) and (iv) respectively.

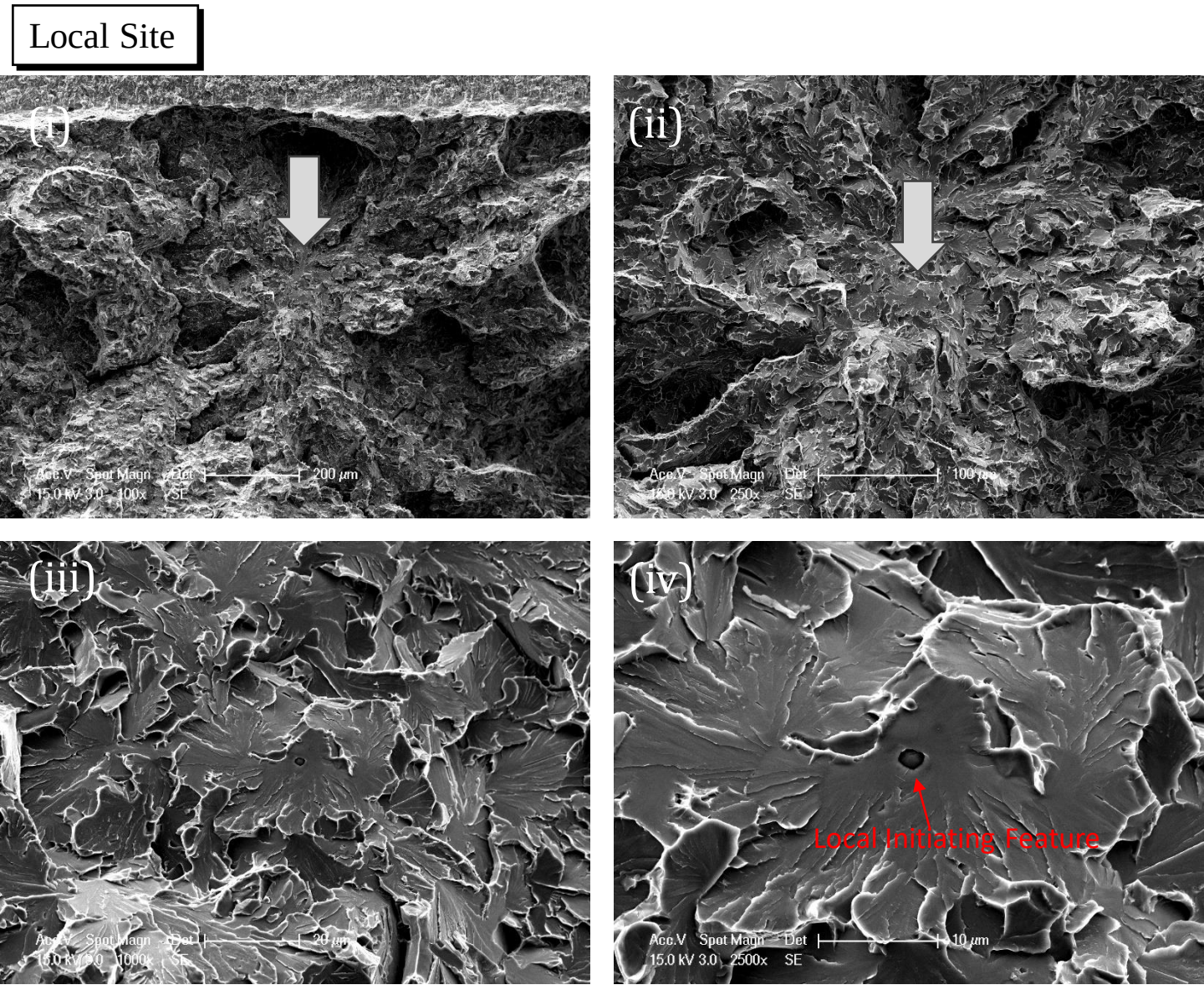


Figure 6-30 (e). Local fracture initiation area at side (A) of the sharp-cracked specimen CT HT1-26, test temperature of -100 °C. A sequential magnification of the white-framed area at (i) 100x, (ii) 250x, (iii) 1000x, and (iv) 2500x are shown.

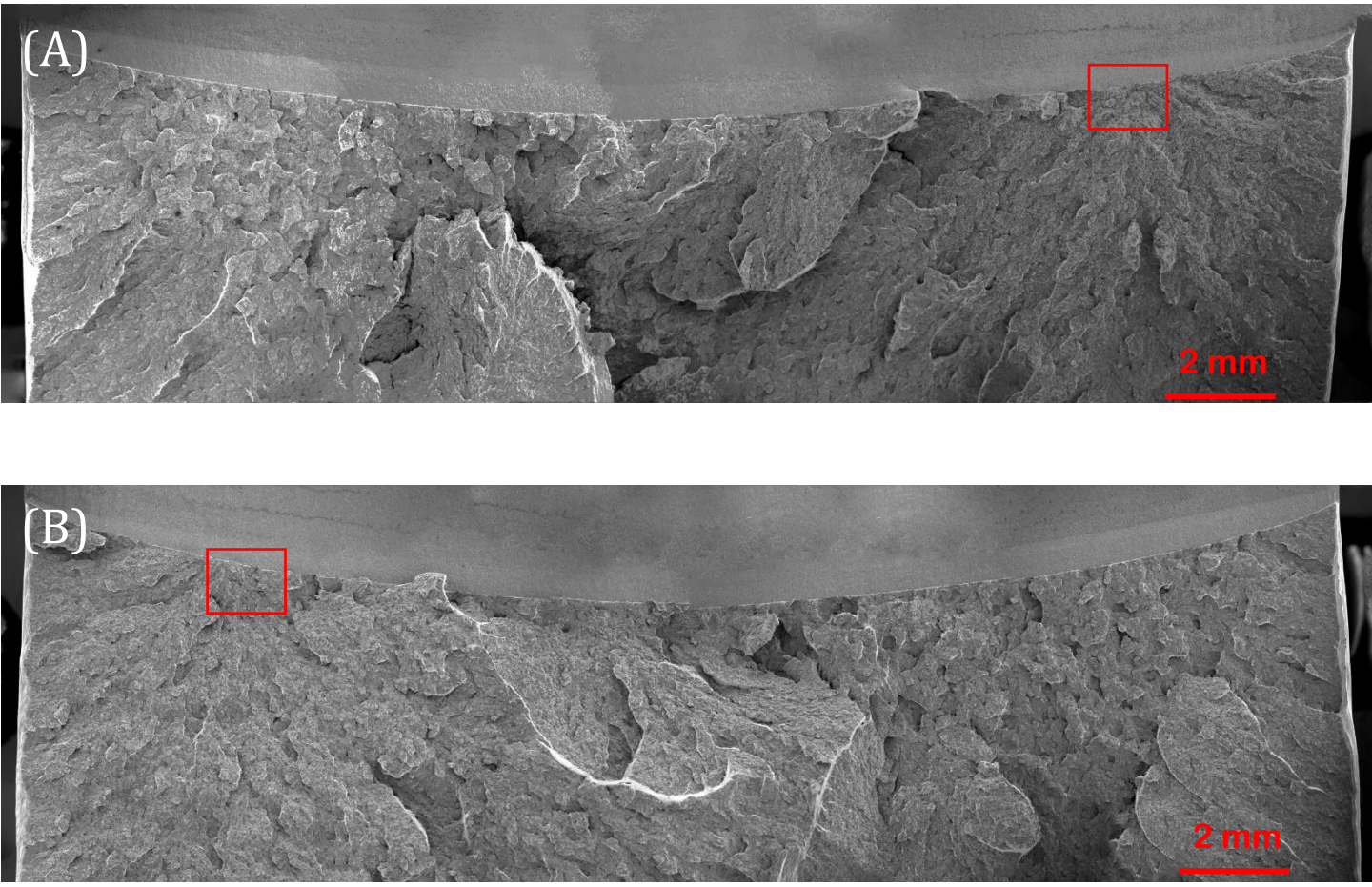


Figure 6-31 (a). Overview of fracture surfaces on a sharp-cracked specimen, designated CT HT1-27, tested at -100 °C. Red frames on matching halves (A) and (B) denote the most probable fracture initiation areas. Test results: Critical J-integral (Jc) value of 37.9 $kJ/m^2$, crack tip opening displacement (CTOD) of 0.029 mm, local cleavage fracture stress of 2285 MPa (n=0.1), fracture initiation distance (X0) of 94 µm, and an average stable crack extension of 9 µm.

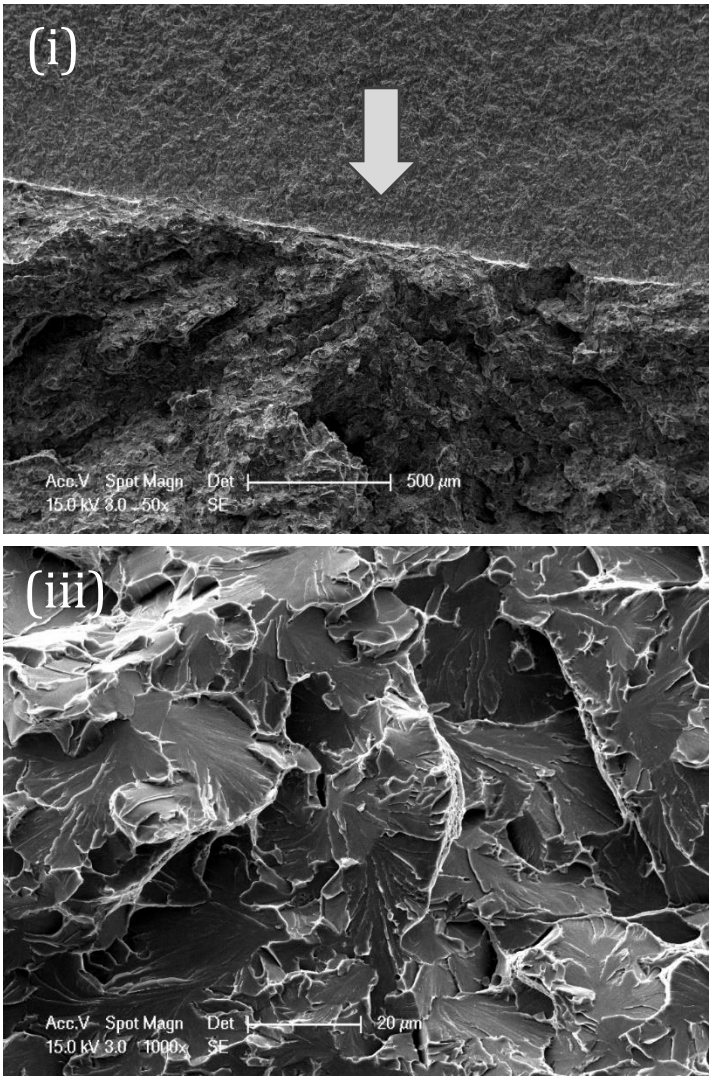


Figure 6-31 (b). Fracture Initiation at side (A) of the sharp-cracked specimen CT HT1-27, test temperature of -100 °C. A sequential magnification of the red-framed area at (i) 50x, (ii) 250x, (iii) 1000x, and (iv) 10000x are shown. Fractographic analysis reveals matrix related feature as the initiation, with the initiating feature's equivalent diameter at 1.5 µm and the initial facet's equivalent diameter at 32 µm.

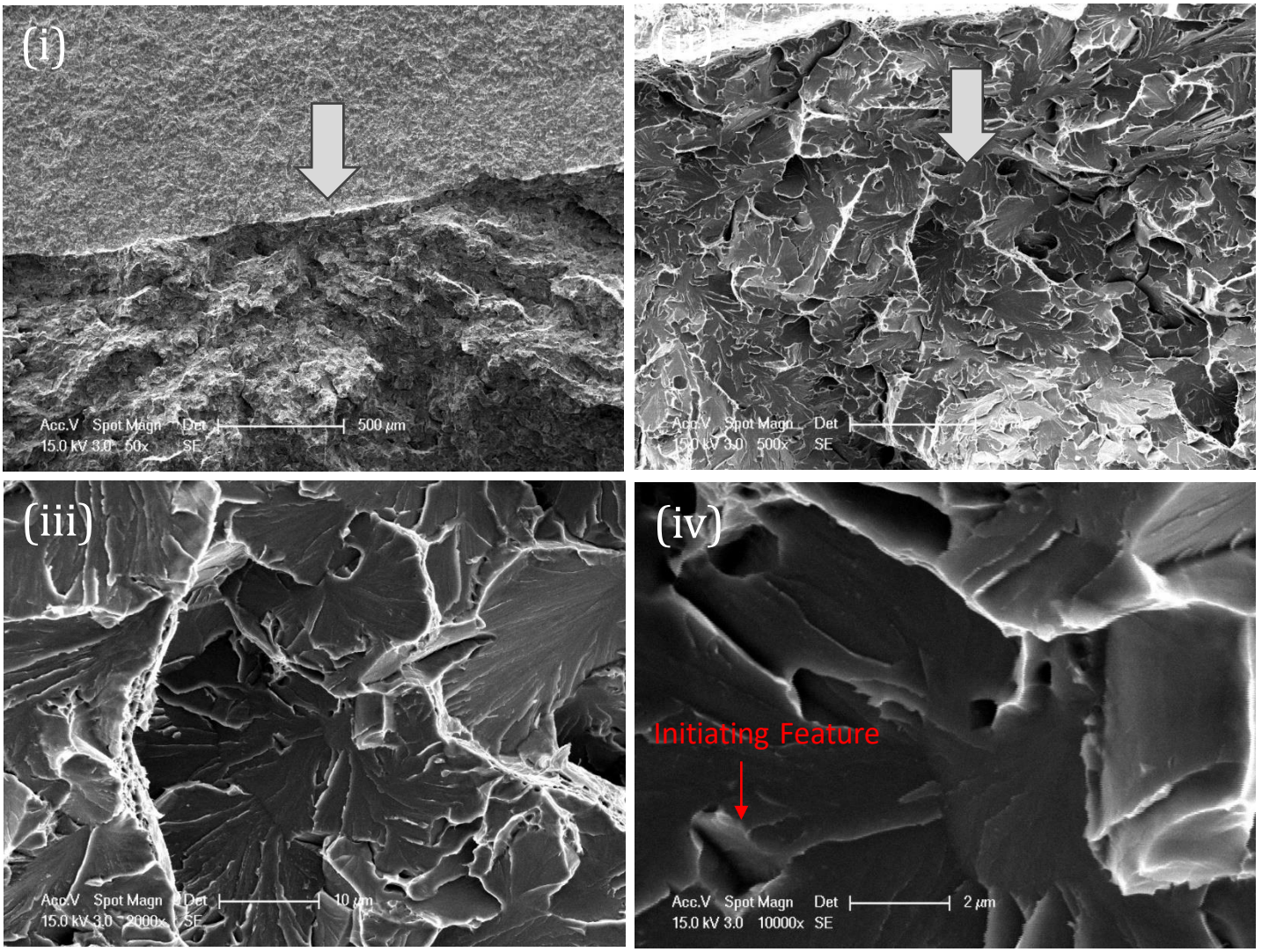


Figure 6-31 (c). Fracture Initiation at matching side (B) of the sharp-cracked specimen CT HT1-27, test temperature of -100 °C. A sequential magnification of the red-framed area at (i) 50x, (ii) 500x, (iii) 2000x, and (iv) 10000x are shown. Fractographic analysis reveals matrix related feature as the initiation, with the initiating feature's equivalent diameter at 1.5 µm and the initial facet's equivalent diameter at 32 µm.

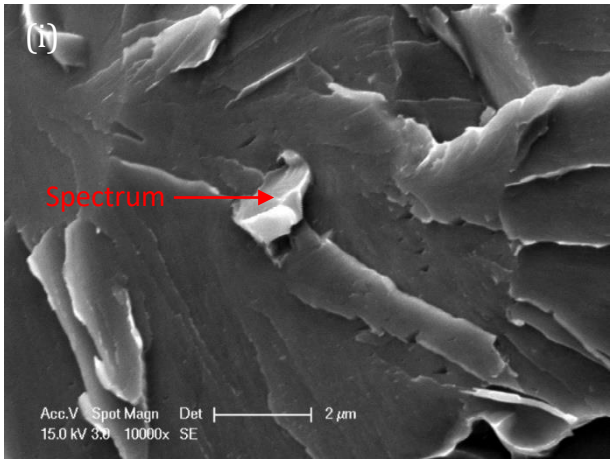


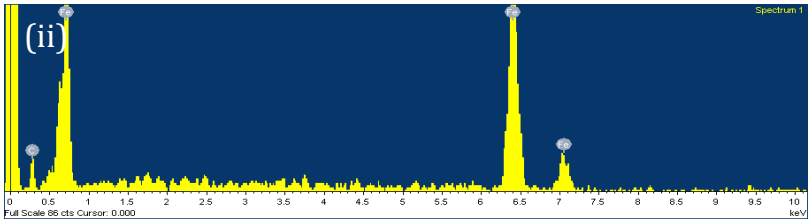


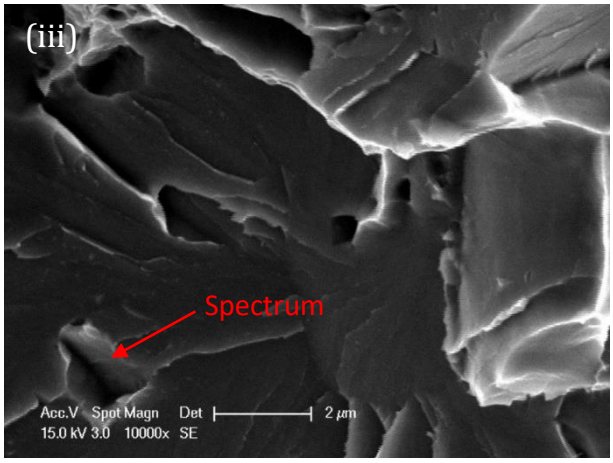


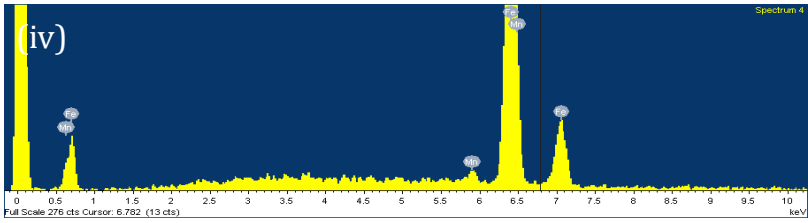


Figure 6-31 (d). Cleavage initiation point (i) and (iii) from matching halves of fracture surfaces of sharp-cracked specimen CT HT1-27 tested at -100 °C with their corresponding EDX spectrums (ii) and (iv) respectively.

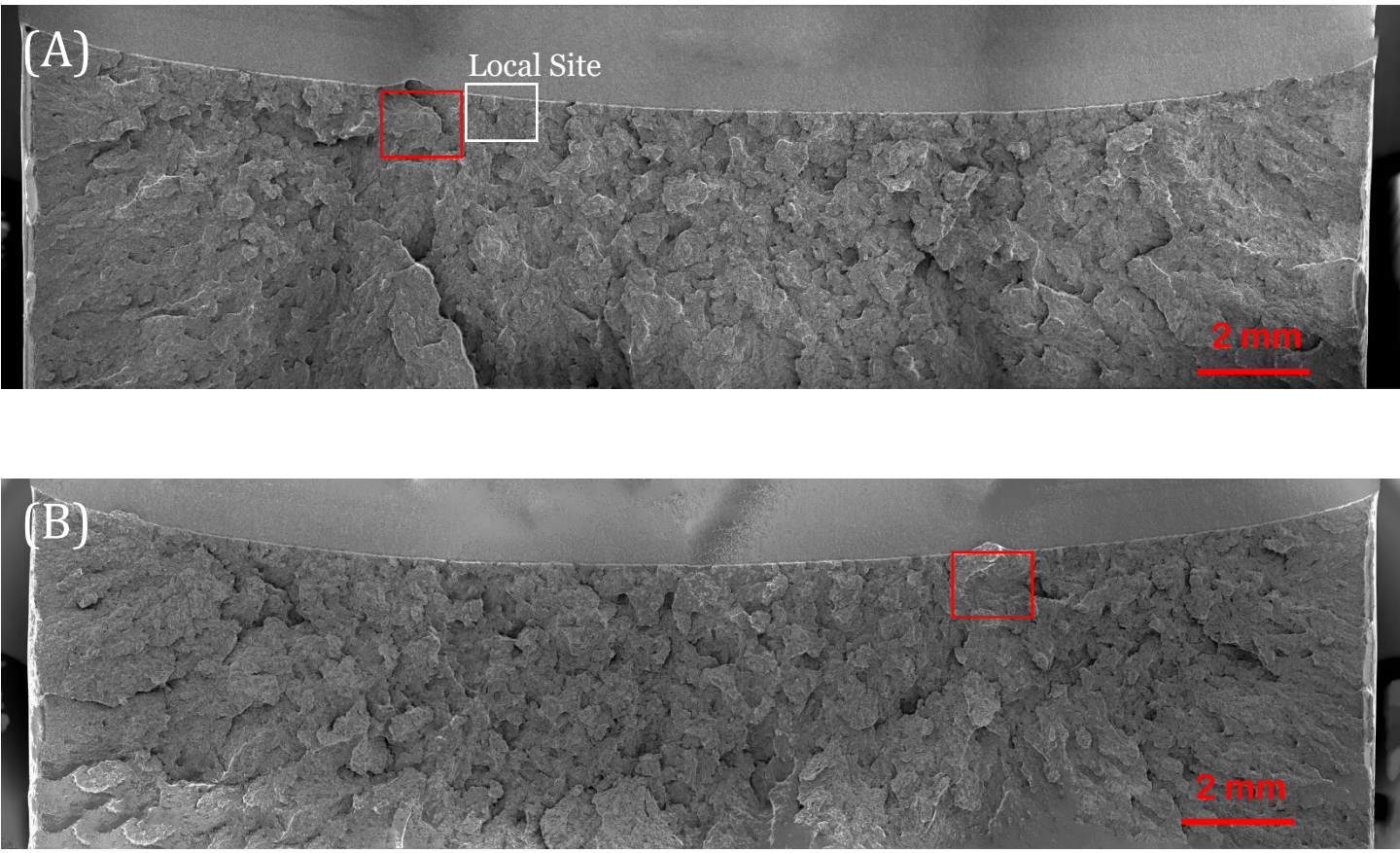


Figure 6-32 (a). Overview of fracture surfaces on a sharp-cracked specimen, designated CT HT2-01, tested at -100 °C. Red frames on matching halves (A) and (B) denote the most probable fracture initiation areas. White frame indicating local cleavage area. Test results: Critical J-integral (Jc) value of 64.9 $kJ/m^2$, crack tip opening displacement (CTOD) of 0.050 mm, local cleavage fracture stress of 1900 MPa (n=0.1), fracture initiation distance (Xo) of 649 µm, and an average stable crack extension of 16 µm.

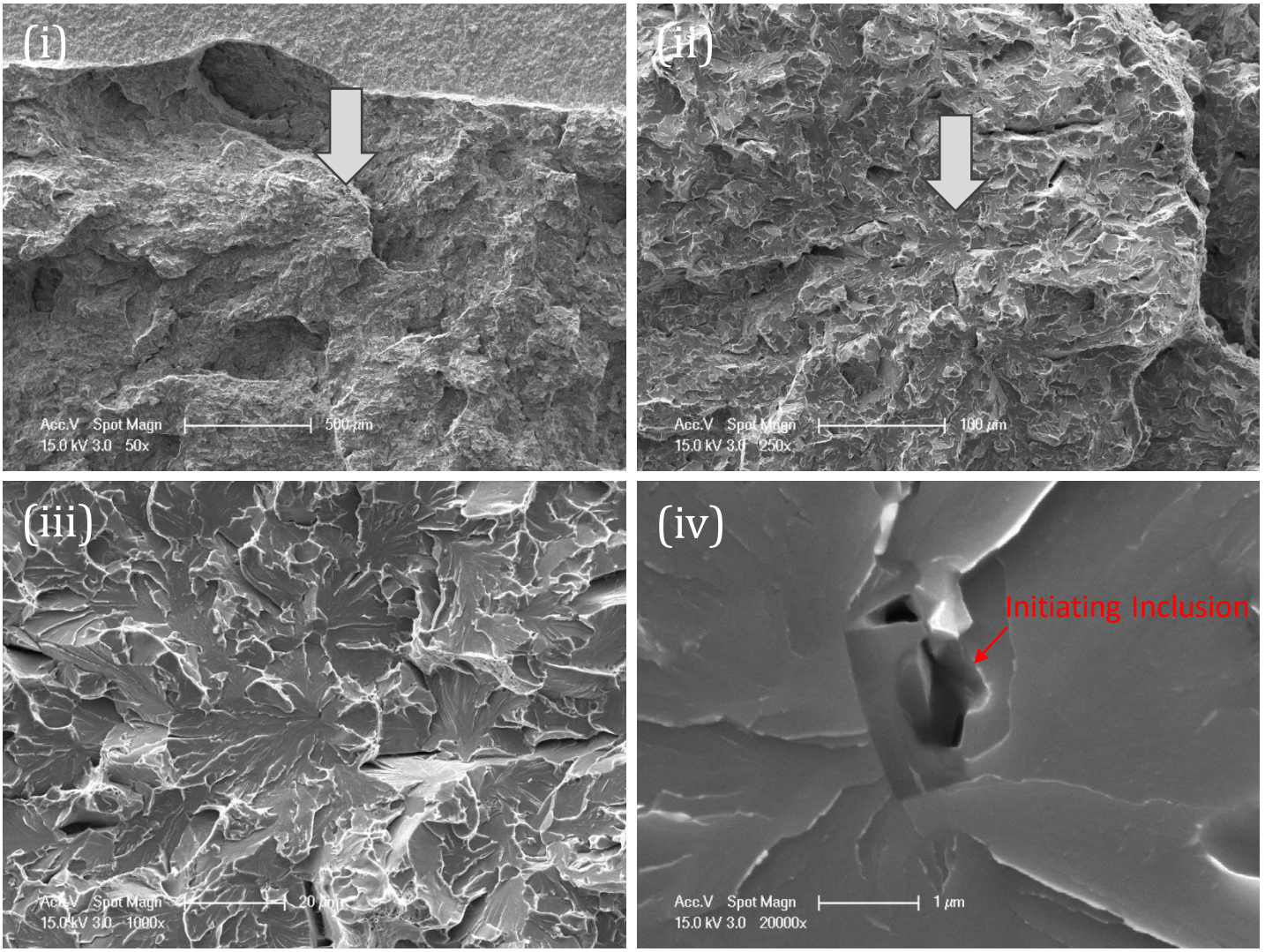


Figure 6-32 (b). Fracture Initiation at side (A) of the sharp-cracked specimen CT HT2-01, test temperature of -100 °C. A sequential magnification of the red-framed area at (i) 50x, (ii) 250x, (iii) 1000x, and (iv) 20000x are shown. Fractographic analysis reveals inclusion cracking as the initiation mechanism, with the inclusion's equivalent diameter at 1.6 µm and the initial facet's equivalent diameter at 34 µm.

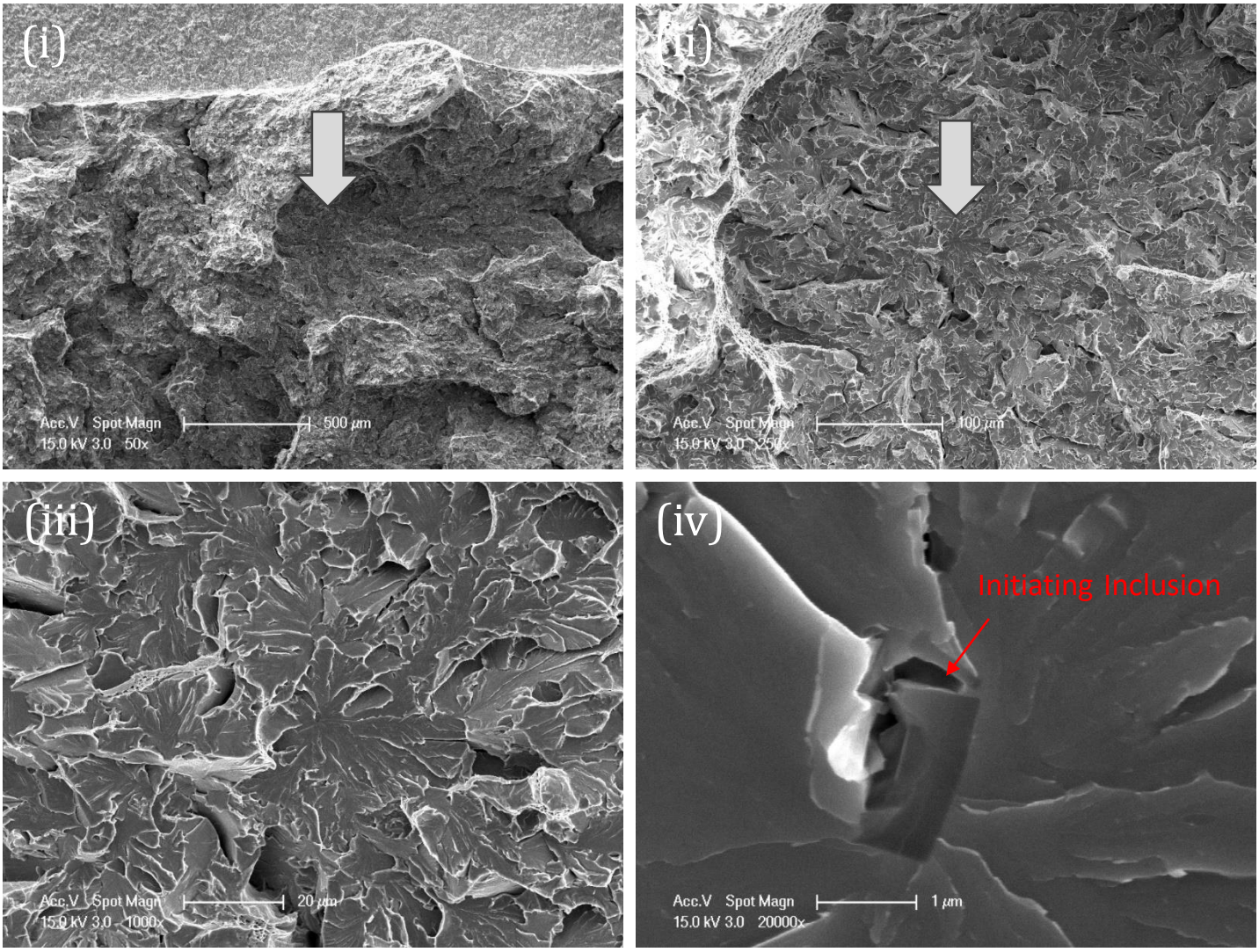


Figure 6-32 (c). Fracture Initiation at matching side (B) of the sharp-cracked specimen CT HT2-01, test temperature of -100 °C. A sequential magnification of the red-framed area at (i) 50x, (ii) 250x, (iii) 1000x, and (iv) 20000x are shown. Fractographic analysis reveals inclusion cracking as the initiation mechanism, with the inclusion's equivalent diameter at 1.6 µm and the initial facet's equivalent diameter at 34 µm.

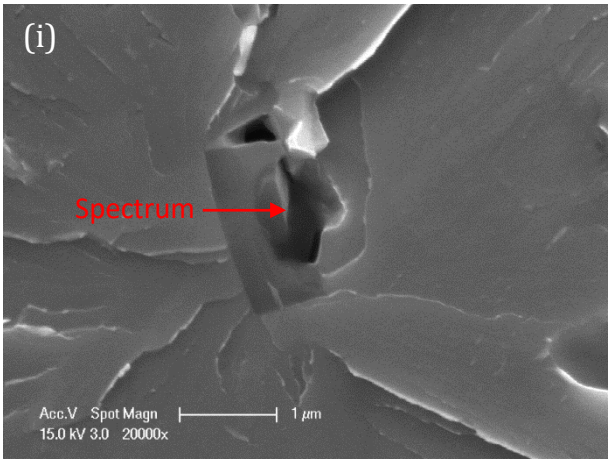


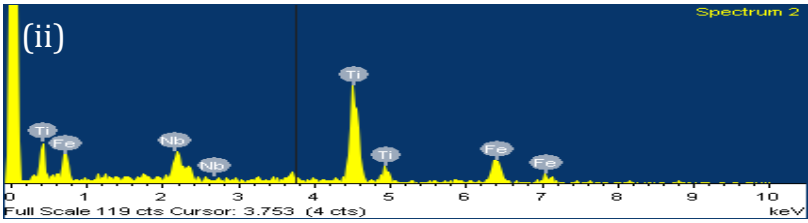


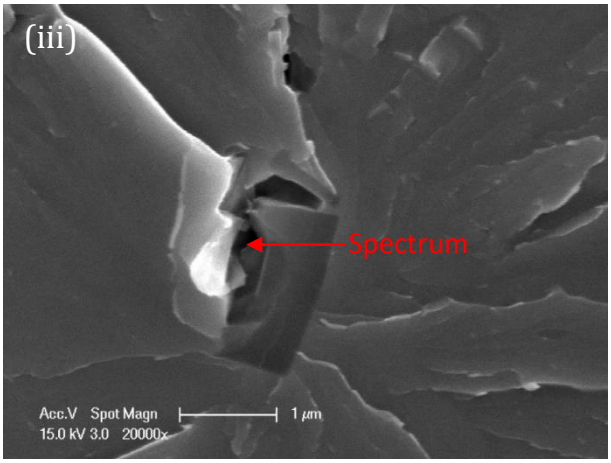


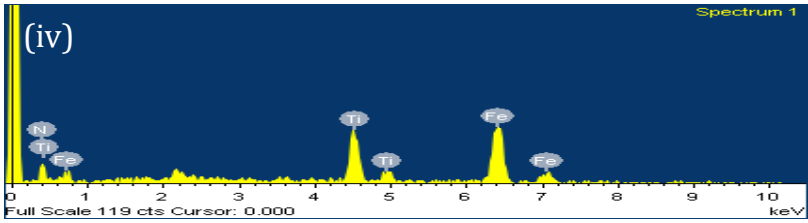


Figure 6-32 (d). Cleavage initiation point (i) and (iii) from matching halves of fracture surfaces of sharp-cracked specimen CT HT2-01 tested at -100 °C with their corresponding EDX spectrums (ii) and (iv) respectively.

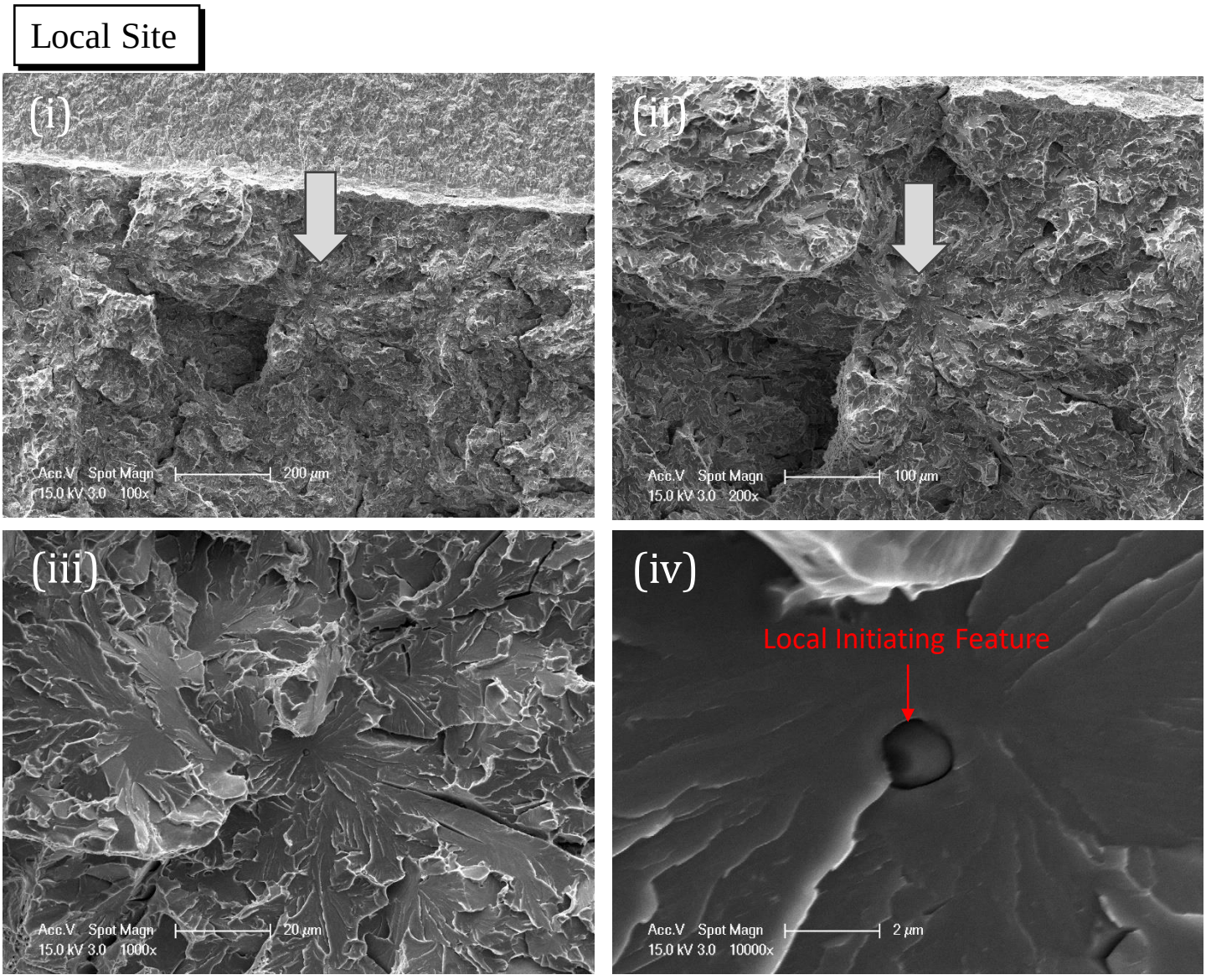


Figure 6-32 (e). Local fracture initiation area at side (A) of the sharp-cracked specimen CT HT2-01, test temperature of -100 °C. A sequential magnification of the white-framed area at (i) 100x, (ii) 200x, (iii) 1000x, and (iv) 10000x are shown.

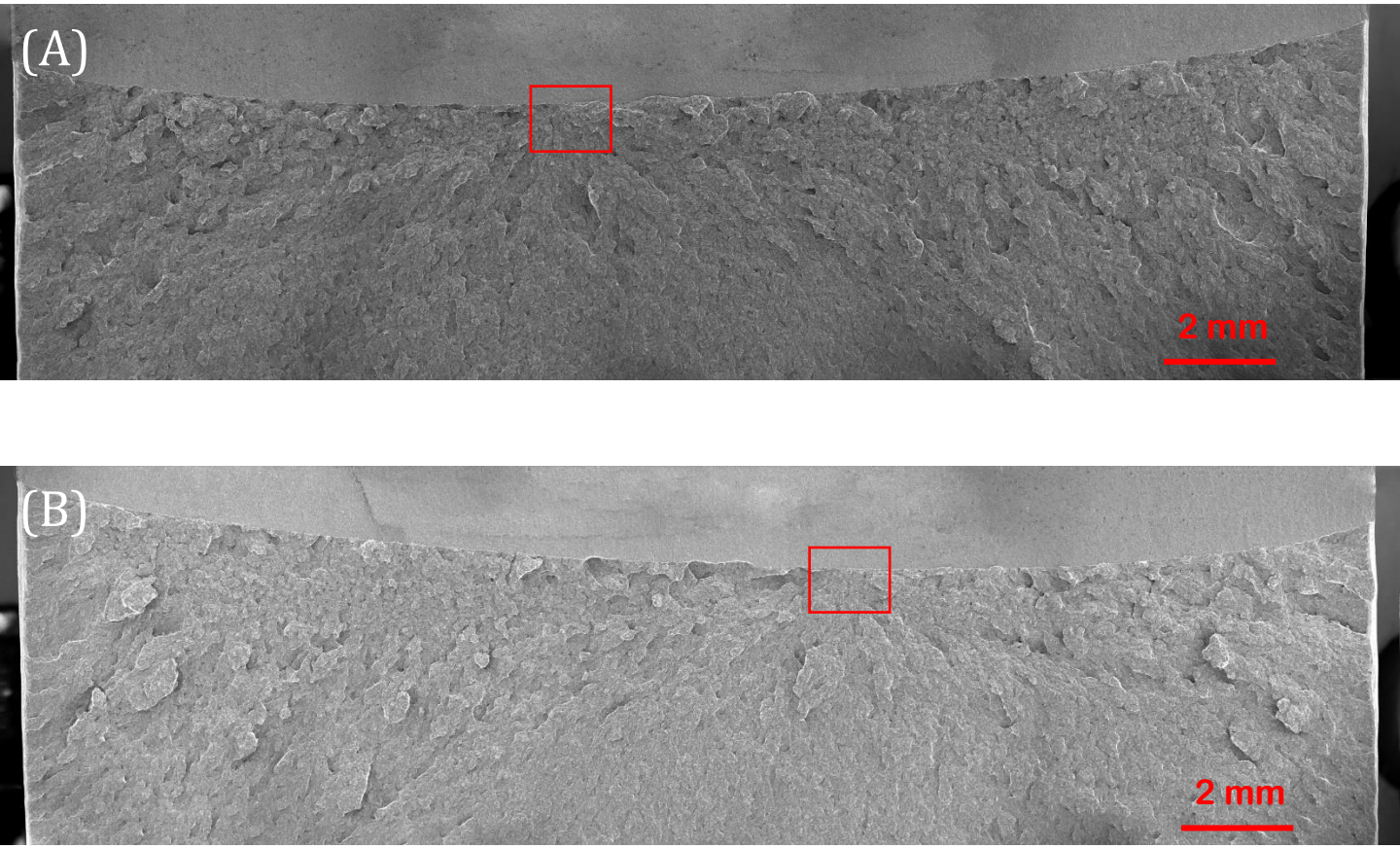


Figure 6-33 (a). Overview of fracture surfaces on a sharp-cracked specimen, designated CT HT2-02, tested at -100 °C. Red frames on matching halves (A) and (B) denote the most probable fracture initiation areas. Test results: Critical J-integral (Jc) value of 17.2 $kJ/m^2$, crack tip opening displacement (CTOD) of 0.013 mm, local cleavage fracture stress of 2145 MPa (n=0.1), fracture initiation distance (Xo) of 63 µm, and an average stable crack extension of 2 µm.

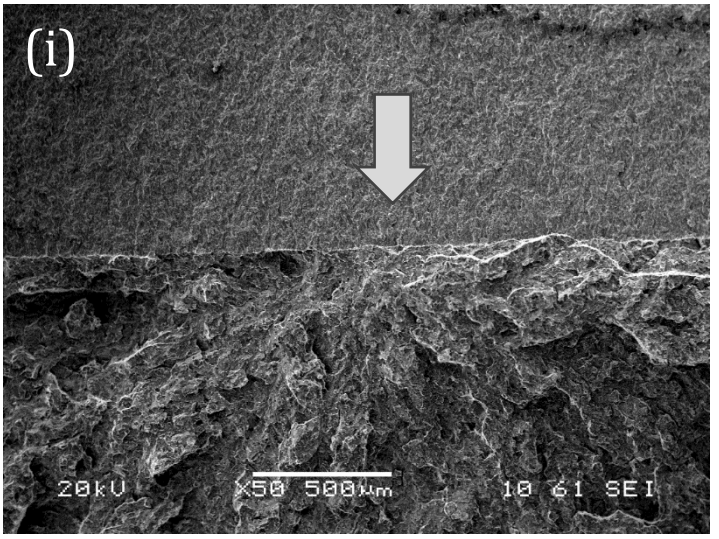


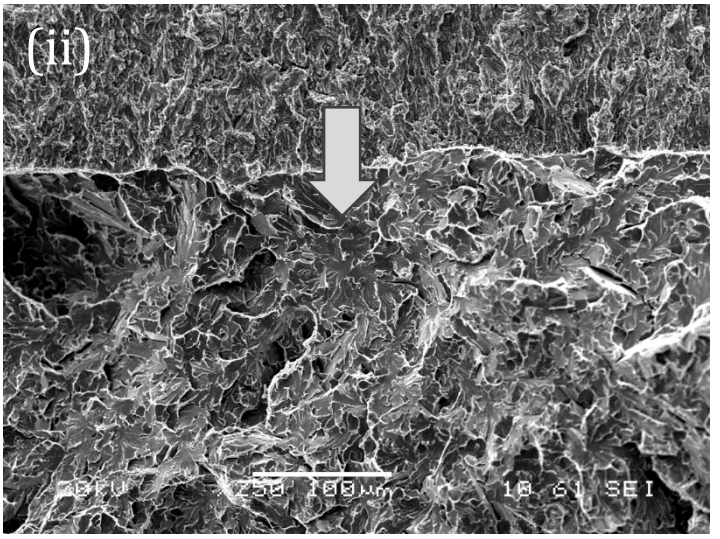


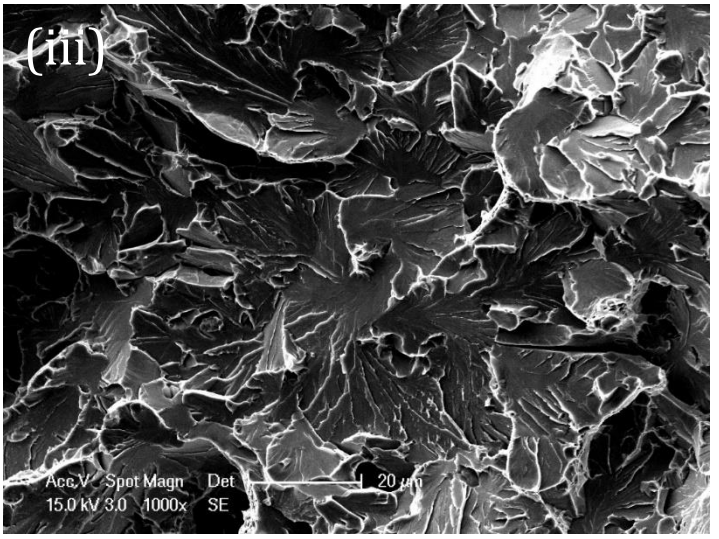


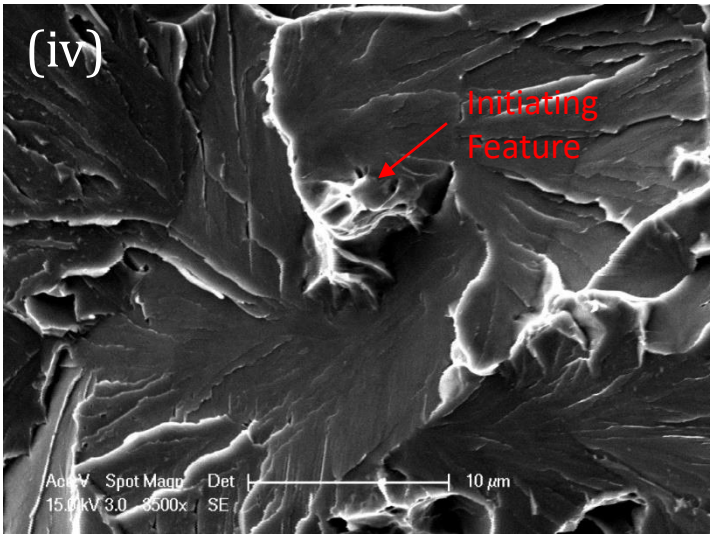


Figure 6-33 (b). Fracture Initiation at side (A) of the sharp-cracked specimen CT HT2-02, test temperature of -100 °C. A sequential magnification of the red-framed area at (i) 50x, (ii) 250x, (iii) 1000x, and (iv) 3500x are shown. Fractographic analysis reveals matrix related initiation mechanism, with the initial facet's equivalent diameter at 43 µm.

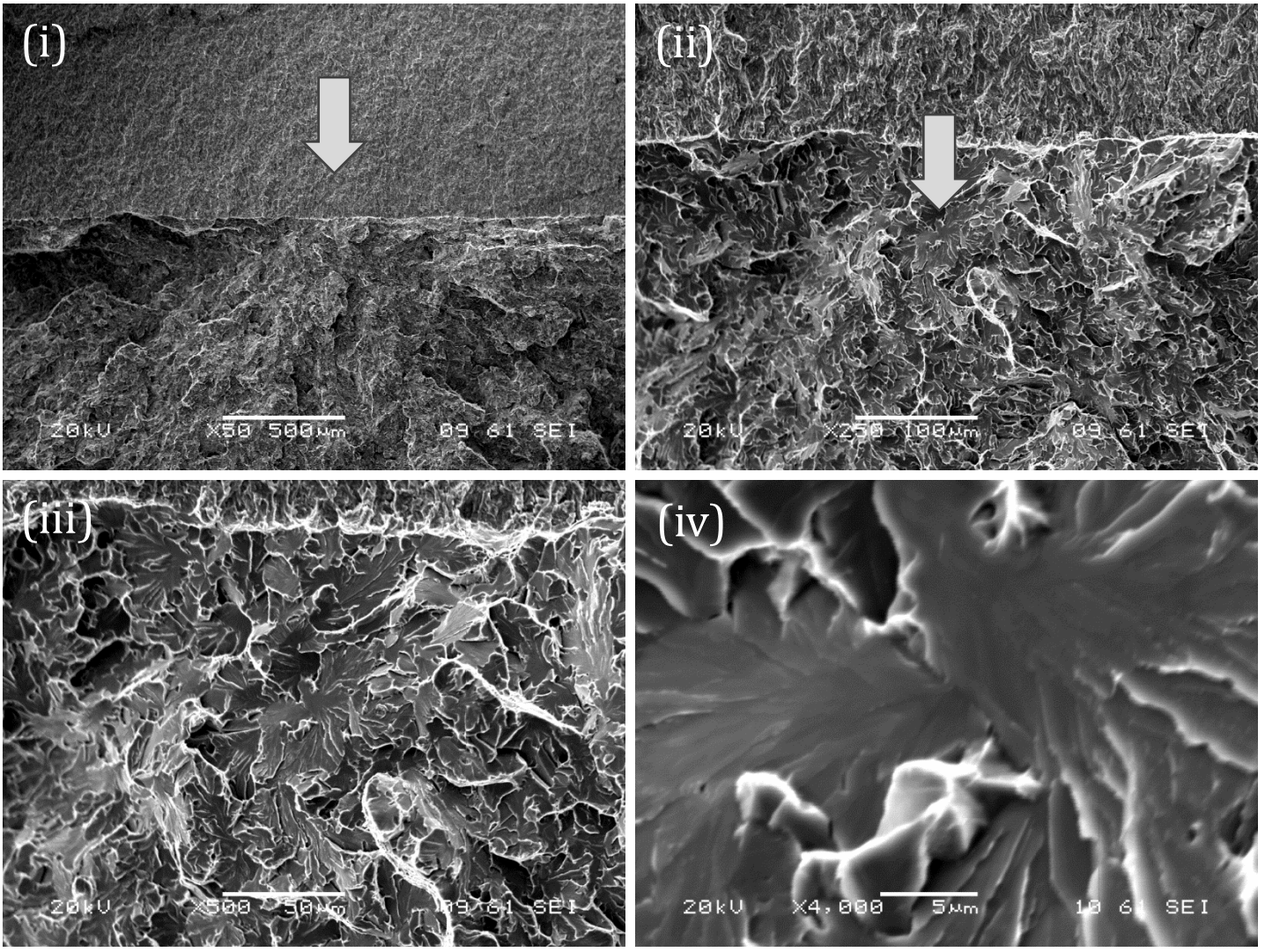


Figure 6-33 (c). Fracture Initiation at matching side (B) of the sharp-cracked specimen CT HT2-02, test temperature of -100 °C. A sequential magnification of the red-framed area at (i) 50x, (ii) 250x, (iii) 500x, and (iv) 4000x are shown. Fractographic analysis reveals matrix related initiation mechanism, with the initial facet's equivalent diameter at 43 µm.

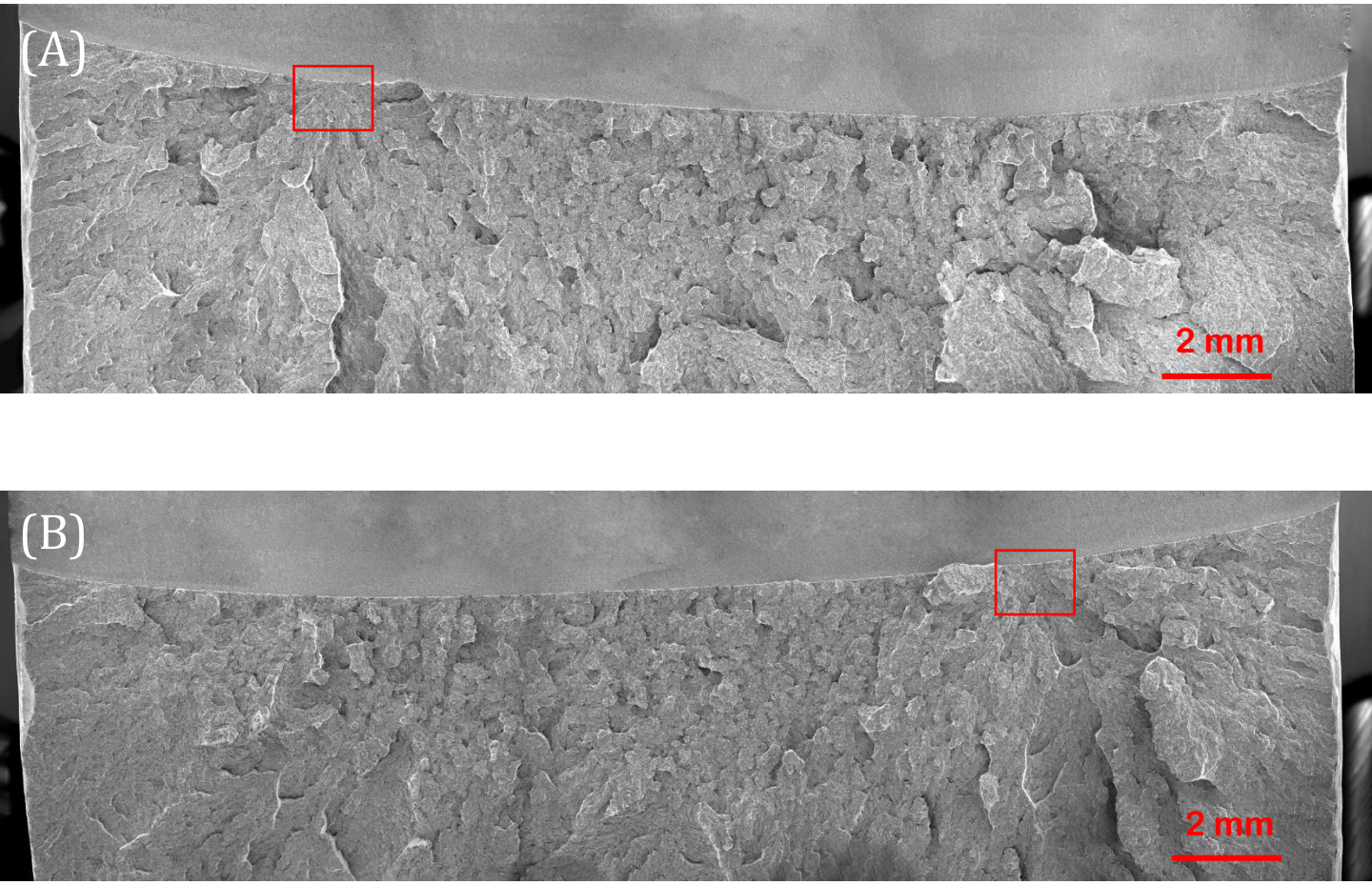





Figure 6-34 (a). Overview of fracture surfaces on a sharp-cracked specimen, designated CT HT2-03, tested at -100 °C. Red frames on matching halves (A) and (B) denote the most probable fracture initiation areas. Test results: Critical J-integral (Jc) value of 40.3 $kJ/m^2$, crack tip opening displacement (CTOD) of 0.031 mm, local cleavage fracture stress of 2322 MPa (n=0.1), fracture initiation distance (Xo) of 53 µm, and an average stable crack extension of 9 µm.

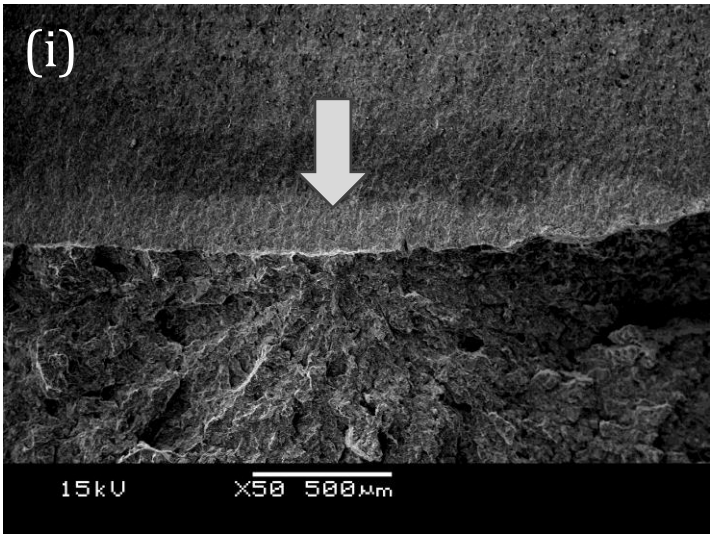


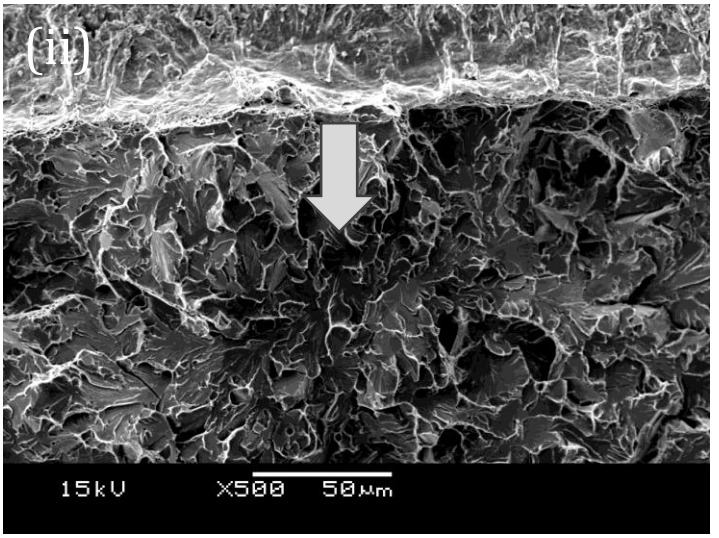


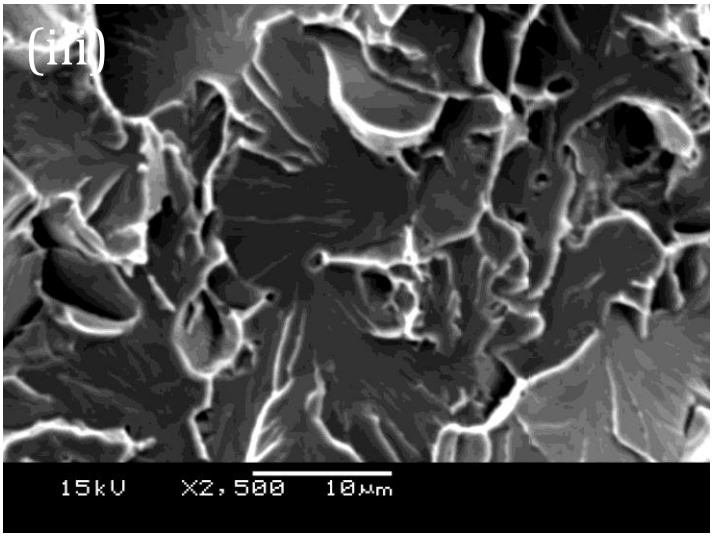


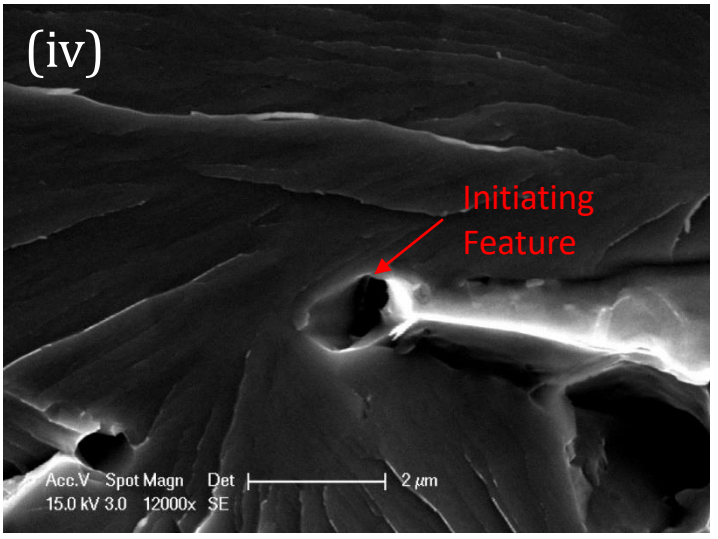


Figure 6-34 (b). Fracture Initiation at side (A) of the sharp-cracked specimen CT HT2-03, test temperature of -100 °C. A sequential magnification of the red-framed area at (i) 50x, (ii) 500x, (iii) 2500x, and (iv) 12000x are shown. Fractographic analysis reveals matrix related feature as the initiation, with the initiating feature's equivalent diameter at 1.1 µm and the initial facet's equivalent diameter at 26 µm.

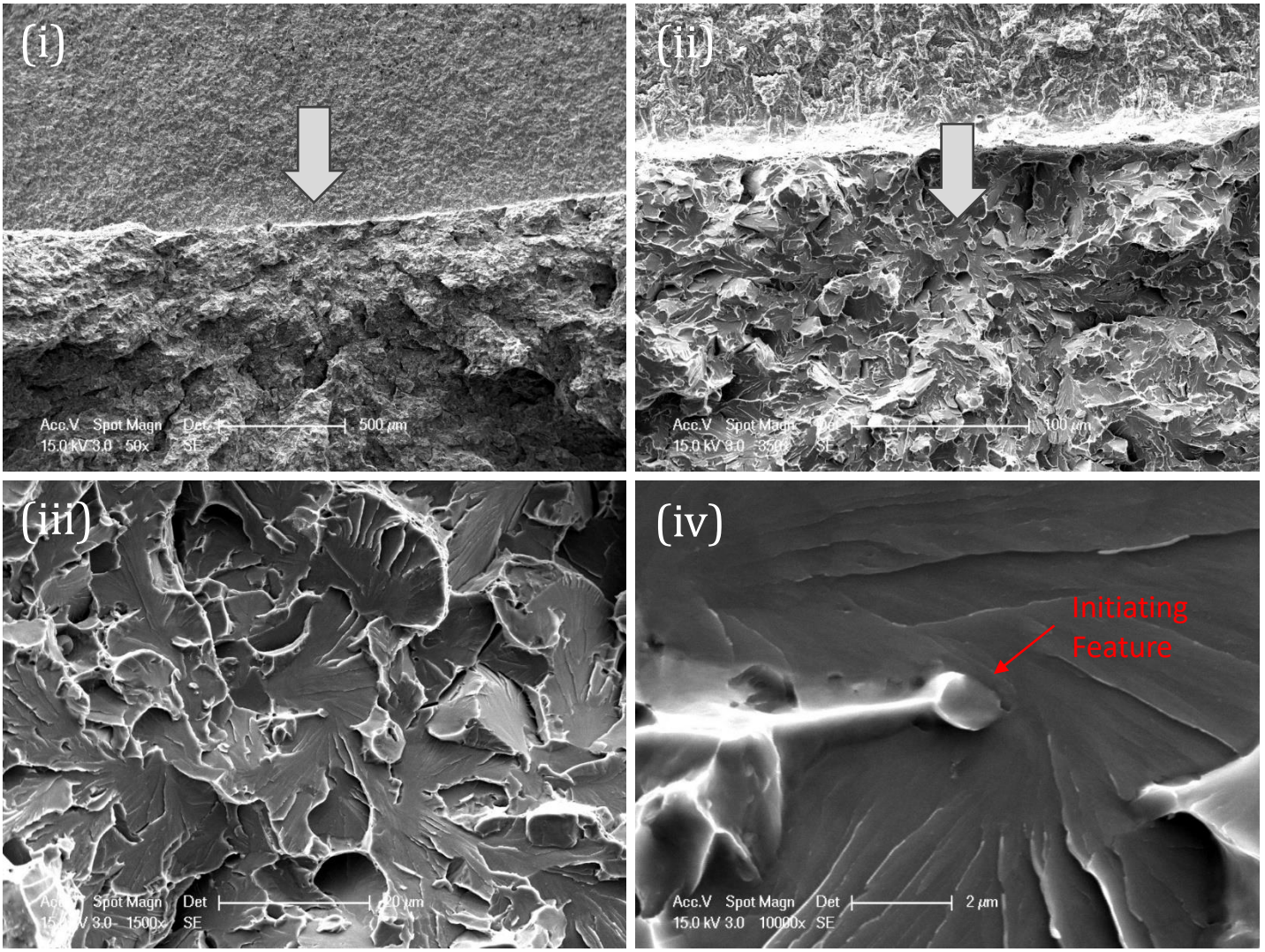


Figure 6-34 (c). Fracture Initiation at matching side (B) of the sharp-cracked specimen CT HT2-03, test temperature of -100 °C. A sequential magnification of the red-framed area at (i) 50x, (ii) 350x, (iii) 1500x, and (iv) 10000x are shown. Fractographic analysis reveals matrix related feature as the initiation, with the initiating feature's equivalent diameter at 1.1 µm and the initial facet's equivalent diameter at 26 µm.

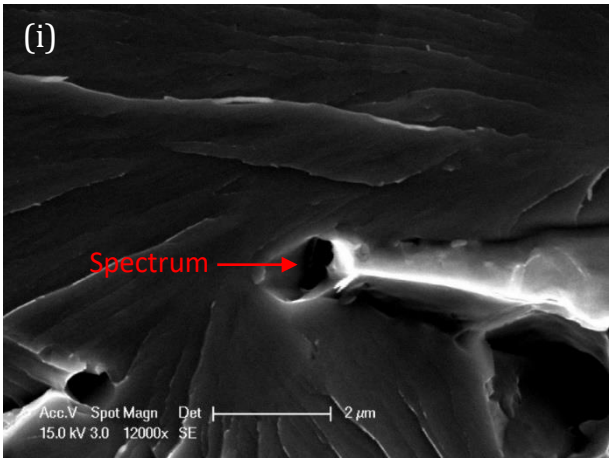


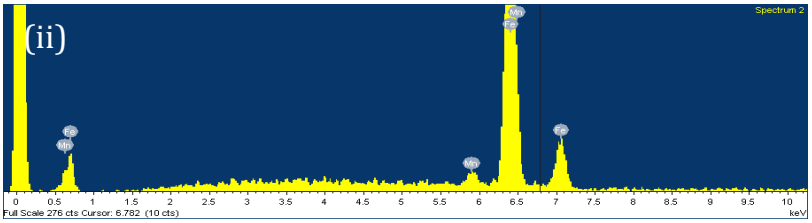


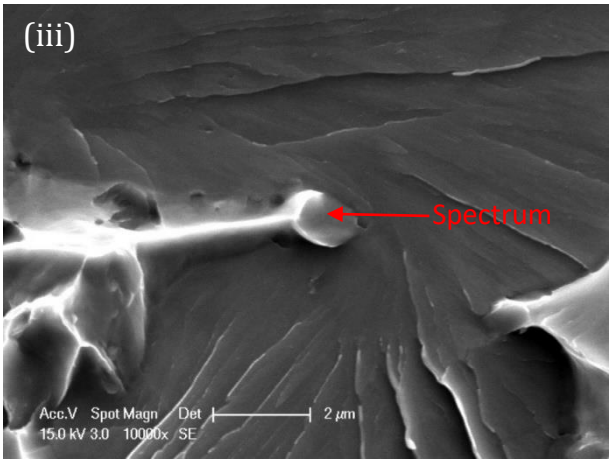


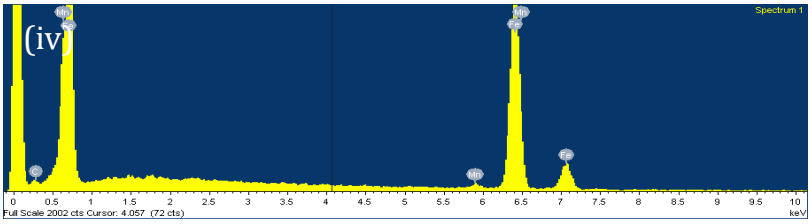


Figure 6-34 (d). Cleavage initiation point (i) and (iii) from matching halves of fracture surfaces of sharp-cracked specimen CT HT2-03 tested at -100 °C with their corresponding EDX spectrums (ii) and (iv) respectively.

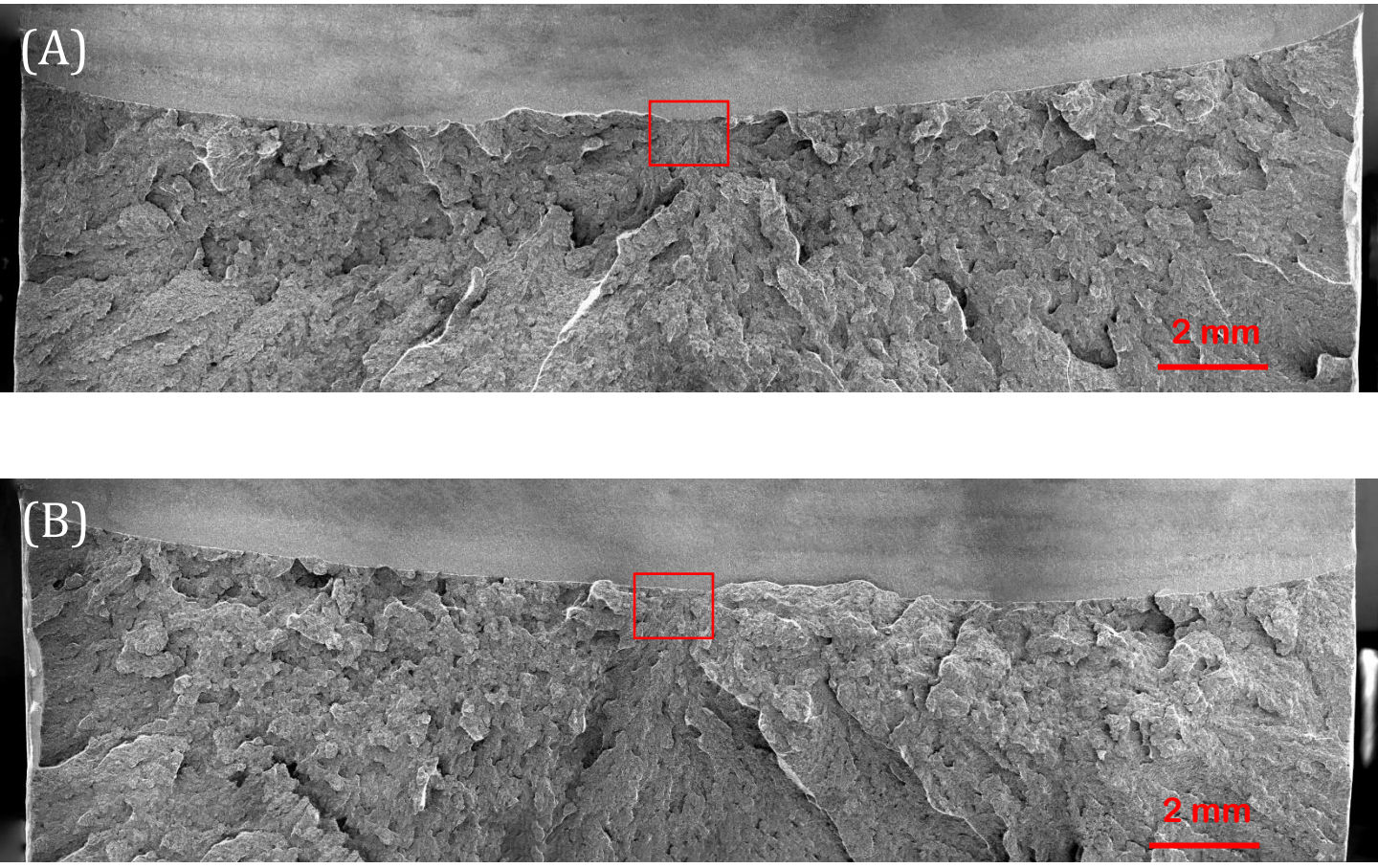


Figure 6-35 (a). Overview of fracture surfaces on a sharp-cracked specimen, designated CT HT2-04, tested at -100 °C. Red frames on matching halves (A) and (B) denote the most probable fracture initiation areas. Test results: Critical J-integral (Jc) value of 42.2 $kJ/m^2$, crack tip opening displacement (CTOD) of 0.033 mm, local cleavage fracture stress of 2340 MPa (n=0.1), fracture initiation distance (Xo) of 78 µm, and an average stable crack extension of 9 µm.

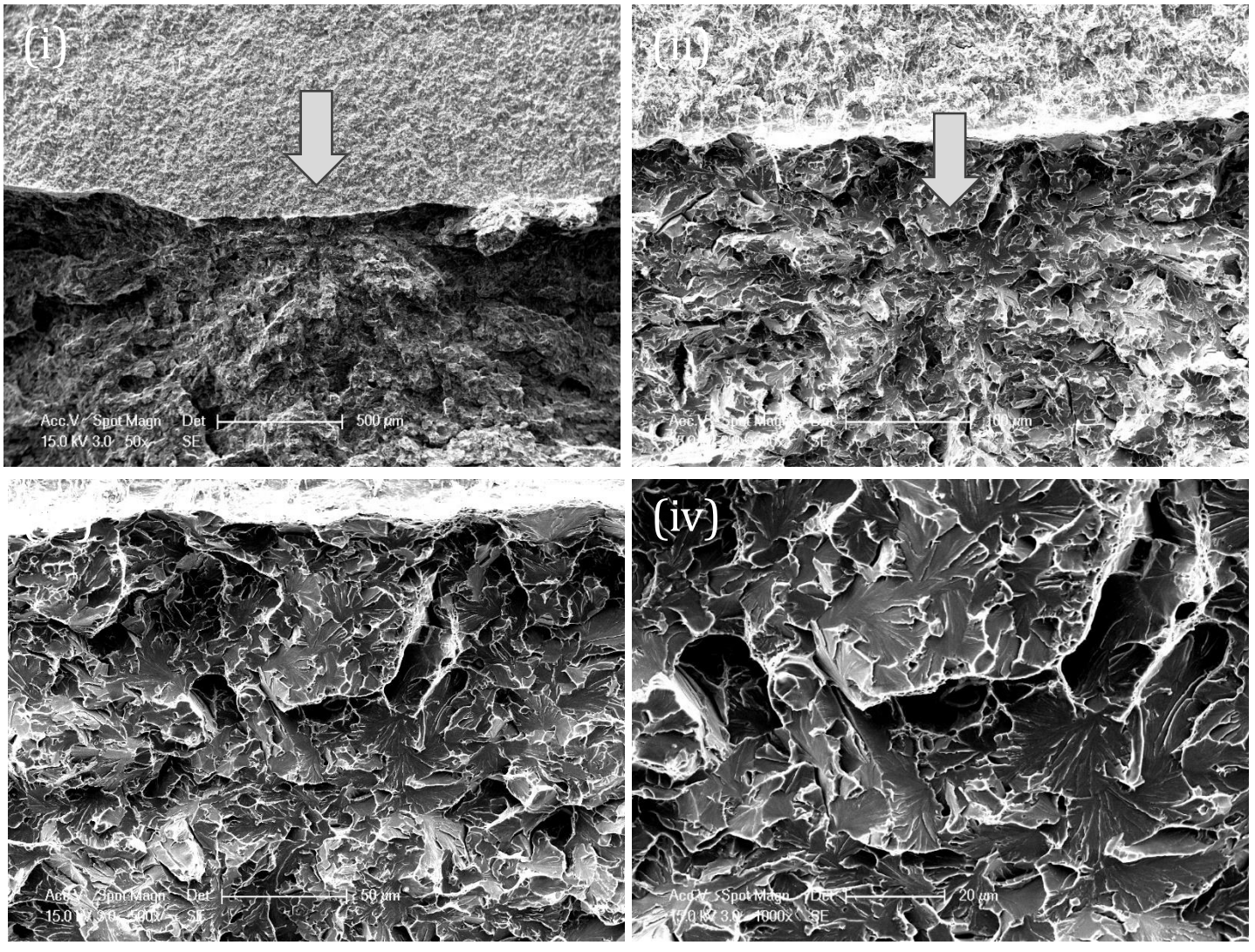


Figure 6-35 (b). Fracture Initiation at side (A) of the sharp-cracked specimen CT HT2-04, test temperature of -100 °C. A sequential magnification of the red-framed area at (i) 50x, (ii) 250x, (iii) 500x, and (iv) 1000x are shown. Fractographic analysis reveals matrix cracking as the initiation mechanism, with the initial facet's equivalent diameter at 20 µm.

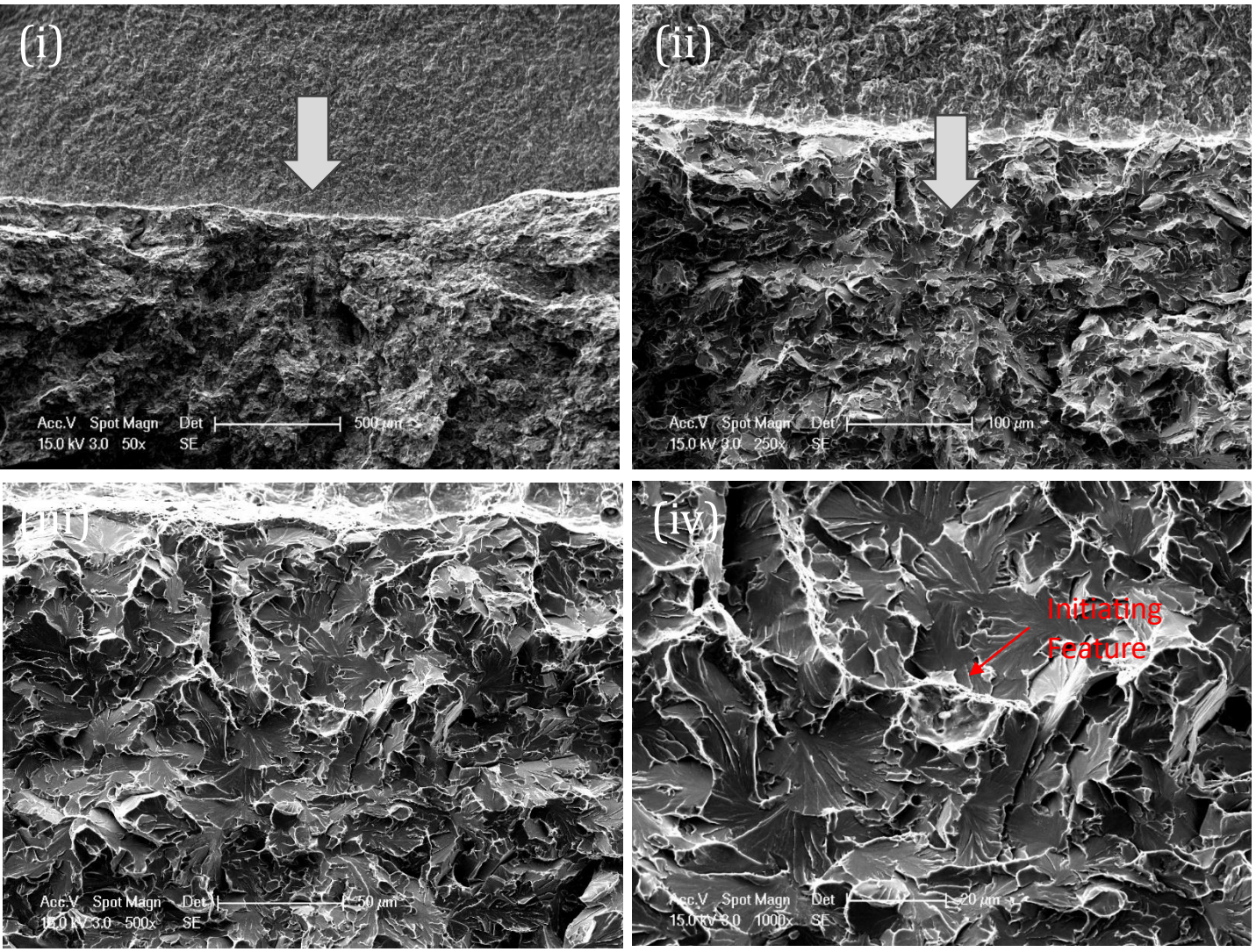


Figure 6-35 (c). Fracture Initiation at matching side (B) of the sharp-cracked specimen CT HT2-04, test temperature of -100 °C. A sequential magnification of the red-framed area at (i) 50x, (ii) 250x, (iii) 500x, and (iv) 1000x are shown. Fractographic analysis reveals matrix cracking as the initiation mechanism, with the initial facet's equivalent diameter at 20 µm.

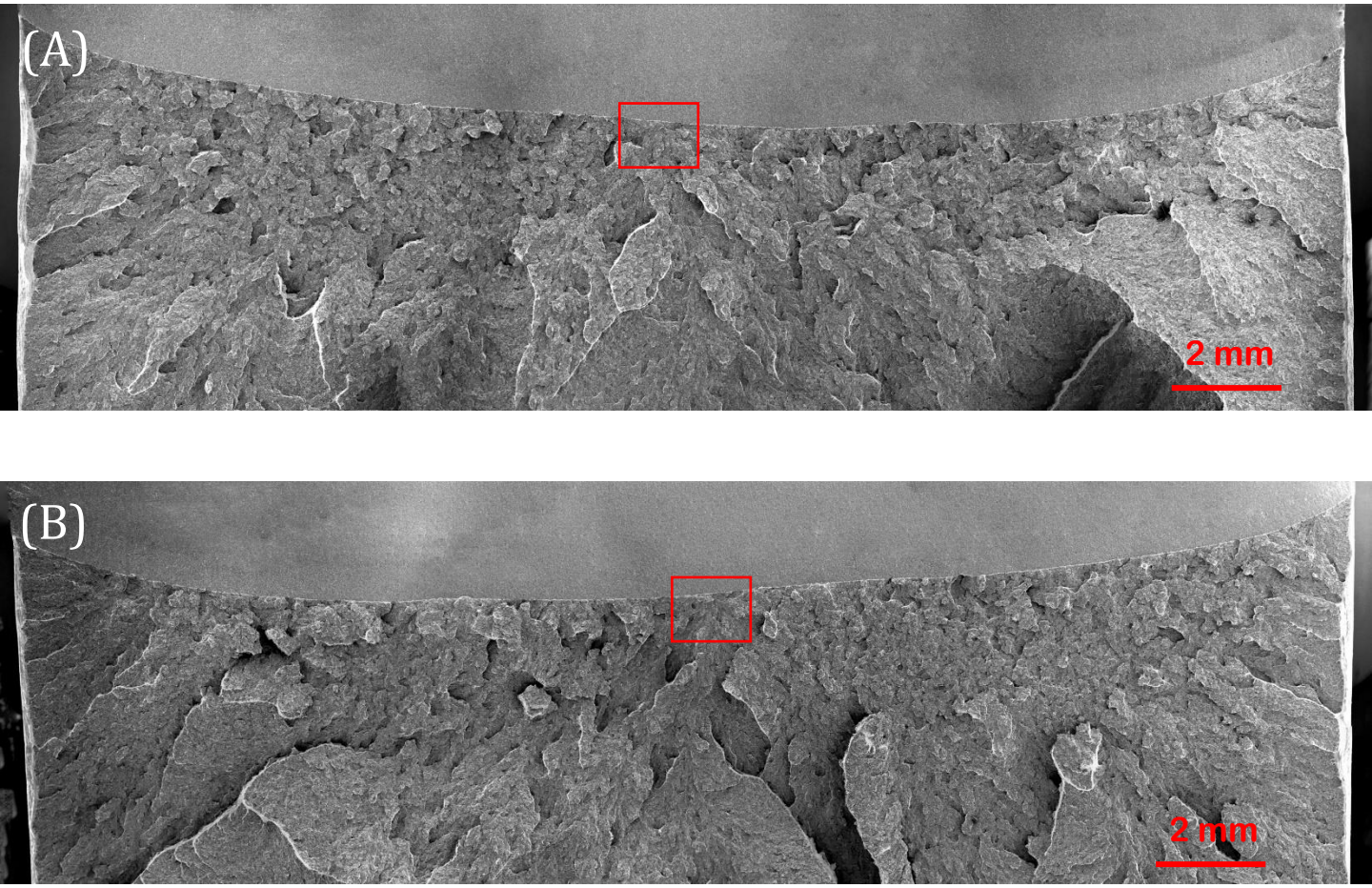


Figure 6-36 (a). Overview of fracture surfaces on a sharp-cracked specimen, designated CT HT2-09, tested at -100 °C. Red frames on matching halves (A) and (B) denote the most probable fracture initiation areas. Test results: Critical J-integral (Jc) value of 36.1 $kJ/m^2$, crack tip opening displacement (CTOD) of 0.028 mm, local cleavage fracture stress of 2206 MPa (n=0.1), fracture initiation distance (Xo) of 115 µm, and an average stable crack extension of 8 µm.

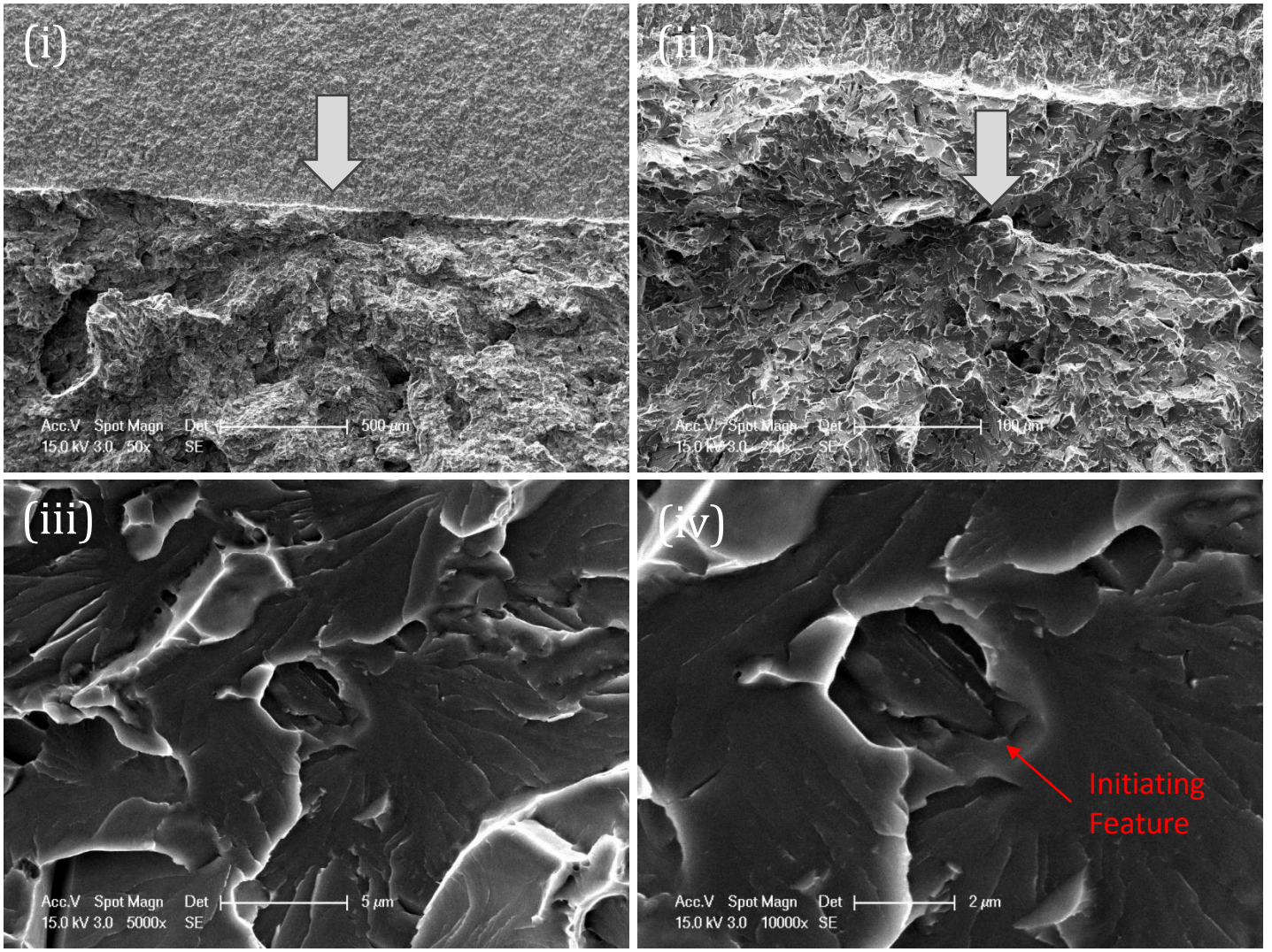


Figure 6-36 (b). Fracture Initiation at side (A) of the sharp-cracked specimen CT HT2-09, test temperature of -100 °C. A sequential magnification of the red-framed area at (i) 50x, (ii) 250x, (iii) 5000x, and (iv) 10000x are shown. Fractographic analysis reveals matrix related initiation mechanism, with the initiating feature's equivalent diameter at 3.2 µm and the initial facet's equivalent diameter at 31 µm.

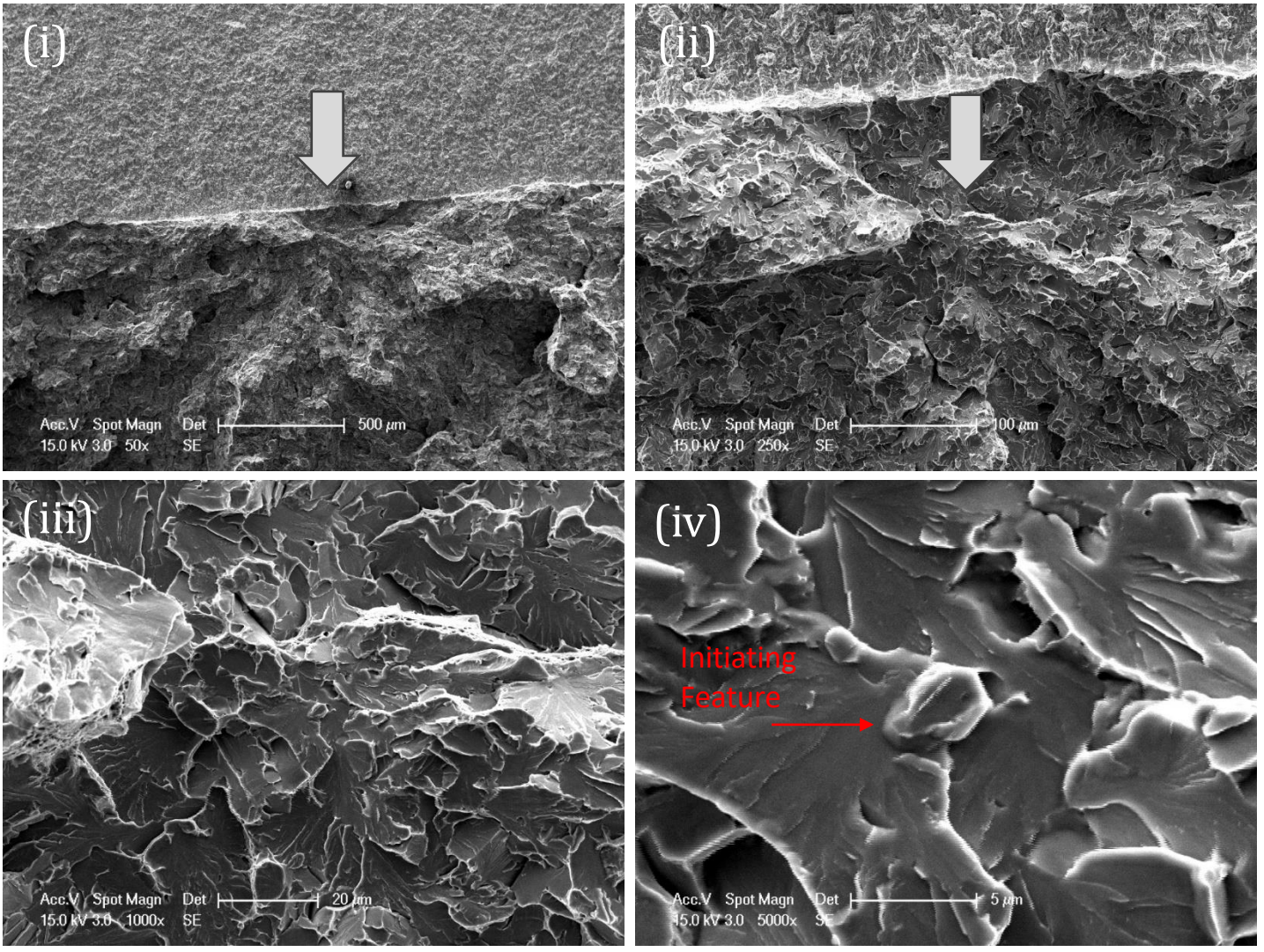


Figure 6-36 (c). Fracture Initiation at matching side (B) of the sharp-cracked specimen CT HT2-09, test temperature of -100 °C. A sequential magnification of the red-framed area at (i) 50x, (ii) 250x, (iii) 1000x, and (iv) 5000x are shown. Fractographic analysis reveals matrix related initiation mechanism, with the initiating feature's equivalent diameter at 3.2 µm and the initial facet's equivalent diameter at 31 µm.

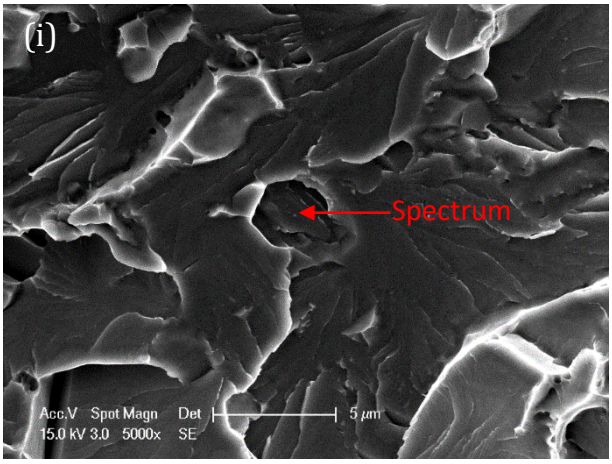


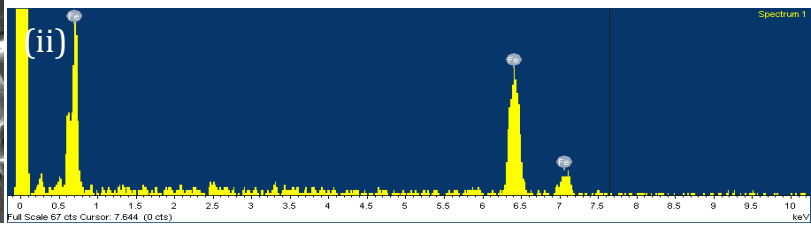


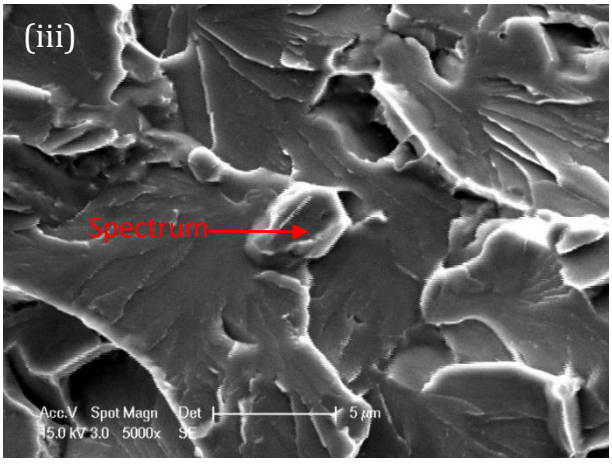


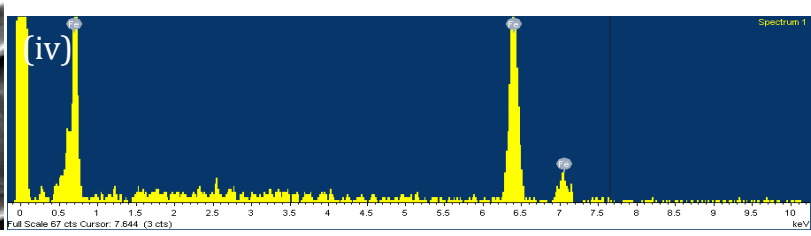


Figure 6-36 (d). Cleavage initiation point (i) and (iii) from matching halves of fracture surfaces of sharp-cracked specimen CT HT2-09 tested at -100 °C with their corresponding EDX spectrums (ii) and (iv) respectively.

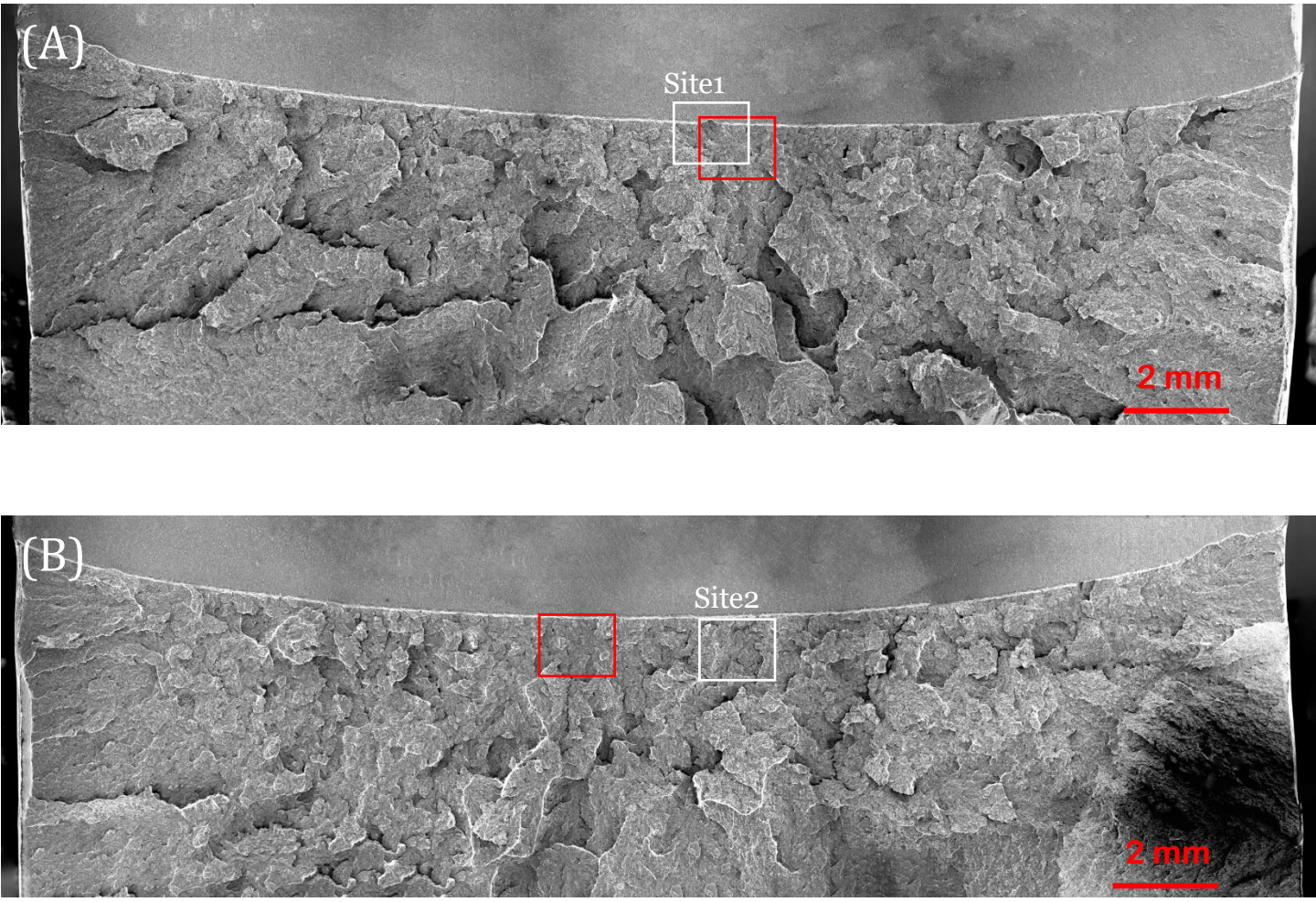


Figure 6-37 (a). Overview of fracture surfaces on a sharp-cracked specimen, designated CT HT2-21, tested at -100 °C. Red frames on matching halves (A) and (B) denote the most probable fracture initiation areas. White frame indicating local cleavage area site1 and site2. Test results: Critical J-integral (Jc) value of 86.2 $kJ/m^2$, crack tip opening displacement (CTOD) of 0.067 mm, local cleavage fracture stress of 2071 MPa (n=0.1), fracture initiation distance (Xo) of 402 µm, and an average stable crack extension of 32 µm.

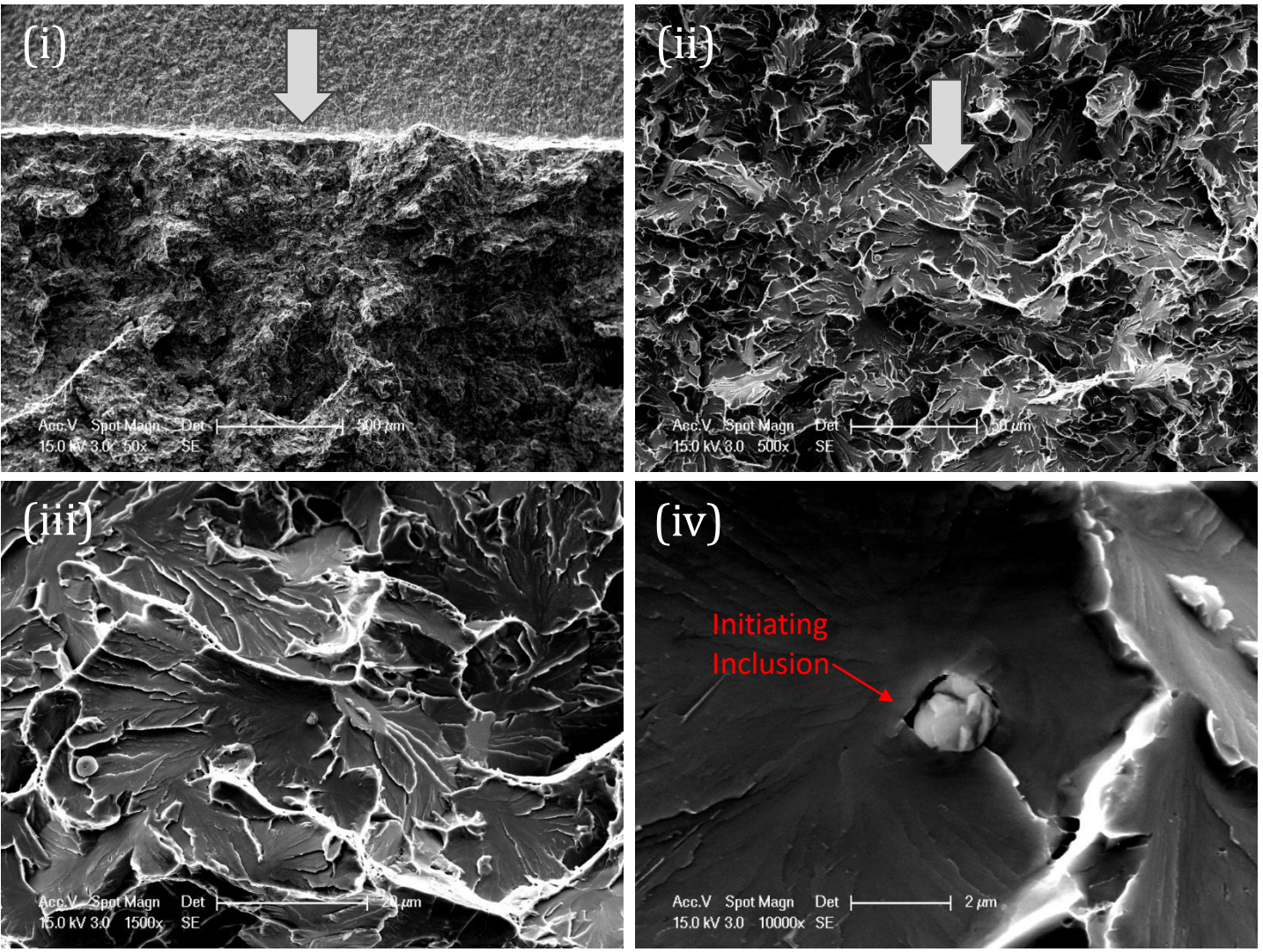


Figure 6-37 (b). Fracture Initiation at side (A) of the sharp-cracked specimen CT HT2-21, test temperature of -100 °C. A sequential magnification of the red-framed area at (i) 50x, (ii) 500x, (iii) 1500x, and (iv) 10000x are shown. Fractographic analysis reveals inclusion cracking as the initiation mechanism, with the inclusion's equivalent diameter at 1.4 µm and the initial facet's equivalent diameter at 35 µm.

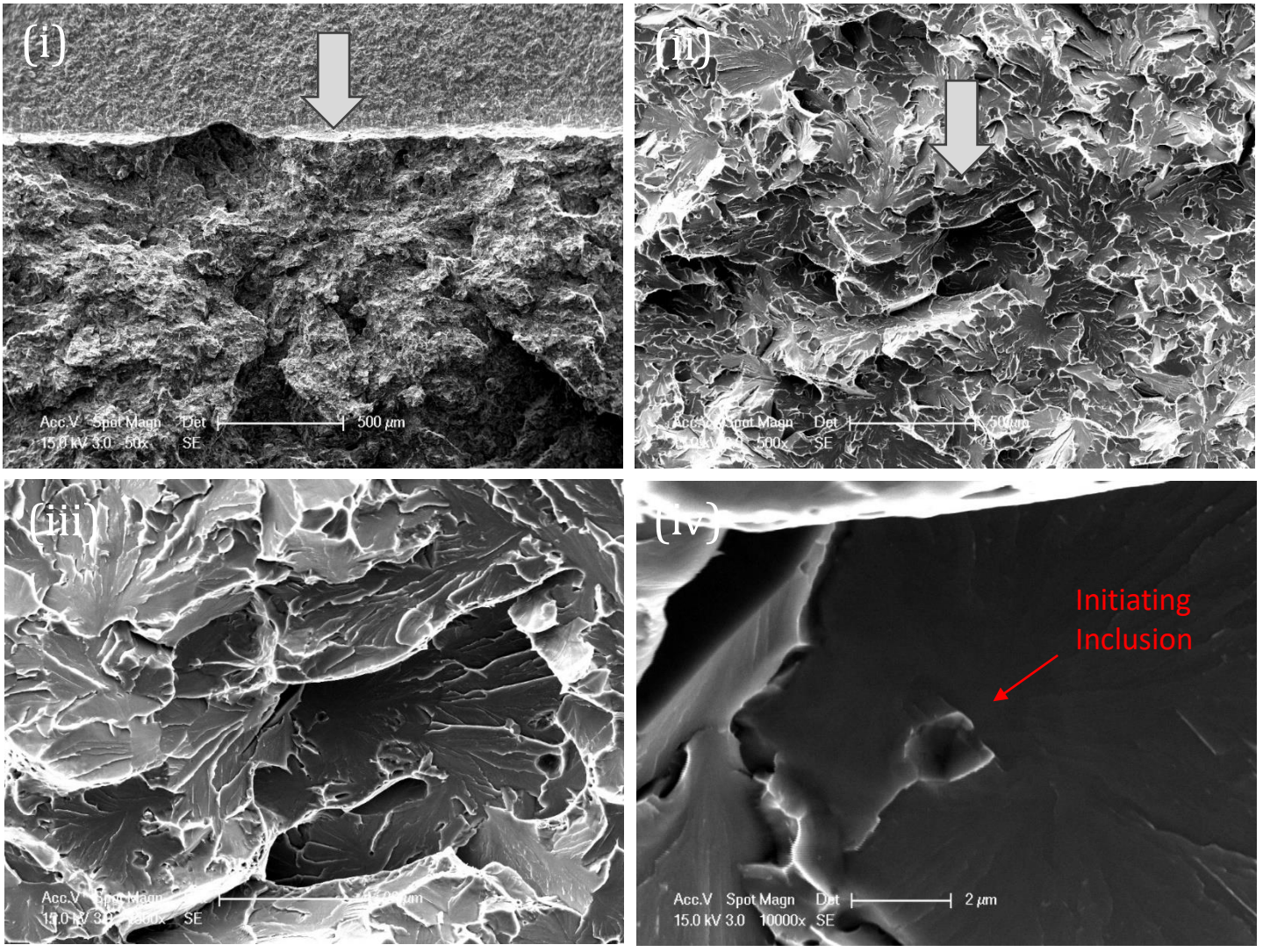


Figure 6-37 (c). Fracture Initiation at matching side (B) of the sharp-cracked specimen CT HT2-21, test temperature of -100 °C. A sequential magnification of the red-framed area at (i) 50x, (ii) 500x, (iii) 1000x, and (iv) 10000x are shown. Fractographic analysis reveals inclusion cracking as the initiation mechanism, with the inclusion's equivalent diameter at 1.4 µm and the initial facet's equivalent diameter at 35 µm.

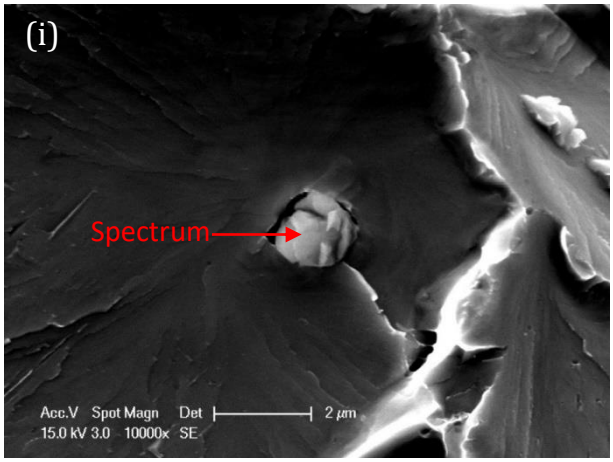


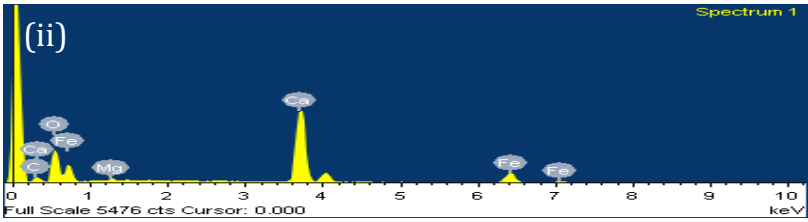


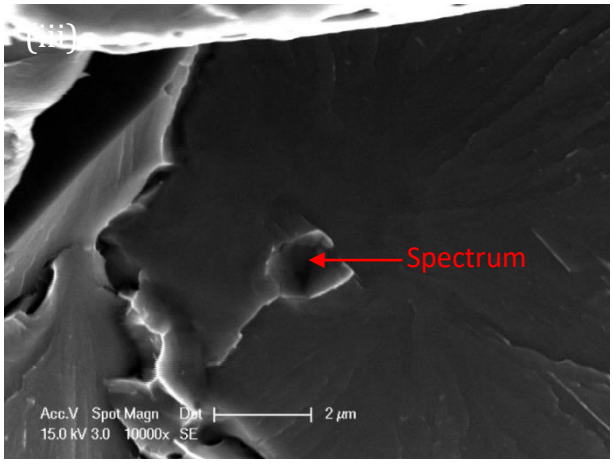


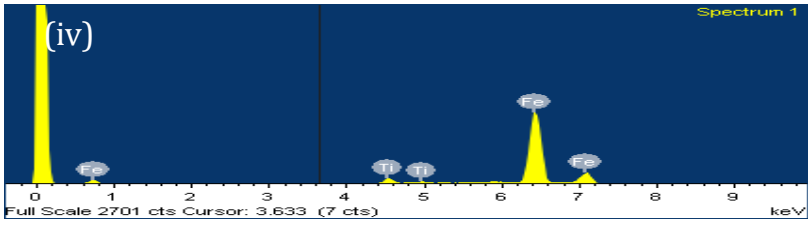


Figure 6-37 (d). Cleavage initiation point (i) and (iii) from matching halves of fracture surfaces of sharp-cracked specimen CT HT2-21 tested at -100 °C with their corresponding EDX spectrums (ii) and (iv) respectively.

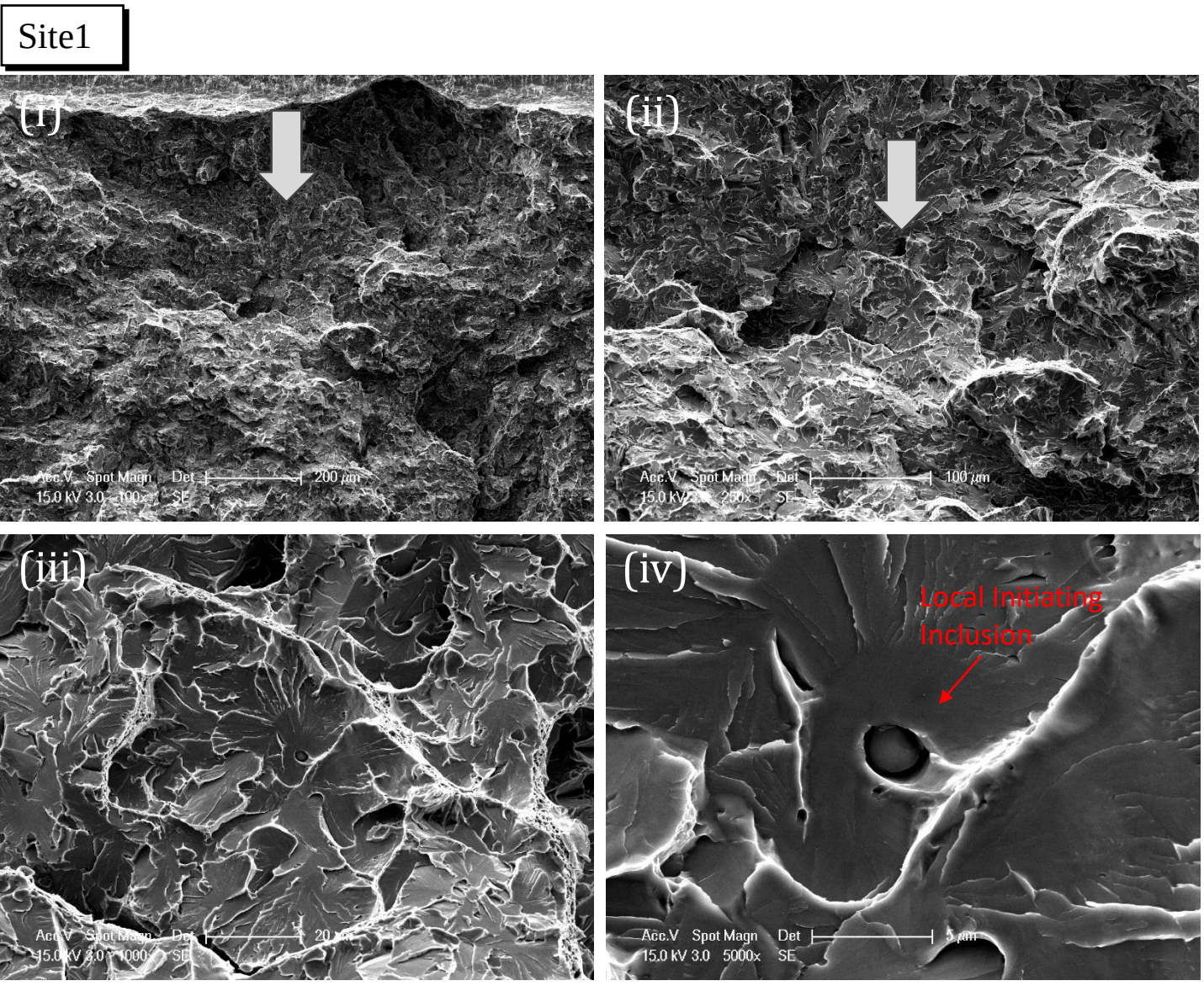


Figure 6-37 (e). Local fracture initiation area at side (A) of the sharp-cracked specimen CT HT2-21, test temperature of -100 °C. A sequential magnification of the white-framed area at (i) 100x, (ii) 250x, (iii) 1000x, and (iv) 5000x are shown.

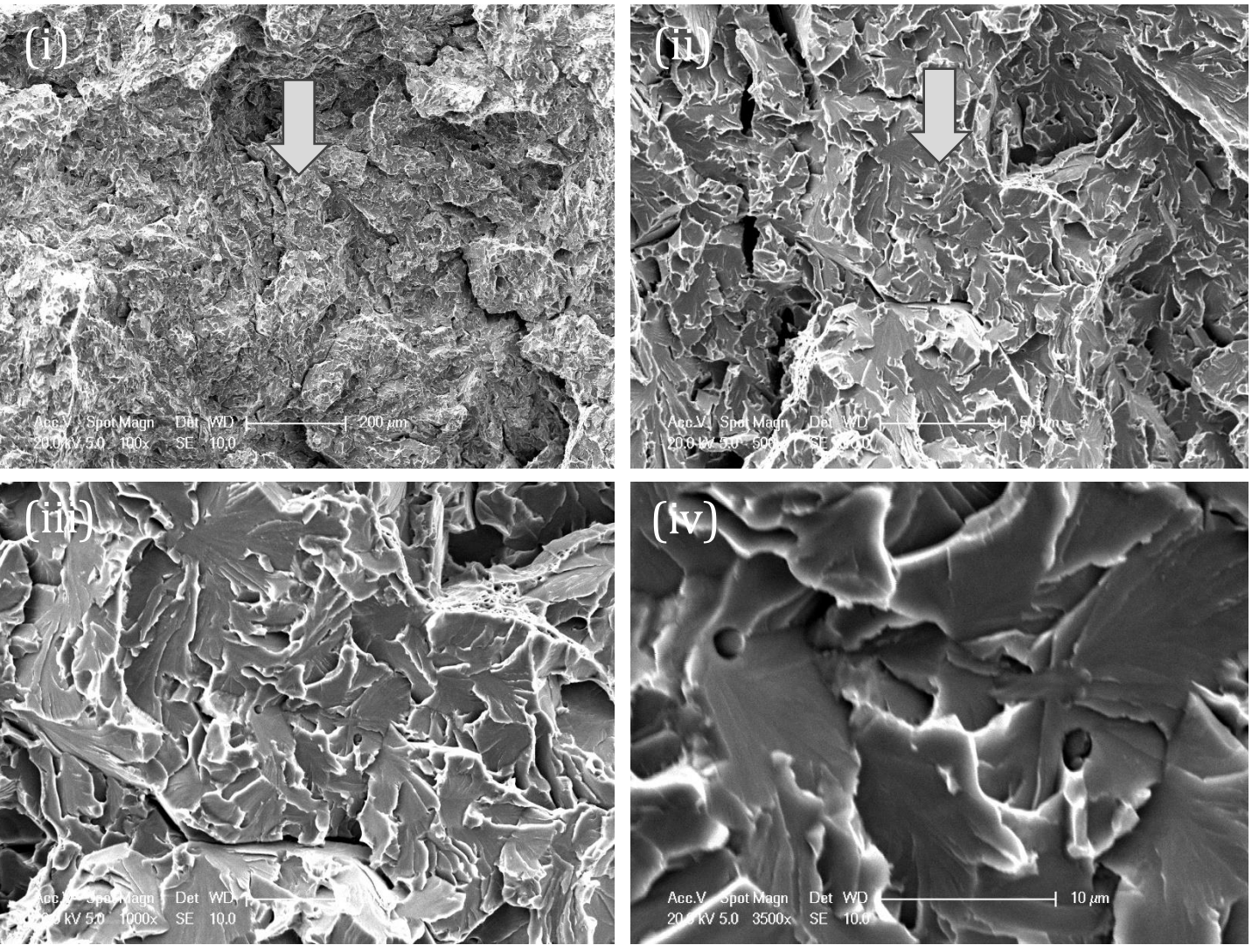


Figure 6-37 (f). Local cleavage area on side (B) of the sharp-cracked specimen CT HT2-21, illustrating regions where inclusions do not initiate cleavage, at a test temperature of -100°C. A sequential magnification of the white-framed area at (i) 100x, (ii) 500x, (iii) 1000x, and (iv) 3500x are shown.

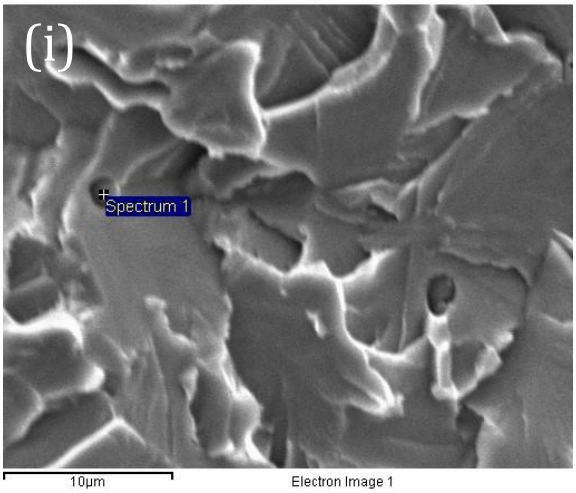


Site2

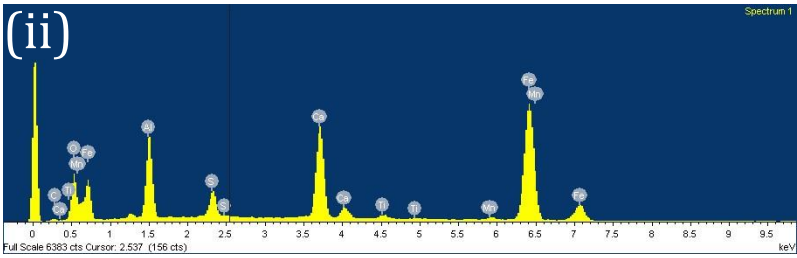


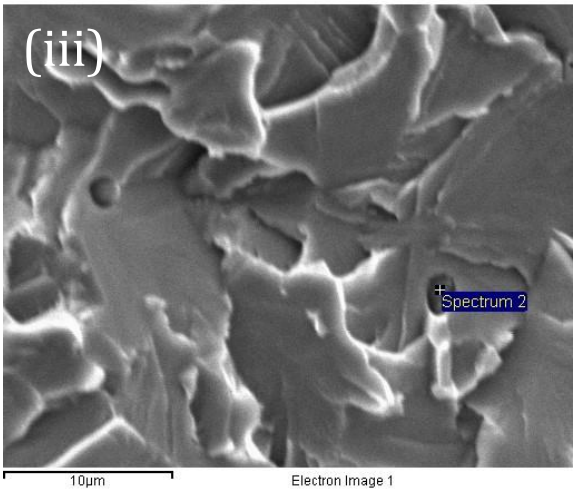


Site2

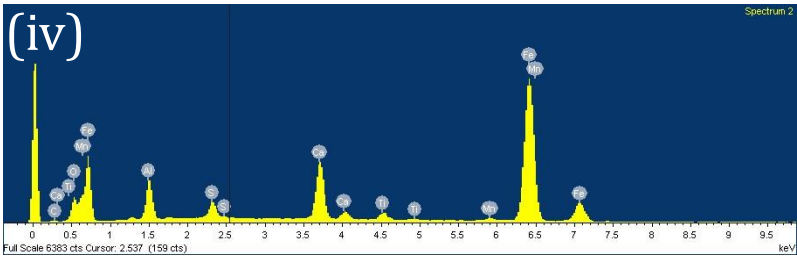


Figure 6-37 (g). EDX analysis results of inclusions within the local cleavage area on side (B) of the sharp-cracked specimen CT HT2-21, tested at -100°C. Image (i) and (iii) display the inclusion along with the location of the spectrum, while (ii) and (iv) present the corresponding spectrum results.

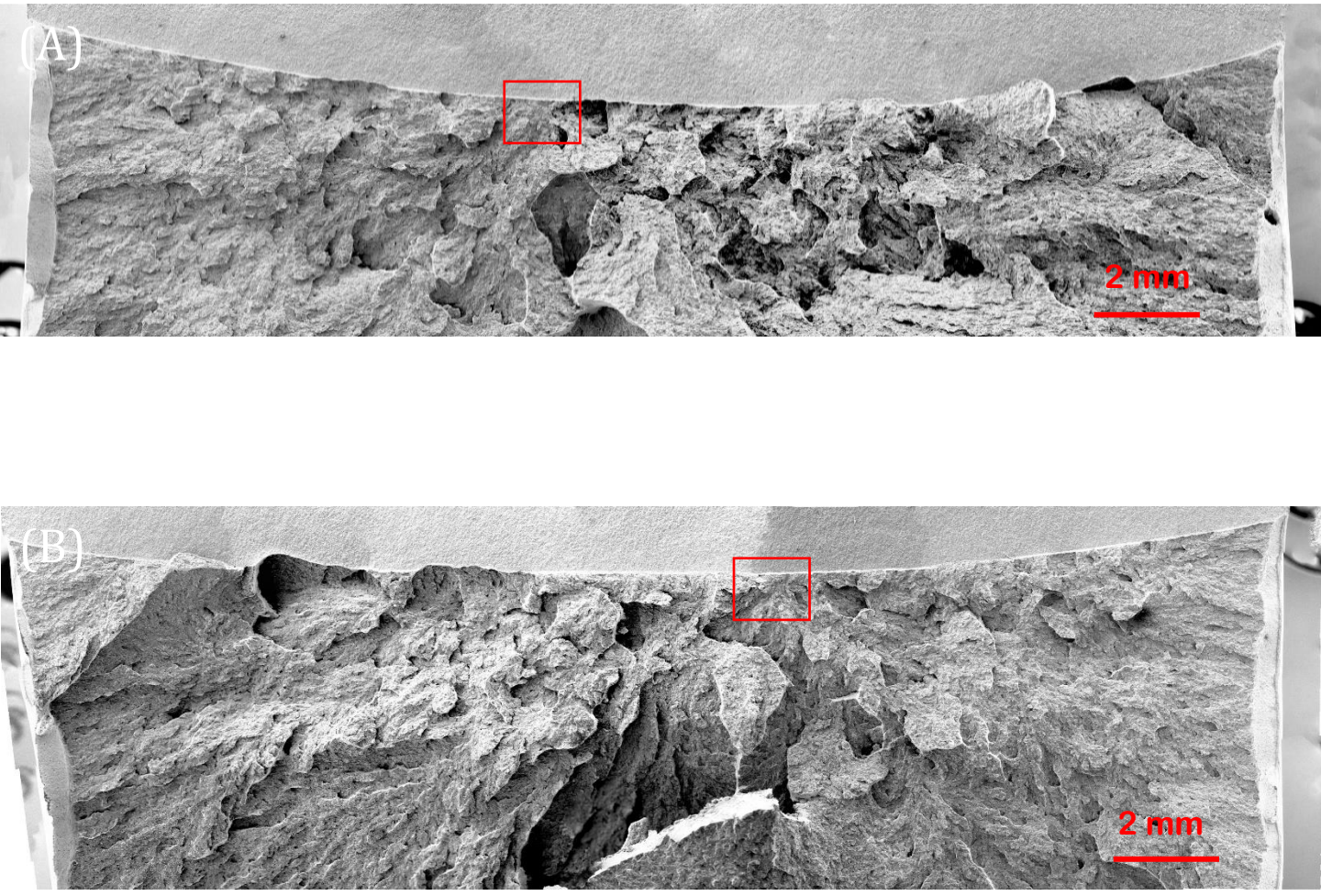


Figure 6-38 (a). Overview of fracture surfaces on a sharp-cracked specimen, designated CT HT1-17, tested at -80 °C. Red frames on matching halves (A) and (B) denote the most probable fracture initiation areas. Test results: Critical J-integral (Jc) value of 70.6 $kJ/m^2$, crack tip opening displacement (CTOD) of 0.056 mm, local cleavage fracture stress of 1992 MPa (n=0.1), fracture initiation distance (Xo) of 295 µm, and an average stable crack extension of 34 µm.

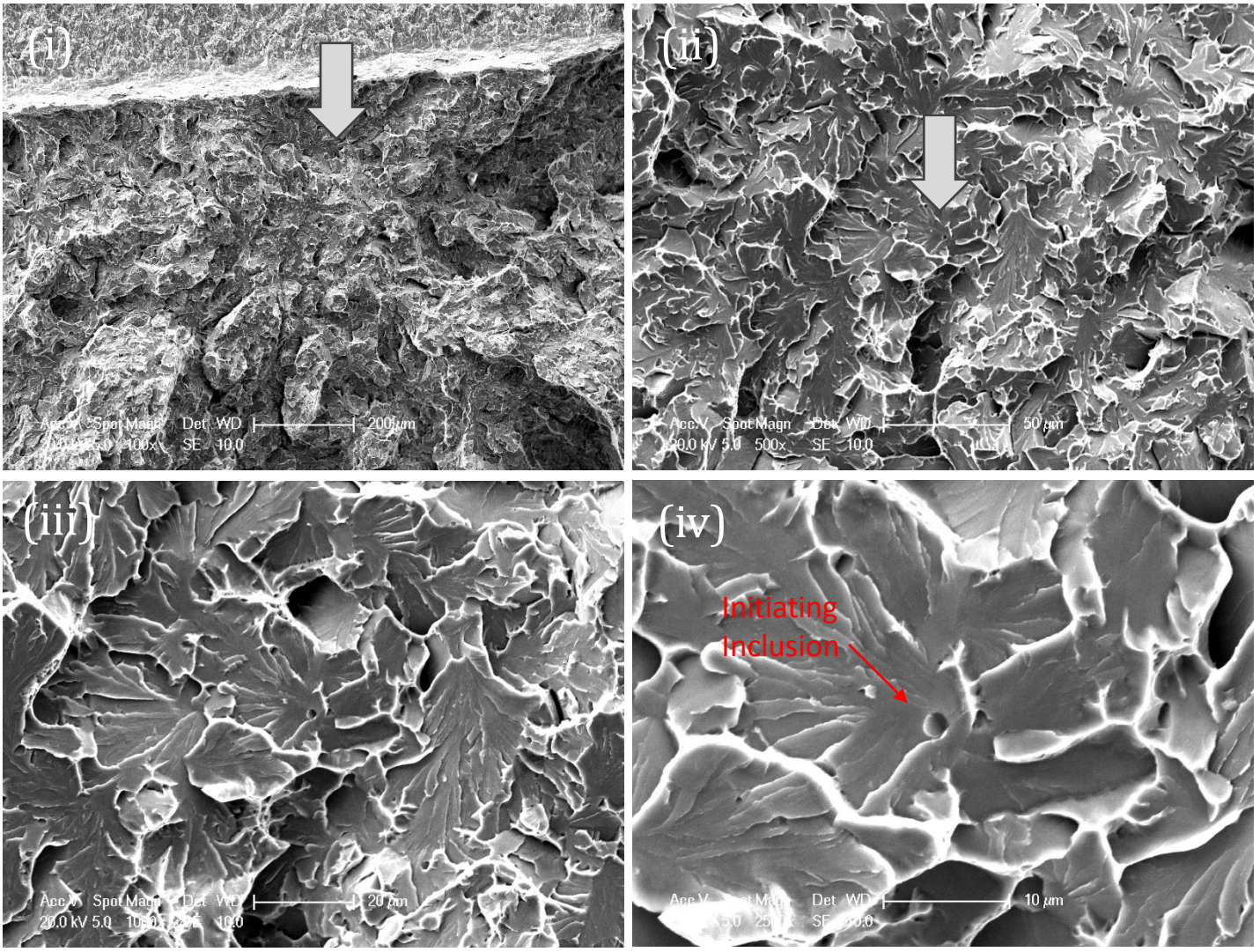


Figure 6-38 (b). Fracture Initiation at side (A) of the sharp-cracked specimen CT HT1-17, test temperature of -80 °C. A sequential magnification of the red-framed area at (i) 100x, (ii) 500x, (iii) 1000x, and (iv) 2500x are shown. Fractographic analysis reveals inclusion cracking as the initiation mechanism, with the inclusion's equivalent diameter at 2.1 µm and the initial facet's equivalent diameter at 29 µm.

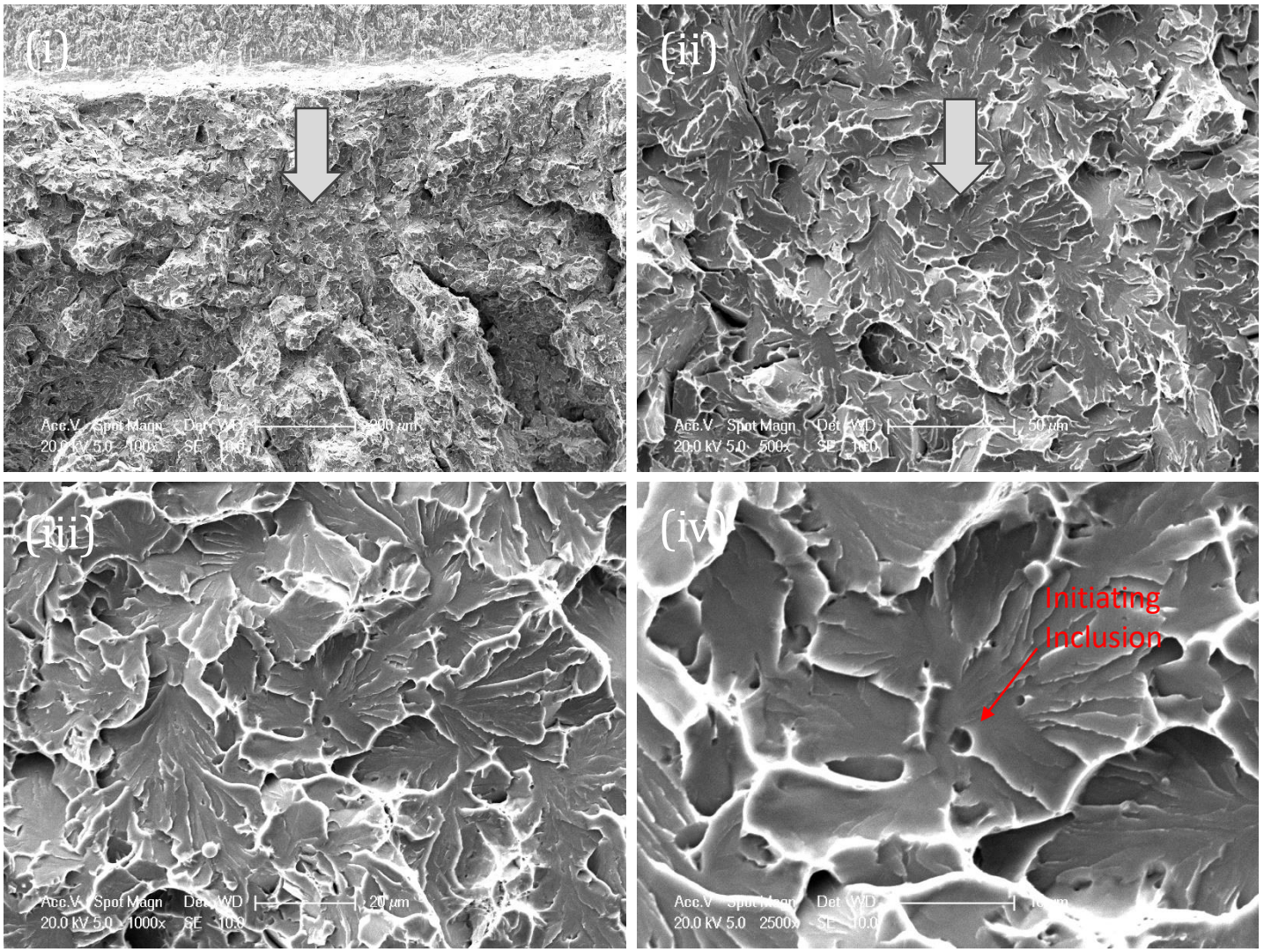


Figure 6-38 (c). Fracture Initiation at matching side (B) of the sharp-cracked specimen CT HT1-17, test temperature of -80 °C. A sequential magnification of the red-framed area at (i) 100x, (ii) 500x, (iii) 1000x, and (iv) 2500x are shown. Fractographic analysis reveals inclusion cracking as the initiation mechanism, with the inclusion's equivalent diameter at 2.1 µm and the initial facet's equivalent diameter at 29 µm.

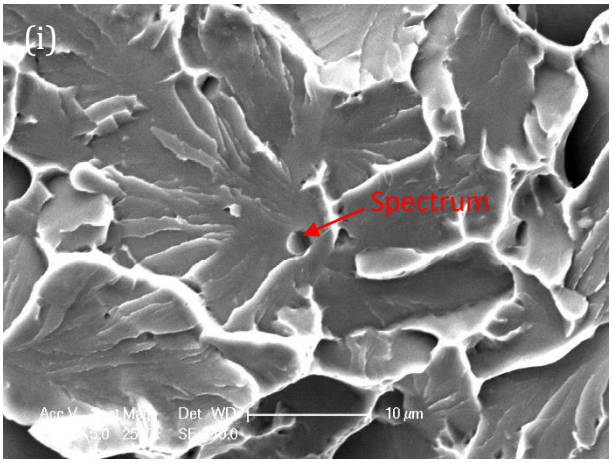


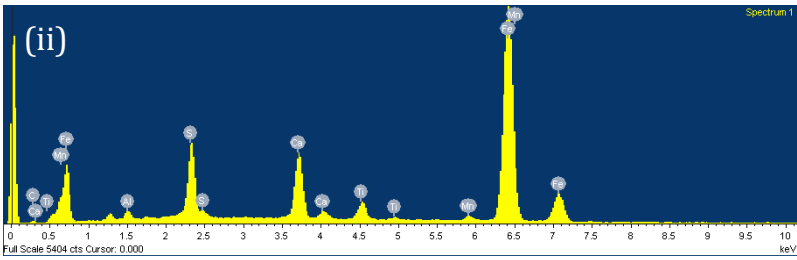


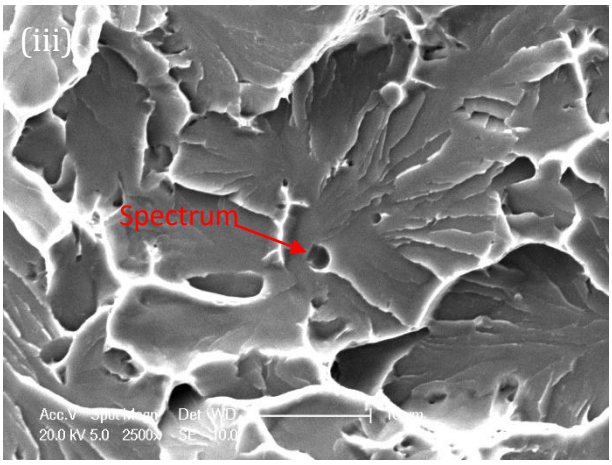


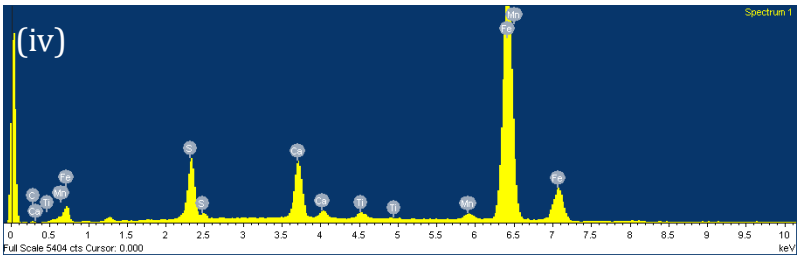


Figure 6-38 (d). Cleavage initiation point (i) and (iii) from matching halves of fracture surfaces of sharp-cracked specimen CT HT1-17 tested at -80 °C with their corresponding EDX spectrums (ii) and (iv) respectively.

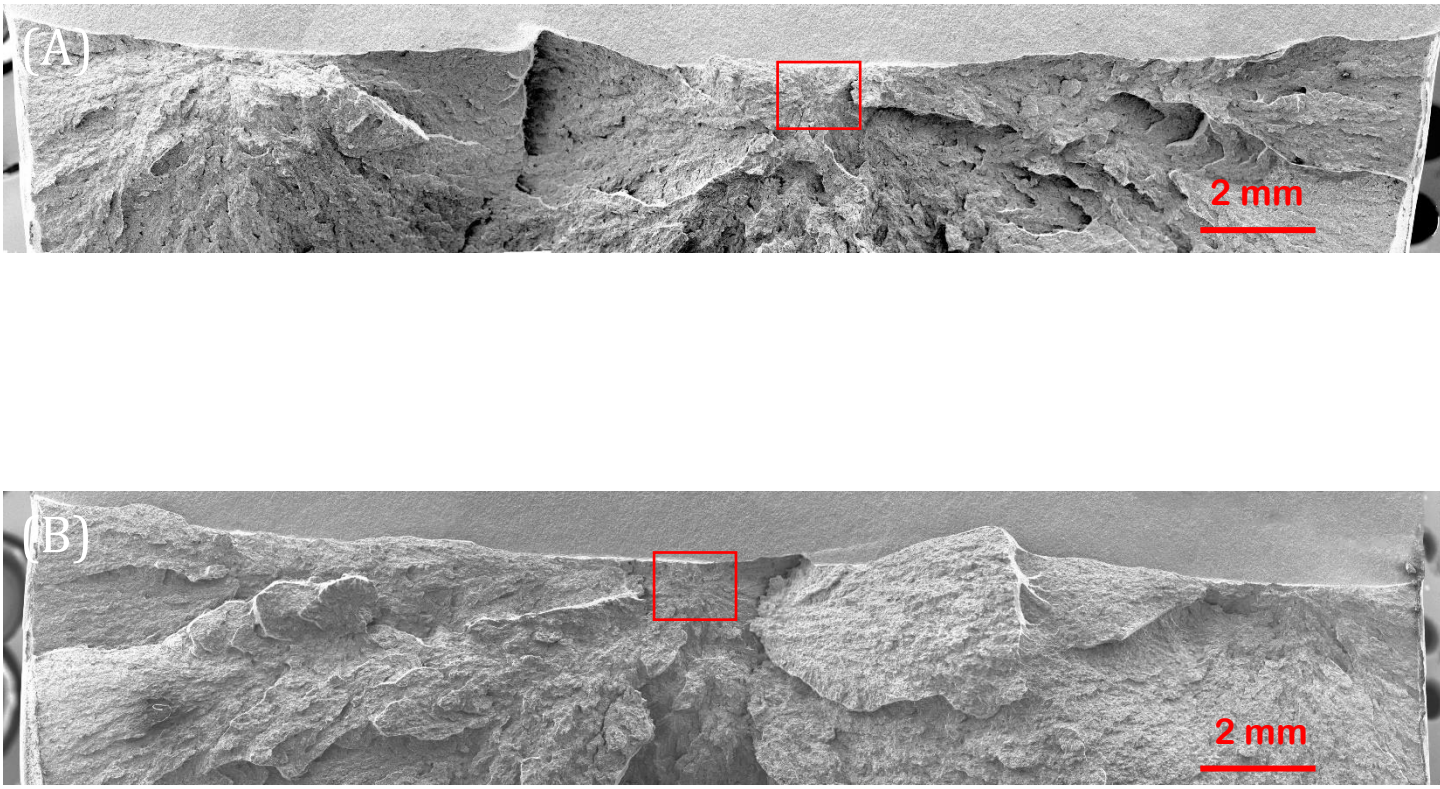


Figure 6-39 (a). Overview of fracture surfaces on a sharp-cracked specimen, designated CT HT2-25, tested at -80 °C. Red frames on matching halves (A) and (B) denote the most probable fracture initiation areas. Test results: Critical J-integral (Jc) value of 155.9 $kJ/m^2$, crack tip opening displacement (CTOD) of 0.120 mm, local cleavage fracture stress of 2078 MPa (n=0.1), fracture initiation distance (Xo) of 486 µm, and an average stable crack extension of 54 µm.

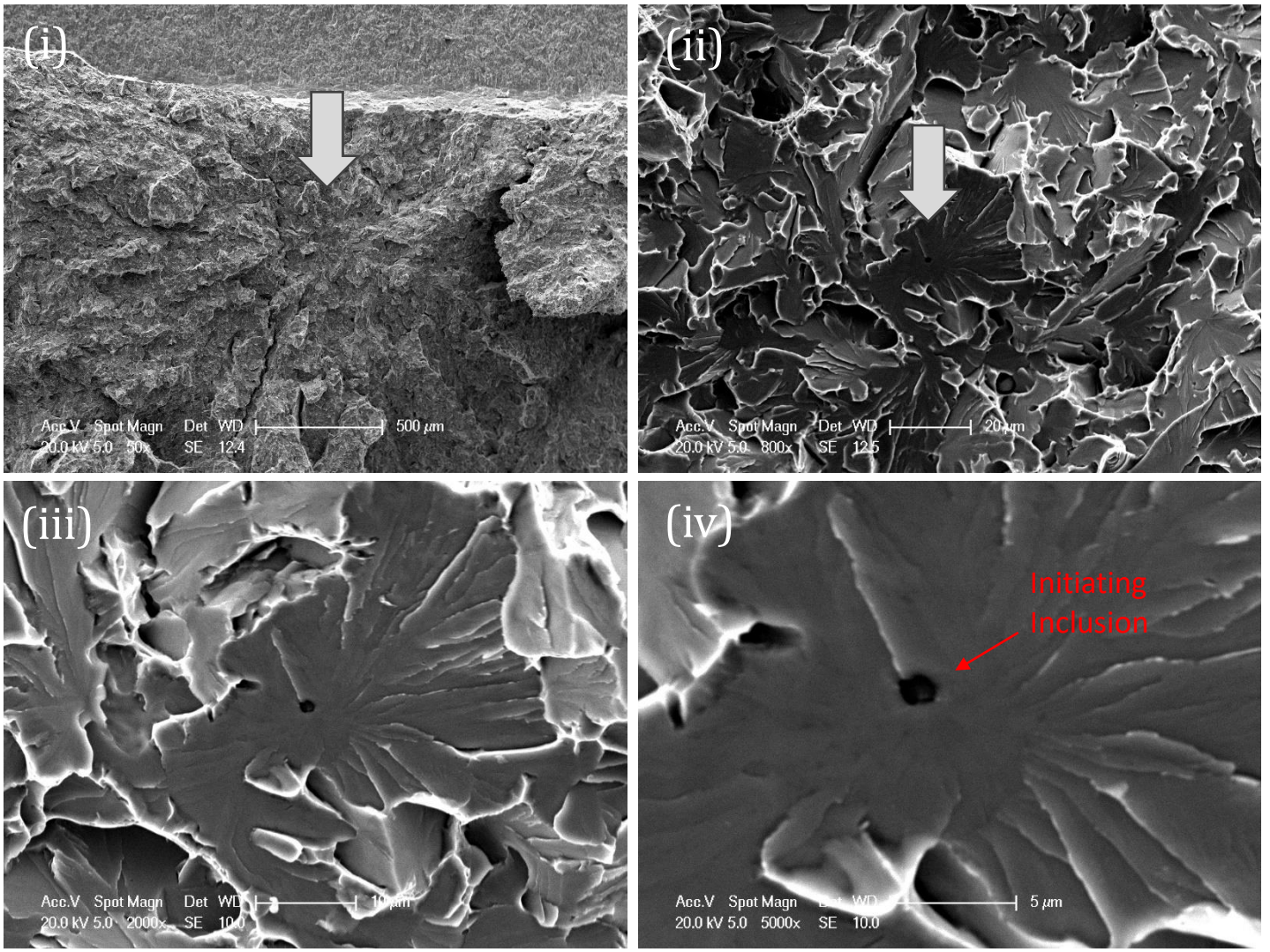


Figure 6-39 (b). Fracture Initiation at side (A) of the sharp-cracked specimen CT HT2-25, test temperature of -80 °C. A sequential magnification of the red-framed area at (i) 100x, (ii) 800x, (iii) 2000x, and (iv) 5000x are shown. Fractographic analysis reveals inclusion cracking as the initiation mechanism, with the inclusion's equivalent diameter at 1.4 µm and the initial facet's equivalent diameter at 39 µm.

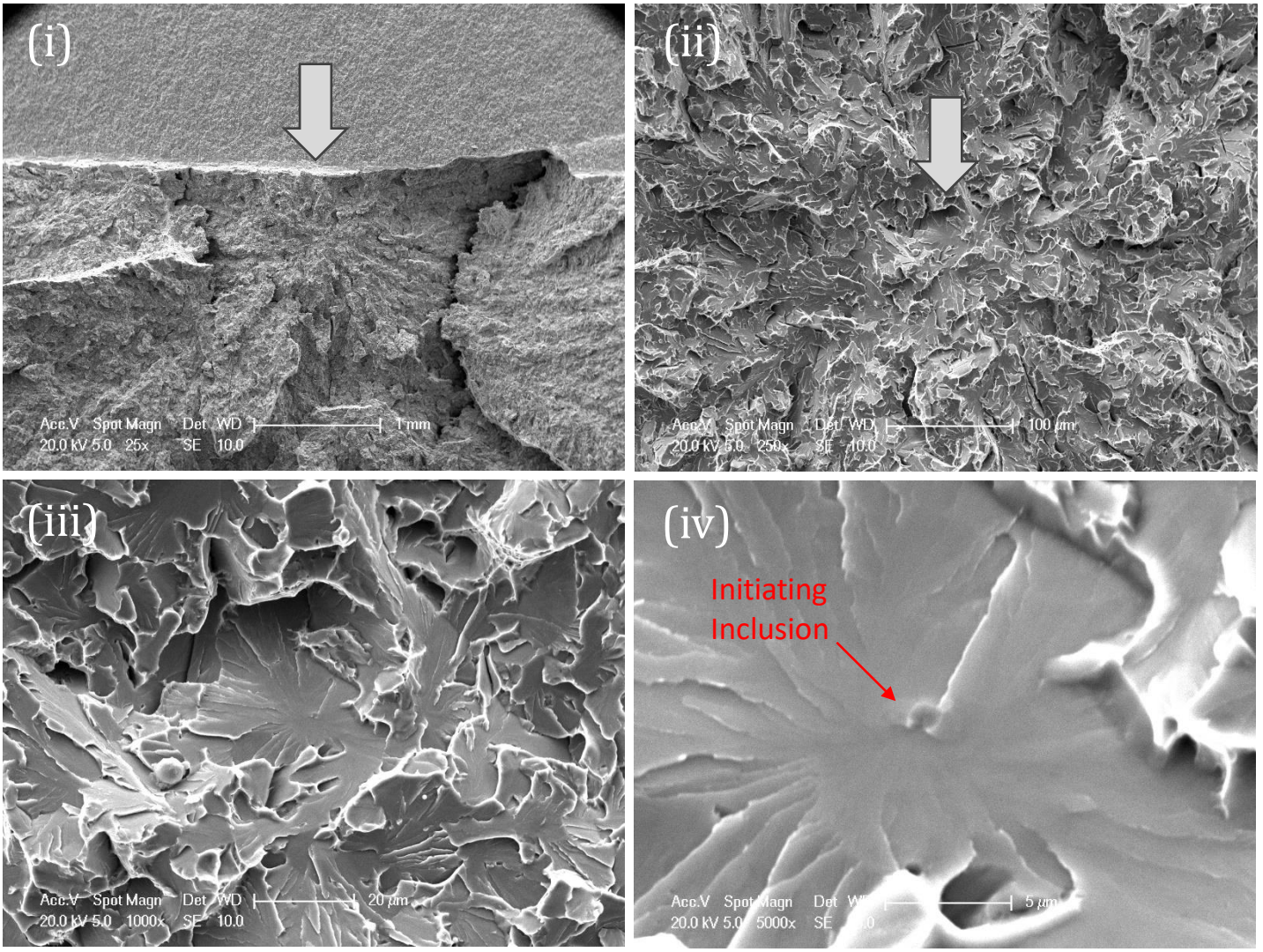


Figure 6-39 (c). Fracture Initiation at matching side (B) of the sharp-cracked specimen CT HT2-25, test temperature of -80 °C. A sequential magnification of the red-framed area at (i) 25x, (ii) 250x, (iii) 1000x, and (iv) 5000x are shown. Fractographic analysis reveals inclusion cracking as the initiation mechanism, with the inclusion's equivalent diameter at 1.4 µm and the initial facet's equivalent diameter at 39 µm.

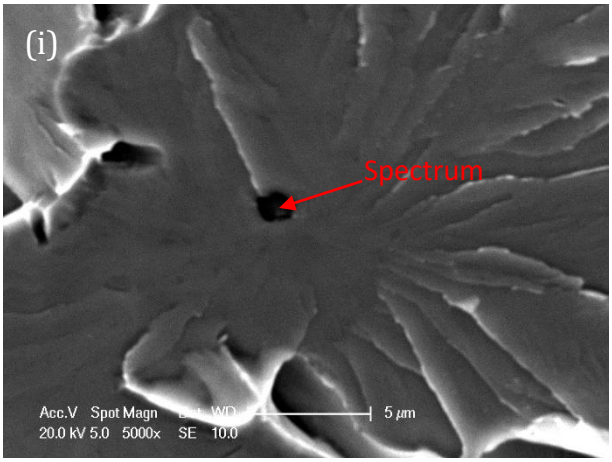


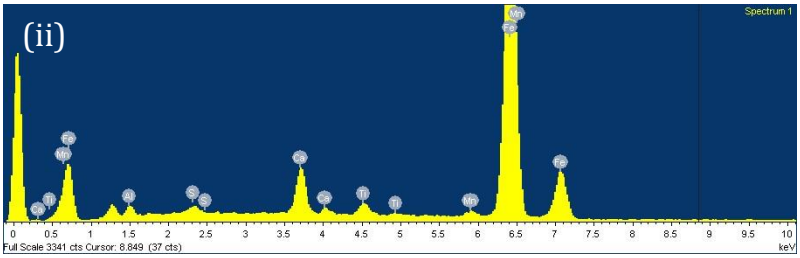


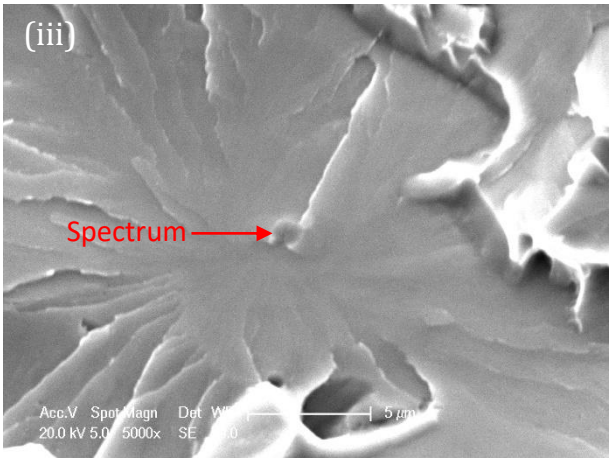


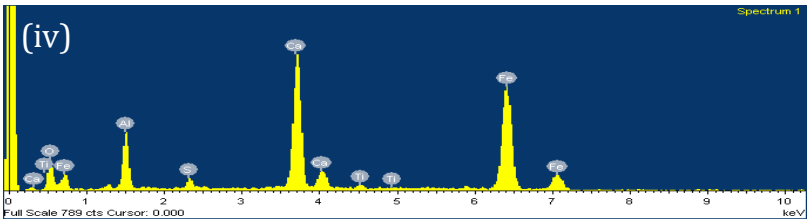


Figure 6-39 (d). Cleavage initiation point (i) and (iii) from matching halves of fracture surfaces of sharp-cracked specimen CT HT2-25 tested at -80 °C with their corresponding EDX spectrums (ii) and (iv) respectively.

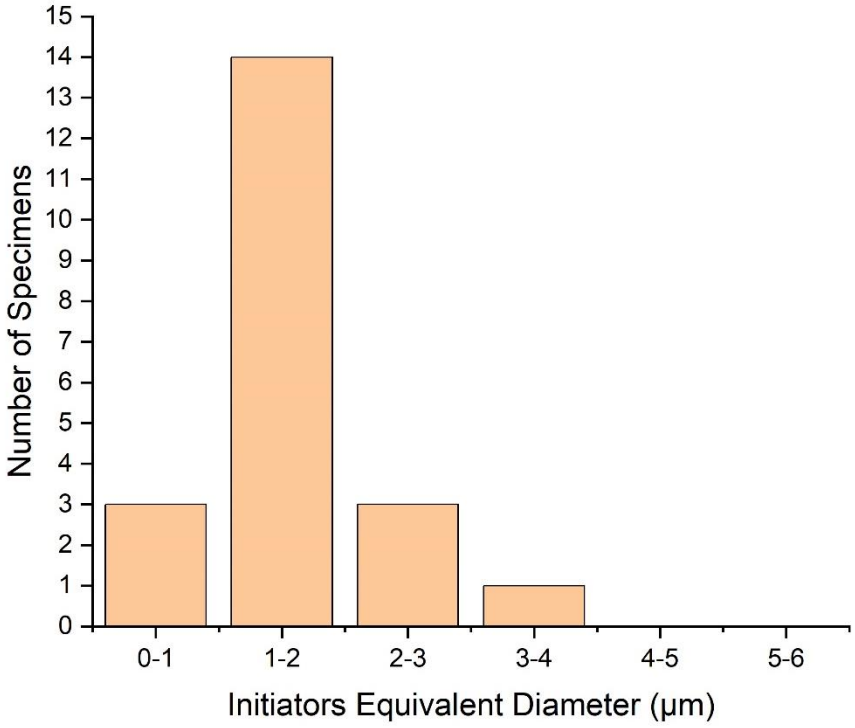


Figure 6-40. Size distribution of initiators in all 26 specimens that initiation sites were identified.

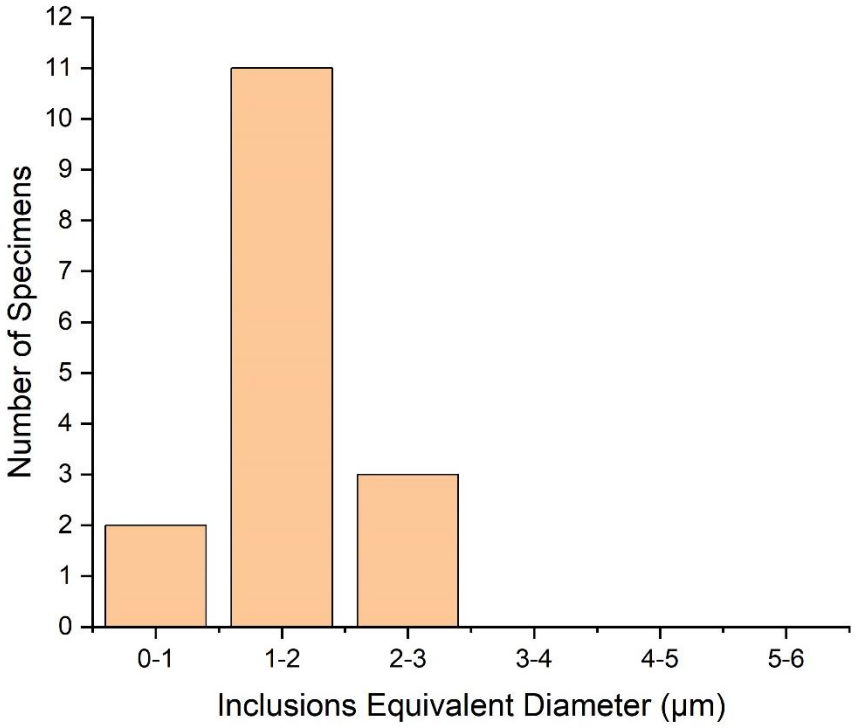


Figure 6-41. Size distribution of inclusions in all 17 specimens which has an inclusion as initiator.

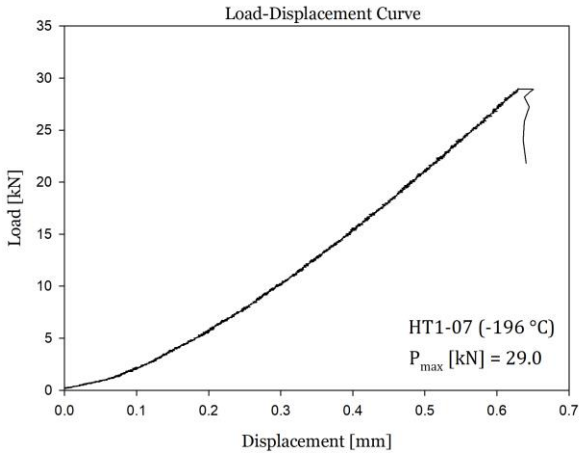
Load-Displacement Curve
Load [kN]
Displacement [mm]
HT1-07 (-196 °C)
P_max [kN] = 29.0

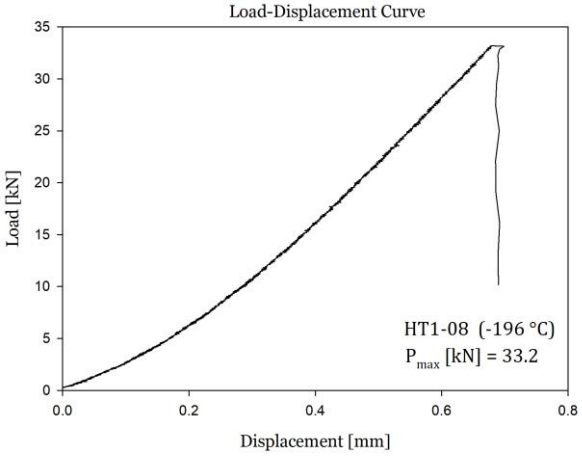
Load-Displacement Curve
Load [kN]
Displacement [mm]
HT1-08 (-196 °C)
P_max [kN] = 33.2

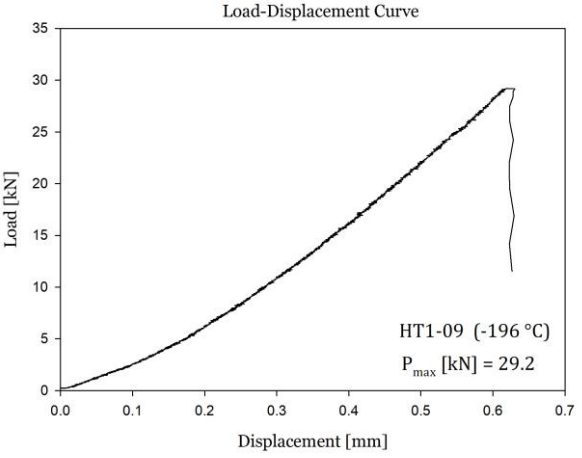
Load-Displacement Curve
Load [kN]
Displacement [mm]
HT1-09 (-196 °C)
P_max [kN] = 29.2

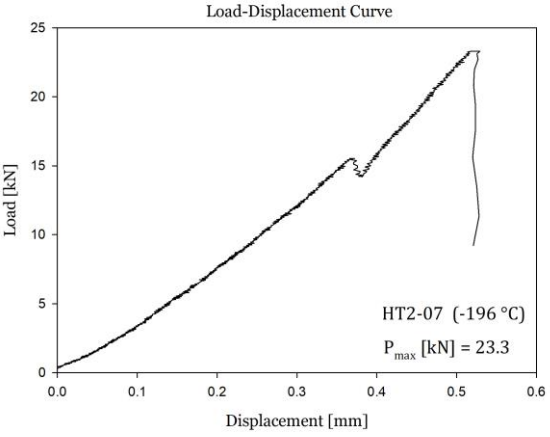
Load-Displacement Curve
Load [kN]
Displacement [mm]
HT2-07 (-196 °C)
P_max [kN] = 23.3

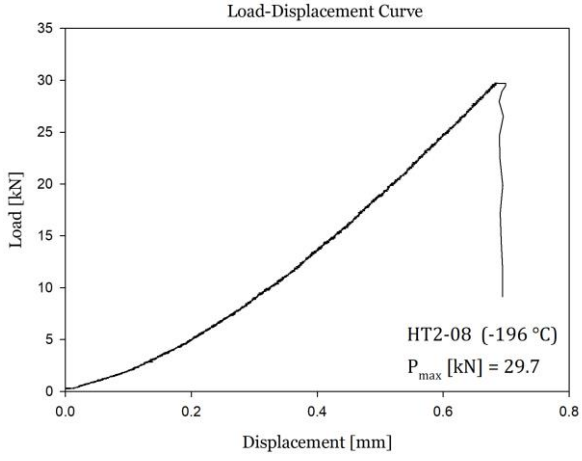
Load-Displacement Curve
Load [kN]
Displacement [mm]
HT2-08 (-196 °C)
P_max [kN] = 29.7

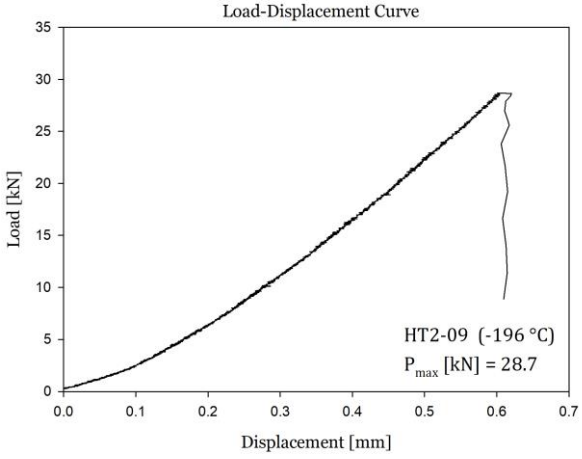
Load-Displacement Curve
Load [kN]
Displacement [mm]
HT2-09 (-196 °C)
P_max [kN] = 28.7

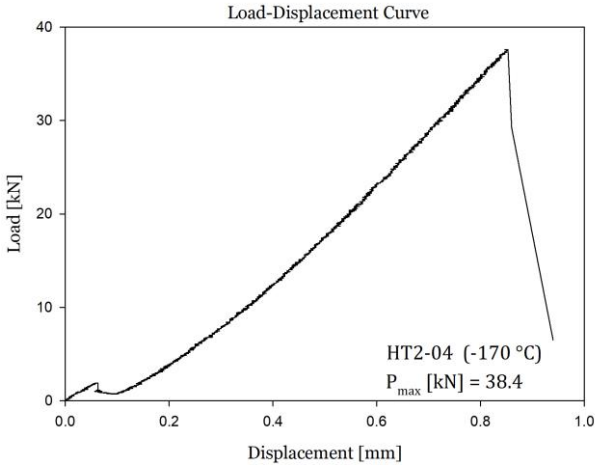


Figure 6-42. Load-displacement curves for blunt-notched specimens HT1-07/HT1-08/ HT1-09/HT2-07/HT2-08/HT2-09 at -196 °C and HT2-04 tested at -170 °C

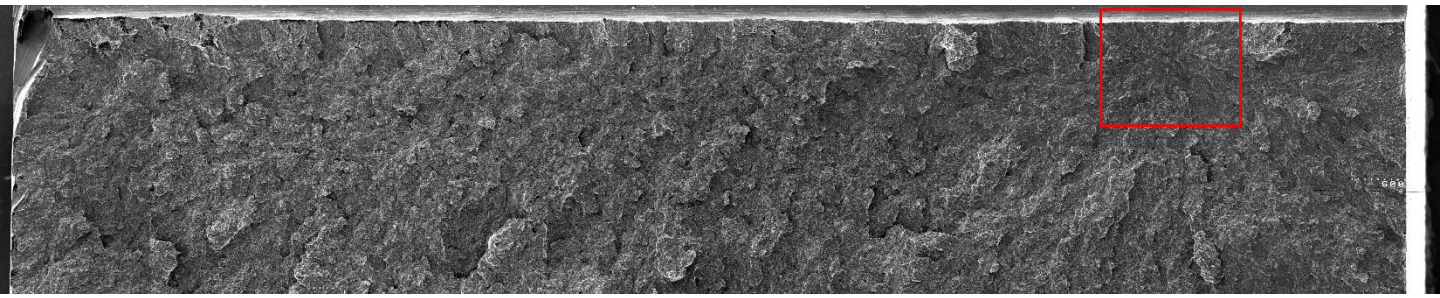

Figure 6-43 (a). Overview of the fracture surface on one side of the blunt-notched specimen FS HT1-07, tested at -196°C, with a red frame highlighting the most probable initiation area. Test results: Local cleavage fracture stress of 1956 Mpa, fracture initiation distance (X0) of 305 µm.

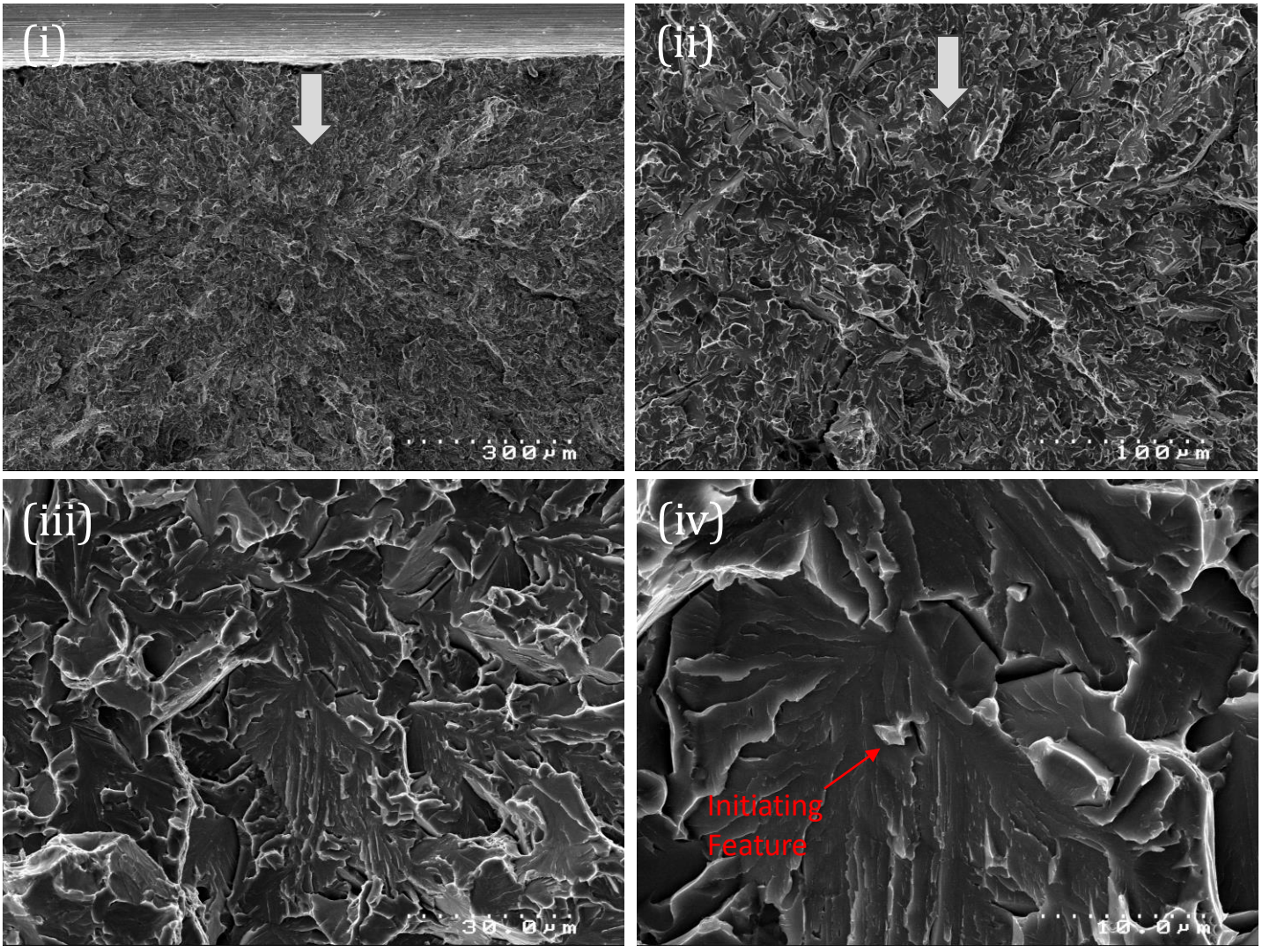


Figure 6-43 (b). Fracture initiation point of one side blunt-notched specimen FS HT1-07 tested at -196 °C; (i), (ii), (iii) and (iv) are sequential magnification of the same red framed area. Fractographic analysis reveals matrix related feature as the initiation, with the initiating feature's equivalent diameter at 1.8 µm and the initial facet's equivalent diameter at 34 µm.

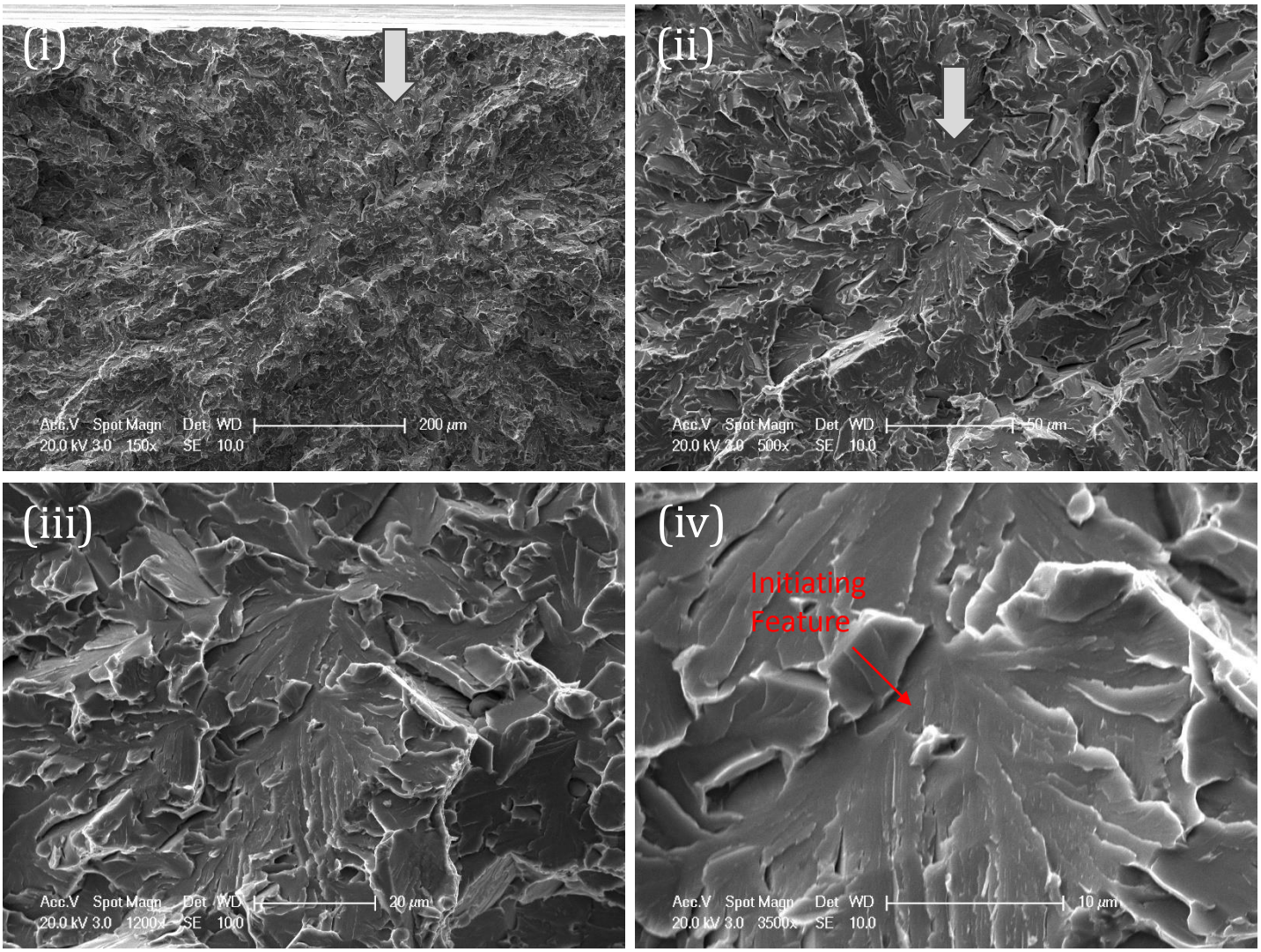


Figure 6-43 (c). Fracture initiation point of the matching side of blunt-notched specimen FS HT1-07 tested at -196 °C; A sequential magnification of the initiation area at (i) 150x, (ii) 500x, (iii) 1200x, and (iv) 3500x are shown. Fractographic analysis reveals matrix related feature as the initiation, with the initiating feature's equivalent diameter at 1.8 µm and the initial facet's equivalent diameter at 34 µm.

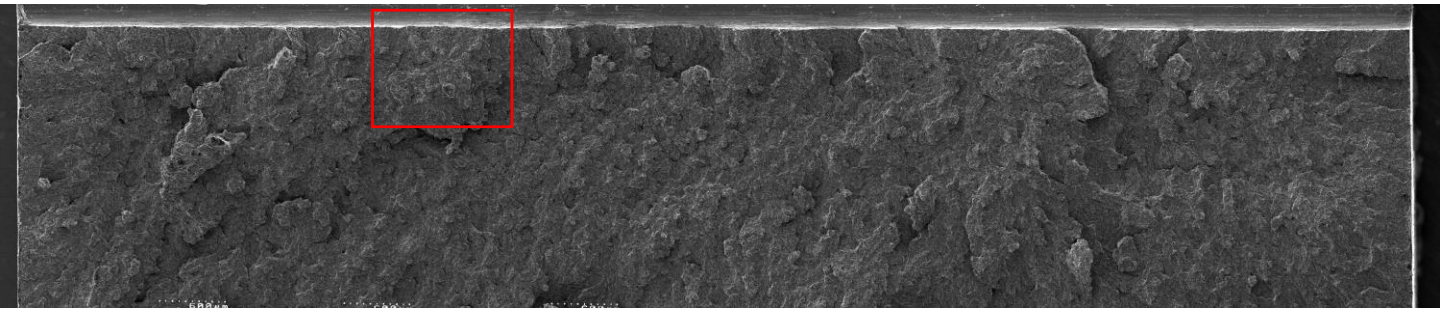

Figure 6-44 (a). Overview of the fracture surface on one side of the blunt-notched specimen FS HT1-08, tested at -196°C, with a red frame highlighting the most probable initiation area. Test results: Local cleavage fracture stress of 2039 Mpa, fracture initiation distance (Xo) of 320 µm.

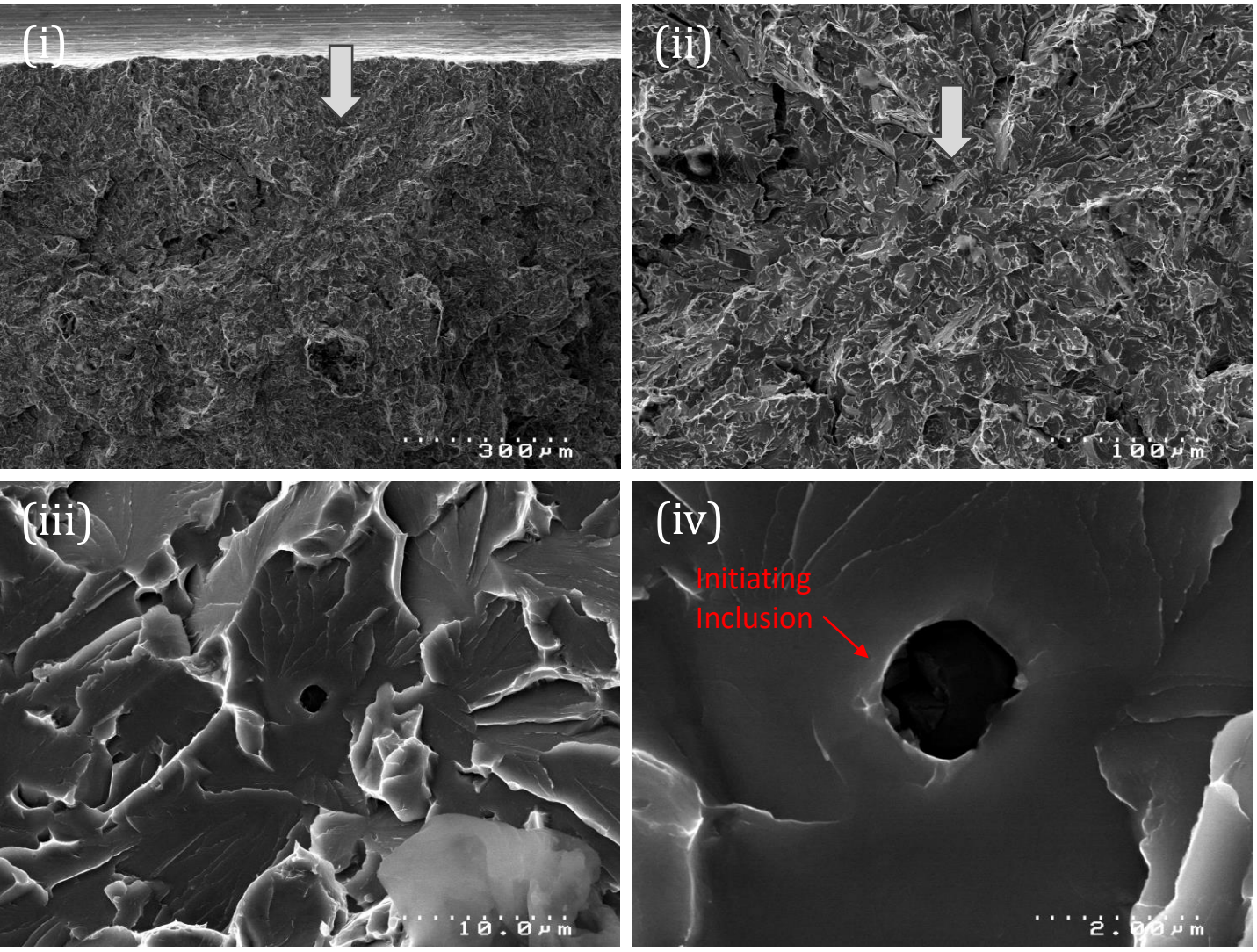


Figure 6-44 (b). Fracture initiation point of one side blunt-notched specimen FS HT1-08 tested at -196 °C; (i), (ii), (iii) and (iv) are sequential magnification of the same red framed area. Fractographic analysis reveals inclusion cracking as the initiation mechanism, with the inclusion's equivalent diameter at 1.8 µm and the initial facet's equivalent diameter at 20 µm.

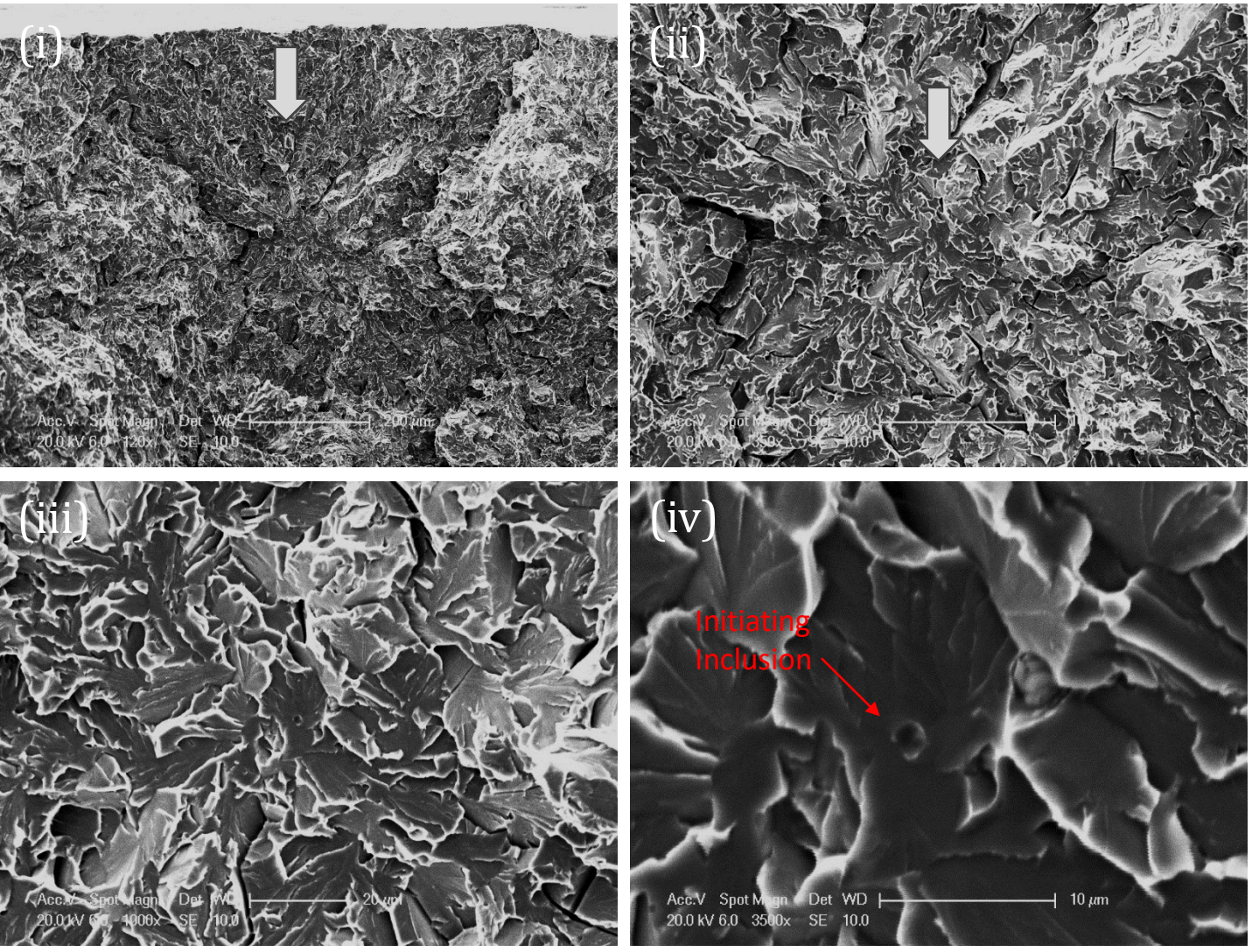


Figure 6-44 (c). Fracture initiation point of the matching side of blunt-notched specimen FS HT1-08 tested at -196 °C; A sequential magnification of the initiation area at (i) 120x, (ii) 350x, (iii) 1000x, and (iv) 3500x are shown. Fractographic analysis reveals inclusion cracking as the initiation mechanism, with the inclusion's equivalent diameter at 1.8 µm and the initial facet's equivalent diameter at 20 µm.

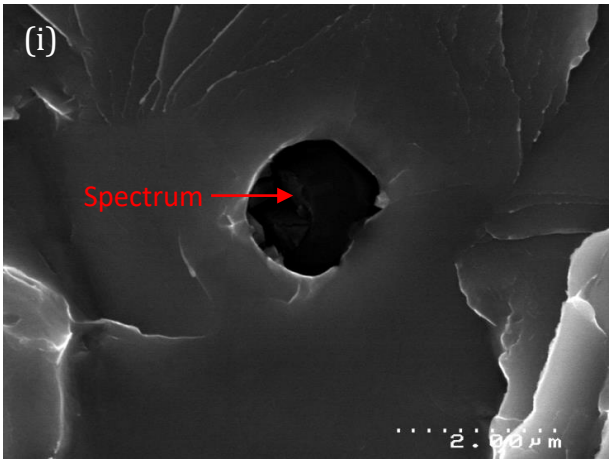


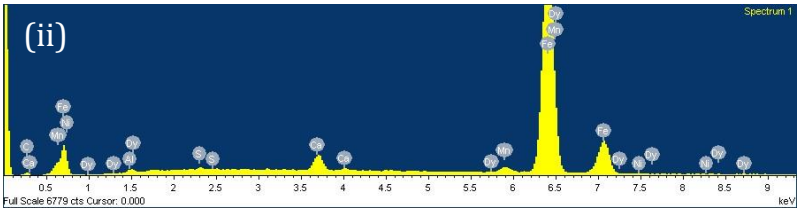


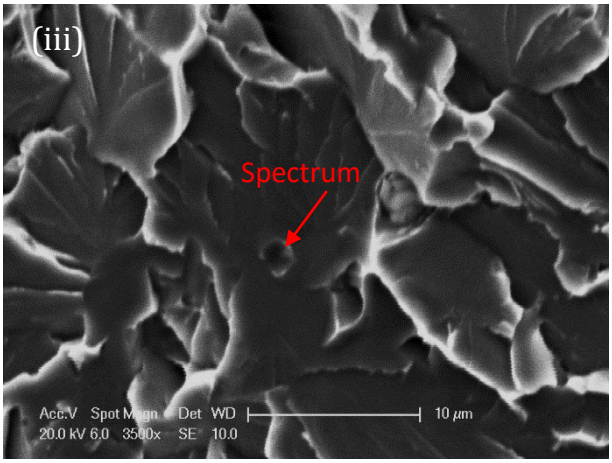


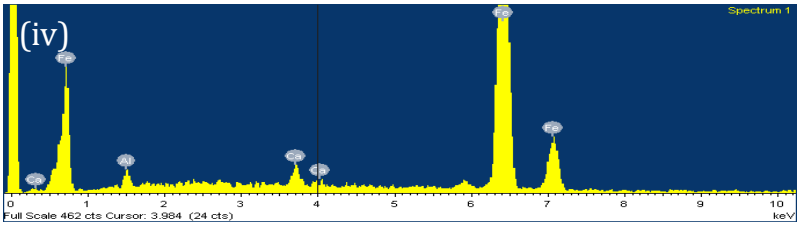


Figure 6-44 (d). Cleavage initiation point (i) and (iii) from matching halves of fracture surfaces of blunt-notched specimen FS HT1-08 tested at -196 °C with their corresponding EDX spectrums (ii) and (iv) respectively.

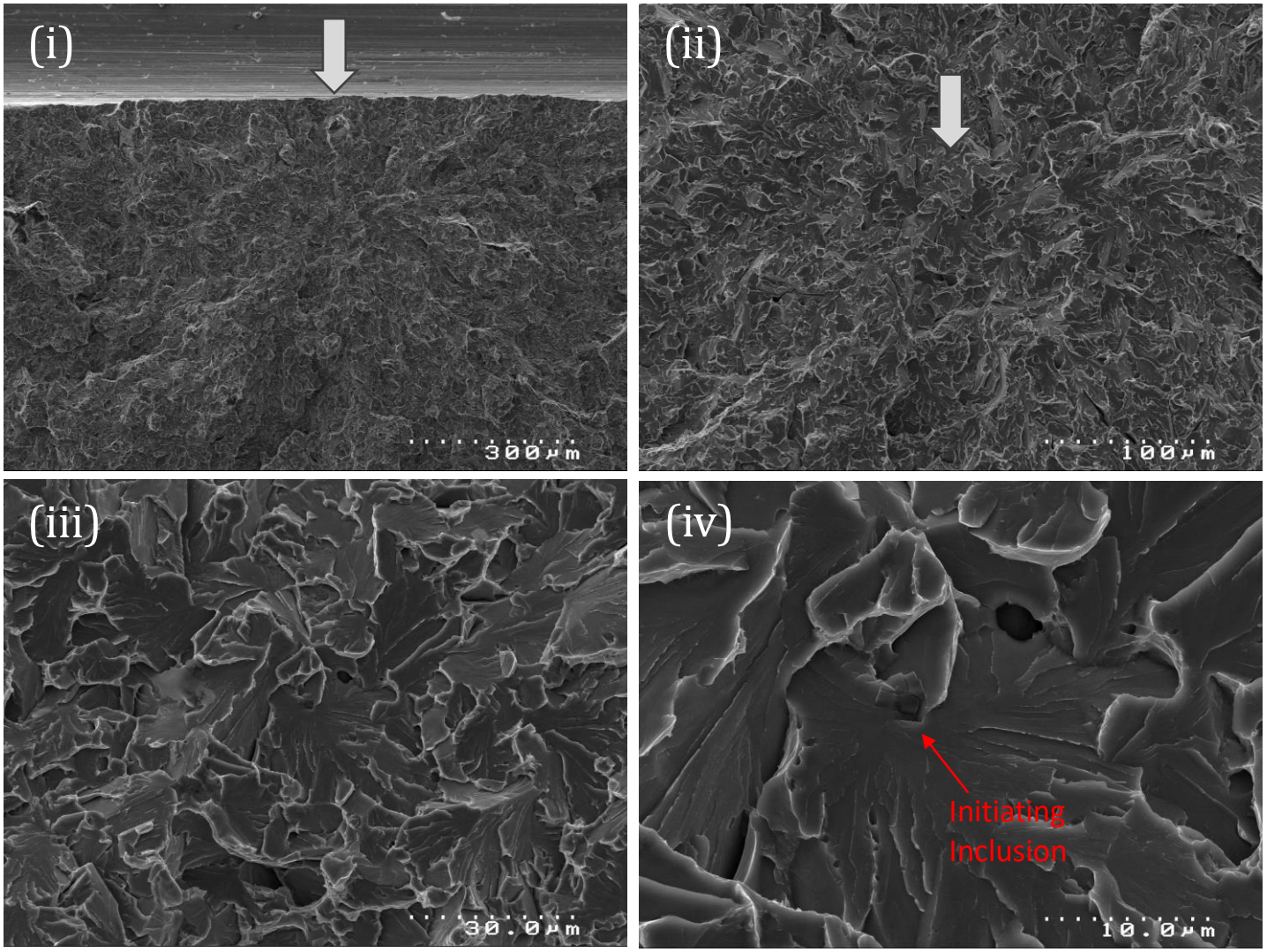


Figure 6-45 (a). Fracture initiation point of one side blunt-notched specimen FS HT1-09 tested at -196 °C; (i), (ii), (iii) and (iv) are sequential magnification of the most probable initiation area. Fractographic analysis reveals inclusion cracking as the initiation mechanism, with the inclusion's equivalent diameter at 1.6 µm and the initial facet's equivalent diameter at 23 µm.

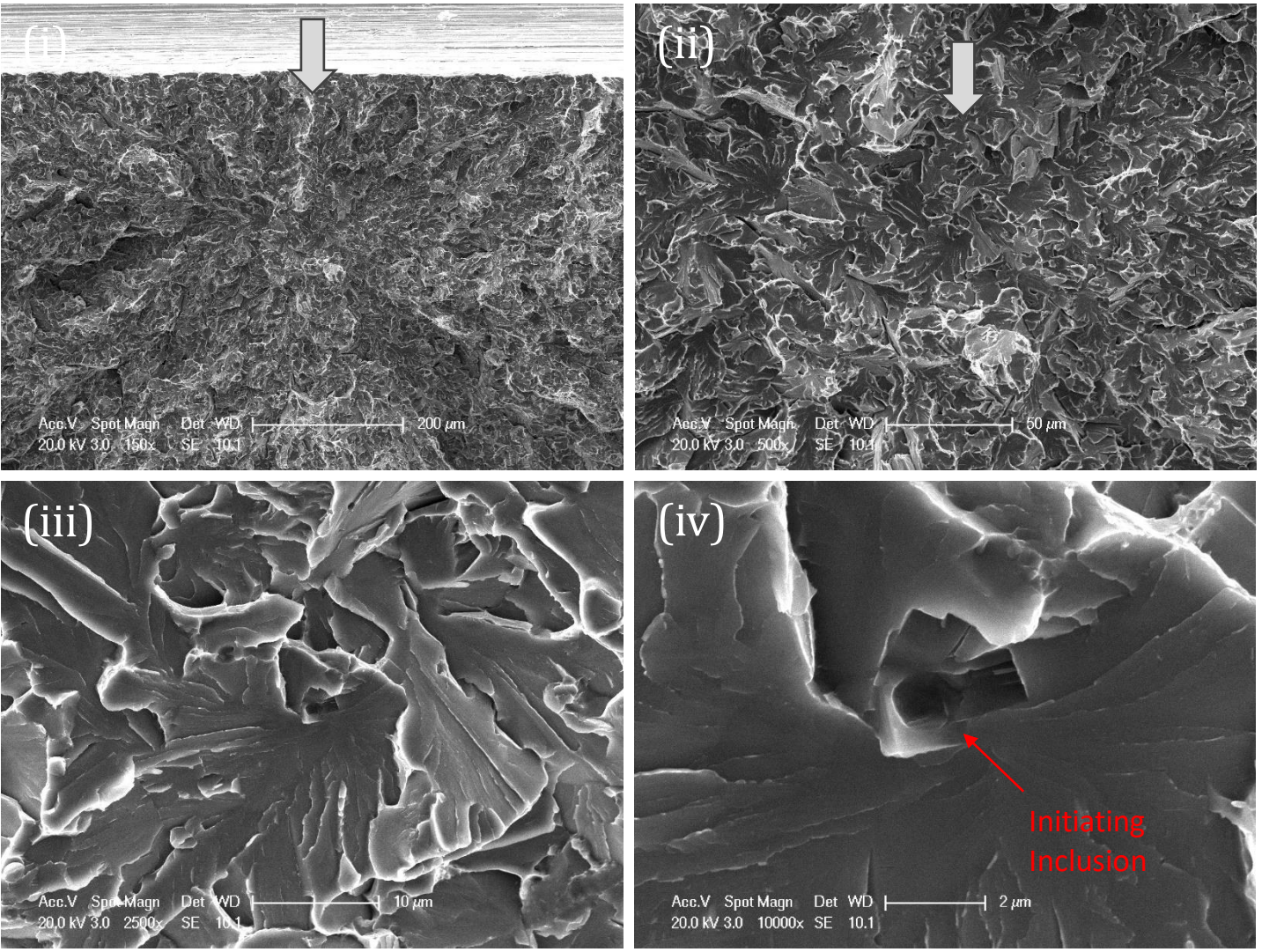


Figure 6-45 (b). Fracture initiation point of the matching side of blunt-notched specimen FS HT1-09 tested at -196 °C; A sequential magnification of the initiation area at (i) 150x, (ii) 500x, (iii) 2500x, and (iv) 10000x are shown. Fractographic analysis reveals inclusion cracking as the initiation mechanism, with the inclusion's equivalent diameter at 1.6 µm and the initial facet's equivalent diameter at 23 µm.

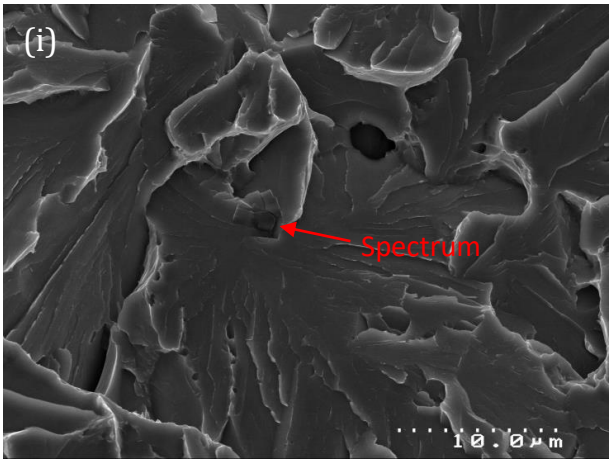


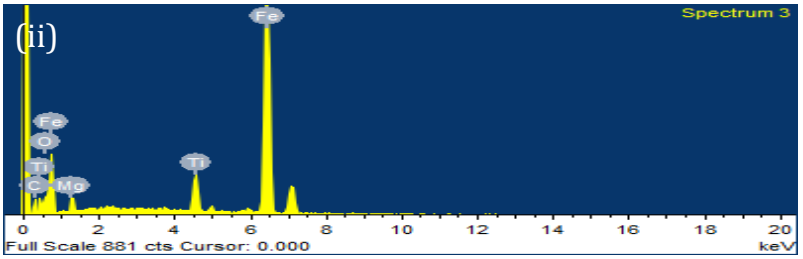


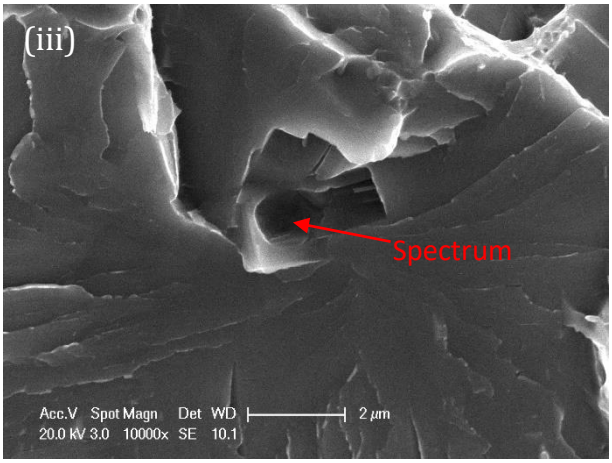


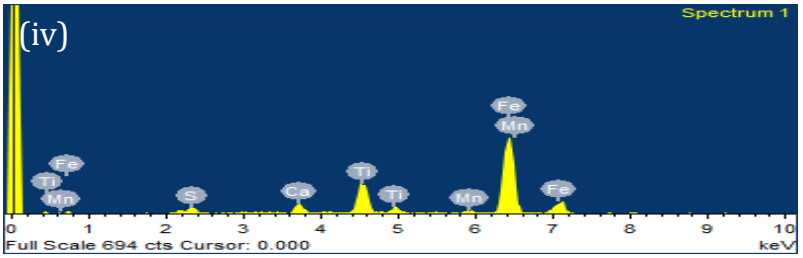


Figure 6-45 (c). Cleavage initiation point (i) and (iii) from matching halves of fracture surfaces of blunt-notched specimen FS HT1-09 tested at -196 °C with their corresponding EDX spectrums (ii) and (iv) respectively.

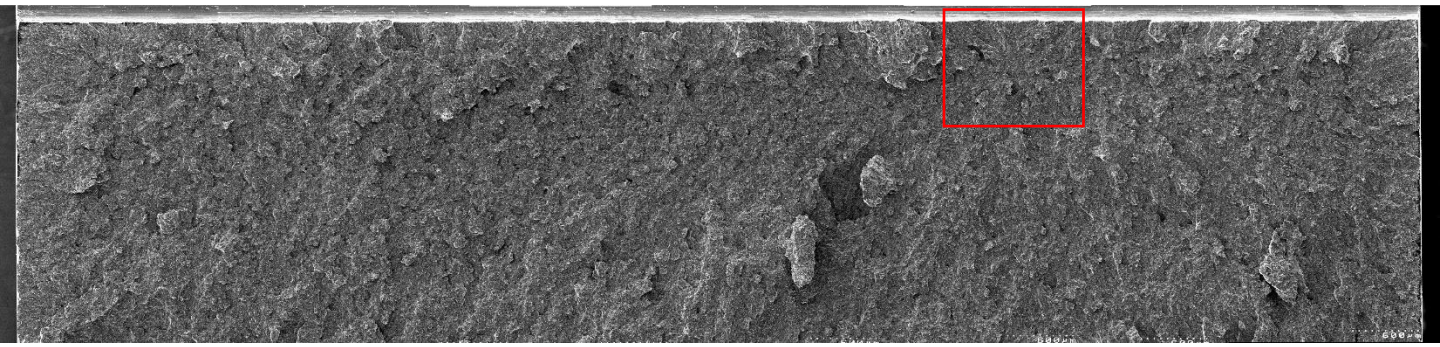

Figure 6-46 (a). Overview of the fracture surface on one side of the blunt-notched specimen FS HT2-07, tested at -196°C, with a red frame highlighting the most probable initiation area. Test results: Local cleavage fracture stress of 1678 Mpa, fracture initiation distance (Xo) of 335 μm.

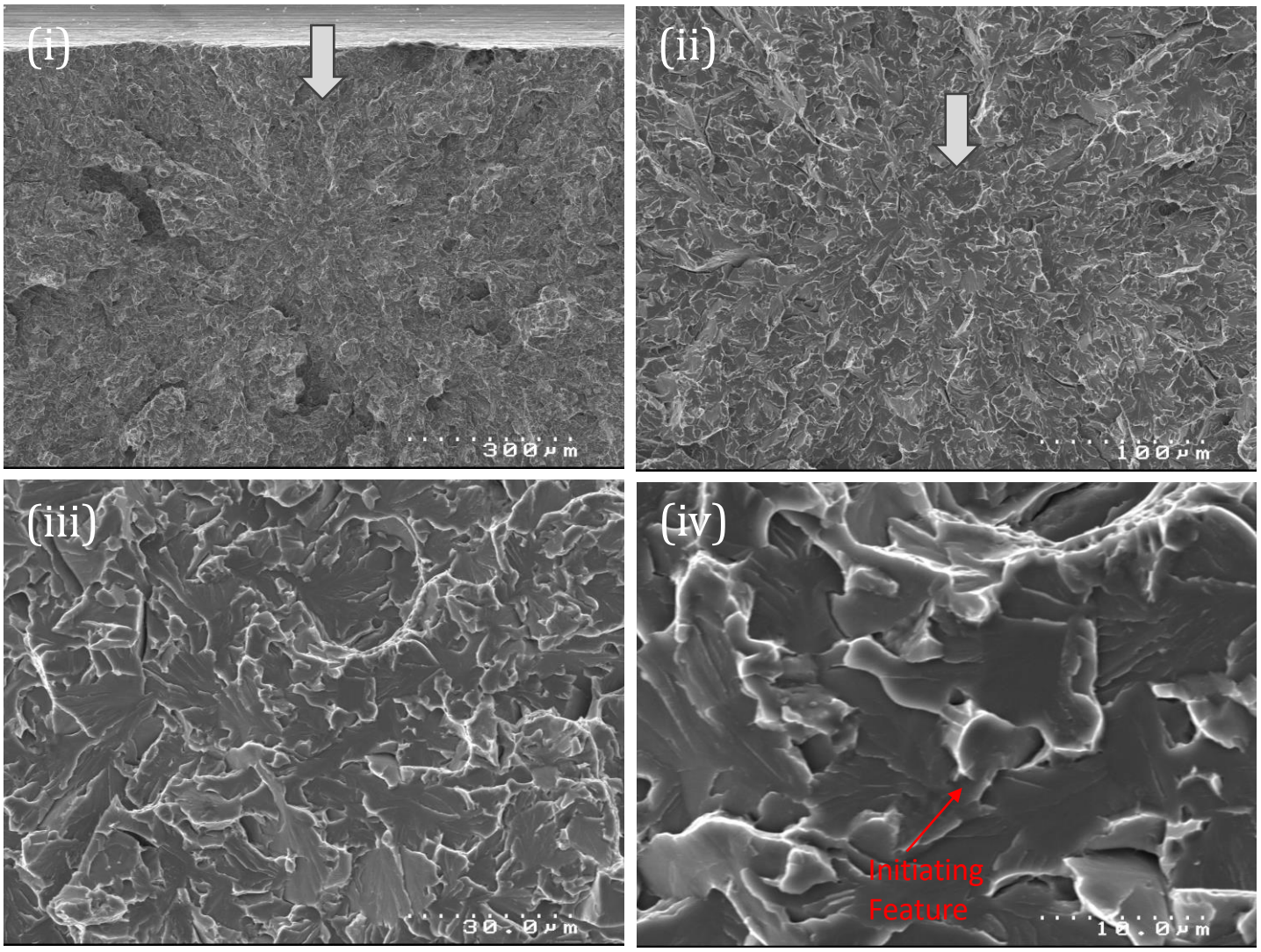


Figure 6-46 (b). Fracture initiation point of one side blunt-notched specimen FS HT2-07 tested at -196 °C; (i), (ii), (iii) and (iv) are sequential magnification of the same red framed area. Fractographic analysis reveals matrix related feature as the initiation, with the initiating feature's equivalent diameter at 1.1 µm and the initial facet's equivalent diameter at 25 µm.

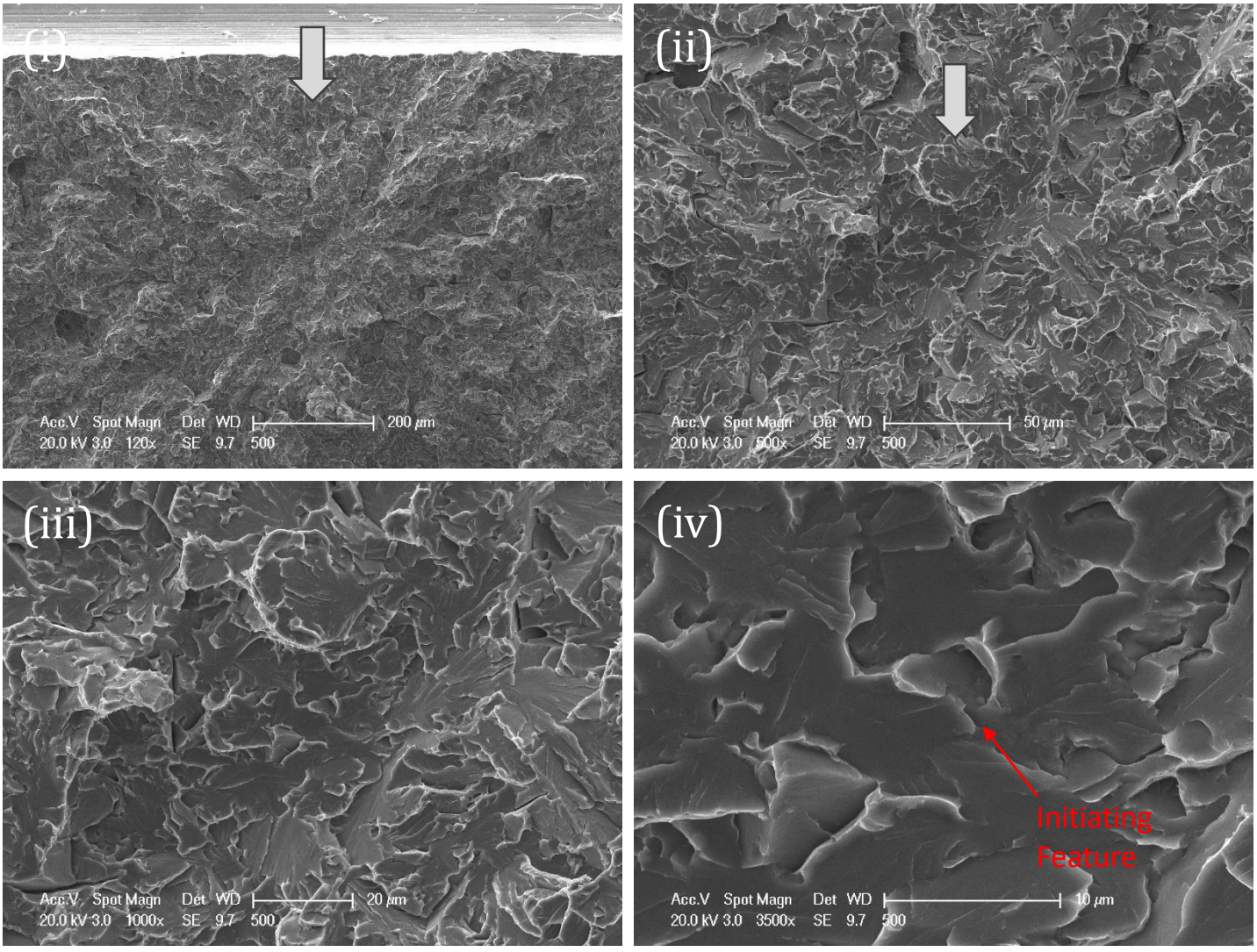


Figure 6-46 (c). Fracture initiation point of the matching side of blunt-notched specimen FS HT2-07 tested at -196 °C; A sequential magnification of the initiation area at (i) 120x, (ii) 500x, (iii) 1000x, and (iv) 3500x are shown. Fractographic analysis reveals matrix related feature as the initiation, with the initiating feature's equivalent diameter at 1.1 µm and the initial facet's equivalent diameter at 25 µm.

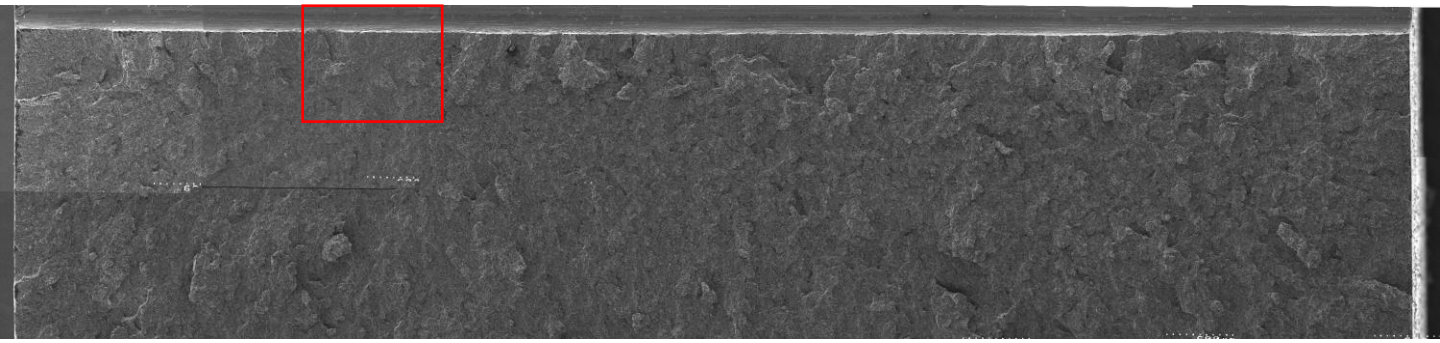

Figure 6-47 (a). Overview of the fracture surface on one side of the blunt-notched specimen FS HT2-08, tested at -196°C, with a red frame highlighting the most probable initiation area. Test results: Local cleavage fracture stress of 1937 Mpa, fracture initiation distance (Xo) of 268 μm.

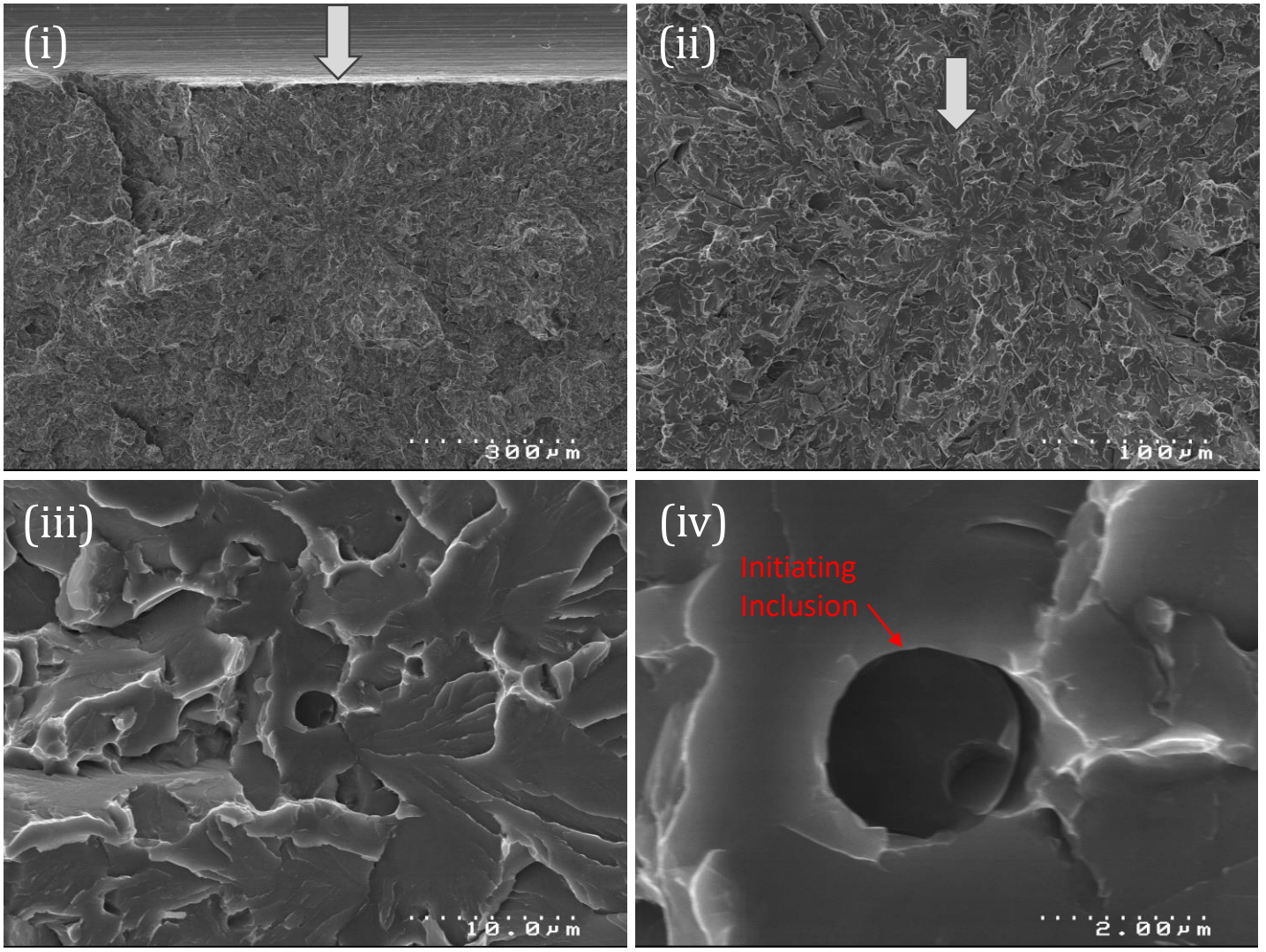


Figure 6-47 (b). Fracture initiation point of one side blunt-notched specimen FS HT2-08 tested at -196 °C; (i), (ii), (iii) and (iv) are sequential magnification of the same red framed area. Fractographic analysis reveals inclusion cracking as the initiation mechanism, with the inclusion's equivalent diameter at 2.6 µm and the initial facet's equivalent diameter at 27 µm.

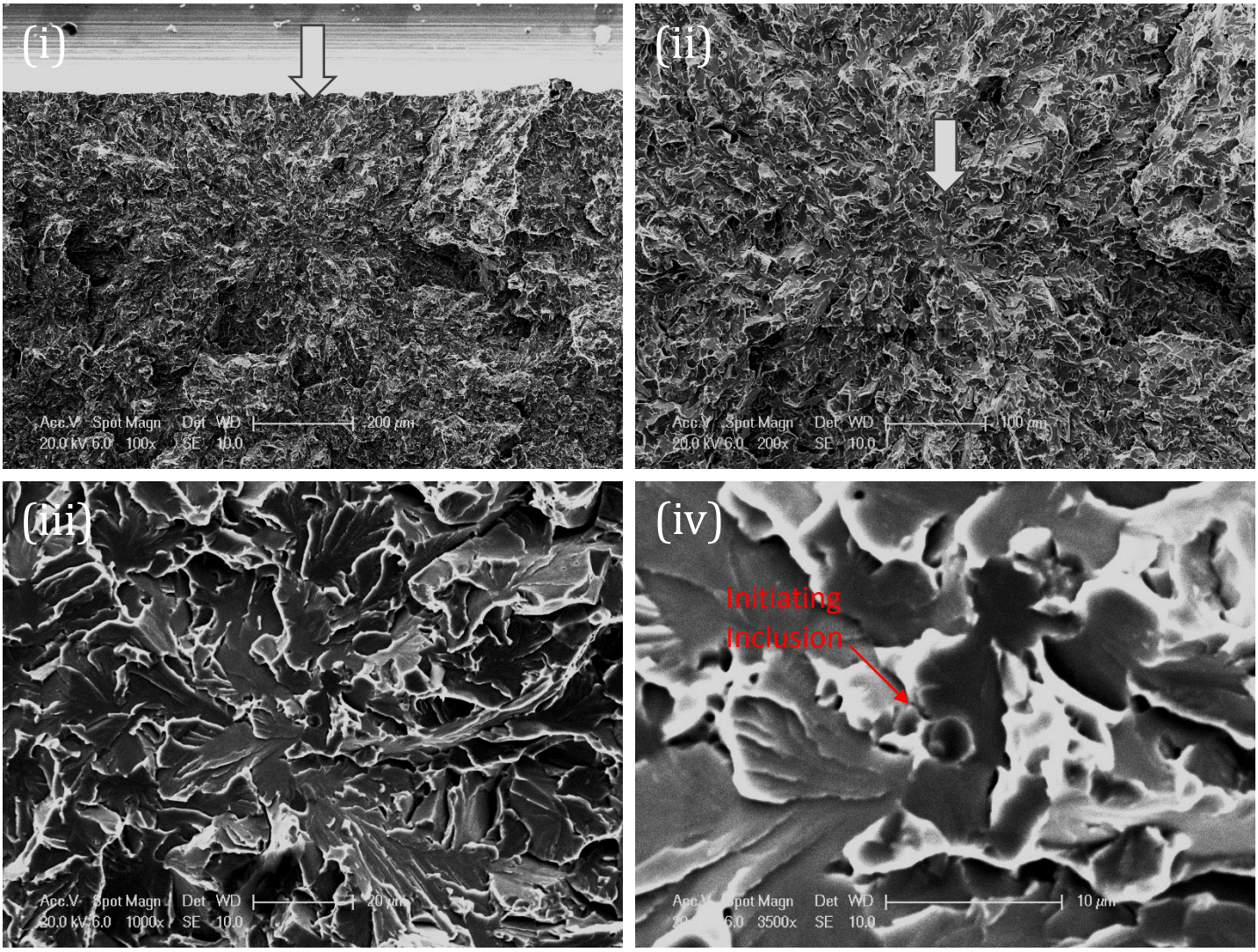


Figure 6-47 (c). Fracture initiation point of the matching side of blunt-notched specimen FS HT2-08 tested at -196 °C; A sequential magnification of the initiation area at (i) 100x, (ii) 200x, (iii) 1000x, and (iv) 3500x are shown. Fractographic analysis reveals inclusion cracking as the initiation mechanism, with the inclusion's equivalent diameter at 2.6 µm and the initial facet's equivalent diameter at 27 µm.

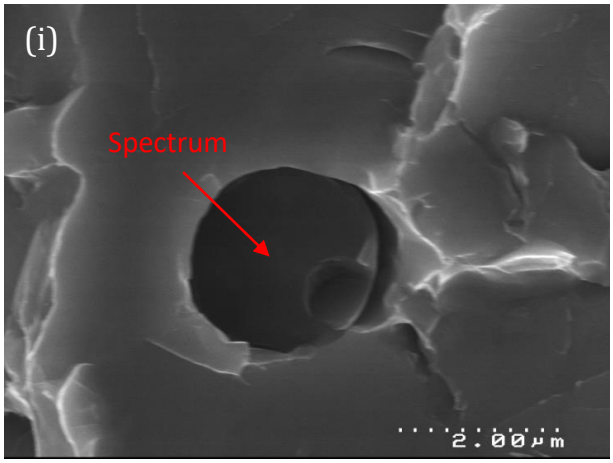


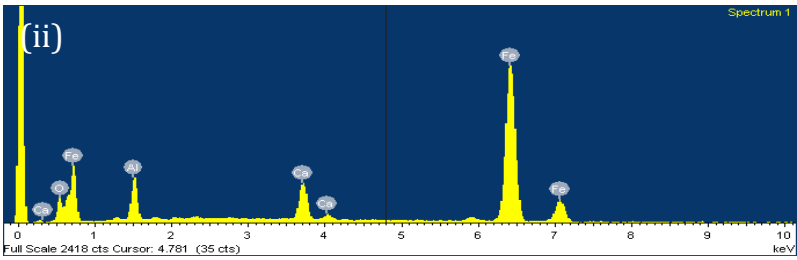


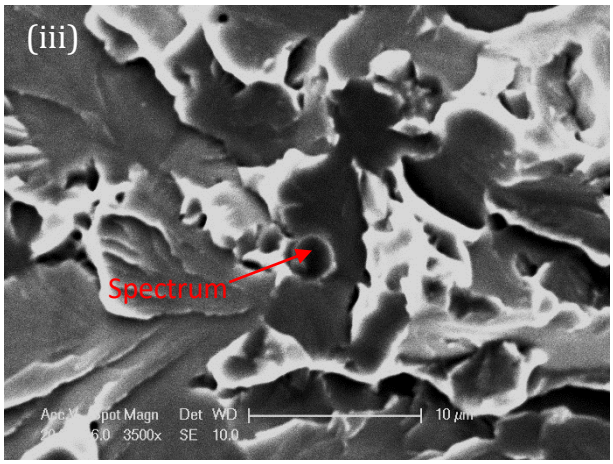


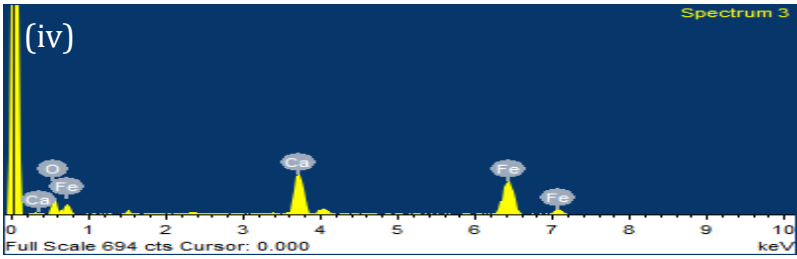


Figure 6-47 (d). Cleavage initiation point (i) and (iii) from matching halves of fracture surfaces of blunt-notched specimen FS HT2-08 tested at -196 °C with their corresponding EDX spectrums (ii) and (iv) respectively.

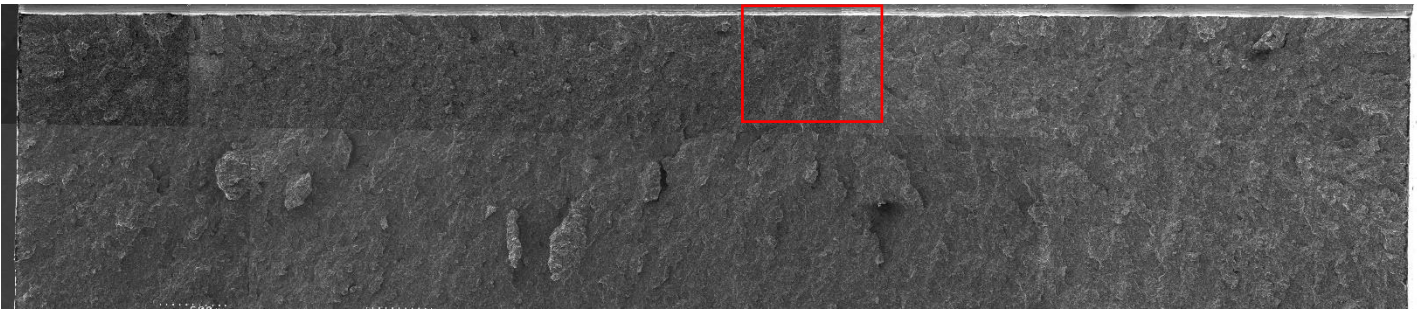

Figure 6-48 (a). Overview of the fracture surface on one side of the blunt-notched specimen FS HT2-09, tested at -196°C, with a red frame highlighting the most probable initiation area. Test results: Local cleavage fracture stress of 1845 Mpa, fracture initiation distance (Xo) of 220 µm.

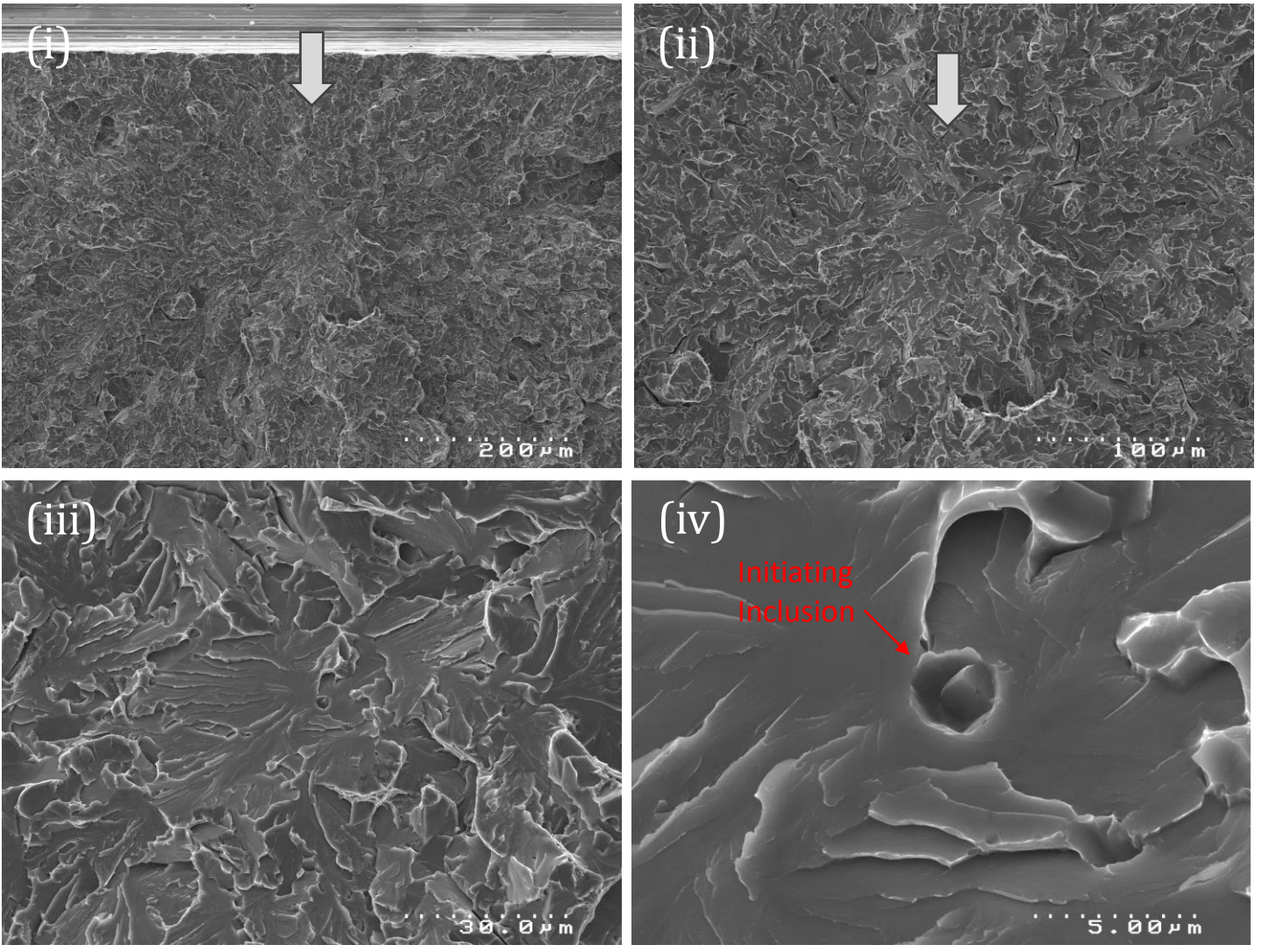


Figure 6-48 (b). Fracture initiation point of one side blunt-notched specimen FS HT2-09 tested at -196 °C; (i), (ii), (iii) and (iv) are sequential magnification of the same red framed area. Fractographic analysis reveals inclusion cracking as the initiation mechanism, with the inclusion's equivalent diameter at 2.6 µm and the initial facet's equivalent diameter at 32 µm.

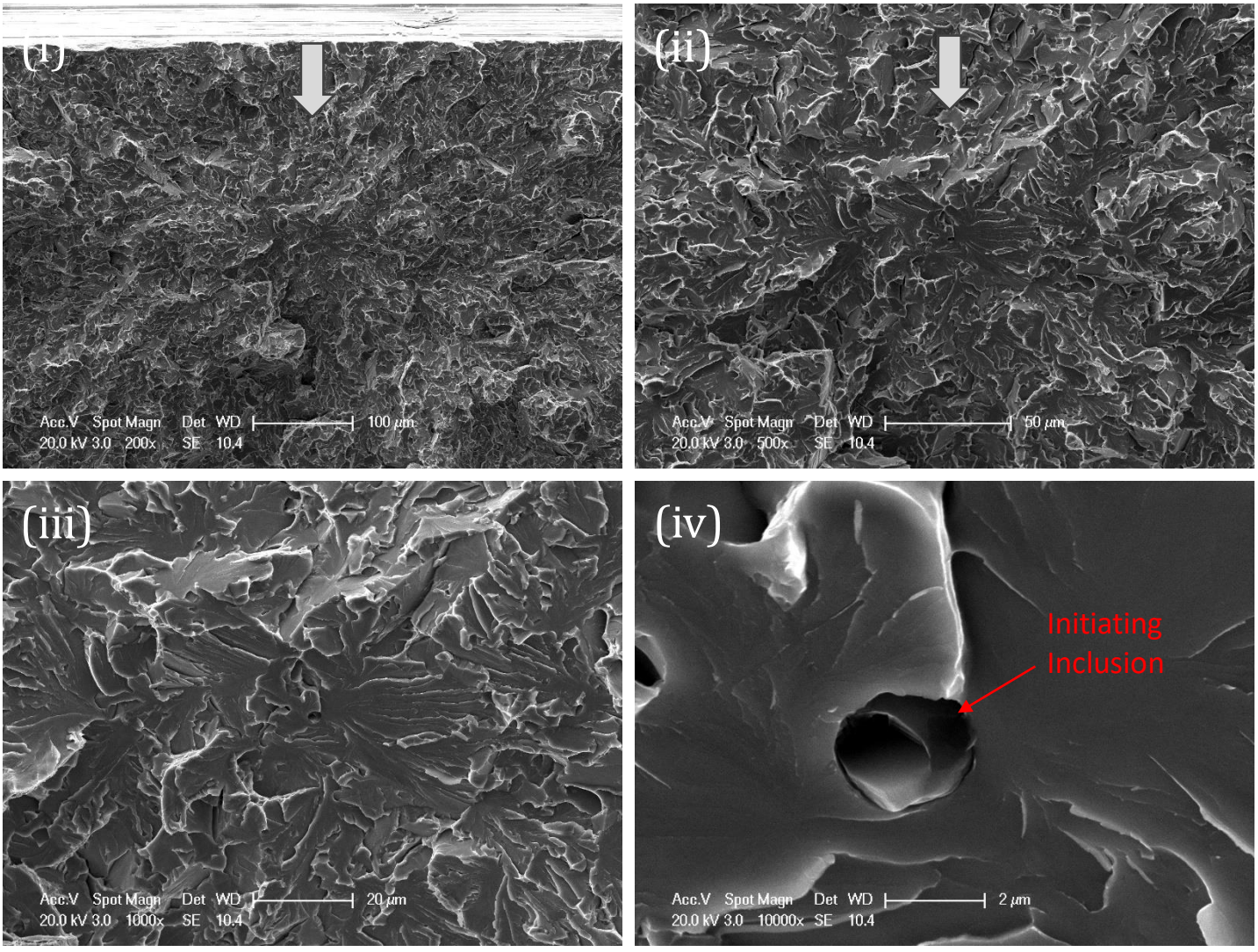


Figure 6-48 (c). Fracture initiation point of the matching side of blunt-notched specimen FS HT2-09 tested at -196 °C; A sequential magnification of the initiation area at (i) 200x, (ii) 500x, (iii) 1000x, and (iv) 10000x are shown. Fractographic analysis reveals inclusion cracking as the initiation mechanism, with the inclusion's equivalent diameter at 2.6 µm and the initial facet's equivalent diameter at 32 µm.

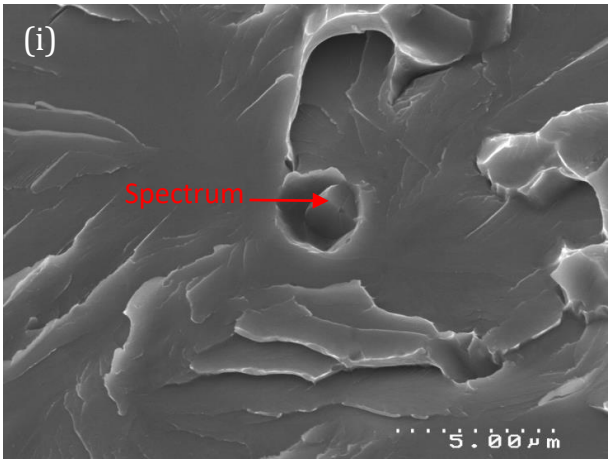


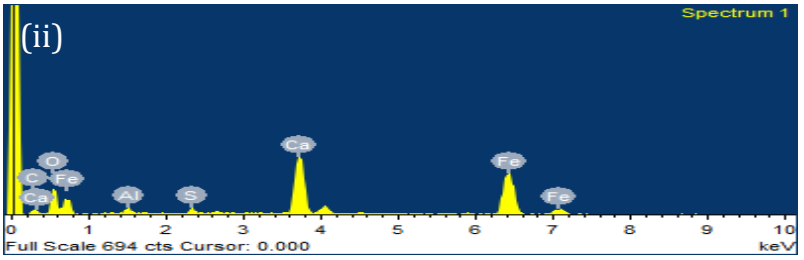


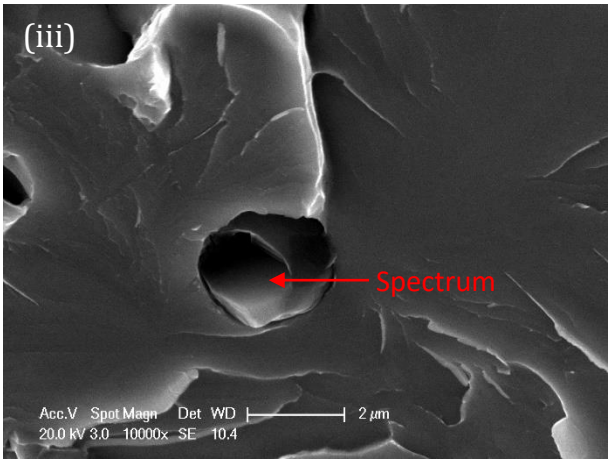


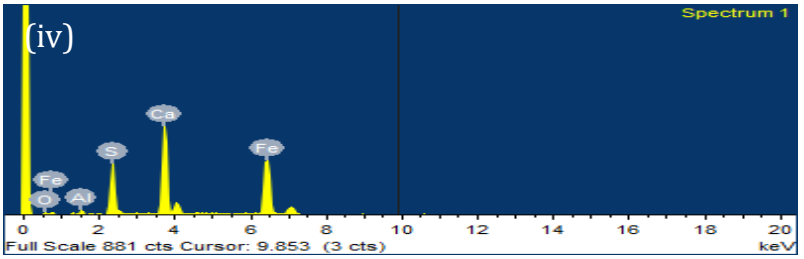


Figure 6-48 (d). Cleavage initiation point (i) and (iii) from matching halves of fracture surfaces of blunt-notched specimen FS HT2-09 tested at -196 °C with their corresponding EDX spectrums (ii) and (iv) respectively.

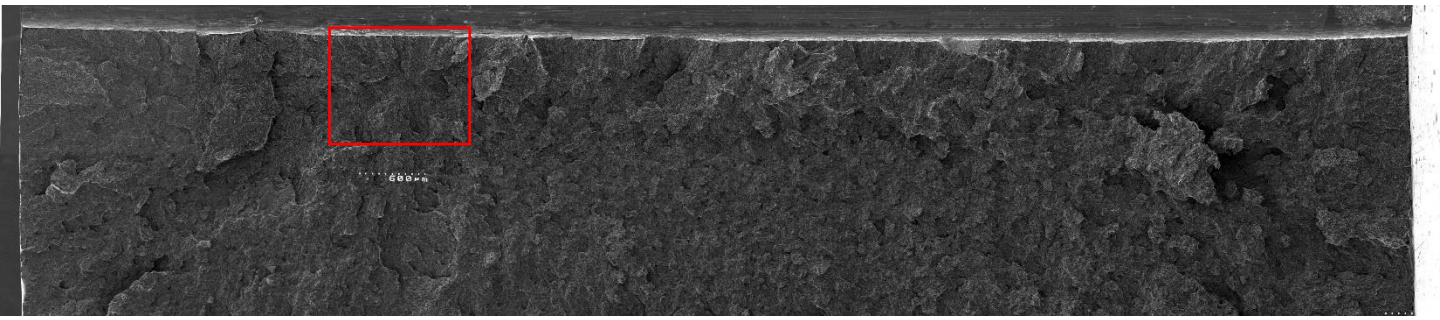

Figure 6-49 (a). Overview of the fracture surface on one side of the blunt-notched specimen FS HT2-04, tested at -170°C, with a red frame highlighting the most probable initiation area. Test results: Local cleavage fracture stress of 1915 Mpa, fracture initiation distance ($X_0$) of 420 µm.

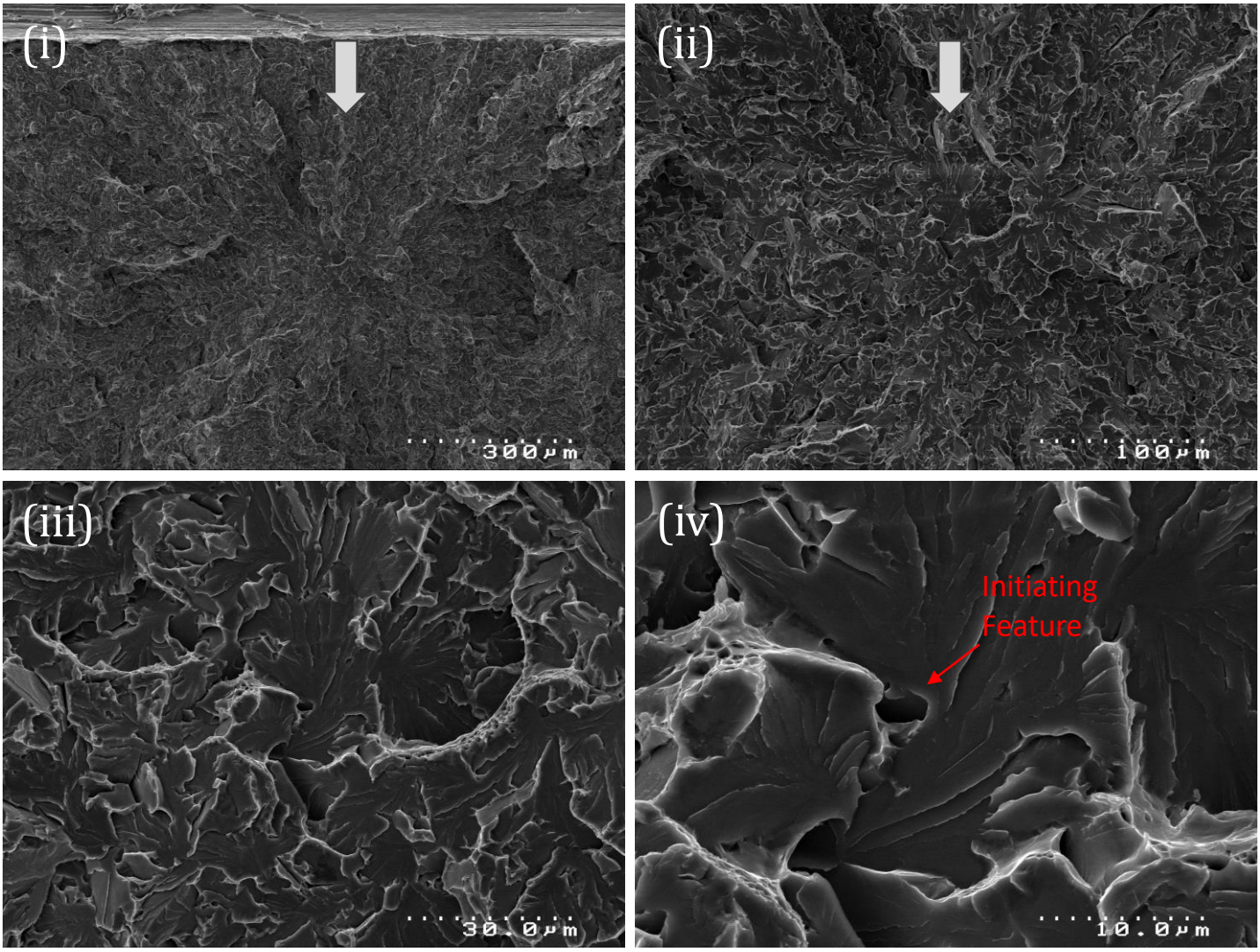


Figure 6-49 (b). Fracture initiation point of one side blunt-notched specimen FS HT2-04 tested at -170 °C; (i), (ii), (iii) and (iv) are sequential magnification of the same red framed area. Fractographic analysis reveals matrix related feature as the initiation, with the initiating feature's equivalent diameter at 2.6 µm and the initial facet's equivalent diameter at 30 µm.

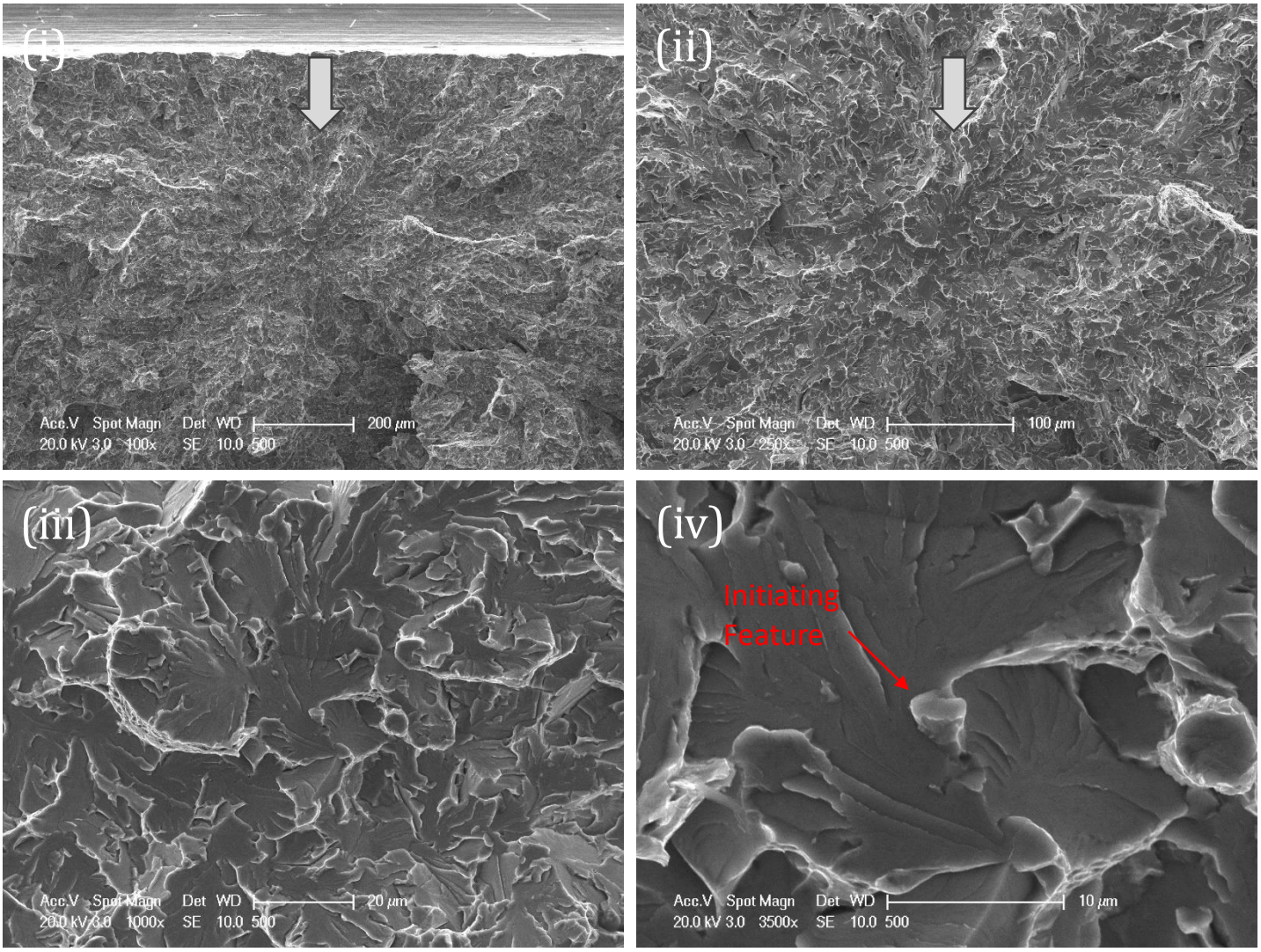


Figure 6-49 (c). Fracture initiation point of the matching side of blunt-notched specimen FS HT2-04 tested at -170 °C; A sequential magnification of the initiation area at (i) 100x, (ii) 250x, (iii) 1000x, and (iv) 3500x are shown. Fractographic analysis reveals matrix related feature as the initiation, with the initiating feature's equivalent diameter at 2.6 µm and the initial facet's equivalent diameter at 30 µm.

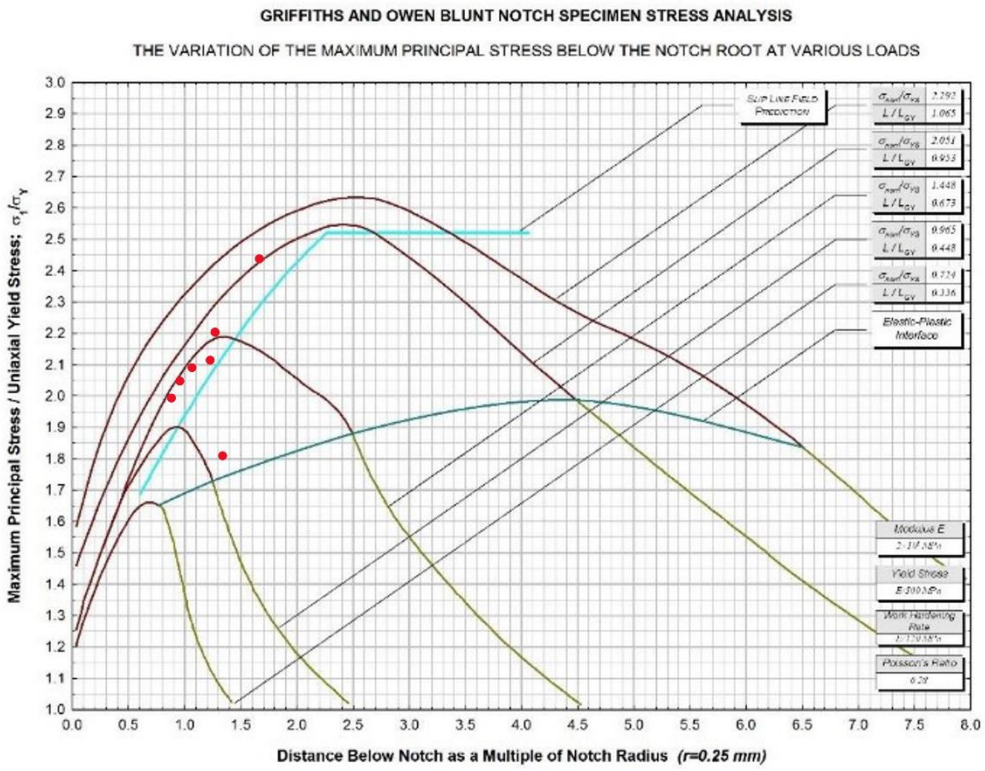


Figure 6-50. Initiation Site Locations in relation to FEM Stress Distribution. (the seven red dots represent the result of each test)

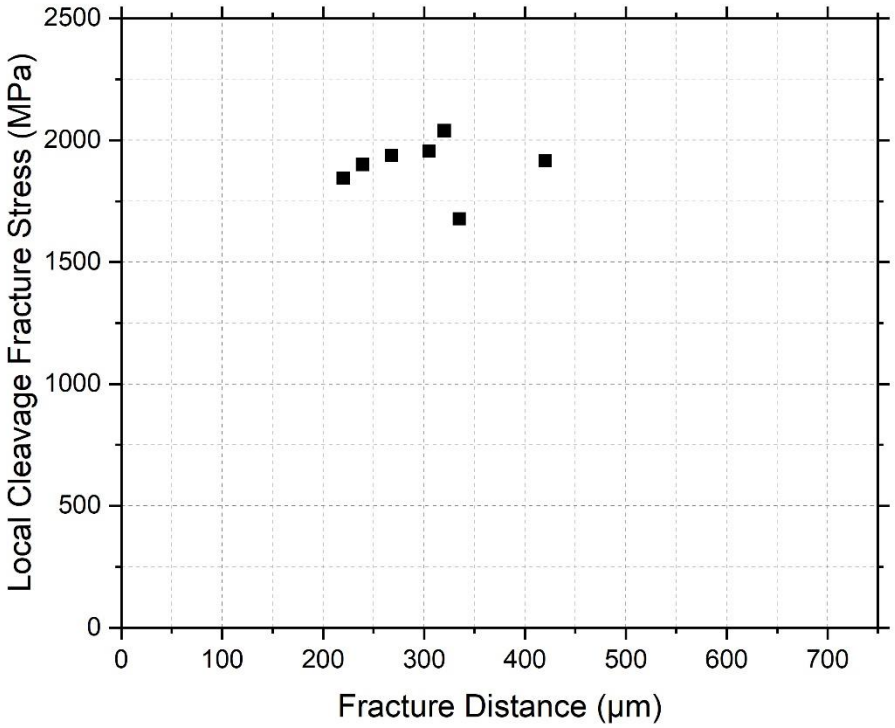


Figure 6-51. Local cleavage fracture stress $\sigma_F$ relation with fracture distance of all seven blunt-notched test specimens. (Fracture distance is measured as the distance from the end of notch root edge to cleavage initiation point)

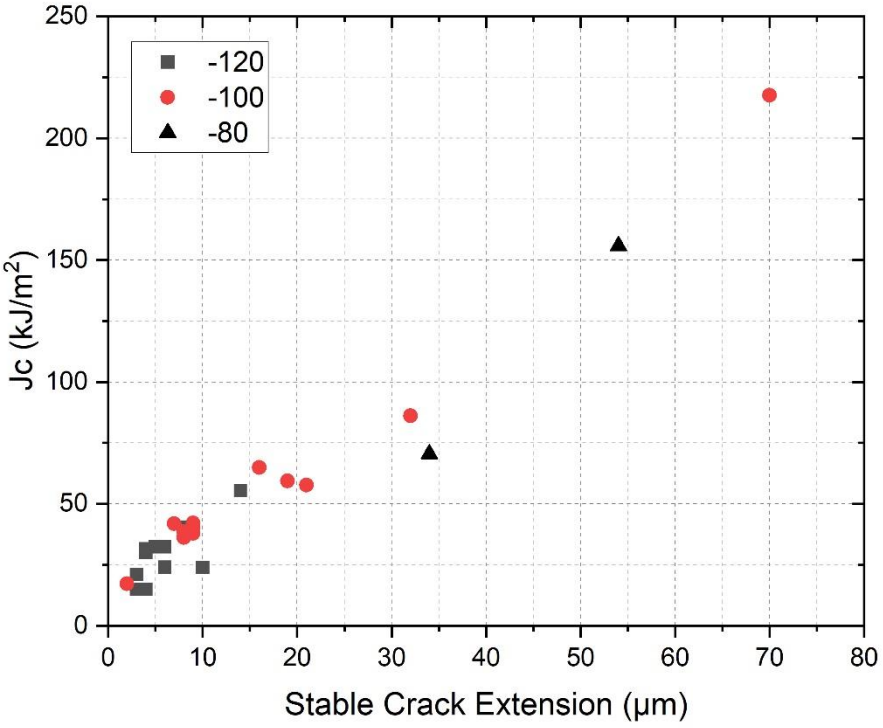


Figure 6-52. $J_C$ relation with stable crack extension $\Delta a$

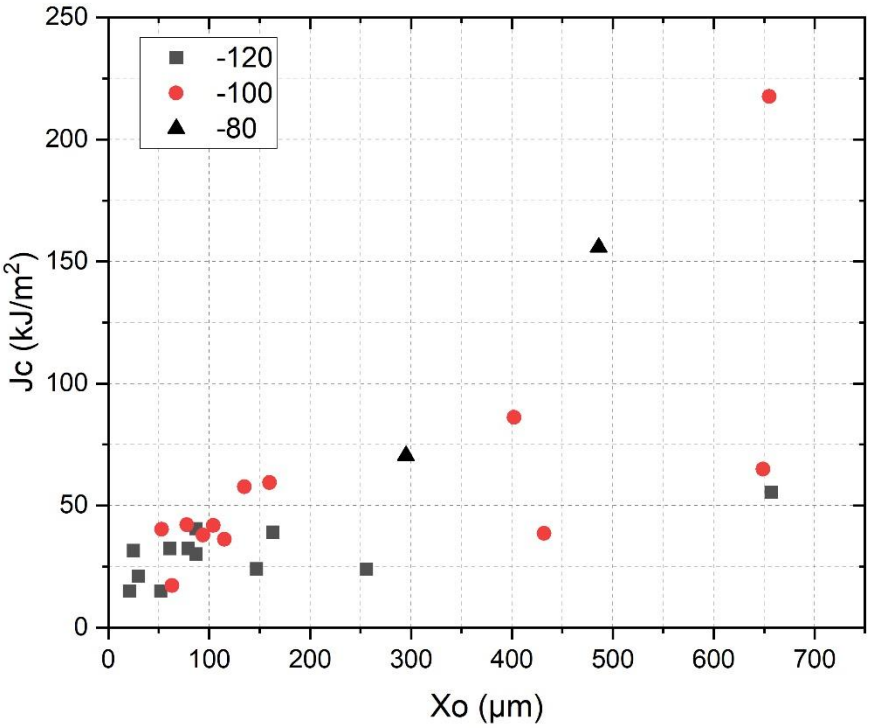


Figure 6-53. $J_C$ relation with Fracture Distance Xo (Distance from end of ductile crack growth to cleavage initiation point)

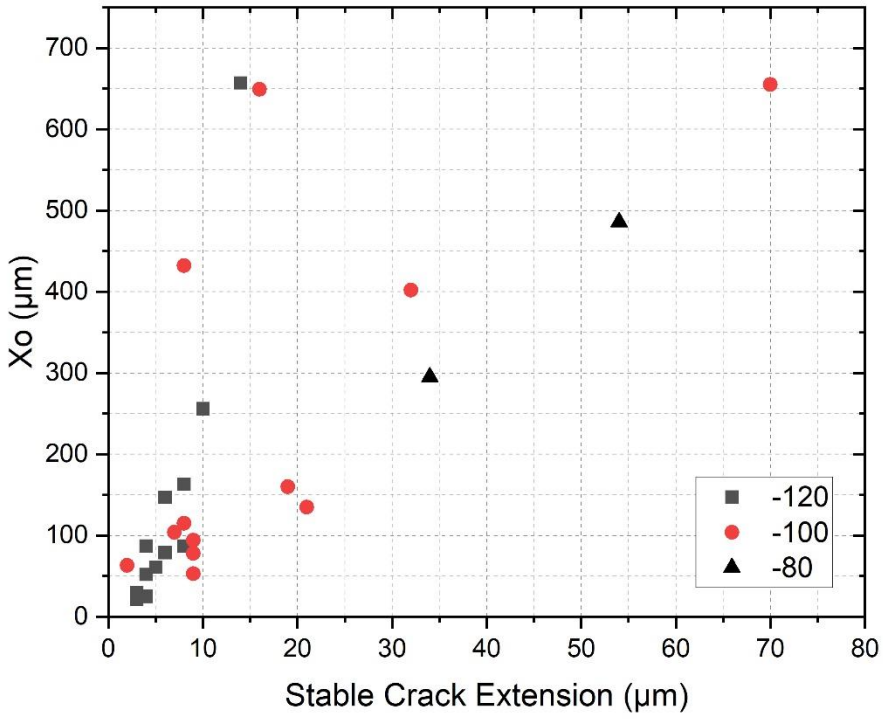


Figure 6-54. Fracture distance $X_0$ relation with stable crack extension $\Delta a$

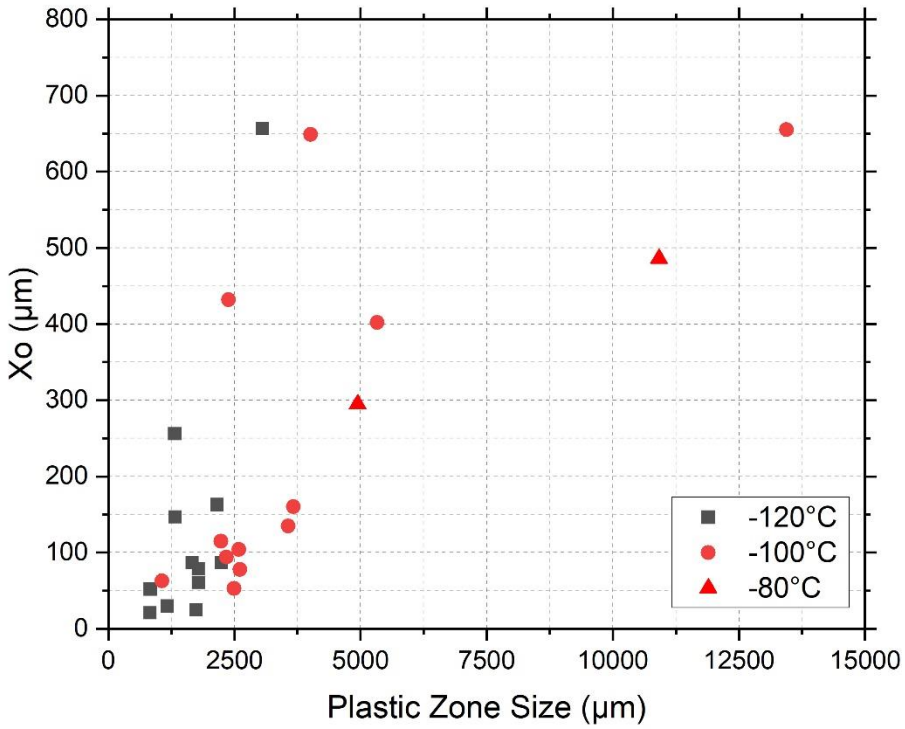


Figure 6-55. Fracture distance $X_0$ relation with the true plastic zone size.

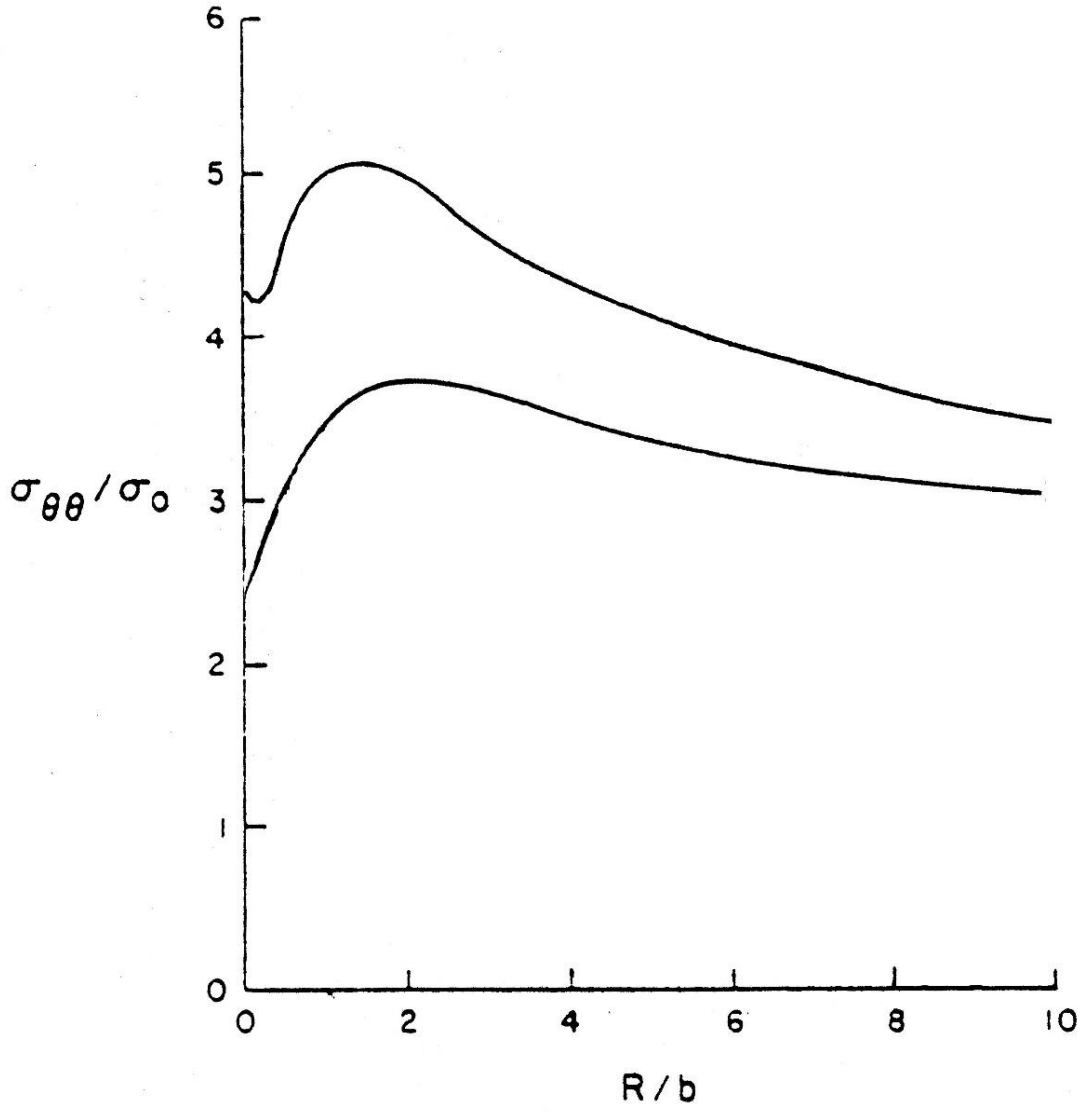


Figure 6-56. Modified McMeeking FEM stress distribution of n=0.1 and n=0.2.

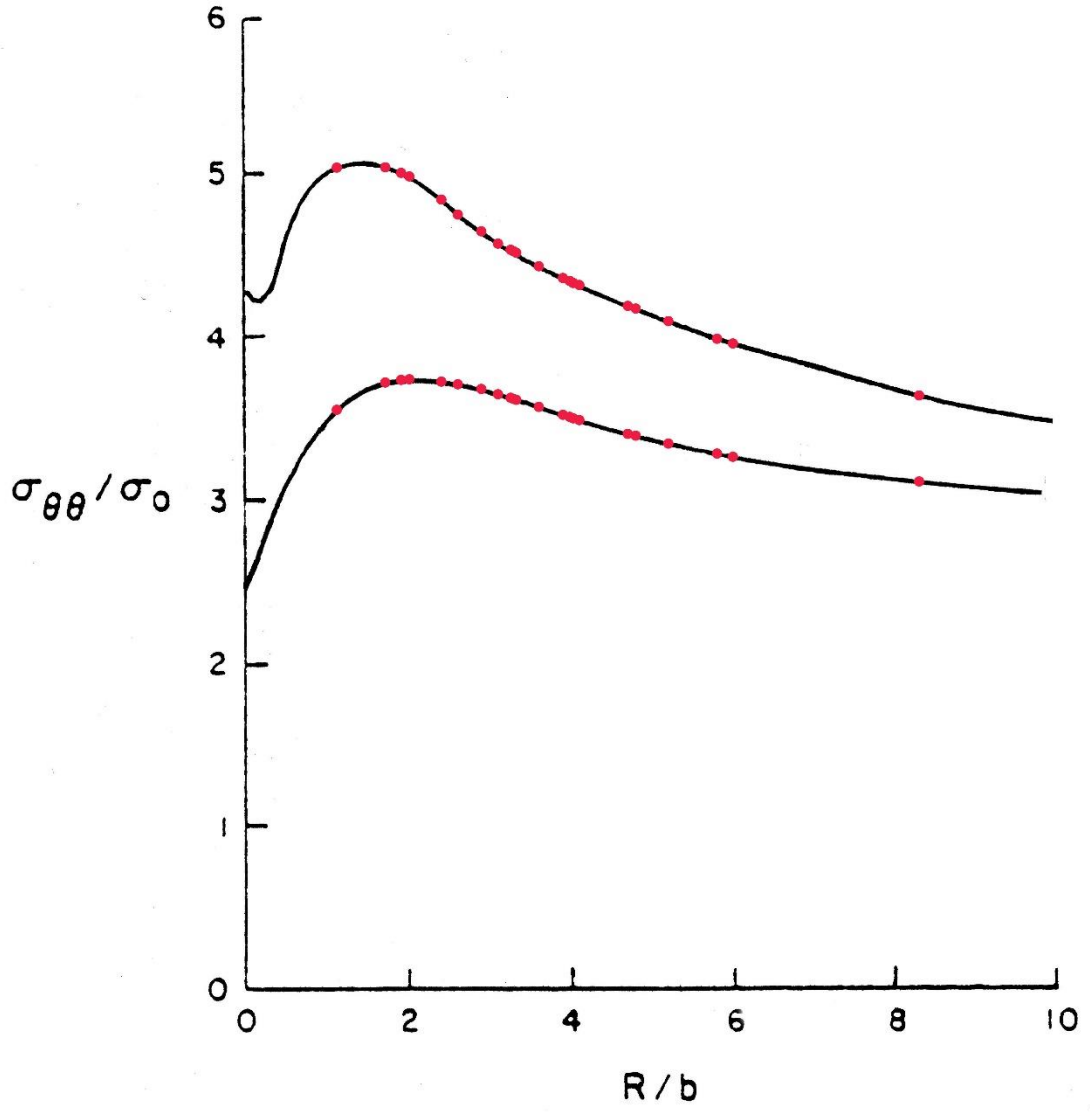


Figure 6-57. McMeeking FEM stress distribution of n=0.1 and n=0.2 with red dots represent the result of each test within the limit of the analysis.

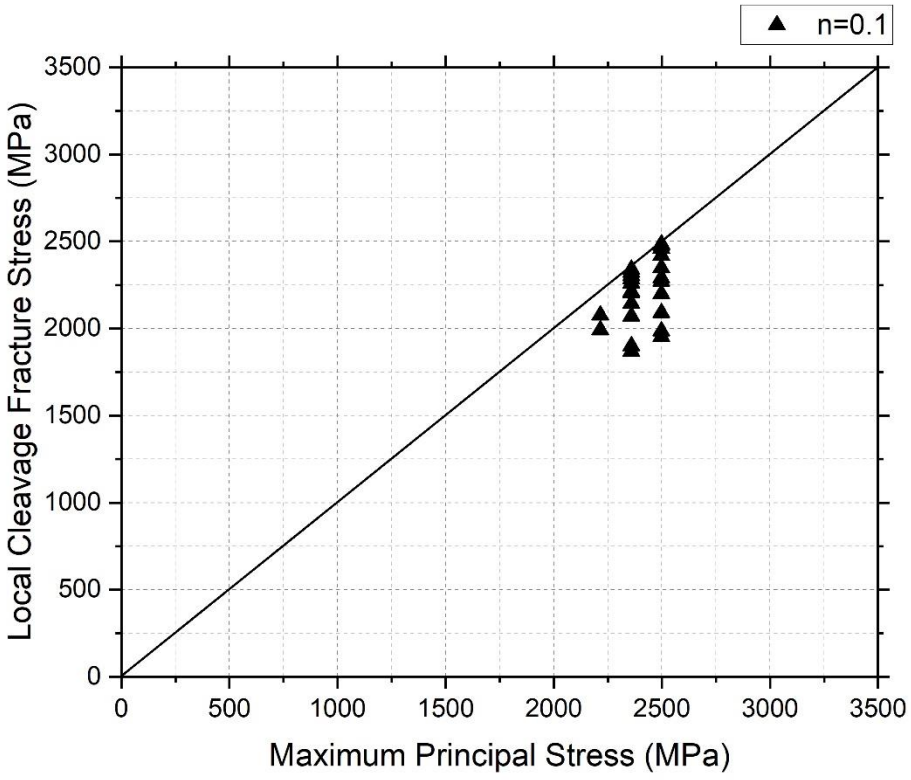


Figure 6-58. Local cleavage fracture stress $\sigma_F$ plotted with maximum principal stress $\sigma_{yy}^{max}$ for sharp-cracked specimens results of n=0.1.

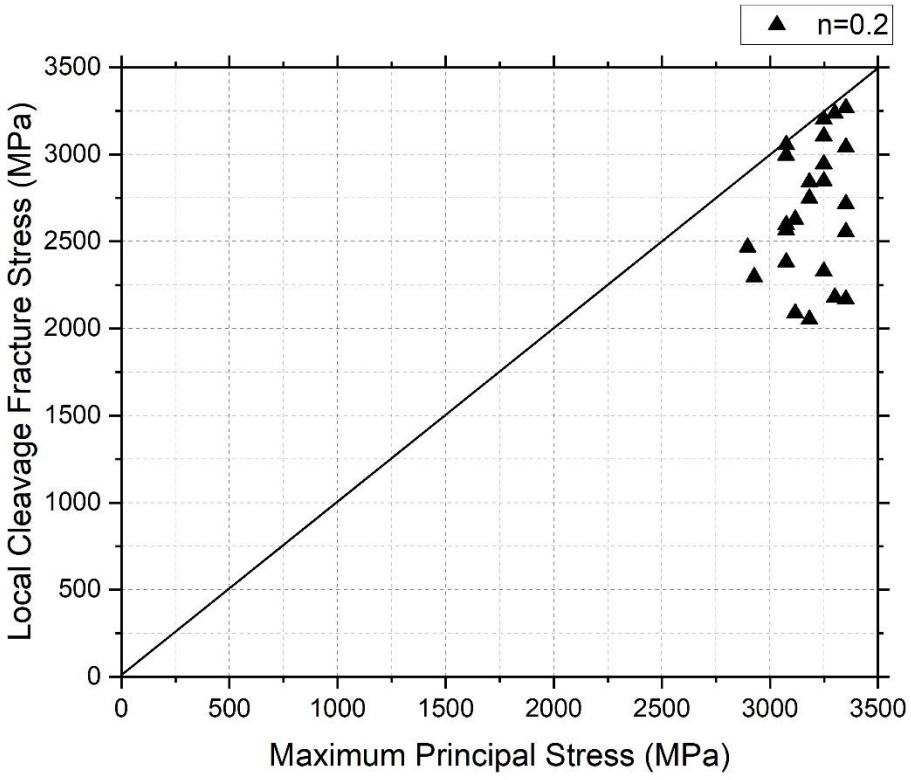


Figure 6-59. Local cleavage fracture stress $\sigma_F$ plotted with maximum principal stress $\sigma_{yy}^{max}$ for sharp-crack specimens results of n=0.2.

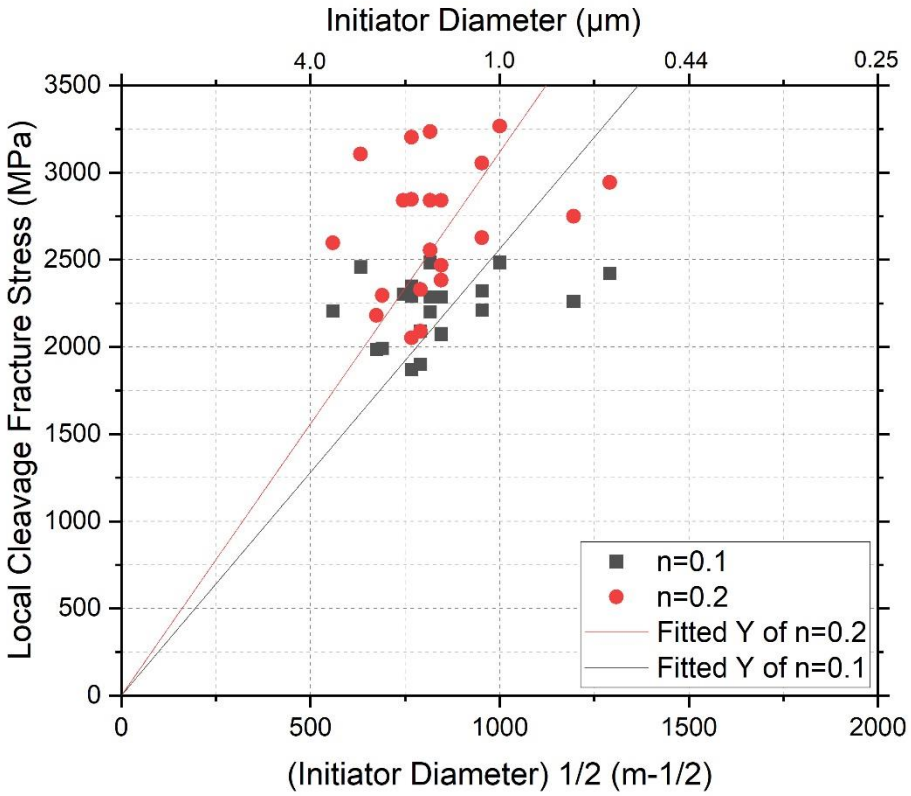


Figure 6-60. Local cleavage fracture stress $\sigma_F$ vs the reciprocal square root of the diameter of initiators. (n=0.1 and n=0.2)

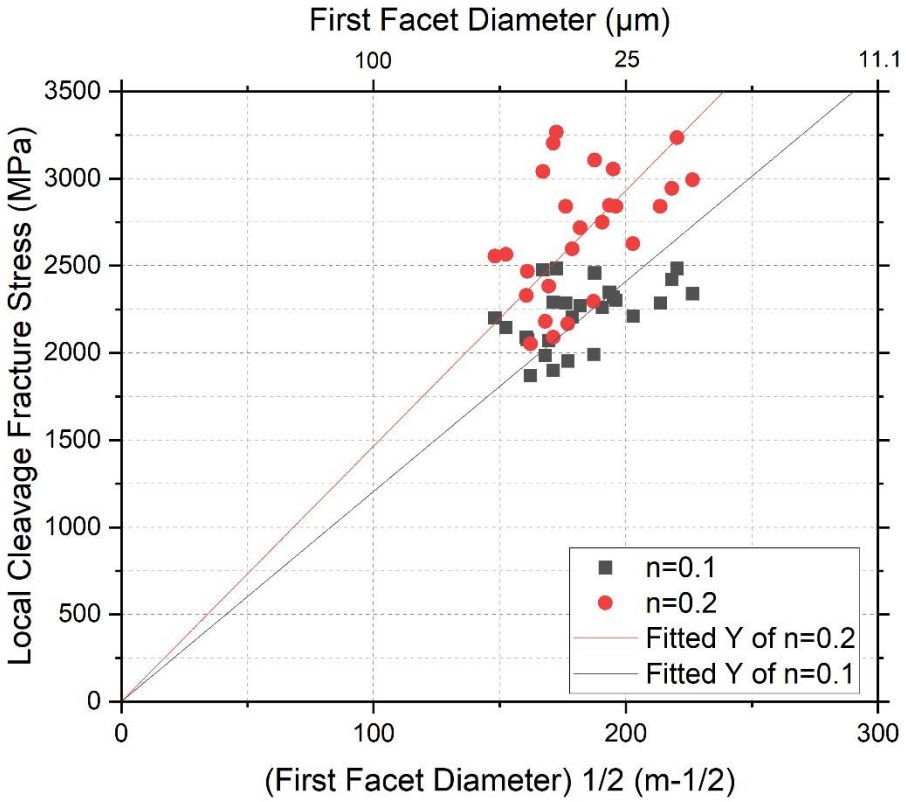


Figure 6-61. Local cleavage fracture stress $\sigma_F$ vs the reciprocal square root of the diameter of initiating facet. (n=0.1 and n=0.2)

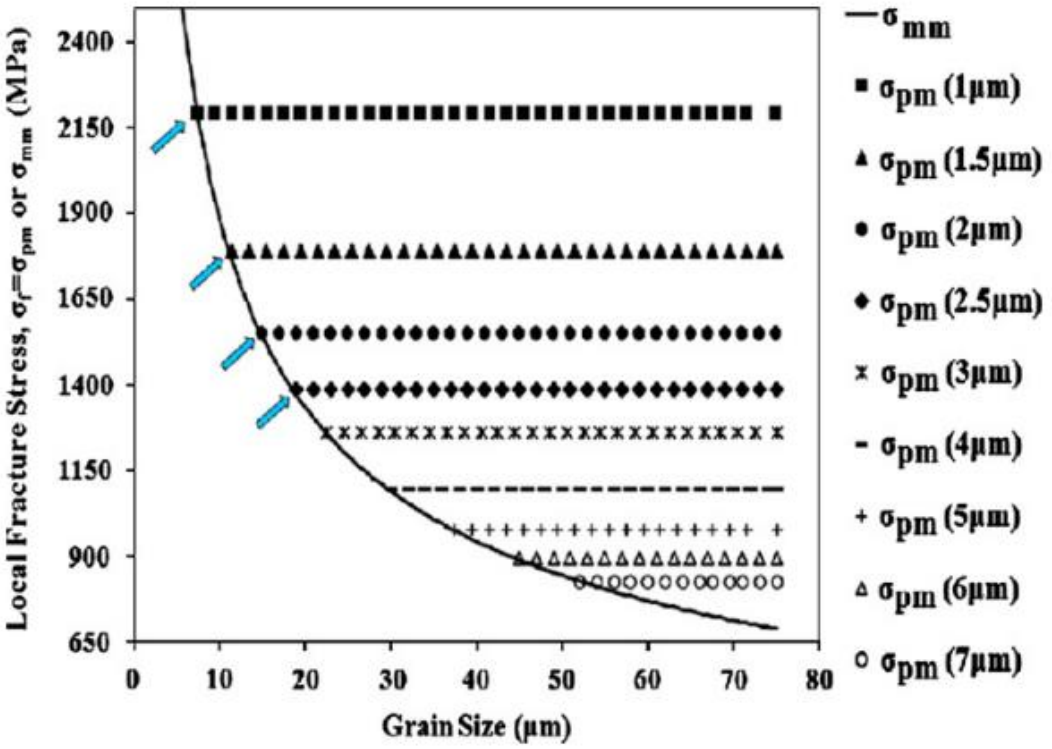


Figure 6-62. Variation of local cleavage fracture stress with grain size and particle size. [117]

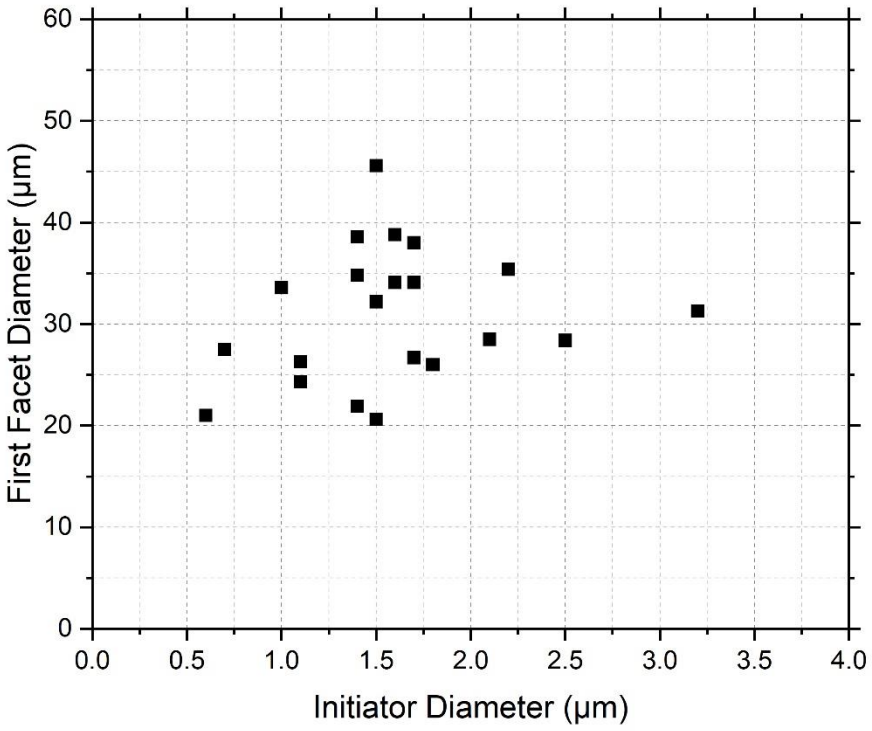


Figure 6-63. Correlation between initiator size and first facet size in 26 specimens that initiation was identified.

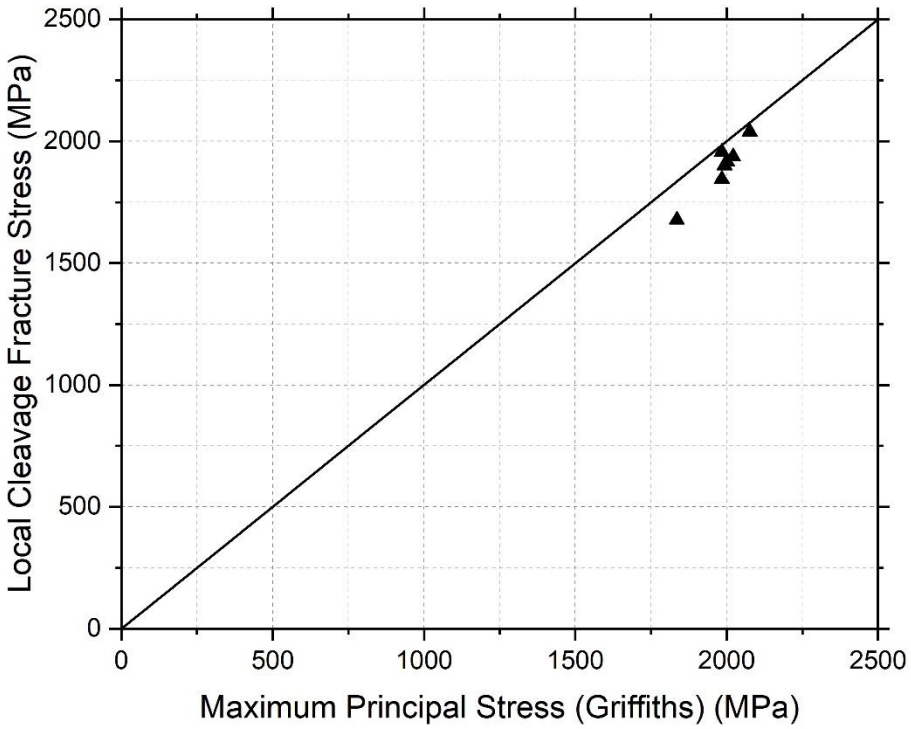


Figure 6-64. Local cleavage fracture stress $\sigma_F$ plotted with $\sigma_{yy}^{max}$ for seven blunt-notched specimens results.

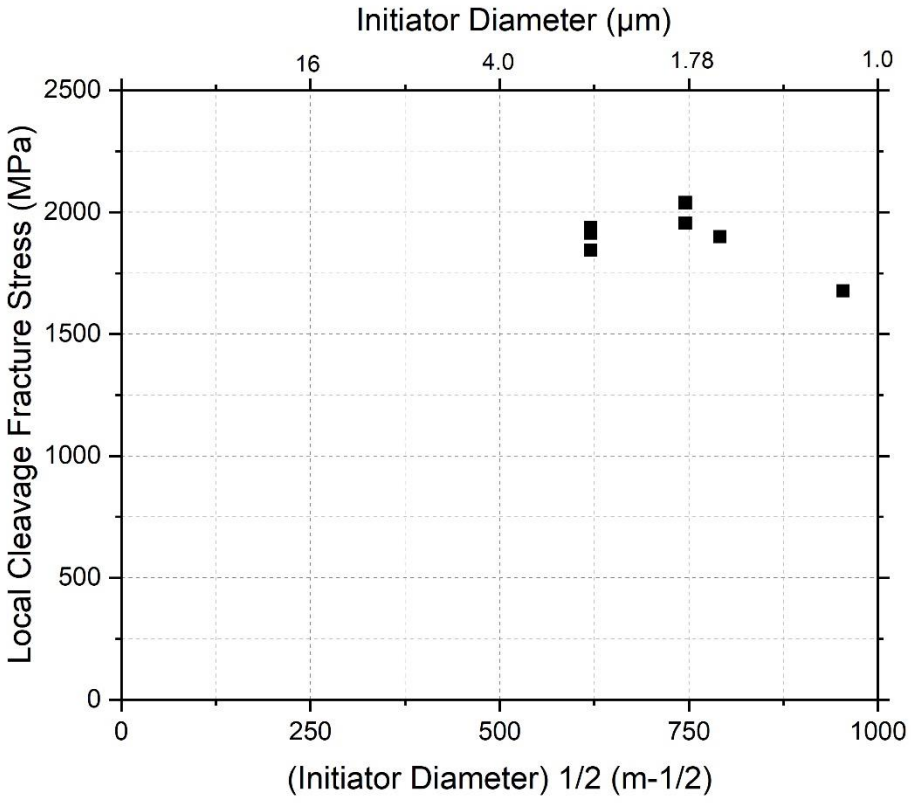


Figure 6-65. Local cleavage fracture stress $\sigma_F$ vs the reciprocal square root of initiator diameter measured from fracture surfaces.

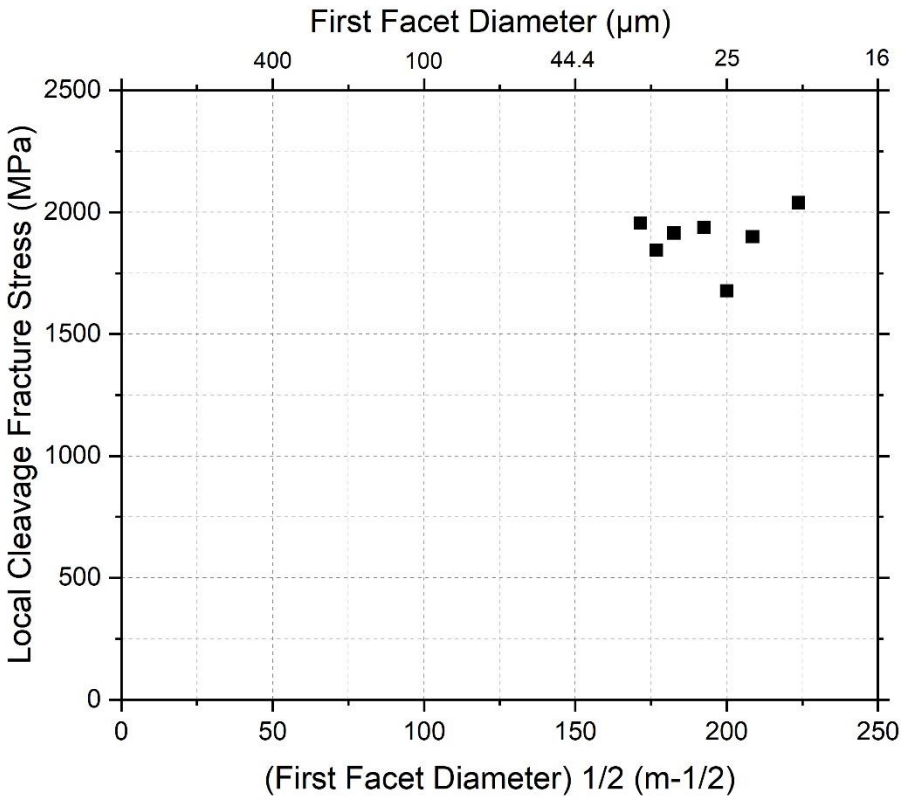


Figure 6-66. Local cleavage fracture stress $\sigma_F$ vs the reciprocal square root of facet diameter measured from fracture surfaces.

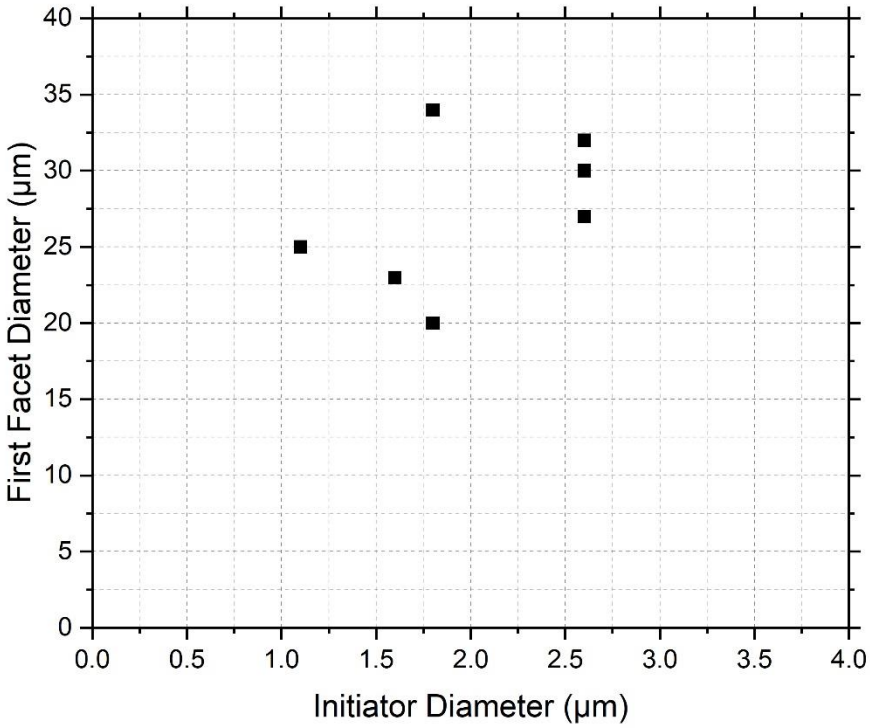


Figure 6-67. The relationship between all type initiators diameter and first facet diameter in seven blunt-notched specimens.

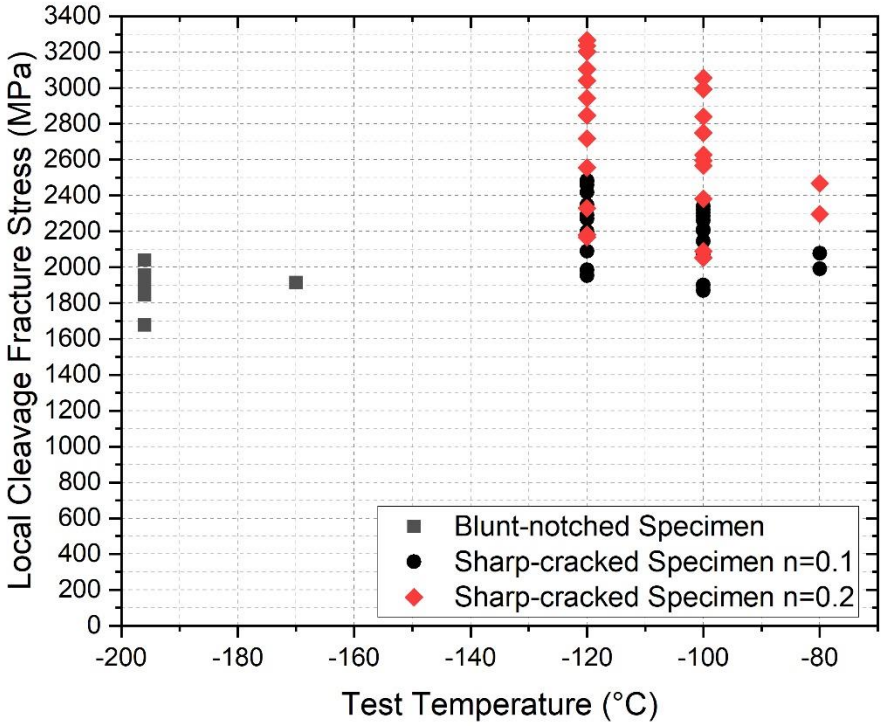


Figure 6-68. Local cleavage fracture stress $\sigma_F$ relation with test temperature for blunt-notched specimens and sharp-cracked specimen of both results from n=0.1 and n=0.2.

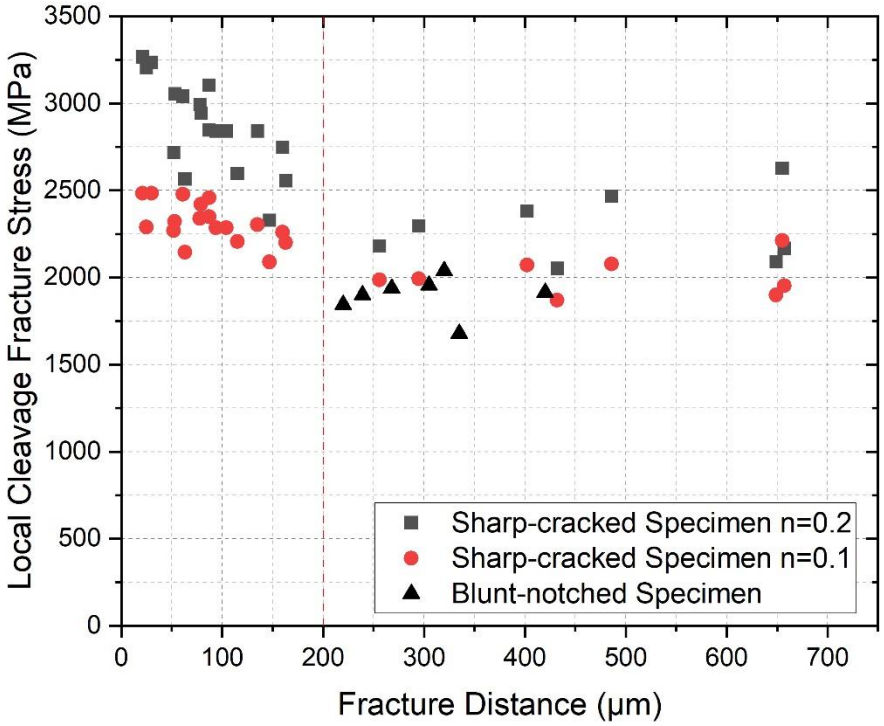


Figure 6-69. Local cleavage fracture stress $\sigma_F$ relation with fracture distance comparison for sharp-cracked specimens of n=0.1 and n=0.2 conditions and blunt-notched specimens.

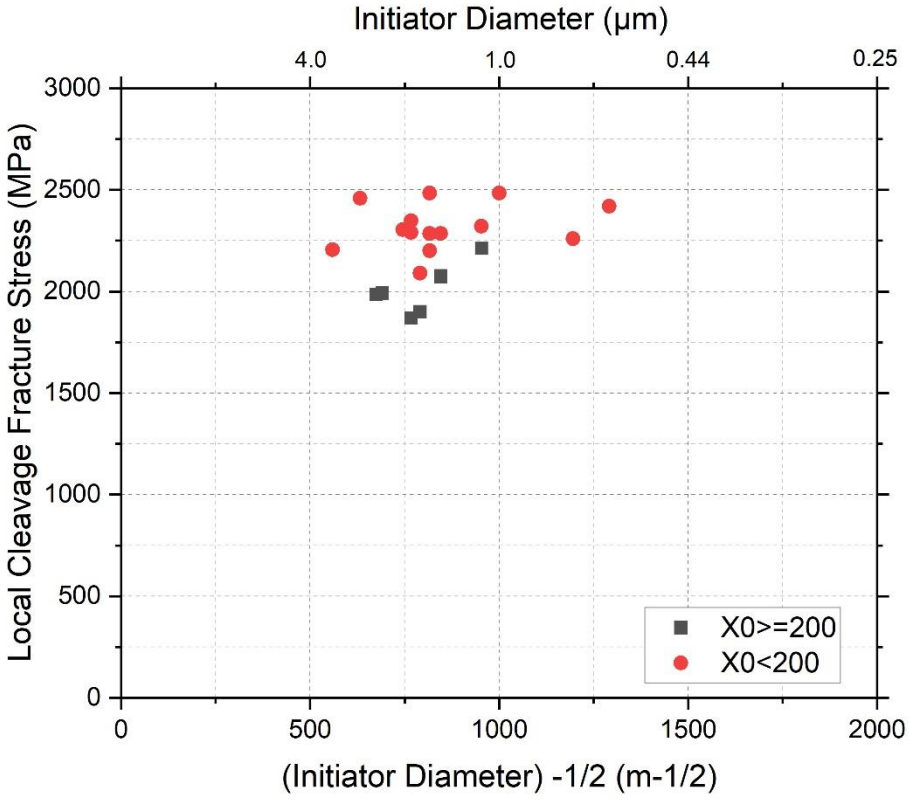


Figure 6-70. Local cleavage fracture stress $\sigma_F$ vs the reciprocal square root of the diameter of all type initiators for sharp-cracked specimens under condition of n=0.1. Distinguish fracture distance of 200μm.

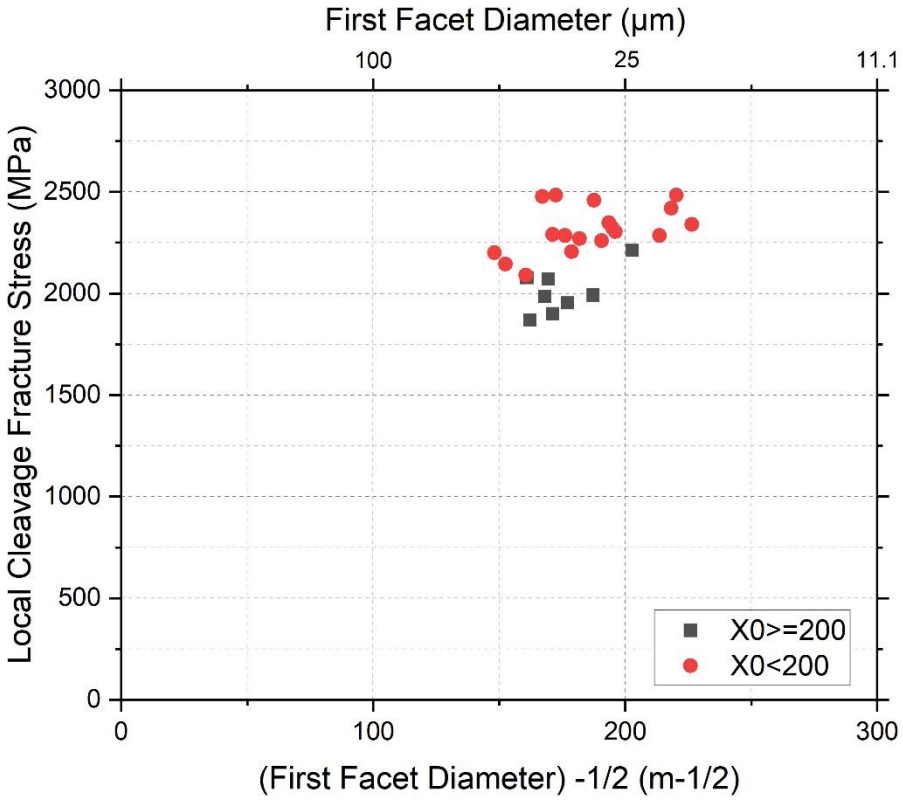


Figure 6-71. Local cleavage fracture stress $\sigma_F$ vs the reciprocal square root of the diameter of the initiating facet for sharp-cracked specimens under condition of n=0.1. Distinguish fracture distance of 200μm.

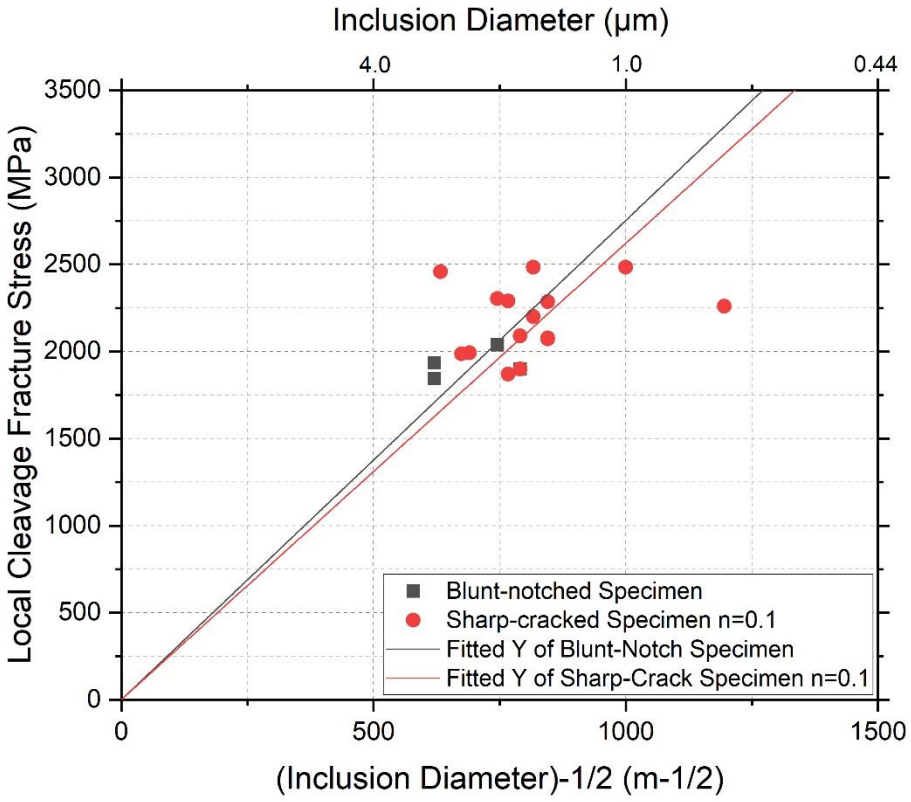


Figure 6-72. Local cleavage fracture stress $\sigma_F$ vs the reciprocal square root of the diameter of **cracked** inclusions for blunt-notched specimens and sharp-cracked specimens with n=0.1.

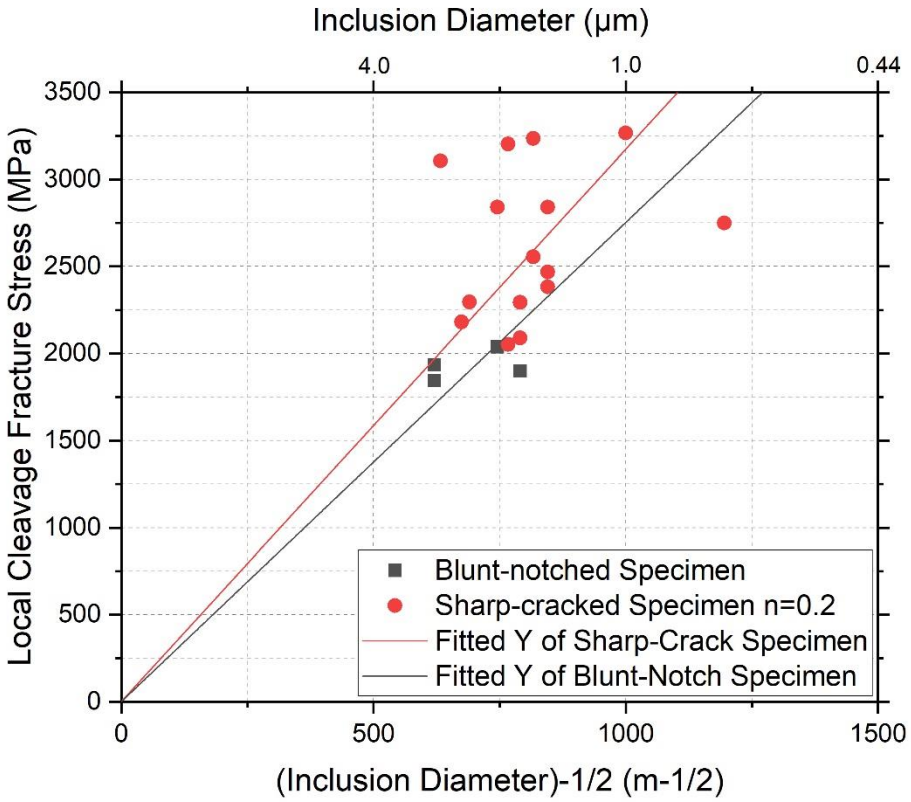


Figure 6-73. Local cleavage fracture stress $\sigma_F$ vs the reciprocal square root of the diameter of **cracked** inclusions for blunt-notched specimens and sharp-cracked specimens with n=0.2.